LYNX X-RAY OBSERVATORY

CONCEPT STUDY **REPORT**

X-RAY OBSERVATORY

LYNX

www.HIDDENCOSMOS.org

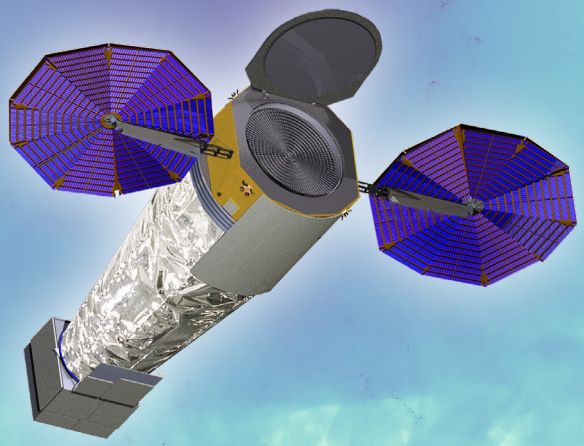

CONCEPT STUDY **REPORT**

SCIENCE & TECHNOLOGY DEFINITION TEAM COMMUNITY CO-CHAIRS

ALEXEY **VIKHLININ**
Center *for* Astrophysics | Harvard & Smithsonian

FERYAL **ÖZEL**
University *of* Arizona

NASA STUDY SCIENTIST

JESSICA **GASKIN**
NASA Marshall Space Flight Center

PRESENTED ON BEHALF *of* THE LYNX TEAM

THE X TEAM

SCIENCE & TECHNOLOGY DEFINITION TEAM (STDT)

co-chair	FERYAL **ÖZEL**	UNIVERSITY OF ARIZONA
co-chair	ALEXEY **VIKHLININ**	CENTER FOR ASTROPHYSICS | HARVARD & SMITHSONIAN
	STEVEN **ALLEN**	STANFORD UNIVERSITY
	MARK **BAUTZ**	MASSACHUSETTS INSTITUTE OF TECHNOLOGY
	W. NIEL **BRANDT**	THE PENNSYLVANIA STATE UNIVERSITY
	JOEL **BREGMAN**	UNIVERSITY OF MICHIGAN
	MEGAN **DONAHUE**	MICHIGAN STATE UNIVERSITY
	JESSICA **GASKIN**	NASA MARSHALL SPACE FLIGHT CENTER
	ZOLTAN **HAIMAN**	COLUMBIA UNIVERSITY
	RYAN **HICKOX**	DARTMOUTH COLLEGE
	TESLA **JELTEMA**	UNIVERSITY OF CALIFORNIA, SANTA CRUZ
	JUNA **KOLLMEIER**	CARNEGIE INSTITUTION FOR SCIENCE
	ANDREY **KRAVTSOV**	UNIVERSITY OF CHICAGO
	LAURA **LOPEZ**	THE OHIO STATE UNIVERSITY
	PIERO **MADAU**	UNIVERSITY OF CALIFORNIA, SANTA CRUZ
	RACHEL **OSTEN**	SPACE TELESCOPE SCIENCE INSTITUTE
	FRITS **PAERELS**	COLUMBIA UNIVERSITY
	DAVID **POOLEY**	TRINITY UNIVERSITY
	ANDREW **PTAK**	NASA GODDARD SPACE FLIGHT CENTER
	ELIOT **QUATAERT**	UNIVERSITY OF CALIFORNIA BERKELEY
	CHRISTOPHER **REYNOLDS**	UNIVERSITY OF MARYLAND / CAMBRIDGE
	DANIEL **STERN**	JET PROPULSION LABORATORY

EX-OFFICIO MEMBERS *of the* STDT

PCOS Representative	TERRI **BRANDT**	NASA GODDARD SPACE FLIGHT CENTER
Lynx Program Scientist	DANIEL **EVANS**	NASA HEADQUARTERS
COPAG Representative	SUVI **GEZARI**	UNIVERSITY OF MARYLAND
PCOS Representative	ANN **HORNSCHEMEIER**	NASA GODDARD SPACE FLIGHT CENTER
SRON Appointee	PETER **JONKER**	RADBOUND UNIVERSITY NIJMEGEN
COPAG Representative	JOSEPH **LAZIO**	JET PROPULSION LABORATORY
CSA Appointee	BRIAN **McNAMARA**	UNIVERSITY OF WATERLOO
DLR Appointee	KIRPAL **NANDRA**	MAX PLANCK INSTITUTE FOR EXTRATERRESTRIAL PHYSICS
ASI Appointee	GIOVANNI **PARESCHI**	INAF BRERA
ESA Appointee	ARVIND **PARMAR**	EUROPEAN SPACE AGENCY
NASA Athena Study Scientist	ROBERT **PETRE**	NASA GODDARD SPACE FLIGHT CENTER
CNES Appointee	GABRIEL **PRATT**	CEA SACLAY
U.S. Athena Representative	RANDALL **SMITH**	CENTER FOR ASTROPHYSICS | HARVARD & SMITHSONIAN
JAXA Appointee	MAKOTO **TASHIRO**	SAITAMA UNIVERSITY

INSTRUMENT WORKING GROUP LEADS

MARK **BAUTZ**
IWG CHAIR
Massachusetts Institute *of* Technology

ABRAHAM **FALCONE**
CO-CHAIR, HIGH DEFINITION IMAGERS
Pennsylvania State University

RALPH **KRAFT**
CO-CHAIR, HIGH-DEFINITION IMAGERS
Center *for* Astrophysics | Harvard & Smithsonian

SIMON **BANDLER**
CO-CHAIR, MICROCALORIMETERS
NASA Goddard Space Flight Center

MEGAN **ECKART**
CO-CHAIR, MICROCALORIMETERS
Lawrence Livermore National Laboratory

RALF **HEILMANN**
CO-CHAIR, GRATING SPECTROMETERS
Massachusetts Institute *of* Technology

RANDY **McENTAFFER**
CO-CHAIR, GRATING SPECTROMETERS
Pennsylvania State University

OPTICS WORKING GROUP, MIRROR TRADE STUDY, & MIRROR DESIGN LEADS

GARY **BLACKWOOD**
NASA Jet Propulsion Laboratory

LESTER **COHEN**
Center *for* Astrophysics | Harvard & Smithsonian

KIRANMAYEE **KILARU**
USRA / NASA Marshall Space Flight Center

GIOVANNI **PARESCHI**
INAF-Brera Astronomical Observatory

PAUL **REID**
Center *for* Astrophysics | Harvard & Smithsonian

MARK **SCHATTENBURG**
Massachusetts Institute *of* Technology

ERIC **SCHWARTZ**
Center *for* Astrophysics | Harvard & Smithsonian

PETER **SOLLY**
NASA Goddard Space Flight Center

WILLIAM **ZHANG**
NASA Goddard Space Flight Center

DEPUTY LYNX STUDY SCIENTIST

DOUGLAS **SWARTZ**
UNIVERSITIES SPACE RESEARCH ASSOCIATION / NASA MARSHALL SPACE FLIGHT CENTER

LYNX CONCEPT STUDY MANAGER

KAREN **GELMIS**
NASA MARSHALL SPACE FLIGHT CENTER

LYNX STUDY OFFICE

LESTER **COHEN**	CENTER FOR ASTROPHYSICS	HARVARD & SMITHSONIAN
ALEX **DOMINGUEZ**	NASA MARSHALL SPACE FLIGHT CENTER
MARK **FREEMAN**	CENTER FOR ASTROPHYSICS	HARVARD & SMITHSONIAN
JESSICA **GASKIN**	NASA MARSHALL SPACE FLIGHT CENTER
KAREN **GELMIS**	NASA MARSHALL SPACE FLIGHT CENTER
ROBBIE **HOLCOMBE**	NASA MARSHALL SPACE FLIGHT CENTER
SAMANTHA **JOHNSON**	NASA MARSHALL SPACE FLIGHT CENTER
VLADIMIR **KRADINOV**	CENTER FOR ASTROPHYSICS	HARVARD & SMITHSONIAN
KEVIN **McCARLEY**	NASA MARSHALL SPACE FLIGHT CENTER
DAN **SCHWARTZ**	CENTER FOR ASTROPHYSICS	HARVARD & SMITHSONIAN
ERIC **SCHWARTZ**	CENTER FOR ASTROPHYSICS	HARVARD & SMITHSONIAN
DOUG **SWARTZ**	NASA MARSHALL SPACE FLIGHT CENTER
HARVEY **TANANBAUM**	CENTER FOR ASTROPHYSICS	HARVARD & SMITHSONIAN
GRANT **TREMBLAY**	CENTER FOR ASTROPHYSICS	HARVARD & SMITHSONIAN
ALEXEY **VIKHLININ**	CENTER FOR ASTROPHYSICS	HARVARD & SMITHSONIAN
MARTIN **WEISSKOPF**	NASA MARSHALL SPACE FLIGHT CENTER
JOHN **ZuHONE**	CENTER FOR ASTROPHYSICS	HARVARD & SMITHSONIAN

The Lynx Study Office is jointly operated by

Marshall Space Flight Center

CENTER FOR ASTROPHYSICS
HARVARD & SMITHSONIAN

Additional contributors are listed at the back of this Report.

The Lynx Team is large and growing. We curate an up-to-date list of members at
WWW.LYNXOBSERVATORY.ORG / TEAM

Contents

X

EXECUTIVE SUMMARY

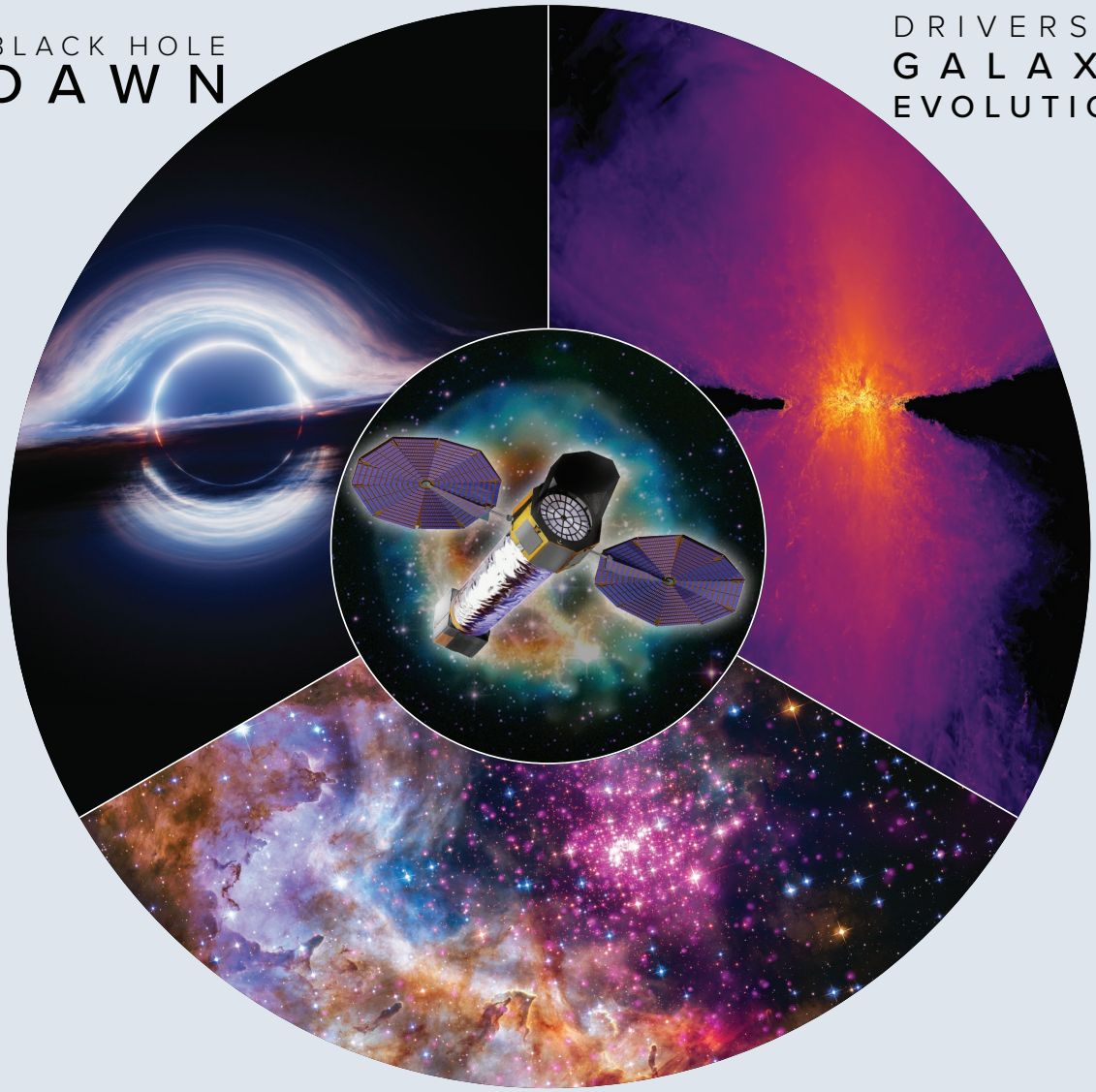

the ENERGETIC SIDE *of*
STELLAR EVOLUTION

Lynx is a revolutionary X-ray observatory with the power to transform our understanding of the cosmos through unprecedented X-ray vision into the otherwise invisible Universe. It is designed to pursue three fundamental science pillars: 1) seeing the dawn of black holes, 2) revealing what drives galaxy formation and evolution, and 3) unveiling the energetic side of stellar evolution and stellar ecosystems. For its spacecraft design and operational concept, *Lynx* leverages the overarching, proven architecture from *Chandra*. The *Lynx* payload provides extraordinary advances in science capabilities thanks to an extremely powerful combination of sub-arcsecond angular resolution and high throughput of its X-ray mirror, and the transformational spectroscopic capabilities of its science instruments. Strong heritage and substantial maturity in key new technologies lead to a credible cost for this Great Observatory-class mission.

A NEW GREAT OBSERVATORY

X-RAY OBSERVATIONS are indispensable for understanding the cosmos. Their power is immense because much of the baryonic matter and the sites for the most active energy releases in the Universe are primarily observable in X-rays. For the 2030s and beyond, an X-ray observatory with power matching the capabilities in other wavebands is a necessary discovery engine for full exploration of the Universe.

JWST and other upcoming major space- and ground-based facilities are expected to greatly expand science frontiers in the coming decades. This presents both a great opportunity and a challenge for a next-generation X-ray observatory. In many areas, such as tracing black holes during the Cosmic Dawn and understanding the formation and evolution of galaxies, an X-ray observatory is the logical next step. The challenge is that the X-ray science at these new frontiers requires expansion of capabilities by orders of magnitude beyond the current state of the art or anything already planned.

Until recently, such gains were not technologically possible. This has changed thanks to recent breakthroughs and sustained maturation of key technologies for X-ray mirrors and detectors. We are reaping the fruits of U.S. investments in these areas over the past 10–15 years. An X-ray observatory that can extend the science frontiers of the post-*JWST* era is now entirely feasible. *Lynx* is the mission concept that realizes this vision. It will fly revolutionary optics and instrumentation onboard a simple, proven spacecraft. In all aspects, *Lynx* will be a next-generation Great Observatory that is certain to make a profound impact across the astrophysical landscape. It will provide the depth and breadth to answer the fundamental questions that confront us today; just as importantly, it will have capabilities to address questions we have yet to even ask.

Lynx is poised to make a particularly strong impact in the following three areas, which serve as its science pillars and are used to define core performance requirements:

- **The Dawn of Black Holes,**
- **The Invisible Drivers of Galaxy Formation and Evolution,**
- **The Energetic Side of Stellar Evolution and Stellar Ecosystems.**

The capabilities required by these *Lynx* science pillars can be implemented within a proven mission architecture derived from *Chandra*. *Lynx* will have a baseline lifetime of 5 years and be provisioned for 20 years of operation. Operation beyond 20 years is possible with the implementation of in-space servicing and/or the redirection before launch of unused mass margins to accommodate additional station-keeping fuel. *Lynx* easily meets the mass and volume constraints of existing and expected heavy-class launch vehicles. If needed, its 10-m optical bench can be designed with an extension mechanism to reduce length in stowed configuration, further increasing flexibility with respect to future launch options.

Lynx Science Pillars

The Dawn of Black Holes — We now realize that black holes define many aspects of cosmic evolution, and that massive black holes were in place very early in the history of the Universe. Understanding their formation and rapid early growth is one of the most important unsolved problems in astrophysics. *Lynx* will be able to detect the first massive black holes in the first generations of galaxies. The first galaxies will be found and characterized in deep optical and infrared surveys that

the DAWN *of* BLACK HOLES

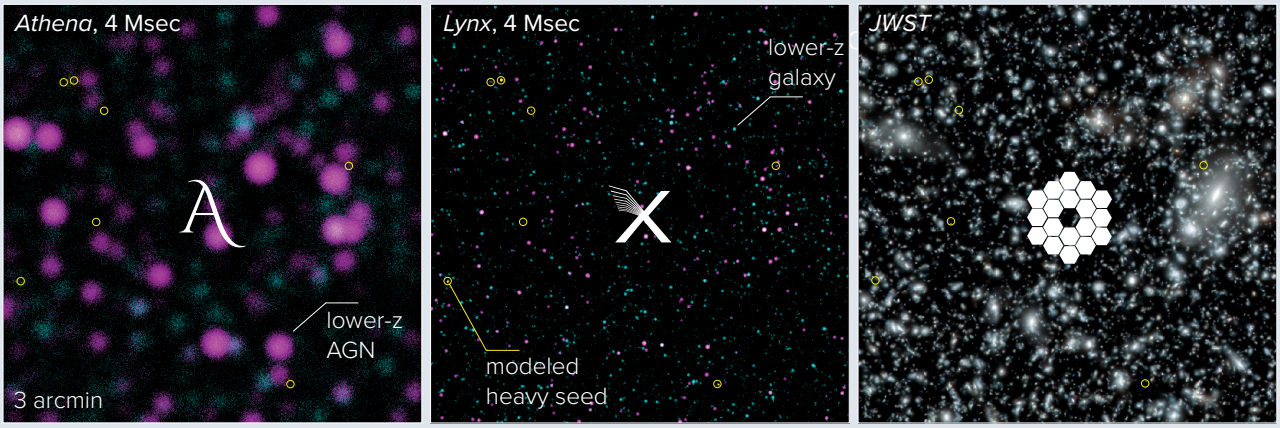

KEY CAPABILITIES

The key observations are deep surveys over ~ 1 deg^2 with flux limit ~ 10^{-19} erg s^{-1} cm^{-2} to detect black hole seeds with M_{BH} = 10,000 $M_\odot$ at z = 10. This requires:

- On-axis PSF ~ 0.5″ (HPD), and sub-arcsecond imaging within 10′ radius FOV to avoid source confusion.
- A_{eff} = 2 m^2 at E = 1 keV to enable completion of deep surveys within one year.

Lynx will provide a sensitivity in X-rays to detect accreting black holes with mass M_{BH} ~ 10^4 $M_\odot$ at z = 10. These observations will open an electromagnetic window into the Dawn of Black Holes. *Lynx*, using X-rays, and *LISA*, using gravitational waves, together will probe the growth of the first black holes by both accretion and mergers, unveiling a complete picture of their early assembly.

Angular resolution is critical for detecting high-z black hole seeds. The panels above show simulated 3′ × 3′ regions in deep surveys by *JWST*, *Lynx*, and *Athena* (a future ESA X-ray observatory with 5″ angular resolution). Unlike *Athena*, *Lynx* will not be affected by "source confusion," and can uniquely associate every X-ray source with a *JWST*-detected galaxy. In the X-ray images, color codes different source populations. In each panel, yellow circles show the locations of high-z black hole seeds (see Fig. 1.3 on p. 21 for more information on how seed models can be tested with *Lynx*). Their fluxes are a factor of ~ 100 below the confusion limit for a 5″ X-ray telescope.

can be obtained with either the almost ready to launch *JWST* or the subsequent *WFIRST* missions. The X-ray flux limits required to detect the first massive black holes are accessible only with *Lynx*.

The Invisible Drivers of Galaxy Formation and Evolution — Unprecedentedly detailed information is now available on the stellar, dust, and cold gas content of galaxies, and yet there is a dearth of understanding of the exact mechanisms of their formation. *Lynx* will expose essential drivers of galaxy evolution which primarily leave imprints in the circumgalactic medium (CGM) extending well beyond the optical size of galaxies and containing most of their baryons. Most of the halo gas in galaxies more massive than the Milky Way is heated above UV ionization states to X-ray temperatures. The energetic processes that define its state are the same ones that regulate growth and create the diversity of galaxy morphologies. While modern UV, optical, and sub-mm observations can map cold and warm gas, these observations are equivalent to seeing only the smoke and sparks in a fire. For a true understanding of the lives of galaxies, we need *Lynx* to see the flame itself.

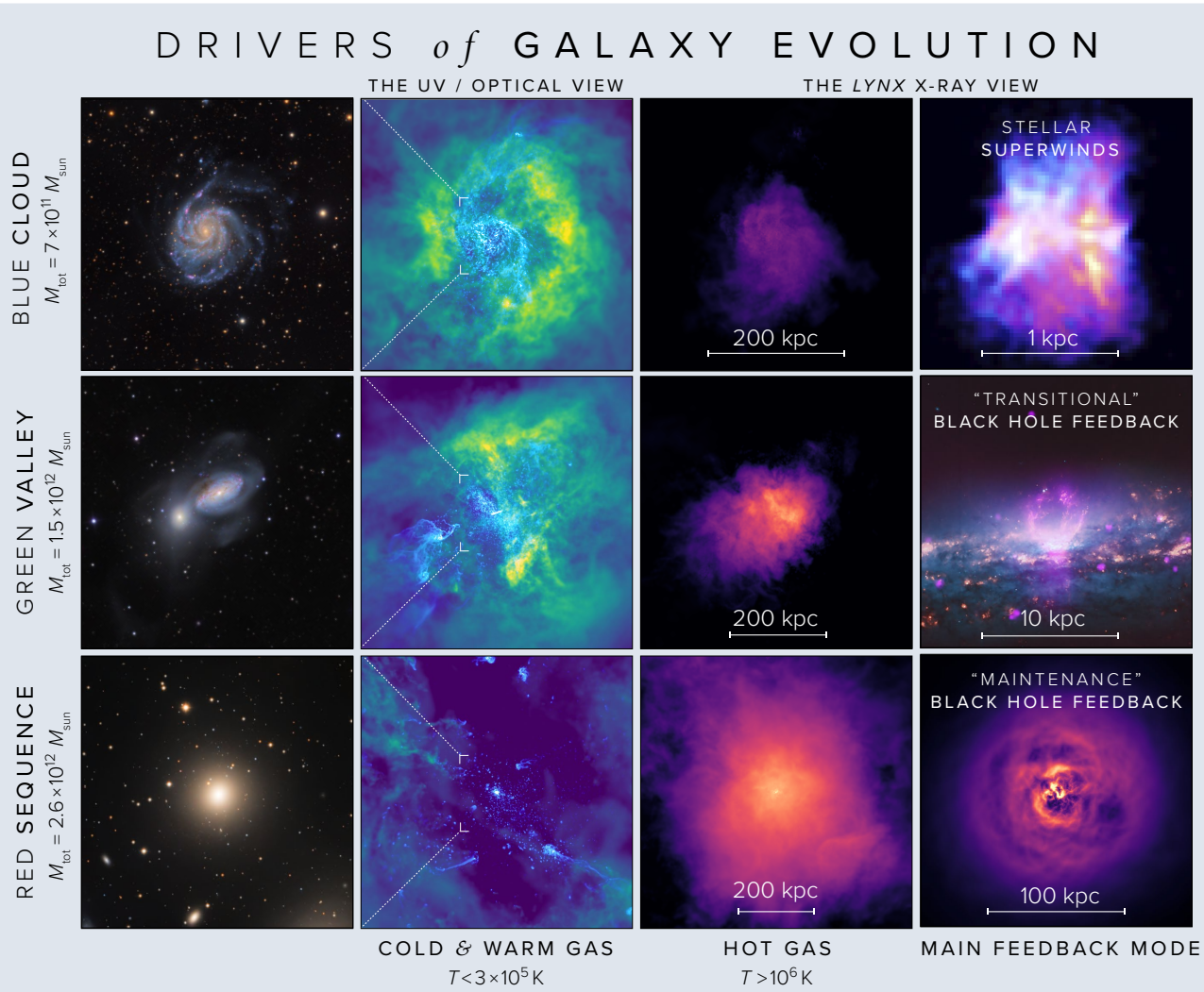

KEY CAPABILITIES

- Map CGM in emission to $0.5r_{200}$: PSF < 1″, A_{eff} = 2 m^2.
- Probe CGM in absorption at ~ r_{200}: gratings with A_{eff} = 4,000 cm^2 and $\lambda/\Delta\lambda$ > 5,000.
- Map velocities in ~ 100 km s^{-1} galactic outflows: microcalorimeter with $E/\Delta E$ = 2,000 at E = 0.6 keV.
- Study AGN feedback in galaxies and clusters: microcalorimeter with 0.5″ pixels.

The sensitivity and spectroscopic capabilities of *Lynx* will enable mapping of the hot galactic halos to ~ 0.5 – 1 virial radii in both emission and absorption. The inner structure of the halos ($\lesssim 0.1r_{vir}$) is where all primary signatures of ongoing feedback are imprinted. The capabilities of the *Lynx* microcalorimeter will be essential for exposing these signatures. It will simultaneously provide 1″ spatial resolution and R = 2,000 resolving power at all key energies required, e.g., to map the kinematic and chemical structure of galactic winds *(right)*.

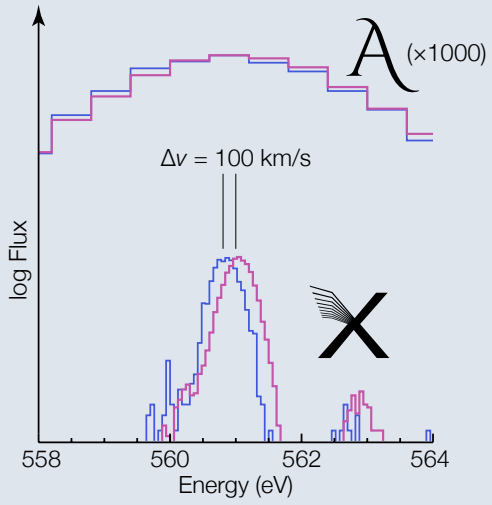

the ENERGETIC SIDE *of* STELLAR EVOLUTION

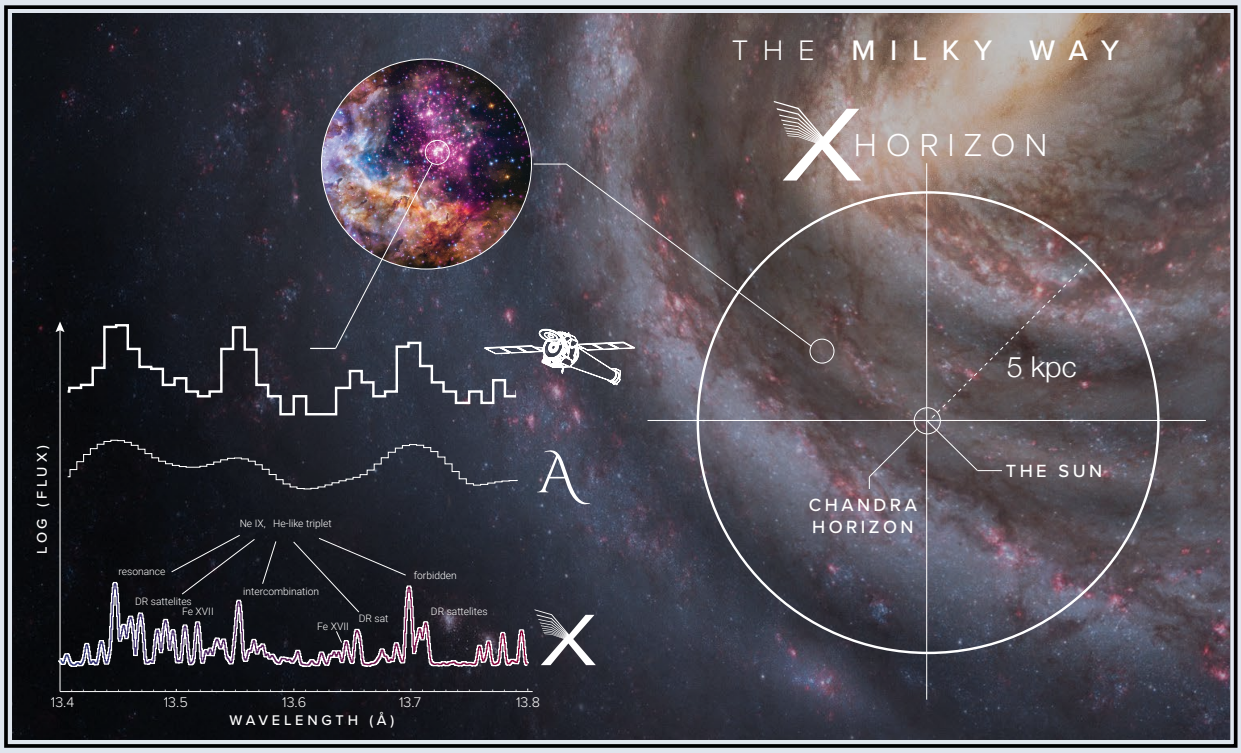

KEY CAPABILITIES

- Spatially resolve star cluster cores: PSF ≈ 0.5″.
- Resolve lines in stellar spectra: gratings with $R > 5{,}000$.
- Map 3D structure of supernova remnants: microcalorimeter with $\Delta E = 3$ eV and 1″ pixels.

Lynx will provide unique new capabilities for studying stellar birth, life, and death. Its sensitivity will be sufficient for detecting low-mass young stellar objects to 5 kpc. It will enable vastly more powerful spectral diagnostics for studies of stellar accretion and coronae. Microcalorimeter observations will fully resolve the 3D structure of supernova remnants in the Milky Way and nearby galaxies.

The Energetic Side of Stellar Evolution and Stellar Ecosystems — As we enter the era of multimessenger astronomy following LIGO detections of gravitational waves, and as studies of exoplanets evolve toward holistic assessment of habitable conditions, orders-of-magnitude expansion in capabilities will be needed to observe key high-energy processes associated with stellar birth, life, and death. *Lynx* will meet this challenge and dramatically extend our X-ray grasp throughout the Milky Way and nearby galaxies. The horizon for detecting X-rays as markers of young stars and for detailed stellar spectroscopy will be extended by an order of magnitude. Spatially resolved spectroscopy on arcsecond scales will offer a three-dimensional view of metals synthesized in stellar explosions, and will enable population studies of supernova remnants in the Local Group galaxies. Sensitive observations of X-ray binaries beyond the Local Group galaxies and detailed follow-up of gravitational wave events will transform our knowledge of collapsed stars. *Lynx* will make all these studies possible by combining, for the first time, the required sensitivity, spectral resolution, and sharp vision to see clearly in crowded fields.

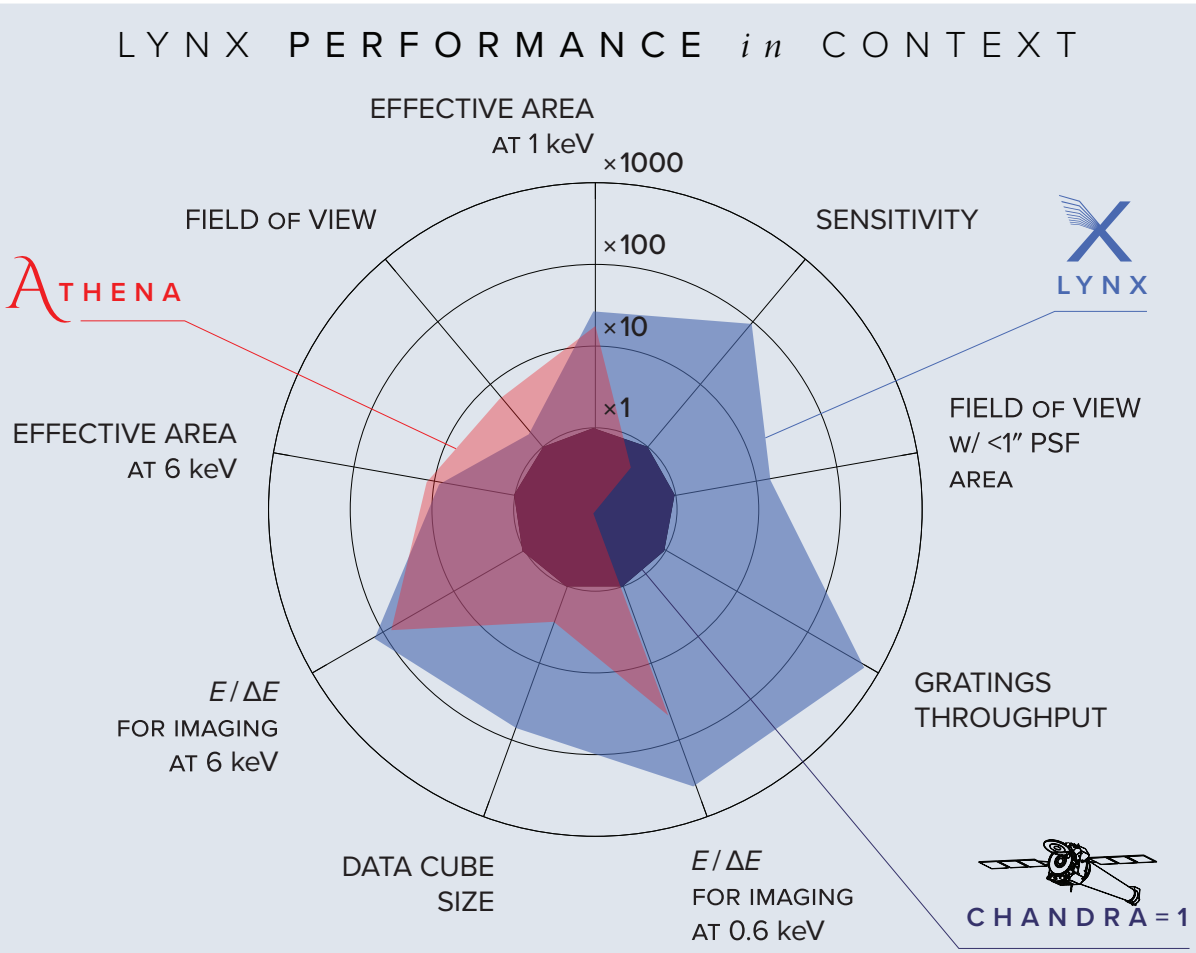

The requirements established by the *Lynx* science pillars translate into the need for orders-of-magnitude performance gains along a number of key axes. The diagram above shows how these gains compare with the performance of *Chandra* (taken to be 1 on all axes) and *Athena* (shown in red). *Athena*, ESA's planned mission, will carry the first large X-ray microcalorimeter and make strides in energy resolution, effective area (especially at high energies), and field of view. It will not, however, make breakthrough gains across the board: not in sensitivity; not in sharp imaging; not in very high spectral resolution. *Lynx* makes primary breakthroughs along these axes, which are precisely the directions required by its science goals. *Lynx* and *Athena* can be viewed as orthogonal missions with different science goals and based on different strengths. *Athena*'s science centers on massive, wide surveys and detailed spectroscopy of relatively bright and isolated objects. With a combination of its high angular resolution, high throughput, and powerful spectroscopic capabilities, *Lynx* opens up the discovery space in the high redshift universe, crowded fields, feedback on galactic scales, and circumgalactic environments.

Mission Design

Lynx will operate as an X-ray observatory with a grazing incidence telescope and detectors that record the position, energy, and arrival time of individual X-ray photons. Post-facto aspect reconstruction leads to modest requirements on pointing precision and stability, while enabling very accurate sky locations for detected photons. The design of the *Lynx* spacecraft is straightforward, with few moving

PAYLOAD & MISSION CHARACTERISTICS

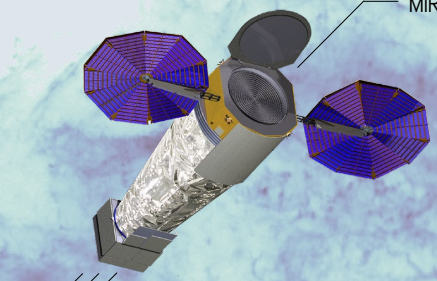

LYNX MIRROR ASSEMBLY

0.5'' on-axis PSF, 2m² effective area at 1 keV, sub-arcsecond PSF over a 22'×22' field of view.

HIGH DEFINITION X-RAY IMAGER

An active pixel array of fine pixels covering a 22'×22' field of view with subarcsecond imaging and providing moderate spectral resolution.

LYNX X-RAY MICROCALORIMETER

An array of 1'' pixels covering a 5'×5' field of view and providing 3 eV spectral resolution. Two additional arrays are optimized for finer imaging (0.5'' pixels) and higher spectral resolution (0.3 eV in the soft band).

X-RAY GRATING SPECTROMETER

Gratings with resolving power of $R > 5{,}000$ and ~ 4,000 cm² of effective area across the critical X-ray emission and absorption lines of N, O, Ne, and Fe L.

THE MISSION

- Orbit: Sun-Earth L2
- Field of regard: 85% of the sky
- Consumables: sized for a 20 year mission
- Data volume: JWST comparable
- Communications: 3 times daily with DSN
- Observing Efficiency: >85%

The *Lynx* spacecraft is built around the X-ray mirror assembly that is followed by a large-area insertable grating array. The science instrument module is attached to the spacecraft by an optical bench. It includes the interchangable prime focus detectors, HDXI and LXM, and the off-center XGS readout array at a fixed location. All risk and new development for *Lynx* is isolated to its optics and science instruments. The spacecraft requires no new inventions and, indeed, can use many existing solutions, including those developed for *Chandra* and other past missions.

parts; all of its elements can be procured today. *Lynx* will operate in a halo orbit around Sun-Earth L2, enabling high observing efficiency in a stable environment. Its maneuvers and operational procedures on-orbit are nearly identical to *Chandra*'s, and similar design approaches promote longevity.

The transformational scientific power of *Lynx* is entirely enabled by its payload — the mirror assembly and a suite of three highly capable science instruments. Each of the payload elements features state-of-the-art technologies, but at the same time represents a natural evolution of an existing instrument or technology, with each already having years of funded technology development. Key technologies are currently at Technology Readiness Levels (TRL) 3 or 4. With three years of targeted pre-phase A development in early 2020s, three of four key technologies will be matured to TRL 5 and one will reach TRL 4 by start of Phase A, achieving TRL 5 shortly thereafter.

The Lynx Mirror Assembly (LMA) — The LMA is the central element of the observatory. It is responsible for leaps in sensitivity, spectroscopic throughput, survey speed, and better imaging than *Chandra* because of much-improved off-axis performance. The LMA can be based on three fully feasible mirror technologies: Silicon Metashell Optics (SMO) developed at NASA's Goddard Space

EYES, SHARP *as a* LYNX

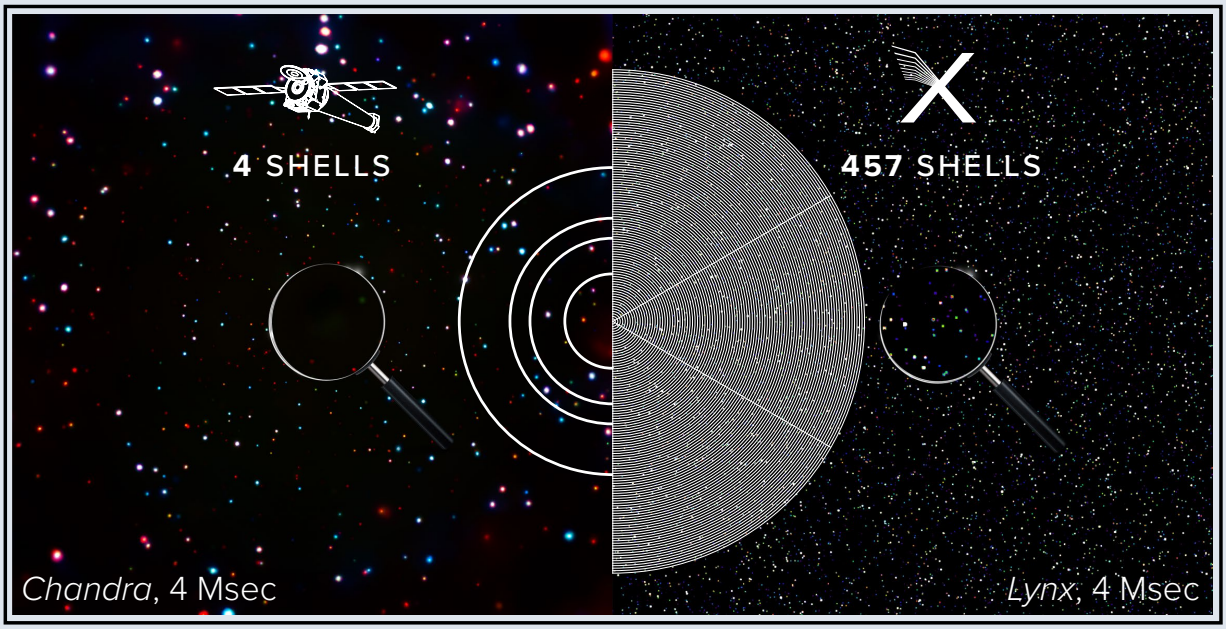

0.5″ PSF on-axis, sub-arcsecond across a 22′ × 22′ FOV

50× *Chandra*'s throughput in soft X-rays

1,000× *Chandra*'s survey speed

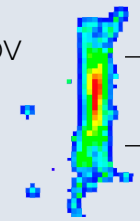

2019 MIRROR PAIR TEST

1.3″ (HPD) at 4.5 keV, dominated by gravity distortions

The *Lynx* Mirror Assembly (LMA) keeps *Chandra*'s sub-arcsecond resolution on-axis while providing orders-of-magnitude gains in throughput and FOV size for sub-arcsecond imaging. The LMA is composed of concentric modular metashells, and each module is populated with multiple mirror pair segments. The repeatable production of mirror segments with a surface quality meeting or exceeding required specifications was recently verified (February 2019). A full-illumination X-ray test of an aligned mirror pair on a flight-like mount has produced a 1.3″ image, for which approximately 1″ is attributed to 1-g gravity distortion in the test configuration. Subtraction of well-modeled gravity distortions indicates sub-arcsecond performance for the tested mirror pair in zero-gravity.

Flight Center (GSFC), Full Shell Optics developed jointly by MSFC and the Italian National Institute for Astrophysics, and Adjustable Segmented Optics developed at the Smithsonian Astrophysical Observatory (SAO) and Penn State. The SMO technology was selected for the design reference mission (DRM) following a comprehensive technology assessment trade study, which evaluated the ability of each approach to meet *Lynx* science requirements, the credibility of technology development plans, and the validity of schedule, cost, and risk estimates. The SMO technology is currently the most advanced in terms of demonstrated performance (already approaching what is required for *Lynx*, see figure above). The SMO's highly modular design lends itself to parallelized manufacturing and assembly, while also providing high fault tolerance: if some individual mirror segments or even modules are damaged, the impact to schedule and cost is minimal.

the HIGH-DEFINITION X-RAY IMAGER (HDXI)

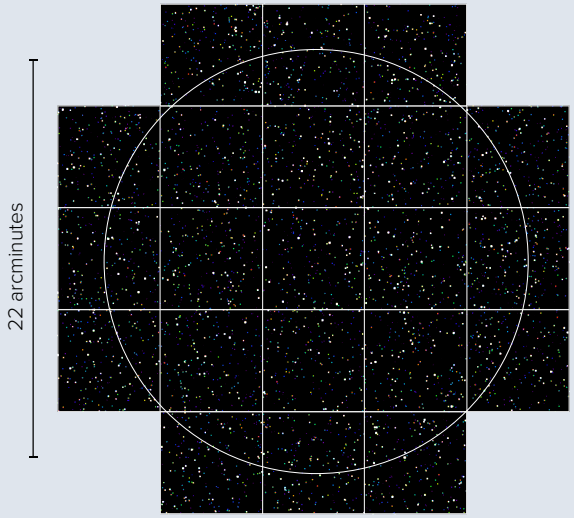

0.3" Pixel size well-matched to telescope PSF.
Large, curved focal plane (22' × 22').

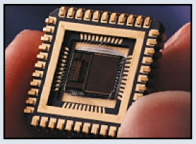

Monolithic CMOS (Sarnoff / SAO & MPE)

High gain (135 μV / e^-), low noise (3 e^- rms) amplifiers.

PMOS devices ready for X-ray testing with < 1 e^- read noise and no RTS noise.

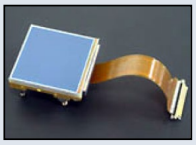

Hybrid CMOS (Teledyne & PSU)

Achieves ~ 80 eV (FWHM) energy resolution at 0.5 keV, in-pixel CDS, no crosstalk. Event-driven readout achieved. Latest scaled-up designs include on-chip digitization.

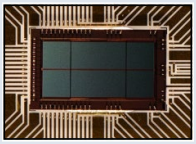

Digital CCD with CMOS Readout
(MIT / Lincoln Lab)

Reduced noise (4.6 e^-). Low-power CMOS clock. Larger (2 Mpix) device in fabrication.

The High-Definition X-ray Imager (HDXI) — The HDXI instrument is the main imager for *Lynx*, providing high spatial resolution over a wide FOV and good sensitivity over the 0.2–10 keV bandpass. Its 0.3″ pixels will adequately sample the *Lynx* mirror PSF over a 22′ × 22′ FOV. The 21 individual sensors are laid out along the optimal focal surface to improve the off-axis PSF. The *Lynx* DRM uses Complementary Metal Oxide Semiconductor (CMOS) Active Pixel Sensor (APS) technology, which is projected to have the required capabilities (i.e., high readout rates, high broad-band quantum efficiency, sufficient energy resolution, minimal pixel crosstalk, and radiation hardness). The *Lynx* team has identified three options with comparable TRL ratings (TRL 3) and sound TRL advancement roadmaps: the Monolithic CMOS, Hybrid CMOS, and Digital CCDs with CMOS readout. All are currently funded for technology development.

The Lynx X-ray Microcalorimeter (LXM) — The LXM is an imaging spectrometer that provides high resolving power (R ~ 2,000) in both the hard and soft X-ray bands, combined with high spatial resolution (down to 0.5″ scales). To meet the diverse range of *Lynx* science requirements, the LXM focal plane includes three arrays that share the same readout technology. Each array is differentiated by its absorber pixel size and thickness, and by how the absorbers are connected to thermal readouts. The total number of pixels exceeds 100,000 — a major leap over past and currently planned X-ray microcalorimeters. This huge improvement does not entail a huge added cost: two of the LXM arrays feature a simple, already proven, "thermal" multiplexing approach where multiple absorbers are connected to a single temperature sensor. This design brings the number of sensors to read out (one of the main power and cost drivers for the X-ray microcalorimeters) to ~ 7,600. This is only a modest increase over what is planned for the X-IFU instrument on *Athena*. As of Spring 2019, prototypes of the focal plane have been made that include all three arrays at 2/3 full size. These prototypes demonstrate that arrays with the pixel form factor, size, and wiring density required by *Lynx* are readily achievable, with high yield. The energy resolution requirements of the different pixel types

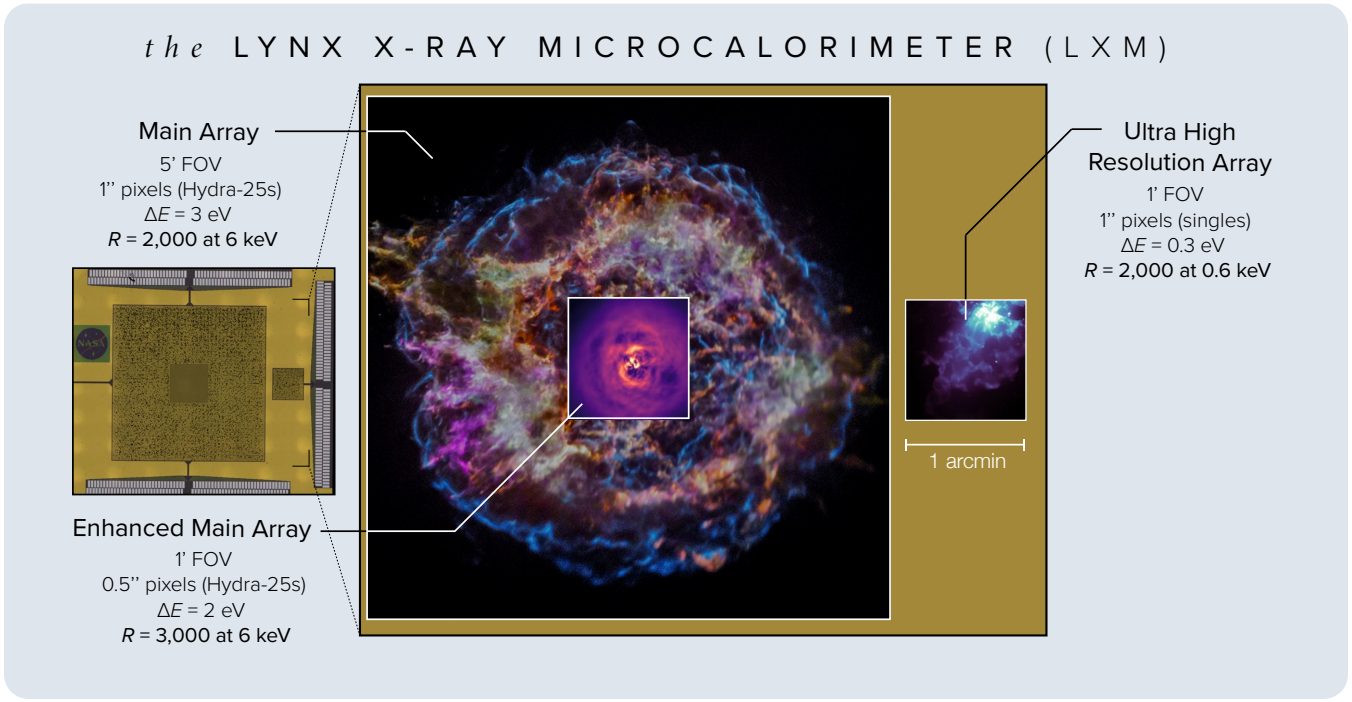

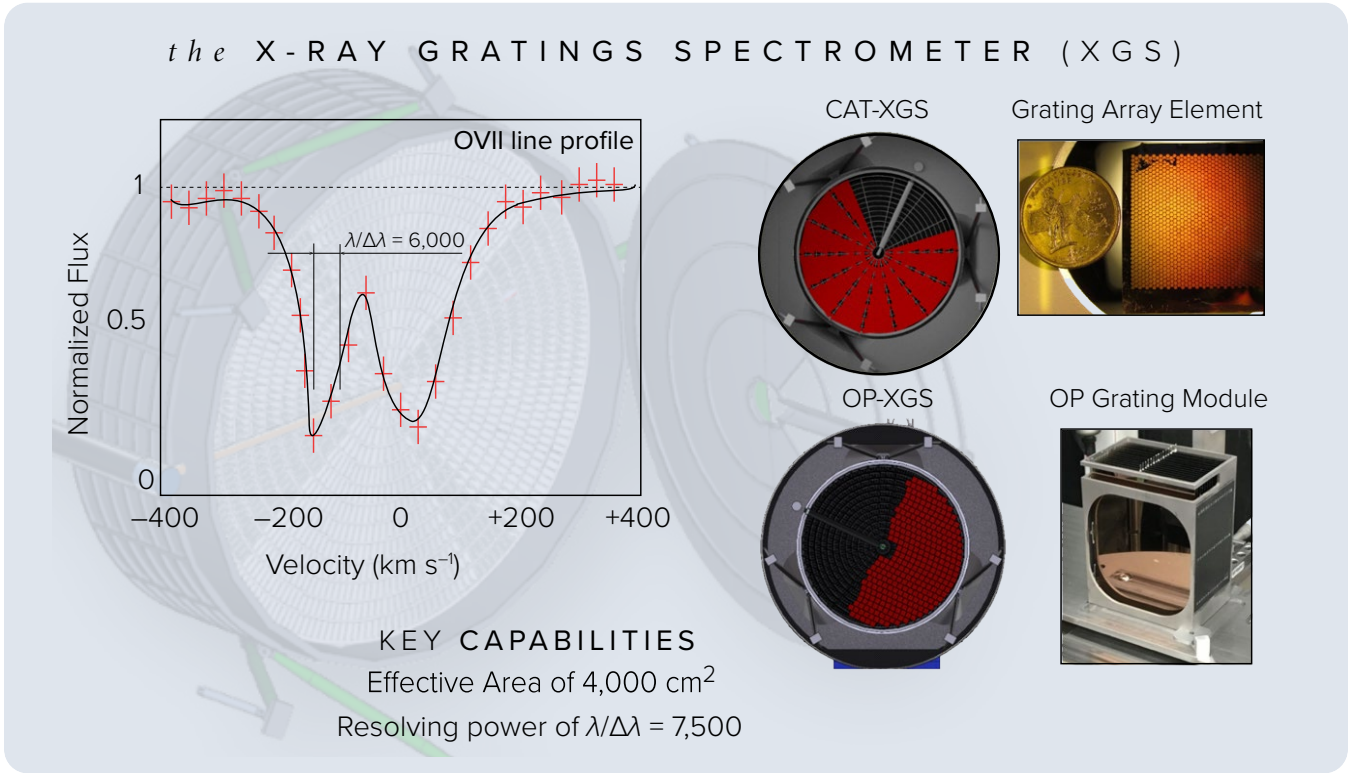

is also readily achievable. Although the LXM is technically still at TRL 3, there is a clear path for achieving TRL 4 by 2020 and TRL 5 by 2024.

The X-ray Grating Spectrometer (XGS) — The XGS will provide even higher spectral resolution (R = 5,000 with a goal of 7,500) in the soft X-ray band for point sources. Compared to the current state of the art (*Chandra*), the XGS provides a factor of > 5 higher spectral resolution and a factor of several

hundred higher throughput. These gains are enabled by recent advances in X-ray grating technologies. Two strong technology candidates are: critical angle transmission (used for the *Lynx* DRM) and off-plane reflection gratings. Both are fully feasible, currently at TRL 4, and have demonstrated high efficiencies and resolving powers of ~ 10,000 in recent X-ray tests.

Mission operations — The *Chandra* experience provides the blueprint for developing the systems required to operate *Lynx*, leading to a significant cost reduction relative to starting from scratch. This starts with a single prime contractor for the science and operations center, staffed by a seamless, integrated team of scientists, engineers, and programmers. Many of the system designs, procedures, processes, and algorithms developed for *Chandra* will be directly applicable for *Lynx*, although all will be recast in a software/hardware environment appropriate for the 2030s and beyond.

General Observer approach to Lynx science program — The science impact of *Lynx* will be maximized by subjecting *all* of its proposed observations to peer review, including those related to the three science pillars. Time pre-allocation can be considered only for a small number of multi-purpose key programs, such as surveys in pre-selected regions of the sky. Such an open General Observer (GO) program approach has been successfully employed by large missions such as *Hubble*, *Chandra*, and *Spitzer*, and is planned for *JWST* and *WFIRST*. The *Lynx* GO program will have ample exposure time to achieve the objectives of its science pillars, make impacts across the astrophysical landscape, open new directions of inquiry, and produce as yet unimagined discoveries.

Cost and Mission Schedule

The *Lynx* team has conducted extensive parametric cost analyses for all aspects of mission cost, with detailed analyses focused on the spacecraft (broken down to the subsystem level), X-ray optics, each of the science instruments, and mission operations. The analysis utilized the industry-standard PCEC Cost Model, the SEER® hardware model, and the PRICE® TruePlanning® Space Missions and PRICE®-H Hardware models. The resulting costs estimated by these models are consistent and, where comparison is possible, in family with the actuals from past NASA missions. The parametric cost, which serves as the primary estimate, has been validated in multiple ways: an end-to-end grassroots estimate based on a mix of analogies and expert input, an MSFC non-advocate independent cost estimate, and an independent cost and technical evaluation. Finally, the *Lynx* team carried out a thorough mission-level comparison to escalated *Chandra* actuals.

The parametric model and validation methods provide point estimates, which are consistent within ±5%. Confidence levels (CL) are available from the parametric modeling, the MSFC non-advocate independent cost estimate, and the independent cost and technical evaluation. All of these methods give consistent costs at $\lesssim$ 50% CL. For example, at 40% CL, the costs are in the range from \$4.8B to \$4.9B (in FY20\$). This consistency reflects a well-developed mission design with a strong heritage and lessons learned from past and planned missions. There is a larger divergence for higher confidence levels. For example, for a 70% CL, the spread is from \$5.1B to \$6.2B. This naturally reflects uncertainties appropriate for this relatively early stage of the mission design. Overall, consistency is excellent and gives credibility to the estimated *Lynx* mission cost. Note that the quoted costs cover the entire mission lifecycle, from start through 5 years of operations. They include reserves and a conservative passthrough from the NASA Launch Service Providers for a heavy-class launch vehicle. The operations cost is ~ \$400M total, including projected funding of ~ \$100M (FY20\$) for grants.

Even with the huge gains in capability provided by *Lynx*, its costs will only modestly exceed the inflated *Chandra* actuals. This is substantiated by the following considerations: *Lynx* technology development and the mission study have directly benefited from a science community and a contractor base with extensive and applicable experience working on *Chandra* and other recent X-ray missions. Even though personnel and contractors will change, an exceptionally solid mission concept and cost basis for *Lynx* are already in place, given the engagement of this experienced team. Observatory-wide error budgets for mass, power, thermal, and end-to-end performance demonstrate that the requirements are well understood and achievable. The spacecraft and two of the *Lynx* instruments (HDXI and XGS) are modest evolutions of the *Chandra* equivalents and do not require breakthroughs or new inventions. The third instrument, the LXM, is quickly gaining technology maturity from laboratory efforts and from other X-ray missions (*Hitomi*, *XRISM*, *Athena*). Mission operations are particularly well understood, with plans, requirements, algorithms, and cost estimates derived from the *Chandra* experience. The ability to produce a *Lynx* mirror at a cost similar to *Chandra* can be tracked to tangible technological breakthroughs, along with an LMA design amenable to mass production. The status already achieved in key technology areas adds credibility to the development plans to reach TRL 6 for the LMA and the science instruments over the next several years. Taken together, these factors explain the relatively small differences between the *Lynx* costs and inflated *Chandra* actuals.

Mission lifecycle schedule — The *Lynx* team has developed a notional mission schedule that includes all required milestones and key decision points. Given their architecture similarities, the *Lynx* schedule for the system-level assembly, integration, and test closely matches that of *Chandra*, after accounting for its larger size and additional complexities. It is also consistent with the *WFIRST* in-guide schedule to a 2025 launch. The *Lynx* schedule includes ≈ 3 years of pre-Phase A studies, during which time key technologies will be maturated to the levels required to enter Phase A. The funding needed is comparable to that provided for *WFIRST* at the same stage. Durations for Phases A&B and C&D are 42 and 103 months, respectively. Assuming this sequence starts soon after the Astro2020 Decadal Survey makes its recommendation, *Lynx* will launch in 2036.

Contents of this Report

- **The Science of *Lynx*** is discussed in §1–§5. This includes a discussion of the three *Lynx* science pillars and the impact of *Lynx* in many other areas of astrophysics, the Science Traceability Matrix, and a notional plan of observations required to execute the pillar science.
- **Design Reference Mission** is presented in §6 and provides a discussion of the overall rationale for the observatory design, detailed account of the spacecraft and payload elements, system-level error budget, system-level analyses and predicted on-orbit performance, discussion of the launch options, and a concept for mission operations.
- **Technologies.** Review of the current state of the art and near-terms plans is presented in §7. Further information is provided in the special section on *Lynx* of the *Journal of Astronomical Telescopes, Instruments, and Systems* [1]. Detailed roadmaps for further maturation of key technologies are available in the supplemental materials and online.
- **Programmatics.** The discussion of programmatics, including the mission lifecycle schedule, cost, risks and mitigations, is provided in §8. The costing methodology and high-level cost range is presented in §8.5. A detailed cost book is available in the supplemental materials.

- **Observatory Configuration Trade Space.** Sections 9 and 10 provide a comparison of science capability and costs for a representative range of possible mission configurations. The analysis demonstrates that the *Lynx* DRM concept optimizes the "science per dollar" metric.

The Impact of *Lynx* Across the Future Astrophysical Landscape

Lynx will profoundly impact many areas of astrophysics. Obviously, it will play a critical role in the topics directly related to its science pillars, such as studies of the Cosmic Dawn, Black Holes, Galaxy Formation, and Origin of Elements. *Lynx* will also make a major impact in other areas, such as Cosmology, Resolved Stellar Populations, Solar System Observations, and Multi-Messenger Astronomy. Its influence will be seen even in less obvious areas, such as studies of the cold interstellar medium, planets, and protoplanetary disks. This wide impact is a result of gains in sensitivity and spectroscopic capabilities of historical magnitude, equivalent to opening a new wavelength band or introducing a new observational technique.

The *Lynx* imaging component provides a factor of 50× higher throughput, 20× the FOV with sub-arcsecond imaging, and a factor of 1,000× greater speed for surveys compared to the current state of the art (*Chandra*). To put this in context, these improvements are bigger than the tremendous gain in survey power from *Hubble* to the future NASA flagship observatory, *WFIRST*. In terms of sensitivity, *Lynx* will detect sources 100× fainter than those seen in the deepest *Chandra* surveys.

Astronomy is undergoing revolutionary changes, driven in large part by movement toward hyper-dimensional datasets. Fully spatially resolved spectroscopic data cubes provided by instruments such as MUSE on ESO's Very Large Telescope (VLT) enable advancements which rival the leap from the first astro-photograph to state-of-the-art imaging from *Hubble*. There is an equivalent development in the X-rays, from *Einstein* to *Chandra* and onwards to *Lynx*. The X-ray microcalorimeter on *Lynx* will provide an X-ray capability comparable to what MUSE provides in the optical, and what the MIRI and NIRspec instruments on *JWST* will provide in the infrared. To put the relative gains in context, the leap from *Chandra* to *Lynx* is the same as going from a 1-m telescope with a CCD imager to an 8-m VLT equipped with a MUSE spectrograph.

Current cutting-edge and major future astronomical facilities — the Extremely Large Telescopes on the ground, *JWST*, *WFIRST*, Advanced LIGO, *LISA*, ALMA, SKA — all make great leaps in sensitivity, and aim at taking exquisite data in their respective wavebands. To be synergistic with these facilities, a future X-ray observatory must aim in the same direction, and this requires the combined firepower of high angular resolution, high throughput, and spectroscopy. This is precisely what *Lynx* will deliver.


the SCIENCE of LYNX

Overview and Motivation

As we survey the past decade of developments in astrophysics to formulate the open questions ahead of us, a few topics jump out that ultimately motivate the development of a next-generation X-ray observatory:

- Very massive, $\sim 10^9\,M_\odot$, black holes are being discovered at ever higher redshifts, currently reaching $z \approx 7.5$. The birth and early evolution of such supermassive black holes are a remarkable, yet poorly understood phenomenon, with strong impacts on the evolution of the first galaxies. The James Webb Space Telescope (*JWST*) will soon dramatically uncover the process of galaxy assembly and star formation in the early universe. After *JWST*, the next logical step in studies of the Cosmic Dawn will be to observe the nearly coeval Dawn of Black Holes.
- The stellar content of galaxies is now extremely well characterized via large-scale projects such as the Sloan Digital Sky Survey (SDSS) and the crowd-sourced Galaxy Zoo. In a few years, the Vera Rubin Telescope (formerly LSST) and Wide-Field Infrared Survey Telescope (*WFIRST*) will provide sensitive optical and near-infrared data for galaxy samples extending to high redshifts. Numerical simulations are making great strides toward reproducing realistic galaxies from the cosmological initial conditions, but have to make unconstrained and wildly varying assumptions about powerful energy feedback. Direct observations of the ongoing feedback and its effect on gas in the galactic halos is the missing ingredient for completing the picture of galaxy formation and evolution.
- The onset of multimessenger astronomy following Laser Interferometer Gravitational-Wave Observatory (LIGO) detections of gravitational wave events from neutron stars and black hole mergers renews the emphasis on the endpoints of stellar evolution, particularly neutron stars and black holes in binary systems. Using all available tools to study compact object properties and following up gravitational wave detections are of crucial importance in this era.
- Exoplanet studies rapidly evolve toward statistical characterization of the planet populations and holistic assessment of habitable conditions. The activity of the host star can significantly deplete planetary atmospheres, and at the same time may be required for primitive biochemistry. Studying the effects of stellar activity on habitability are especially important for planets around dwarf stars, the very population whose atmospheres will be accessible for studies in the 2020s with large, ground-based optical telescopes and *JWST*.

These developments serve as a guide for formulating the critical science questions to be addressed in the following decades: How and when do the first black holes in the Universe light up? How do they grow and interact with galaxies? How do feedback processes shape galaxies? What are the properties of the gas that reside outside of galaxies? How do stellar-mass black holes and neutron stars form? What are the evolutionary paths that lead to LIGO sources? What are the mechanisms of activity of young stars and what is the impact of stellar activity on the habitability of their planets?

The best, and often the only, way to address these questions is via observations with a sensitive, high angular resolution X-ray telescope. This leads to the three pillars of *Lynx* science: 1) *The Dawn of Black Holes*, 2) *The Invisible Drivers of Galaxy Formation and Evolution*, and 3) *The Energetic Side of Stellar Evolution and Stellar Ecosystems*. These science pillars require revolutionary capability advances that enable *Lynx* to make impact across the astrophysical landscape of the 2030s and maximize the scientific return from *JWST*, *WFIRST*, and other major future observatories.

1 *The* Dawn *of* Black Holes

Massive black holes, with $M_{\rm BH} = 10^6 - 10^{10}\,M_\odot$, are ubiquitous in the nuclei of galaxies in the local Universe, but their ultimate origin remains one of the most intriguing and longest-standing unsolved puzzles in astrophysics. Observations over the past two decades have revealed that massive black holes are common by the time the Universe is several Gyr old, and many were in place very quickly, within the first Gyr after the Big Bang. Their quick assembly has been attributed to a range of "seeding" mechanisms such as the rapid collapse of gas into the nuclei of early protogalaxies, accretion and mergers of stellar-mass black holes in early cosmic structures, and the runaway collapse of early, ultra-dense stellar clusters. However, the relative importance of these seeding processes, and thus the origin of massive black holes, remains unclear.

- *Lynx* is designed to provide definitive tests for discerning between black hole seeding models using *electromagnetic* observations. The most direct answers will be obtained through detection of black holes with masses of $\lesssim 10^5\,M_\odot$ at the redshifts $z \gtrsim 10$ where we expect them to form. Reaching these high redshifts and low masses is crucial because black holes are expected to "lose" the memory of their initial assembly by the time they grow well above $\sim 10^5\,M_\odot$ and are incorporated into higher-mass galaxies.

  The best way to study a population of $10^{4-5}\,M_\odot$ black holes at high redshifts is by a sensitive X-ray survey. Black holes are most readily observed when they grow by accretion, and X-ray emission is a direct tracer of the rate of black hole growth that can be detected above the light from their host galaxies. The properties and environments of black hole host galaxies provide additional important constraints on seeding models, and can be obtained with deep optical and IR (OIR) imaging using the planned *JWST* and *WFIRST* missions. The X-ray emission from $10^{4-5}\,M_\odot$ black holes at cosmic dawn will be extremely faint (as low as $\sim 10^{-19}$ erg s^{-1} cm^{-2}) and thus accessible only with a next-generation X-ray observatory which has both high angular resolution ($\lesssim 1''$) and high throughput — *Lynx*.

  Deep X-ray surveys, augmented by the OIR surveys, will be capable of probing several of the most characteristic markers of the black hole seed scenarios. They will thus resolve the long-standing puzzle of the origin of massive black holes. These electromagnetic observations will also be highly synergistic with *LISA* detections of high-z black hole mergers through gravitational waves [2]
- To understand the origin of massive black holes, it is essential to trace their evolution beyond the seed stage and through the epoch of maximal black hole and galaxy growth at $z \sim 1$–2. The exquisite sensitivity and angular resolution of *Lynx* will enable a complete census of black hole masses, growth rates, and their host galaxies from $z = 2$ to 6 and higher. These observations will show whether all massive black holes emerge at high redshifts ($z > 6$), or whether some low-mass "seeds" begin significant growth phases only at lower redshifts. *Lynx* AGN surveys will elucidate not only black hole origins, but also the role of black hole feedback in the early evolution of galaxies.
- Fast-forwarding to the present epoch, *Lynx* can probe the origin of massive black holes using cosmic archaeology in the local Universe. All viable paths to producing supermassive black holes require a stage with their masses in the range $10^{2-5}\,M_\odot$, and a certain fraction of black holes and their hosts are expected not to grow much thereafter. Therefore, the population of intermediate-mass

black holes in *dwarf* galaxies can retain residual memory of the predominant seeding mechanism even into the present epoch [3–6]. Sensitive, high-resolution X-ray observations with *Lynx* can detect these black holes [4], joining next-generation radio [6] or stellar-dynamics studies [5].

1.1 An Electromagnetic Window into the Dawn of Black Holes

1.1.1 Demographics of massive black holes, theories of their origin, main questions

The local population of massive black holes in galaxies is now well studied down to masses of $\sim 10^6\,M_\odot$ [7]. Black holes with $M = 10^{6-10}\,M_\odot$ are commonly found in the nuclei of big galaxies, and are believed to be the remnants of high-z quasars that underwent rapid growth in brief (10^{7-8} years), bright episodes of accretion at $z \sim 2$–3 [8–10]. However, the physical mechanism through which SMBHs acquired the first $\sim 10^6\,M_\odot$ of their mass remains a mystery [11, 12]. At least some SMBHs with $M = 10^{8-9}\,M_\odot$ are in place as early as redshift $z = 7.5$ [13–18], only $\lesssim 700$ Myr after the Big Bang. Several distinct physical mechanisms to form high-redshift $\sim 10^5 M_\odot$ SMBHs are under consideration [11]. These include models for *"light seeds,"* namely

- sustained Eddington-rate accretion onto an initially stellar-mass black hole,

and several models for *"heavy seeds"* that can all produce a much more massive ($10^{4-5}\,M_\odot$) seed black hole within < 1 Myr. These include:

- direct collapse of a gas cloud into a black hole seed without fragmentation or star formation.
- rapid gas collapse into a black seed via an intermediary stage of a supermassive star.
- rapid gas collapse onto a pre-existing stellar-mass black hole at super- or hyper-Eddington rates.
- runaway collapse and merger of an ultra-dense stellar cluster.

Note also that there may be a continuum between the light and heavy-seed scenarios [20]. Understanding which of these mechanisms are responsible for the first SMBHs at $z > 6$ is one of the most important unsolved problems in astrophysics [12, 19, 21–26].

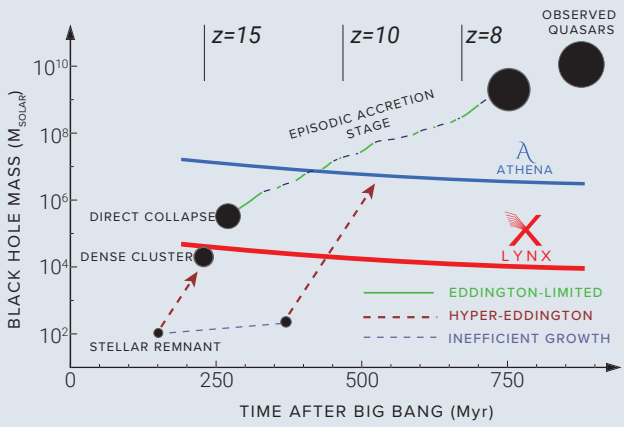

Fig. 1.1— Schematic of main classes of SMBH formation models (adapted from Smith, Bromm, & Loeb [19]).

The light-seed scenario is the simplest possibility because one does expect an abundance of 10–100 $M_\odot$ black holes formed as remnants of massive and short-lived Population III stars as early as $z \sim 30$ [27]. However, this scenario is challenging [28] on several grounds. It requires sustained accretion near the Eddington rate from $z \sim 30$ through $z \sim 6$. Population III stars are born in small "mini-halos," in which the gas fuel for a future black hole is easily unbound by feedback [29–32]. Gravitational radiation recoil during black hole mergers can easily eject them from low-mass host halos [33] and thus stunt further growth. Because of challenges with the light-seed scenario, channels involving heavy seeds for some or all of the first black holes are also attractive.

All heavy-seed scenarios share a common feature: they take place in "atomic cooling halos" (ACHs) at $z \gtrsim 10$–12, in which gas cools efficiently via line emission (e.g., Lyα) of atomic hydrogen. Such halos exist in a narrow range of virial temperatures $T_{\rm vir} \approx 8{,}000$ K, corresponding to $M_{\rm vir}$ = few $\times 10^7\, M_\odot$ at $z = 10$. Analytic arguments and numerical models show that rapidly cooling self-gravitating gas collapses into ACHs at rates as high as $\dot{M} \approx 1 M_\odot\,{\rm yr}^{-1}$ ($\approx c_{\rm s}^3/G$ where the sound speed $c_{\rm s} \approx 10\,{\rm km\,s}^{-1}$ for $T = 8{,}000$ K). This inflow can feed formation of a massive black hole seed, but the necessary condition is that the gas is prevented from fragmenting into normal stars [34–36], which is challenging. This can be achieved in a small subset of ACHs by exposing them to extremely intense Lyman-Werner radiation [37–40] from a bright neighbor [41–43], and/or by intense heating from an unusually violent merger history [44–46], aided by the streaming motions between gas and dark matter [47–49]. When these conditions are met, the ACHs can quickly (within a few Myr) produce black holes with masses as high as $10^{4-5}\, M_\odot$.

Note that *none* of the heavy seed formation channels are expected to promptly yield black holes with masses well above the $10^{4-5}\, M_\odot$ range. For direct collapse, the total gas supply in the $M_{\rm tot}$ = few $\times 10^7\, M_\odot$ ACH is limited [50]. The collapse of a supermassive star into a black hole is initiated by general relativistic instability at $\approx 10^5 M_\odot$ [51–54]. Hyper-Eddington accretion onto a lower-mass black hole ceases once a similar mass is reached [55–57]. Finally, an ultra-dense nuclear stellar cluster in the core of the ACH cannot contain more than $10^5\, M_\odot$ of stellar material [58, 59].

1.1.2 Observational diagnostics of black hole seeds

Electromagnetic tracers of black holes at high redshift focus on detecting actively accreting black holes (AGN). X-rays are the best tracer for multiple reasons: The X-ray emission is ubiquitous. It is relatively insensitive to obscuration, especially at the high rest-frame energies probed at high redshift. There is a large contrast between the AGN light and galactic starlight in the X-ray band, so the two are not easily confused. Combined with multiwavelength and gravitational wave probes, X-ray observations provide a set of powerful diagnostics of the black hole seed scenarios:

- *AGN luminosity functions at very high redshift ($z \gtrsim 10$)*, expected to show a sharp drop at high L (or $M_{\rm BH}$) in the light-seed case [60] and different shapes of the faint end for different formation channels [61, 62]. The constraining power of the luminosity functions derives from the fact that the AGN luminosities reflect the black hole masses via the Eddington limit.
- *Characteristic optical and IR spectral signatures for ongoing heavy seed formation events* in the dense cores of ACHs [63, 64], due to unusually heavy obscuration expected in these objects.
- *Event rates, mass, and spin distributions of mergers* detectable by *LISA* [60, 65–70].

The key aim for *Lynx* on the Dawn of Black Holes is determining the relative importance of heavy and light-seeding processes, which will dramatically expand our knowledge for the ultimate origin of massive black holes. Confirmation that any early black holes formed through a heavy-seed channel would be especially interesting, as rapid formation of a massive black hole via any of these mechanisms would be among the most spectacular events in the history of the Universe.

- *Properties of black hole host galaxies.* As discussed above, in all heavy-seed scenarios, the initial SMBH with $M = 10^{4-5} M_\odot$ is born in a few $\times\, 10^7 M_\odot$ halo whose total gas content is few $\times\, 10^6 M_\odot$. In the light-seed models, similar $10^{4-5} M_\odot$ SMBHs are assembled by numerous mergers and slower accretion, and thus are located inside much more massive hosts by $z = 10$ [71].
- *Cross-correlation of the redshifted 21-cm background with the residual X-ray background* [72].
- *Fossil evidence* from the local population of intermediate-mass black holes [4–6].

Each of these probes provides independent constraints, but also includes large theoretical uncertainties and degeneracies. Particularly challenging are predictions for "mixed" models, in which early black holes form through both heavy and light-seed channels. Therefore, it is best to use a combination of techniques and rely on the most characteristic markers of different seeding scenarios.

Catching the formation or early evolution of a heavy seed while it stays in the original host can yield an exceptionally clean test ([73–76] and Fig. 1.2). This phase is hard to catch, but there are still expected differences at both the faint and bright ends of the luminosity function [61, 62, 70, 71, 77–79] and very distinct differences in the number densities and properties of the host galaxy. The host galaxies of heavy seeds remain strong outliers for $\gtrsim 100$ Myr after the black hole birth, with BH-to-stellar mass ratio of order unity. This contrasts sharply with the light-seed scenario, in which $M_{\rm BH}/M_\star$ is of order 10^{-3}, consistent with the local black hole vs. galaxy mass relation [76].

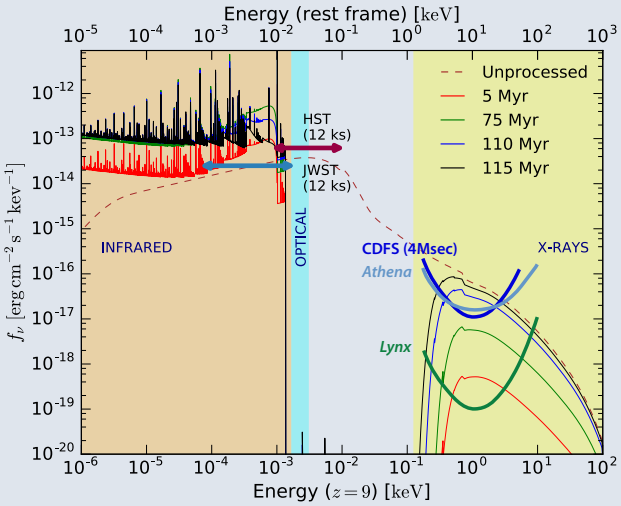

Fig. 1.2— Spectral predictions for a heavy-seeded black hole shortly after the initial collapse (adapted from [73]).

A key requirement for any observational test of seed models is to **detect black holes with mass ~ $10^5 M_\odot$ or below at $z > 10$**, because the memory of initial assembly is lost after the black holes grow well above their initial seed mass. In particular, the heavy seed hosts become incorporated into massive, metal-enriched galaxies, similar to those hosting the SMBHs that had grown from light seeds. The special conditions for the black hole growth which existed in the ACH are destroyed, and rapid star formation is enabled. The subsequent growth of the black hole and its host galaxy quickly makes their properties indistinguishable from those expected in the light-seed scenarios.

1.1.3 The *Lynx* experiment to probe the nature of SMBH seeds

Four of the six observational diagnostics of the black hole seed models discussed above can be implemented via a combination of a sensitive X-ray survey which identifies high-z black holes accreting at or near the Eddington rate and associates them with their host galaxies through multiwavelength observations (Fig. 1.3). Such as survey should have the following components:

- The sensitivity in the X-rays must enable detection of $M_{\rm BH} \approx 10^4\, M_\odot$ black holes accreting near Eddington at $z = 10$. This corresponds to $f_x \approx 10^{-19}$ erg s^{-1} cm^{-2}. At this sensitivity, a significant

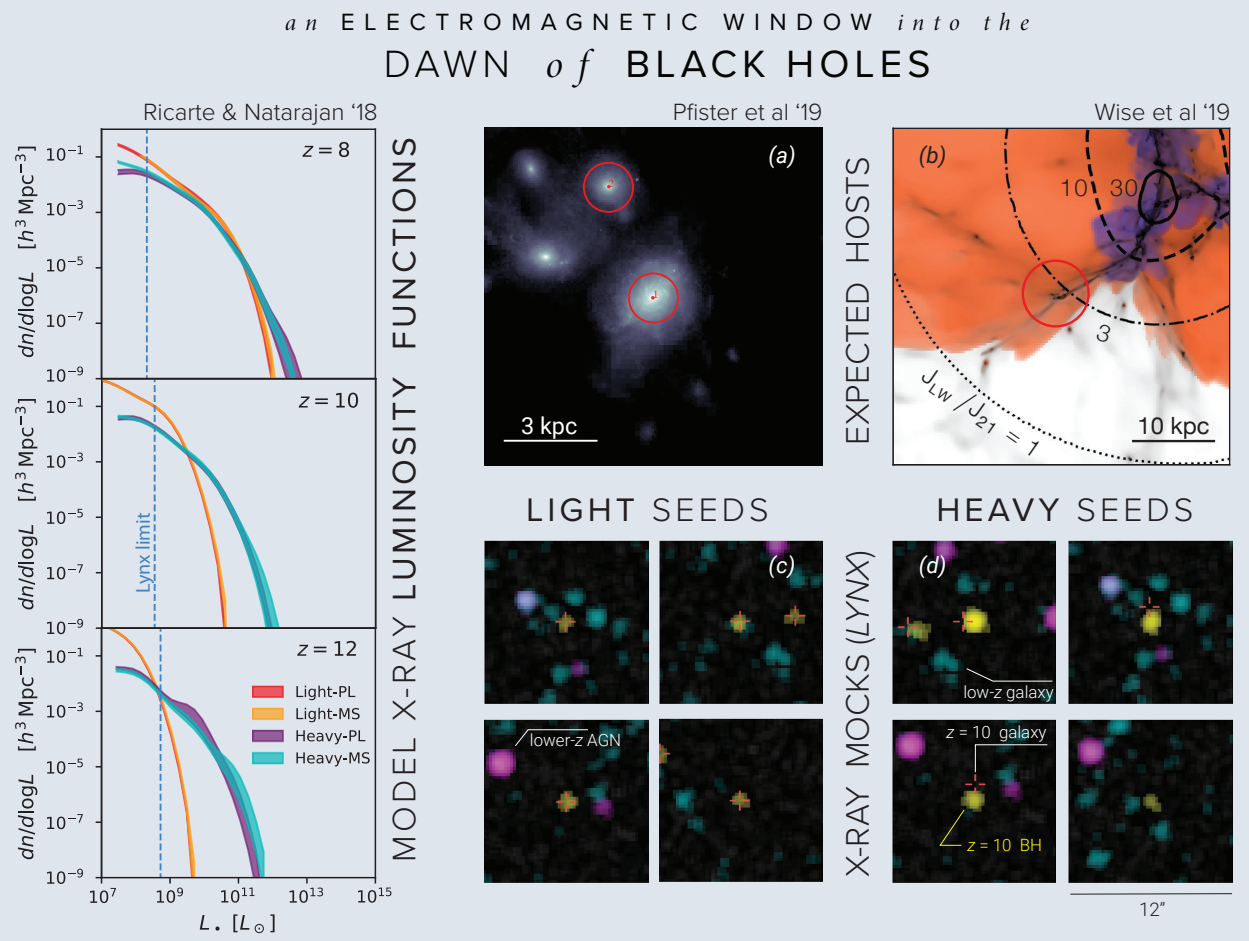

Fig. 1.3— X-ray surveys with *Lynx* will reach into the early Universe at $z = 10$ and above, close to the formation epoch of the first massive black holes. One expects distinct observable differences between light- and heavy-seeded models in the distribution of black hole masses (and hence, luminosities) and in the properties of their host galaxies probed by OIR observations. *Left:* model X-ray luminosity functions (adapted from [60], hereafter RN18b). There are large differences at $z \geq 10$ for high L_X, which disappear by $z = 8$ when black holes "lose" memory of their initial assembly. *Top panels:* Locations of the black holes in their immediate galactic environment when they reach $M_{\rm BH} \sim 10^5\,M_\odot$ (*red circles*). *(a)* Light-seeded black holes are within massive, $M_{\rm tot} \approx 10^{10} M_\odot$, galaxies detectable in the IR with *JWST* or *WFIRST*. *(b)* Newly born heavy-seeded black holes are in low-mass atomic-cooling halos located near (tens of kpc) strong sources of Lyman-Werner radiation such as groups of galaxies [46]. The initial host is undetectable in the IR, except perhaps by stacking on a large number of X-ray locations. *Lower panels:* 12″ cutouts around four brightest $z = 10$ black holes in a $3' \times 3'$ region in a 4 Msec *Lynx* exposure. The X-ray mocks start with the Illustris TNG light cone simulation [80], which provides NIR magnitudes, star formation rates (= L_X from X-ray binaries [81]), and SMBH accretion rates for $z < 8$ galaxies. Black holes at $z = 10$ are added using the RN18b model. *(c)* In the light-seeds case, X-ray detections (*yellow*) are co-located with OIR-detectable galaxies (locations marked by *red crosses*). *(d)* In the heavy-seeds case, one expects fewer but brighter X-ray detections. By the time these black holes are caught in a survey, they typically have grown, but are still within small, $M_{\rm tot} \approx 10^8 M_\odot$ and faint, $M_\star \approx 4 \times 10^5 M_\odot$, galaxies which are often about to merge with a larger galaxy 5–10 kpc away [76]. The host remains undetectable (lower-right panel), but the larger nearby galaxy can be seen as an OIR counterpart noticeably offset ($\sim 1''$) from the X-ray position (other three panels). The Galactic or low-redshift origin of the X-ray source in this case can be ruled out by X-ray spectral hardness ratios and *JWST* magnitude limits.

number of detections are expected in all models [60, 70] at redshifts $z \gtrsim 10$ where large differences in the luminosity function are generally expected [60]. At somewhat lower redshifts ($z \approx 8-9$), such a survey provides good sampling of the faint end of the luminosity function, which also is a constraint on seed models [61, 62]. X-ray positions must be determined to a fraction of 1″ for identification with host galaxies.

- To probe the expected differences in the host galaxy properties, the sensitivity in the OIR survey in the same region should be sufficient to identify counterparts of detected X-ray sources at least down to the galaxy mass limits expected in the light-seed case. In the heavy-seed case, where neither the host galaxies, nor the recently born $\sim 10^5\,M_\odot$ seed black holes are expected to be detectable even with *JWST*, it will be possible to isolate the corresponding population as (brighter) X-ray point sources with no OIR counterparts (see Figure 1.3). Furthermore, it will be possible to test the offsets between black holes and their bright galactic neighbors, anticipated in the close vicinity (up to tens of kpc or a few arcseconds) of faint hosts of heavy seeds [41, 46, 82].
- There is a reasonable chance of catching ongoing direct collapse events in such a survey (Fig. 1.2, [73]). In this case, spectral signatures may be detectable (including a strong Lyα line [75]).
- Finally, *Lynx* surveys are an excellent dataset for cross-correlations of weak unresolved X-ray emission from high-z black holes with atomic gas detected in future 21-cm surveys ([72], §4.3).

Capability requirements — The basic requirements for such a program include the following:

- *An X-ray sensitivity sufficient to detect* $10^4\,M_\odot$ *black holes at* $z = 10$. For reasonable assumptions about underlying X-ray spectral shapes, expected levels of obscuration, and spectral energy distributions, the required observed-frame 0.5–2 keV fluxes (corresponding to penetrating rest-frame $\approx$ 5–20 keV X-rays) are $\approx 10^{-19}$ erg cm^{-2} s^{-1}. These fluxes are just above those expected for X-ray binary populations in high-z galaxies ([61], Appendix A.2). In heavy-seed scenarios there is likely a population of X-ray sources without a co-located OIR counterpart. Their reliable identification requires extremely high sample purity which is typically achieved at flux levels $\approx$ a few $\times$ the nominal detection threshold (Appendix A.3 and Fig. A.5). The proposed survey limits will therefore easily probe $10^5\,M_\odot$ black holes expected in the heavy-seed scenarios.
- *Sufficient angular resolution to protect against X-ray source confusion by the large numbers of foreground galaxies.* Current estimates (e.g., [61, 81]) forecast a sky density for such sources of (120–450)$\times 10^3$ deg^{-2} at the relevant X-ray flux levels. Avoiding source confusion in this regime requires a $\lesssim 1''$ (50% power diameter) point spread function (Appendix A.1). A coarser PSF quickly destroys the ability to detect X-ray sources at the required fluxes. Sub-arcsecond angular resolution is also essential for matching the positions of X-ray detections with potential host galaxies.
- *Sufficiently large solid angle to conservatively probe an expected range of black hole occupation fractions.* At $z \approx 10$, the space density of potential hosts of heavy seeds ($M_{\rm halo}$ = few $\times\, 10^7 M_\odot$) is $\approx 1\,{\rm Mpc}^{-3}$. More massive hosts of light-seeded $10^{4-5}\,M_\odot$ black holes ($M_{\rm halo} \sim 10^{10} M_\odot$) have a number density of $\approx 10^{-3}\,{\rm Mpc}^{-3}$. To provide a sufficient cushion to model uncertainties, a reasonable target is a 1 deg^2 survey that covers a volume of 6.5×10^6 Mpc^3 per $\Delta z = 1$ around $z = 10$. It will be sensitive to source densities of $\sim 10\,{\rm deg}^{-2}$, corresponding to occupation factors of actively accreting black holes of $f = f_{\rm occ} \times f_{\rm duty} \approx 10^{-6}$ and 10^{-3} for the heavy- and light-seed models, respectively. These factors are 2 orders of magnitude below the upper end of the range predicted in several studies (e.g.,

[46, 49, 60, 71, 82, 83]), $f_{\rm heavy} \approx 10^{-4}$ and $f_{\rm light} \approx 10^{-1}$, resulting in ~ 1,000 sources per deg^2. Ideally, the survey should be conducted across 3–5 distinct fields that are widely separated in the sky to minimize the effects of cosmic variance (e.g., [84, 85]). Some optimizations will be possible with a "wedding cake" survey strategy depending on the precise mission parameters.

- *Sensitivity in the OIR to characterize host galaxies, or lack thereof.* As discussed above, the OIR survey must reach sensitivities sufficient for detecting at least the light-seed hosts at $z = 10$, and reliably determining their photo-z. These hosts galaxies are expected to be faint, with near-infrared magnitudes of ≈ 28.5–29.5. Such magnitudes should be reachable over the required solid angles by *JWST* "wide" and *WFIRST* "deep" surveys in well-studied multiwavelength survey regions (e.g., [86]). Maintaining a low fraction (< 1%) of low-redshift interlopers is essential, as is the case with studies of high-z galaxy populations in general. Photometric-redshift and Lyman-break techniques have promise for enabling such a challenging discrimination, but ultra-deep multi-band OIR imaging and optimal redshift-estimation approaches will be essential.

The X-ray requirements discussed above can be met only with a new, next-generation X-ray observatory. To conduct the required deep X-ray survey in less than 1 year of total exposure time, an X-ray observatory should combine high throughput with sub-arcsecond angular resolution that is stable across a large field of view. *Chandra*'s grasp falls short of the requirements by three orders of magnitude. *Athena*'s sensitivity is insufficient by a factor of 200 due to its 5″ spatial resolution. *Lynx* is designed to meet all of these requirements.

Finally, we note that the survey approach suggested here is highly synergistic with future gravitational wave studies: while the X-ray signal probes accretion (but is blind to mergers), *LISA* will be able to directly track mergers (but will be blind to accretion and cannot identify galaxy counterparts). These two probes together can unveil a complete picture of the early SMBH assembly.

Lynx is uniquely capable of probing the earliest massive black holes by directly detecting their accreting seeds in X-ray observations. Combined with OIR studies of their host galaxies and environments as well as gravitational wave probes of black hole mergers, sensitive surveys with *Lynx* will have great potential to solve the long-standing puzzle of the origin of massive black holes.

1.2 Black Holes from Cosmic Dawn to Cosmic Noon

1.2.1 Probing the full range of massive black holes near the cosmic star formation peak

Beyond the origin of massive black holes, studying their growth from "Cosmic Dawn" at z ~ 10 to "Cosmic Noon" at z ~1–2 is essential for understanding their co-evolution with galaxies near the peak of cosmic star formation. A recent breakthrough in our understanding of AGN shows that they are not "on/off" like light bulbs, but instead "flicker" across a wide range of Eddington ratios on relatively short time scales (< 10^{5-6} years [87]). Thus, to understand the entire AGN population, the full dynamic range in accretion rates and hence X-ray luminosity needs to be probed at all epochs. This approach has been critical for understanding the connection between black hole and galaxy growth, the nature of AGN obscuration, and the evolution of AGN in large-scale structures [88–90].

As discussed above, X-rays are uniquely capable of probing a wide range of black hole masses and accretion rates, due to their high contrast and penetrating power. To cover the complete growing black hole population from $z = 6$ to 2 requires the sensitivity and angular resolution of *Lynx*.

Over the past 20 years, *Chandra* and *XMM-Newton* X-ray surveys have successfully collected clean and largely unbiased samples of AGN to $z = 5$ [91–96]. They cover a broad range of luminosities (down to $L_X = 10^{44}$ erg s^{-1} at $z = 5$ and $L_X = 10^{39}$ erg s^{-1}at $z = 0.5$; see Fig. 1.4) and include large numbers of both unobscured and obscured AGN. In the next few years, *eROSITA* [97] and *ART-XC* [98] will constrain the bright end of the luminosity function ($> 10^{45}$ erg s^{-1}) with 10^6 AGN over a broad redshift range.

The next frontier is to probe deeper, below the "knee" of the luminosity function at redshifts $z > 3$. Such observations require large numbers of very faint sources (many thousands compared to the few hundreds available now [62, 99]). This will enable efficient coverage of large areas down to the flux limits of the current deepest X-ray survey (the *Chandra* Deep Field-South), identifying thousands of distant AGN over several deg^2, down to fluxes of 10^{-18} erg s^{-1} cm^{-2}. These limits are factor of 10 below what is currently achievable with *Chandra* only in pencil-beam surveys. The counterparts for even the highest-z sources in the *Lynx* wide surveys will be readily available from next-generation facilities such as *WFIRST* and *Euclid*.

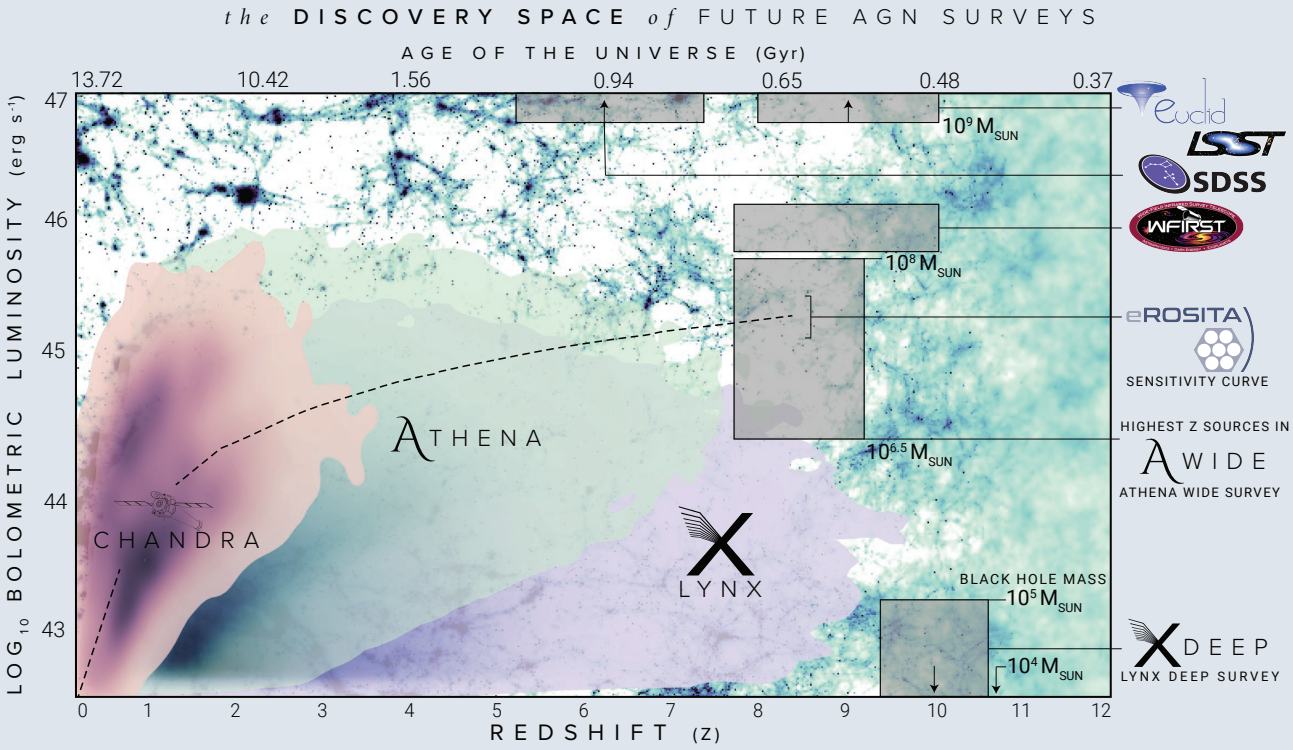

Fig. 1.4— Redshift and bolometric luminosity distributions (with corresponding SMBH masses for Eddington-limited accretion) to be probed by future experiments, compared with current *Chandra* surveys and the expected *eROSITA* limit in the Ecliptic Pole regions.

The abundance of future imaging and spectroscopic surveys (e.g., LSST, DESI, 4-MOST) will allow us to explore the distribution of AGN accretion rates as a function of key galaxy host properties (i.e., star formation rate, stellar mass, morphology). With sensitive radio measurements, such as those to be provided by SKA or ngVLA, an empirically derived fundamental plane of black hole activity [100] can be used to estimate both the black hole mass and kinetic energy output, in addition to the radiative energy output immediately available from the X-ray measurements (see e.g., [101] for a recent application). A connection between AGN and their environment can then be established via a statistical analysis of their clustering properties [102–106].

Finally, large OIR samples and wide *Lynx* surveys will enable X-ray stacking analyses, pushing down to extremely faint mean fluxes, 10^{-20} erg s^{-1} cm^{-2}. Stacking has been powerful in constraining the connection between galaxy mass, star formation, and black hole accretion rates up to $z \sim 3$ and $L_X = 10^{41-42}$ erg s^{-1} [89, 107]. *Lynx* will reach down to luminosities of $L_X = 10^{38} - 10^{39}$ erg s^{-1} — close to the level expected from individual X-ray binaries and so will cover the full range of accretion, down to emission from weakly accreting, lower mass black holes.

1.2.2 Unveiling obscured accretion

Another important avenue toward understanding the AGN-galaxy connection is to probe the most obscured AGN across cosmic time. A significant number of AGN are "hidden" by dust, so that only high energy X-rays can penetrate. Theoretical models predict phases of high obscuration during gas-rich galaxy mergers, when feedback from AGN may play an important role in regulating galaxy growth [108, 109]. Understanding what role black hole feedback plays in regulating galaxy formation is a significant component of the second *Lynx* science pillar. In addition to studies and tests outlined in §2, observations of the "hidden" AGN up to high-z is an important input to assessing what role the central black holes play in regulating galaxy formation.

At low redshift, roughly 30% of AGN are so highly obscured as to be undetected even in the 2–10 keV band (e.g., [110]). Very little information is available on the populations of these sources at higher redshift [111, 112]. Reprocessed IR emission offers one way of detecting such heavily-obscured AGN [113–116], but IR observations suffer from both contamination and dilution by the host galaxy. The reprocessed emission can be also observed in high-energy X-rays via the "Compton hump" at 20–40 keV and a ubiquitous Fe-K recombination line at $E = 6.4$ keV (see [117–119] for pioneering work using *NuSTAR*). At $z > 2$, the Compton hump is redshifted below 10 keV, where *Lynx* will provide leaps in sensitivity, pushing the census of heavily-obscured AGN out to $z = 4$ and revealing the least luminous of these hidden black holes.

1.3 Black Hole Seeds Archaeology in the Local Universe

A complementary strategy for understanding black hole seed formation comes from observing the relics of the first black holes in the local Universe. For this census, it is necessary to understand both the occupation fraction of black holes in galaxies and the fraction of those black holes that are actively accreting. Because of their smaller sphere of influence and lower accretion-powered luminosity, the occupation fraction becomes progressively harder to measure at lower black hole

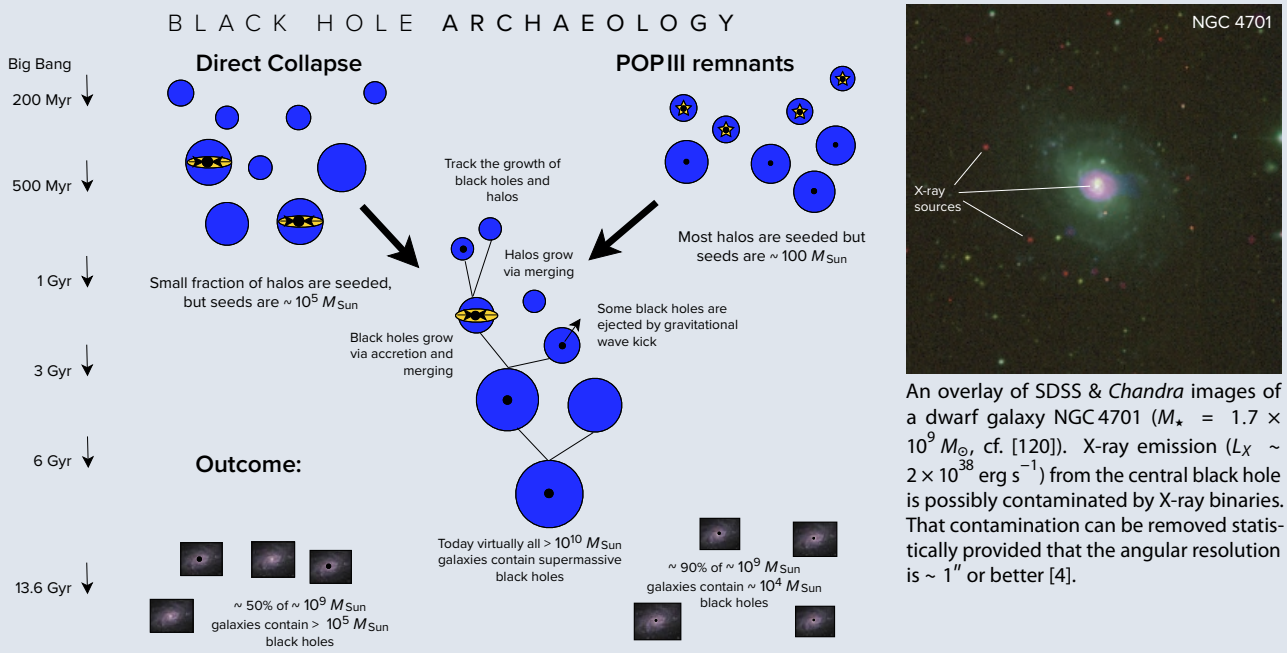

An overlay of SDSS & *Chandra* images of a dwarf galaxy NGC 4701 ($M_\star$ = 1.7 × 10^9 $M_\odot$, cf. [120]). X-ray emission (L_X ~ 2×10^{38} erg s^{-1}) from the central black hole is possibly contaminated by X-ray binaries. That contamination can be removed statistically provided that the angular resolution is ~ 1″ or better [4].

Fig. 1.5— Qualitative predictions for the properties of the local black hole occupation fraction in low-mass galaxies (adapted from Greene 2012 [3]). Unlike more massive galaxies, dwarfs are expected to retain residual memory of the predominant black hole seeding mechanism, and therefore serve as promising sites for black hole archaeology. Because of the complexity of the evolutionary path leading even to the low-mass dwarfs, this method requires statistical studies of large samples. The census of 10^{4-5} $M_\odot$ black holes in local dwarf galaxies and globular clusters can be obtained via sensitive X-ray imaging (a serendipitous project with *Lynx* [4]), or from radio synchrotron detections with ngVLA [6], or by stellar dynamics measurements with ELTs [5]. *Lynx* will be able to contribute to the radio method by enabling black hole mass estimates via the black hole activity fundamental plane [100]. Dynamical measurements at $D < 5$ Mpc with ELTs will provide a calibration between the black hole mass and X-ray luminosity, and constrain the accretion duty cycle. *Lynx* will then extend the studies to much greater distances.

masses, particularly in dwarf galaxies. This measurement, to a few percent accuracy, is uniquely enabled by *Lynx*.

As envisioned by Gallo et al. [4], the occupation fraction can be determined by the empirical relationship between the black hole X-ray luminosity and the stellar mass of its host galaxy, $M_\star$. This relation likely results from relations between $M_{\rm BH}$ and $M_\star$, and between $M_\star$ and the amount of "fuel" available to power the black hole. To measure the occupation fraction, it is essential to account for stochastic flickering of the accretion onto the black hole as well as contamination by actively accreting X-ray binaries [121, 122]. The high sensitivity and angular resolution of *Lynx* are critical for overcoming these challenges. Moreover, with high angular resolution maintained over a large field of view, the search for black hole seed relics can be performed as a serendipitous *Lynx* project.

Measurements of the black hole occupation fraction provide an essential probe of early black hole formation. For $9 < \log(M_\star/M_\odot) < 10$, the fraction of galaxies hosting black holes is expected to depend on the predominant black hole seeding mechanism at high redshifts (Fig. 1.5). This reflects the residual memory of the early stages of assembly still retained by dwarf galaxies. Semi-analytic models [21, 24, 60, 123–126] suggest that by $z = 0$, low-mass galaxies are still more likely (by a factor

of ~ 2) to contain massive black holes in the light seed scenario than in the heavy seed scenario (recall that at $z \sim 10$, that factor is $\sim 10^{3-4}$, see §1.1.3). Furthermore, the occupation fraction of black holes in dwarf galaxies provides a key constraint on the black hole mass density at low redshift, one that is essential to calibrate both numerical and semi-analytic models of their growth [24, 127, 128]. It is also essential in assessing the dominant mechanism responsible for quenching star formation in low-mass galaxies: if the occupation fraction is close to 100%, black holes alone can provide the required amount of energy feedback [129, 130]. Finally, the expected rates of events, such as tidal disruption events of SMBH mergers, are hugely sensitive to the black hole occupation fraction at the low mass end of the galaxy population (e.g., [131]).

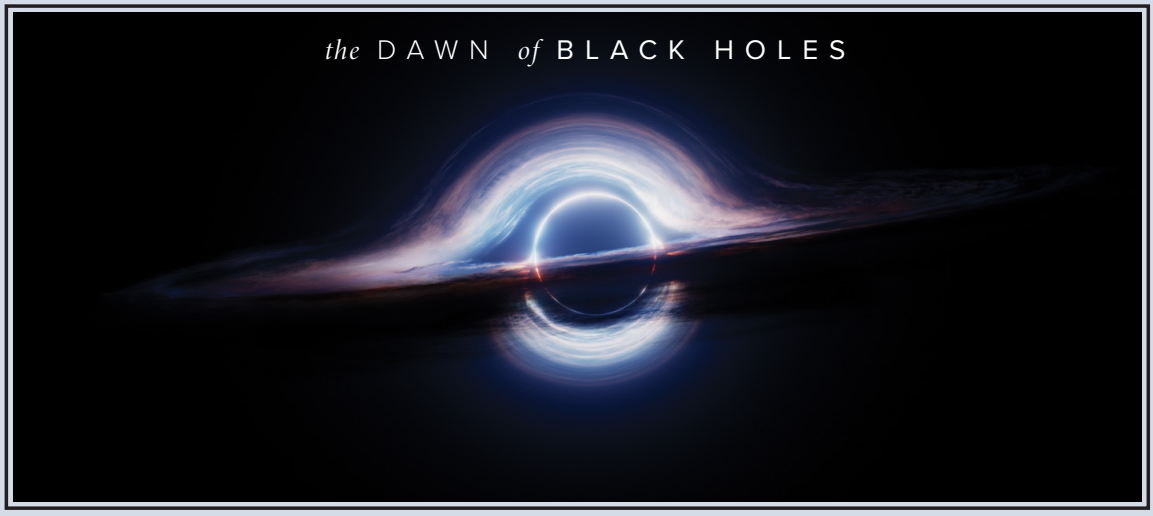

A custom, artistic black hole rendering made for the Lynx Team's public outreach efforts by artist Niko Maisuradze

Lynx will provide a conclusive view on how black holes form, evolve, and shape the evolution of their host galaxies, from the epoch of Cosmic Dawn to our cosmic neighborhood.

2 *The* Drivers *of* Galaxy Evolution

The past decade began with the first light of ALMA and will end at the start of the new era of hyperdimensional astrophysics. The movement toward highly multiwavelength, multidimensional datasets has enabled immense progress in many science frontiers, particularly with regard to the cycle of baryons in galaxies and the energetic feedback processes thought to drive their evolution. Facilities like ALMA and the next generation of optical/NIR integral field unit (IFU) spectrographs enable mapping the physical conditions and kinematics of cold molecular and warm ionized gas in galaxies in unprecedented detail. *JWST*'s launch at the start of the coming decade will push this capability to the rest-frame UV at redshifts $z > 6$, mapping the birth of the first galaxies (see §4.3 for a discussion of *Lynx* observations of Cosmic Dawn). Understanding their subsequent evolution, however, awaits an ability to map the processes that transform galaxies directly, rather than the *consequences* of those processes in isolation. Doing so requires an equivalent revolution in our ability to map the morphology and kinematics of the *hot* plasma that pervades galaxies, the atmospheres in which they reside, and the feedback processes that are the engines of their evolution.

Lynx will ignite this new epoch in our understanding of galaxies. As a long-lived, flexible platform combining extreme sensitivity with sharpest-ever angular and spectral resolution in X-ray bands, *Lynx* will *directly* observe the fundamental drivers of galaxy evolution. It will do so across nearly *all* characteristic size scales, epochs, and modes. *Lynx* will be the catalyst for the next great paradigm shifts across nearly every sub-field of galaxy evolution, including:

Extended circumgalactic halos — The thermodynamic state and chemical composition of hot gas in galactic halos encodes a record of the feedback-modified assembly history that shapes galaxy evolution. *Lynx* will probe the hot circumgalactic medium (CGM) to a large fraction of the virial radius in halos of virial mass $M_{\rm tot} \gtrsim 3 \times 10^{12}\,M_\odot$ through direct imaging in emission, and for $M_{\rm tot} \approx 1 \times 10^{12}\,M_\odot$ or below in absorption using bright background AGN as sightline backlights. We discuss this further in §2.1.

The Cosmic Web and its interface with galaxies — Cosmic Web sheets and filaments represent the typical environment for most "field" galaxies. Hot gas contained within them is a major reservoir of baryons in the low-redshift Universe, but it remains largely unexplored. Sub-regions of this gas feed accretion *into* galaxies, while other regions harbor the ejecta of strong feedback events that have pushed enriched gas *out of* galaxies. The thermodynamic state and metallicity of this hot gas, therefore, serves as a critical constraint for galaxy formation models. *Lynx* will have the sensitivity to *map* the Cosmic Web in emission above an overdensity threshold of ~ 50, as well as detect it in absorption against virtually *every* X-ray bright background AGN (Appendix A.5). A multi-megasecond Cosmic Web imaging campaign with *Lynx* would produce a Legacy-class, epochal dataset that would reign among its greatest scientific achievements. Because this program would be so revolutionary and impact so many sub-fields in astrophysics, we discuss it further in §4.4. See Fig. 4.7 on page 78 for a realistic simulation of what we are calling the *Lynx* Legacy Field.

High-redshift probes — In addition to detailed low-redshift measurements, we must also obtain additional constraints on the hot gas near the epoch of peak cosmic star formation at $z = 2 - 3$. *Lynx* will do this through observations of high-redshift galaxy groups down to a mass scale of $M_{\rm tot,500} = 2 \times 10^{13}\, M_\odot$ at $z > 3$ (§4.4.1). This is close to the galactic mass scale, and so strong feedback operating in galaxies will generally result in signatures observable in the intragroup medium.

As galaxies fall into clusters, gas in their halos is shock-heated, stripped, and mixed with halo gas from a large number of other galaxies. These processes can completely erase information on the thermodynamic state of gas prior to accretion onto the cluster, but not on its *chemical* composition. Metallicity measurements in outer cluster regions can therefore provide a strong constraint on the average metallicity of the CGM at $z > z_{\rm cluster}$ [132–135], and hence on the feedback history. *Athena* will make metallicity measurements in clusters to $z \approx 1$. Approximately 60% of stars observed at $z = 0$ are formed by $z = 1$ [136], so while some trends in metallicity can be expected, they will likely be weak (as indeed seen in *Chandra* observations [137–139]). *Lynx* can make *spatially resolved* metallicity measurements in clusters across ~ 11 Gyr of cosmic history to $z = 3$ (§4.6) using samples provided by upcoming large-area surveys (§4.4.2). Dramatic redshift trends in the chemical composition of cluster gas at $1 < z < 2$ and beyond are expected because less than 10% of the present-day stars were in place at $z \geq 2$ [136]. Observations of this trend, *uniquely* possible with *Lynx*, will greatly advance our understanding of galaxy wind feedback at the critical epoch of peak star formation.

Feedback signatures in gas near and within galaxies — The physical conditions and kinematics of hot gas in and around galaxies is sculpted by ongoing and recent episodes of energetic feedback from star formation and black holes. On scales from a few parsecs to tens of kiloparsecs, *Lynx* will observe galaxy-scale winds driven by stellar, supernovae (SNe), and black hole feedback, including detailed measurements of their energetics and constraints on their launching mechanisms. Winds have rich structure and *must* be observed in the X-ray band in order to be fully understood, but because they are so tenuous, their X-ray surface brightness is ubiquitously low [140, 141]. These critical measurements therefore require the extreme sensitivity of *Lynx* coupled to its exquisite angular resolution, enabling spatial mapping on all relevant scales. The LXM's ~ 0.3 eV spectral resolution will meanwhile place many resolution elements across the characteristic velocity widths of these winds, giving a truly multidimensional understanding of how they operate (§2.2).

On ~ 100 pc to ~ 1 kpc scales, *Lynx* will resolve and characterize extended narrow line emission regions in nearby AGN, providing a key diagnostic for shock excitation and therefore a new understanding of where and to what degree AGN outburst energy is dissipated in the interstellar medium (ISM). Another diagnostic of AGN energy feedback on galaxy-wide scales will be *Lynx* observations of AGN-inflated bubbles in the hot ISM of nearby elliptical galaxies. Both types of observations require sub-arcsecond imaging capabilities, unique to *Lynx*. On the smallest scales, *Lynx* will track the hot interstellar medium in active star forming regions of the Milky Way and nearby galaxies (§3.1). Observing the interface between the hot ISM that surrounds dense molecular clouds will advance our understanding of how energy feedback from star formation locally shuts down *new* star formation. Futhermore, *Lynx* observations of large samples of young supernova remnants in Local Group galaxies will establish a compregensive view of the relationship between recent SNe activity and star formation (§3.3).

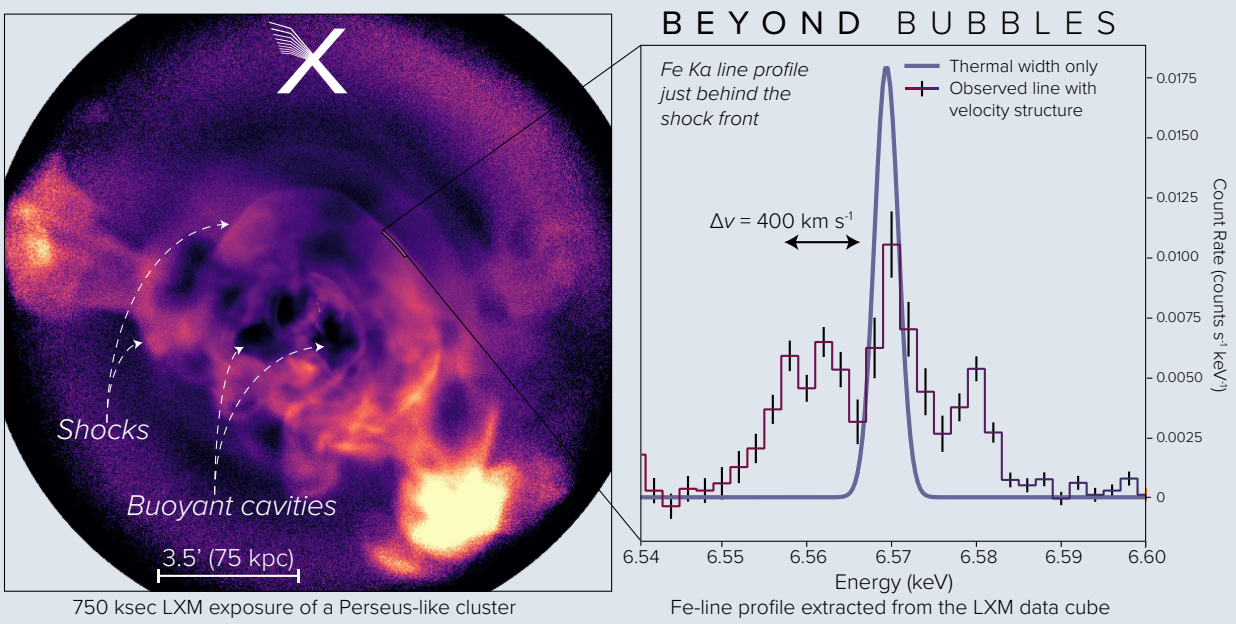

Fig. 2.1— The high spatial resolution characterization of buoyant X-ray cavity networks and sound waves in galaxy groups and clusters remains one of *Chandra*'s great scientific legacies. These kpc-scale shocks and bubbles, mechanically inflated by radio-bright jets launched from supermassive black holes, act as calorimeters for the total energy input by black hole feedback in the central galaxy. *Lynx* is the *only* planned mission with the combined angular and spectral resolution needed to finally understand how AGN mechanical energy, via bubble enthalpy and shock dissipation, is thermalized in the intracluster medium (ICM). (*Left*) Maps of adiabatic (sound waves) and isothermal (bubbles) fluctuations based on a mock 750 ksec *Lynx* LXM observation of a Perseus-like cluster [142, 143]. *Chandra* could hypothetically observe Perseus for nearly *fifteen megaseconds* and the result would still not remotely approach the richness of this *Lynx* datacube, given the > 50-fold improvement in spectral resolution of the LXM relative to ACIS. (*Right*) The image at left shows how *spatially* rich this mock *Lynx* datacube is, while here we show how *spectrally* rich it would be. The panel shows an extracted profile for the Fe Kα line observed with the LXM subarray from a region immediately behind the shock front, showing the effect of velocity broadening originating from the expanding front. Such measurements, only feasible within a few arcseconds of the front because of the brightness contrast effects, provide the expansion velocity and the density structure of the shock.

Microphysics of feedback dissipation — The most energetic examples of black hole feedback are found in galaxy clusters (reviews by, e.g., McNamara & Nulsen [144] and Fabian [145]), which also serve as astrophysical laboratories for studies of plasma physics effects coupled to turbulent energy dissipation from feedback (e.g., [146]). *Chandra* observations of cool cores in the nearby galaxy clusters show that this is a remarkably complex process, where plasma microphysics (e.g., viscosity, dissipation of turbulence, heat conduction) plays a major role. *Hitomi* observations of Perseus provide a glimpse of the power of high resolution spectroscopy, even with coarse angular resolution, for these studies [147]. *XRISM* and then *Athena* will bring X-ray spectroscopic capabilities to the next level, providing superb measurements of the total energy of gas motions in a large sample of galaxy clusters. However, as the *Chandra* experience convincingly shows, the key to better understanding the energy dissipation microphysics lies in the ability to resolve structures down to the Spitzer mean free path scale, λ_{sp}. *Chandra* is often limited by statistics, not angular resolution, in probing gas on the λ_{sp}

scales. *Lynx* will eliminate this problem (Fig. 2.1, §4.10, [142]). More importantly, it will provide gas velocities on a similar angular scale, providing a third dimension to the data. New handles on the plasma physics effects provided by *Lynx* observations of nearby galaxy clusters will be used to inform the "subgrid" treatment of feedback in numerical models of galaxy formation.

AGN mechanical power in the fastest outflows — AGN winds span a wide range of ionization and kinematic states (§2.2), but it is likely that the high-ionization, ultra-fast outflows act in ways most directly relevant for galactic feedback [148]. Their mass and energy budgets, however, remain poorly understood, and largely inaccessible without *Lynx*. The main diagnostic of these flows is the blue shifted K-shell lines of Fe XXV and Fe XXVI between 6 – 9 keV (rest frame). These observations will be a major goal for the microcalorimeters on both *Athena* and *Lynx*. However, the current quality of X-ray data results in uncertainties an order-of-magnitude higher in the derived energy and momentum flux of the wind, because these quantities are degenerate with the distance and density of gas in the wind, which cannot be independently determined. Only the high-resolution *soft* X-ray spectra obtained by the *Lynx* microcalorimeter and gratings will provide access to density diagnostics in hot AGN winds, greatly reducing uncertainties in the determination of the instantaneous AGN mechanical output, and therefore *greatly* constraining black hole feedback models (§4.2.3).

Fueling and triggering of AGN feedback — *Lynx*'s sharp angular resolution will allow it to determine the gas state at or near the sphere of influence of SMBHs in nearby galaxies. While it is likely that the accretion flow within this radius significantly deviates from the Bondi solution, $\dot{M}_{\rm Bondi}$ can still serve as a useful proxy for the instantaneous accretion rate on the black hole. *Chandra* observations indeed reveal a strong correlation between the derived Bondi accretion rate and AGN jet power for a small sample of nearby elliptical galaxies [149]. The Bondi-Hoyle-Lyttleton accretion rate is typically used as a proxy for black hole feedback in numerical models of galaxy formation with a free efficiency factor (e.g. Springel et al. 2005 [150]): $\dot{E}_{\rm feed} = \epsilon_f \times \epsilon_r \dot{M}_{\rm Bondi}\, c^2$. The efficiency factor ϵ_f cannot be determined from first principles. It is uncertain by approximately an order of magnitude, with the correspondingly uncertain consequences for the AGN feedback effect on galaxies. Dramatically better sensitivity and new spectral gas diagnostics available with *Lynx* will make it possible to derive $\dot{M}_{\rm Bondi}$ much more reliably and in a larger sample of galaxies. These observations will be used to guide subgrid parameterizations of the AGN feedback in numerical models.

* * *

All observations mentioned above are at the core of *Lynx*'s ability to expose the drivers of galaxy formation. Below, we expand on the most demanding programs that partly define the observatory's requirements: characterization of the CGM in emission and absorption, the detailed measurements of galaxy winds driven by stellar and black hole feedback, and observations of the very *nearest* examples of galaxy-scale feedback — that within our own galaxy.

2.1 The Imprint of Galaxy Evolution Drivers on the Circumgalactic Medium

The majority of baryons reside beyond the optical extent of a galaxy in the circumgalactic and intergalactic media. Gaseous halos are inextricably linked to the appearance of their host galaxies

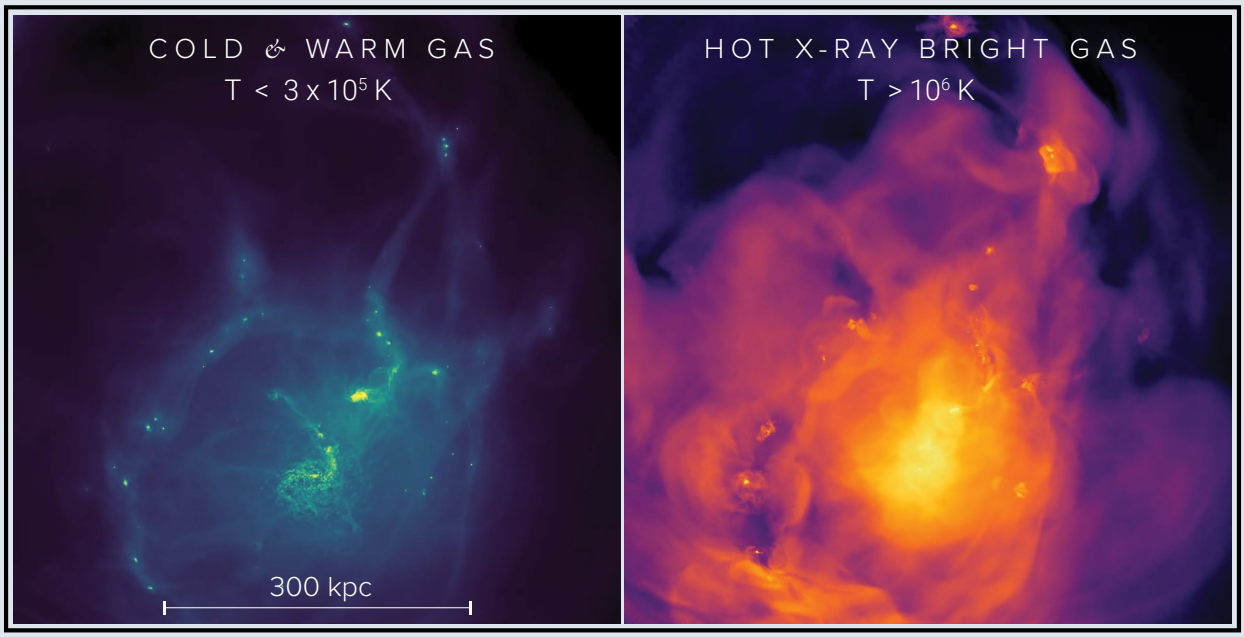

EAGLE Super-HighRes zoom simulation of the virial radius surrounding a newly formed Milky Way-mass galaxy. The left panel shows the cold and warm component, while the right panel shows the equivalent X-ray view of the hot gas, whose morphology and kinematics encode a history of the processes that drive the galaxy's evolution.

Credit: B. Oppenheimer & Collaborators

Detailed information is now available on the stellar, dust, and cold gas content of galaxies, and yet there is a dearth of understanding of the exact mechanisms of their formation. *Lynx* will expose essential drivers of galaxy evolution which primarily leave imprints in the X-ray bright CGM, extending well beyond the optical size of galaxies and containing most of their baryons.

through a complex story of accretion, feedback, and continual recycling. These energetic processes, which couple strongly to the state of gas in the CGM, are the same ones that both: (1) regulate stellar growth so that it is not over-efficient, and (2) partially create the diversity of today's galaxy colors, star formation rates, and morphologies that span the Hubble types. They work in concert to regulate the evolution of a galaxy, ushering it across the so-called "Green Valley" and maintaining its quenched appearance on the "Red Sequence" (Fig. 2.2, top panel).

Understanding of the CGM is rapidly expanding, thanks to exquisite UV absorption line studies (reviewed by, e.g., Tumlinson, Peeples & Werk 2017 [158]). However, the majority of baryons in halos more massive than ~ 10^{12} $M_{\odot}$, along with their critically important physical conditions and dynamics, remain *invisible* because that gas is heated above UV ionization states. Information on many of the essential drivers of galaxy evolution is primarily contained in this thus-far inaccessible hot gas phase.

Completing the picture of galaxy formation requires uncovering the physical mechanisms behind stellar and SMBH feedback driving mass, metals, and energy into the CGM. By opening galactic hot halos to new wavebands, we not only obtain archival records of more than ~ 13 billion years of evolution, but we can observe ongoing accretion, the deposition of superwind outflows into the CGM, and the re-arrangement of baryons by SMBH feedback. A description of the flows of mass, metals,

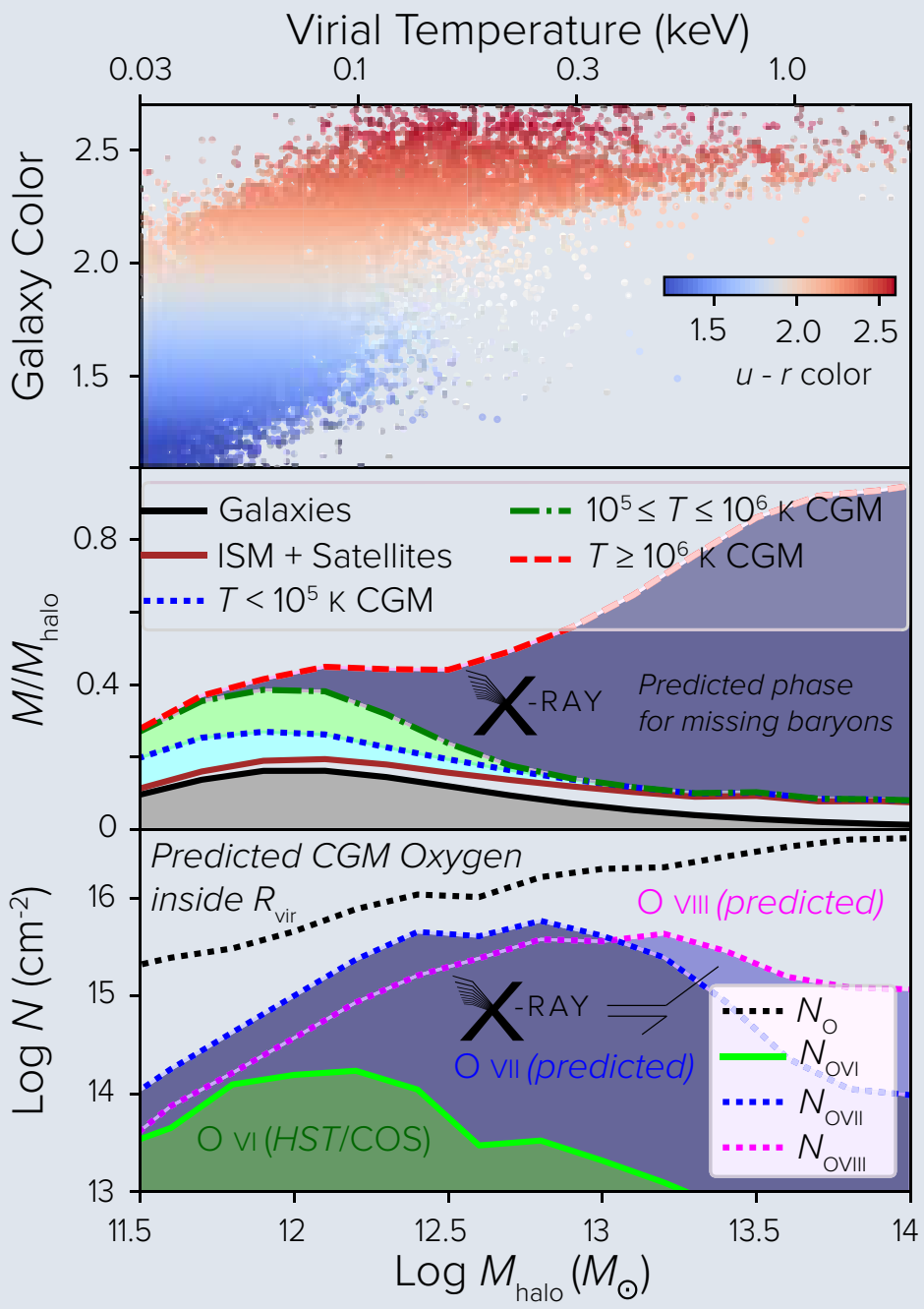

Fig. 2.2— Current observations and theory predictions indicate a dramatic transition in the properties of galaxies at a mass scale of ≈ the Milky Way. (*Top*) Low-z galaxies show the greatest variety of colors, SFRs, and morphologies in the mass range $(1-3)\times10^{12}\,M_\odot$ [151]. (*Center*) Abundance matching analyses [152] show that star formation efficiency peaks around $10^{12}\,M_\odot$. A decline at higher masses is thought to be associated with the growing importance of hot baryons (red line with purple shading) over the cool ($T < 10^5$ K [153]) and warm ($10^5 \le T < 10^6$ K [154]) CGM phases. The white area above the red dashed line are the expected baryons ejected beyond $R_{\rm vir}$. (*Bottom*) The average column density of oxygen in different ionization states within $R_{\rm vir}$. While O VI has been observed around normal galaxies with *HST*/COS [154], much larger reservoirs of O VII and O VIII, accessible only via a highly sensitive X-ray observatory like *Lynx*, dominate the predicted CGM oxygen budget [155–157].

and energy will *only* be complete by observing the thermodynamic states, chemical compositions, structure, and dynamics of $T \geq 10^6$ K halos. These measurements are uniquely possible with a next-generation X-ray observatory *only* if it provides the sensitivity needed to detect extremely low surface brightness CGM emission, *only* if it has the spectroscopic power to resolve spectral lines and therefore measure gas motions, and *only* if it has the high spatial needed resolution to resolve the critical scales on which a panoply of feedback effects operate. *Lynx* is designed to meet this challenge.

2.1.1 The current state of the art in our understanding of the CGM

An intimate connection between properties of the stellar component in galaxies and their extended gas halos has long been predicted by analytic theories of galaxy formation. A transition of galaxy properties at the $\sim 10^{12}\ M_\odot$ dark matter halo mass scale can be related to the maximum in the baryonic cooling curve at corresponding virial temperatures [159, 160]. The formation of a hot ($T > 10^6$ K), ambient gaseous halo should accompany a decline in the efficiency of accretion onto a galaxy, and of star formation within it [161–163]. These analytic models also reveal one of the central conundrums in our understanding of galaxies: the so-called "over-cooling" problem, wherein cooling and condensation of halo gas averaged over cosmic time is expected to proceed at *much* higher rates than that of the observed star formation [164]. Effectively all likely solutions to the over-cooling problem leave an observable imprint in the CGM, as stellar winds and radiation pressure [165–167], along with black hole-driven radiative and mechanical outflows [144, 168, 169], all eject baryons from the galaxy into the CGM.

UV-based CGM observations enabled by *HST*'s Cosmic Origins Spectrograph (COS) has re-defined our understanding of galactic halos. UV absorption lines from hydrogen and metals are ubiquitous in quasar spectra intersecting the CGM. COS has now observed the multiphase gaseous content of several galactic halos, revealing a rich set of dynamical processes like gas accretion, outflows, and recycling that correlate with galaxy type [158].

Fig. 2.3— *(next page)* A drastic transformation of galaxies from the star-forming blue cloud, to the green valley, and finally to the red sequence happens in a relatively narrow range of masses around $M_{\rm tot} = 1 \times 10^{12}\ M_\odot$. The diverse optical appearances (top panels) are intimately tied to their circumgalactic gas reservoirs. Numerical simulations predict rich structure of all CGM phases (see the second and third panel rows, which show outputs from three EAGLE Super-HiRes zooms). This structure reflects the "invisible" drivers of galaxy formation: accretion, feedback, and recycling flows of gas. The CGM in its full glory remains largely unobserved. The structure of cold ($T < 10^{4.5}$ K, white-blue) and warm ($T \sim 10^{5.5}$ K, green-yellow) gas is probed via UV absorption in individual sight lines; while the hot phase is routinely observed in the X-rays only in more massive ellipticals. As galaxy mass increases, we expect a dramatic transformation of the CGM from warm-cold dominated for $M < 10^{12}\ M_\odot$ to hot-dominated for $M \gtrsim 2 \times 10^{12}\ M_\odot$. Energy feedback, which plays a major role in this transformation, changes predominant types around the $M_{\rm tot} = 1 \times 10^{12}\ M_\odot$ mass scale (bottom panels). In all cases, the main signatures of ongoing feedback are imprinted in the inner structure of the hot halo. Their observations require a combination of high spatial and spectral resolution, uniquely provided by *Lynx*.

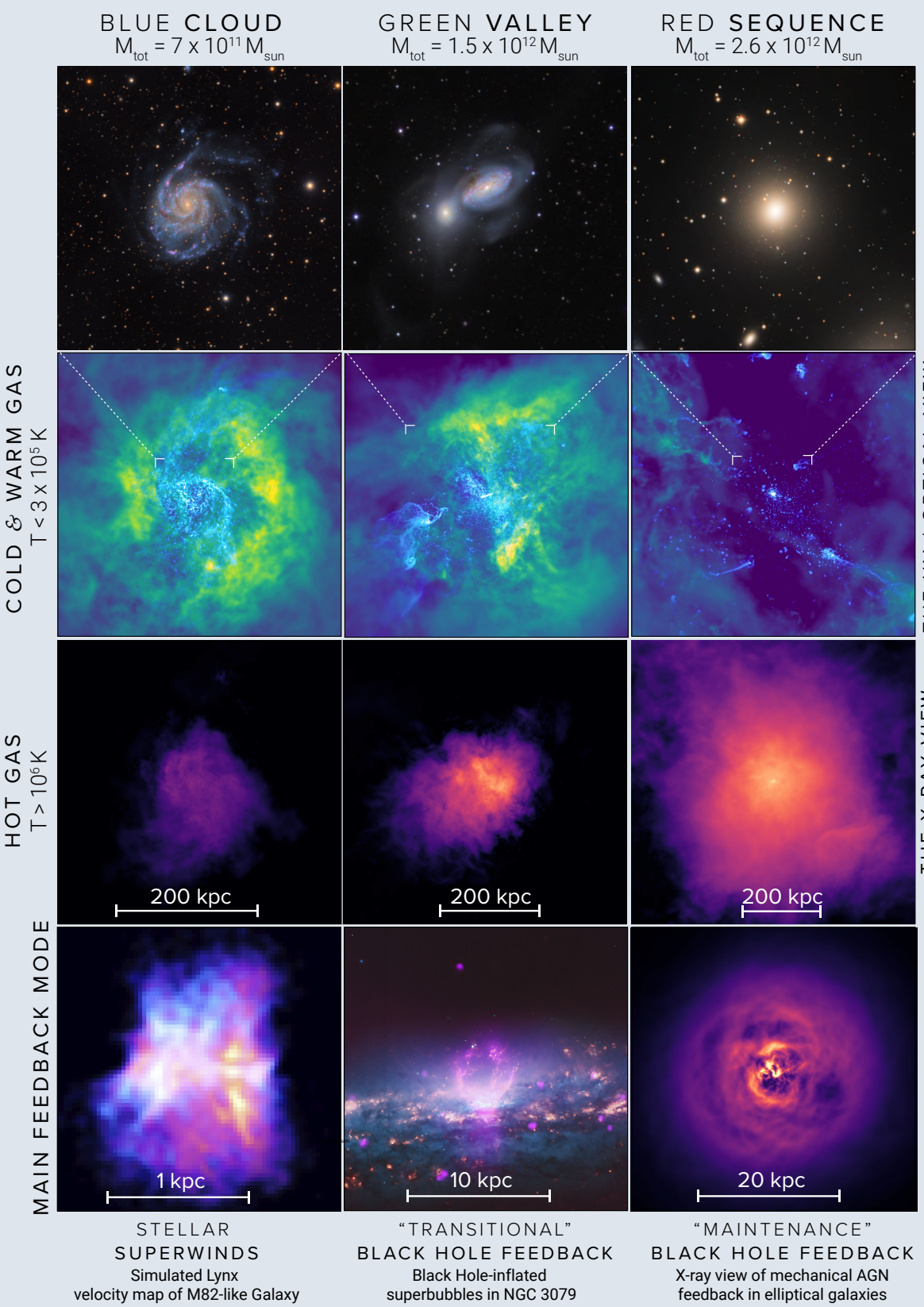
BLUE CLOUD
M_{tot} = 7 x 10^{11} M_{sun}
GREEN VALLEY
M_{tot} = 1.5 x 10^{12} M_{sun}
RED SEQUENCE
M_{tot} = 2.6 x 10^{12} M_{sun}
COLD & WARM GAS
T < 3 x 10^5 K
THE UV / OPTICAL VIEW
HOT GAS
T > 10^6 K
THE X-RAY VIEW
200 kpc
200 kpc
200 kpc
MAIN FEEDBACK MODE
1 kpc
10 kpc
20 kpc
STELLAR SUPERWINDS
Simulated Lynx velocity map of M82-like Galaxy
"TRANSITIONAL" BLACK HOLE FEEDBACK
Black Hole-inflated superbubbles in NGC 3079
"MAINTENANCE" BLACK HOLE FEEDBACK
X-ray view of mechanical AGN feedback in elliptical galaxies

State-of-the-art cosmological hydrodynamic simulations have applied increasingly sophisticated feedback schemes tied to star formation and SMBH accretion [e.g., 170–172]. They reproduce detailed properties of galaxies and provide very specific predictions for the physical properties of the CGM. Basic theory (i.e. $T_{\rm vir} \approx 10^6 \times (M_{\rm halo}/10^{12} M_\odot)^{2/3}$ K) and multiple simulation suites, including EAGLE [173], Illustris-TNG [174], and FIRE-2 [175] all predict that the *majority* of CGM gas and metals lies in the hot phase of halos at or above the Milky Way (MW) mass scale, $M_{\rm halo} \approx 10^{12}\, M_\odot$ (Fig. 2.2). At least some simulation suites [e.g., EAGLE, see 176] simultaneously reproduce the UV absorption line statistics for the cool/warm ($T \leq 10^{5.5}$ K) phase of the CGM [e.g. 153]. We therefore expect that the "COS era" is just the dawn of our understanding of the baryon physics regulating, transforming, and quenching galaxies. Despite the rich array of ions detected by UV absorption, the majority of CGM baryons and metals remain undetected in the hot ($T \geq 10^6$ K) phase. Their physics, dynamics, and energetics contain essential clues on how galaxies assemble, evolve, and transform.

2.1.2 Toward a new understanding of how galaxies evolve

A full description of the formation and evolution of galaxies depends on mapping a range of high-energy processes that operate on vastly different scales. Our understanding of these processes awaits an ability to observe accretion physics onto $10^{5-9} M_\odot$ SMBHs, the energetic yet diffuse stellar and SMBH-driven superwinds emanating from galaxy disks, and the complex tapestry of mass, metal, and energy flows exchanging phases in the CGM. The calibration of fundamental relations between galaxies, their central black holes, and *all* phases of the CGM remain unconstrained by competing theoretical models. It is essential that new observational capabilities are developed to enable their direct study. *Lynx* is designed to deliver this paradigm-shaping power.

The current generation of simulations all agree that a confluence of high-energy processes operate to evolve and transform a galaxy's optically observed properties: color, morphology, and star formation rate. A blue cloud galaxy regulates its star formation through a balance of accretion from the CGM (both cold, $T \sim 10^4$ K, and hot, $T > 10^5$ K), and star formation-driven superwind outflows. The formation of a virialized hot halo at $M_{\rm vir} \sim 10^{12}\, M_\odot$ curtails this cycle as the gas cooling becomes inefficient. At this stage, the SMBH is predicted to grow much faster than the galaxy due to the decline of bursty star formation-driven winds [177] and/or the collection of nuclear hot gas [178], leading to AGN feedback that drives jets, shocks, and bubbles tens to hundreds of kpc into the CGM [e.g., 179]. This amount of energy and momentum imparted to MW-mass gaseous halos can (1) shred the cool/warm CGM accretion supply, (2) uplift and eject baryons from the CGM [180], and (3) secularly transform a galaxy across the green valley [181]. Such a re-arranged, quasi-stable, and high entropy halo — from which accretion becomes inefficient — leads to the transition of the central galaxy into the red sequence, where "maintenance-mode" AGN feedback may be required to maintain the galaxy's quenched appearance. The main goal of future observational programs should be to show *how* these processes work in concert to drive the evolution of the galaxy.

2.1.3 The X-ray-bright reservoirs of mass, metals, and energy

As noted above, the majority of baryons and metals remain undetected in $\geq 10^{12} M_\odot$ halos [182], most likely because they are in the hot phase. How much could a future X-ray observatory find? The maximum fraction of baryons locked in stars is ~ 20%, and is found in MW-mass halos (Fig. 2.2,

middle panel). Budgeting the baryons out to the virial radius of MW-mass halos ($R_{\rm vir} \sim 200 - 250$ kpc) from COS UV surveys [153, 183] finds another 10–20%. Therefore, at least 50% of the expected baryons associated with a $1 - 2 \times 10^{12} M_\odot$ halo are not accounted for. Their location and physical state is expected to be a very powerful diagnostic of the physics that regulates galaxy formation.

The mismatch of metals observed within galaxies with yields predicted from stellar populations [184] indicates that a significant (and probably major) fraction of metals reside in the CGM. Metals detected in UV quasar absorption spectra account for ~ 10% of the total output from star formation [185]. Similarly, the significant gaseous halo O VI masses observed by COS [154] are only a small percentage of the total circumgalactic oxygen budget. Cooling functions of hot gas predict far more O VII and O VIII [186], which will dominate the oxygen budget above $M_{\rm vir} = 10^{12} M_\odot$ (Fig. 2.2, lower panel). These ions are detectable at high abundance in our own halo, but their distances are poorly constrained [187]. Only by observing them around a large variety of galaxies as a function of impact parameter can we reveal the amount and location of these invisible circumgalactic metal reservoirs. Only *Lynx* can do this.

Moreover, the gaseous halo energy budget, which should be dominated by $T \geq 10^6$ K gas, is unconstrained by at least an order of magnitude. Completely absent from such an energy census are turbulent velocities [188], bulk motions, and rotation [189] of the hot gas, as well as magnetic fields [190] and non-thermal particles [191]. Knowing the mass, metal, and energy budget will depend on measurements of the detailed thermodynamic state of the hot halo — the dominant medium by volume and mass. Required observations include radial profiles of gas density, temperature, and metallicity. In addition, we must have a facility with the combined sensitivity spectral, and angular resolution to truly *map* the CGM. The expected kinematic and morphological structure of all CGM components is very rich, and directly related to dynamical processes coupled to both stellar and black hole feedback (Fig. 2.3). In order to truly understand the involved physics while avoiding incorrect inferences as to the bulk properties of the CGM, individual objects must be observed and spatially mapped. These persistent gaps in our understanding will finally be addressed by *Lynx*.

2.1.4 A new understanding of the CGM with *Lynx*

The coming years will see UV absorption line studies of the CGM continue, growing the *HST*/COS archive and enabling future cross-correlation with ground-based follow-up surveys. The *new* frontier, however, will be observations of the hot phase. UV studies fundamentally *cannot* provide direct information on this phase because the gas is ionized above all observable UV transitions for the relevant range of temperatures, as shown in the phase diagram in Fig. 2.4.

Observations of the Sunyaev-Zeldovich (SZ) effect are soon to grow in power. Detection of *individual* galactic halos through their SZ decrement is impossible even with the largest scale future SZ experiments, though attempts to detect the *stacked* thermal and kinetic SZ effects may have been successful ([192, 193]). These detections will likely become routine in the upcoming Cosmic Microwave Background (CMB) "Stage 3" and "Stage 4" experiments [194], although these surveys will focus more on higher mass objects ~ 10^{13} $M_\odot$. Angular resolution also will be an issue for this work. The optimal redshift range for stacking the SZ signal is at $z \sim 0.5$ or above. At this redshift, the ~ 1 arcminute beam of the "Stage 4" CMB experiment corresponds to ~ 350 kpc, too coarse to constrain the structure of the CGM within the virial radius, even in a stack.

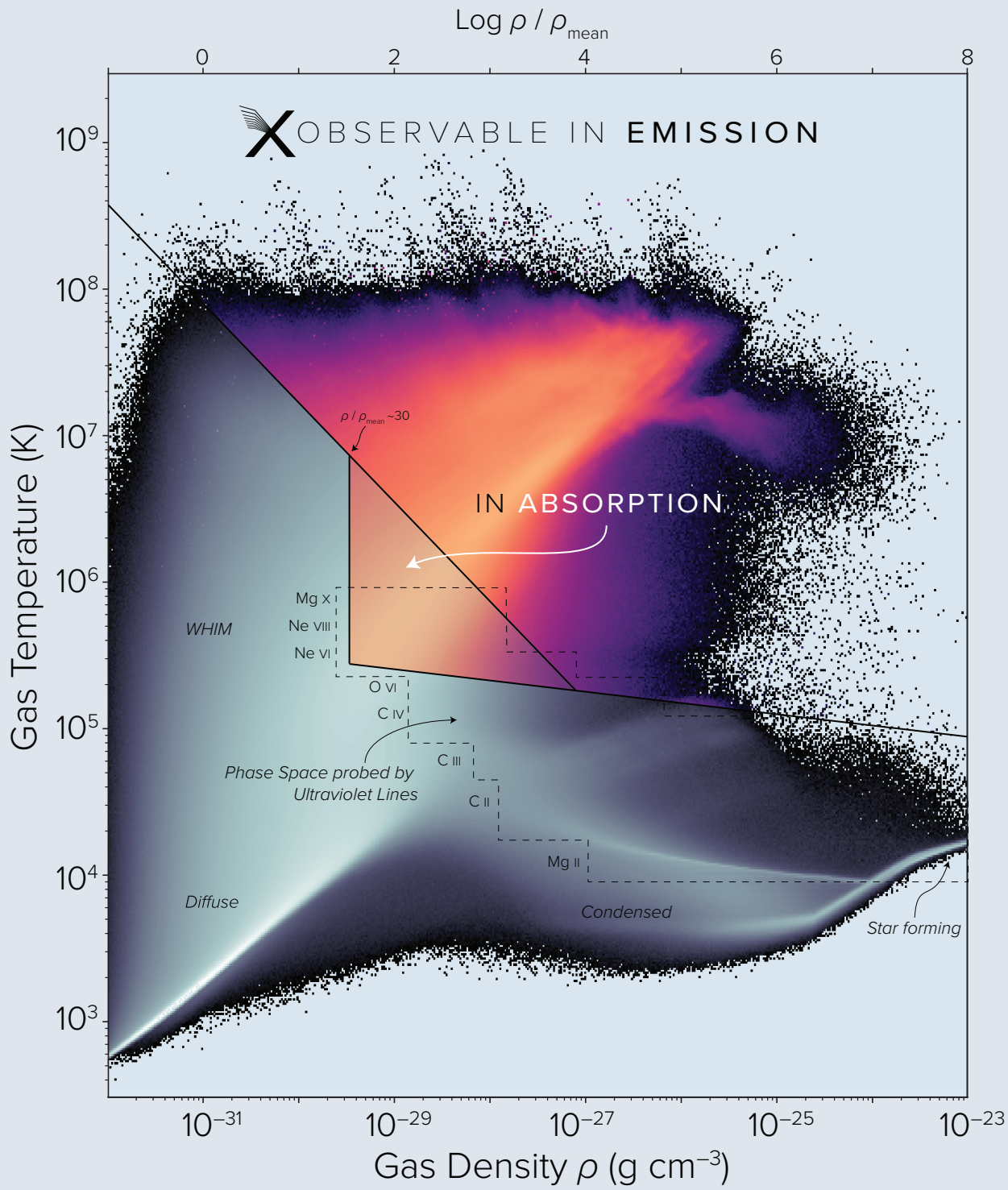

Fig. 2.4— By $z = 0$, over 50% of all baryons in the Universe are hotter than $10^{5.2}$ K, and the *vast* majority (located in the ICM and Cosmic Web) have yet to be detected. This density-temperature phase diagram generated from EAGLE — and generic of all cosmological simulations — shows that most of these hot hidden baryons will be revealed by *Lynx* in emission. Using absorption lines of O VII, O VIII, and other X-ray ions, *Lynx* will uncover a unique regime of lower-temperature diffuse baryons down to an overdensity of ~ 30. At temperatures around the lower boundary of the range that can be probed in X-rays, the sensitivity of the UV and optical absorption line method takes over (dashed rectangular regions reproduced from Tumlinson, Peeples, & Werk 2017 [158]). The simulated baryons shown here are extracted from a 100 Mpc^3 volume at $z = 0$.

Therefore, while ongoing and future studies of the CGM using UV absorption lines and the SZ effect are important, critical observations of the *hot* CGM in *individual* galaxies must be obtained elsewhere. A reasonable *minimum* set of goals for an X-ray observatory capable of doing so includes deep images in the soft X-ray band for characterization of multiple modes of feedback operating inside $0.25R_{\rm vir}$ of a $10^{12}M_{\odot}$ halo (50 kpc), as well as to map the structure of hot halos out to $0.5R_{\rm vir}$ for a $10^{12.5}M_{\odot}$ galaxy (150 kpc). Moreover, detections in multiple bands over the $\sim 0.4-1.5$ keV range will be needed to independently determine the CGM temperature, density, and metallicity. Spectroscopic observations are also essential. Sensitive absorption line measurements — at spectral resolving powers $R > 5{,}000$ only accessible with X-ray gratings — can extend characterization of the CGM in MW-mass galaxies to at least the virial radius and provide additional kinematic data [195]. X-ray microcalorimeter measurements in the inner halo can resolve structures associated with feedback and gas accretion onto galaxies. Such a microcalorimeter should have at least an ≈ 0.3 eV energy resolution to observe gas motions with the expected of order $\lesssim 100$ km s^{-1} velocities and provide 1″ spatial sampling to resolve expected structures ([196], §2.2.1).

The limiting factor for imaging observations of diffuse gas in galactic halos and in Cosmic Web filaments is its expected low contrast relative to both astrophysical and instrumental backgrounds (Appendix A.5). *Chandra*'s capabilities are insufficient by 1.5–2 orders of magnitude. *Athena* will be severely affected by residual cosmic X-ray background fluctuations caused by sources fainter than the confusion limit and by large-scale non-uniformities of stray light. *Athena* also lacks X-ray gratings, and its microcalorimeter provides a resolving power of only $R \sim 250$ at O VII, insufficient to measure gas velocities expected to be on the order of ~ 100 km s^{-1}. The only facility powerful enough to revolutionize our understanding of the hot CGM is *Lynx*, which will fly a combined package of outstanding imaging, X-ray gratings with $R > 5{,}000$, and a sub-arcsecond microcalorimeter with energy resolution as sharp as 0.3 eV, enabling velocity centroiding to ~ 10 km s^{-1}.

2.1.5 Pushing to lower densities: X-ray absorption studies of the CGM

At its outermost radii, the CGM becomes so tenuous that the large fraction of baryons and metals that reside there can no longer be observed in emission, even with an observatory as sensitive as *Lynx*. The gas near and outside of the virial radius in galaxies and galaxy groups, as well as baryons in lower-density regions of the Cosmic Web, nevertheless encodes key imprints of galaxy evolution drivers that have thus far remained unobservable. Were we able to observe this gas, we could detect reservoirs of hidden metals and mass, as well as quantify complete unknowns like turbulence, hot gas flows, and rotation velocities in the outer halos of galaxies *including our own* (see §2.3). These environments have virial temperatures $\gtrsim 10^{5.5}$ K, so the gas should be ionized to X-ray states (§ A.4). While no observatory could ever observe these faintest regions in emission, *Lynx* is designed to detect and characterize this gas by X-ray *absorption* against background AGN, which will serve as backlights that place this previously unseen gas in silhouette (Fig. 2.4). We describe this key capability below.

The tenuous CGM in silhouette: the need for next-generation X-ray gratings — In order to match the thermal width of key lines, the optimal resolving power for absorption studies of intergalactic gas is $R \gtrsim 5{,}000$ (see Appendix A.4 and A.5 for detailed discussions as to why). Currently, the primary

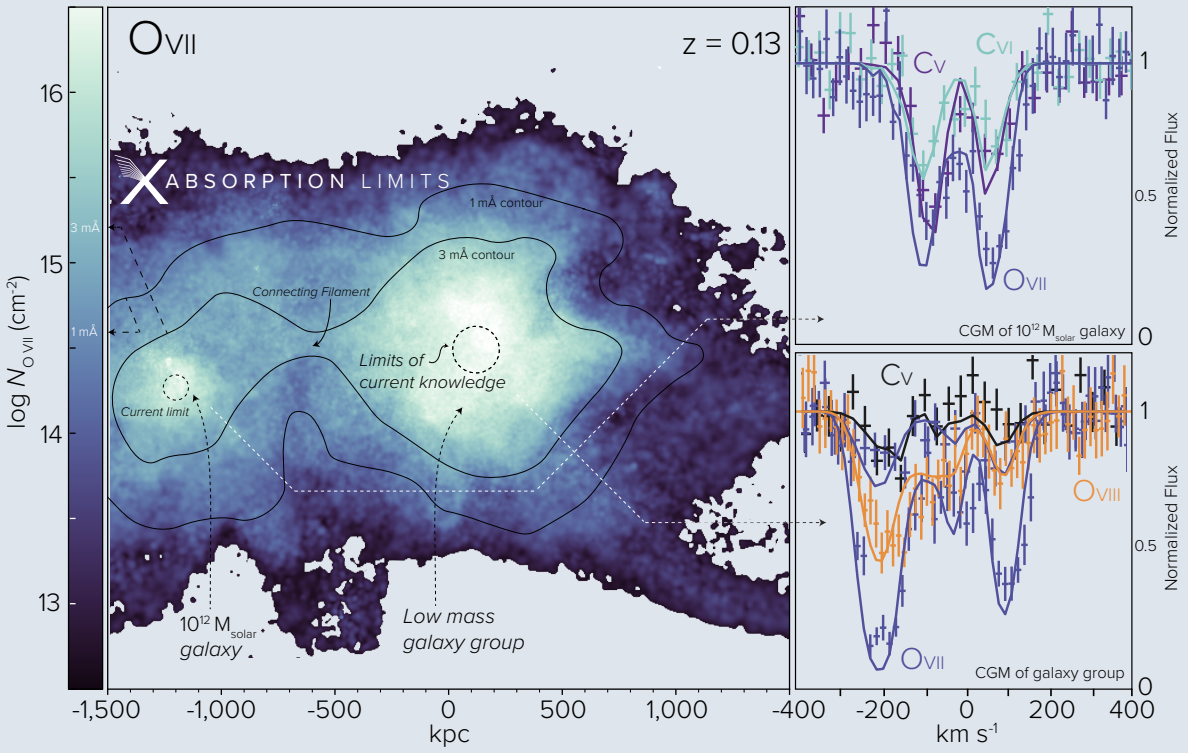

Fig. 2.5— X-ray absorption studies can probe a large fraction of the baryons and most of metals in the Universe, which likely lie near or outside of the virial radius in extended galaxy halos, galaxy groups, and the Cosmic Web. These environments have virial temperatures $\gtrsim 10^{5.5}$ K, so the gas should be observable primarily in the X-rays. However, its density is so low that the gas will be undetectable in emission even with *Lynx*. However, it should be detectable in absorption provided that a reasonable level of metal enrichment has occurred. Breakthrough capabilities of the *Lynx* X-ray Grating Spectrometer (XGS) will enable detection of these reservoirs of hidden metals and mass. Additionally, *Lynx* will be able to quantify hot gas flows, turbulence, and rotation around the Milky Way and external galaxies. (Adapted from [195]).

X-ray spectrographs for intergalactic absorption studies are the *XMM-Newton* and *Chandra* gratings. Their resolving power is lower than this optimal R by more than an order of magnitude. Their collecting area is also far too low: 45 cm^2 and ~ 7 cm^2 for *XMM-Newton* and *Chandra*, respectively. These instruments have nevertheless led to major advances, despite their limitations.

In the near future (2022), a microcalorimeter with a ΔE = 5 eV resolution will be launched on *XRISM*, followed by *Athena*'s X-IFU with 2 eV resolution [197]. X-ray microcalorimeters have approximately constant energy resolution, (ΔE) as a function of energy. Therefore, *XRISM* and *Athena* will resolve the thermal width (~200 km s^{-1}) for high ionization Fe lines at $E > 6$ keV, but below 1 keV (where most X-ray transitions lie) they cannot do so. For example, their resolution is only ~ 300 for O VIII Lyα, which is *worse* than that provided by *Chandra*.

The low collecting area of currently available gratings, and the inability of upcoming microcalorimeters to resolve the thermal width for soft X-ray transitions, has been a primary motivation for adding the X-ray Grating Spectrometer (XGS) to *Lynx*'s revolutionary payload. Available technologies are now approaching the capability to provide a resolving power of R = 7,500 (constant across the soft

X-ray energy band), more than enough to resolve the thermal widths of key lines. New grating technologies also achieve high grating *efficiencies*, so the instrument can provide an effective area large enough to probe hot gas in the lowest density regions of the CGM and Cosmic Web (Fig. 2.4).

***The CGM in absorption with* Lynx** — One approach for a *Lynx* campaign to detect the CGM in absorption will be to observe a sufficiently large sample of bright background AGN whose sightlines intersect halos of lower-redshift galaxies that span a range of masses and impact parameters. Expected temperatures and oscillator strengths imply that O VII and O VIII will be the key ions to observe. Data quality will be high enough to observe the structure of O VII line (e.g., thermal and turbulent broadening, multiple kinematic components, etc.), as well as high enough to clearly detect the O VIII line. The few X-ray absorption lines detected so far [e.g. 198, 199] prove our feasibility calculations, but remain inadequate for anything beyond an initial detection. In terms of equivalent width, these requirements translate approximately into the detection limits for narrow lines of $\lesssim 1$ mÅ.

As discussed further in Appendix A.5 and [200], one can select ~ 100 bright background AGN with a median redshift of $z \sim 0.3$ and extending to $z = 2$ for such a program. More than one absorption system will be measured for most of the sightlines, providing rich sampling of the CGM across a range of masses and impact parameters. Identification will be aided by UV absorption line studies of lower ionization lines (when available) and by optical redshift determinations of the likely host systems. Most of the absorption lines associated with galaxies will come from $z < 0.6$ galaxies with $M > 2 \times 10^{11}\, M_\odot$, based on models [201]. Such galaxies are generally brighter than $m_r = 22$ mag and are therefore already detected in large photometric surveys, allowing for spectroscopic follow-up.

Once absorbers have been associated with hosts, it will be possible to study the properties of the gas in galaxy halos, galaxy groups, and the Cosmic Web. The anticipated quality of data will enable measurements of the column densities and kinematics beyond R_{200} (Fig. A.8 on p. 291). For reference, the Milky Way is currently the only L^* system studied in X-ray absorption, and the absorption is dominated by gas within 50 kpc [182]. Measurements of the infall, rotational, and turbulent velocities of the hot gas, and constraints on its volume filling factor provide direct tests of galaxy formation models and enable a search for hot outflows.

To conduct this survey with a reasonable time allocation (e.g., ~ 5 Msec), an effective area of 4,000 cm^2 for the XGS instrument is required. Such a spectroscopic survey can incorporate the broad science goals of many other science programs, such as those measuring the structure and kinematics of the Milky Way halo (§2.3), studies of the Cosmic Web (§4.4.1), blind surveys of $10^{5.5}$ – $10^{6.5}$ K gas in the Universe, and searches for heavy elements in the CGM and IGM aimed at solving the "missing metals" problem ([184], §4.6)

Lynx will unleash a revolution in observations of the CGM. Its hot component, now predominantly undetected, will be richly mapped around normal galaxies. These observations, augmented by advances in the radio and a continued progress in the UV and millimeter regimes, will expose the missing pieces for understanding galaxy formation.

2.2 Galaxy Winds Powered by Stellar and Black Hole Feedback

Galaxies grow as stars form amid dense clouds of cold molecular gas, and age toward quiescence when this gas is disrupted, expelled from the galaxy, or prevented from forming in the first place (e.g., Somerville & Davé 2015 [202]). At all mass scales, galaxy evolution models now routinely invoke various forms of stellar and black hole energy feedback to reconcile observations with a theory that would otherwise over-predict the size of galaxies and the star formation history of the Universe [144, 145, 203]. The past decade has seen stellar and black hole feedback achieve paradigmatic status in the field of galaxy evolution, yet both remain largely a black box with regards to how, for example, stellar superwinds or AGN mechanical energy might couple to the entropy of the ambient ISM or intracluster medium at low- and high-mass scales (respectively), or how this energy deposition is tied to the fate of cold molecular gas from which all stars are born.

Progress in this vital science will be reliant on a better understanding of the hot circumgalactic and intra(group/cluster) medium, which serves as a fuel reservoir powering the processes that drive them (§2.1). However, *direct* observations of ongoing feedback are required to truly understand the underlying physics. Ultraviolet and sub-mm data, while clearly important, are equivalent to observing only the sparks in a fire. We must now observe and map the *flame*. It is therefore vitally important to spatially map the kinematics and physical conditions of the hot phase of galaxy winds across a wide range in redshift and across decades in the galaxy mass scale, achieving parity with a capability that already exists for the warm ionized and cold molecular gas phases.

2.2.1 The kinematic structure of galaxy winds

Simulations provide guidance that the structure in winds is rich and abundant, containing observables that are fundamental for understanding how these winds operate. Because those structures often subtend ~ an arcsecond even for nearby objects like M82, sub-arcsecond resolution (coupled to very high soft X-ray sensitivity) is needed to enable direct comparison with data from flagship ground-based IFUs like MUSE and interferometers like ALMA at matching spatial scales. The science enabled by such a parity in capability would be entirely transformational for the understanding of galaxy evolution, and capitalize on the discoveries that (e.g.) *JWST*, ALMA, and the Extremely Large Telescopes (ELTs) will make in the decades to come. Sub-arcsecond spatially resolved spectroscopy at ~ 30 km s^{-1} velocity resolution in X-rays will enable these paradigm-shaping advancements along multiple fundamental questions relevant to both stellar and black hole feedback at all mass scales.

One of these major, overarching questions relates to how much energy lies in the winds, where it is deposited, and how this deposition takes place [203]. While both stellar and black hole feedback launche winds that are inherently multiphase, thermalization and coupling efficiency between the wind driver (e.g., clustered supernovae; jets launched by black holes) and the ambient gas is highest for the hot gas [207, 208]. X-ray observations are therefore a direct observation of the bulk of the energy carried by superwinds, and a probe of the most efficient mechanism by which metal-rich gas is transported on galaxy-wide scales and beyond. In addition to the energy budget, these data are also crucial for understanding the physics of wind launching. As an example, the structure of winds launched with and without a significant cosmic ray component can be compared in Figs. 2.6 and 2.7.

Fig. 2.6— A composite of mock *Lynx* and actual *HST* images of M82, the canonical (and first-known) stellar superwind in a galaxy. (*Bottom left*) A GPU simulation, using the CHOLLA Galactic Outflow simulation suite [204], of an M82-like galaxy at 5 pc resolution over a scale of 20 kpc. Colors in the outflow encode its absolute velocity. Figure adapted from work by Schneider and collaborators [205, 206]. (*Bottom right*) A 100 ksec mock observation of the same simulated galaxy with the LXM. The instrument would be capable of resolving the line-of-sight velocity of hot gas in the outflow at ~ 30 km s^{-1} velocity (spectral) resolution on arcsecond scales, an unprecedented leap in current capability.

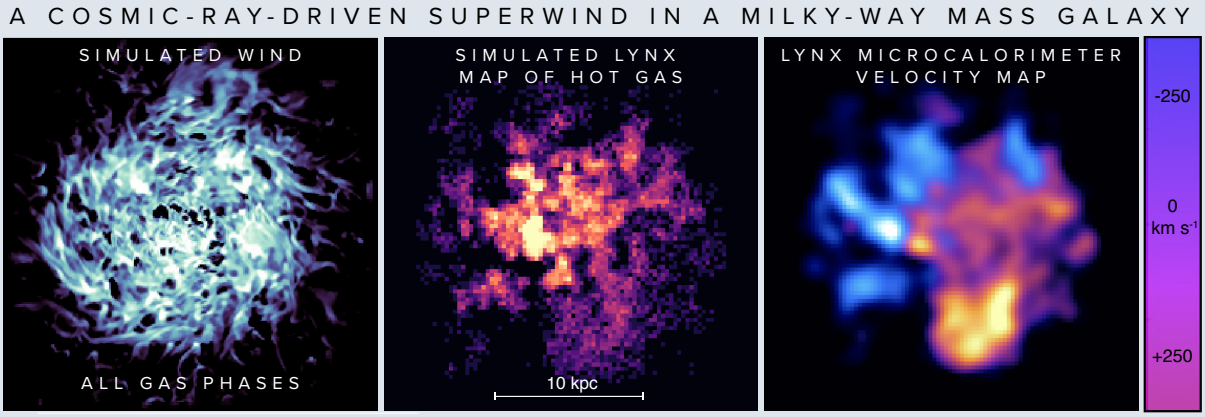

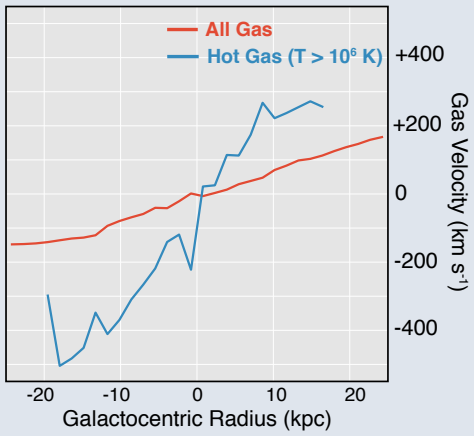

Fig. 2.7— (*Above*) A simulated galactic wind in a Milky Way-mass galaxy, courtesy of Ruszkowski and collaborators, that features cosmic ray advection, streaming, and streaming instability heating of the ISM. The simulation results in major observable predictions that can cleanly discriminate between the outflow model shown in Fig. 2.6, which does not incorporate cosmic ray heating. (*Center*) A mock *Lynx* image of X-ray surface brightness associated with the simulation at left. The *Lynx* microcalorimeter would provide 0.3 eV spectral resolution and 1″ pixel size, resulting in a line-of-sight velocity map for the hot gas like that shown in the top-right panel. Because of coupling efficiency, the velocity profile of the hot phase is clearly distinct from that of the cooler gas phases, as can be seen on the right.

The observable discriminants between these two wind drivers are largely found in the velocity structure, clumpiness of the hot plasma, and how it couples to the cold gas. These signals are mappable only by a sub-arcsecond, high spectral resolution X-ray microcalorimeter in space — a requirement that only the X-ray microcalorimeter on *Lynx* will meet. Such an instrument can also measure the shock strength (and thus wind velocity) at the boundary of the wind and cooler phases of the ISM/CGM. Multiple spatial and spectral resolution elements would be needed across the wind cone to map (e.g.) the iron lines that trace turbulent broadening in the wind fluid (e.g., Doppler b, see also Fig. 2.1), as well as its non-equilibrium ionization. For individual galaxies, shocks heat gas within a few kpc of the nucleus, such that only a sub-arcsecond X-ray telescope can measure the shock strength on scales associated with the nuclear regions of galaxies beyond Virgo. The issue of spatial resolution is similarly important in measurements of the thermalization efficiency across the galaxy mass scale and throughout galaxy disks, as well as the mass loading factor in winds and fountains as a function of galactocentric radius.

2.2.2 The chemical structure of galaxy winds

The CGM and on-going feedback is progressively more difficult to probe in lower-mass galaxies [203], and because hot winds become so tenuous, this is particularly true for the X-ray band. The ability to map galactic winds in the dwarf regime (i.e., galaxies with total masses ~ 10^9 – 10^{10} $M_\odot$)

is nevertheless critical for understanding galaxy formation, given that some mechanism is clearly needed to preferentially suppress star formation in halos less massive than the Milky Way (e.g., [209]) In that sense, *Lynx*'s unique ability to directly observe hot winds and the physics that drive them becomes even *more* important at lower galaxy mass scales.

As an over-pressured fluid, typical wind terminal speeds can easily exceed the escape velocity of a dwarf galaxy [203, 210]. The chemical richness and structure of these winds can further preserve a record of the processes that launch them. Winds that are clearly metal-enriched relative to the local ISM are likely to be driven by supernova ejecta, for example [211], while the opposite is true for a wind powered by black hole feedback. Measuring metal abundance in hot winds is an *exquisitely* challenging observational problem, due largely to their extremely low X-ray surface brightness. Only two such measurements — one in NGC 1569 [212] and I Zw 15 [213] — have successfully been made (both were with *Chandra*). The primary reason for this scarcity is the low X-ray luminosity of the diffuse wind emission *relative to the point source population* in these galaxies. Clean separation of diffuse and point X-ray source components *absolutely requires* sub-arcsecond angular resolution. *Chandra* is the only instrument to have thus far provided this capability, but it suffers greatly from insufficient effective area and relatively poor spectral resolution. The launch of *Lynx* and the LXM would *immensely* advance our ability to measure the chemical composition of winds in low mass galaxies. Until that time, this issue will remain both a critical and urgent observational question.

* * *

The above examples demonstrate *Lynx*'s transformational ability to directly observe feedback across all modes and across all relevant scales, from dwarfs to very massive galaxies in cluster centers. However, the story of feedback and CGM studies with *Lynx* is incomplete without considering what it can do in the galaxy we call home.

2.3 The *Lynx* View of the Milky Way

A completely unique view of both circumgalactic gas and on-going feedback will be offered by *Lynx* observations of the Milky Way. Our galaxy resides in a hot halo that extends at *least* ten kiloparsecs outward, and probably all the way to the virial radius. It is the very nearest example of a CGM. It also contains the nearest example of galaxy-scale feedback in action, as evidenced by the *Fermi* Bubbles. *Lynx*, therefore, has the opportunity to observe a hot halo from a truly unique perspective — from *within* — and enable the first high fidelity map of its kinematic structure. Meanwhile, *Lynx* observations of the *Fermi* bubbles will uncover aspects of galactic-scale feedback that are beyond observability in external galaxies. These observations are discussed below.

The nearest Circumgalactic Medium — The kinematics of the Milky Way's hot halo were first observed using *XMM-Newton* grating spectra of background AGN, which act as bright backlights that place the Milky Way's hot halo in silhouette. The results indicate that the inner hot halo is co-rotating at ~ 180 km s^{-1}, implying that the hot gas within 100 kpc holds as much angular momentum as the total stellar and H I disks [189]. While the observations are still sparse and heterogeneous with the $R \sim 300$ grating spectrometers of *XMM-Newton*, the results carry extraordinary implications for the Milky Way's evolutionary path toward a Grand Design Spiral morphology, as well as for how it accretes

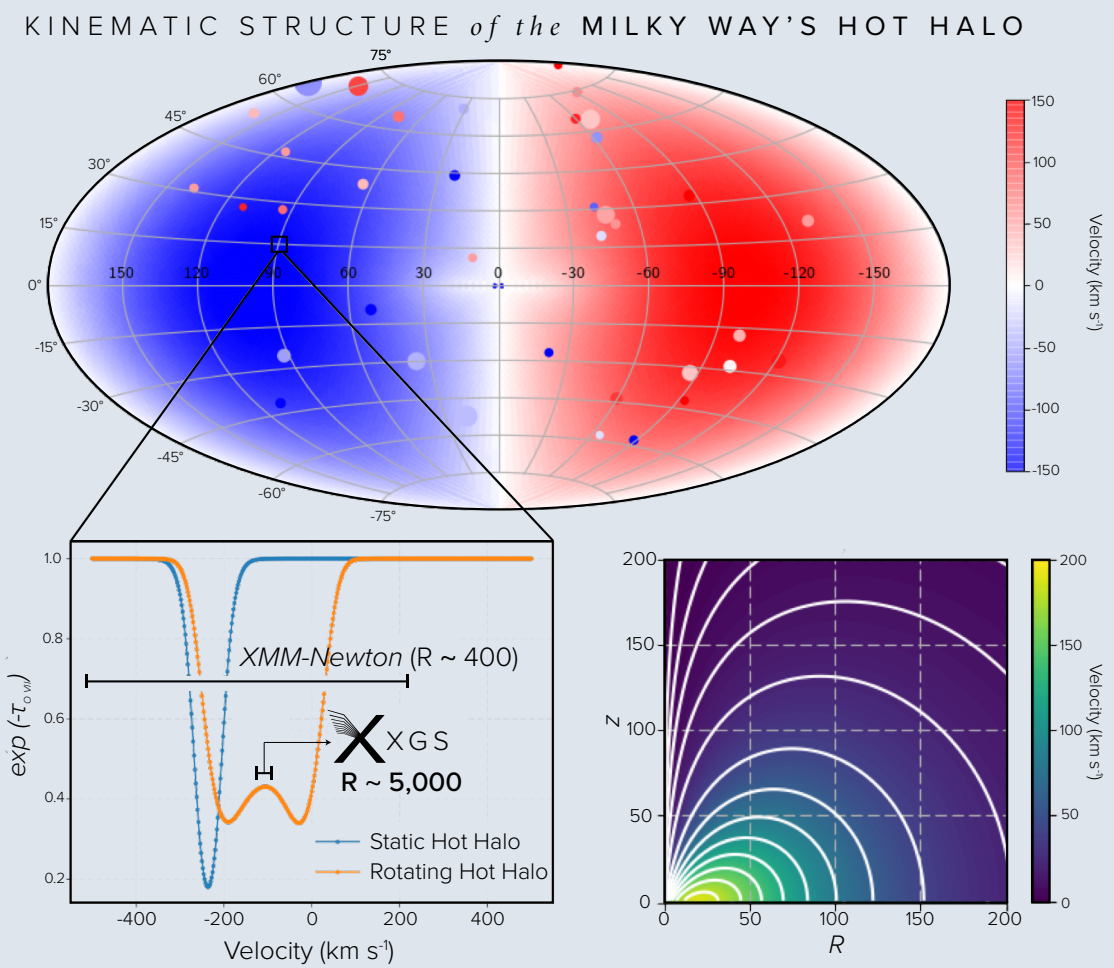

Fig. 2.8— *Lynx* will open the Milky Way's hot halo to tomographic mapping via absorption line spectroscopy toward thousands of AGN/QSOs. (*Top*) Data points from the *XMM-Newton* sample compiled by Hodges-Kluck et al. 2016 [189], where the color of each point indicates centroid velocity and the size is O VII strength. These are overlaid on a velocity map from the favored rotating hot halo model from Sormani et al. (2018) [214]. (*Bottom left*) *Lynx* X-ray grating spectroscopy is necessary to resolve the detailed velocity structure needed to distinguish a static hot halo (blue) from a rotating hot halo model (orange). (*Bottom right*) The dynamically stable rotating halo model predicts a co-rotating inner halo, giving way to a mostly static outer halo. These and other non-static hot halo models with kinematics including rotation promote the formation of high-velocity clouds observed in the UV, which supply the Milky Way with fuel for continued star formation [215]. Existing observations of the Milky Way's CGM cannot be fully understood without X-ray observations from a facility as powerful as *Lynx*.

material from the CGM to fuel present-day star formation. State-of-the-art simulations like EAGLE show that co-rotating hot halos are quite typical [216], and correlate with spiral morphologies and stellar disk sizes [217]. Dynamic hot halo models [214, 218] show that rotation promotes [189, 215] formation of cool-warm ($T \sim 10^4 - 10^5$ K) high-velocity clouds (HVCs) that are best observed in the UV [219, 220].

The *Lynx* gratings will provide a factor of ~ 1,500 higher spectroscopic power (i.e., effective area times spectral resolution) compared to the current state of the art for MW halo studies (brought

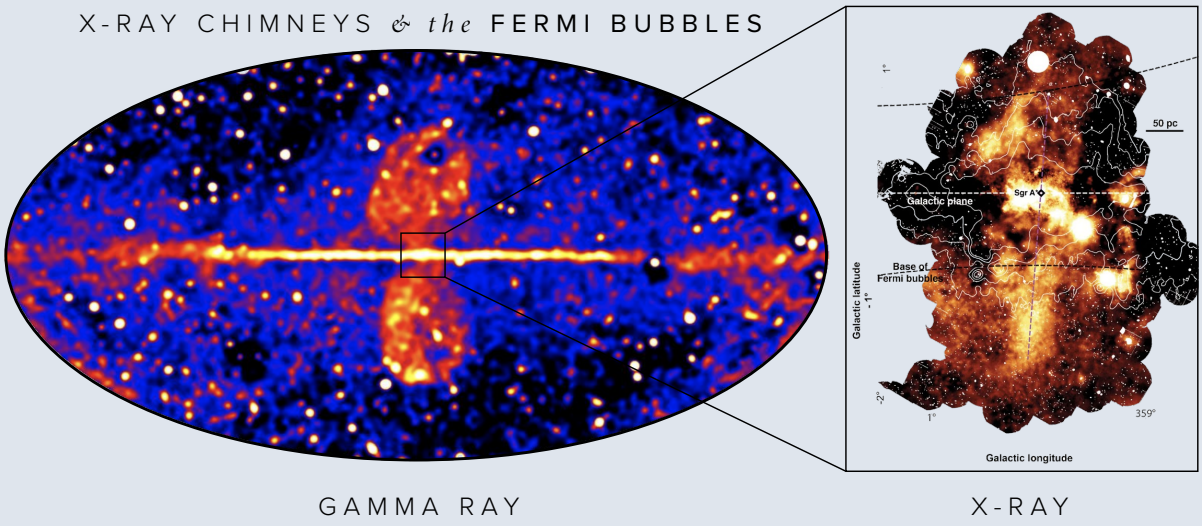

Fig. 2.9— (*Left*) Hardness ratio of the *Fermi* LAT all-sky map of the > 100 MeV sky including 8 years of observations [221]. The *Fermi* bubbles are clearly visible, extending thousands of light years above and below the Galactic Center. (*Right*) X-ray observations of the galactic center [222], showing the X-ray "chimneys" which potentially feed the bubbles. The angular resolution, spectral resolution, and sensitivity of *Lynx* are required to discern the chemical and kinematic properties of these structures.

by the RGS instrument aboard *XMM-Newton*). *Every* extra-galactic spectroscopic target observed by *Lynx* will provide a R = 5,000 measurement of the O VII absorption line from the Milky Way's halo, providing not just velocity centroids, but also exquisitely resolved line profiles, as shown in Fig. 2.8. Using this in combination with other lines (O VIII, Ne IX, C V, C VI), *Lynx* will create an exquisitely detailed thermal-kinematic map with sightlines scattered across the entire sky. The LXM high resolution array, meanwhile, will provide a lower spectral resolution ($R \sim 2{,}000$ for O VI) but much higher throughput complimentary observation, enabling measurements along a far larger number of sightlines, if needed. These data will enable the creation of three-dimensional tomographic models that will reveal the structure, stability, and evolution of the Milky Way's hot halo.

The nearest example of AGN feedback: the Fermi Bubbles — Originally discovered as a faint haze and then a sharp-edged excess of gamma ray surface brightness in all-sky maps from the *Fermi Gamma Ray Observatory*, these bipolar plumes of high energy particles, symmetric about the Galactic center, extend 10 kpc above and below the plane of the Milky Way ([223, 224] and Fig. 2.9). These bubbles are driven either by nuclear star formation (e.g., [225, 226]) or even a past epoch of AGN activity by accretion onto Sgr A* (e.g., [227]).

The *Fermi* Bubbles are the setting for studying physical processes relevant to galactic feedback with a level of detail impossible in other galaxies. Archival maps from *XMM-Newton*, *Chandra*, and *ROSAT* reveal X-ray "chimneys" (Fig. 2.9, right panel) extending from the inner parsecs of the galaxy to the base of the *Fermi* Bubbles, serving as potential exhaust channels for the transport of energy and mass to the kpc-scale structures [222]. Future observations with *XRISM* and *Athena* will enable

measurements of heavy element abundance in the bubbles, helping to discriminate between the competing nuclear star formation and black hole activity models that seek to explain their origin [228]. Line-of-sight velocity profiles can provide additional constraints on both the bubble's origin and their energetics, but a *great* many unanswered questions as to the *Fermi* Bubbles' true nature requires X-ray mapping to extremely faint surface brightness levels. How, for example, is energy channeled through the apparent X-ray "chimneys" and further into bubbles? How do the *Fermi* Bubbles interact with the CGM and ISM of the Milky Way? The observations needed to answer these questions will be impossible with low angular resolution X-ray telescopes, particularly in the very crowded regions of the Galactic Center and MW Bulge, due to confusion with discrete sources (see, for example, a clear illustration of this challenge in [229]). *Lynx* will have the combined sensitivity and angular resolution needed to isolate the diffuse emission component, reaching surface brightness levels 1–2 orders of magnitude fainter than any current or future X-ray mission (see Appendix A.5). *Lynx* can do this with both the HDXI and LXM instruments, and while the latter would cover a smaller angular region on the sky per pointing, it will enable detailed kinematic and chemical mapping of the bubble gas.

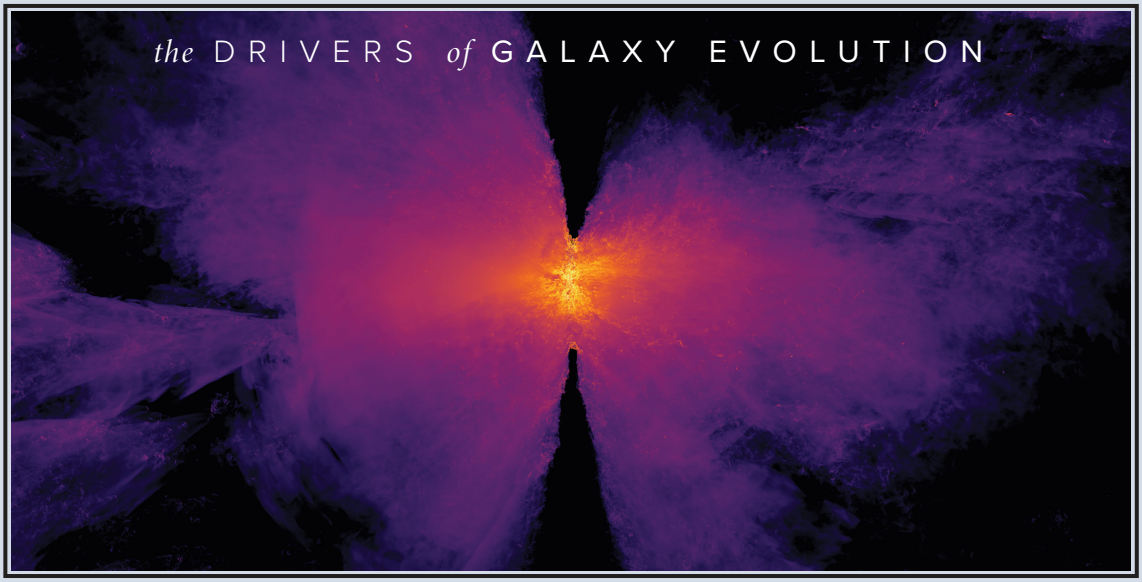

X-ray surface brightness of a starburst-driven wind in an M82-like galaxy, simulated with the Cholla GPU-based hydrodynamics code.
Credit: E. Schneider & Collaborators

Ultraviolet, optical/infrared, and sub-mm data on galactic halos and feedback at galactic scales are equivalent to observing the sparks in a fire. We now need *Lynx* to observe and map the flame itself.

3 *The* Energetic Side *of* Stellar Evolution *and* Stellar Ecosystems

Investigating the fundamental aspects of stellar structure and evolution has been an essential cornerstone of 20th century astrophysics with NASA's Great Observatories. Their phenomenal success has expanded the field of stellar astrophysics, as new discoveries challenge our understanding of this fundamental process.

Observations of star-forming regions are among the most challenging in modern astronomy. These regions are very crowded, with two-dimensional source densities exceeding 100 pc^{-2}, while their dynamic range is large, with pre-main sequence brown dwarfs residing in the vicinity of massive O stars. The overall range in stellar luminosity can easily cover 20 M_V. Furthermore, these regions are often filled with hot gas which creates spectroscopic difficulties, as well as cold dust that complicates the interpretation of the observed data and obscures some objects completely. While NASA's Great observatories have focused on many of these complex regions, discoveries have been restricted to the nearest ones due to limited sensitivity and spectral resolution.

Lynx is uniquely capable of addressing several open questions in star formation. A complete census of star-forming regions in X-rays, combined with well matched IR data, will advance our understanding of disk survival times and dissipation mechanisms. In addition, *Lynx* will enable direct observations of the effects of X-ray irradiation on circumstellar grain growth to compare with grain evolution models in both high- and low-UV environments. X-rays are native to stars at all phases of star formation and affect planet-forming disks, especially through flares. X-rays trace magnetic fields which weave through the flares, providing a unique, non-gravitational feedback mechanism between disk and star. Moreover, the bright X-ray emission emanating from the hot plasma associated with massive stars can have large scale impacts on the topology of star-forming regions and their interface with the ISM.

A furthering of research in stellar magnetic activity is necessary to understand the fundamental processes controlling observable quantities, which is a necessary first step in gauging their impact on stellar ecosystems, including potentially habitable planets. As summarized in the National Academy's Committee on the Astrobiology Science Strategy for the Search for Life in the Universe:

> *Indeed, because the host star has a significant impact on planetary habitability, and the star's activity and luminosity evolve considerably, it will be important to determine and observe stellar activity indicators in systems of all ages and to understand evolutionary pathways, particularly for M-type stars, to feed back into the overall picture of the evolution of habitable terrestrial planets.*

X-ray spectroscopy with *Lynx* can uniquely address a number of open questions in stellar magnetic activity. The answers to these questions are important for stellar astrophysics, but also have important implications for for where planets form and whether they are potentially habitable. In the coming decades it will be important to understand the interplay between stars, planets, and planetary systems to make progress in the Search for Life. New observing capabilities are required to go beyond the several tens of normal stars which *Chandra* has gathered at high spectral resolution over its two

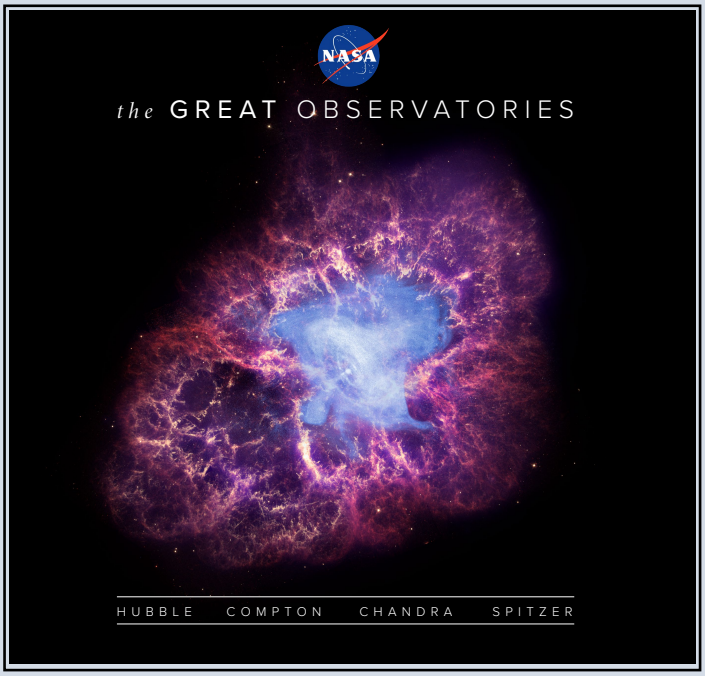

A new understanding of the birth, life, and death of stars counts as one of the everlasting triumphs of the NASA's Great Observatories program. *Lynx* will build upon this grand tradition. *By itself*, it will revolutionize wide swaths of stellar astronomy. Yet its greatest strengths will manifest themselves through multiwavelength synergies with the flagship facilities of the future.

decades of operations. Specific stellar astrophysics questions include: what controls accretion and magnetic activity in young stars? what factors control the coronal emission of stars? how do the characteristics of stellar flares and winds change with time?

Lynx will also provide a new window onto stellar death. Supernovae (SN) play an essential role in the Universe. Metals synthesized during the explosion chemically enrich galaxies, supplying fodder for dust and the next generation of stars. Their shock waves plow through the ISM for thousands of years, accelerating particles to extreme energies (~10^{15} eV) and amplifying magnetic fields up to a thousand times that of the ISM. These shocks also heat surrounding gas and impart momentum, altering the phase structure of the ISM, shaping galaxies, and driving kpc-scale galactic winds.

Supernova remnants (SNRs) offer the means to study SN explosions, dynamics, and shocks at sub-parsec scales. X-ray observations probe the hot metals synthesized in the explosion and the TeV electrons accelerated by the shocks, and thus are key to testing recent, high-fidelity three-dimensional SN simulations. X-ray imaging spectroscopy at arcsecond scales, uniquely possible with *Lynx*, will revolutionize SNR science, offering a three-dimensional view of metals synthesized in explosions and enabling SNR population studies in Local Group galaxies. *Lynx* will also provide an unparallel view of shocks and energetic particle acceleration in SNRs (§4.10).

Properties of X-ray binary (XRB) populations provide another avenue for studies of the end points of stellar evolution and the evolution of binary stellar systems. A complete census of XRBs requires that we study populations of these objects in external galaxies. However, even in M31 (780 kpc away), a full range of XRB luminosities is barely accessible with *Chandra*. In other nearby

massive galaxies, no existing X-ray telescope can probe down to $L_X \sim 10^{34}$ erg s^{-1} required to sample a full distribution of XRB accretion states. *Lynx* will bridge this gap and provide the needed sensitivity for observations throughout the Local Group, and well beyond it for brighter objects.

3.1 Understanding Star Formation in the Milky Way

Understanding the fundamental aspects of star formation and evolution has been a major success story for multiwavelength astronomy. Infrared (IR) space-based missions (*Herschel*, *Spitzer*) have been critical in identifying young stellar objects (YSOs) with excess emission from circumstellar envelopes and disks. Modern ground-based instruments (ALMA, Gemini/GPI, VLT/SPHERE, Subaru/HiCIAO) are capable of resolving circumstellar disks around nearby young stars at AU spatial scales. They have revealed unprecedented view of disk structure and ongoing planet formation. In the near future, *JWST* will provide a remarkable view of these systems in the mid-IR. The IR indicators of stellar youth are limited to ages less than the disk dissipation timescale, ~ 3–5 Myr. X-ray observations identify young stars by completely independent fingerprints that last tens to hundreds millions of years, covering a wide variety of stellar masses and environments.

Young stars are ubiquitously bright X-ray sources. X-rays in lower-mass stars originate from the corona, which has its origin at the dynamo. Modeling based on recent data indicates that the dynamo takes different forms depending upon the mass of the star [231]. For the most part, X-ray luminosity is seen to decrease with age following a power law, $L_X \propto t^{-0.5}$ [232]. This decrease is driven by the convective turnover rate and indicates that late M stars have elevated X-ray fluxes for up to 5 billion years [233]. This long-term X-ray luminosity allows the identification of young stars long after they lose their dust disks but before they evolve onto the main sequence. In one simple example, Kuhn et al. [234, 235] find that *Chandra* typically identifies a factor of ~ 2 more young stars than the IR-excess sources detected with *Spitzer*.

For low-mass stars in the accretion phase, X-ray emission associated with accretion shocks are observed and specific X-ray line ratios act as temperature and density diagnostics. These measurements allow direct inference of the infall rate and constraining mechanisms [236]. This phase is also associated with enhanced flaring in which 100 MK long-lived flares are likely responsible for rapid heating of protoplanetary disks and can have deleterious effects on young planets. Moreover, X-ray emission in general impacts circumstellar disk chemistry [237] and eventually disk dispersal [238].

For high-mass stars, most of the X-ray energy originates from wind shocks and wind-wind collisions. The winds interact with the ISM, depositing thermal energy and creating turbulence (e.g., Mac Low & Klessen [239]). This turbulence inhibits other ongoing star formation.

Multiwavelength studies of clusters such as the Orion Nebula with well-matched observatories are extremely powerful. They offer a complete view of the star-formation process and its relation to the ISM [240–243]. In particular, X-rays are crucial to probe highly embedded sources, which have unique X-ray signatures. This is demonstrated by direct X-ray detections of protostars [244] as well as the detection of 6.4 keV iron fluorescence, which is from circumstellar disk material being irradiated by stellar flares and exciting iron fluorescence [245]. Consequently, it is possible to apply the reverberation mapping technique, used in studies of active galactic nuclei, to resolve AU-scale details on stellar disks that are several kpc from the Sun.


RCW 49 & Westerlund 2
4.2 kpc away
Spitzer
15 arcmin (60 ly)
Westerlund 2
HST + Chandra
15 ly
Westerlund 2
412 pc away
1 ly
Orion
412 pc away
1 ly

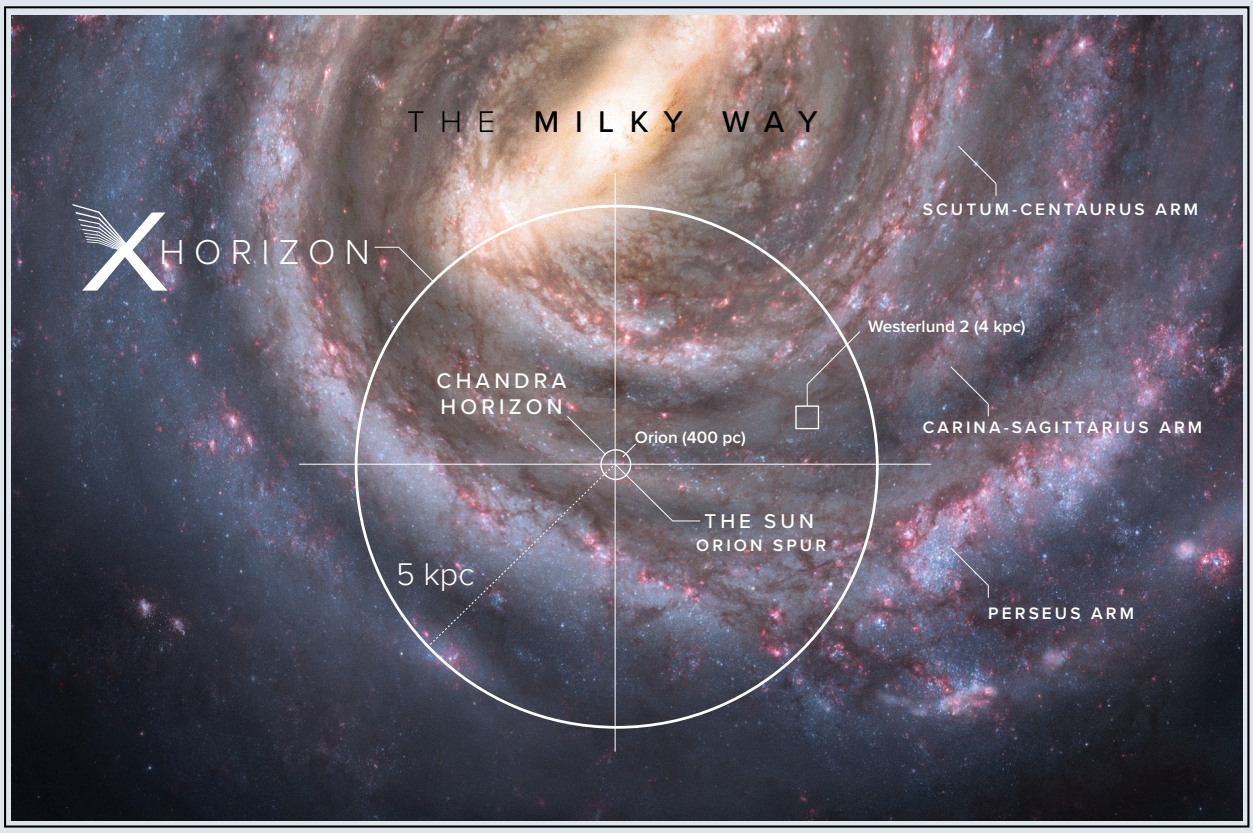

Fig. 3.1— Sensitive X-ray telescopes are indispensable tools for finding young stars and observing the earliest stages of star formation. Similar to our Sun, X-ray emission from young stars (t < 600 Myr) is generated in their active coronae powered by magnetic dynamos. Unlike our Sun however, young stars are brighter in fractional X-ray luminosity, $L_X/L_{\rm bol}$. For pre-main sequence stars, $L_X/L_{\rm bol} \sim 1{,}000 \times L_{X,\odot}/L_{\rm bol,\odot}$. Their bright X-ray emission is capable of piercing through dense molecular clouds. The *Spitzer*, *HST*, and *Chandra* image of Westerlund 2 (*facing page*) illustrates the great potential of multiwavelength studies of a young star forming region. The *Spitzer* IR image (*top*) shows the Westerlund 2 star cluster embedded in the RCW49 nebula. The *middle* panel shows the star cluster itself, as viewed by *Hubble* and *Chandra*. Optical images (green and blue) reveal patchy thick clouds where stars are born. *Chandra* (*purple*) detects dozens of young stars in this ~ 2 Myr old star-forming region [230], and reveals hot plasma which interacts with molecular clouds — the local feedback in action. While the X-ray emission is perhaps the best way to find young stars in regions such as Westerlund 2, the sensitivity of *Chandra* is only sufficient to probe the full stellar mass range in a single region, the Orion Nebula Cluster. In Orion (d = 410 pc), *Chandra* is sensitive down to a mass scale of ~ 0.02 $M_\odot$ while in Westerlund 2 (d = 4.2 kpc), it only reveals the tip of the mass functions (cf. images in the *bottom* panels). *Lynx* will expand our X-ray view of young star forming regions in the Milky Way by an order of magnitude (*above*). It will reach into the Carina-Sagittarius, Perseus, and Scutum-Centaurus arms, observing a large number of star forming regions with a wide range of ages, masses, and star formation rates. For brighter objects, *Lynx*'s high-resolution spectroscopic capabilities will enable characterization of X-ray emitting plasma temperatures, electron densities, coronal abundances, and intervening absorbing columns. These observable quantities provide direct constraints on stellar magnetic field activity, circumstellar disk geometry and chemistry, stellar chemical evolution, mass accretion and mass loss, and planet formation and habitability.

For *Chandra*, the Orion Nebula Cluster is the only massive cluster close enough ($d \sim 400$ pc) for detailed studies in the full stellar mass range. While clusters further away have been observed (the furthest being NGC 1893 at 3.6 kpc), the evidence is clear that *Chandra*-generated samples quickly become incomplete at distances beyond Orion [234, 235]. The limiting factor for *Chandra* is low effective area. *Athena* will dramatically improve the throughput but will be source-confused in Orion's core. Because of its angular resolution limitations, *Athena* will be incapable of detailed studies in star clusters beyond Orion's distance. All other X-ray missions under development are even more limited by angular resolution. Extending the horizon of sensitive X-ray studies beyond the Orion Nebula Cluster, which is uniquely possible with *Lynx*, is crucial for the future of the field.

The Orion Nebula is only one cluster. Many studies need a statistical approach, and fundamentally require observations of more than one object. For example, constraints on circumstellar disk survival times, a crucial factor to halt planet formation, were obtained for a small number of clusters within 1 kpc of the Sun [246]. This work needs to be extended to more distant and/or more massive clusters, naturally leading into the study of "transition disk" [247, 248] timescales. The increased statistics of well-observed clusters will enable studies of how high-energy illumination affects dust grain growth [249], and how hot plasma interacts with the colder ISM and dust ([250, 251], Fig. 3.1). The X-ray based census of stellar clusters as an additional advantage of being insensitive to the interstellar dust and ionized emission around young stars that limits, e.g., *Gaia*'s ability to map even the closest clusters near the Galactic plane.

Requirements — Sensitivities reaching to X-ray luminosities of $L_X = 10^{27}$ erg s^{-1} are needed to probe the stellar mass range down to $\sim 0.1\,M_\odot$. This translates to flux limits of $f_X = 1.3 \times 10^{-18}$ and 3.3×10^{-19} erg s^{-1} cm^{-2} at distances 2.5 and 5 kpc, respectively. These limits are achievable in 100 ksec to Msec-class exposures (§A.3). The requirements on angular resolution are even more demanding. The X-ray luminosity function of young stellar objects in the Orion Nebula is flat near the faint end of the observed range [252]. The confusion limit for a 0.5″ PSF in this case (Appendix §A.1) corresponds to a source density of 5.5×10^6 deg^{-2}, or 40× the observed peak density in the Orion Nebula [252]. Therefore, a star cluster similar to the Orion Nebula will be unaffected by source confusion in *Lynx* observations out to $D \approx 2.6$ kpc. At $D = 5$ kpc, it will still be unaffected by confusion outside of the cluster core (0.13 pc). The effective horizon for *Lynx* observations of young star forming regions in the Milky Way, in terms of sensitivity and spatial resolution, extends to ~ 5 kpc, and that 0.5″ PSF is required to avoid confusion in the cluster cores.

* * *

Lynx will fundamentally change the X-ray view of star formation, keeping pace with expected improvements in technology at other wavelengths. The LXM pointings to clusters such as Orion will yield enough signal for ~ 1,000 stars to detect critical temperature and density sensitive lines. Sensitive imaging will be possible to much greater distances than the Orion Nebula. Surveys complete to $M_\star \sim 0.1\,M_\odot$ could be carried out on clusters such as Carina (2.4 kpc), NGC 281 (2.1 kpc), NGC 3603 (6.9 kpc). The effective "horizon" for such surveys will be extended into the Carina-Sagittarius spiral arm, giving immediate access to a large number of star forming regions spanning a wide range of masses, star formation rates, and ages. Less detailed, but still rich, datasets can be generated for clusters in the Magellanic Clouds, such as 30 Doradus (50 kpc).

3.2 Fundamental Physics of Stellar Coronae, Accretion, and Winds

Plasma heating and the processes occurring in the coronae of stars are of fundamental importance in understanding the physics of stellar surfaces and their outer atmospheres. Decades of study by high-energy satellites have revealed the ubiquity of stellar coronae around stars on the lower half of the stellar main sequence. Even on our well-studied Sun, the origin of this hot plasma is not settled, though it is clear that X-ray/Extreme Ultraviolet (XEUV) emission impacts planetary atmosphere evaporation [253]. Stellar magnetic properties (global magnetic field distributions, coronal levels, and variability) cannot be predicted based solely on fundamental stellar parameters [254]. Instead, because magnetic activity signatures are produced as the result of magnetic reconnection (an inherently nonlinear process), an observational approach is needed. While we have one spectacularly well-studied star, it is a singular case observed at one point in its 4.5 billion year-old history. Recent evidence even indicates that its magnetic activity cycle may not be representative of other solar-like stars, further underlining the need to study magnetic signatures in other stars.

High-resolution X-ray spectroscopy can uniquely address a number of open questions in stellar magnetic activity. The answers to these questions are important for stellar astrophysics, but also have implications for exoplanet habitability. In the coming decades it will be important to understand the interplay between stars, planets, and planetary systems as a way to make progress in the Search for Life. Table 3.1 summarizes the stellar astrophysics questions, measurements needed to answer these questions, instrument capabilities that would enable these measurements, and the implications of the answers for exoplanet habitability studies.

3.2.1 What controls accretion and magnetic activity in young stars?

X-ray emission in young (pre-main sequence) stars is more complex than for sources on the main sequence. There is a significant excess of soft emission in accreting sources [268], which are surrounded by accretion disks. This emission is usually attributed to a shock where the magnetically funneled accretion stream impacts the stellar surface. Since the shock occurs at higher densities than typically found in the corona, high-resolution X-ray spectroscopy can be used to disentangle the shock and coronal components. However, in TW Hya (the only young star density diagnostics for several elements and temperatures can be robustly studied using current instrumentation), the distribution of densities cannot be explained by the current accretion models (Brickhouse et al. [236]). To pursue this question, line flux ratios need to be measured from different elements in different ionization stages. An effective area an order of magnitude higher than *Chandra*/HETG would allow a sample size of a few dozen targets, but ultimately kinematic components in the lines need to be resolved to distinguish accretion flows, static coronal structures, and outflows (Fig. 3.2).

Young stars not only accrete mass, they also gain angular momentum. The magnetic coupling of the accretion streams to the disk provides an energy reservoir that can power X-ray/Far-UV (XFUV) emission. This emission can penetrate deep into the disk and alter the chemistry in regions where planets are building up. The magnetic connection also allows the star to launch outflows, spin up or down, and provide feedback to the inner disk region, potentially changing the disk lifetime and thus the time that planets have to form.

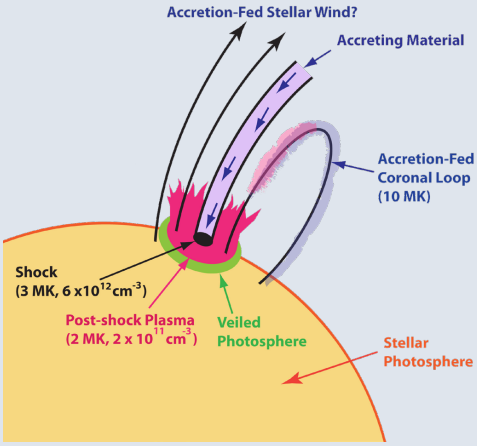

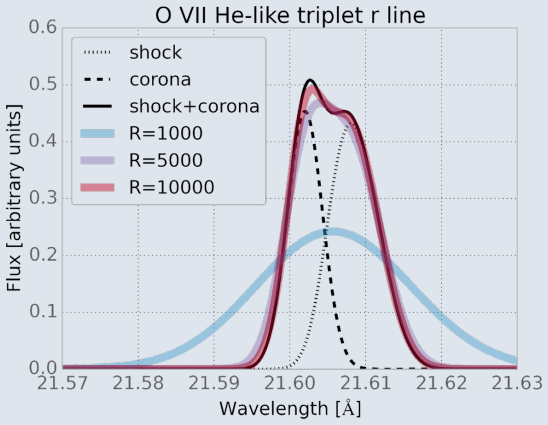

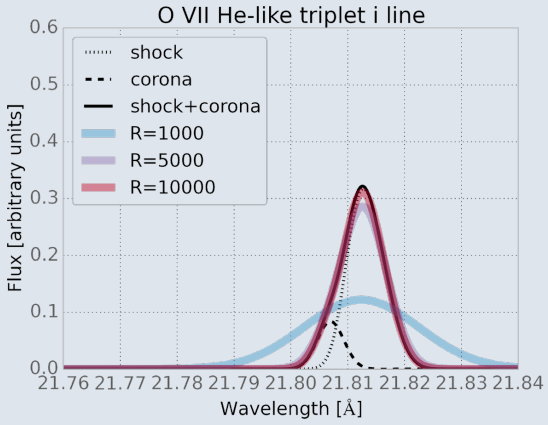

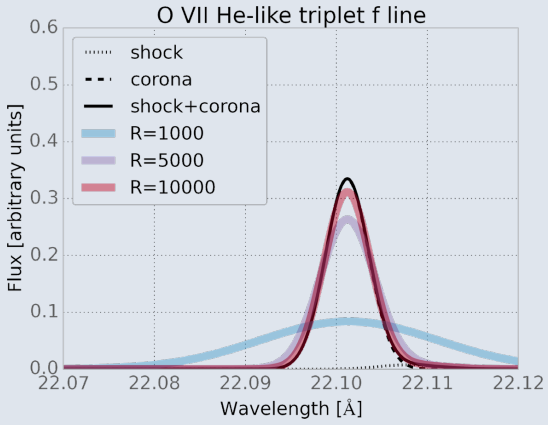

Fig. 3.2— The magnetically funneled accretion model is a standard component of the accepted picture of evolution of low-mass stars. Magnetically controlled accretion onto solar-type stars occurs in the first ~ 10^7 years after the star's birth. During this time, the stellar magnetic field and ionizing radiation are key factors in the protoplanetary disk dynamics. They drive the accreting material onto the star and enable instabilities in the disk which catalyze the build-up of planetary cores. Stellar rotation is regulated by interaction with the inner disk through magnetic field lines and though outflows which can remove angular momentum.

In the standard scenario, the stellar dipolar magnetic field truncates the inner disk radius (at ~ 5 stellar radii) and controls the flow of material toward an accretion spot. This material reaches supersonic speeds and produces a shock near the stellar surface. The shocked plasma initially reaches ~ 3×10^6 K temperatures. It then flows into the stellar atmosphere, radiatively cools, and recombines. UV and OIR signatures of the heated stellar atmosphere below the shock provide estimates of the mass accretion rate. However, X-rays provide the only direct measurements of the shocked material itself [255, 256].

The story told by currently available X-ray data is more complicated than expected in the simple model. Not all systems show the presence of hot gas at high densities [257, 258]. O VII fluxes are higher than what is expected from the radiatively cooling plasma column [259]. Derived accretion rates are usually lower than those determined from OIR data [260] (but see also [261]). In TW Hya, the derived shock structure is inconsistent with the expectations of the accretion column model [256]. However, a crucial caveat for assessing all these discrepancies is that the shock emission can be mixed with the coronal emission and can be affected by absorption from the pre-shocked gas. Other possible effects have been proposed, including emission line opacity [262], absorption by the stellar chromosphere/photosphere [263], dilution of the dipole field near the stellar surface by higher multipole field components [264, 265], and additional coronal heating by the shock itself [256]. Clean measurements of the shock emission require radically better data quality (statistics, spectral resolution), which are impossible to obtain now, but are fully feasible with *Lynx*. *Lynx* will enable entirely new diagnostics of the accretion flow, e.g., the separation of the coronal and shock components in the velocity space *(e.g., spectra shown on the right, based on shock models from [266])*. Velocity-resolved measurements in multiple series of lines from the same ion species will provide absorption column measurements for different velocities, thus constraining the structure of accretion flow. The *r* line contains both shock and coronal emission, and the *Lynx* XGS will easily see this as a broadened line. The *i* line is dominated by the dense accretion shock and is thus redshifted, while the *f* line is dominated by the corona and is observed at its rest wavelength. For TW Hya, these measurements will be time-resolved, allowing one to track the blobs of material falling onto the star on time scales of hours.

Image credit: Brickhouse et al. [256] and Günter et al. [267].

Pushing down in mass scale: magnetic activity in brown dwarfs — To understand what role convection and other factors play in controlling stellar magnetic activity, it is useful to push down in mass scale: below the fully-convective limit in M-dwarfs ($M < 0.35 M_{\odot}$) and further down to the brown dwarfs (BD) regime. Magnetic activity of BDs is not only of fundamental astrophysical interest, but is also important for understanding the possible influence of magnetic star spots in the interpretation of surface features on BDs generally interpreted as clouds.

X-ray observations of BDs indicate changes in the activity pattern at the very low range of stellar masses. Young BDs have been detected in sensitive X-ray surveys of young star-forming regions. These objects are still in the contracting phase. They have a higher luminosity and earlier spectral type than mature, fully-contracted objects, and their X-ray behavior is similar to M dwarfs of a similar spectral type. However, the detection of a flare on the 500 Myr old BD LP 944-20 [269] demonstrated that mature BDs host relatively strong, persistent magnetic fields that at least occasionally dissipate stored magnetic energy through magnetic reconnection. LP 944−20 also shows an extremely low quiescent L_X/L_{bol} ratio despite its fast rotation, which puts it severely out of line with fully-convective and earlier M dwarfs [270]. There is evidence [271] for an anti-correlation between rotation and X-ray activity in BDs, in addition to a large scatter in L_X/L_{bol} at a given rotation rate. BDs are also over-luminous in radio by factors of 100 compared with their X-ray output [272].

Further progress is stymied by the X-ray faintness of BDs. All but the closest are generally too faint to be detected by *Chandra*. A *Lynx* survey of BDs will increase the sample of objects by orders of magnitude and address fundamental outstanding questions in BD magnetic activity. *Lynx* will reveal how the energy is partitioned between plasma heating and particle acceleration, how dynamos work in the regime between stars and giant gas planets, and help to understand how magnetic dissipation works in the near neutral atmospheres of BDs.

3.2.2 What stellar factors control coronal emission?

Changes to the quiescent coronal emission of stars occur over both evolutionary and shorter timescales. The well-known stellar activity-rotation-age relationship can roughly predict a star's X-ray emission, given its age and internal structure [274]. The star's magnetic field creates an ecosystem, which helps set the environment that planets (and life) experience [275]. Changes in the star's X-ray to EUV luminosity with time directly affect erosion of planetary atmospheres [276]. Stellar magnetospheres influence the inner edge of the traditional habitable zone [277]; thus a fine-grained approach to understanding the structure of stellar magnetospheres and their influence on conditions for habitability is required. Recent studies have demonstrated that stellar twins are not magnetic twins: stars with essentially identical stellar ages, masses, radii, and rotation periods have different large-scale and local magnetic field topologies [254], and consequently differing levels and amounts of X-ray variability. X-rays trace magnetic structure directly, provide the "ground-truth" to compare with extrapolations of photospheric magnetic field structures, such as from Zeeman Doppler Imaging (e.g. [278]) or dynamo simulations (e.g. [279]). Figure 3.3 shows the different impact of magnetic field configurations — whether compact or evenly distributed, and the associated scale heights — which can be discerned in velocity space for a binary system given sufficient counts and spectral resolution. Stellar atmospheres are multi-temperature and multi-density, spatially structured, turbulent, dynamic, and contain multiple abundances. Understanding this complexity requires high spectral

Table 3.1— Stellar X-ray spectroscopy informs stellar and planetary studies.

Science question	Measurements needed	Capabilities required	Implication for habitability
What controls accretion & magnetic activity in young stars? §3.2.1	DEM, n_e, N_H, abundances of coronae as function of stellar age, mass, accretion/activity levels	$\lambda/\Delta\lambda > 2{,}000^*$; λ coverage 10–60 Å	Heating timescale of protoplanetary disks, where planets form, migrate
What factors control the coronal emission of stars? §3.2.2	Broad temperature constraints for DEM analyses as a function of age, rotation, $T_{\rm eff}$, magnetic geometry	$\lambda/\Delta\lambda > 2{,}000$; λ coverage 1–40 Å	Energy balance in corona, extrapolation into XEUV, planetary atmosphere irradiation
	Density constraints at multiple temperatures	$\lambda/\Delta\lambda > 2{,}000^*$	Energy balance, characteristics of magnetospheric structures
	Coronal length scales	$\lambda/\Delta\lambda > 5{,}000$ for line broadening	Influence of stellar magnetosphere on habitable zone
How do the characteristics of flares change with time? §3.2.3	Systematic variation of $T_{\rm max}$, $E_{\rm flare}$, $L_{X,\rm max}$ on flares and distributions of flare energies of stars with varying mass, age, magnetic configuration	$<$ 5 eV spectral resolution at $E > 2$ keV; $\sim$ 1 day-long observations with few interruptions	Individualized approach to determining likely planetary atmosphere evolution
	Influence of energetic particles	$\lambda/\Delta\lambda > 5{,}000$ for line broadening & shifts	Space weather, potentially enhanced planetary atmosphere erosion
How do stellar winds change with time? §4.8	Detect charge exchange emission to constrain $\dot{M}$ from a steady wind for the nearest stars	0.5″ spatial resolution	Impact on exoplanet conditions, updated stellar astrophysics
	Study stellar coronal mass ejections over a broad range of stars via changes in column density, coronal dimming, and/or velocity signatures in line profiles	For N_H: broad λ coverage; sensitivity below 1 keV. For dimming: broad λ coverage; $\lambda/\Delta\lambda > 2{,}000^*$. For velocity signatures: $\lambda/\Delta\lambda > 5{,}000$	Solar-stellar connection for magnetic activity, habitability, exospace weather

* — spectral resolution listed is minimum required to reproduce current capabilities; $\lambda/\Delta\lambda > 5000$ would enable significant advances.

resolution observations sufficient to disentangle the vast sea of weak emission lines in the 10–60 Å region. A wide bandpass provides access to transitions spanning the range of temperatures found in the corona for accurate determination of the differential emission measure (DEM) distribution. Velocity broadening in line profiles probes turbulence as well as extended spatial structure. Chung et al. [280] have provided the only evidence to date of excess broadening of a cool star (Algol).

3.2.3 How do the characteristics of flares change with time?

Flares on stars are processes that encompass the entire atmosphere of the star and are the most dramatic processes of energy release experienced by normal stars during their time on the main

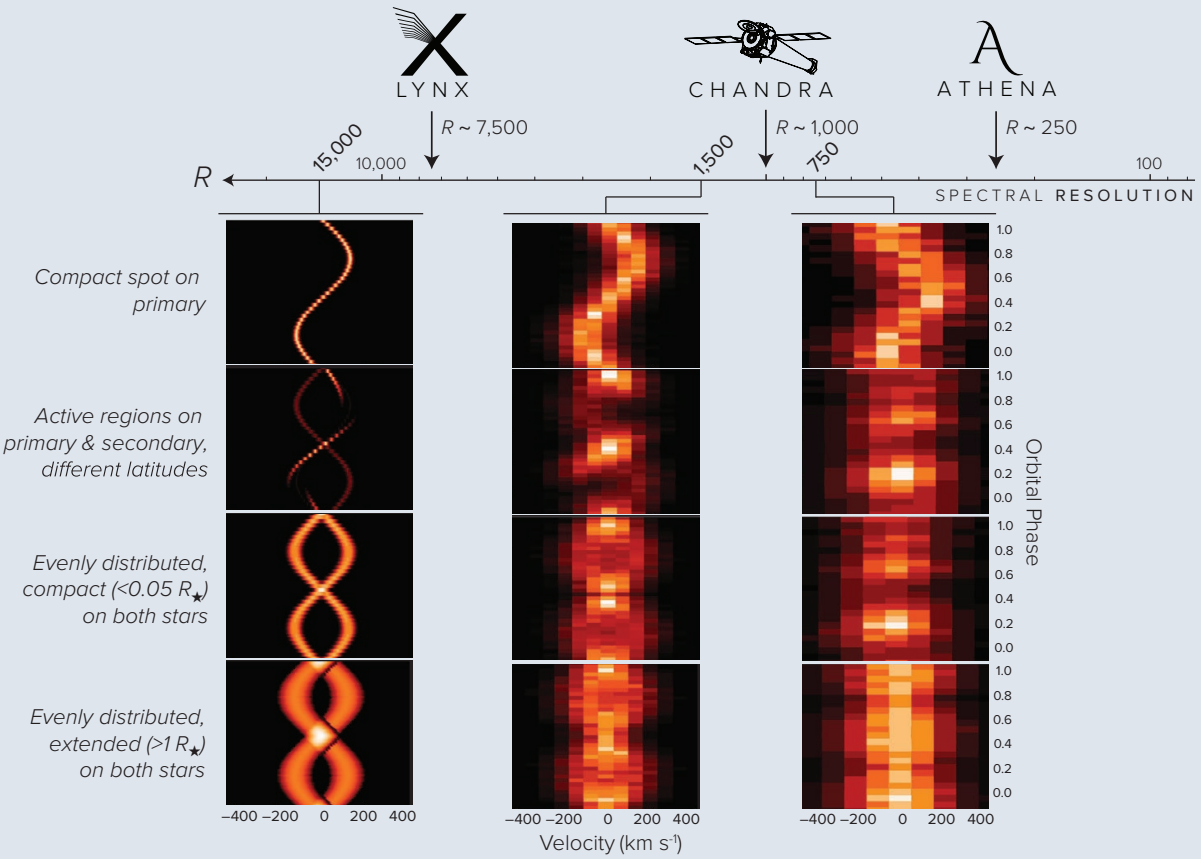

Fig. 3.3— The impact of X-ray spectral resolution on the ability to deduce coronal structures and the contribution from each member of a binary. Discriminants between various scenarios, such as those described in the leftmost column of text, are found only when the X-ray spectral resolution is sufficiently high. The panels, adapted from Fig. 10 of Hussain et al. [273], illustrate this effect for the case of the nearby binary YY Cen. The panels are arranged on a logarithmic axis of spectral resolution ($R = \lambda/\Delta\lambda$) that increases toward the left. Only the exquisite spectral resolution delivered by the *Lynx* X-ray Grating Spectrometer, with a goal of $R \sim 7{,}500$, will enable us to clearly distinguish between these scenarios. *Chandra* and *Athena* are entirely unable to do so.

sequence. Optical results from *Kepler* and now *TESS* are providing systematic probes of flare occurrence as a function of stellar properties. The associated X-ray emission is key for understanding the increased planetary atmospheric erosion beyond what is expected based on a star's evolving quiescent X-ray emission. Measuring the maximum plasma temperature, energy, and luminosity on a sample of stars will inform this study; the apparent connection of the distribution of flare energies to magnetic topology [281] will characterize the extent of the Solar Analogy; temperatures in excess of 10^7 K (up to and exceeding 10^8 K) are the domain of X-ray spectra. Energetic particles are a previously unexplored "dark energy" in stellar flares, with implications for stellar particle acceleration and space weather around other stars. Blueshifts in solar flares of up to several hundred km s^{-1} coincide with the start of nonthermal hard X-ray emission from accelerated particles [282]. Similarly, the peak in nonthermal line broadening in solar flares occurs at the same time as the maximum amount of hard X-ray emission [283]. Measuring line broadening and studying its variation with time in stellar flares opens up the study of the space weather environment that stars create.

3.2.4 The effects of stellar activity on planet atmospheres

Several effects of the host star's activity on planet habitability conditions have been mentioned above, and a more detailed summary is given in §4.8. *Lynx* will not only radically improve measurements of the high energy processes impacting planets, but will also characterize the structure of upper planet atmospheres via the X-ray transit spectroscopy [285], calibrating how the atmospheres respond to the high-energy bombardment.

The very first detection of X-ray transits in the "hot Jupiter" system HD 189733b [284] showed the potential of this method. The eclipse is much deeper in X-rays than in the optical, ~ 7% vs. 2%. This implies that soft X-rays are blocked at a radius ≈ 1.75 of the planet's optical size. The most likely origin of this difference is additional obscuration due to C, N, and O in a spherically symmetric exosphere with a density of ~ 10^{11} cm^{-3} and a temperature of ~ 20,000 K. Such measurements of the upper atmospheres of exoplanets are unique to X-rays that can probe the upper extended atmosphere even if its hydrogen is ionized (as should be the case for slow evaporation). UV measurements probe either much lower depths [286, 287], or very strong outflows that are only partially ionized [288, 289].

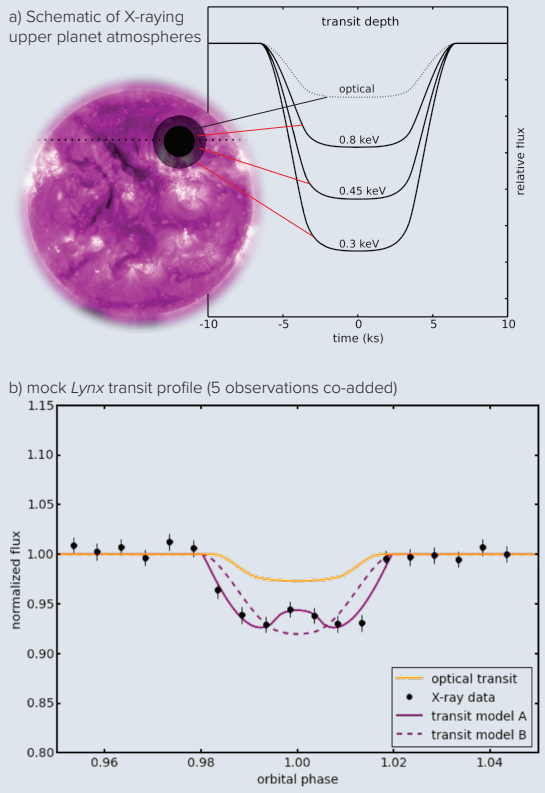

Fig. 3.4— Schematic of X-ray observations of transiting exoplanets, and a simulated *Lynx* measurement for a system similar to HD 189733b. See [284] for description of X-ray transit model profiles.
(Image credit: K. Poppenhaeger)

Lynx will dramatically improve the data quality (Fig. 3.4) and enable new types of measurements because of its ability to observe X-ray planet transits in individual spectral lines. Measurements at different energies will probe different atmospheric levels. Asymmetries in X-ray eclipses can potentially be detected, pointing to stellar wind-induced atmospheric depletion, comet-like sublimation tails, or bow shocks around planets. Statistically, X-ray eclipses can be detected with *Lynx* down to the super-Earth regime (see [285] for discussion of observing strategies). Using these observations and modeling as a guide, one can constrain the loss of atmospheres in exo-Earths for different levels of high-energy impacts.

The physical processes responsible for stellar X-ray emission are complex. Their understanding will play a fundamental role as new, multiwavelength telescopes focus on the abundance of planets being detected every year. *Lynx* will provide an unprecedented view of magnetic activity of planet-hosting stars and, combined with future multiwavelength missions, will play an essential role in the Search for Life.

3.3 Supernova Remnants in High Definition and Beyond the Milky Way

Hundreds of supernovae are found each year at optical wavelengths by dedicated surveys, but most of them are too distant to resolve the SN ejecta and the immediate surroundings of the exploded stars. Studies of the closest SNe, such as SN 1987A [290], have advanced the field tremendously, but our understanding of SN progenitors and explosion mechanisms is hampered by the infrequency of nearby events. Supernova remnants offer the means to study SN explosions, dynamics, and shocks at sub-pc scales. They are an important tool to explore the relationship between compact objects and their explosive origins. Observations of SNR morphologies, kinematics, and chemical abundances are crucial to test and constrain recent, high-fidelity 3D SN simulations. Metals synthesized in the explosions are shock-heated to ~10^7 K temperatures, and TeV electrons accelerated by the forward shock emit synchrotron radiation at X-ray energies. Thus, X-ray observations are a crucial means to probe the bulk of SNR ejecta material and the particle acceleration process.

Lynx will enable major advancements in SN science. Detailed investigation of > 600 faint and distant SNRs in the Milky Way and Local Group galaxies [291–295] will be possible. Sub-arcsecond spatial resolution will enable proper motion studies over a baseline of several decades, and will facilitate a resolved view of the thin synchrotron filaments around the periphery of young SNRs. The LXM will image SNRs in individual spectral lines, facilitating 3D mapping of metals synthesized in the explosions. With these capabilities, the sample size of young SNRs with morphological, kinematic, and nucleosynthetic measurements will dramatically increase, probing SN feedback and chemical enrichment in different environments and providing crucial information for SN explosion models.

Resolving Galactic SNRs — Since *Chandra*'s first-light image of Cassiopeia A (Cas A) showing narrow, non-thermal filaments, small ejecta knots, and a neutron star at its center, the scientific benefit and beauty of high spatial resolution at X-ray energies has become increasingly evident. However, a prime limitation of current facilities is that CCD energy resolution is insufficient to resolve He-like and H-like line complexes of heavy elements, and gratings spectrometers are only useful if SNRs have minimal angular extents [296] or to study isolated ejecta knots [297].

X-ray microcalorimeters will revolutionize SNR studies. *Hitomi* provided a tantalizing glimpse of the power of high-resolution spectro-imaging capabilities by showing bulk redshifted iron in the young SNR N132D, indicating a highly asymmetric explosion [298]. Within the Milky Way, the *Athena* microcalorimeter (with 5″ spatial resolution) will obtain superb spectra that will enable characterization of the individual SNR components, such as the Si-rich jet, the concentration of Fe ahead of the forward shock, and the synchrotron filaments around the periphery of Cas A.

The *Lynx*LXM instrument will resolve these features will be resolved in full detail and without confusion, enabling precise measures of the kinematics, shock heating, ejecta mixing, chemistry, and non-thermal radiation. In particular, it will be possible to obtain accurate radial velocities of ejecta knots in young, ejecta-dominated SNRs. Given the limitations associated with dispersed spectra from extended objects, current studies have only measured radial velocities for the brightest knots in a handful of SNRs [297]. The combination of a few eV spectral resolution and 1″ spatial resolution in the un-dispersed spectrum will truly revolutionize SNR studies, expanding the view of SNRs from two dimensions into 3D. An example is shown in Fig. 3.5.

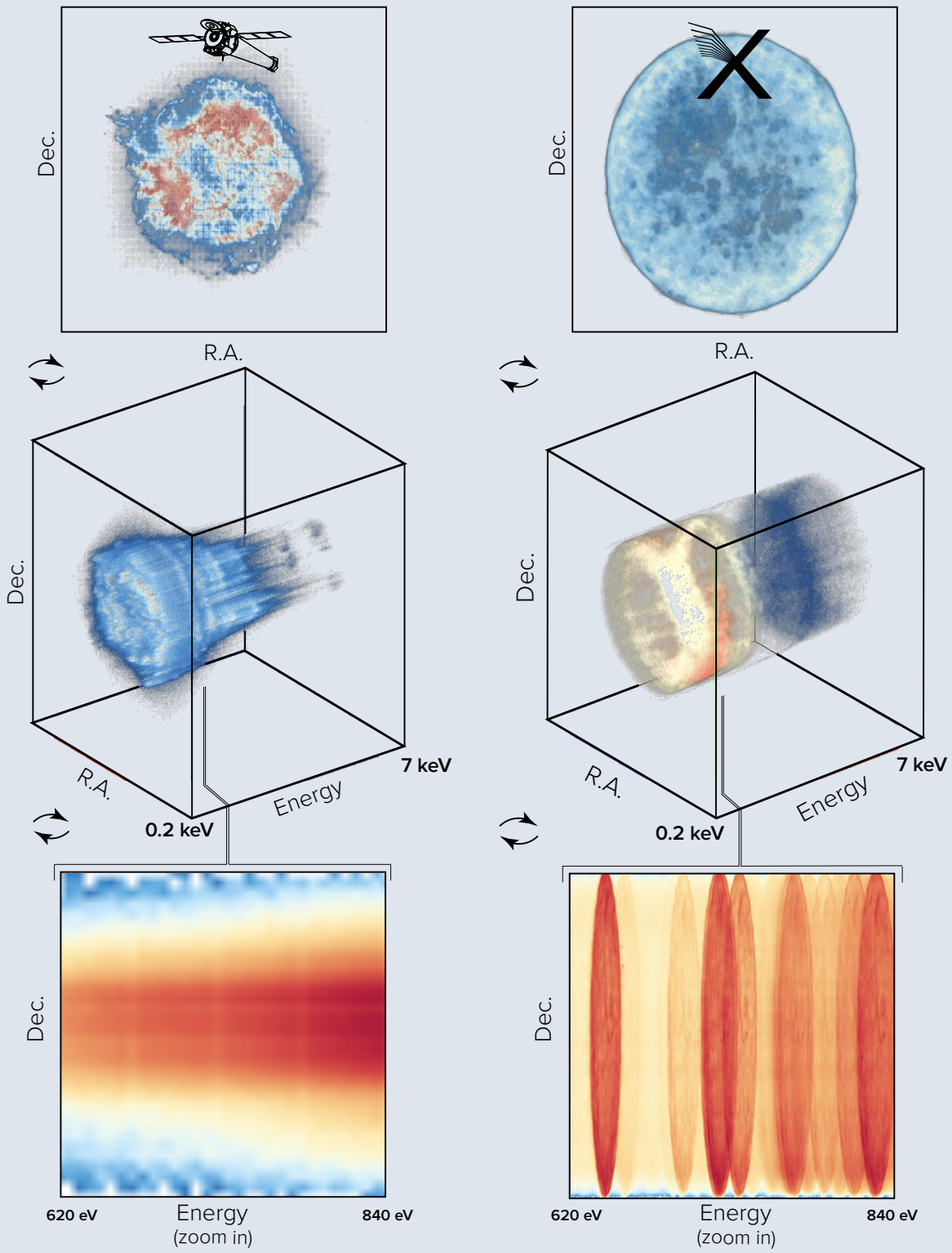

Fig. 3.5— The *Lynx* LXM will collect multidimensional datacubes many times richer than those obtained by ACIS aboard *Chandra*. Here, we show a three-dimensional representation of the (real) *Chandra*/ACIS datacube for Cassiopeia A (left), compared with an LXM observation of a similar, numerically simulated remnant (right, courtesy S. Orlando). Beginning with the counts images (top panels), rotating off-axis (center panels) reveals the energy axis, and a zoom into a small band (bottom panels) shows that the spectral resolution of LXM is vastly superior to that of ACIS, resolving spectral lines and the velocity structure of the remnant.

Proper motions over baselines of several decades — While the LXM spectral resolution will enable measurements of line-of-sight velocities in the SNRs, a sub-arcsecond spatial resolution will enable *Lynx* to measure proper motions of SNR shocks, knots in the ejecta, and neutron star kicks over a 30–40 year baseline, using *Chandra* data as a reference point, $v = 3.16'' \times (D/1\,\mathrm{kpc})^{-1}\,(v_t/500\,\mathrm{km\ s^{-1}})$. Depending on the morphology of the object, displacements can be measured better than the telescope PSF. For example, *Chandra* was used to derive an expansion rate of 0.1″ over 17 years for the LMC remnant 1E 0102.2−7219 [300], corresponding to v = 1,600 km s^{-1}. Thus, ~ 500 km s^{-1} will be measurable with *Lynx* out to D = 10 kpc, and velocities of > 1,000 km s^{-1} will be observable out to the Magellanic Clouds. Combined with LXM radial velocity measurements, proper motions will reveal the true 3D structure of the SNR ejecta. First results for a small number of SNRs are already coming from *Chandra* [301]. *Lynx* will enable high-fidelity measurements, which will serve as a powerful new tool for understanding the physics of supernova explosions.

Taking detailed SNR studies extragalactic — Spatial resolution is especially important to probe the morphologies and distinct spectral components in extragalactic SNRs. For example, Fig. 3.6 shows simulated *Athena* and *Lynx* images of the young SNR N103B in the Large Magellanic Cloud (LMC). In this case, ~ 1″ spatial resolution is crucial to disentangle the ejecta and circumstellar medium spectra. At the distance of the LMC, 1″ ≈ 0.3 pc; with that resolution, maps of the youngest parsec-scale sources can be obtained, such as for SN 1987A (3″ ≈ 1 pc across by the 2030s, [302]).

The large increase in effective area of *Lynx* over *Chandra* will enable detailed studies of large extragalactic populations of SNRs. For example, a 100 ksec exposure with *Lynx* will yield > 10^3 counts from dozens of SNRs in M31 and M33. In the Magellanic Clouds, X-ray imaging and microcalorimeter observations can achieve similar signal-to-noise to what current facilities achieve for Milky Way sources. *Lynx* measurements of SNR morphologies can be used to determine the parent supernova types [303], as well as measurements of O, Ne, Mg, and Fe lines [304]. High spectral resolution measurements of the centroid energies of the Fe line complex [305] can also be

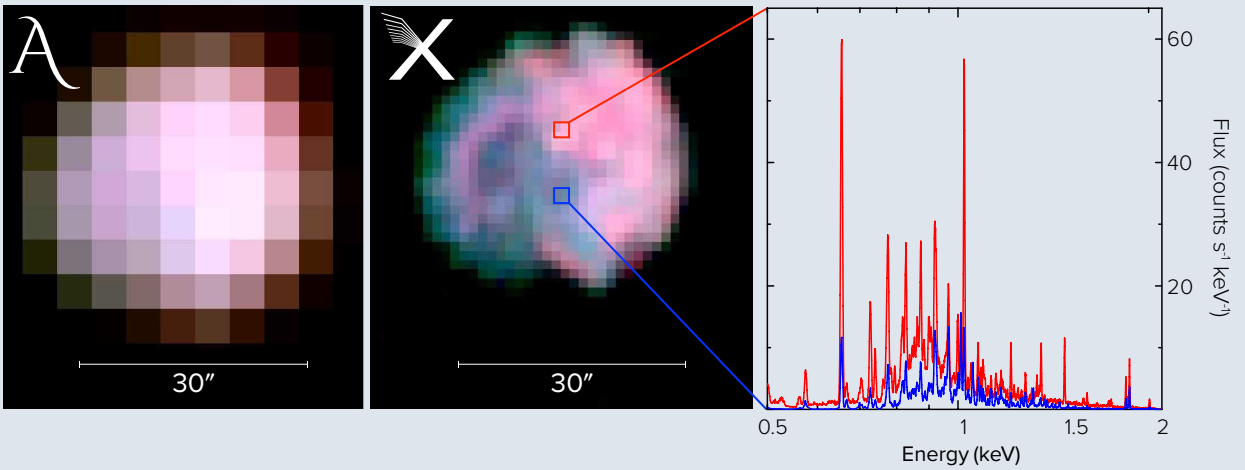

Fig. 3.6— Simulated *Athena* (left) and *Lynx* (middle) images of the Type Ia SNR N103B in the LMC. The right panel shows simulated microcalorimeter spectra from two locations in N103B. A 1″-pixel microcalorimeter is vital to obtain distinct spectra from the ejecta and CSM components.

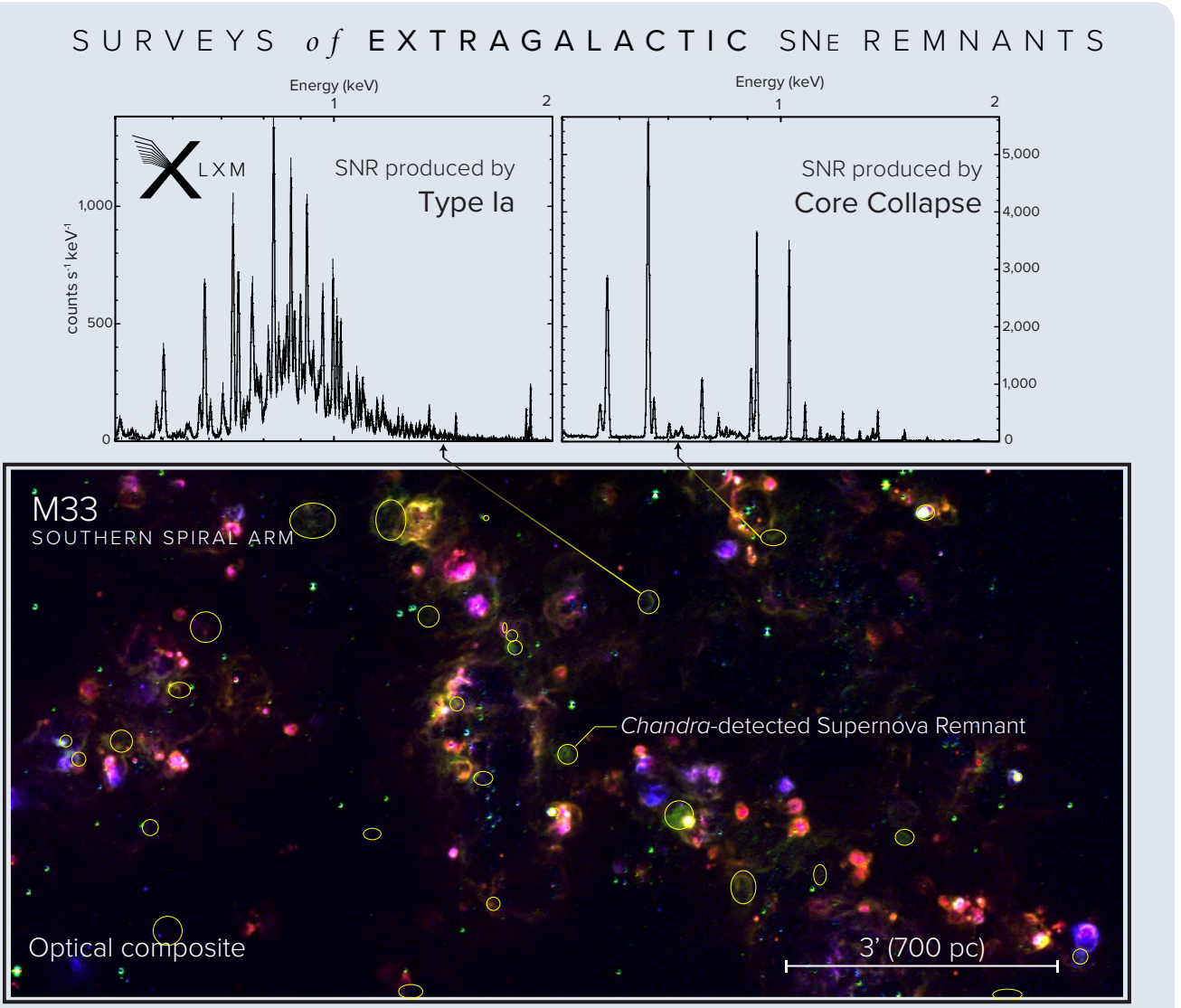

Fig. 3.7— A *Lynx* survey of supernova remnants in a Local Group galaxy like M33 will reveal a panoply of exquisite spectra with rich and highly diagnostic forests of lines. (*Top*) Two typical spectra of remnants from Type Ia and Type II explosions, extracted from a simulated 100 ksec *Lynx* X-ray Microcalorimeter survey of a galaxy at the distance of M33. The exquisite soft-band spectral resolution of the instrument enables unique classification of the parent supernovae. (*Bottom*) The view of SNRs and ongoing star formation in the Southern spiral arm of M33 (*Credit:* Long et al. [299]). The field measures $12.2' \times 5.8'$. The SNRs (yellow ellipses) were identified by optical spectroscopy. *Chandra* detects 44% of these at a 3 σ confidence level. *Lynx* will detect *all* SNRs and determine the types of parent supernovae.

used to type SNRs. A *Lynx* survey of SNRs in the Local Group will enable a detailed exploration of the SN activity in the past ~ 10^4 years in relation to galactic environments, and to probe its effect on energy feedback and metal enrichment.

New insights into supernovae explosion mechanisms — The fundamental questions about supernova explosions are: which stars explode, and how do they explode? *Lynx* will provide new critical information on both questions:

- Type Ia SNe are generally believed to form through two possible scenarios [306]: the single-degenerate channel (a white dwarf plus a stellar companion) and the double-degenerate (two white dwarfs). Modeling of the explosion mechanisms [307, 308] indicates that the yield of neutron-rich isotopes, such as ^{58}Ni and ^{55}Mn, is sensitive to the central density of the white dwarf, which varies strongly between the single- and double-degenerate channels. For instance, Ni/Fe and Mn/Fe ratios in SNR 3C 397 indicate that the progenitor likely had a high central density [309] — a scenario which rules out the double-degenerate channel. This and other similar results (e.g., [310]) are based on CCD-resolution spectra of a handful of remnants with the associated large uncertainties from moderate resolution spectra. High-resolution, spatially resolved X-ray spectroscopy offers the possibility of probing the products of explosive nucleosynthesis at high significance. *Lynx* will enable such measurements in the Magellanic Clouds and nearby SN Ia's such as S Andromedae in M31.
- For core-collapse SNe, the explosion mechanism remains uncertain. Possibilities include the neutrino mechanism, energy injection via a central engine, and the growth of turbulence via standing accretion shocks (e.g., [311]). Regardless of the exact mechanism, it is widely accepted that the quasi-spherical symmetry of the progenitor must be broken at some point in order to revive the shock which forms during core bounce. The primary observational constraint provided by *Lynx* will be 3D spatial and velocity maps of ejecta. Each explosion mechanism seeds asymmetries differently, and these seeds persist into the remnant phase.

Pioneering work on the ejecta distribution of the brightest Galactic SNR Cas-A has been done using *Chandra* [312, 313]. Both of these studies suggest significant overturning of the ejecta with high-Z material at larger radii than low-Z material, likely the result of convection of ^{56}Ni-rich material driven to the surface during the explosion. As discussed above, such measurements will be revolutionized by *Lynx* because of its combined high spatial and spectral resolution.

- A unique observational insight into the early stages of the core-collapse supernova explosions is provided by neutron star kick measurements [314]. *Lynx* can identify neutron stars in and near the MW and Magellanic Clouds SNRs by their unique featureless spectrum. For the MW remnants, *Lynx* can use proper motions for determining the neutron stars kick velocities (expected to be $\langle v \rangle \approx 380$ km s^{-1}, [315]). This must be done in the X-rays because many young neutron stars, such the central compact object in Cassiopeia A, are radio quiet.

Recent studies of neutron star kicks [316, 317] use an approximate approach by measuring the apparent displacement of the neutron stars from the remnants' geometric centers, assuming a remnant age, distance, and a spherically-symmetric explosion. *Lynx* will revolutionize this field by providing full 3D information about ejecta, along with the spatial resolution and sensitivity necessary to yield accurate constraints on young neutron star proper motions.

3.4 Detailed View of X-ray Binary Populations in Nearby Galaxies

Binary stellar systems are key tools for several areas of astrophysics: star-formation processes, the late stages of stellar evolution, compact object formation, and compact object mergers. At advanced stages of evolution, many binary systems pass through an X-ray emitting phase, where one of the stars is turned into a compact object that accretes material from its companion. This X-ray binary (XRB) phase is the most efficient observational probe of binary stellar systems outside of direct observation

of photometric or spectroscopic binary stars in our Galaxy. The XRB phase is also critical for the evolution of close binaries which may eventually become compact-object mergers and hence sources of gravitational waves and short γ-ray bursts [319].

Detailed data on the XRBs in the Milky Way is being provided by specialized X-ray observatories such as *RXTE*, *NICER*, *INTEGRAL*, *Swift/BAT* and a host of earlier satellites dating back to *Uhuru*. However, a census of XRBs in the Milky Way still provides only a partial view. Observations of external galaxies are essential to achieve the complete picture necessary for understanding compact object formation. This is especially critical for modeling the populations of gravitational wave progenitors (Fig. 3.8). The evolutionary channels of accreting X-ray sources are a key component for understanding the demographics of compact objects, particularly their mass and spin distributions [320–322]. Though detailed modeling of individual sources in our Galaxy have already given a basic framework for the different phases in the evolution of binary stellar systems [323, 324], the small number of objects, combined with the limited parameter space covered by the stellar populations in our Galaxy, does not represent conditions in other galaxies where the majority of the gravitational wave progenitors are expected to originate.

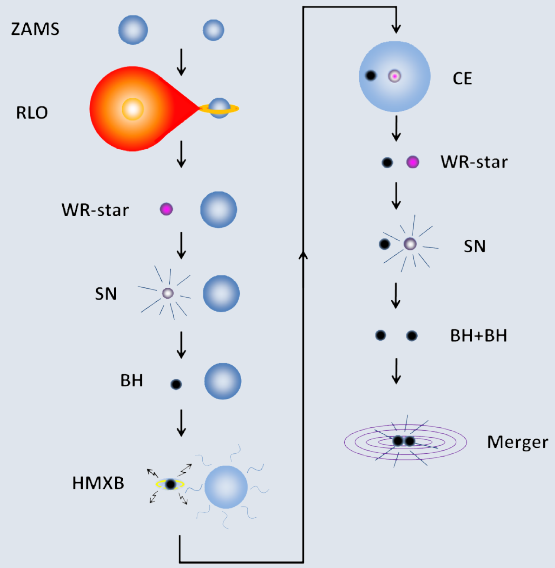

Fig. 3.8— Indicative evolution of a binary stellar system through the X-ray phase to the final compact object merger [318]. Each of the shown phases are key for the outcome of the evolution. The only phases that can provide observational constraints on the physical parameters of the system are the initial binary star phase and the X-ray binary phase.

Therefore, the best way to make the next leap forward in understanding the formation rate of these objects is with *Lynx* which can efficiently observe the bulk of the active XRB populations in a representative sample of nearby galaxies with a spatial resolution of 0.5″ or better, allowing the identification of their multiwavelength counterparts.

Lynx surveys of XRBs in nearby galaxies are not only a tool for exploring end points in stellar evolution and the evolutionary paths to the gravitational wave-detected merger events. They also will serve as key calibration points for *Lynx* observations of the Cosmic Dawn epoch that rely on the XRB populations in high-redshift galaxies (§4.3).

X-ray emission, in purple, from million year old stars in Westerlund 2.

Credit: X-ray: NASA/CXC/SAO/Sejong Univ./Hur et al; ; Optical: NASA/STScI

From the birth of infant suns to the wreckage of their deaths, *Lynx* will reveal the high-energy side of stellar evolution.

4 *The* Impact *of Lynx across the* Astrophysical Landscape

The science requirements for *Lynx*, when translated to instrument requirements, result in performance gains of historic magnitude. The imaging component provides a factor of 50× higher throughput, 20× the FOV with sub-arcsecond imaging, and a factor of 1,000× greater speed for surveys compared to the current state of the art (*Chandra*). To put this in context, this is higher than the hundred-fold gain survey power of the future NASA flagship observatory, *WFIRST*, relative to *Hubble*. In terms of sensitivity, *Lynx* will detect sources 100× fainter than those seen in the deepest *Chandra* surveys (Fig. 4.1).

Turning to spectroscopy, we observe that astronomy is undergoing revolutionary changes driven in large part by movement toward hyper-dimensional datasets. Fully spatially-resolved spectroscopic data cubes, provided by instruments such as MUSE on ESO's VLT, enable advancements which rival the leap from the first astro-photograph to state of the art imaging from *Hubble*. There is an equivalent development in the X-rays from *Einstein* to *Chandra* and onward to *Lynx*. The *Lynx* X-ray Microcalorimeter will provide an X-ray capability comparable to what MUSE provides in the optical, and what the MIRI and NIRSpec instruments on *JWST* will provide in the infrared. To put these relative gains in context, the leap from *Chandra* to *Lynx* is the same as that from a 1-m telescope with a CCD imager to an 8-m VLT equipped with a MUSE spectrograph.

Gains in sensitivity and spectroscopic capabilities of such magnitude are equivalent to opening a new wavelength band or introducing a major new observational technique. *Lynx* will play a critical role not only in the areas directly related to its science pillars, such as studies of the Cosmic Dawn, Black Holes, Galaxy Formation, and Origin of Elements. It will also make a major impact in other areas, such as Cosmology, Stellar Populations, Solar System, and Multi-Messenger Astronomy. The impact of *Lynx* will be felt even in less obvious areas, such as studies of planets and protoplanetary disks. A sample of examples given below shows that *Lynx* is not simply an X-ray telescope for X-ray astronomers: it is a new Great Observatory which will make a profound impact across the astrophysical landscape. Indeed, it is designed to be long-lived and flexible enough to pursue answers to the questions we have yet to even ask.

4.1 Multimessenger Astronomy

Lynx will operate in an astrophysical landscape already transformed by upcoming capabilities in the time domain and by the emergence of the era of multimessenger astronomy following LIGO detections of gravitational wave events from neutron stars and black hole mergers, and IceCube detections of astrophysical neutrinos. *Lynx* will enable unique advances in the transient sky discovery space. The main strength of *Lynx* is not a very fast response time, although it can respond to some targets of opportunity (ToO) within 3 hours (§6.7.2). Its ToO and multi-messenger astronomy capabilities will instead capitalize on extreme sensitivity and sharp angular resolution. We highlight two examples focusing on *Lynx* synergies with ground- and space-based gravitational wave experiments.

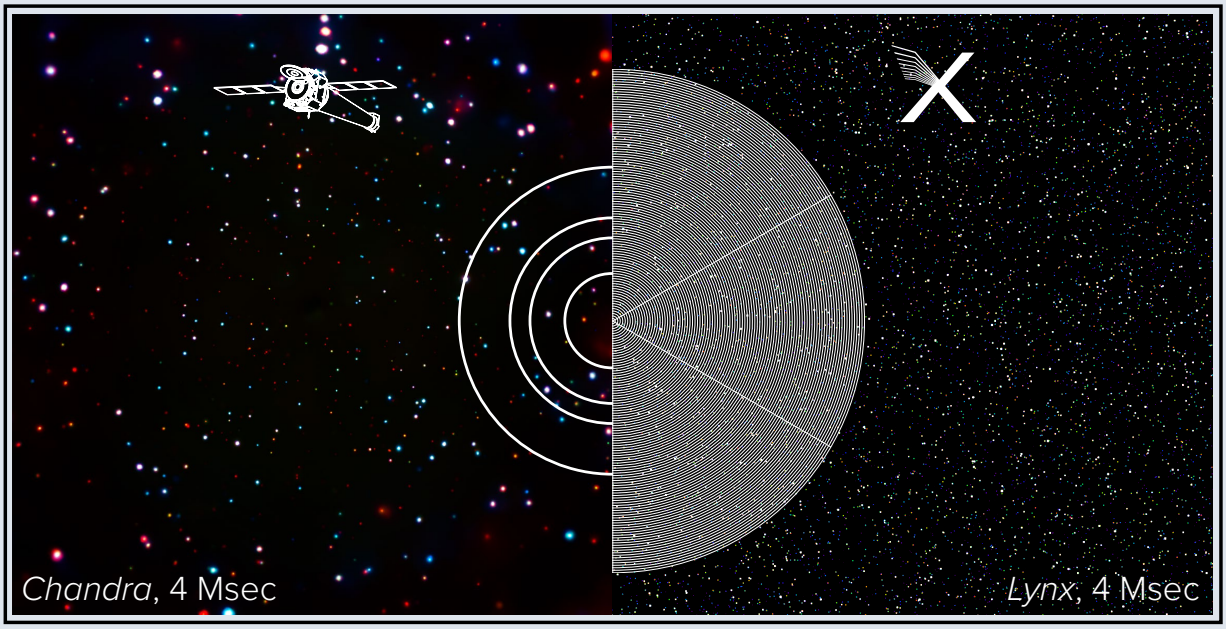

0.5″ PSF on-axis, sub-arcsecond across a 22’ × 22’ FOV

50× *Chandra*’s throughput in soft X-rays

1000× *Chandra*’s survey speed

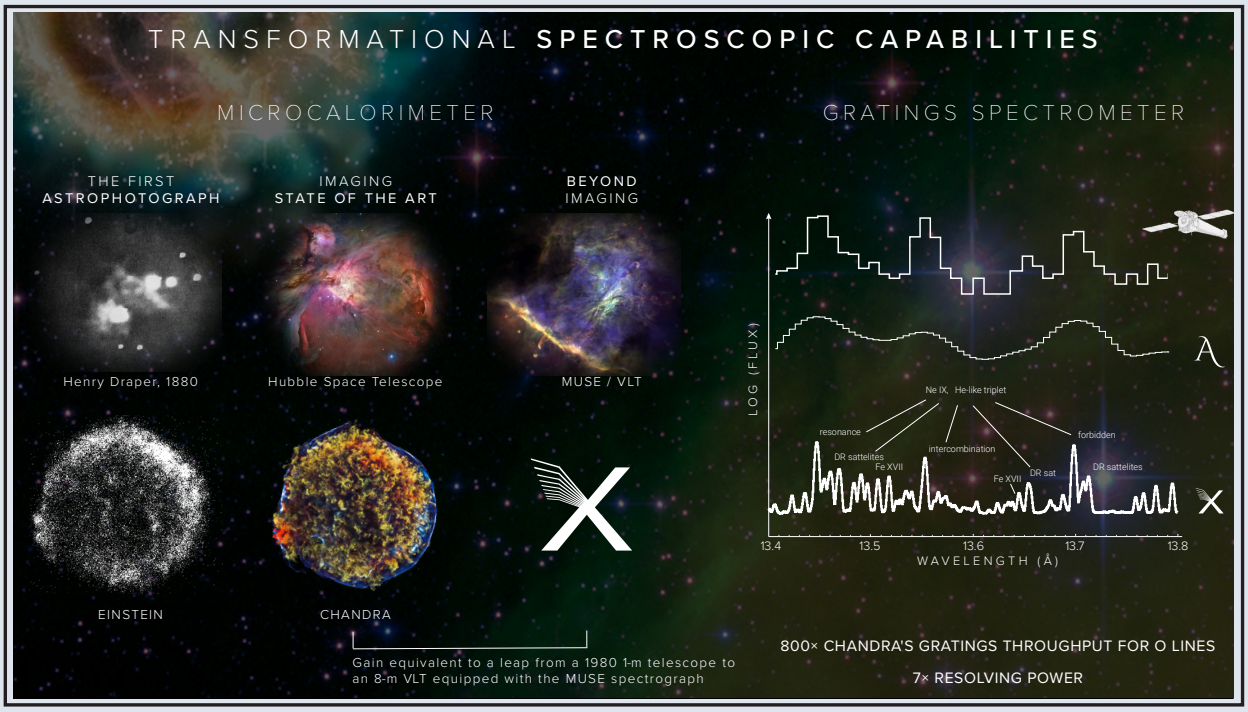

Fig. 4.1— *Lynx* imaging and spectral capability gains in context.

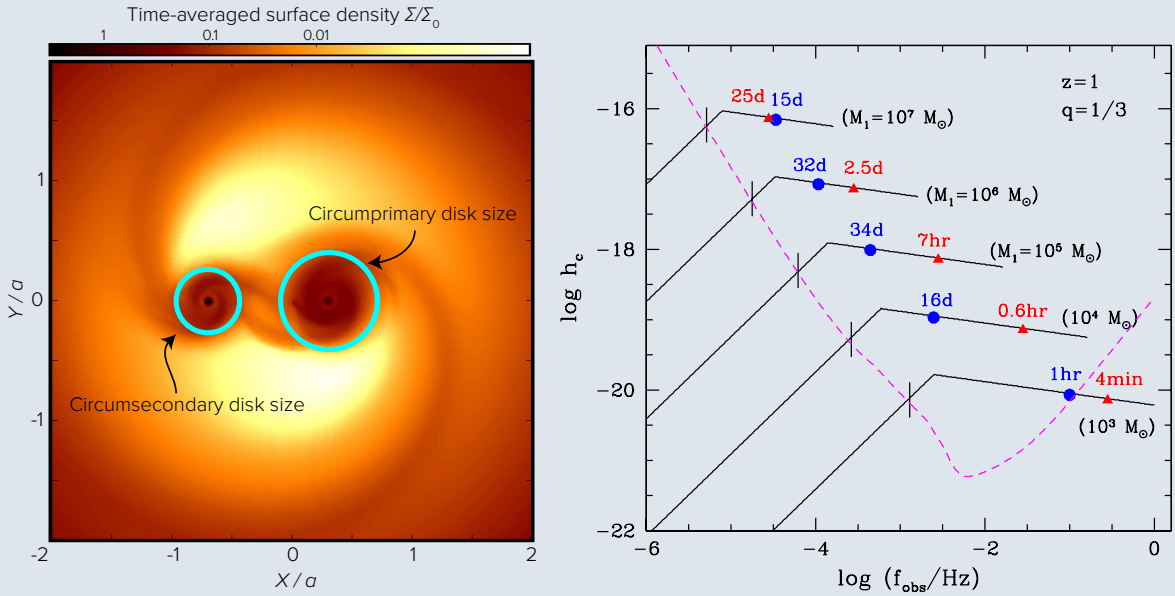

Fig. 4.2— (*Left*) The surface density of an accretion disk near a binary supermassive black hole, shown on a logarithmic scale. The binary has a mass ratio of $q = M_2/M_1 = 0.43$. Circles indicate the expected tidal truncation sizes of the circumprimary and circumsecondary disks. This panel has been adapted from Farris et al. (2014) [325]. (*Right*) Tracks of characteristic strain, h_c, across the *LISA* band of binaries at $z = 1$ with mass ratios of $q = 1/3$ and different primary masses M_1, as labeled. The break in h_c marks five years prior to the merger. Along each track, various marks indicate times when (*i*) the binary enters the *LISA* band (vertical line), (*ii*) it is localized to 10 deg^2 (blue circle), and (*iii*) the tidal truncation radius of the circumprimary disk becomes smaller than $10\,R_g$ (red triangle). The dashed magenta curve shows the projected sensitivity of *LISA* [69]. This panel has been adapted from Haiman (2017) [326].

4.1.1 X-ray chirp signal from merging supermassive black holes

LISA will be exceedingly sensitive to mergers of SMBHs with masses $\sim 10^6\,M_\odot$ [69]. As argued in [326] and summarized briefly below, there should be a distinct X-ray "chirp" that accompanies the gravitational wave (GW) signal in these mergers. SMBHs with $M \sim 10^6\,M_\odot$ are predominantly located in gas-rich disk galaxies [7], and their binary black hole mergers should also proceed in gas-rich environments [330], resulting in a high accretion rate on the binary BH. A number of recent MHD simulations have concluded that while the inner structure of the binary's accretion disk is modified [331], the BHs continue to accrete at high rates via narrow streams [325, 332–339], and this continues even in the late stages of the merger, when the binary inspiral is driven by the GW radiation [340, 341]. Each BH forms its own "minidisk" that is truncated by the tidal forces of the companion BH (Fig. 4.2). Truncation radii are $\sim 100\,r_g$ when the binary enters the *LISA* band [342, 343]. This is a factor of $\approx 10\times$ the size of the region where X-rays are produced by quasars [326, 344–348], but comparable to the optically emitting region. The truncation radius moves into the X-ray emitting region only 2–3 days prior to the merger.

These considerations suggest that $M_{\rm BH} \sim 10^6\,M_\odot$ black hole binaries should be uniquely visible in the X-rays for much of the duration of the *LISA* event (c.f. Fig. 4.2). Relativistic Doppler modulations and lensing effects will inevitably imprint periodic variability in the X-ray light curve, at the tens of percent level, tracking the phase of the orbital motion and thus the GWs [326]. Modulations will be especially strong for unequal-mass binaries, with components moving at high orbital speeds.

For nearly equal-mass binaries, the accretion rates onto the individual SMBHs will also be strongly modulated at the binary's orbital period, yielding even stronger, order-unity variability, independent of inclination [341].

LISA should be able to localize a typical black hole binary with $M_{\rm BH} \sim 10^6\,M_\odot$ and $z \approx 1$ to within several square degrees starting several weeks before the merger [349–351]. Monitoring this area, *Lynx* will be able to uniquely identify a near-Eddington, quasar-like, X-ray source, with periodic flux variability. The X-ray periodicity will initially be ~ hours, and its phase will track the GW chirp. The GW and X-ray chirp signals can then be observed in tandem for several hundred cycles. Detecting the X-ray chirp accompanying the GWs will help uniquely identify the electromagnetic counterpart of the *LISA* source, thus enabling a wide range of new science [352].

4.1.2 Followup of LIGO events

GW information on the neutron star (NS) merger event GW170817 and identification of its electromagnetic counterpart [353] presented unprecedented opportunities to learn about the post-merger physics of this type of events (see [354] for review). Observed signatures in the γ-rays, X-rays, OIR, and radio included tell-tale signs of the propagation of a relativistic jet [355, 356], synthesis of r-process elements, and interactions of relativistic jet with the ISM [329, 357–359]. Perhaps the most fundamental question is: what is the final remnant of the event? In the case of GW170817, the merged object has a mass of $2.74^{+0.04}_{-0.01}\,M_\odot$ [353] and can be either a hyper-massive neutron star or a black hole.

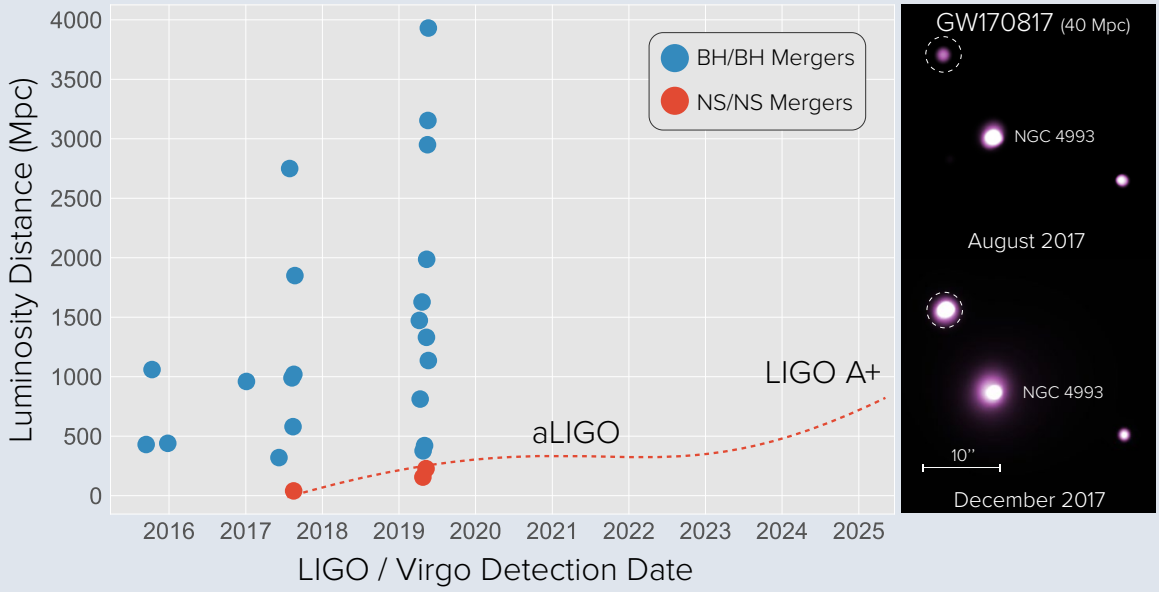

Fig. 4.3— Distribution of distances to LIGO GW events, and a projected size of the "horizon" for neutron star mergers ([327]). By 2030, most events detected by LIGO A+ will be at distances that require the sensitivity and angular resolution of *Lynx* for long-term monitoring of the post-merger evolution [328]. The right-hand panels show the *Chandra* detections of GW170817, whose measured fluxes are many hundred times lower than expected for a rapidly spinning, merged neutron star, implying that a black hole likely formed instead (*Credit:* NASA/CXC/Trinity University/D. Pooley et al.; [329]).

Unambiguously determining the nature of the final remnant requires long-term X-ray monitoring. In addition to the jet emission expected for any type of final remnant, a fast-spinning NS will produce additional X-ray emission via its spin-down [329], on time scales of up to years later. Even a slowly-spinning NS is expected to produce additional flaring X-ray emission via the untwisting of the toroidal magnetic field [360]. A black hole, on the other hand, should not produce substantial additional X-ray emission.

Upcoming NS merger discoveries will no doubt yield many insights and surprises. Electromagnetic signatures of other types of LIGO events are yet to be detected. Any adequate followup of future events will require an X-ray observatory with sub-arcsecond resolution and a sensitivity well beyond *Chandra* (which had to spend several hundred ksec to followup GW170817, at only 40 Mpc). As GW detectors are updated and the horizon for detection of NS-NS mergers extends to 10× the distance to GW170817 (Fig. 4.3), the electromagnetic emission will be ~ 100× fainter, with separations from unrelated X-ray sources ~ 10× smaller. Following up such events will require a combination of throughput and angular resolution that is offered only by *Lynx*.

4.2 Black Hole Accretion Physics

Studies of black hole accretion in the X-rays are typically done with facilities emphasizing a bandpass extending to high energies, very high throughput, and fast timing [361]. However, just as in the case of Multimessenger Astronomy, *Lynx* will make unique contributions which capitalize on its sensitivity, angular resolution, and high-resolution spectroscopic capabilities. The structure of inner accretion disks and hot coronae can be probed via quasar microlensing. Long-term monitoring of tidal disruption events (TDE) tracks accretion state transitions in a well-controlled experiment. Grating spectroscopy of AGN and Galactic X-ray binaries is key for inferring the density structure of accretion outflows.

4.2.1 Structure of the inner disk and hot corona using quasar microlensing

However exquisite X-ray imaging with *Lynx* will be, it is insufficient for resolving black hole accretion disks. *Lynx* nevertheless will enable a unique probe of the inner disk and hot corona structure using quasar microlensing. This technique offers one of the most straightforward and efficient ways to measure the sizes of the emitting regions in accretion flows [363, 364]. It probes angular scales which are ~ 1 order of magnitude below even those resolved by the Event Horizon Telescope in M87 [365], enabling studies of disks around quasars accreting at high rates. Microlensing measurements will nicely complement those made via the X-ray reverberation method [366, 367] that best probe a different black hole demographic (Galactic stellar-mass black holes and the nearest AGN typically with a low intrinsic luminosity).

The microlensing method uses strongly lensed, multiply imaged quasars, and relies on the motion of the quasar relative to the network of high-magnification caustics generated by stars in the lensing galaxy (see Fig. 4.12 below). Corresponding flux variations are on timescales of days to years. X-ray microlensing measurements are inherently interesting because they probe the innermost and hottest structures in the accretion flow. Opportunities for quasar microlensing studies will drastically expand in the 2020s, as new samples of multiple-imaged quasars are generated by LSST [368]. There are

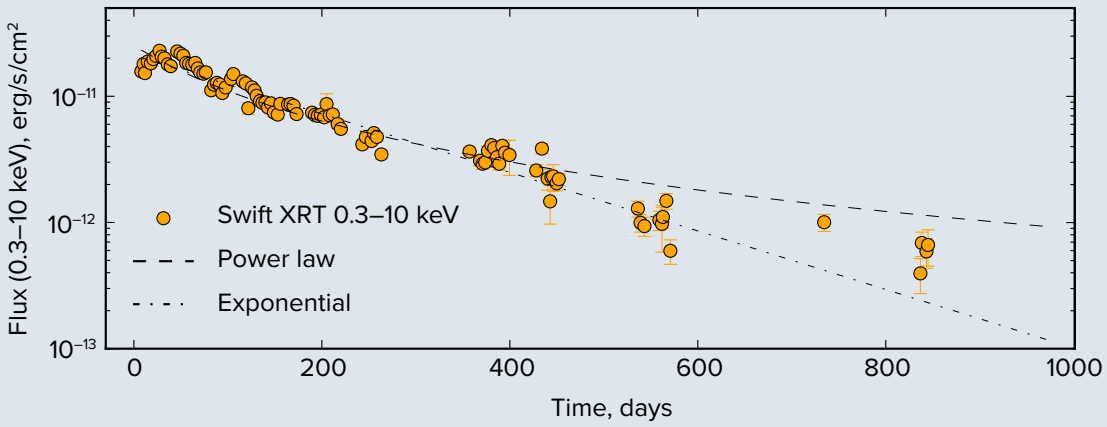

Fig. 4.4— X-ray light curve of the ASASSN-15li TDE event (adapted from [362]). Smooth behavior of the X-ray flux reflects a gradual, predictable decrease in the accretion rate. *Lynx* will have the sensitivity to monitor events such as ASASSN-15li for 15+ years. These observations will constitute a well-controlled experiment for probing accretion physics in very sub-Eddington regimes.

two basic measurements: sparsely sampled and densely sampled light curves. Measurements of the X-ray fluxes of the individual images (typically separated by ~ 1″) taken every several months to years will provide ~ micro-arcsecond constraints of the X-ray emitting regions. In the event of a knife-edge caustic sweeping across the quasar, high-cadence sampling of the light curves will provide nano-arcsecond measurements of the emitting regions [368]. *Lynx* is ideally suited to make measurements of both types.

Lynx can also simultaneously probe the two distinct components in the accretion flow because they can be separated spectrally. The hot corona produces X-ray continuum whose microlensing light curves constrain the corona size. The fluorescent Fe Kα line originates in the accretion disk itself. As a caustic moves across regions of the accretion disk with different Doppler boosts, the observed line centroid shifts. This provides a unique constraint on the inner disk structure [369]. Initial detections of this variability have already been made with *Chandra* [370], but the capabilities of *Lynx* are required to realize the full potential of this method [371].

4.2.2 Accretion state transitions in tidal disruption events

Stellar tidal disruption by a central SMBH is a natural outcome of orbital dynamics in dense stellar systems [372–374]. Among many other astrophysical applications, tidal disruption events (TDEs) provide a unique opportunity for studying transitions between the accretion disk states [375]. As the TDE event evolves, the accretion rates decline from super-Eddington, to modestly sub-Eddington, to very sub-Eddington levels in a very predictable way. Therefore, their accretion disks might exhibit state changes analogous to those seen in stellar-mass black holes in X-ray binaries [376].

For most TDEs detected in the X-ray regime at early stages, the observed spectra are consistent with the simple picture of a compact, classical accretion disk [377]. X-ray observations at later stages of evolution have only started to come in and provide indications that state transitions have occurred within 4–9 years of the initial stellar disruption [375, 378]. Radically better statistics are needed to

track how state transitions occur, and to track the evolution of TDE accretion disks in the regime of the very low rates expected > 10 years after the event.

Two factors are relevant for future TDE observations. First, the recently launched *eROSITA* telescope onboard SRG [97] should provide tens or even hundreds of X-ray detected TDEs per year [375, 379], while the Vera Rubin Telescope will provide an abundance of optical TDE detections in the 2020s. Second, the large theoretical uncertainties associated with circularization and disk formation in TDEs becomes less important at times long after the peak of the mass return rate, and the behavior will be regular and well-modeled by a quasi-circular disk approximation, even in the presense of complicating factors initially [380–382]. Indeed, a very regular evolution of the X-ray flux from TDEs at late times has been observed (e.g., Fig. 4.4).

Therefore, there will be no shortage of suitable TDE targets for *Lynx* at times as late as 15 years after the event. This will open a unique window for studying accretion on SMBH in the now-prevalent very low $\dot{M}$ regime. But long-term monitoring requires sensitivity and high spatial resolution to isolate the TDE source within the host galaxy. These capabilities are exclusive to *Lynx*.

4.2.3 Structure of accretion disk outflows using soft-band X-ray spectroscopy

The highly energetic outflows from AGN are one of the key mechanisms regulating galaxy formation (§2). They are the central mechanism by which the SMBH interacts with the host galaxy. AGN

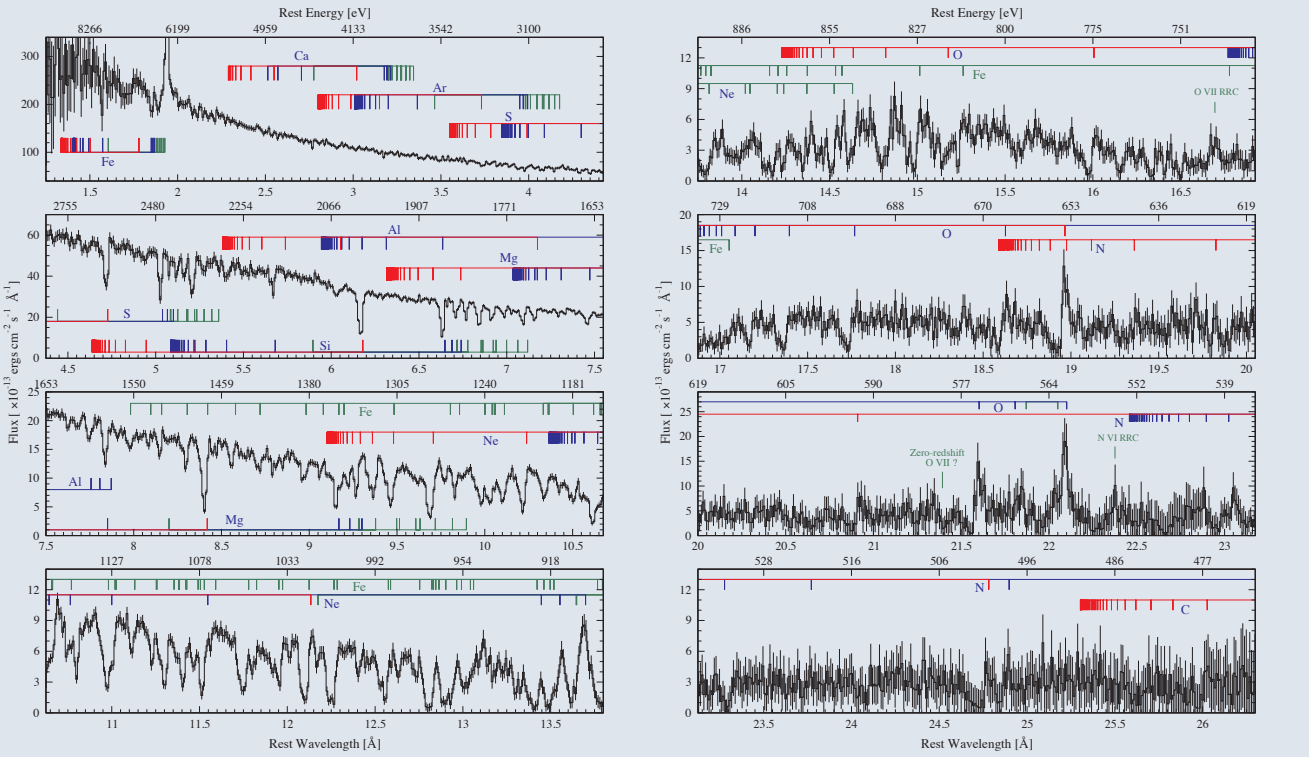

Fig. 4.5— A 900 ksec *Chandra* grating spectrum of the AGN in NGC 3783 from Kaspi et al. [383], showing a rich series of soft X-ray absorption lines from Ne to Fe. The relative strengths of these lines are used to determine the ionization parameter of the gas. *Lynx* will obtain higher quality spectra in under 10 ksec. Additional spectral information accessible with *Lynx* can be used to determine density in the outflow and distance from the black hole.

outflows are complex and multiphase. Observations show that the bulk of energy and momentum flux is carried by their hot gas component. This is exemplified by the detection of ultra-fast, $v > 0.033c$ outflows in the X-ray spectra [148, 384]. However, the current quality of X-ray spectral data (e.g., Fig. 4.5) generally does not allow independent establishment of the distance and density of gas in the outflow, because the easily measured quantity is X-ray ionization parameter $\xi_X = L_X/(n_e R^2)$. This makes the derived energy and momentum flux in the wind uncertain by an order of magnitude or more. Three possible solutions are offered by the powerful soft X-ray spectroscopic capabilities of *Lynx* that provide access to density diagnostics in the AGN winds:

- Detections of density-sensitive line doublets, spanning an energy range of 0.245–1.05 keV, probe densities $10^7 - 10^{15}$ cm^{-3}. These lines are faint and have been detected only once (in the Galactic black hole GRO J1655–40 [385]), but *Lynx* will make a nearly 1,000× leap in high-resolution spectroscopic capability compared to the current state of the art.
- Rapid fluctuations in the ionizing flux from the AGN will change the ionization state of the wind. If changes in the ionization parameter can be tracked on the time scales of recombination, they can be used to infer the gas density. *Lynx* has the capability to measure ξ in 1–10 ksec or less in a typical AGN, and will thus provide a sensitivity to densities $n_e = 10^8 - 10^7$ cm^{-3}, respectively.
- For yet higher densities, recombination times are short and the outflow will always be in ionization equilibrium. However, long-term correlations of the outflow ionization state with black hole luminosity can still be used to infer densities. Both long- and short-term variability of ξ can also be used to constrain filling factors [386].

These three types of measurements will greatly improve determinations of the instantaneous AGN mechanical output. Similar approaches can be used in studies of accretion disk winds in Galactic X-ray binaries.

4.3 Cosmic Dawn

The Cosmic Dawn and the Epoch of Reionization (EoR) which marks its end are widely considered an area with great discovery potential [389]. A number of radio experiments are under development to study the EoR via the redshifted 21-cm background. Detection of galaxies at the EoR is one of the main science goals of *JWST*. The primary contribution of *Lynx* to the Cosmic Dawn studies will be the detection of the first generations of supermassive black holes (§1). However, the sensitivity of *Lynx* will be also sufficient to detect XRB populations in the same redshift range, either individually, in a stack, or as residual diffuse X-ray background. This leads to additional X-ray probes relevant for the multiwavelength push to study the Cosmic Dawn. Extrapolations of population synthesis models [390, 391] predict that the XRBs will dominate the X-ray emissivity of the Universe at $z \gtrsim 6$, surpassing the contribution from AGN [81, 392]. Therefore, XRBs are expected to be the main source of heating to the neutral intergalactic medium (IGM) prior to the EoR [388, 393–396]. This X-ray output can have a dramatic effect on the 21-cm signals from neutral hydrogen, as shown in Fig. 4.6. Reliable projections of the XRB flux from high-redshift galaxies is, therefore, critical for extracting maximal information from future 21-cm experiments. *Lynx* will be instrumental for this task, as discussed below.

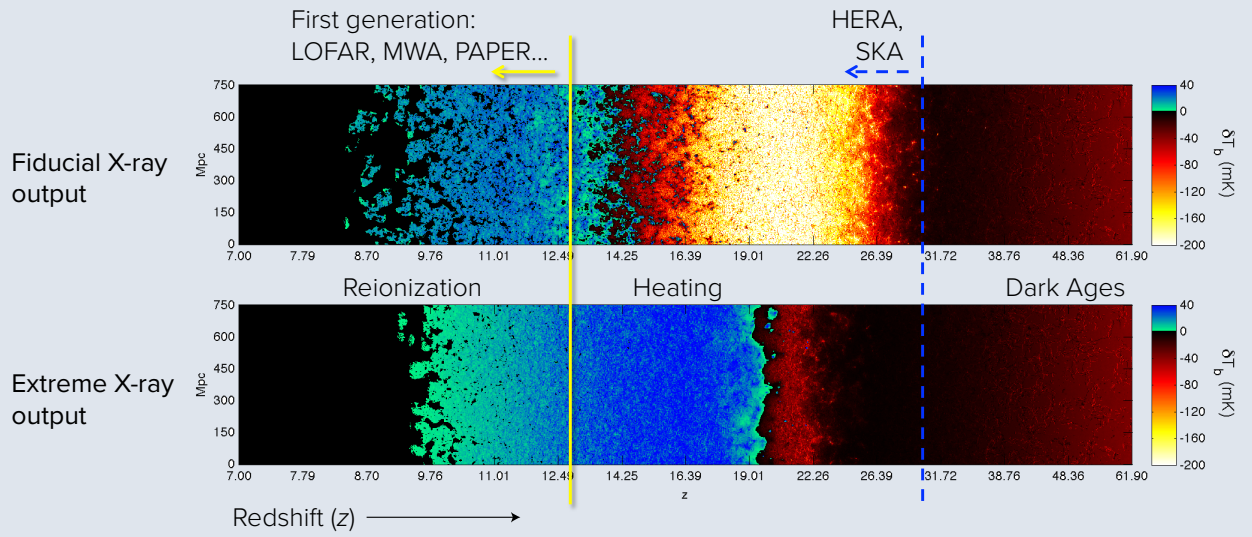

Fig. 4.6— X-rays can have a dramatic impact on the intergalactic gas in the early Universe, as illustrated by light-cone simulations of the 21-cm signal brightness temperature (adapted from [387]). The horizontal axis shows evolution along the line of sight, from $z \sim 62$ to $z \sim 7$. The Epoch of Heating is the interface between yellow and blue, and the EoR is the interface between blue and black. The vertical lines show the reach of various 21-cm interferometer experiments. The top panel corresponds to the "fiducial" model of [388] in which the L_X/SFR ratio is calibrated to local starburst galaxies. The lower panel corresponds to an "extreme X-ray" model in which primordial galaxies are much more luminous, with harder X-ray spectra.

High-redshift star formation — Deep surveys with *Lynx* and *JWST* will have strong synergies for studies of high-redshift galaxies. *Lynx* is expected to detect the integrated XRB flux from *JWST*-detected galaxies with star formation rate (SFR) as low as $2\,M_\odot\,\mathrm{yr}^{-1}$ at $z = 10$ (Appendix A.2). Even lower SFRs will be accessible through stacking analysis. The XRB output per unit star formation rate is a strong function of the high-mass end of the IMF and of the average metallicity of the stellar populations ([390, 391], see also Appendix A.2). For example, the $L_{\rm XRB}$/SFR ratio is expected to increase by an order of magnitude as the average metallicity of newly born stars decreases to $\sim 0.03 - 0.04\,Z_\odot$ at $z = 10$ (c.f. Fig. 1 in [391]). The rest-frame UV output, observed by *JWST*, changes only mildly [136]. Therefore, the ratio of X-ray and NIR fluxes will constrain the properties of stellar populations in the first galaxies.

Extrapolations to EoR — Tracking the $L_{\rm XRB}$/SFR ratio over a wide redshift range, from $z \approx 0$ to $z \approx 10$, also has practical implications in that it will be possible to reliably extrapolate it well into the EoR. Another critical ingredient to the theoretical 21-cm predictions is the shape of the X-ray spectral energy distribution (SED) in the soft band. Soft X-rays dominate the IGM heating because the Universe effectively becomes transparent to ionizing radiation at $E > 1.5 - 2\,\mathrm{keV}$ [397]. Different X-ray SEDs will result in markedly different impacts on the 21-cm signal (Fig. 4.6). The SED of X-rays emerging from a galaxy is a product of the intrinsic SED of accreting objects and the absorption by the interstellar medium of the host galaxy. For the intrinsic SED, the low-redshift census of XRBs in nearby galaxies (§3.4) will be instrumental. The ISM absorption effects in a wide

range of galaxy properties can be assessed using a multitude of intermediate-redshift galaxies found in wider *Lynx* and OIR surveys (e.g., with *WFIRST*).

Cross-correlation with 21-cm signals — Finally, there is a prospect of detecting X-rays from galaxies at $z > 10$ via cross-correlation of the residual X-ray background with the 21-cm signals from experiments such as HERA and SKA [398, 399]. This signal will be possible to extract only using X-ray observatories that offer a high contrast of sky signal to the instrumental background, and only after maximally complete elimination of the X-ray background components originating at higher redshifts, e.g., from intrinsically faint $1 < z < 3$ foreground objects. The capabilities of *Lynx* in this area are unsurpassed by a wide margin (Appendix A.5).

4.4 Large Scale Structure

Lynx is not designed for very wide (more than ~ 100 deg^2) surveys. However, it *will* make distinct contributions to studies of the Large-Scale Structure (LSS) of the Universe through its ability to achieve great sensitivities and dense object sampling in regions of a few tens of deg^2. An example of such program, the *Lynx Legacy Field*, and its multifaceted impact, is discussed below. Additionally, *Lynx* will enable very efficient followup observations of objects discovered in wide multiwavelength surveys, as illustrated below by two examples: high-z galaxy clusters and connection between AGN activity and LSS.

4.4.1 *Lynx* Legacy Field

A *Lynx* Legacy Field is a notional 10 Msec survey in a 10 deg^2 region of the sky with existing multi-wavelength and optical spectroscopic coverage, centered at a massive galaxy cluster at $z = 0.1 - 0.2$ (Fig. 4.7). Continuous coverage with HDXI pointings would result in at least 100 ksec exposure at each location. The sensitivity achieved in this dataset would enable a number of unique investigations within a single observing program, of which four are highlighted:

Cosmic Web filaments — In 100 ksec exposures, *Lynx* will reach sensitivity levels for faint surface brightness emission that are limited not by statistics but by residual uncertainties in the background modeling (Appendix A.5). Rich galaxy clusters form at the intersection of the Cosmic Web filaments, which are expected to be filled with hot gas at X-ray temperatures [401]. Clipping the mock X-ray brightness derived from the the Hydrangea simulation [400] at the *Lynx* surface brightness sensitivity cutoff shows that the Cosmic Web will be exposed *in emission* in the Legacy Field (upper panel in Fig. 4.7).

The application of the Cosmic Web observations to understanding galaxy formation was discussed in §2. The filaments detected in the Legacy Field would be classic examples of the warm-hot intergalactic medium [402–404], on which significant effort has been expended in the UV, probing the lower end of this temperature distribution via broad Lyα [405] and O VI [406] absorbers in individual sightlines toward background AGN. However, UV absorption line studies cannot *map* the Cosmic Web structure, and they still cannot account for all the baryons expected in the intergalactic medium [158].

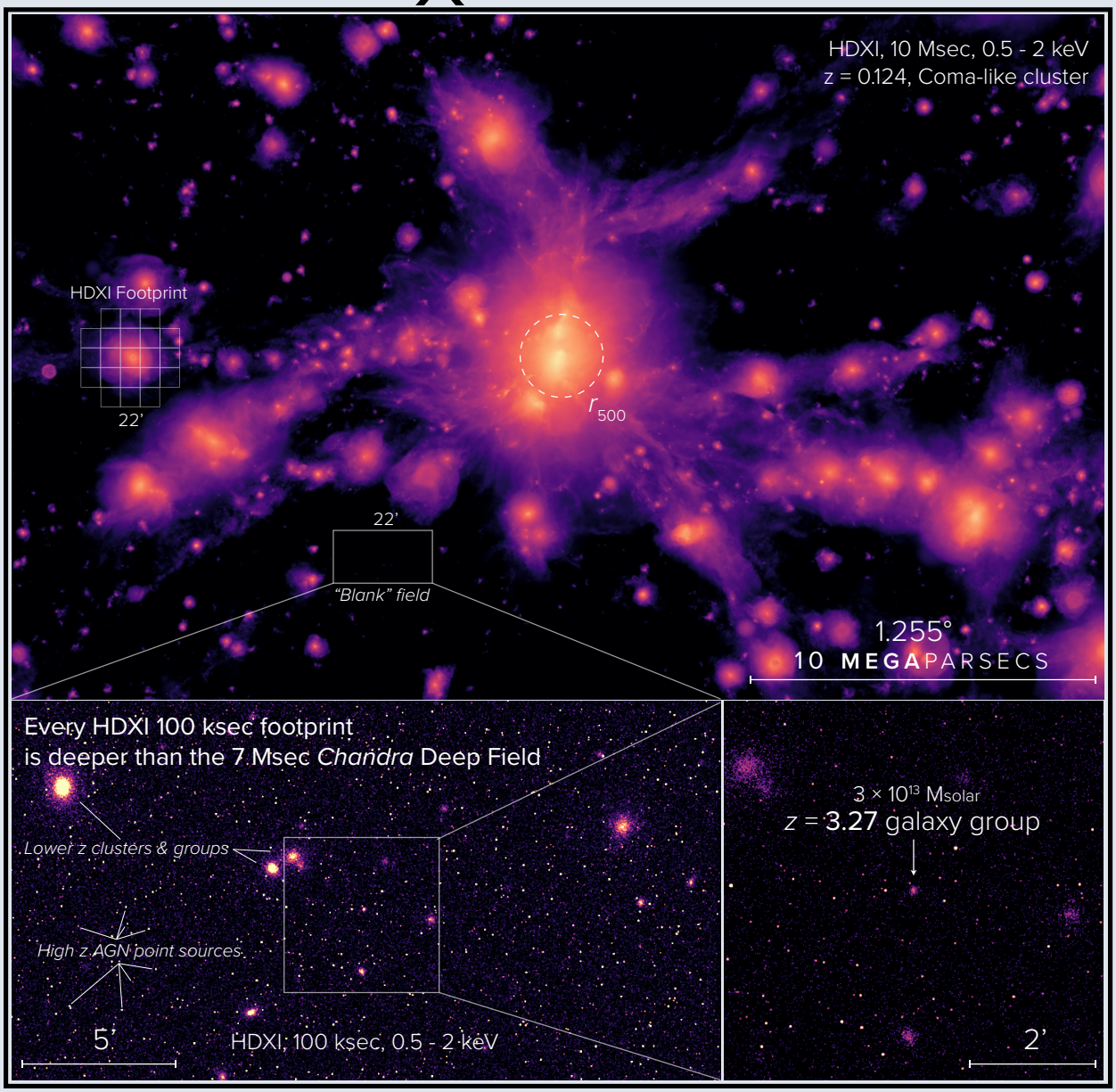

Fig. 4.7— The *Lynx* Legacy Field, a 10 square degree map of the largest structures in the Universe, is a notional 10 Msec program that would reign among the Observatory's most revolutionary achievements. Focused on a previously identified low-z large scale structure, this survey will reveal a massive galaxy cluster anchored to the void by Cosmic Web filaments that have, thus far, never been truly observed. The panel above shows a realistic mock of the soft X-ray surface brightness from the Hydrangea simulation [400], with a true *Lynx* surface brightness sensitivity cutoff applied (see Appendix A.5). A large mosaic of individual 100 ksec HDXI exposures, the Legacy Field will maintain sub-arcsecond imaging across the *entire* field, and *every* individual 100 ksec footprint in the mosaic will reach a greater depth than the deepest region of the 7 Msec *Chandra* Deep Field South. While the image of the filamentary web and its cluster-scale node will be a revolutionary achievement on its own, even "blank" regions of the image would contain an exquisite array of high- and low-redshift AGN, clusters, and groups (§1.2). This is illustrated in the bottom two panels, which show (at bottom left) a zoom-in on a simulated single 100 ksec HDXI footprint of a "blank" region of the Legacy Field. Nearly seven thousand discrete sources will be detected in a single $22' \times 22'$ field of view. It is the ability to detect and mask these sources that gives *Lynx* access to the very low surface brightness levels needed to reveal the Cosmic Web (Appendix A.5). The lower right panel shows a further zoom-in on this "blank" field exposure, revealing a blindly detected $3 \times 10^{13}\ M_\odot$ galaxy group at redshift $z = 3.27$, the epoch of formation of the earliest galaxy groups and protoclusters. The *Lynx* Legacy Field will be among the richest X-ray datasets ever obtained, and reign as a lasting triumph of science.

The *Lynx* Legacy Field maps will go well beyond establishing the full baryon budget: they will reveal a complex and rich array of substructures and dynamics at the interface of Cosmic Web filaments and the virialization regions of galaxy groups and clusters. Note that a 100 ksec *Lynx* observation surpasses the depth of a 5 Msec *Chandra* exposure, reaching an unprecedented level of statistical quality[1]. The most interesting regions can be subsequently observed with LXM to obtain high-resolution spectral information.

Evolution of X-ray source populations — Detection of Cosmic Web filaments in the Legacy Field will be possible only thanks to the ability of *Lynx* to detect and mask discrete X-ray sources. The filament emission itself will be faint, $\lesssim$ 10% of the residual background. Therefore, detectability of faint background sources in most of the Legacy Field's area will not be affected by the presence of extended foreground structure. In terms of sensitivity to point sources, a 100 ksec *Lynx* HDXI observation will surpass the levels achieved in the very central region of the 7 Msec *Chandra* Deep Field South [95]. Note that sensitivity will be provided over a full 10 deg^2 area (lower-left panel in Fig. 4.7). Therefore, the point source catalog from the *Lynx* Legacy Field will be a definitive dataset for studies of evolution of AGN (§1.2) and XRB populations in normal galaxies (§4.3) to moderately-high redshifts.

AGN clustering — The expected number density of detected point sources in the Legacy Field is $\sim 50\,000$ deg^{-2}, of which $\sim$ 50% will be AGN (Fig. A.1 in Appendix A.1). It will therefore be a dataset with an unprecedentedly dense sampling of the LSS using AGN as tracers in a field of a substantial size, uniquely suited for the spatial correlation and cross-correlation studies discussed in §1.2.

Highest-redshift galaxy groups — Properties of distant galaxy groups are an important high-z probe of galaxy formation models (§2). The most useful objects are those with the lowest mass. At high redshifts, these cannot be reliably detected other than in highly sensitive X-ray surveys. The sensitivity of *Lynx*, along with its ability to separate point-like and extended sources, makes it a unique tool for such studies. Cosmological numerical simulations predict that in the Legacy Field alone there will be $\sim$ 10 galaxy groups at $z > 3$ detected down to a mass limit of $M \gtrsim 2 \times 10^{13} M_\odot$. Some of them (e.g., the one shown in the bottom-right panel in Fig. 4.7) will yield a sufficient number of photons for measurements of the thermodynamic state of the intra-group medium.

4.4.2 High-redshift galaxy clusters

Over the next decade, dedicated survey instruments will increase the number of known clusters and groups out to high redshift, constraining cosmology and providing a more complete picture of the early stages of galaxy formation. Examples include *eROSITA* in X-rays, LSST and Euclid in the OIR [410], and several "Stage 3" ground-based mm-wave observatories. The SZ-effect surveys, in particular, will break new ground by providing the first large, robustly selected catalogs of clusters at $z > 1.5$, as well as the first informative absolute mass calibration from CMB-cluster lensing. They will find > 3,000 clusters at $z > 1$ and $\sim$ 50 at $z > 2$ [411–414]. Further in the future, SZ surveys with greater sensitivity and improved spectral coverage (such as CMB-S4 [415]) will probe even deeper.

[1] By comparison, the deepest *Chandra* observation of a galaxy cluster is the 1.4 Msec exposure of Perseus [407]

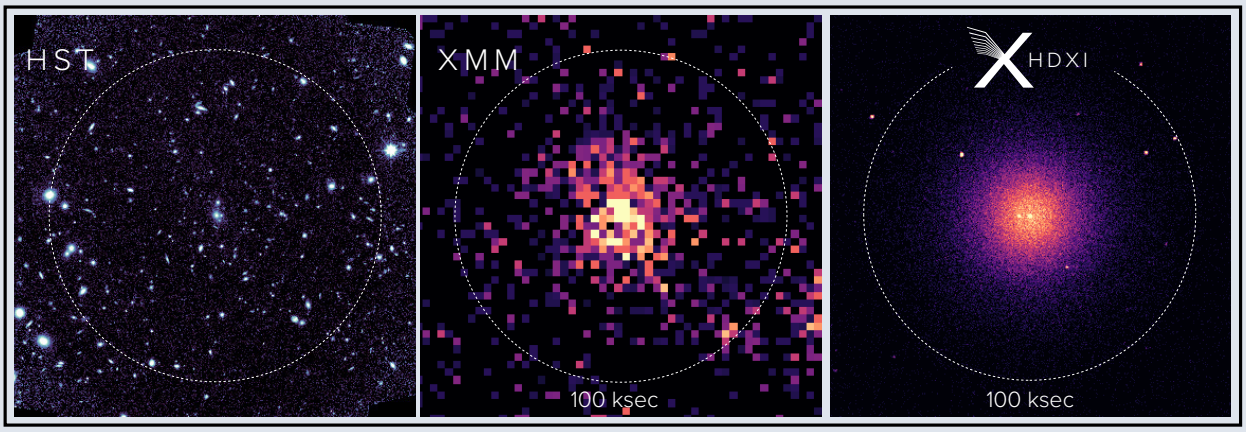

Fig. 4.8— Images of the $z = 2$ cluster XLSSC 122 [408]. (*Left*) *Hubble Space Telescope* F140W map of the cluster; (*center*) a 100 ksec *XMM-Newton* X-ray observation of the cluster; (*right*) a simulated *Lynx* HDXI map of the same cluster with a realistic AGN population expected at high-z. Dashed circles show the characteristic radius, $r_{200} \sim 54''$. The *XMM* and *Lynx* images are adapted from [409], while the *HST* data, used with permission, is from Willis et al. (2019, in prep.).

Once discovered, these systems will be primary candidates for X-ray observations [416]. Tracking cluster evolution to $z \approx 2$ is one of the prime science goals for *Athena* [417, 418]. However, beyond this redshift, *Athena* data will start to be hampered by its poor angular resolution, inability to cleanly separate the hot gas emission from embedded and background AGN, and limited ability to track low surface brightness at the cluster outskirts. *Lynx* will have the angular resolution required to bring X-ray cluster measurements to the highest redshift of the upcoming catalogs (Fig. 4.8). *Lynx* will also resolve the thermodynamic and kinematic structure of these earliest systems, as well as determine the role of feedback from AGN and stars [419, 420].

4.4.3 AGN-LSS connection

Clustering studies can connect the AGN and LSS in a statistical way [102–106], but *Lynx* will enable more direct observations that probe the sub-halo habitats of accreting SMBHs within the LSS. The growth of SMBHs is most strongly affected by environmental processes in the dense nodes of the Cosmic Web — galaxy clusters and groups. As discussed above, these objects can be observed with *Lynx* out to $z \sim 2 - 3$. This epoch is of the utmost importance: it hosts the highest star-formation rate density in galaxies and accretion density in AGN [421], and thus presents a great opportunity to directly understand the interplay between SMBHs, galaxies, and structure formation. The observations required for this science must characterize the mass and dynamical state of parent structures and detect AGN within them. This is best done in X-rays, but the throughput and angular resolution of *Lynx* will be necessary (Fig. 4.8). Current *Chandra* results [422] provide an initial indication that AGN in clusters and in the field evolve differently, which possibly ties the AGN trigger mechanism to galaxy mergers. These results still suffer from statistical uncertainties that *Lynx* will overcome. More importantly, *Lynx* will push these studies in new directions.

At low redshift, the majority of galaxies reside in the group environment. Groups are a sweet-spot for frequent galaxy-galaxy interactions. Probing groups, especially at low masses, requires sensitivity

which only *Lynx* can provide. In fact, *Lynx* will also enable studies of less dense, non-virialized nodes in the Cosmic Web — the protocluster environments. Protocluster structures are already being identified with ALMA and with Lyα observations [423, 424] at $z = 4 - 6$. Only *Lynx* will have the combination of sensitivity and spatial resolution in X-rays to probe the SMBH growth in these environments.

4.5 Cosmology

Cosmology in the coming decades will be a multiwavelength endeavor, with cornerstones provided by millimeter, OIR, and X-ray measurements. In combination, these observations should enable the construction of large, clean, complete source catalogs, with precise redshifts and accurate mass calibration. The exquisite statistical precision of these measurements will turn the emphasis for cosmological studies ever more toward robust systematic controls: only with such controls can apparent tensions between measurements (e.g., [425, 426]) be taken as indicative of new physics. Multiwavelength observations enabling complementary measurements across a broad suite of cosmological probes will be essential, dramatically reducing the impact of systematics that limit the utility of measurements made in any single waveband or with any single technique.

Observations of galaxy clusters provide one of our most powerful probes of cosmology and fundamental physics. The future of multiwavelength cluster science is compelling (§4.4.2, [416]), but to unlock the full power of upcoming $z > 2$ cluster samples, X-ray measurements will be absolutely essential. *Lynx*'s unique capabilities will enable it to cleanly resolve and separate the emission from galaxies, AGN, and diffuse gas in high-z clusters, enabling precise cross-matching with ground- and space-based measurements across all wavebands. *Lynx* measurements of the cluster dynamic, thermodynamic, and chemical structure will provide an unparalleled view of the evolving baryonic matter content within them, spanning the epochs when star formation and AGN activity peaked. Critically for cosmology, *Lynx* measurements will also enable the extraction of precise, low-scatter mass proxies for these systems, thus bringing transformative power to hierarchical modeling of the mass function and baryonic matter content. Potential *Lynx* cosmology programs include: studies of early dark energy and modified gravity, combining measurements of structure growth and expansion history during this early epoch; studies of inflation, utilizing signatures of primordial non-Gaussianity in the highest mass, highest redshift objects; and refined measurements of neutrino masses from their impact on the evolving growth of structure (see [427] for a review).

4.6 The Cycle of Elements

Heavy elements are synthesized in supernova explosions and in mergers of neutron stars [428]. These events disperse heavy elements into the ISM, where a fraction becomes locked into newly formed stars, and another fraction escapes via winds. These processes transport heavy elements into the CGM and IGM, where they can remain for a long time. Some of the intergalactic gas is accreted back onto galaxies, fueling new star formation. *Lynx* will provide a uniquely detailed view of all of the stages in this grand cosmic cycle of elements (Fig. 4.9). The supernova leg of this cycle is discussed in §3.3. The capabilities of *Lynx* for observing winds ejecting metals from

galaxies are discussed in §2.2. This section concentrates on the third leg: heavy elements dispersed in the intergalactic medium.

To put studies of the cycle of elements in context, one should consider the cosmic inventory of heavy elements. It is estimated to be significant — heavy elements contribute ~ 1% of all baryons by mass [429]. A large fraction of heavy elements are trapped in stellar remnants (white dwarfs, neutron stars, black holes), but the remaining "loose metals" are significant enough to enrich all cosmic baryons to a mean metallicity of $0.2 - 0.4\,Z_\odot$ at low redshift. While stars today have an average metallicity of $\sim 1\,Z_\odot$ [430], they account for only 20 – 30% of loose metals. By implication, the gas phase of the present-day Universe should be enriched to a level of $\sim 0.15 - 0.3\,Z_\odot$. However, the total amount of metals detected in damped Lyα absorbers [431] and Lyman-limit systems [432] accounts for less than 10% of the expected cosmic budget [433]. The molecular ISM within galaxies is far less massive and is not a significant cosmic metal reservoir. Therefore, the vast majority of metals should be dispersed elsewhere. Most of these metals presumably reside in the CGM and the IGM [184].

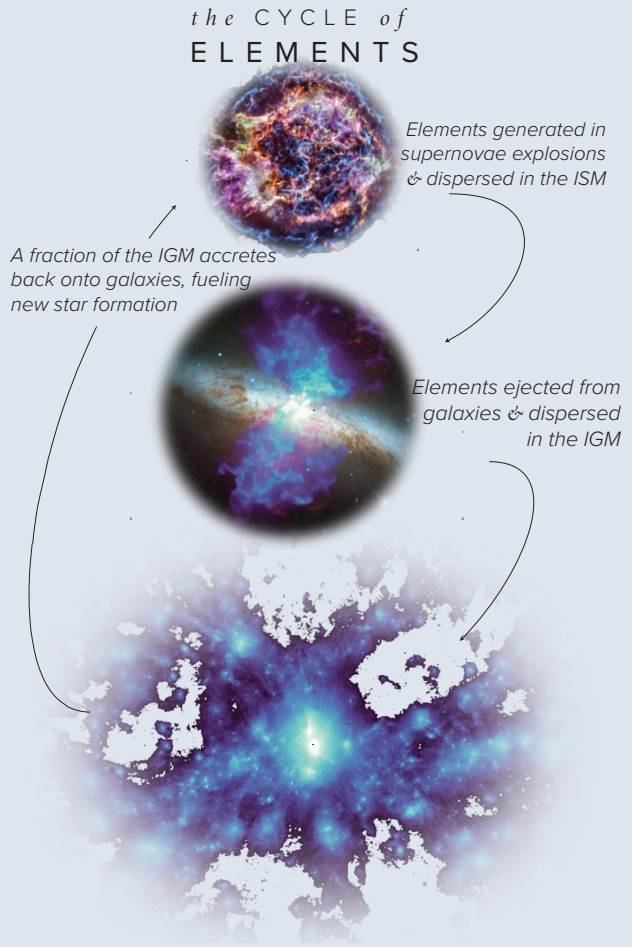

Fig. 4.9— Schematic of the cosmic cycle of elements. Elements heavier than Lithium are synthesized in stars and supernova explosions and dispersed into the ISM. A fraction of the ISM escapes via winds into the CGM and IGM. Some of the intergalactic gas cools and accretes back onto galaxies, fueling new star formation. *Lynx* will provide unique ways to look at all stages of this cycle.

Lynx is poised to drastically improve our view of extragalactic metals. At low redshift, it will perform a census of metals in the hot phase of the CGM and Cosmic Web. At high redshift, it will enable observations of enrichment in galaxy clusters near the peak of cosmic star formation.

Metals in the CGM and Cosmic Web — The main tool for *Lynx* observations of diffuse metals at low redshift is absorption line spectroscopy of background AGN. This method directly detects heavy elements such as oxygen, and also probes intergalactic gas to lower densities than is possible in emission (Fig. 2.4 on p. 38). With the AGN spectroscopic survey discussed in §2.1.5, *Lynx* will perform a blind survey of absorption lines up to $z = 1.6 - 2$ for O VII and O VIII lines, respectively. Structure formation simulations predict a distribution of equivalent widths of extragalactic absorbers.

Lynx will probe lines down to $EW \sim 0.5 - 1$ mÅ. Both simulations [434, 435] and simple analytic estimates predict a detectable system every $\Delta z \approx 0.06$ for $EW > 1$ mÅ. The AGN sample identified for the *Lynx* CGM-in-absorption program (§2.1.5, Appendix A.5) will have a total redshift depth of ~ 26; therefore ~ 400 blind line detections are expected. The same dataset can be used for a blind census of $10^{5.5} - 10^{6.5}$ K gas in the Universe [195].

Early enrichment of galaxy clusters — Hot intracluster gas in rich galaxy clusters contains a fossil chemical record of all previously accreted intergalactic gas, even the initially warm/cold gas. In the local Universe, the intracluster medium (ICM) outside the central ≈ 100 kpc appears to be uniformly enriched to $\sim 0.3\,Z_\odot$ [132–135]. Recent studies indicate that the bulk metal content of clusters has not changed over the past ~ 10 Gyr [137–139]. These results imply that the bulk of metals in the ICM originates from early times. Even combining all available data on high-z clusters from *Chandra* and *XMM-Newton*, one can only put a lower limit on the characteristic redshift of enrichment [137–139], $z > 1.5$.

The bulk of metal enrichment in the Universe should have happened at $z \sim 2.5$, during the epoch of peak cosmic star formation, and one expects a correspondingly strong change in the ICM metallicities around this epoch. As discussed in §4.4.2, *Lynx* is uniquely capable of making detailed measurements of the ICM in clusters at $z > 2$, including spatially resolved profiles of the ICM metallicity. These observations will provide a direct observation of the intergalactic gas enrichment by metals at its peak epoch.

4.7 ISM and Stellar Astronomy

A wide range of energetic processes provide a unique perspective on stellar birth and death. For each of these, *Lynx* will provide a unique perspective (§3). There are also large swaths of galactic and stellar astrophysics, such as the physics of cold ISM or statistics of stellar populations, that do not directly involve high-energy processes. The traditional tools of research in these areas are sensitive OIR, UV, and radio observations. However, the unique capabilities of *Lynx* will enable a view from new, often unexpected angles, using the tools of X-ray astronomy. Three examples are highlighted below.

4.7.1 ISM structure via X-ray reflection

Dense molecular clouds are the primary stellar nurseries. Understanding their internal structure is a key component of understanding star formation. But this structure is determined by a complex, scale-dependent interplay between several processes, which are not well understood, despite their fundamental importance for a range of astrophysical contexts [440, 441]. To determine the overall star formation efficiency, particularly crucial are scales from 10 pc down to 0.1 pc [442, 443]. These scales bracket the transition from quasi-isothermal supersonic turbulence to self-gravity of individual dense cores leading to coherent (rather than turbulent) motions [444]. Physical conditions and hence emission properties of the gas vary across spatial scales, making it hard to construct an unbiased probe free of opacity and projection effects. This applies even to 1″-scale interferometric observations

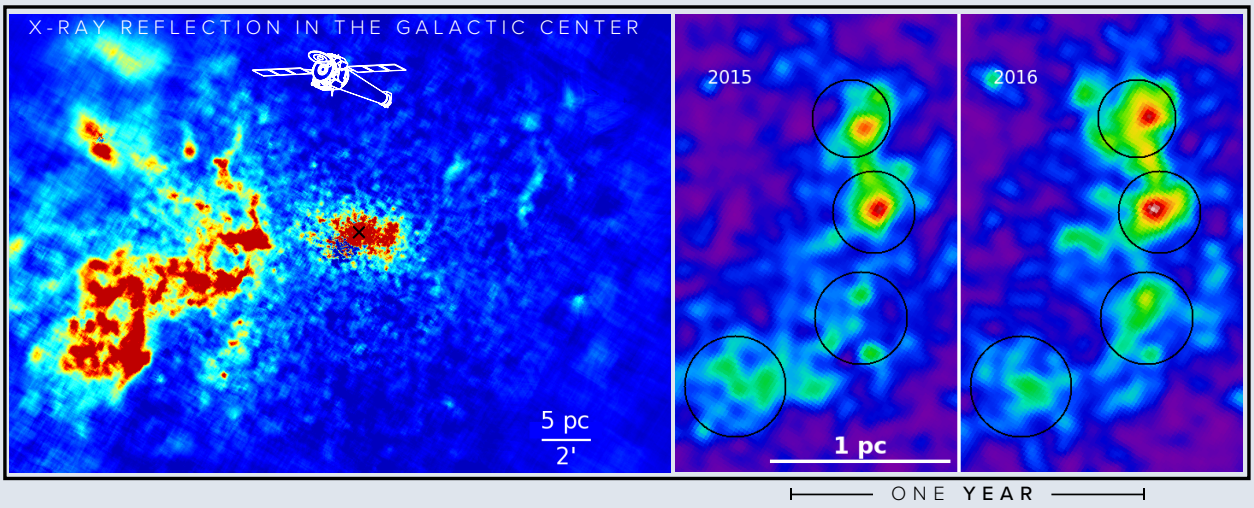

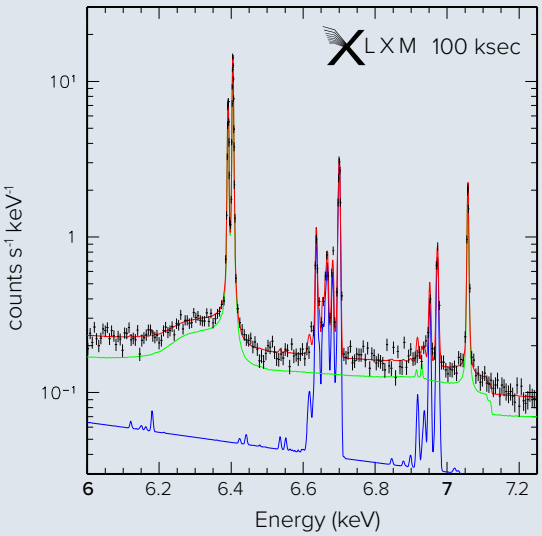

Fig. 4.10— *Above: Chandra* image of the reflected component in the central region of the Galaxy. This component can easily be separated from other background and foreground components using its distinct spectral shape. Right panels show changes in the 4–8 keV images on a time scale of one year in a small patch located ~ 20 pc from Sgr A*. The geometry of the illuminated region is uniquely set by the time delay due to propagation of scattered light from Sgr A* to the cloud, and then to the observer. Knowing the age of the outburst allows reconstruction of the 3D location of the reflecting molecular gas with respect to Sgr A*.

Right: Predicted X-ray reflected emission, which will be observed from the circles shown above in a 100 ksec LXM observation. The model shown in blue corresponds to the contribution of unresolved compact sources in the GC region (i.e., the background for X-ray reflection measurements). Figure adapted from [436].

with ALMA [445, 446], where reconstruction of the 3D density probability distribution function (PDF) is problematic because of leakage of the large scale power [447].

However, Nature offers us a unique diagnostic tool for studying clouds in the Central Molecular Zone of the Milky Way. They reflect X-rays from short and powerful past outbursts of Sgr A* that are short enough to remove all adverse projection or opacity effects in the "reflected" signal (Fig. 4.10). This reflected X-ray emission has a very characteristic spectral shape, which facilitates its clean separation from other background and foreground components. As a result, the evolving X-ray surface brightness distribution is tightly linked to the underlying density field of the molecular gas. This offers a truly unique opportunity to determine the 3D location of the illuminated clouds with ~ 10 pc accuracy and to reveal their internal structure down to 0.1 pc scales.

The first application of this method using *Chandra* produced results consistent with the expectations for quasi-isothermal supersonic turbulence, although statistical noise was still high [448]. Measurements with the *Lynx* microcalorimeter will be orders of magnitude more accurate because of a higher throughput, LXM spectroscopic capabilities on 1″ spatial scale, and a longer baseline for

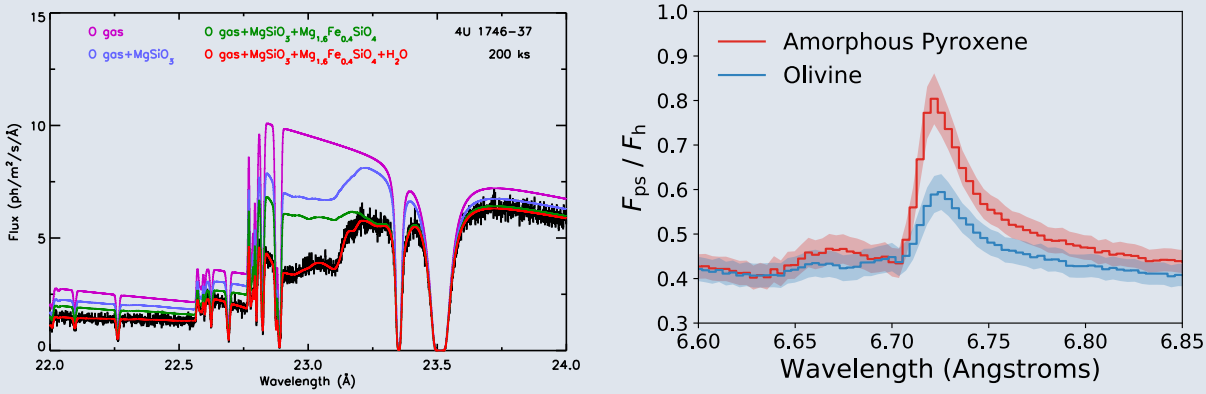

Fig. 4.11— Interstellar dust studies with *Lynx*. *Left, adapted from [437]*: Simulated *Lynx* absorption spectrum of Galactic XRB 4U 1746-37 showing the effects of absorption due to dust at the oxygen K edge. If water ice on grains near the diffuse ISM/cloud interface accounts for the "missing oxygen" (see Jenkins [438]), *Lynx* will easily detect it. *Right, adapted from [439]:* Simulated 20 ksec LXM spectrum of the scattering halo for GX 340+0 (F_h), normalized by the apparent spectrum of the central source. The peak in the scattering cross-section can be used to differentiate between common amorphous and crystalline silicate minerals.

the temporal evolution of the reflected signal (see Fig. 4.10 and [449]). An exciting frontier for the LXM is mapping the gas velocity field using the centroid shift of the reflected 6.4 keV Fe line. Typical turbulent velocities on the order of a few km s^{-1} will probably remain unmeasurable in the X-ray. However, the shear velocity in the Galactic Center region is much larger and can be mapped. This is true not only for clouds separated by tens of pc, but also for the velocity variations within individual clouds [449].

4.7.2 Interstellar dust via X-ray absorption and scattering

Despite decades of study, many questions remain about how cosmic dust is formed, its composition, and its longevity in the ISM of galaxies. *Lynx* will enable a new set of tools to measure the composition, size, and structure of the interstellar dust in the Milky Way [437, 439]. High-resolution X-ray spectroscopic measurements of absorption features in the ISM can probe the interstellar heavy elements in both gaseous and solid form over a broad range of ISM column densities ($N_H \sim 10^{20}$–10^{24} cm^{-2}). Studying these X-ray absorption features yield the constituent compounds, crystallinity, size, and shape of interstellar dust grains [450–454]. An example of application of this method using the *Lynx* X-ray gratings is shown in Fig. 4.11.

Another X-ray probe of the interstellar dust involves the scattering halos around bright sources. The halo intensity and shape depend on grain composition, size, distribution along the line of sight, and column density [455–457]. The sensitivity of *Chandra* and *XMM-Newton* is insufficient to probe the most interesting sightlines through the ISM (e.g., those with existing multiwavelength data). This situation will dramatically improve with the *Lynx* LXM instrument [439]. It will directly reveal resonant features in the scattering cross-section that can be used to identify different mineral components of interstellar dust grains (Fig. 4.11).

4.7.3 Stellar IMF via quasar microlensing

The stellar initial mass function (IMF) — the mass distribution of the newly born stars — is a key ingredient for the interpretation of stellar elemental abundances, the history of stellar populations, galaxy evolution, and for predicting stellar transients at all redshifts [459]. A memorable quote from C. Frenk[1] well summarizes the central issue regarding extragalactic measurements of the stellar mass:

> *Nobody ever measures the stellar mass. That is not a measurable thing; it's an inferred quantity. You measure light, OK? You can measure light in many bands, but you infer stellar mass. Everybody seems to agree on certain assumptions that are completely unproven.*

Quasar microlensing is the *only* way to determine the stellar mass-to-light ratio — a sensitive probe of the IMF slope at low masses — beyond the solar neighborhood [458].

When a massive galaxy gravitationally lenses a distant quasar (Fig. 4.12), it produces multiple images and introduces a magnification to each one. Each of the quasar "macroimages" is the sum of multiple microimages of the quasar formed by the stars in the lensing galaxy. These microimages are the gravitational analog of the speckles produced by the Earth's atmosphere. The movement of the galaxy relative to the quasar causes fluctuations in the brightness of the speckles. Their frequency is a function of the clumpiness of matter in the lensing galaxy, and hence of the stellar-to-dark matter ratio. The total mass distribution can thus be inferred from the separation of quasar macroimages. Therefore, a combination of the macro- and microlensing measurements provides a determination of the amount of mass in compact form (stars, stellar remnants, etc.) at specific locations in the lensing galaxy, typically several kpc from the center.

[1] 2017 May 15, `https://tinyurl.com/y6jx4j8y` (44:48)

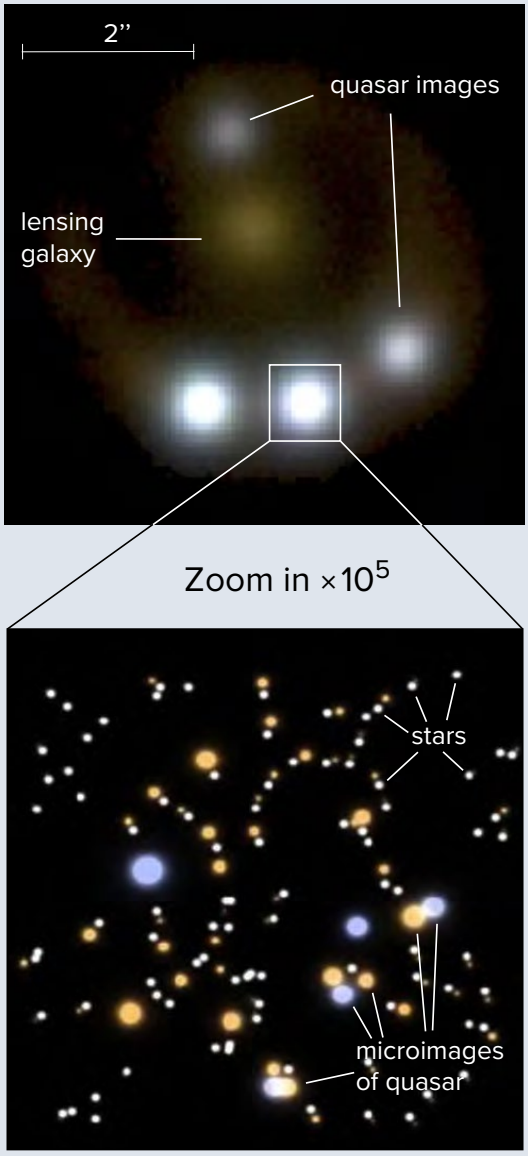

Fig. 4.12— Schematic of quasar microlensing adapted from [458]. *Top:* Magellan image of RX J1131–1231. *Bottom:* Simulated 60 μas × 60 μas region of the lensing galaxy where the macroimage forms. The stars causing microlensing are shown in white. Quasar microimages are shown in red and blue (saddle-points and minima in the lensing field, respectively).

Quasar macroimages are the sum of all the individual, unresolved microimages. Order-of-magnitude variations in brightness of the macroimages are produced when the stellar field shifts by tens of μas. Quasar lensing can characterize both the total mass of the lensing galaxy (via the separation of macroimages) and its stellar population (via microlensing).

The amplitude of microlensing scintillations is the highest in X-rays [363] because the quasar X-ray emitting region is compact. This makes *Lynx* observations unique for determinations of the stellar mass in external galaxies, reaching to $z \sim 1.5$ (detailed strategies are outlined in [458]). As was discussed in §4.2.1, the future prospects for microlensing observations with *Lynx* are excellent. They will radically improve the present measurements done with *Chandra* ($M_\star/L = 1.2 \pm 0.6$ of the Salpeter value [460]).

4.8 Impact of Stellar Activity on the Habitability of Planets

The recent National Academies' report on Exoplanet Science Strategy [461] puts a strong emphasis on the holistic characterization of all factors that may affect habitability of exoplanets. *Lynx* can strongly contribute to one aspect of this problem: the characterization of the effects of stellar activity on planetary atmospheres. This is a particularly important factor for planets around M-dwarf stars, i.e., the very population which will become accessible for transit spectroscopy studies with *JWST* and ground-based ELTs. Energetic stellar photons and particle radiation evaporate and erode planetary atmospheres and control upper atmospheric chemistry. Key exoplanet host stars are too faint in the X-ray band for accurate characterization using existing and already planned X-ray telescopes. *Lynx* is the only facility that can: (1) characterize by proxy the crucial and difficult to observe EUV stellar flux, as well as its history and variations for planet hosting stars, (2) observe the stellar wind, and (3) detect the subtle Doppler signatures of coronal mass ejections. Relevant stellar activity measurements are discussed in [462], and a short summary is reproduced below.

Measurements of EUV irradiating flux — The dominant thermal process in planetary atmospheric loss is hydrodynamical outflow, energized by extreme ultraviolet (EUV; 100–912 Å) and X-radiation (0.1–100 Å) that heats the exoplanet's thermosphere, levitates gas against the exoplanet's gravitational potential [463], and photodissociates heavier molecules into lighter atoms that are more easily lost to space. Most of the thermospheric heating is by EUV photons that cannot be observed directly because of interstellar absorption, while chromospheric UV and FUV are inadequate EUV proxies. The strength and spectral energy distribution of a star's EUV emission can instead be inferred from X-rays originating in the transition region and corona (Fig. 4.13). Detecting the relevant lines requires high-throughput and high-resolution spectroscopic capabilities that are unique to the *Lynx* XGS instrument. *Lynx* can make these measurements for stars of different ages and with different rotation periods, which is critical for understanding the range of likely radiation doses throughout planet evolutionary tracks.

Measurements of stellar winds — The flow of ionized stellar wind electrons and protons also erodes an exoplanet's atmosphere. An example in the Solar system is Mars, where recent measurements by the MAVEN satellite [465] show that the primary mass-loss mechanism for water is erosion by the solar wind. The data on extra-solar winds for stars on the lower half of the main sequence are scarce. There are indirect estimates of up to $\sim 100\,\dot{M}_\odot$ for four G and K stars with strong magnetic fields, based on Lyα absorption in the "wall" of hydrogen at the stellar analogy of the heliopause [466]. There are only two estimates using this technique of mass-loss rates for M stars: $8\,\dot{M}_\odot$ for

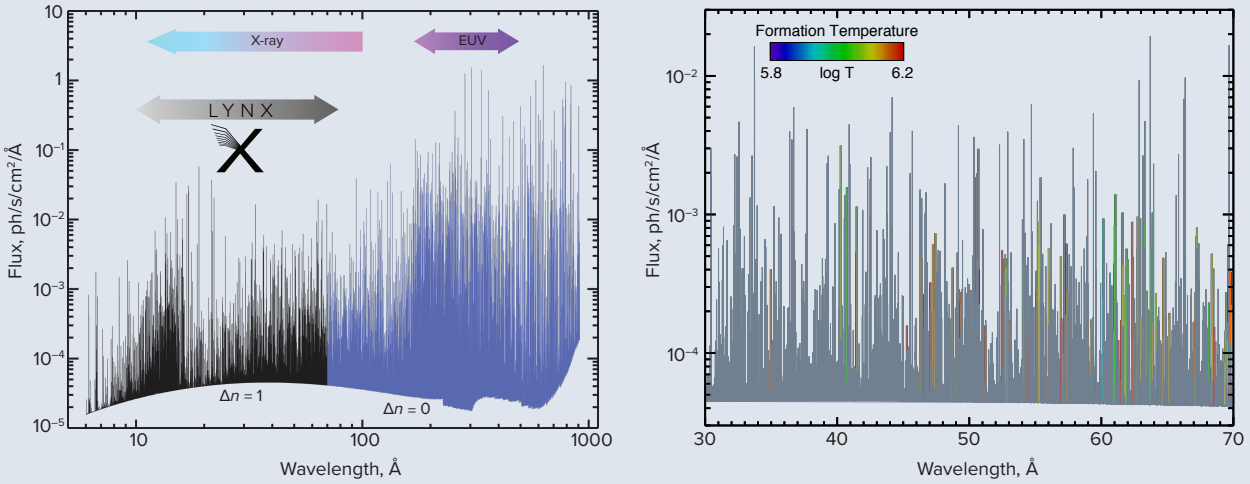

Fig. 4.13— *Left:* The key X-ray-to-EUV spectral region computed for Proxima Centauri b, responsible for upper planetary atmospheric ionization, heating and loss. Coverage at high spectral resolution in soft X-rays is essential for understanding the EUV emission: The 30-60 Å range exhibits transitions of the same ions that dominate the shorter EUV wavelengths. *Right:* The soft X-ray range, highlighting in color lines formed at temperatures below log T = 6.2 that could be observed by a sensitive soft X-ray grating spectrometer and used to measure by proxy the EUV flux. Adapted from [464].

EV Lac and an upper limit of $< 10\,\dot{M}_\odot$ for Proxima. There is suggestive evidence of an increase in mass loss rate with stellar surface X-ray flux [467], up until a critical value where $\dot{M}$ decreases precipitously.

Lynx provides a new method of measuring the winds in a much larger sample of stars. Interaction of the ionized stellar wind with neutral atoms in the ISM generates X-rays via the charge exchange process. The resulting X-ray spectrum is dominated by K-shell emission from H-like and He-like ions of C, O, N, and Ne. The conversion of detected X-ray flux to wind mass loss rate is direct. Using *Chandra*, only an upper limit of $20\,\dot{M}_\odot$ was derived for Proxima [468]. *Lynx* will provide a much larger throughput and the ability to image in the specific spectral lines expected from charge exchange. Drake et al. [462] estimate that winds with Solar-type rate can be observed with *Lynx* to at least 10 pc, and to larger distance for higher rates.

Stellar coronal mass ejections — Solar flares are usually accompanied by the ejection of cooler material ($T \approx 10{,}000$ K) that had previously been confined by magnetic fields that became disrupted during the flare. These so called coronal mass ejections (CME) may also contain high energy protons accelerated in the flare and CME shock front. CME differ from the quasi-steady solar wind in two respects: they are orders of magnitude denser and are spatially confined. Scaling between solar and stellar flare energies, and then between solar flares and CME, implies that CMEs are potentially a major impact to the stellar kinetic energy budget [469], as well as a severe habitability concern [470, 471]. Yet they are not observed as often as they are expected to be on stars [472, 473].

There is thus an acute need for direct observations of stellar CME events. Searches currently underway at low frequency radio band are yet to produce detections. The only detection of an event with extreme power has been made recently with *Chandra* using Doppler shifts of S XVI, Si XIV,

Mg XII, and O VIII lines [475]. There are two previous detections of probable CMEs where the cool dense material is seen in absorption as it passes in front of the flaring corona: from Proxima Cen [476] and from Algol during a superflare [477]. *Lynx* will introduce dramatic improvements in the high resolution X-ray spectroscopy and will routinely and definitively observe the tell-tale Doppler shifts of CMEs or their coronal compression waves.

4.9 Solar System

X-ray observatories have repeatedly demonstrated their benefits in Solar System studies as a means to probe local high-energy environments. Solar System objects are known to emit X-rays through several unique mechanisms which have been directly observed from numerous sources, including: planets (Mercury, Venus, Earth, Mars, Jupiter, Saturn), satellites (the Moon, Io, Europa, Ganymede), comets (Encke, Ikeya-Zhang, Levy, McNaught-Hartley) asteroids (Eros, Itokawa), and space environments (planetary radiation belts, satellite plasma tori, boundary layers such as Earth's magnetopause) ([478] and references therein). The wide variety of both physical systems and emission mechanisms enables Solar System X-ray science to provide invaluable insights into surface and atmospheric compositions [479, 480], magnetospheric and auroral dynamics [481–484], and energy and mass transport [485–488].

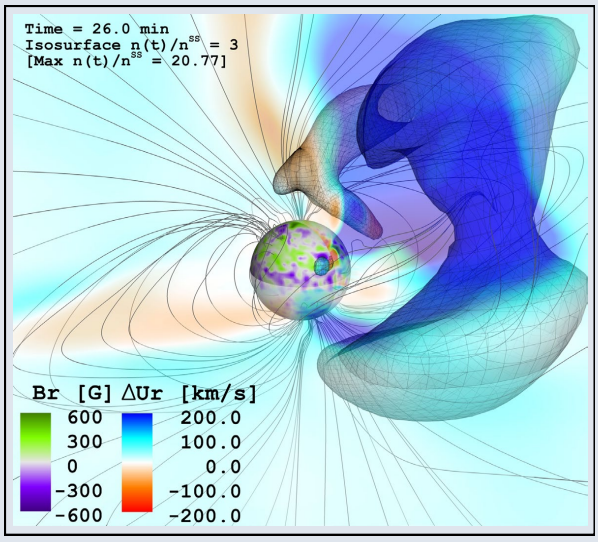

Fig. 4.14— Modeling of CMEs in M-dwarfs predicts a set of distinctive observational signatures, even for cases in which the CMEs are fully suppressed by the large-scale magnetic field [474]. A dramatic gain in the X-ray grating spectroscopy capabilities will allow *Lynx* to systematically detect these CME signatures:

- A factor of 5–10 or more increase in the integrated soft X-ray coronal emission, with durations between tens of minutes up to an hour.
- In weakly-suppressed CME events, a rapid ($<$ 1 hour) evolution of Doppler shifts from red to blue, with velocities up to 200 km s^{-1}, transitioning from hotter ($\log T \gtrsim 6.8$) to cooler ($\log T \simeq 6.0$) coronal lines. Lower velocities (< 100 km s^{-1}), and longer durations ($\gtrsim 1$ hour), are expected for more strongly suppressed eruptions.
- Fully confined CME events would lead to a gradual brightening of the soft X-ray corona by factors of $\sim 2-3$ over the course of several hours. This emission would be redshifted (< -50 km s^{-1}), indicative of infalling material (the so-called coronal rain cloud).

Adapted from [474]. The figure shows a simulated weakly suppressed CME event, with colors indicating Doppler shifts and surface magnetic field strength.

The utility of both *Chandra* and *XMM-Newton* for Solar System observations is strongly limited by either low effective area at soft X-rays, limited spatial resolution, or low spectral resolution. As a result, Solar System objects require lengthy observing campaigns, often spanning multiple days/weeks and extensive modeling. These factors ultimately limit the overall impact of Solar System X-ray studies for broader scientific application. *Lynx* is uniquely poised to make major advances in Solar System science in a manner not possible with other X-ray observatories. Its high throughput and angular resolution will enable time-domain X-ray studies in which particle transport and short-term variability will be resolvable for the majority

Fig. 4.15— (*Left*) *Chandra* High Resolution Camera image of X-ray emission from the northern Jovian aurora, superimposed on a *Juno* image of the planet. (*Right*) An observation of Comet C/2012 S1 (ISON) showcasing optical and X-ray emission [488]. The X-ray emission was detected with *Chandra* using a 24 hour exposure during the comet's closest approach with Earth. The notable increase in soft X-ray effective area of *Lynx* will allow them to detect the daily fluctuations within comet atmospheres out to a distance 3× what is presently possible, while advances in spatial resolution will provide details at resolution of 1,000 km.

of Solar System objects. For example, *Lynx* will resolve X-ray emission from return currents in Jupiter's magnetosphere which are known to fluctuate on minute timescales [484, 489]. *Lynx* will also search for Jovian-type aurorae (Fig. 4.15) in other gas giants, where current observations are inconclusive [490–492].

X-ray emission serves as a unique beacon for surface elemental composition via fluorescence emission lines, as demonstrated by *Chandra* measurements of the Lunar surface [479]. *Lynx* will provide high-quality data for the Moon and extend similar measurements throughout the Solar System. For example, on Europa, X-ray fluorescence studies of the surface ice can be used to model its elemental composition, and potentially even that of the sub-surface ocean if the regolith or ice is significantly mixed with cryovolcanic ejecta (c.f. [493]).

Lynx will also provide a glimpse into the early Solar System elemental and molecular composition via X-ray emissions from comets (Fig. 4.15). Comets are known to emit X-ray through mechanisms that track cometary chemical composition and comet-Solar Wind interactions [488, 494–497]. Orders-of-magnitude higher throughput of *Lynx* will enable, for the first time, statistical analyses of cometary X-rays as a function of composition, outflow rates, origin, orbit, and chemical evolution.

4.10 Physics of Space Plasmas, Shocks, and Particle Acceleration

X-ray observations provide the opportunity to probe space plasmas in a range of parameters inaccessible with traditional *in situ* measurements in the Solar system. Examples include very energetic shocks and particle acceleration in supernova remnants, and plasma with very low (but non-zero)

magnetic pressure in massive galaxy clusters. These are key regimes for understanding the physics of shock waves, particle acceleration, and transport processes in a variety of astrophysical settings. The plasma physics effects in clusters and SNRs can be studied in X-rays in such systems, but *Lynx*'s subarcsecond angular resolution will be required to probe the relevant length scales near the Coulomb mean free path and below [498, 499].

Magnetic fields and transport processes — Plasma transport processes can potentially have a profound effect on evolution and formation of galaxies and galaxy clusters [501, 502] (but see [503–505] for predictions in the opposite extreme). However, the thermal conductivity and viscosity of the hot intergalactic and intracluster gas remain poorly constrained observationally. It is nevertheless clear that the presence of a magnetic field and its topology play a critical role [506–509]. The most useful measurements are, therefore, in settings where the magnetic topology is expected to be simplified. For example, near contact discontinuities, magnetic fields are expected to be parallel to the interface [510, 511]. Such a setting is where the angular resolution and sensitivity of *Lynx* can be used efficiently to constrain the parallel conductivity Observations of precursor temperature gradients on kpc-scales ahead of shocks gives an opportunity to constrain heat conduction for a different magnetic field topology.

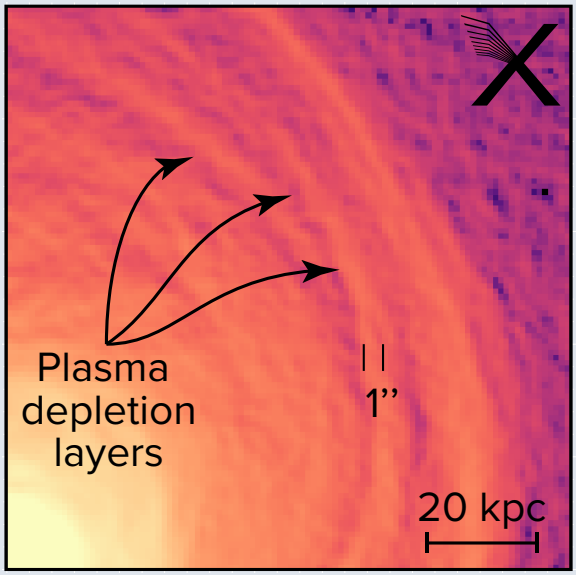

Fig. 4.16— Simulated image of a cold front in a nearby, $kT \sim 2$ keV cluster with *Lynx*, filtered to show surface brightness gradients. The plasma depletion layers with high magnetic pressure and low surface brightness revealed in the *Lynx* image but are lost in the noise for *Chandra*. *Adapted from [500].*

Plasma viscosity is one of the key parameters required for understanding how the kinetic energy generated by AGN feedback is dissipated into heat (§2). *Lynx* will vastly improve upon *Chandra*'s viscosity constraints obtained via resolved signatures of fluid instabilities [512, 513], ram-pressure-stripped tails of galaxies [514, 515], and surface brightness fluctuations [516, 517]. It will also enable new types of measurements via a combination of high spatial and high spectral resolution data [142].

Finally, *Lynx* can provides indirect measurements of the magnetic field strength in "plasma depletion layers," created when magnetic fields are stretched and amplified by strong velocity shears (Fig. 4.16). Tantalizing evidence for such layers have been provided by *Chandra* [513, 518–520], but the large effective area and high angular resolution of *Lynx* are required to make definitive detections. The depth of the surface brightness depressions provide an estimate of the magnetic field strength, and the structure of the layers will constrain viscosity and thermal conduction [500].

Particle equilibration — Cosmological structure formation commonly leads to a situation in which ions and electrons can be heated to different temperatures (e.g. [521]). The electron-

ion non-equilibrium affects the subsequent evolution of these objects and interpretation of their observations (e.g. [522]). The equilibration process can be tested with low-Mach shocks in galaxy clusters, where spectroscopy on arcsecond scales can establish if the equilibration timescale is due to Coulomb collisions or a faster plasma process. While current results from *Chandra* are inconclusive and limited by statistics [523–525], *Lynx* will drastically improve the statistics and enable new observational tools, such as direct measurements of T_i from thermal line widths.

Particle acceleration in SNR and galaxy clusters — X-rays can also probe sites of cosmic ray acceleration. In the case of SNRs, they are seen in continuum synchrotron emission at the location of the remnant's forward shock [526]. *Chandra* observations of Tycho show an even more intriguing pattern of synchrotron radiation: a series of "stripes" or ripples that may be interpreted as a signature for the presence of 10^{14} – 10^{15} eV protons (Fig. 4.17, [527, 528]). *Lynx* can search for similar structures in other SNRs, thanks to its much higher sensitivity and an improved ability to separate thermal and non-thermal emission spectrally while maintaining arcsecond angular resolution. Observations with *Lynx* will also provide a long baseline for detections and studies of secular motions of shocks and ripples.

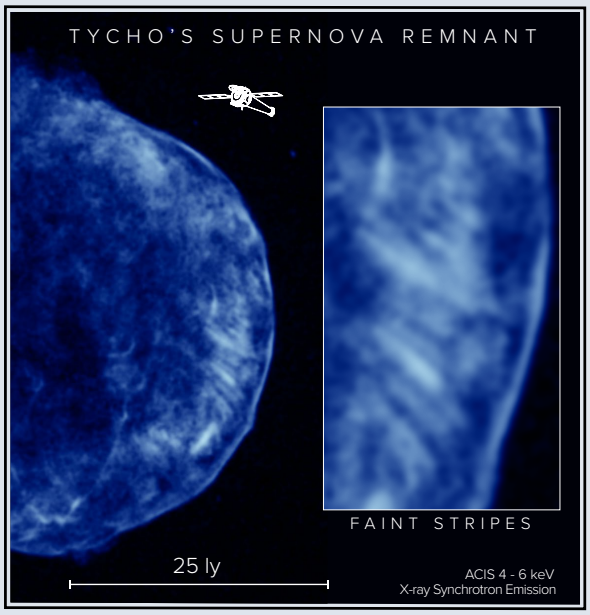

Fig. 4.17— *Chandra* 4–6 keV X-ray image synchrotron radiation in Tycho Supernova Remnant from 2011. "Stripes" are clearly seen on the west limb, as shown in the inset panel.

Credit: CXC

The weak shock waves driven by galaxy cluster mergers can also accelerate cosmic ray electrons, as evidenced by their radio synchrotron emission, which appears in the form of "radio relics" tracking the shock waves [529]. The physical mechanisms by which particles are accelerated so efficiently at these relatively low-Mach shocks remains unclear. To distinguish between various acceleration mechanisms, precise measurements of the shock Mach numbers and radio synchrotron properties are crucial. Radio measurements are now fully feasible with a new generation of telescopes. To obtain X-ray data of matching quality requires the angular resolution and sensitivity of *Lynx*. The LXM data also can be used to test for the presence of supra-thermal electrons [530] that may be key for understanding the high efficiency of particle acceleration.

Yet another opportunity to study particle acceleration is provided by the diffuse radio halos in clusters, where the radio synchrotron emission arises from the second-order Fermi acceleration of relativistic electrons by MHD turbulence [531, 532]. The LXM can track the turbulent cascade down to the relevant scales for efficient acceleration and show how the turbulence is distributed spatially.

5 Science Traceability Matrix

Table 5.1 provides a list of observing programs required to execute the *Lynx* pillar science discussed in §1–§3. These programs are generally multipurpose and multi-object, with the targets ranging from stars in our cosmic neighborhood to deep surveys penetrating into the epoch of reionization. Exposure times for individual targets range from short snapshot observations to very deep pointings.

The notional observing plan is used to define the mission performance requirements. As a very general summary, execution of the pillar science requires and X-ray observatory operating in the "standard" X-ray band, 0.2–10 keV, which combines high angular resolution, high throughput, and transformational spectroscopic capabilities. For imaging and deep surveys, the required angular resolution is similar to *Chandra*'s but the grasp (product of effective area and the size of the FOV with sub-arcsecond imaging) needs to be nearly 1,000× higher. On the spectroscopy side, *Lynx* needs $R > 5{,}000$ for point-like sources. Spatially resolved spectroscopic capabilities are also needed, reaching down to sub-arcsecond spatial scales, and providing resolving powers $R \sim 2{,}000$ for key astrophysically important lines both in the hard and soft X-ray bands.

With the projected state of X-ray detector technology in the next ~ 10 years, a minimum observatory configuration capable of providing the capabilities summarized above includes three science instruments: an imaging camera, an X-ray microcalorimeter, and X-ray grating spectrometer. The instruments are placed in the prime focus of the advanced X-ray mirror and take full advantage of its angular resolution and throughput. A complete discussion of the mission configuration and design choices for the optics and science instruments is presented in §6 below. The overall *Lynx* mission configuration trade space is discussed in §9.

The *Lynx* science traceability matrix (STM) is presented in Table 5.2. Note that only the main science drivers for each of the major performance requirements are listed in the STM. There are multiple science programs in the notional plan for the pillars relying on each of the capabilities, but typically with less demanding requirements (Table 5.1). Additional notes on the mirror and science instruments requirements are given below.

Lynx Mirror Assembly — The prime science driver for *Lynx* angular resolution is detecting early supermassive black holes at the seed stage or soon after. The required X-ray sensitivity is $\approx 10^{-19}$ erg s^{-1} cm^{-2}. To avoid source confusion at these fluxes, and to uniquely associate detected X-ray sources with high-z galaxies requires an angular resolution of 0.5 arcsec (HPD), and better than 1 arcsec across the FOV used for sensitive surveys (Appendix A.1). Many *Lynx* programs need a large FOV with sub-arcsecond imaging. Here, the *Lynx* requirement is better than 1 arcsec (HPD) PSF maintained to an off-axis radius of at least 10 arcmin.

As discussed is §9, there will be a great value for the Observatory/Discovery portion of the *Lynx* program that goes beyond execution of the science pillars, increases the breadth of *Lynx* science impacts, and provides opportunities for observations that address today's "unknown unknowns" — those questions one has yet to even ask. Therefore, for the DRM configuration, the mirror effective area is sized to 2 m^2 at $E = 1$ keV, such that the pillar science can be executed in ≈ 50% of the observing time of a nominal five-year mission (Fig. 5.1).

Table 5.1— Notional observing plan required to execute science pillars

Pillar	Program	Typical Observation	Instrument	t_{exp}
The Dawn of Black Holes	**Origin of SMBH seeds*** §1.1	Surveys over 1 deg^2 to depth $f_x = 1.6 \times 10^{-19}$ erg s^{-1} cm^{-2} [0.5–2 keV band] plus a deeper survey over 400 $arcminute^2$ to $f_x = 7 \times 10^{-20}$ erg s^{-1} cm^{-2}	**HDXI**	23 Msec
	SMBH growth from Cosmic Dawn to the Present. AGN & environments. Triggering, quenching, relation to galactic star formation. §1.2	Survey down to $f_x = 2 \times 10^{-18}$ erg s^{-1} cm^{-2} over 2 deg^2	**HDXI**	2 Msec
Drivers of Galaxy Formation and Evolution	**State of diffuse baryons in galactic halos — direct imaging*** §2.1	Survey of ~ 15 low-redshift isolated (spiral) galaxies, pushing 10% thermodynamic (gas density) measurements to 0.5 r_{500} for $M \sim 3 \times 10^{12}$ $M_\odot$ and to r_{200} for $M \sim 1 \times 10^{13}$ $M_\odot$.	**HDXI**	7.5 Msec
	State of diffuse baryons in galactic halos — absorption line spectroscopy* §2.1.5	Observe ~ 80 AGN ($f_{agn} \sim 1 \times 10^{-11}$ erg s^{-1} cm^{-2}) to detect ~ 30 absorption line systems in $M \sim 10^{12}$ $M_\odot$ galaxy halos down to ~ 1 mÅ EW. Use same sightlines to characterize the Milky Way Halo and for blind detections of the Cosmic Web.	**XGS**	5 Msec
	State of gas and feedback in high-redshift galaxy clusters and groups. §2, 4.4.2, 4.6	Gas temperature, density and metallicity profiles in ~ 30 clusters and groups at $z > 2$	**LXM**, main array	6 Msec
	Characterization of the first galaxy groups at $z = 3 - 4$. §2, 4.4.1	Imaging observations of ~ 10 high-z galaxy groups	**HDXI**	2 Msec
	Spectroscopic survey of AGN to determine energetics of the AGN feedback. §2, 4.2.3	Soft-band spectroscopy with $R > 1{,}000$ down to 0.2 keV to measure density-sensitive spectral features	**XGS**, **LXM**, ultra-high resolution array	3 Msec
	Characterize the supply side of AGN energy feedback. §2	Measure thermodynamic state of diffuse gas near the Bondi radius of SMBHs in nearby elliptical galaxies	**LXM**, enhanced spatial resolution array	2 Msec
	Measure the energetics and effects of AGN feedback on galactic scales* §2	Observe AGN-inflated bubbles in the ISM of low-redshift elliptical galaxies	**LXM**, enhanced spatial resolution array	2 Msec
		Spectro-imaging of extended narrow emission line in nearby spiral galaxies		2 Msec
	Energetics and mechanics of galactic winds*. §2.2	Observe galaxy winds in ~ 20 objects, with the ability to characterize velocities to < 100 km/s on arcsecond scales	**LXM**, ultra-high resolution array	2.5 Msec
	Galaxy cluster-scale feedback §2, 4.10	LXM observations of nearby galaxy clusters to constrain plasma physics effects in the cluster cores	**LXM**, main array	2 Msec
The Energetic Side of Stellar Evolution and Stellar Ecosystems	Young star forming regions §3.1	Surveys to detect entire mass distribution of stars in active star forming regions to $d = 5$ kpc	**HDXI**	2 Msec
	Stellar coronal physics, impact of stellar activity on planet habitability, accretion on young stars. §3.2	Spectroscopic survey of 80 stars within 10 pc	**XGS**	2 Msec
		Transit spectroscopy of planets around dwarf stars down to super-earth regime	**XGS**, **LXM**, ultra-high resolution array	1 Msec
	Endpoints of stellar evolution: SNRs*. §3.3	Targeted observations of the youngest SNRs in the Milky Way, up to ~ 50 objects	**LXM**, main array	2 Msec
		Statistics and typing of SNRs in different environments in nearby galaxies		1 Msec
	Endpoints of stellar evolution: X-ray binary populations. §3.4	Survey of X-ray binary populations in nearby galaxies	**HDXI**, **LXM**	2 Msec

* — highlighted in bold are *Lynx* performance drivers (see Science Traceability Matrix, Table 5.2).

HDXI — The High-definition X-ray Imager needs pixels < 0.33 arcsec to adequately sample the mirror PSF and a FOV ≥ 20 arcmin × 20 arcmin to meet the requirement for surveys and imaging objects with large angular extent. Energy resolution requirements are lax. The HDXI plus the optical blocking filter system needs to have good quantum efficiency, especially in the soft band, to meet the overall effective area requirements. The need for thin optical blocking filters introduces indirect frame rate requirements for the HDXI, which translate into good timing capabilities (§6.3.2).

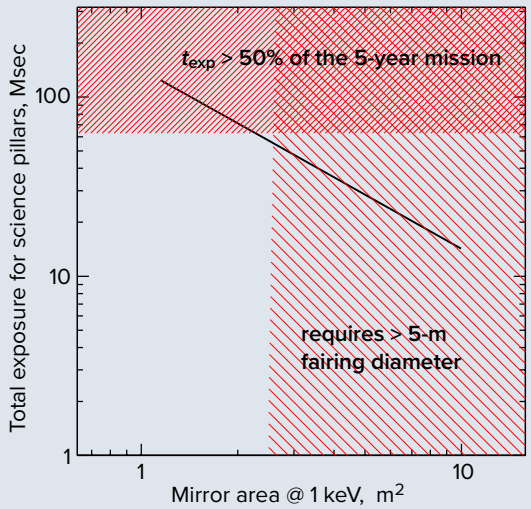

Fig. 5.1— Total exposure time of the notional observing plan from Table 5.1, as a function of the mirror effective area at E = 1 keV. An effective area of 2 m^2 represents an appropriate design choice because such a telescope can fit inside the dynamic envelope of the standard 5-m fairings, while still enabling a dynamic and exciting observing program (see text and Chapter 9). Exposure time available in a 5-year mission shown here assumes 85% observing efficiency §,6.6.2.

LXM — The *Lynx* X-ray Microcalorimeter will provide non-dispersive spectroscopy, required by many science programs. The main array simultaneously needs < 3 eV energy resolution over the 0.2–7 keV band, and 1 arcsec spatial resolution over a 5arcmin × 5arcmin FOV, driven equally by requirements of the SNR, galaxy cluster, and ISM studies. Major components of the pillars program, especially energy feedback studies, will require even more demanding specialized capabilities. These will be achieved by introduction of two additional arrays. The enhanced imaging array with 0.5 arcsec pixels, 1 arcmin × 1 arcmin FOV, and an energy resolution of 2 eV over the 0.2–7 keV band is required, e.g., to characterize the effects of AGN feedback on galactic scales. The ultra-high spectral resolution array with 1 arcsec pixels and a 1arcmin × 1arcmin FOV will provide 0.3 eV energy resolution in the 0.2–0.75 keV band required, e.g., for studies of supernovae-driven galaxy winds and density diagnostics in AGN outflows.

XGS — A spectral resolution higher than what is achievable with X-ray microcalorimeter technology in the foreseeable future is required for absorption-line studies of diffuse baryons in galactic halos, physics of stellar coronae, and assessing the impact of stellar activity on habitability of their planets. This capability will be provided by the X-ray Grating Spectrometer. The XGS applications are broad but the performance requirements are driven by absorption line studies of diffuse baryons in galactic halos. Approximately 4,000 cm^2 of system throughput is required at the astrophysically important X-ray lines in the 0.2–2 keV band, especially O VII and O VIII absorption lines. A resolving power of $R \approx 5{,}000$ is needed to match the expected thermal line widths, and $R \approx 7{,}500$ is desired.

X SCIENCE TRACEABILITY MATRIX

Science Goal	Science Objective	Key Observations	Measurement Requirements	Mirror and Instrument Requirements		
				Instrument	Property	Value
See the Dawn of Black Holes	**Observe progenitors of supermassive black holes at their seed stage at z=10**	Detection of black holes in z=10 galaxies down to a mass limit of M_{BH}=10,000 M_{Sun} over a volume with 10^4–10^7 potential host galaxies. §1.1.3, Appendix A.3	Surveys with flux limits (0.5–2 keV): • 1.6×10^{-19} erg/s/cm^2 over 1 deg^2 • 7×10^{-20} erg/s/cm^2 over 400 arcminutes^2	Mirror+ HDXI	**Angular Resolution (HPD)**	**<1 arcseconds across the field**
					Grasp @ 1 keV	**~2 m^2 × 300 arcminutes^2**
					Imager pixel size	**0.33 arcseconds**
Reveal Invisible Drivers of Galaxy and Structure Formation	**Determine the state of diffuse baryons in galactic halos to guide the galaxy formation models**	Direct imaging observations of 15 low-*z* galaxies with M_{tot}~3×10^{12} M_{Sun}. §2.1.4, Appendix A.5	Reach 10% accuracy for derived thermodynamic parameters of hot gas at 0.5 r_{200}	Mirror+ HDXI	**Effective Area @1 keV**	**2 m^2**
					Field of View	**10 arcminute radius**
					Spectral Resolution @1 keV	**60 eV (FWHM)**
					Particle Background @0.5-2 keV	**< 0.0005 cnt/s/arcmin^2/keV**
		Characterization of hot halos beyond the virial radius in ~30 galaxies with mass $10^{11.5}$–$10^{12.5}$ M_{sun} at z=0-1. §2.1.5, Appendix A.5	Observe 80 bright AGN sight lines to reach the sensitivity of 1 mÅ for OVII and OVIII absorption lines	XGS	**Spectral Resolving Power**	**5,000**
					Effective Area at 0.45-0.7 keV	**4,000 cm^2**
	Establish the energetics, physics, and the impact of energy feedback on galactic scales	Spatially and spectrally resolve the structure of starburst-driven winds in low-redshift galaxies. §2.2	Measure the outflow velocity profile in 20 galaxies with 100 km/s accuracy, and derive the momentum and energy flux	LXM / Ultra High Resolution Array	**Spectrometer Pixel Size**	**1 arcsecond**
					Energy Resolution @0.2-0.75 keV	**0.3 eV (FWHM)**
					Spectrometer Subarray Size	**1 arcminute × 1 arcminute**
		Determine the effects of AGN energy feedback on ISM, and determine the physical state of gas near the SMBH sphere of influence in nearby galaxies. §2	In 30 nearby galaxies, resolve extended emission line regions, AGN inflated bubbles, and characterize the thermodynamic state of gas with 10% precision at or close to the Bondi radius from the central black hole	Mirror + LXM / Enhanced Main Array	**On-axis Angular Resolution**	**0.5 arcseconds (HPD)**
					Spectrometer Pixel Size	**0.5 arcseconds**
					Energy Resolution @0.6-7 keV	**3 eV**
					Spectrometer Subarray Size	**1 arcminute × 1 arcminute**
Unveil the Energetic Side of Stellar Evolution and Stellar Ecosystems	**Constrain SN explosion physics, the origin of elements, and a relation between SN activity and local environment**	Survey of young SNR in Local Group galaxies. §3.3	Measure spatial structure of SNRs in spectral lines of individual elements (e.g. Fe-Kα), and in non-thermal emission	LXM / Main Array	**Spectrometer Pixel Size**	**1 arcsecond**
					Spectrometer Field of View	**5 arcminutes × 5 arcminutes**
					Energy Resolution @0.6-7 keV	**3 eV (FWHM)**
					Effective Area @6 keV	**1,000 cm^2**

Mission Functional Requirements

Operate and survive in the science orbit, with a minimum observing efficiency of 85%, for the duration of the 5-year mission

Accommodate payload in the Launch Vehicle

Provide data collection that is sufficient for uninterrupted observations by all science instruments

Provide pointing attitude control and knowledge consistent with sub-arcsecond imaging, as well as stability consistent with a 1 arcminute FoV

Table 5.2


LYNX MISSION DESIGN

6 *Lynx* Design Reference Mission

The *Lynx* X-ray Observatory will inspire extraordinary new science investigations that are not possible through existing or planned missions. The Design Reference Mission will deliver revolutionary scientific returns across all three science pillars driving *Lynx* mission requirements. The approach detailed here leverages extensive spacecraft and mission operations heritage, all while requiring only four key technologies to be advanced to Technology Readiness Level 6. This approach will greatly reduce risk posture while maximizing mission success.

6.1 *Lynx* Design Rationale

The *Lynx* science pillars address some of the most profound science questions facing the astronomy community today. These science pillars set the mission goals and observatory requirements for the notional Design Reference Mission (DRM) (Figure 6.1), defined here as the science program, observatory architecture and telescope design, and the notional mission profile. The DRM is designed to achieve transformational science with low risk by (1) prioritizing a General Observer (GO) program with a long mission lifetime and high observing efficiency, (2) capitalizing on advanced payload technologies with clear development paths, (3) embracing heritage architecture and operations paradigms, and (4) incorporating proven spacecraft technologies.

A team of dedicated engineers, technologists, and scientists from NASA Centers, government institutions, universities, and industry has generated a mission concept and preliminary observatory design. The *Lynx* team started with a broad trade space, including key technology, mission profile, and spacecraft options. Exhaustive trades were carried out at the component, system, and mission levels (§9 and Appendix B), resulting in a streamlined, highly capable DRM that will perform science befitting a flagship mission for a cost and schedule that permits a balanced astrophysics portfolio.

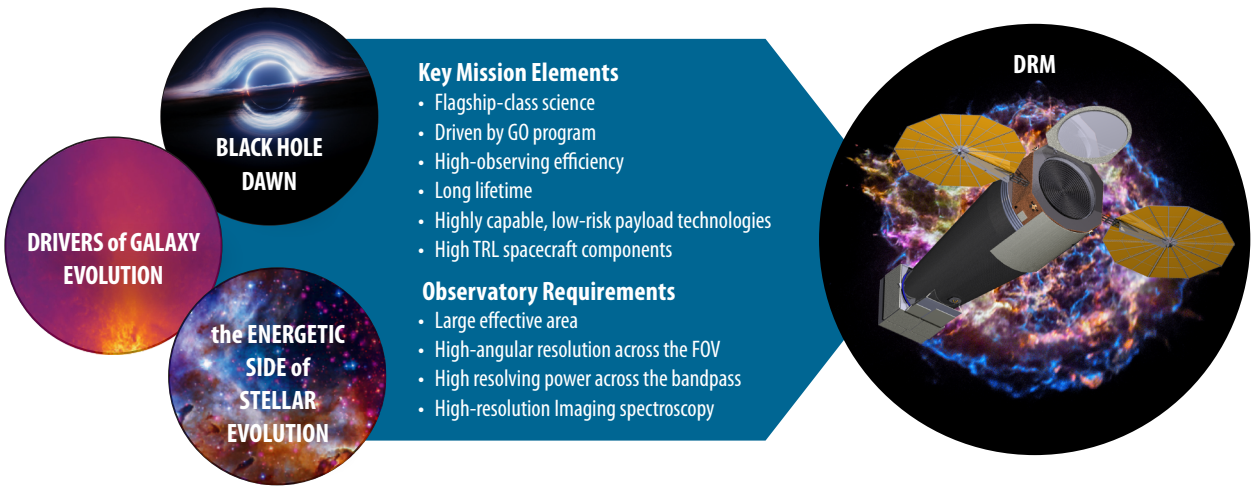

Figure 6.1. The *Lynx* DRM stems from the challenging science drivers defined by the science pillars. At a high level, these requirements present a need for an extremely sensitive X-ray telescope with a large collecting area coupled with high angular resolution across the field of view and unprecedented spectral resolution. The resulting architecture enables a broad range of science across the field and serves as an Observatory for the astrophysics community.

6.1.1 Mission Architecture

Lynx will provide the worldwide astronomical community with a flexible and efficient observing platform: an X-ray observatory with a large effective area coupled with high angular resolution across a large Field of View (FOV) and unparalleled spectral resolution. *Lynx* will operate at a halo orbit at Sun-Earth-L2 (SE-L2), an orbit that allows high viewing efficiency (>85%), an extended mission duration, a benign thermal environment, and easily managed communications. *Chandra*-proven mission operations and infrastructure will be implemented to ensure efficient, queued observation scheduling; *Chandra*-like pointing attitude control, stability, and knowledge consistent with sub-arcsecond imaging; and robust communication infrastructure to rapidly acquire and distribute processed data to observers (Figure 6.2).

Like all NASA flagships, *Lynx* will be a mission of high national priority. The *Lynx* mission architecture and spacecraft design therefore adopt a Risk Class A profile, which allows no credible single-point failures to prevent mission success. This means following strict implementation of risk management and mission assurance practices with redundancies on credible critical single-point failures. This also means that the *Lynx* design will use flight-proven hardware and operational procedures where feasible

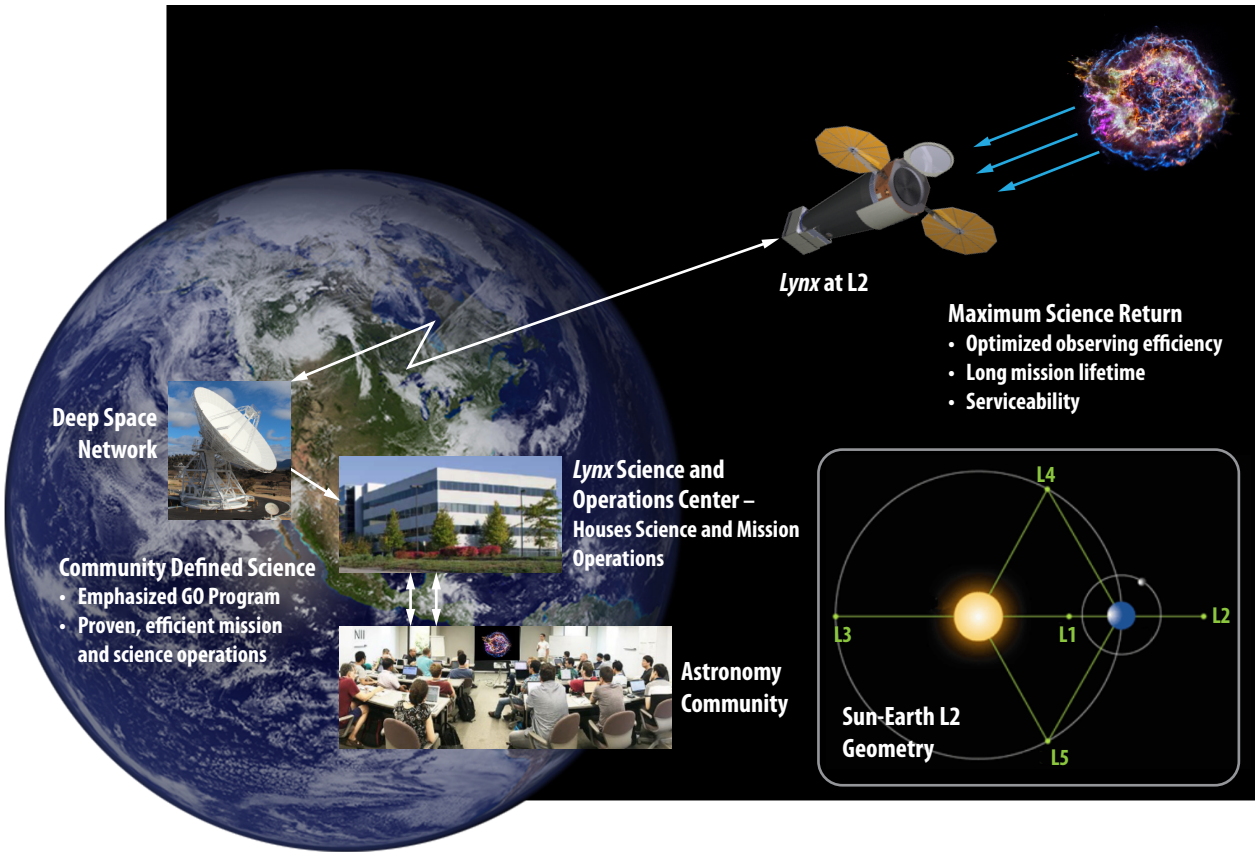

Figure 6.2. Depiction of *Lynx* at SE-L2 (not to scale). *Lynx* operation goals and leveraging of previous mission heritage processes are highlighted.

and will aim for mission longevity in a relatively benign operating environment. Key *Lynx* mission parameters are summarized in Table 6.1.

Table 6.1. Defining *Lynx* Mission Parameters. High-observing efficiency, long lifetime, dedicated GO program, and launch vehicle flexibility are among the high-priority *Lynx* mission attributes.

Mission Parameter	Value
Mission Risk Class	A
Orbit	SE-L2
Observing Efficiency	>85%
Mission Lifetime Baseline Provisioned	 5 years operation 20 years operation
Science Program	GO driven
Launch Vehicle Class	Heavy

Lynx will operate as a GO facility, allowing for a broad range of community-driven observing programs that include the both the science detailed in the pillars outlined in §1 – §3 and the Observatory/Discovery science (§4). In keeping with the GO program philosophy, all *Lynx* observations will be subject to peer review, including those related to the three science pillars. Time pre-allocation can be considered only for a small number of multi-purpose key programs, such as surveys in pre-selected regions of the sky.

Although *Lynx* will be a large observatory, estimates of its mass and volume have ensured its compatibility with multiple future heavy-class launch vehicles anticipated to be available in the 2030 timeframe, including the Space Launch System (SLS). This flexibility significantly reduces *Lynx*'s mission risk and cost by eliminating the historical single-source constraint. The success of new launch vehicle systems such as the Falcon Heavy has greatly changed the landscape, and *Lynx* is designed to take full advantage of the likely 2030 launch market.

6.1.2 Observatory Architecture

The *Lynx* science program requires an observatory that is significantly more capable than any other X-ray mission, previous or planned. Capabilities include high sensitivity for sub-arcsecond imaging over a wide FOV and milli-Angstrom resolution spectroscopy. On-axis angular resolution of 0.5-arcsecond Half-Power Diameter (HPD) is required to avoid source confusion (i.e., the noise generated by the numerous sources that are too faint to be detected individually (Appendix A)) and background limitations at the faintest fluxes, and to uniquely associate X-ray sources with counterparts at other wavelengths. A mirror effective area of 2 m^2 at 1 keV and an FOV with arcsecond or better imaging extending to ~10 arcminutes off-axis are needed to adequately sample the population of supermassive black hole seeds at high redshift in a reasonable amount of time. The combination of arcsecond or better angular resolution with up to R = 2,000 spectral resolution is needed to map the thermodynamic state of hot gas flows in nearby stellar nurseries, extragalactic winds, Active Galactic Nuclei (AGN) outflows, and the cores of clusters of galaxies. An even higher resolving power (R = 5,000) is needed to probe low-density circumgalactic and intergalactic gas in absorption against background AGNs and to resolve all major emission line diagnostics of plasma physics in the soft X-ray band (§6.3.3).

The *Lynx* Observatory meets the requirements necessary to achieve these science goals due to the careful integration of the spacecraft and telescope and through the use of advanced technologies. The spacecraft and telescope elements must be designed in unison and guided by trades that maximize system capability. Understanding the impact of the spacecraft elements (e.g., thermal regulation, vibration, and dynamic operation) on the telescope is essential to achieving the necessary performance. The error budgets necessary to achieve the required imaging and spectroscopic performance are exacting, and are shown in §6.6.1.

The *Lynx* spacecraft is designed to meet the telescope demands with a low-risk design posture. While recent advances in propulsion systems, power systems, avionics, Command and Data Handling (C&DH), and many other areas will be implemented, all spacecraft systems will be high Technology Readiness Levels (TRLs), i.e. 7–9. Minimizing on-orbit operational risk is also a mission priority. The *Lynx* mission has been specifically designed to avoid unique orbital or pointing maneuvers and complicated deployments. Onboard mechanisms needed for standard deployments such as solar array panels and instrument and mirror contamination doors will all have strong spaceflight heritage (high TRL), and flight-heritage mechanisms will be employed for focal plane instrument translation and focusing as well as for grating array insertion and retraction.

The underlying *Lynx* architecture is dictated by the nature of X-ray light from astronomical sources (Figure 6.3). Though the paths of X-rays are not easily altered, X-rays can be reflected and focused by grazing incidence mirrors at incident angles that are less than the critical angle of total external reflection. At X-ray energies, this angle is on the order of arcminutes to a few degrees from parallel to the reflecting surface. Therefore, for practical focal ratios, focal lengths are measured in meters, the effective collecting area for a single mirror is modest, and the resulting paucity of focused X-rays puts every photon at a premium. Meeting the *Lynx* effective collecting area requirement requires nesting large numbers of thin, lightweight, co-aligned, co-axial mirrors in order to optimize the available aperture and to achieve acceptably low mass.

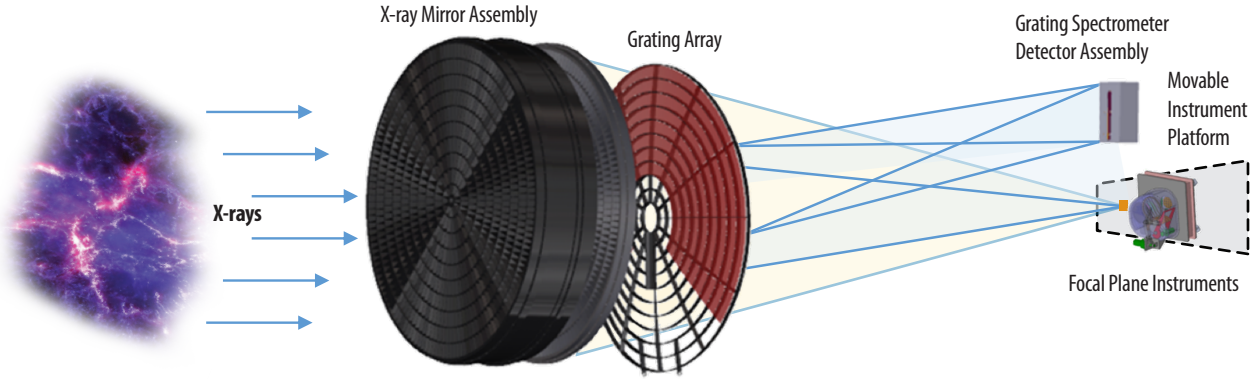

Figure 6.3. Diagram tracing X-ray photons through a generic X-ray mirror assembly and onto a detector located at the focal plane. A translation stage can be used to translate different instruments into the focal point. X-ray gratings can be deployed to intercept the X-rays leaving the mirror assembly, diffracting them onto a detector assembly at a fixed location on the focal plane.

X-ray detectors measure each photon's arrival time, energy, and location in the focal plane. A given detector can only be optimized for a subset of these capabilities. Since different science objectives require different instrumentation, the *Lynx* design envisions a single X-ray mirror assembly and a suite of science instruments that can be individually placed within the optical path when requested for an observation. Accordingly, *Lynx* requires a high-angular resolution, large-effective-area mirror assembly and a science instrument suite that collectively is capable of fine imaging, high-resolution dispersive grating spectroscopy at low energies, and high-resolution imaging spectroscopy across the *Lynx* waveband in order to meet all *Lynx* science goals.

This architecture is similar to most past and present X-ray observatories. The *Lynx* team has leveraged the demonstrated *Chandra* legacy elements, including placing a retractable grating array for dispersive spectroscopy; adopting an updated, State-of-the-Art (SOA) pointing and aspect determination system conceptually identical to *Chandra*'s Pointing Control and Aspect Determination (PCAD) system; and implementing the *Chandra* operations and mission planning paradigm, among others.

Achieving leaps in capability requires improvements beyond the current SOA in X-ray mirrors and science instrumentation. The *Lynx* team recognizes that the path to achieving flagship-class science while also maintaining an acceptable cost and risk posture requires the *Lynx* telescope elements to be well defined, have relatively mature candidate technologies at the present time, and well-defined maturation paths over the next several years. Technology development paths, schedules, and cost estimates to reach TRL 6 by mission Preliminary Design Review (PDR) are summarized in §7 and in comprehensive technology development plans. Further risk reduction for the *Lynx* concept may be attributed to the multiple candidate technology alternatives for payload elements and science instrument components, and due to the fact that all instrument technologies baselined for the *Lynx* DRM have evolved from either flight-proven heritage or from designs destined for near-term, space-based missions. A special section of the *Journal of Astronomical Telescopes, Instruments, and Systems* (*JATIS*) details ongoing efforts to develop these technologies specifically for the *Lynx* mission [533].

6.2 Observatory Configuration

The *Lynx* Observatory consists of the telescope and the spacecraft. The telescope includes all elements related to the *Lynx* Mirror Assembly (LMA), science instruments, and Optical Bench Assembly (OBA), while the spacecraft provides all basic systems to support the telescope and operations, including propulsion; Guidance, Navigation, and Control (GN&C); power; thermal; avionics and flight software; and C&DH. The GN&C also provides the data necessary to compute a highly accurate aspect solution on the ground, modeled after the *Chandra* PCAD system. As *Lynx* is a Class A mission, the Observatory has been designed with redundancies for all credible single-point failures (summarized in Table 6.14).

The *Lynx* Observatory configuration is defined primarily by the science requirements for effective area, FOV, and angular and spectral resolution over a 0.2- to 10-keV energy range. To meet these requirements, *Lynx* has baselined its telescope to have a 3-m-diameter mirror assembly with a 10-m focal length, coupled to a suite of science instruments with a fixed optical bench structure. These three science instruments are known as the High-Definition X-ray Imager (HDXI), the X-ray Grating Spectrometer (XGS), and the *Lynx* X-ray Microcalorimeter (LXM).

Additional configurations (§9) were considered, and a trade study on the achievable science as a function of cost was carried out. Baselining the 3-m diameter mirror assembly with 10-m focal length was determined to provide the most science per dollar and will allow the science outlined in the *Lynx* science pillars (§1 – §3) to be completed within ~50% of the 5-year baseline mission, reserved for Observatory/Discovery science (§4). This configuration will also allow for an observatory architecture with a realizable, near-term implementation plan and is optimized for a x5-m heavy-class launch vehicle fairing. Primary *Lynx* Observatory resources are summarized in Table 6.2.

The *Lynx* Observatory configuration (expanded in Figure 6.4) illustrates a straightforward design with a stable platform capable of maintaining the alignment between the mirror assembly and the focal plane instruments (via a fixed optical bench) within tolerances needed to maintain the exacting imaging performance. This design allows for stable pointing over timescales needed for typical observations, and for either focal plane instrument to be easily translated into and out of the focal point (§6.3.5).

The *Lynx* spacecraft will provide the structure and environment needed to support the telescope, as well as all the necessary mechanisms to ensure the spacecraft can meet the science requirements. Key mechanisms include

Table 6.2. LXO resources.

Observatory Resource	Parameter
Overall dimensions (solar panels stowed)	4.5-m diameter × 12.7-m long
Predicted total mass (includes 23% Mass Growth Allowance (MGA)	7,713 kg
Predicted Power (includes 34% margin)	7,421 W
Data Volume	240 Gbits/day (500 Gbits data storage)
Pointing accuracy	10 arcsec (3σ)
Ground aspect knowledge (Post-facto)	1 arcsec RMS absolute to sky
Image reconstruction	0.2 arcsec HPD within 10 arcmin radius
Stability (between LMA & focal plane)	±1/6 arcsec per s, per axis (3σ)
LMA	3-m outer diameter and 10-m focal length
Science instrument suite	• HDXI • XGS • LXM

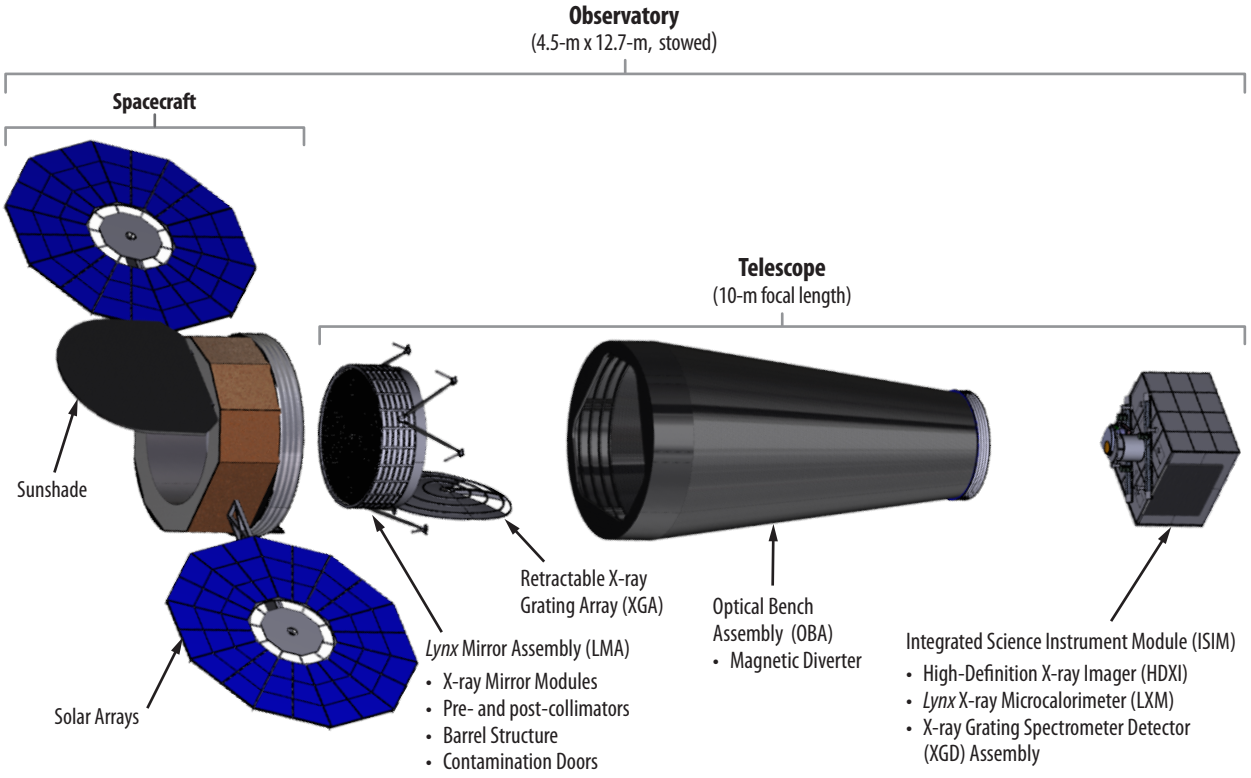

Figure 6.4. *Lynx* configuration expanded to show the telescope and spacecraft portions of the Observatory. The LMA is surrounded by the spacecraft and consists of a high-resolution, large-area mirror assembly with pre- and post-collimators and contamination doors. A retractable X-ray Grating Array (XGA) is attached just after the LMA. A fixed OBA ties the LMA to the science instruments that include HDXI, LXM, and XGS, where the XGS is comprised of the XGA and X-ray Grating Detector (XGD) assembly. [Credit: NASA/M. Baysinger]

those used to deploy the sunshade door to prevent sunlight from illuminating the telescope entrance aperture, insert and retract the X-ray Grating Array (XGA), and to translate the science instruments into and out of the focal point. A summary of primary mechanisms is provided in §6.4.7 (Table 6.20). All of these mechanisms are at TRL 6 or higher (most are at TRL 9) and require little to no maturation.

Equally vital to achieving the *Lynx* science requirements is the overall system integration and interface design (§6.6). This includes the impact on the Observatory from the SE-L2 natural environment (e.g., global deformations due to system-wide thermal gradients), as well as the impact on the telescope performance from the telescope system interfaces and spacecraft elements (e.g., the thermal and mechanical interfaces between the LMA and the OBA and those between the OBA and the spacecraft). Error budget allocations have been generated to identify requirements on system elements and to allocate performance budgets to each element; these are detailed in §6.6.1, and provide allocations for the on-axis imaging performance, spectroscopic performance, and LMA effective area. Elements within these error budget allocations are examples of key driving science requirements that will be tracked as Technical Performance Measures (TPMs) as the *Lynx* design matures. Tracking these TPMs using the *Lynx* Model-Based Systems Engineering (MBSE) tool (Appendix C) will allow monitoring of reserve usage and trends of margin changes. This allows rapid, proactive design assessment and reduces technical risk.

6.3 Design of the Telescope Elements

Given that the spacecraft design is relatively straightforward and that minimal to no development is required, *Lynx*'s success lies primarily in the design and implementation of the telescope. The primary elements requiring some degree of development in order to meet *Lynx* science requirements are the X-ray mirrors and the three science instruments.

The LMA is a fixed structure attached to the OBA. Figure 6.5 shows the attachment of the LMA to the OBA and of the OBA to the spacecraft using bipods. Forward and aft contamination doors are used to control contamination on the X-ray mirrors while on the ground, and en route to SE-L2. Once on-orbit, these doors and a sunshade attached to the spacecraft will be opened and will remain open throughout the mission. A single retractable grating array, the XGA, has the ability to move into and out of the optical

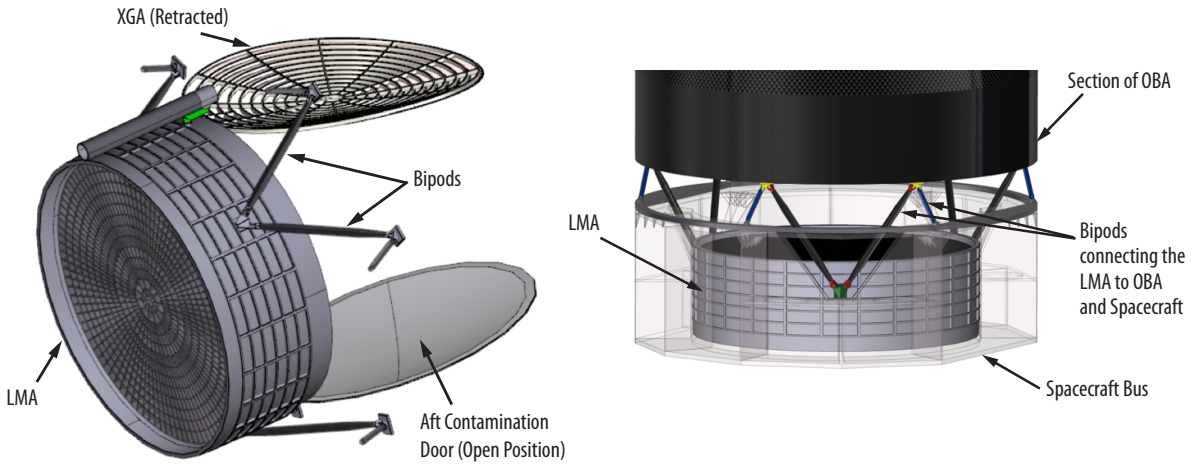

Figure 6.5. Drawing of the LMA with the XGA in the retracted position and aft-contamination door open. Bipods are used to attach the LMA to the OBA and from the OBA to the spacecraft bus.

path as required. The XGA will launch in the retracted position and will have a failsafe mechanism that automatically retracts if the controlling mechanism fails.

The Integrated Science Instrument Module (ISIM) provides an interface to the OBA and houses the focal plane instruments (HDXI, the X-ray Grating Detector (XGD) assembly, and LXM), their electronics, radiators, and supporting structure (Figure 6.6). Two of the science instruments—HDXI and LXM—along with their electronics and radiators are mounted on a moveable platform that is part of the ISIM, while the XGD assembly is located on a fixed platform. The ISIM also provides interfaces for thermal, power, and data for these instruments. More detail is found in (§6.3.5).

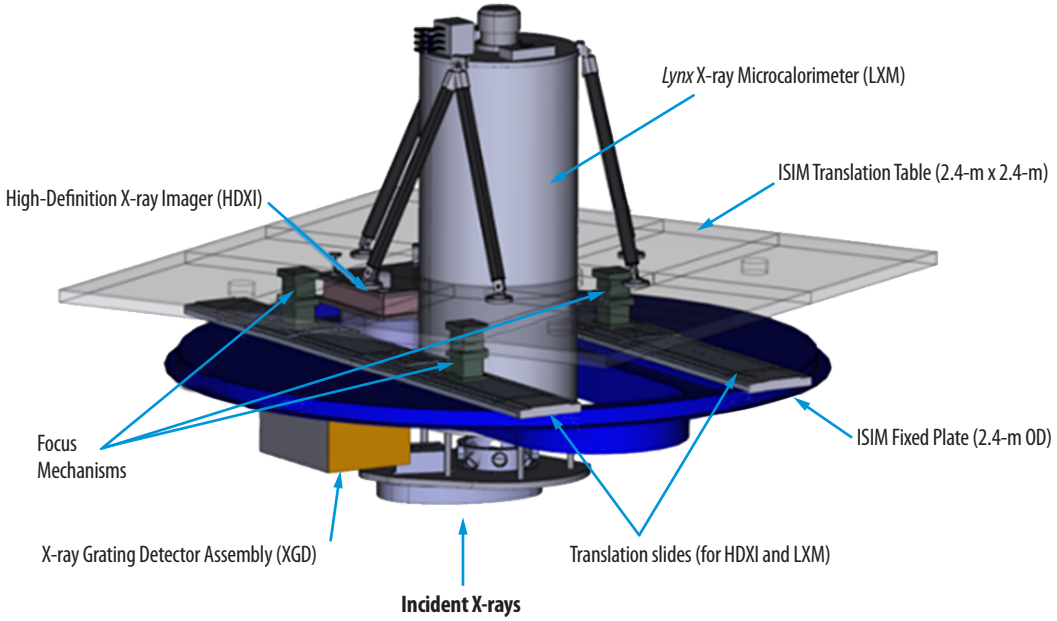

Figure 6.6. ISIM with the translation table shown in translucent-gray, to which HDXI and LXM are attached. The HDXI and LXM can be translated on-axis, depending on the desired science measurement. Three focusing mechanisms allow for fine focus of the HDXI and LXM. The XGD assembly is mounted to the ISIM fixed plate, and has a focus mechanism built into its housing. The electronics boxes for the instruments and the radiators are not shown in this view.

6.3.1 *Lynx* Mirror Assembly

The *Lynx* Mirror Assembly design incorporates fine angular resolution across the full field of view with large effective area. These capabilities empower synergistic observations with 30-m-class, ground-based telescopes planned for operation in the 2030s.

The LMA will be the most advanced of its kind, designed to preserve the sharp vision of *Chandra* on-axis but extended over the entire FOV while increasing the collecting power with significantly larger effective area.

These requirements flow directly from the *Lynx* science goal of observing the first supermassive black hole seeds and unambiguously associating them with the first galaxies observed by the *James Webb Space Telescope (JWST)*. *Lynx*'s on-axis angular resolution of 0.5 arcseconds (HPD) is required

to avoid source confusion at the faintest fluxes and to uniquely associate X-ray sources with high-redshift optical and near-infrared (IR) galaxies. A mirror effective area of 2 m^2 at 1 keV and an FOV with arcsecond or better imaging extending to ~10 arcminutes off-axis will allow for the population of supermassive black hole seeds at high redshift to be adequately sampled in a reasonable amount of time (§1).

LMA requirements (Table 6.3) will enable the next generation of X-ray astronomy and will deliver synergistic observations with ground- and space-based observatories with high angular resolutions.

Table 6.3. LMA primary requirements.

LMA Parameter	Requirement
Energy range	0.2–10 keV
Angular Resolution: On-Axis Across the FOV	 0.5 arcsecond HPD < 1 arcsecond HPD
Grasp at 1 keV (effective area × FOV for <1 arcsec HPD)	~600 m^2 $arcminutes^2$
Field of View (FOV)	20 arcminutes diameter
Effective area at 1 keV	2 m^2
Effective area at 6 keV	0.1 m^2

6.3.1.1 LMA Design Overview

The LMA gain in performance over existing and planned missions is acquired through the use of advanced silicon X-ray mirror technology combined with a precise mirror prescription and modular assembly. *Chandra* achieved on-axis sub-arcsecond angular resolution with four nested pairs of full-shell mirrors that were directly fabricated out of Zerodur® glass, cut and polished to thicknesses ranging from 16- to 24-mm and coated with iridium [534]. *Lynx* will achieve the same angular resolution with much thinner (0.5 mm) mirrors that allow for greater nesting of mirror pairs and larger effective area while simultaneously reducing mass per collecting area.

Lynx's large FOV and off-axis angular resolution are enabled through the use of shorter mirror segments and by changing the telescope geometry from a Wolter Type I (used by *Chandra*) to a Wolter-Schwarzschild configuration. The Wolter-Schwarzschild configuration provides a much flatter best-focus surface because it does not suffer from comatic aberration [535]. The *Lynx* Point Spread Function (PSF) for the low-energy end of the bandpass (0.2 to ~2 keV) is expected to be better than 1 arcsecond HPD at 1 keV to a field radius of at least 10 arcminutes. The flatter *Lynx* response is required for wide-field surveys and efficient imaging of extended sources at high-angular resolution. Figure 6.7 illustrates how the PSF varies as a function of off-axis

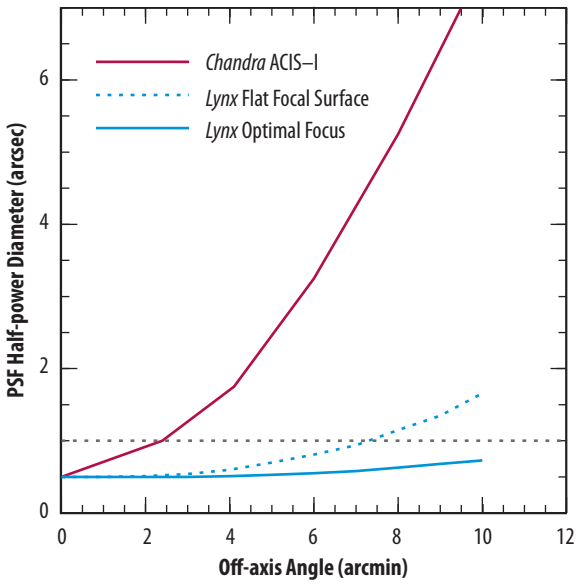

Figure 6.7. The *Chandra* PSF (HPD) resulting from the use of Wolter Type I mirror prescription and the focal surface of ACIS-I, compared to the predicted *Lynx* PSF that will use a Wolter-Schwarzschild prescription coupled to a curved "optimal" focal plane detector assembly. *Lynx* will achieve sub-arcsecond angular resolution across the required FOV.

angle and includes the effect of the detector focal plane geometry for both *Chandra* (coupled with the Advanced CCD Imaging Spectrometer (ACIS-I) [536]) and *Lynx* (coupled with HDXI; §6.3.2.1).

The achievable angular resolution is highly dependent on the mirror technology—fabrication, coating, alignment, and mounting processes. During this concept study, the *Lynx* team focused on three mirror technologies that have a long history of development and are currently being funded: Silicon Meta-shell Optics [537], Full Shell Optics [538, 539], and Adjustable Segmented Optics [540, 541]. A trade study considered each technology's ability to meet *Lynx* science requirements as well as their capacity for overcoming technical challenges and meeting programmatic constraints. Members of the *Lynx* Science and Technology Definition Team (STDT), NASA program and technology experts, industry partners, independent consultants, and members from the Silicon Meta-shell Optics, Full Shell Optics, and Adjustable Segmented Optics technology teams carried out this assessment. Over 5,000 manhours over 6 months were spent on this study, with over 100 documents produced. All three technologies met the *Lynx* requirements and were deemed viable options. The recommendation, then, was to use the most mature technology, the Silicon Meta-shell Optics, to focus the design (see Appendix B.2.1 for more detail on this trade study). The availability of alternative feasible technologies, however, reduces the risk to development and enhances the *Lynx*'s ability to meet its requirements with a design that meets cost and schedule constraints.

The *Lynx* Silicon Meta-shell Optics are mature, and their modular design is highly amenable to mass production. Multiple parallel production lines at multiple locations will optimize mirror segment fabrication and assembly.

The Silicon Meta-shell Optics technology combines advanced polishing technology with monocrystalline silicon, whose near-zero internal stress enables the fabrication of extremely thin (lightweight) optics using advanced deterministic polishing technology, and is actively being developed by a team at NASA Goddard Space Flight Center (GSFC). Silicon also has other highly desirable properties, including a low Coefficient of Thermal Expansion (CTE), high elastic modulus, high thermal conductivity, and low density, making it the best material choice for the *Lynx* mirrors.

Silicon Meta-shell Optics use a modular design in which modules are built by layering mirror segment pairs of nearly identical size on top of one another. The first mirror pair is kinematically supported for alignment and then permanently bonded at eight locations onto a silicon plate, which serves as the structural backbone of a mirror module. Subsequent layers are built up in the same manner. A baffle is included to reduce stray X-ray photons (i.e., unwanted photons that originate from the diffuse cosmic X-ray background that scatter onto the mirror aperture). Multiple modules are mounted into a meta-shell ring-like structure of a given diameter. Multiple meta-shells are nested together to attain the required

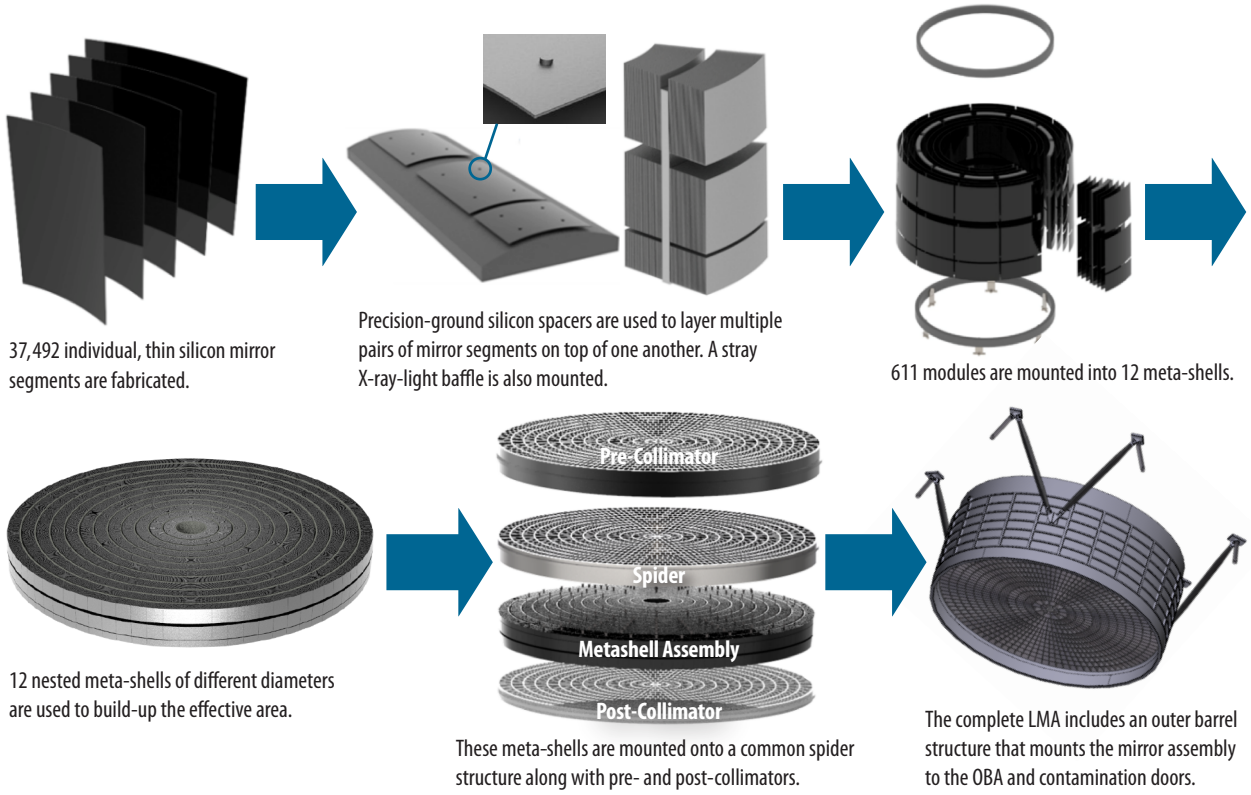

Figure 6.8. The LMA mirror segments are mounted into modules along with baffles that reduce the amount of scattered X-ray light onto the focal plane. These modules are mounted into multiple meta-shells of different diameters to build-up effective area. These meta-shells are mounted onto a common support structure called the 'spider,' along with pre- and post- collimators for thermal control. The entire assembly is mounted inside a barrel that interfaces to the OBA.

effective area (Figure 6.8). A significant advantage of this modular design is that it is highly amenable to mass production. Multiple, parallel production lines will be used to optimize mirror segment fabrication and assembly. As part of this study, a manufacturing optimization algorithm has been developed and is being refined to assess the trade between production time and the cost of the LMA [542].

The LMA will include pre- and post-collimators to help regulate the thermal response of the mirror on-orbit and a barrel structure that mounts the mirror assembly to the OBA using flight-proven (TRL 9) flexures and forward and aft contamination doors for ground operations. LMA design characteristics are summarized in Table 6.4.

Table 6.4. Key LMA design characteristics. The Silicon Meta-shell Optics use a modular design that uses many mirror segments that mount into meta-shells, which are nested into the mirror assembly.

Mirror Assembly Parameter	Value
Optical Assembly Geometry	Wolter-Schwarzschild
Mirror Segment Material	Mono-crystalline Silicon
Segment Size	100-mm x 100-mm
Segment Thickness	0.5 mm
Number of Mirror Segments	37,492
Number of Modules	611
Number of Meta-shells	12
Meta-shell Radius Range	120-mm (inner) – 1,500-mm (outer)
Total Length (pre- to post- collimator)	0.85 m
Predicted LMA Mass (includes collimators, support structure, and contamination doors)	2,035 kg
Steady-State Temperature	293 K ± 0.25 K
Contamination Limit (based on *Chandra*) Molecular Particulate	 ~40 Å $< 10^{-5}$ surface coverage

This design exceeds the *Lynx* LMA requirements for effective area and FOV and is made possible using thin (0.5-mm) mirror segments that are also relatively short. The effective area for this geometry at 1 keV is 2.1 m^2 (Figure 6.9); the ghost-free FOV, which accounts for structure blockage, is 22 arcminutes in diameter.

A description of the current performance for Silicon Meta-shell Optics and an overview of the development path to TRL 6 are provided in §7.2.1. A comprehensive technology development plan is provided in the *Silicon Meta-shell Optics Technology Roadmap*.

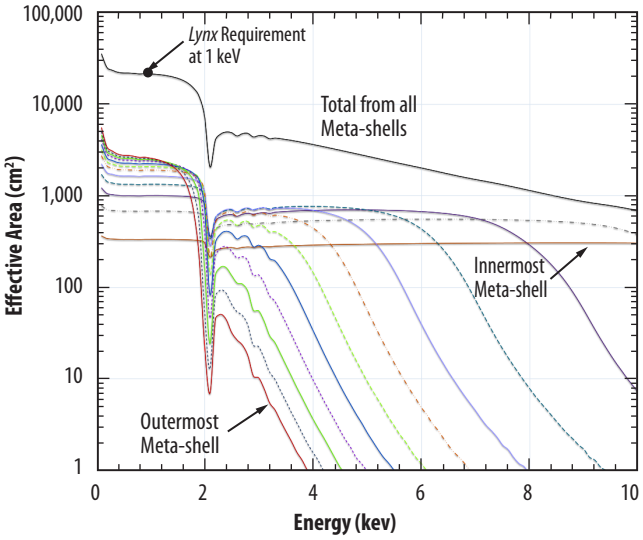

Figure 6.9. The total LMA effective area as a function of energy and the effective area for each of the 12 meta-shells are shown.

6.3.1.2 *Lynx* Mirror Assembly Performance Considerations

The baseline design for the LMA is a product of multiple engineering studies that included detailed structural, dynamics, and thermal designs. The results of these studies have been compiled into the *DRM Supplemental Design Package*. Critical design features include mitigating contamination on the mirror assembly (both on the ground and on-orbit), thermal control, and launch survivability.

Contamination Control — Contamination control on the mirrors is needed on the ground and on-orbit, as molecular and particulate contaminants on X-ray optical surfaces can degrade performance, and changes in contamination levels can compromise calibration stability. To control contamination, doors have been incorporated into the LMA that allow for a dry nitrogen purge on the ground, with the covers remaining closed post-calibration through the completion of a post-launch outgassing phase. In operation, the *Lynx* thermal control subsystem maintains the LMA at approximately room temperature—higher than the surrounding subsystem structure by around 10 °C — to minimize particulate and molecular adhesion to mirror surfaces over time.

Thermal Analysis — The LMA thermal operation on-orbit is 293 K ± 0.25 K, necessary to maintain the fine angular resolution required by the *Lynx* science goals. A detailed thermal analysis on the optics spider and pre-collimator was conducted to optimize their geometries and to improve thermal performance and minimize power requirements for the optical system. The design uses the mirror support element (or spider) to double as the active, heated portion of a thermal pre-collimator to radiatively

heat the LMA, plus a passive portion forward of the spider to minimize the heat lost to space (Figure 6.10). Similar pre-collimator designs have been used previously on multiple X-ray telescopes, including the *Einstein* Observatory and *Chandra*. In addition, the LMA will have a post-collimator (with similar geometry to the spider) to thermally control the exit aperture of the telescope and the grating array. The results of this analysis were used to size the heater controllers and power system (§6.4.3).

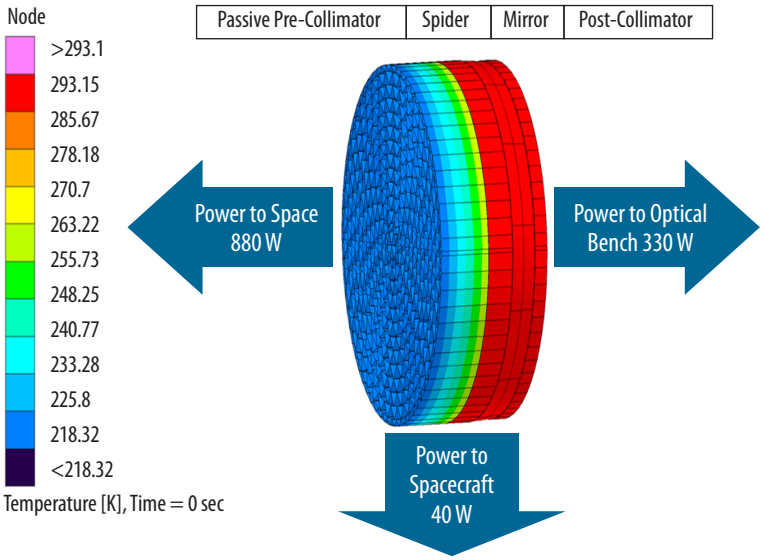

Figure 6.10. Results of LMA thermal analysis.

Launch Survivability and Structural Considerations — Factors that impact analyses related to LMA launch survivability require knowledge of the specific launch vehicle environment, as well as a more detailed design than is practical for this design concept phase. However, initial high-level assessments have been made based on the current design and assumed launch vehicle loads provided by the NASA Launch Services Program (LSP) Office (§6.5). Analyses indicate that the LMA would survive launch assuming standard engineering design practices are followed. All safety factors are per NASA-STD-5001B W [543].

Two specific areas were investigated for this analysis: (1) quasi-static strength of LMA subcomponents and (2) individual mirror strength and relative motion. These areas were assessed via linear static stress analyses and frequency response analyses.

Quasi-static Strength — Structural details and analysis of the LMA are presented in the *Lynx DRM Supplemental Design Package*. Analyses performed to assess LMA launch survivability included linear static stress analyses based on Mass Acceleration Curve (MAC) load factors that were developed by the Silicon Meta-shell Optics design team at GSFC as shown in Table 6.5. The loads are reflective of the Atlas V and Delta IV launch vehicles. These MAC load factors are intended to include transients, quasi-static ascent, and random vibrations. These are first-cut estimates and are expected to be conservative. As the project evolves and detailed structural dynamic analyses are performed, these loads will be tailored for the more detailed design.

Table 6.5. LMA MAC load factors for the 12 meta-shells.

Meta-shell	Mass (kg)	MAC Curve Load Factor (G's) Atlas V/ Delta IV
1	31.3	19.8
2	44.5	18.1
3	54.8	16.4
4	63.7	15.9
5	72.0	15.3
6	79.6	14.8
7	85.3	14.3
8	91.2	13.8
9	97.9	13.3
10	103.7	13.3
11	108.7	12.9
12	115.5	12.9

Post Bonds between Mirror Segments — As shown in Figure 6.8 (middle of the top row), precision ground spacers (or posts) are used to layer multiple segment mirror pairs on top of one another for assembly into a module. The applicable MAC quasi-static load factors were applied to each meta-shell in a static stress analysis to optimize the size of the posts and to calculate the adhesion shear/tension interaction margin of safety in the post bonds. Each meta-shell was analyzed as an independent "component" to the supporting spider. The minimum predicted margin of safety was +0.002 in the post bonds. The positive margin was indicative of an acceptable design, indicating that the posts meet the strength requirements.

Spider and Flexures — Static strength analyses were performed for the LMA spider and flexures, which are used to attach the meta-shells to the spider. This was done using International X-ray Observatory (IXO) Coupled Loads Analysis (CLA) results with a 2.0 modeling uncertainty factor, resulting in 12.3 G axially and 3.4 G laterally that were applied simultaneously. The predicted margin of safety for the spider was +6.55, and that of the flexures ranged from +0.53 to +2.25.

Mirror Segments — Due to the uncertainties related to structural analysis of brittle materials such as silicon, the LMA development plan will include steps to proof-test each mirror segment as it is fabricated. Only qualified mirror segments that pass flight-level stresses will be integrated into the assembly.

Mirror Segment Strength and Relative Motion — The mirror segments have a radial spacing of 5 mm within each of the mirror module assemblies. A high-level frequency response analysis of mirror segment vibration during launch was performed to estimate motion of these segments relative to one another. Using conservative estimates of the dynamic environment and a rigid input to the LMA barrel, it was determined that there were no issues regarding relative motion between mirror components or assemblies. A detailed analysis during Phase A will incorporate more realistic damping as well as a fully coupled loads analysis that will provide more realistic inputs to the launch locks.

6.3.2 High-Definition X-ray Imager

Together with the LMA, the HDXI will enable the high-angular resolution across the *Lynx* FOV required for the deepest surveys to detect the seeds of supermassive black holes, carry out the wider medium-depth surveys needed to study the evolution of black holes and galaxies, and mapping of the diffuse extended structures ranging from massive clusters of galaxies and galaxy halos to large star-forming clouds. The HDXI requires a FOV of 20×20 arcminutes^2 and a small pixel size that adequately oversamples the mirror 0.5-arcsecond PSF. The HDXI will also provide the necessary spectral resolution at soft energies to enable measurement of the thermodynamic properties of hot gas in galactic halos and other extended objects. High time resolution is needed to maintain single-photon counting when observing bright X-ray binaries and compact sources, avoiding event pileup. Like the LMA, the *Lynx* HDXI will combine the best heritage technology (specifically X-ray Charge-Coupled Device (CCD) technology) with ongoing sensor technology development efforts, which will provide the lowest risk/lowest cost path to the required measurement capabilities.

6.3.2.1 HDXI Design Overview

The *Lynx* High-Definition X-ray Imager's advanced megapixel X-ray sensors are natural extensions of legacy CCDs but with higher readout rates, improved spectroscopic performance, lower noise, and are intrinsically radiation hard.

Silicon-based X-ray imaging spectrometers are standard for nearly every recent X-ray observatory. Examples include *Chandra's* ACIS [544], *XMM-Newton's* EPIC MOS [545] and PN Cameras [546], and *Suzaku's* X-ray Imaging Spectrometer (XIS) [547]. All of these instruments use traditional X-ray CCDs with acceptable spectroscopic performance and imaging capability but relatively low readout rates. For X-ray observations with next-generation telescopes such as *Lynx* and *Athena*, the current generation of pixelated silicon sensors offer high readout rates, high-broadband quantum efficiencies, and minimal crosstalk compared to traditional CCDs, and have thus been baselined for the *Lynx* DRM.

The *Lynx* HDXI requires a detector array with small-pixel sensors that can appropriately oversample the telescope's PSF with low noise, large FOV, and high-count rate capability (Table 6.6). Based on the SOA and maturation path, the natural choice is to use an array of monolithic or hybrid pixelated Complementary Metal-Oxide Semiconductor- (CMOS-) based active sensors or advanced CCDs with CMOS readout. For purposes of costing and schedule, the hybrid CMOS sensor and associated Application-Specific Integrated Circuit (ASIC) has been adopted for the DRM. This choice was made simply because engineering interface information on the visible-band version of this technology is in the public domain and readily available. The HDXI detector candidate technologies are described in §7.3.1 and are detailed in the *HDXI Technology Roadmap* and elsewhere in the literature [548, 549, 550, 551]. All three of these technologies require similar resources from the spacecraft, are at the same

Table 6.6. HDXI meets the *Lynx* requirements as outlined in the STM.

HDXI Parameter	Capability
Energy Range	0.2–10 keV
Quantum Efficiency (excl. optical blocking filter)	≥ 0.85 0.5–7 keV
Field of view	22-arcmin diameter
Pixel size	≤ 16 μm x 16 μm (0.33 arcsec)
Read noise	< $4e^-$ (RMS)
Energy resolution at 0.3 keV at 5.9 keV	 < 70 eV (FWHM) < 150 eV (FWHM)
Full-field event rate	>8,000 ct/s
Time resolution (20 × 20-arcsec window)	≤ 100 μs
Framerate: Full-field mode Window mode (20 × 20 arcsec)	 >100 frames/s >10,000 windows/s
Filling factor/ chip gap	> 95%
Radiation tolerance	5 yrs at L2 (baseline) 20 yrs at L2 (goal)
Optical/UV Blocking	10^{-6} in U- and V-bands
Filter(s)	Open aperture, optical blocking filter, closed position and calibration

level of maturity, and are currently funded for development. Having three technologies available for consideration for the HDXI significantly reduces the risk to development, ensuring that *Lynx* requirements will be met.

The design reference HDXI focal plane features 21 abutted advanced silicon sensors tiled to approximate the mean curved focal surface of the telescope (Figure 6.11) [548]. The 22-arcminute-diameter FOV is set by the FOV of the LMA. The HDXI focal plane sensor array and readout electronics are housed inside a vacuum enclosure with a circular aperture entrance window.

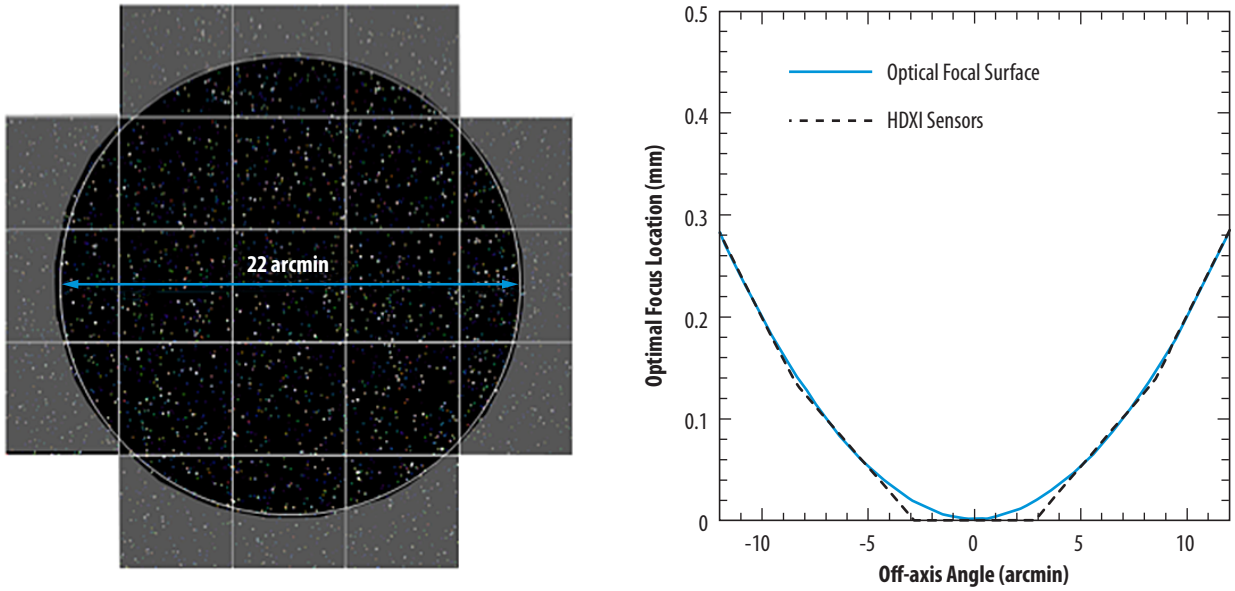

Figure 6.11. (Left) Simulation of a 4 Msec deep field with HDXI array of 21 sensors superimposed. The sensors have a pixel size that is well matched to the telescope PSF of 0.5 arcsec HPD. (Right) The sensors are tilted to approximate a curved focal plane, needed to optimize the angular resolution across the entire 22-arcminutes diameter FOV.

A schematic block diagram of the reference HDXI design is shown in Figure 6.12. The sensors are connected to the Front-End Mother Board (FEMB) via flexprint interconnections. Digitized sensor data from the FEMB are sent to Event Recognition Processers (ERPs) that filter non-X-ray events and empty pixels, reducing the telemetered data volume by 3 to 4 orders of magnitude. Processing is under the control of Detector Electronics Units (DEUs) commanded from the spacecraft and incorporating dedicated firmware and software. The HDXI has a high-speed windowing capability in which a 20-×-20-arcsecond region of a sensor can be read out in <100 μs, which will eliminate pileup from bright sources and allow high-resolution timing measurements of pulsars and magnetars. This windowing capability can be run simultaneously with the full-field readout so that events from the bright source are processed rapidly, but the entire FOV is also read out at the nominal ~100-frames/s cadence. The HDXI system is capable of sustained throughput up to 8,000 cts/s, allowing continuous, pileup-free observations of any extended X-ray source in the sky . Finally, the system will be capable of transferring full sensor frames to the ground for diagnostic purposes. X-ray event data and auxiliary and diagnostic metadata will be formatted into Consultative Committee for Space Data Systems- (CCSDS-) compliant packets for transfer to the spacecraft onboard memory.

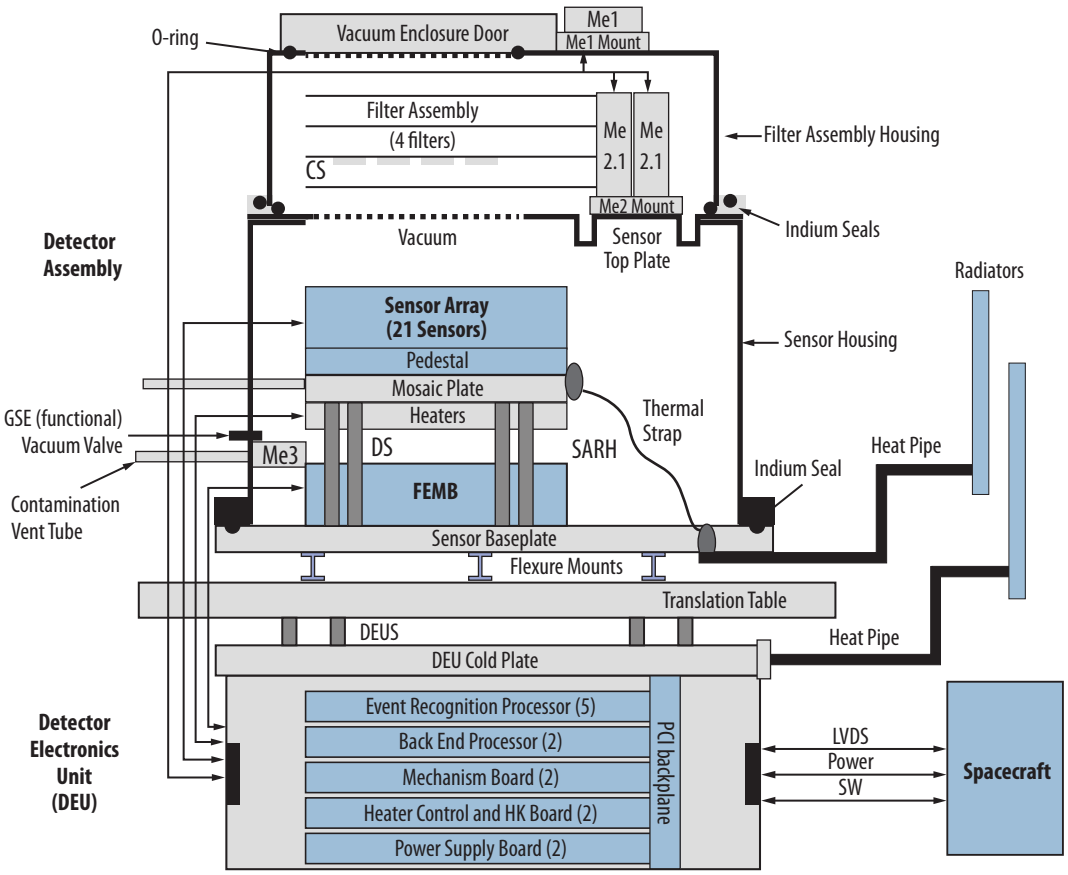

Figure 6.12. Block diagram of the *Lynx* HDXI system. The HDXI DEU and all radiators are attached to the ISIM translation table. Flex cables between the translation table and spacecraft provide power, control, and data. The filter mechanism allows for individual filters or a calibration source to be inserted in front of the sensor array.

The HDXI sensor array and FEMB are located inside an aluminum vacuum enclosure that also contains a filter mechanism (Figure 6.13). Cooling is provided through a cold strap connection between the sensor array which is conductively coupled to a silicon-carbide mosaic plate and the enclosure.

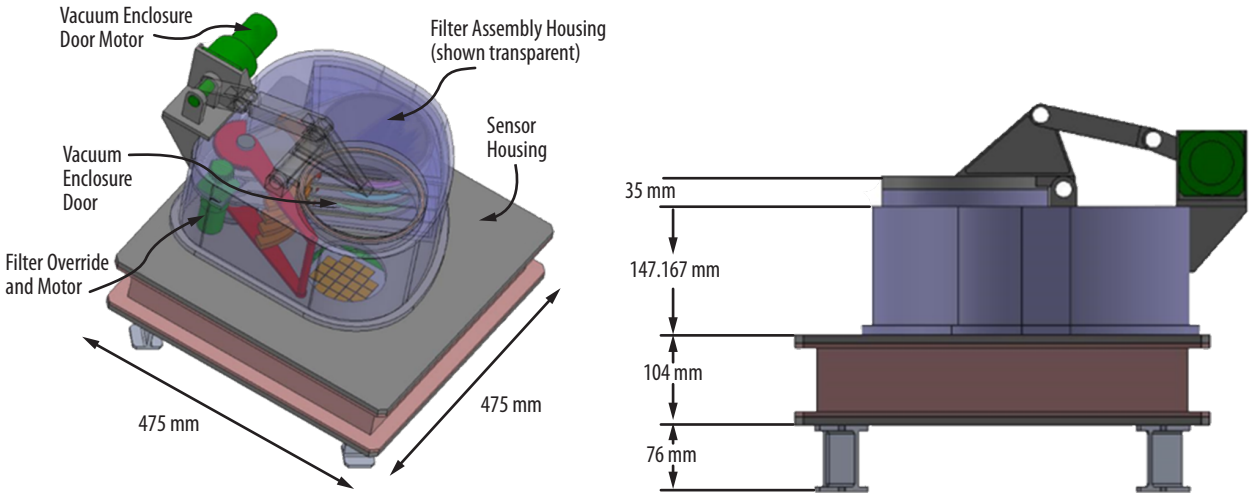

Figure 6.13. The HDXI showing the filter mechanism and vacuum housing. The DEU is not shown, as it is located on ISIM.

This enclosure, along with its thermal load from the rest of the instrument, is passively cooled via external radiators that are connected to the instrument through heat pipes that move along with the translation table. This scheme allows the sensors to be cooled to their nominal operating temperature of –90 °C.

The filter mechanism is a unique design capable of supporting multiple filters that can be used in combination with one another. Though the DRM design includes an open aperture, an optical blocking filter, a ^{55}Fe calibration source, and a closed position, additional filter types will be studied during Phase A to maximize the science value.

The ISIM's translation table enables the HDXI (along with its support electronics and radiators) to be moved on- and off-axis as needed. A focus mechanism on the ISIM allows for axial translation of ±1 cm, more than enough to establish the telescope focus and correct unpredicted variations that may arise due to thermal and structural displacements on-orbit. HDXI instrument features and spacecraft resources are detailed in Table 6.7.

Table 6.7. Reference HDXI design includes an array of 21 advanced silicon X-ray imaging sensors. Required spacecraft resources are listed.

HDXI Resource	Value
Sensor configuration	Back-illuminated, fully-depleted, CMOS-compatible
Detector material	Silicon
Number sensors in array	21 (curved focal plane)
Pixel elements per sensor	1,024 × 1,024
Size	~ 48 × 48 × 36 cm
Mass (includes sensors, structures, filter mechanism, DEU, and harnesses)	80 kg (104 kg with margin)
Power (with margin): Nominal Safe hold Survival	 249 W 7 W 7 W
Focal plane operating temperature	–90°C
Data rates: Nominal Peak	 600 kbps 6 Mbps
Contamination limit Molecular Particulate	 ~100 Å < Level 600

6.3.2.2 HDXI Performance Considerations

The HDXI design uses standard elements for active pixel sensors. Detailed studies that include thermal, mechanical, electrical, flight software, and instrument reliability are provided in the *DRM Supplemental Design Package*. HDXI longevity to 20 years without loss of performance is crucial. Primary considerations that may affect performance over time are radiation damage (which can result in degraded imaging and spectral resolution) and contamination on the sensor surface (which can degrade the low-energy response). With proper design and lessons learned from *Chandra*, however, both of these potential risks will be mitigated.

Radiation Considerations — At SE-L2, there is an appreciable flux of charged particles, primarily in the form of moderate-energy protons (§6.6.2.1). These charged particles exist as an omnidirectional flux, a portion of which can be concentrated through the LMA directly onto the focal plane. Relatively low (–90 °C) sensor operating temperature and shielding on the HDXI enclosure will be used to mitigate the ambient particle flux, and a magnetic diverter (§6.3.6) will be used to "sweep" the charged particle flux away from the focal plane. This technique has been successfully implemented on nearly every focusing X-ray observatory (e.g., *Chandra* [552] primarily for electron flux). The magnetic diverter design for *Lynx* will be similar to what will be used for *Athena*, with a focus on diverting the low-energy proton flux to reduce background on the focal plane instruments [553]. In addition, the HDXI will use CMOS-based sensor technology that is inherently radiation hard, primarily because charge is not transferred across these devices but is instead read out directly from each pixel. The advanced

CCDs are in principle also sensitive to the effects of displacement damage on charge transfer efficiency. This is mitigated through a number of radiation-hardening features, as described in detail in [550]. Radiation tolerance testing is an integral part of the technology development path detailed in the *HDXI Technology Roadmap*. It is expected that the charged particle environment will be similar to that seen by *Chandra*, and therefore is not expected to be an issue, even over the extended 20-year lifetime. However, detailed designs of the HDXI and surrounding structure are required to accurately model the impact of the charged particle population on the sensor array over time. These studies will be performed during Phase A.

Contamination Considerations — A contamination control engineering study for HDXI was carried out as part of an Instrument Design Lab (IDL). Detailed results may be found in the *DRM Supplemental Design Package*. Contamination on the sensor array throughout mission lifetime will be minimized by venting of the HDXI filter and detector assemblies; careful temperature control of the sensor array, FEMB, and surrounding structure; and by the ability to bake out the sensor assembly to remove contamination buildup over time. Keeping the sensor array warmer than the rest of the surrounding structure during cruise will prevent outgassing materials from contaminating the detector. An early on-orbit bakeout in this configuration will drive off any water or other contaminants accumulated during launch processing. On-orbit, the filters, which are in close proximity to the sensor array, will be held at room temperature to mitigate contamination from the rest of the Observatory. The filters and mechanisms will be kept clean, and the filter housing interior will be coated with a molecular absorber coating. The HDXI has been designed with filter and detector bakeout capabilities, further mitigating contamination. During bakeout, when the instrument temperature is raised to evaporate contaminants, the instrument will be translated to one side of the translation table assembly, where the detectors will view a plate coated with a molecular absorber coating affixed to the stationary part of the ISIM. This plate will be in direct line-of-sight of the detector, minimizing contamination accumulation. During normal operation, the FEMB will be kept at a temperature that is ~10 °C warmer than the sensor array. A more detailed temperature analysis and contamination study will be carried out during Phase A.

6.3.3 X-ray Grating Spectrometer

The *Lynx* X-ray Grating Spectrometer will be the most advanced of its kind, with $R > 5{,}000$ and a large effective area of 4,000 cm^2 at 0.6 keV.

The *Lynx* XGS will characterize the warm gas in galactic halos out beyond their virial radius through absorption line studies of background AGNs — which require high spectral resolution of $R > 5{,}000$ — and sensitivity (effective area of 4,000 cm^2 at 0.6 keV) in the 0.2- to 2.0-keV band, capable of 1-mÅ sensitivity in key absorption lines of OVII and OVIII. The XGS will carry out transformational science that includes these studies on the Warm Hot Intergalactic Medium (WHIM) and will expand our knowledge on active star-forming regions, stellar coronae, and the impact of X-ray and extreme ultraviolet flux and winds on planet habitability.

6.3.3.1 X-ray Grating Spectrometer Design Overview

The *Lynx* XGS will provide the highest-throughput, highest-resolution spectra at soft energies of any X-ray spectrometer ever flown to date (Figure 6.14). For comparison, the Reflection Grating Spectrometer (RGS) on *XMM-Newton* has a resolving power from R = 150 to 800 over the 0.33- to 2.5-keV band with an effective area of ~150 cm² at 0.83 keV [554]. The High-Energy Transmission Grating (HETG) on *Chandra* provides spectral resolving power up to R = ~65 to 1,070 over the 0.4- to 10-keV range with an effective area of 59 cm² at 1 keV [536].

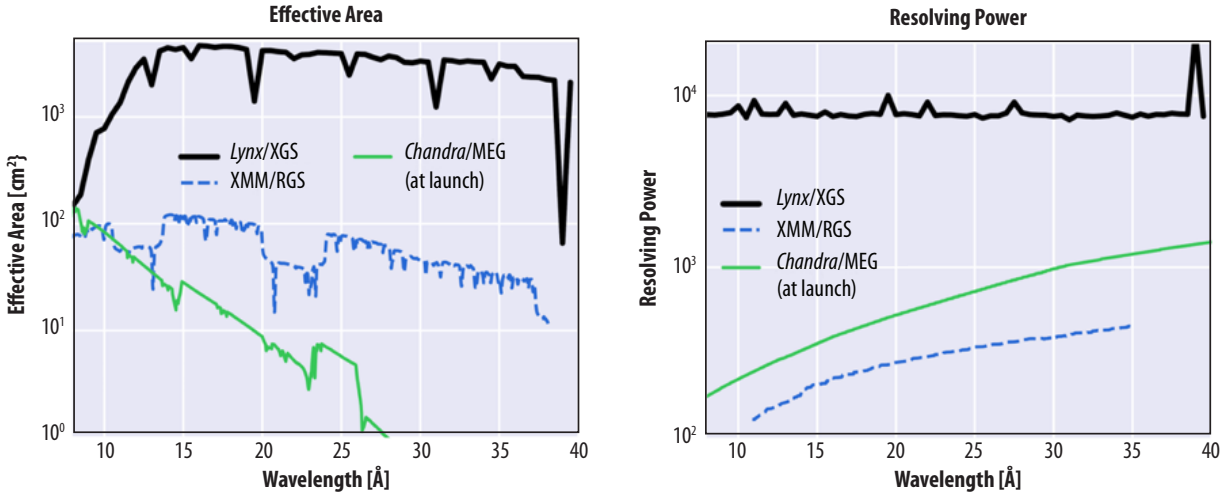

Figure 6.14. Plots comparing (Left) the CAT-XGS effective area summed over all detected diffraction orders, and (Right) resolving power averaged over all detected diffraction orders to that of *Chandra* and *XMM*. The XGS has orders of magnitude more effective area and unprecedented resolving power.

These increases in performance are made possible through recent developments in transmission [555] and reflection [556] grating technologies, both of which are able to meet *Lynx* requirements. Critical-Angle Transmission (CAT) gratings, currently being developed at the Massachusetts Institute of Technology (MIT), have been selected for the *Lynx* DRM for project costing and scheduling purposes (see Appendix B.5.1 for trade study details). Reflection gratings that operate in an Off-Plane (OP) geometry, currently being developed at Pennsylvania State University (PSU), offer equally high performance. Having two technologies that are similarly mature provides a low risk posture related to the development of this instrument.

A comprehensive *CAT-XGS Technology Roadmap* and an *OP-XGS Technology Roadmap* are summarized in §7.3.2 and §7.3.3. Much like the *Lynx* mirrors, the XGS technology will be competed once *Lynx* has been selected for funding.

The XGS consists of two major elements: (1) a large XGA located immediately after the LMA on a retractable structure and (2) the XGD assembly that is located on a fixed location on the ISIM. Defining characteristics are given in Table 6.8.

Table 6.8. Key CAT-XGS characteristics. XGS will meet the *Lynx* requirements as outlined in the STM.

XGS Parameter	Capability
Energy range	0.2 – 2 keV
Resolving power	R > 5,000 (R = 7,500 goal)
Effective area @ .6 keV	~4,400 cm² (4,000 cm² required)
XGD Parameter	**Capability**
Sensor Pixel size	≤ 16 μm × 16 μm (0.33 arcsec)
Read noise	< 4e⁻ (rms)
Energy resolution for resolving spectral orders	≤ 80 eV (FWHM) @ 0.3 keV
Radiation tolerance	5 yrs at L2 (baseline) 20 yrs at L2 (goal)

X-rays that are focused by the LMA pass through the XGA, which diffracts the X-rays according to wavelength. The diffracted spectrum is observed by an array of sensors located on the focal surface (Figure 6.15). The gratings in the XGA are blazed such that most photons are diffracted into high-diffraction orders at large distances from the focal point, increasing the spectral resolving power. The line spread function of the diffracted orders determines the grating performance. Spatially overlapping diffraction orders with different wavelengths are "order-sorted" using the energy resolution of the sensors [555].

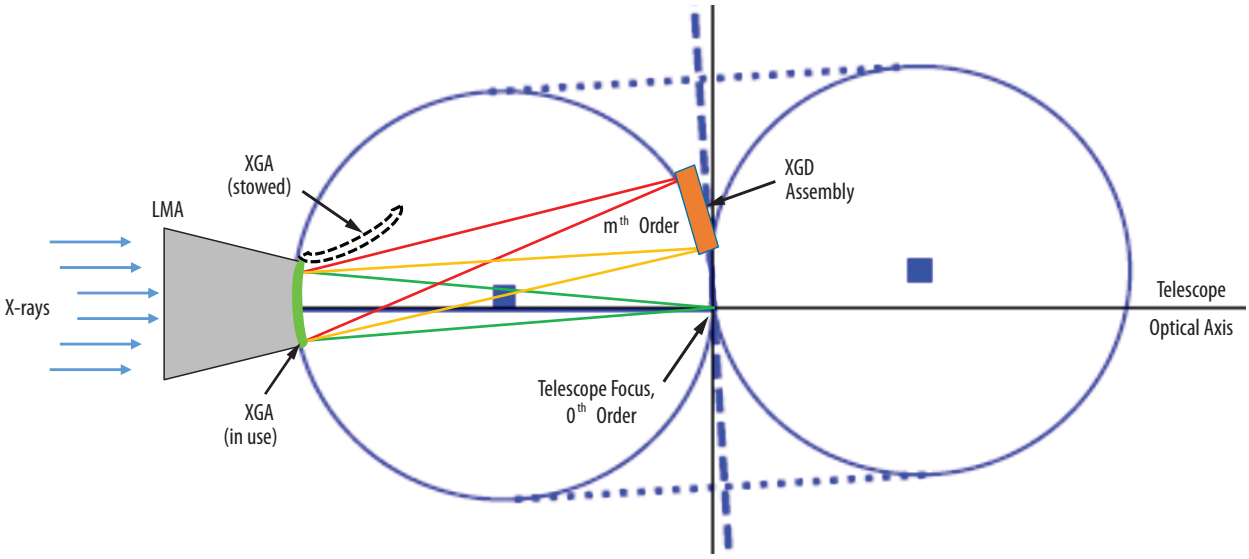

Figure 6.15. Conceptual sketch of the XGS "tilted Rowland torus" design optimized for blazed transmission gratings. The telescope focus is located at the origin of the coordinate system. The dotted lines represent the position of the torus. This design minimizes aberrations by bringing the torus surface close to tangential to the blazed grating facets.

The XGS design is based on the *Chandra* HETG spectrometer [557], which is a Rowland torus design but optimized for blazed transmission gratings (i.e., "tilted Rowland torus"). The Rowland torus is a three-dimensional extension of the Rowland circle geometry, which is necessary to avoid aberrations related to the incoming focused X-rays. In this configuration, the gratings are mounted on one side of the torus, while the detectors are located on the other side (for detailed descriptions see [558, 559]). The gratings, telescope imaging focus, and readout array share the same torus surface. The transmission geometry is comparatively insensitive to grating misalignment and grating non-flatness, leading to relaxed alignment and figure tolerances.

When deployed, the gratings cover roughly 73% of the LMA area (covering 264° in azimuth), leaving areas with the largest aberrations uncovered. The gratings are placed close to the mirrors because a longer distance between the gratings and the detector improves the spectral resolving power. Since individual grating facets are flat and the torus is curved, most points on the grating array do not match the Rowland torus exactly. Using a geometry with a tilted torus reduces this error.

The *Lynx* X-ray Grating Array (XGA) uses state-of-the-art grating technology that exceeds *Lynx* requirements. The X-ray Grating Array deployment heavily leverages heritage from *Chandra*, resulting in a simple, elegant design that provides repeatable deployment and relaxed alignment tolerances between the gratings and optics.

The *Lynx* XGA consists of ~2,100 individual grating facets (50 × 50 mm in size are baselined) mounted into a large grating array structure (or grating array door). Smaller gratings could be arranged to follow the surface of the Rowland torus better, which would reduce optical aberrations but increase the area blocked by support structures. Ray-traces for the XGS indicate that larger sized gratings can be used to achieve a resolving power of up to R = 7,500, which could reduce photon loss due to mounting structures and reduce fabrication cost [555]. A more detailed study involving a more detailed design of the LMA and XGD will be carried out during Phase A.

The single retractable grating array is attached to the LMA structure (Figure 6.16). Effort has been made to keep the mechanism simple while maintaining precise positioning each time the gratings are deployed. The actuator used to deploy the grating array allows for 1.2-µm-level positioning for high repeatability. A second actuator has been added for redundancy. CAT gratings have an alignment tolerance of roughly 100–200 µm along the optical axis, well within the capability of these actuators. Table 6.9 lists key spacecraft requirements for the XGA.

Mechanical stops at the deployed position ensure that the gratings are held stably at the precise axial spacing relative to the mirrors. The XGA insertion mechanism includes a spring-loaded feature that allows the stepper motor to overdrive and provide a constant preload force against the stops. Lateral position control of the grating array is handled passively with design constraints in the hinge-line, as well as the selection of grating metering path structures that match the thermal expansion or contraction of the LMA. Active features such as thermal control heaters may be added to the grating support structure to provide additional stability.

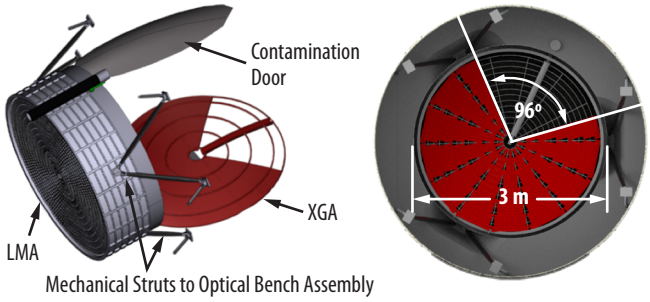

Figure 6.16. (Left) Conceptual drawing of the LMA with the XGS grating array shown. The XGA will be stored outside of the contamination door and launched in the open position. (Right) The grating array covers ~73% of the mirror area to provide the required effective area and can be retracted when not in use. [Credit: NASA MSFC/M. Baysinger/J. Rowe].

Table 6.9. *Lynx* spacecraft resources required by the CAT grating array. CAT gratings have relatively relaxed alignment tolerances and operational temperatures.

XGA Characteristic	Value
Number of gratings (with facets)	~2,100
Grating size	50 × 50 mm
Grating array inner/outer radius	~0.13 m/~1.5 m
Azimuthal LMA coverage	265°
Alignment stability (along optical axis)	200 µm
Alignment tolerance to optics (along optical axis)	10 mm
Deployment repeatability	100 µm
Grating door operational cycles	10,000 cycles (5,000 on ground, 5,000 on-orbit)
Grating door Fail Safe	Non-deployed (or "open") position
Operational temperature	20 ± 4 °C
Survival temperature	-18 to 55 °C
Grating array mass (with door structure)	69 kg (87 kg with margin)

The grating array will be launched out of the FOV in the retracted position and held in place for launch with pin-puller mechanisms that will be released once on-orbit. The insertion method is through a drive mechanism at the hinge-line once unlocked. The grating array door will also include a failsafe device to remove it from the FOV should both the primary and redundant mechanisms fail.

Chandra and *XMM-Newton* serve as excellent examples of X-ray missions that have successfully flown and operated large-scale grating spectrometers, demonstrating that scaling individual gratings to large arrays is a surmountable challenge. Scaling to the large areas required by the *Lynx* XGS is addressed by both CAT and OP technologies in §7.3.2 and §7.3.3, respectively, and in their respective technology development plans. The same manufacturing algorithm to be applied to the *Lynx* mirror segments will also be applied to the XGS gratings to optimize cost and schedule and to reduce risk [542].

The *Lynx* XGS will have a dedicated detector assembly with an array of active pixel sensors enclosed in a vacuum housing on a fixed platform on the ISIM. An optical blocking filter will be deposited directly onto the X-ray sensors to block stray light that could adversely affect the background level. The detector array will also have an independent focus adjustment mechanism that is sufficient to establish the telescope focus on-orbit and for overcoming unpredicted thermal and mechanical deviations.

The detector will use the same sensor technology as that of the HDXI to save cost and schedule. As such, the *HDXI Technology Roadmap* serves as the development plan for the XGD. The HDXI pixel size of 16 × 16 μm is such that it oversamples the 100-μm (Full Width at Half Maximum (FWHM)) line spread function required for R = 5,000 by more than a factor of 6, making it much more capable than required by *Lynx* [555]. The XGD detector type will be revisited during Phase A when a detailed trade study can be conducted to determine the most optimal technology type for a given cost and schedule.

The XGD mechanical layout is consistent with the Rowland torus defined by the gratings. The zeroth-order for the CAT gratings will be detected using HDXI or LXM, while blazed higher orders are dispersed onto a detector array located as close as possible to the zeroth-order without occulting the HDXI or LXM (Figure 6.17). Since the gratings mostly disperse soft x-rays and become highly transparent for shorter wavelengths, the zeroth-order contains most of the incident flux at higher energies and can be used for simultaneous spectroscopy, in addition to the flux from the mirror area not covered by the XGA.

The XGD assembly is similar to that of HDXI, with the primary differences being the reduced number of sensors (i.e., from 21 for HDXI to 18 for XGD). The XGD does not have a filter wheel, but does have a built-in focus mechanism. The sensor array is electrically connected to a front-end motherboard (FEMB) that contains the readout electronics. Heaters, heat pipes, and radiators regulate the sensor array temperature.

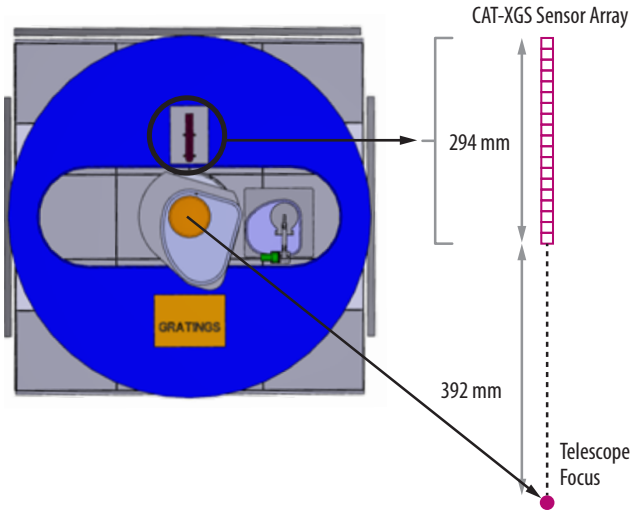

Figure 6.17. Drawing of the layout for the XGD, located on the fixed plate of the ISIM (in blue). The zeroth-order is located at the telescope focus and is detected by the LXM or HDXI. Higher orders are dispersed into the linear array offset from the focal point.

The DEU containing ERPs, backend processors, VERSA-Module Europe card (VME) -based controllers, detector controllers, and power supplies receives power from the spacecraft and allows for command and data flow (Figure 6.18). A more detailed design is found in the *DRM Supplemental Design Package*.

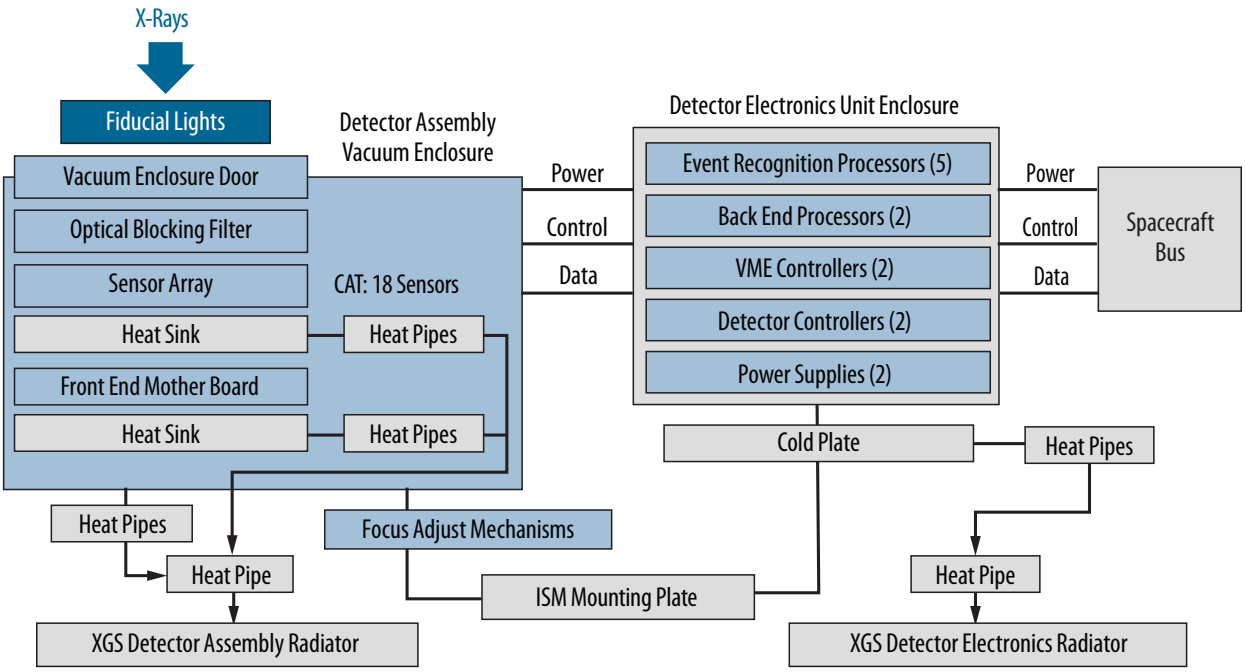

Figure 6.18. CAT-XGS detector assembly block diagram. This architecture is similar to that of HDXI, the main differences being fewer sensors than the HDXI, the lack of a filter wheel, and the inclusion of a focusing mechanism.

Spacecraft resources required for the XGD are similar to those for the HDXI (Table 6.10). Maximum data rates are conservatively set to be the same as that of HDXI, given that the gratings will be always be less efficient than direct detection. A more detailed study to refine these rates will be conducted during Phase A.

6.3.3.2 XGS Performance Considerations

XGS is designed for high performance (large effective area coupled with high resolving power) and longevity (20-year extended mission). Three key considerations have been factored into the XGS performance: (1) launch survivability, (2) ability to maintain alignment between the LMA and XGA on-orbit, and (3) ability to mitigate contamination sufficient to maintain the required performance throughout the mission lifetime.

Table 6.10. XGD spacecraft requirements are listed. Required temperatures and expected data rates are consistent with those of HDXI.

XGD Resource	Value
Number of sensors	18 (with 0.5-mm gaps in between)
Power (with margin): Nominal Safehold Survival	 190 W 7 W 7 W
Operating Temperature	–90°C
Data rates: Nominal Peak	 600 kbps 6 Mbps
Detector Focus Range	± 1 cm
Focus Stability	3 µm
Assembly enclosure size (L×W×H)	40 × 27 × 15 cm
Mass (sensors, structures, DEU, fine focusing motor, and harnesses)	65 kg (80.4 kg with margin)

Launch Survivability — The XGA is made up of many relatively small, thin gratings mounted to a larger structure. The concept leverages the grating design used on *Chandra*, which grants confidence in its feasibility. As the XGA concept matures, static strength analyses will be performed to size the hardware per MAC load factors, and random vibration analyses will be performed to ensure that any potential unique dynamics are identified and considered. MAC load factors are intended to be a combined design load covering transients, quasi-static ascent, and random vibrations. As the project evolves and detailed structural dynamic analyses are performed, loads will be tailored for the evolving design. Random vibration environments known to envelope potential launch vehicle environments will be utilized until *Lynx*-specific environments are defined.

Alignment to Mirrors — The gratings are arranged on the surface of a torus. Shifts of the entire XGS grating structure of 1 cm along the optical axis or several millimeters perpendicular to it do not significantly affect the line spectra function keeping the resolving power of the spectrograph within requirements. The acceptable translation of several millimeters corresponds to an angular precision of a few arcminutes' rotation with respect to the mirrors given the size of the XGA [555]. Additionally, misalignment along the optical axis can be corrected with the focusing mechanism in flight, making this a very robust design that reduces cost and scheduling risk by minimizing the steps required for relative alignment of mirrors and the XGA.

Radiation Considerations — The natural radiation environment at SE-L2 is the primary consideration regarding the XGD. As these sensors are the same as those used for the HDXI, the same mitigation applies (§6.3.2.2).

Contamination — On-orbit, the grating arrays will be kept at higher temperatures than the surrounding subsystems to minimize particulate and molecular adhesion to mirror and grating surfaces. A detailed thermal analysis will be carried out during Phase A to optimize the thermal control system. Additionally, the XGA has an effective area of 4,400 cm^2, which is more than the 4,000 cm^2 required to meet *Lynx* science goals. If a fraction of the XGA does become contaminated over time, the remaining effective area should still meet the requirement. Contamination on the XGD will be minimized using the same considerations as those for the HDXI, that is, through proper venting and careful thermal control of the assembly and surrounding structure (§6.3.2.2).

6.3.4 *Lynx* X-ray Microcalorimeter

The *Lynx* X-ray Microcalorimeter will be the most advanced X-ray microcalorimeter ever flown. With over 100,000 pixel elements arranged into three separate arrays, the *Lynx* X-ray Microcalorimeter will provide an extensive range of imaging and spectroscopic capabilities. Due to recent advances in technology and heavy leveraging of previous and present day microcalorimeter design elements, this design is highly feasible.

The *Lynx* science pillars require a range of angular and energy resolution capabilities and rely heavily on the LXM's performance. The LXM will be capable of: spatially resolving AGN feedback signatures from surrounding hot gas and jets in galaxies, groups, and clusters on 1-arcsecond or finer scales with

2-eV energy resolution; resolving starburst-driven winds in low-redshift galaxies at a high spectral resolution of ~0.3 eV over ~1-arcminute FOVs (at 1-arcsecond imaging resolution); mapping metallicity gradients (3 eV resolution over a 5-arcminute FOV) in circumgalactic, group, and galaxy cluster fields; and surveying young Supernova Remnants (SNRs) in local group galaxies.

The *Lynx* team has performed multiple simulations showing the feasibility of spectroscopic observations on arcsecond and sub-arcsecond resolution scales, which have been highlighted in the text (e.g., in §2.2 and §3.3).

6.3.4.1 LXM Design Overview

A feasible LXM design has been developed for the *Lynx* DRM that meets the combinations of spectral, spatial, and FOV required to enable this transformational science. Though unique, this design borrows heavily from flight heritage and design elements for other X-ray microcalorimeters currently in development, and uses high-TRL elements whenever possible [560].

The most important LXM element required to meet the *Lynx* science goals is its focal plane. The LXM focal plane is composed of a large array of pixels (or absorbers) with sensors attached that determine the energy of individual incident photons by precisely measuring the temperature rise from the heat deposited. As the thickness of the absorber decreases, so does its heat capacity and usable energy range. Thus, there is a tradeoff between energy resolution and energy range in order to achieve the best possible energy resolution for a given energy.

The LXM Focal Plane Assembly (FPA) has three sensor arrays, each designed to meet particular *Lynx* science requirements. The Main Array (MA) is designed to provide a large FOV with good angular resolution and energy resolution across the *Lynx* bandpass. The Enhanced Main Array (EMA) has a narrower FOV, but an angular resolution that is precisely matched to that of the *Lynx* telescope. The Ultra-High-Resolution Array (UHRA) has the same reduced FOV as the EMA, but with much higher energy resolution at lower energies, achieved with thinner absorbers (Figure 6.19).

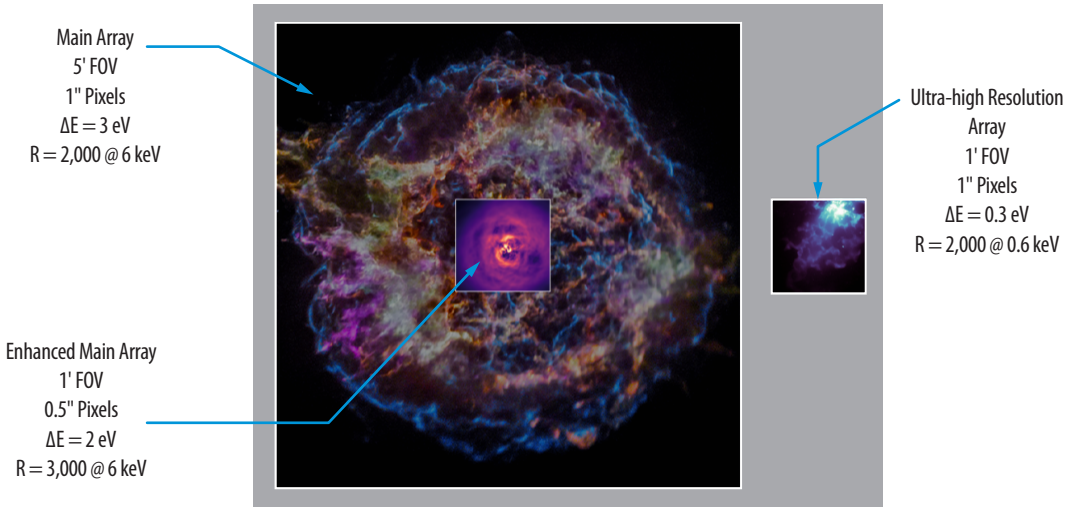

Figure 6.19. LXM will have three sensor arrays that share the focal plane. The Main Array will provide a large FOV with good angular resolution and energy resolution across the *Lynx* bandpass. The Enhanced Main Array has a narrower FOV but an angular resolution that is precisely matched to that of the *Lynx* telescope. The Ultra-High-Resolution Array has the same reduced FOV as the Enhanced Main Array but with much higher energy resolution at lower energies.

The count rate capability is much higher for the UHRA than for the MA and EMA, and is a derived value based on the intrinsic design of the arrays. The design of the UHRA pixels is inherently a few times faster than the MA and EMA hydra designs due to the lower heat capacity of the UHRA absorbers and also due to the small size of the UHRA Transition Edge Sensors (TESs). The UHRA count rate capability ranges from 80 cts/s to 1,000 cts/s per 1-arcsecond pixel, depending on the required energy resolution. The UHRA is useful up to ~2 keV based upon the Quantum Efficiency (QE) and energy resolution, with the energy resolution degrading slowly with energy to ~3 eV. For all three arrays, a lower energy resolution requirement would allow for a higher count rate capability.

Using three arrays for the LXM design not only meets the *Lynx* science goals, but also provides a feasible design that can be fabricated in the relative near-term. By contrast, if one were to design an X-ray microcalorimeter capable of achieving 0.3-eV resolution up to 7 keV across the full LXM FOV, it would require 360,000 pixels and 360,000 TESs, which is currently not practical. Additionally, many of the LXM-expected science observations would result in photon-starved pixels, effectively negating any benefit from the higher angular resolution; this was not considered an acceptable design trade.

A trade study examined the potential benefits of extending the LXM response to higher energies of ~15 to 20 keV. The science case for this is broad and includes improving black hole spin measurements [561], expanding our understanding of the X-ray-emitting corona associated with accreting black holes [562], improved feedback measurements [563], studies of obscured AGN [564, 565], X-ray reverberation mapping to uncover the geometry of the central engine [566], and studies of ultraluminous X-ray sources [567]. A higher energy response can be achieved without modifying the current instrument design (and by operating the microcalorimeters at a slightly higher heatsink temperature); however, modifying the LMA via additional mirrors or multilayer coatings would be required. This trade is documented in Appendix B.2.2.1.

The true power of the X-ray microcalorimeter was first realized by the Soft X-ray Spectrometer (SXS) on the JAXA *Hitomi* (Astro-H) mission, when it revealed the high-resolution (4.9 eV FWHM at 6 keV) spectrum of the core of the Perseus cluster, tightly constraining the velocity dispersion of the cluster gas [568]. Building on the successful implementation of *Hitomi's* SXS, the European Space Agency's (ESA's) planned *Athena* Observatory will include an X-ray microcalorimeter (the X-ray Integral Field Unit (X-IFU)) in its payload that is well matched to *Athena's* large FOV and higher angular resolution [569]. The X-IFU focal plane has a different design than the SXS, with many more pixel elements to read out and requiring an even higher energy resolution. The LXM will be the most capable yet, as the *Lynx* science case requires an FOV comparable to the X-IFU, but matched to the order of magnitude higher angular resolution expected for the *Lynx* telescope. The LXM will also deliver an even higher energy resolution, which will be necessary to address some of the most compelling and unanswered science questions regarding the fundamental drivers of galaxy and large-scale structure formation and evolution. However, a finer angular resolution combined with a relatively large FOV translates into an increased number of pixel elements over that of the X-IFU. Due to innovative thermal multiplexing, the number of sensors (TESs) read out in the LXM will be twice that of the X-IFU [560].

Thermal multiplexing will be performed using hydras in the form of TESs [570, 571] (Figure 6.20). These have been baselined due to their relatively high maturity levels compared to other thermometer technologies. Multi-pixel TESs, or hydras, reduce the number of TESs that need to be read out. This multiplexing allows for wider focal plane coverage (or finer sampling of the FOV for the same coverage) without a commensurate increase in the number of wires or readout components.

Superconducting Quantum Interference Devices (SQUIDs) in resonators allow the multiplexed readout of hundreds of sensors on a single electronics chain. In a microwave SQUID multiplexed readout, the current signals from sensors biased with DC voltage stimulate Radio Frequency- (RF-) SQUIDs that change the resonant frequency of the microwave resonators coupled to a common feedline [572, 573].

A comb of microwave tones probe the resonators, and a shared semiconductor amplifier (e.g., a High-Electron Mobility Transistor (HEMT) or a Silicon-Germanium Heterojunction Bipolar Transistor (SiGe HBT)) measures the summed tones. The maximum assumed number of HEMTs powered on at a single time is 16. Minimal to no energy resolution degradation from the readout is expected for this design [572].

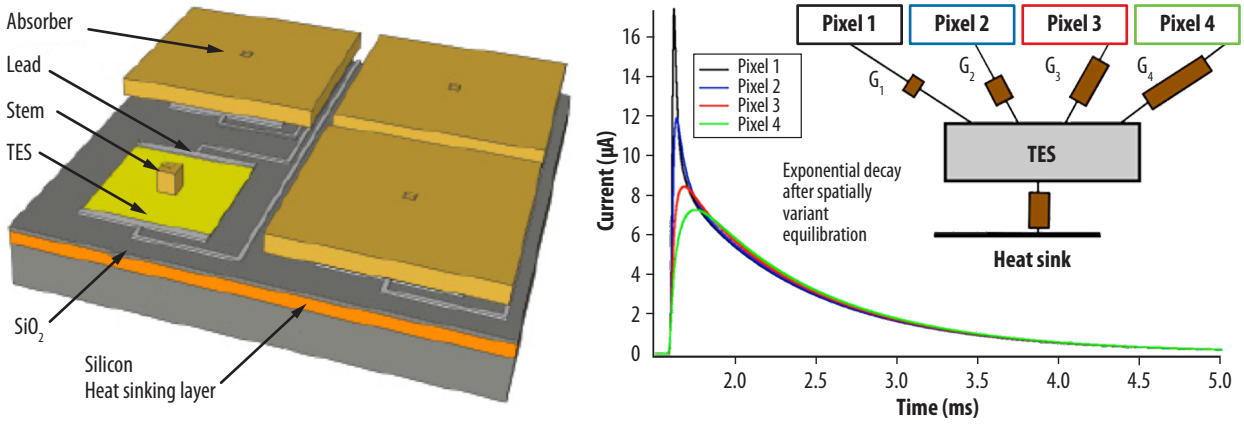

Figure 6.20. (Left) Schematic showing components of a TES calorimeter that uses the thermal boundary between the TES film and the substrate to decouple the TES from the substrate. (Right) Schematic representation of the TES hydra. (Inset Top-Right) Thermal model of a multipixel TES consisting of four X-ray absorbers connected to a single TES via varied thermal conductance Gi = 1…4. The TES is weakly thermally coupled to a heatsink via conductance. The measured average X-ray pulse shapes for a 4-pixel hydra at 6 keV is shown. The differences in pulse shapes before equilibration are used to determine the pixel that absorbed the X-ray photon. *Lynx* will use 25 hydras for the MA and EMA, and no hydras for the UHRA.

The combined capability of the three LXM sensor arrays (Table 6.11) highlights the LXM's full potential to achieve the *Lynx* science pillars and to make new discoveries. The design's technical feasibility has been established through numerous recent breakthrough technologies, not only for the sensor, but also for the supporting elements. The technology development path is described in detail in §7.3.4 and in the *LXM Technology Roadmap*.

Table 6.11. Key characteristics for LXM for the three arrays. The energy resolution and count rate capability are inversely related. A lower energy resolution allows for a higher count rate. The range of this trade space is indicated by the terms 'high-res', 'mid-res,' and 'low-res'. The design of the UHRA pixels are inherently a few times faster than the MA and EMA hydra designs due to the lower heat capacity of the UHRA absorbers and also due to the small size of the UHRA TESs.

Characteristic	Main Array (MA)	Enhanced Main Array (EMA)	Ultra-high Resolution (UHR) Array
Energy range (keV)	0.2 – 7 keV	0.2 – 7 keV	0.2 – 0.75
Quantum efficiency: Area fill factor Vertical QE	 > 90% > 80% at 6 keV	 > 80% > 80% at 6 keV	 > 90% > 99% at 0.75 keV
Field of view	5 × 5 arcmin [1.5 cm x 1.5 cm]	1 × 1 arcmin [3 mm × 3 mm]	1 × 1 arcmin [3 mm × 3 mm]
Pixel size (arcsec)	1 × 1 [50 µm × 50 µm]	0.5 × 0.5 [25 µm × 25 µm]	1 × 1 [50 µm × 50 µm]
Energy resolution: High-res Mid-res Low-res	 3 eV (FWHM) at 6 keV 5 eV (FWHM) at 6 keV 10 eV (FWHM) at 6 keV	 2 eV (FWHM) at 6 keV 4 eV (FWHM) at 6 keV 10 eV (FWHM) at 6 keV	 0.3eV (FWHM) at 0.75 keV 0.8 eV (FWHM) at 0.75 keV 2 eV (FWHM) at 0.75 keV
Number of pixel elements (number of TES readouts)	86,400 (3,456)	14,400 (576)	3,600 (3,600)
Number of hydras per pixel	25	25	N/A
Count-rate capability: High-res Mid-res Low-res	 10 cts/hydra (0.1 mC) 40 cts/hydra (0.4 mC) 150 cts/hydra (1.5 mC)	 10–20 cts/hydra (0.1–0.2 mC) 40–80 cts/hydra (0.4–0.8 mC) 150–300 cts/hydra (1.5–3.0 mC)	 80 cts/s/pixels (0.8 mC) 320 cts/s/pixel (3.2 mC) 1,000 cts/s/pixel (10 mC)
Absolute energy calibration	1 eV	1 eV	0.25 eV
Timing resolution Timing accuracy	2 µs 50 µs		
Instrument background	$<5 \times 10^{-3}$ cts cm^{-2} s^{-1} keV^{-1}		

Achieving high energy resolution across the *Lynx* bandpass requires that the LXM focal plane array be cooled to 50 mK. The LXM FPA is housed within a cryostat designed to minimize the LXM's overall footprint on the ISIM. The architecture has roots in previous X-ray missions such as *Hitomi*, but has a cryogen-free operation (i.e., there are no expendable cryogens that limit mission lifetime).

The key components in the cooling system, shown in Figure 6.21, are the cryocooler, which cools from room temperature (~283 K) down to 4.5 K, and then a multi-stage Adiabatic Demagnetization Refrigerator (ADR), which provides continuous cooling down to 50 mK [574].

A thrust tube design provides mechanical support to the various temperature stages to minimize the diameter of the LXM (Figure 6.22), which allows the XGD to be placed closer to the telescope optical axis. The use of these canonical thrust tubes (and verification of the thermal and structural performance) will be confirmed in pre-Phase A and Phase A. The Advanced Cryocooler Development Program (ACTDP) four-stage (Mega4-1) pulse tube cryocooler developed by Lockheed Martin is already at a relatively high TRL and has been baselined for providing 4.5-K cooling. As there are a number of different options for providing this cooling — such as the Turbo-Brayton Cryocooler developed by Creare — a trade study will be conducted during Phase A to assess the state of these technologies and the advantages and disadvantages of each. The dominant heat loads from the detection chain at 4.5 K come from the HEMTs (estimated to dissipate 16 mW) and the harnesses (estimated to conduct 3 mW) [574].

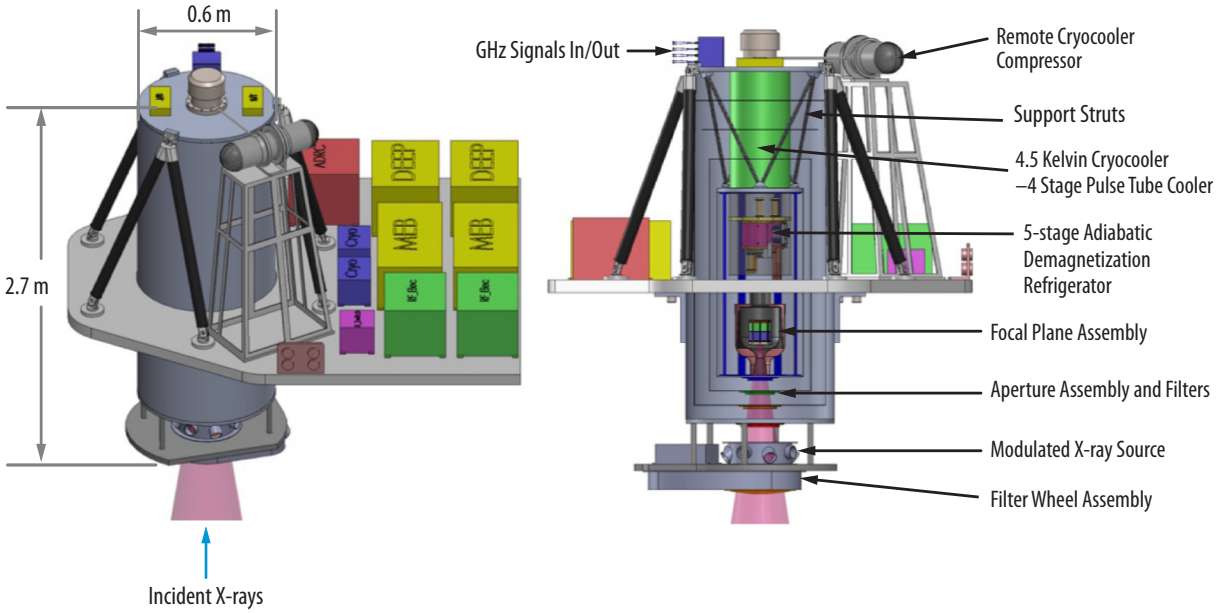

Figure 6.21. (Left) Overview of the LXM cryostat and readout electronics. (Right) Side-on view of the LXM, including a cross-sectional view of the cryostat. The X-rays enter the cryostat from the bottom. The filter wheel and modulated X-ray source (with its electronics) are located a small distance below the bottom of the main cryostat on a separate mounting plate, which is attached to the main cryostat.

At one end of the cryostat are a gate valve and an aperture assembly that incorporates thin-film filters similar to those on *Hitomi* to block IR and optical photons. An engineering study was conducted to determine the optimum IR-blocking filter design to provide a high system (filter + detector) QE across the *Lynx* bandpass [575]. Outside of the gate valve, the LXM will include an external filter wheel and a modulated X-ray source capable of providing pulsed X-ray lines at multiple energies similar to that used on *Athena's* X-IFU [569] and *Hitomi's* SXS [576] for in-flight calibration.

The LXM detector assembly, cryostat, and the full complement of readout electronics are located on the translation table on the ISIM. When the LXM is translated into the optical axis, its electronics and radiators move along with it, minimizing the overall complexity of the ISIM. A block diagram for the

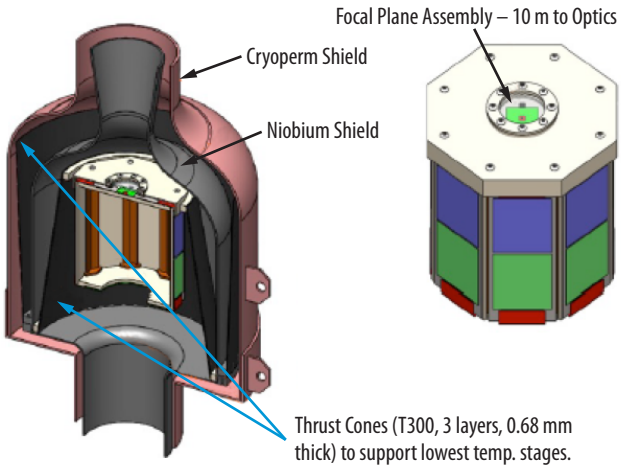

Figure 6.22. (Left) LXM FPA cross section. The high-magnetic-permeability Cryoperm shield is at 4.5 K, and the superconducting niobium shield is at 0.6 K. (Right) View of the FPA 50-mK stage. The MA, EMA, and UHRA are visible on the top surface through an IR-blocking filter that is transparent in this figure. The multiplexer readout components are on each of the eight side panels shown in blue and green.

entire LXM is shown in Figure 6.23. The block diagram shows the FPA design for housing the detector array also includes the cold readout and an anticoincidence detector utilized to reduce the background X-ray events [577]. Two redundant electronics boxes for controlling the cryocooler and the redundant Main Electronics Boxes (MEBs) are also shown. Most of the electronics boxes consist of standard circuits and components used frequently for space, such as control microprocessors, conditioned power sources, and control signals for all of the various components and mechanisms. The Digital Electronics and Event Processor (DEEP) and the analog RF electronics boxes are the only ones that are technically demanding, and thus in need of technology development, as described in the *LXM Technology Roadmap*.

The primary resources required for the spacecraft to support the LXM are listed in Table 6.12. The largest mass contributions for the LXM come from the cryostat and the electronics boxes. Power estimates are dominated by the DEEP boxes (615 W) and the cryocooler (653 W), followed by the RF electronics boxes (141 W), other electronics boxes, and operational heaters. The choice for the Field Programmable Gate Arrays (FPGAs) — a main part of the DEEP electronics — was conservative. Future processors are likely to become available that could reduce the power needed. Similarly, it is very possible that future cryocoolers will require less power. A reduction in power leads

Table 6.12. LXM spacecraft resources.

LXM Resource	Value
Total mass (with margin)	468 kg (585 kg)
Cryostat	164 kg
Electronics Boxes	146 kg
Thermal (heat pipes, etc.)	72 kg
Misc. (harnesses, structures, filters)	86 kg
Power (with margin)	
Nominal	1,575 W (2,205 W)
Safehold	310 W (434 W)
Survival	10W (14 W)
Operating temperature:	
Cryocooler	Cools from 283 K to 4.5K
Multistage ADR	Cools form 4.5 K to 50 mK
Data Rates	
Nominal	20 kbps
Peak	8 Mbps
Detector Focus Range	± 1 cm
Focus Stability	3 µm
Cryostat Size (length x diameter)	1.43 m x 0.6 m

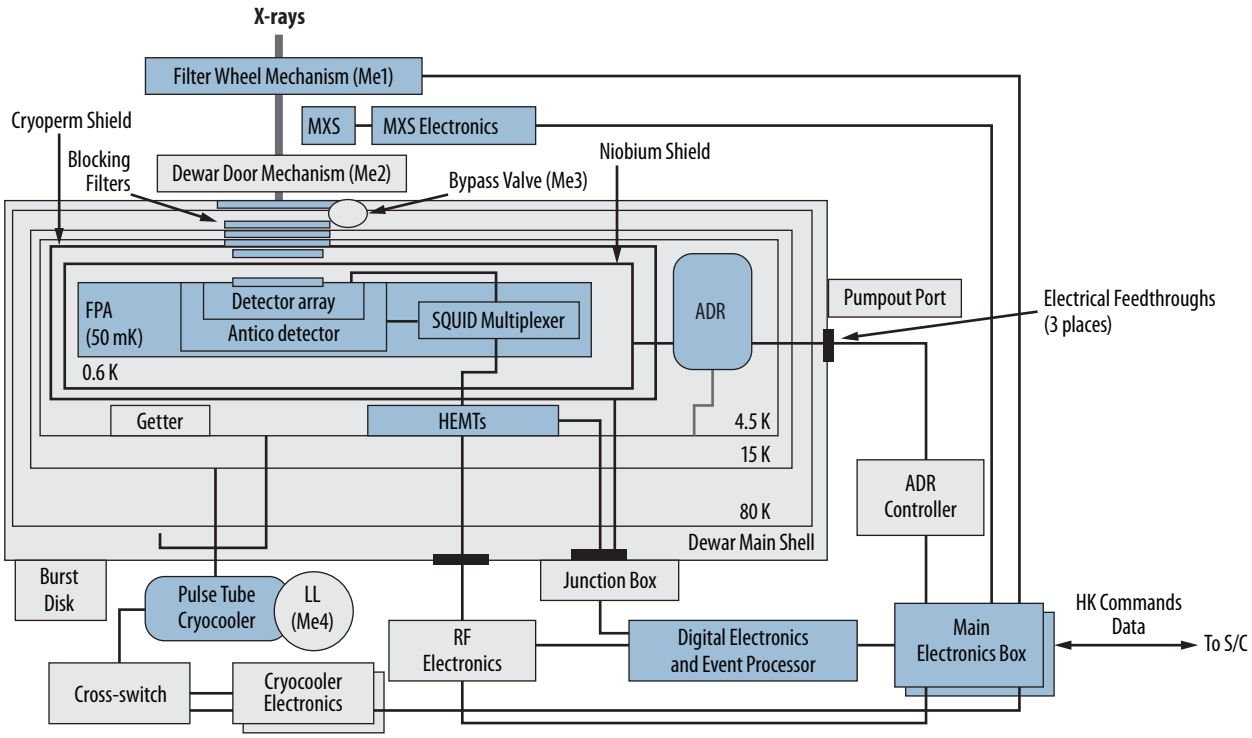

Figure 6.23. LXM block diagram.

to a reduction in the mass of the radiators, which have a margin of 40% and are part of the ISIM. The LXM is assumed to launch warm and only needs about 10 W of housekeeping power until the Observatory is en route to SE-L2.

The assumed maximum data rate for the LXM is based upon a total maximum count rate for the whole array of 100,000 cts/s and an assumption that 80 bits are needed to describe each event. Therefore, the LXM has a maximum data rate of 8 Mbps. When looking at the brightest sources such as Sco X-1, the instantaneous data rate may be higher. In these instances, it is assumed that the other instruments are turned off and that there is a limit on exposure such that the total volume of data collected is <240 Gbps per day, which matches *Lynx's* telemetry limit.

The LXM design is a natural progression from *Hitomi's* SXS, the *X-ray Imaging and Spectroscopy Mission's (XRISM's)* Resolve, and *Athena's* X-IFU. One example of how *Lynx* will leverage technology development from these other payload is through the use of the Modulated X-ray Source (MXS), which will be included on the LXM FPA for in-flight calibration by providing pulsed X-ray lines at multiple energies. The LXM will also leverage the X-IFU readout layout (similar wire density and flex cable technologies) due to the similar focal plane size. This also allows for the mechanical, thermal, magnetic shielding, anticoincidence detector, and IR filter designs from the X-IFU to be leveraged. Cooling the LXM focal plane will be met with a cryostat that uses heritage from SXS and Resolve, and design details from the X-IFU. Other cooling system elements will be achieved via a thrust-tube-type design mounted in a fashion similar to that used for *Spitzer*.

6.3.4.2 LXM Performance Considerations

The LXM performance relies not only on the performance of the instrument itself, but also on how the LXM interfaces to the Observatory. The LXM must survive launch and must have adequate vibration and thermal isolation from the ISIM.

Launch Vibration — The cryocooler will use the same staging configuration as the ACTDP four-stage cooler. This configuration is robust and straightforward to design, assemble, and test. The LXM cryocooler may be required to support significant masses during launch vibration, so design iterations during Phase A are expected in order to meet minimum resonant frequency requirements.

Vibration and Thermal Isolation — Vibration and thermal isolation between LXM and the ISIM are necessary to ensure that Observatory performance is not affected by vibrations from the LXM cryocooler. Isolation is addressed in the design through the use of three bipods to connect the cryostat to the ISIM and by locating the cryocooler compressor, rotating valve, and all moving parts onto a separate stand from the cryostat. The cryocooler is only coupled to the cryostat though a flexible tube, allowing the cryostat to remain vibrationally isolated. As an alternate option, the turbo-Brayton cryocooler by Creare is also being considered for the 4.5-K cooling. There is an inherent lack of vibration generated by the cryocooler, as it is based upon the use of extremely low-mass parts generating extremely small vibrations at frequencies in excess of 1 kHz, and the use of gas bearings and clearance seals that prevent mechanical contact and thus eliminate wear. This is a slightly lower TRL than the ACTDP; however, Creare is currently funded to mature this technology.

The cryostat design utilizes heritage from *Hitomi's* SXS regarding the design of the vibration and thermal isolation. However, detailed analyses will need to be conducted in Phase A to optimize this scheme for *Lynx*. The TES sensor technology used by the X-IFU and the LXM is based upon a first-stage SQUID amplifier with a low impedance input, which is inherently less sensitive to vibrations of the sensor and its wiring.

Contamination — The LXM contamination control requirements are based upon those previously set by *Hitomi*. These requirements are driven primarily by the sensitivity of the detector system and the optical blocking filters. The detector is subject to degradation if the filter or calorimeter surfaces are contaminated with particles or residue.

Surface contamination requirements for the thin film optical filters, associated carriers, and the aperture assembly will be designed to minimize filter obscuration, prevent particles from physically damaging the filters, and limit end-of-life film thickness for non-volatile residue and ice to 500 Å. To meet these limits, the filters will be kept visibly clean. For the particulate contamination requirement, no particles larger than 50 μm will be allowed. For the molecular contamination requirement, the molecular limit will be determined by analysis and X-ray transmission tests. The FPA and carrier surfaces will be cleaned and verified upon final assembly and will subsequently be maintained at that level through filter integration. The detector system must meet the surface contamination requirements similar to that of the thin film filters. Therefore, upon assembly, detector system surfaces will be visibly clean with no particles larger than 10 μm. Detector system surface cleanliness will be maintained by keeping the assembly in controlled environments and periodically cleaning surfaces where feasible.

The ADR contamination control requirements will be designed to minimize contaminant redistribution to sensitive filter or detector surfaces. To minimize such contaminant redistribution, internal dewar surface contamination and outgassing levels will be limited. Vent paths for dewar pump-down will be designed such that the flow of outgassed molecules and particulate contamination across thin film filter surfaces is minimized. Proper venting of helium gas will be designed to avoid thermal conduction caused by vented gaseous molecules. The LXM cryostat outgassing levels will be limited by selecting low-outgassing materials and by baking out assemblies that contain significant quantities of nonmetallic materials. For materials selection, the criteria that should be applied are a maximum of 1% total mass loss and 0.1% collected volatile mass. Vacuum bakeout tests will be conducted for harnessing and Multilayer Insulation (MLI).

Radiation Considerations — Superconducting detectors and electronics are generally considered more resistant to radiation than semiconducting electronics because they do not depend on the mobility of individual electrons and holes and because the material properties of a superconductor are averaged over spatial scales of the coherence length, which greatly exceeds the small size of damage features created by ionizing radiation. Research on radiation effects has focused on superconducting tunnel junctions because their nanometer-scale barriers are the only features whose size approaches the scale of radiation damage. Irradiation tests have been performed on tunnel junctions by a number of researchers, including by those on the *Lynx* team. These results are summarized below:

- A Japanese research team exposed two Nation Institute of Standards and Technology- (NIST-) series SQUID arrays to 160 MeV protons, delivering a 10-krad dose. Their performance before and after irradiation was statistically consistent. More tests of this type are planned for the *Athena* project.

- The Gravity Probe B team exposed three cold DC SQUIDs to 105 to 107 protons/s/cm^2 with proton energies of 50–280 MeV. They concluded, "No changes of the type to be expected from critical current variations were observed, nor was any permanent damage noted in the SQUIDs." [578]
- For Herschel, "More than 100 junctions have been irradiated with [10 MeV proton] doses between 109 and 1,013 protons/cm. According to the analysis, a 2×1,010 protons/cm dose would correspond to … 4 years mission with a 1-mm thick Al shielding. After the tests, only small and not significant changes (about 1%) were observed on the junctions I-V curves." [579]
- Frunzio et al. 1998 summarized irradiation experiments. Two proton-irradiation experiments on niobium-based tunnel junctions (as are planned for *Athena*) delivered doses of 77 and 500 Mrad without causing damage. A third experiment that delivered 5,000 Mrad resulted in damage [580].

One estimate [581] for the radiation dose from four years at L2 with 1-mm-thick aluminum shielding is about 50 krad (given for silicon, but assumed applicable here, too). Frunzio determined the damage threshold for niobium junctions to between 500 and 5,000 Mrad. Hence, the damage threshold is at least a factor of 104 greater than the expected mission dose [580].

In regard to radiation effects, the LXM's main potential sensitivity is to the effects of radiation damage in the room temperature electronics. All LXM electronics will meet the radiation tolerance requirements necessary for the flight electronics to operate over the lifetime of the *Lynx* mission at SE-L2. The processors, Analog-to-Digital Converters (ADCs), and Digital-to-Analog Converters (DACs) needed for microwave SQUID readouts are the critical electronics components that require high performance and must be radiation-tolerant. A detailed discussion of the flight-compatible components identified as an initial baseline are described in [582].

The HEMTs are the main remaining components that are potentially sensitive to the radiation environment. Based upon the known radiation sensitivity properties of semiconducting devices similar to the HEMTs currently baselined for LXM, space-qualifying the SOA HEMTs is not expected to be a problem. However, this still needs to be verified, and this verification process has been included as an important component of the *LXM Technology Roadmap*.

6.3.5 Integrated Science Instrument Module

The ISIM is the support structure for the focal plane instruments that interfaces to the OBA and places the required focal plane camera in the proper position for each observation.

The HDXI and LXM are mounted on a translating table, while the XGD assembly is mounted on a fixed platform. Both the translation table and the XGS platform will be capable of focus adjustment to establish the best focus on-orbit and to allow for offsets of the focal planes for those three cameras. ISIM resources are summarized in Table 6.13.

Table 6.13. ISIM resources are summarized. The ISIM mass of 1,460 kg interfaces to the optical bench. The total number of moves and distances for translation and focus include ground testing and 20 years on-orbit.

ISIM Resource	Value
Total mass (with margin)	1,460 kg
Translation table and interfaces	108 kg
Fixed table	73 kg
Housing	123 kg
Radiators, and thermal hardware	194 kg
Mechanisms	193 kg
Instruments (total)	769 kg
Average operating temperature	283 K
Focus range	± 1-cm
Focus stability	3 µm
Focus accuracy	0.01 mm
Focus total number of moves	20,000
Focus total distance	200 m
Translation range	75 cm
Translation stability	3 µm
Translation accuracy	5 µm
Translation total number of moves	20,000
Translation total distance	15,000 m

This translation table assembly allows any point along a line to be chosen as the celestial target aim point. This allows, for example, selection of the desired LXM subarray, or optimizing the focus over the FOV of the tilted HDXI chips. The XGD is mounted in a fixed location on the ISIM offset from the optical axis to intercept the dispersed spectrum regardless of whether the HDXI or LXM is at the primary focus. The XGD has an independent focus mechanism built into its housing. The positioning requirements and lifetimes are easily met with standard design practices and high-TRL mechanisms. The placement of the instrument electronics boxes was optimized to minimize the distance between each of the instruments and their electronics (shown in Figure 6.24). A more detailed design will be carried out during Phase A and will also include the heat pipe placement. Mechanisms for translating and focusing the instruments have dual-redundant motors (§6.4.7).

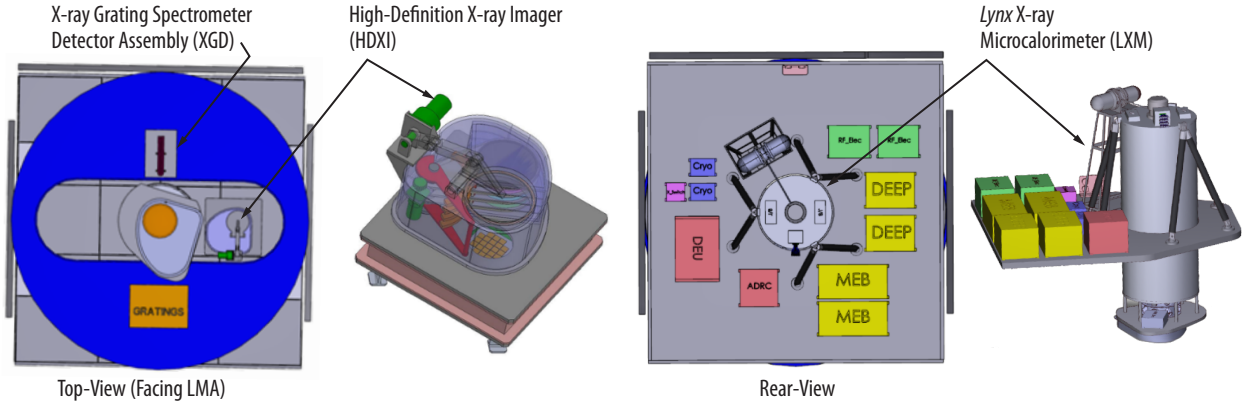

Figure 6.24. Views of the ISIM with HDXI, XGD, and LXM mounted, along with a view of their electronics boxes. An elliptical opening, seen in the top-vie in the ISIM fixed plate allows for the HDXI and LXM to translate across the focal plane.

The ISIM also provides a protective, light-tight cover for the instruments, as well as mounting surfaces for the radiators required by the cold LXM focal plane detectors and the cryocooler. Radiators will be placed on the three coldest sides of the ISIM based on the temperature requirements and proximity to the instruments they serve. For those requiring significant heat transfer from instrument to radiator panel (e.g., the LXM DEEP boxes), heat pipes will be employed as both the primary path and for spreading heat over a large radiator panel. The size of the radiators sets the size of the ISIM translatable platform, resulting in ample real estate for supporting electronics and thermal management.

The Sun-exposed surfaces of the ISIM will be treated with low-absorptance, high-emittance external treatments such as Optical Solar Reflectors (OSRs) or zinc-oxide-filled painted coatings (e.g., Z-93). Overall, the ISIM's temperature will be cold-biased to support colder focal plane detectors as well as reduce the overall heat load of the instruments to the radiators.

6.3.6 Optical Bench Assembly

The OBA's function (depicted in Figure 6.25) is to maintain precise control of the geometric alignment between the optical elements of the LMA and the science instruments within the ISIM. To perform this function, the OBA design uses a near-zero CTE, lightweight, high-tensile, compressive strength carbon fiber composite (M46J) structure additionally supported by ring stiffeners. To provide stability against vibration and high-frequency jitter while maintaining the required rigidity, the LMA is optimally anchored to the OBA by three pairs of bipods, while the ISIM is attached directly to the OBA. To minimize thermal gradients and rapid localized temperature excursions due to Observatory reorientation, the OBA is cold-biased and uses passive thermal insulation and active, autonomous thermal control via resistive heaters. The OBA is opaque to stray light.

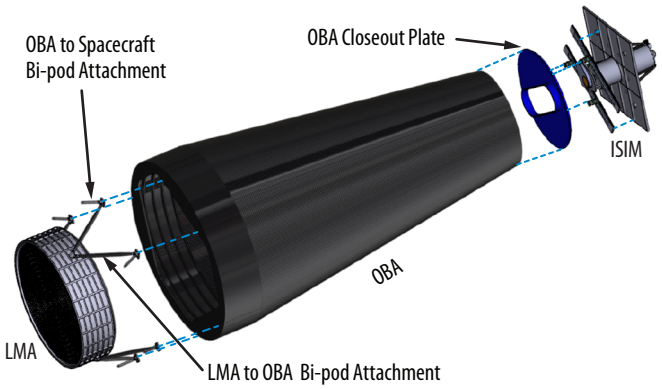

Figure 6.25. OBA provides geometric alignment between the optics and science instruments.

The OBA presents the largest outward surface area toward both hot and cold (Sun and anti-Sun) sides of the Observatory. It therefore potentially suffers the largest amplitude deformations due to induced thermal gradients and other disturbances that affect the alignment of the optical elements along and perpendicular to the optical axis.

Thermal effects are minimized by placing MLI blankets on top of the low-CTE OBA composite structure. In addition, to maintain positive thermal control within the OBA over a longer lifetime of 20 years, the MLI is augmented with a one-time-deployed siliconized Kapton® sunshade (§6.4.4). The sunshade deployment uses a simple series of spring ribs along the length of the OBA, with the ribs and sunshade held just above the MLI with single-shot actuators during launch, which then release the sunshade to its flat shape upon deployment. This arrangement keeps the outer layer of the MLI blanket under 10 °C so that the net heat flow is from the OBA to the exterior for all allowable Observatory orientations. The sunshade extends as needed to allow the full field of regard adopted for the mission, including the ±15° roll capability.

Thermoelastic analysis of the Observatory indicates that maximum deformations do not exceed 2.4 μm along any principle axis due to changes in orientation relative to the Sun. Critically, along the optical axis, these maximum deformations are much less than the telescope depth of focus and will not compromise the *Lynx* PSF. *Lynx* is more tolerant of deformations perpendicular to the optical axis because lateral placement is monitored by the Fiducial Transfer System (FTS).

Chandra and *XMM-Newton* experience beyond Earth's radiation belts shows that charged particle flux through the open aperture of telescope optics can be substantial. *Chandra* utilizes a magnetic diverter located within the OBA between the mirror assembly and the focal plane instruments to deflect electrons from paths toward the on-axis science instrument. A similar magnetic diverter for soft protons is planned for *Athena* [553]. *Lynx* can accommodate a similar magnetic diverter within the OBA cavity. Though no specific design has yet been considered, a mass with ample mass growth allowance based on *Chandra's* magnetic diverter as a first-order approximation has been assumed and incorporated into the Master Equipment List and cost estimate.

As described in §6.4.2, to monitor the alignment of the optical system, the *Lynx* GN&C system has adopted the *Chandra*-heritage PCAD system. The PCAD system includes an FTS, as depicted in Figure 6.26. The FTS places images of Light Emitting Diodes (LEDs) located near each science instrument in the FOV of the star-tracking camera. These diodes serve as points of reference of the instrument's lateral position with respect to the star camera boresight.

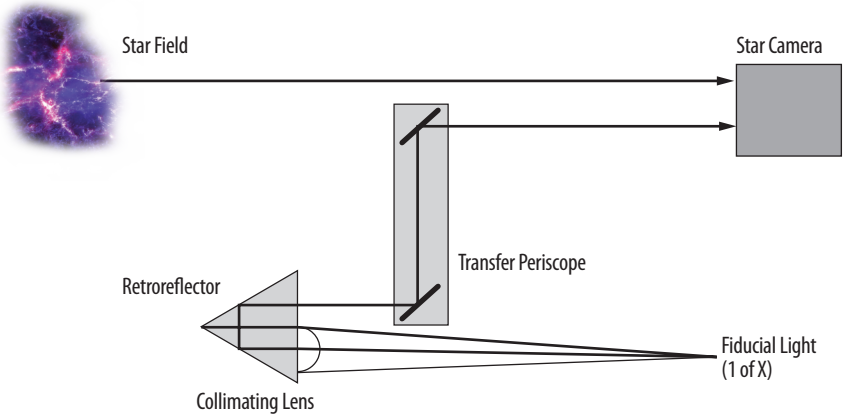

Figure 6.26. Schematic demonstrating the principle of the *Lynx* FTS. In addition to imaging the tracking starfield, the star camera images light from LEDs located near each science instrument. The fiducial light passes through a collimating lens and retroreflector mounted at the node of the LMA before being transferred via a highly stable periscope to the star camera.

6.4 Design of Spacecraft and Subsystems

The Spacecraft will meet *Lynx* requirements with high TRL, low risk design solutions. *Lynx* will take advantage of emerging subsystem technologies to enhance performance and reduce risk without expensive architecture changes. Subsystem elements have been designed to provide 20 years of on-orbit operation and to maximize launch flexibility.

The spacecraft includes all necessary subsystems to enable the scientific and operational functionality of the Observatory, as shown in Figure 6.27. The *Lynx* system block diagram is shown in FO2, illustrating the system dependencies.

Following a trade study on configuration architecture, a *Chandra*-like spacecraft was selected (Appendix B.1.1). This layout is straightforward, with no complicated deployments and provides for standard thermal management of the LMA. The design of the spacecraft and individual subsystems is robust, with extensive use of low-risk, high-TRL, heritage, and commercially available components. However, the architecture itself is not dependent on obsolescent technologies, and newer technologies can be incorporated as available during detailed design. The application of Risk Class A design requirements and industry-standard margins have been used throughout, and credible single-point failures have dual-redundant systems (summarized in Table 6.14).

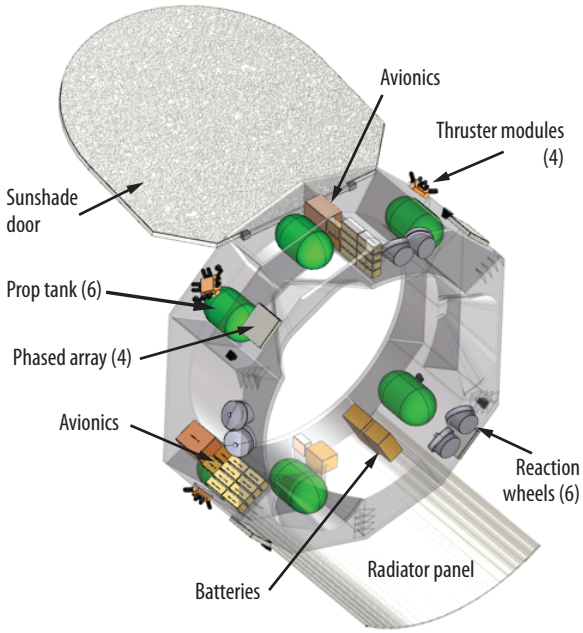

Figure 6.27. *Lynx* spacecraft schematic. All spacecraft subsystems are at high maturity levels or modified heritage.

6.4.1 Propulsion

The propulsion subsystem is a monopropellant blowdown system utilizing hydrazine as fuel and gaseous nitrogen as the pressurant, and can be realized through existing high-TRL and/or modified heritage components. The current design utilizes six modified ATK 80274 propellant tanks, two (plus two redundant) Northrop Grumman MRE-15 main engines, and eight (plus eight redundant) MRE-1.0 Reaction Control System (RCS)/Attitude Control System (ACS) thruster modules. The ATK 80274 standard model tank is flight-proven, but *Lynx* will utilize a modified version to extend the height to allow for the 489-kg load of propellant. The propulsion system is sized to meet the delta-V required to reach the SE-L2 orbit and perform an initial de-spin (also called de-tumble, the negation of unwanted motion after separation from the launch vehicle), with sufficient residual propellant to perform station-keeping and momentum unloading maneuvers for a minimum of 20 years on-orbit.

Table 6.14. Redundant systems have been developed for every credible single point failure on *Lynx*.

Subsystem	Provisions for Fault Tolerance
Mechanisms	• Forward Door Assembly (FDA): Dual-redundant motors • Aft Door Assembly (ADA): Dual-redundant motors • Grating Arrays: Dual-redundant motors • Horizontal translation table mechanisms: Redundant horizontal drive motors in series • Drive screw itself considered non-credible failure • Vertical translation table mechanisms: Dual-redundant vertically stacked actuators • Instrument fine focusing motor: Dual-redundant motors
CD&H	• Flight Computer: Dual-redundant Spacecraft Flight Computers + Redundant Safe Mode Backup Controllers • Solid-state Recorder: Internally redundant with redundant power, control, and data I/O connections Redundancy provided by blocks of independently addressable memory • Data Acquisition Units: Dual-redundant for spacecraft + aft DAU • Main Propulsion System Controller: Dual-redundant • Reaction Control System Controller: Dual-redundant • Reaction Wheel Controller: Dual-redundant • LMA Heater Controller: Internally redundant • SC/OB/ISIM Heater Controller: Internally redundant • Avionics/Propulsion Heater Controller: Internally redundant • Translation Table Mechanisms Controller: Dual-redundant • Solar Panel Array Drive: Dual-redundant • Remote Command and Telemetry Units: Internally redundant
Communication	• X-Band Transponder: Dual-redundant • Ka-Band Transceiver: Dual-redundant • Ka-Band Diplexer: Dual-redundant • X-Band traveling-wave tube amplifier: Dual-redundant • X-Band traveling-wave tube: Dual-redundant • Ka-Band traveling-wave tube: Dual-redundant • Ka-Band traveling-wave tube amplifier: Dual-redundant • Ka-Band PAA: With 4 antennas, a loss of one reduces available FOV. Operational maneuvers may be required to establish Earth link with remaining antennas • X-Band antennas: Passive components, failures are not expected
Power	• Solar Array Drive Actuators: Dual-redundant actuators • Power distribution: Separate distribution to spacecraft and science instruments • Batteries: One additional battery added for fault-tolerance
Propulsion	• Main Engines: Dual-redundant set of 2 thrusters • Thrusters: Dual-redundant set of 8 thrusters; allows momentum unloading after worst-case 3 failures
GN&C	• Control Actuators: Six-wheel reaction wheel pyramid allows for single wheel failure; Any 3 wheels can control vehicle, with reduced momentum envelope and increased slew times. • Coarse Sun Sensors: One additional sensor for fault tolerance • Ultra-fine Sun Sensor: Dual-redundant • Inertial Measurement Unit: Any 2 of 6 gyro channels allow for 3-axis rate measurement • Aspect Star Camera: Redundant Focal Planes and Electronics.
Thermal	• Foil resistance heaters and heater controllers are internally redundant. Redundant temperature sensors provided for each heater zone. Fault detection and switching functions performed within the heater controllers or by command • Heat pipe radiators are inherently fault tolerant. Transport and header heat pipes are shielded. Heat rejection hardware failures are non-credible

Mission analyses used to determine delta-V are based on the *JWST* and the *IXO*, while estimates of de-spin and momentum unloading propellant mass are provided by analysis of the *Lynx* insertion scenario. Figure 6.28 shows the *Lynx* mission profile with all maneuvers and delta-V budget.

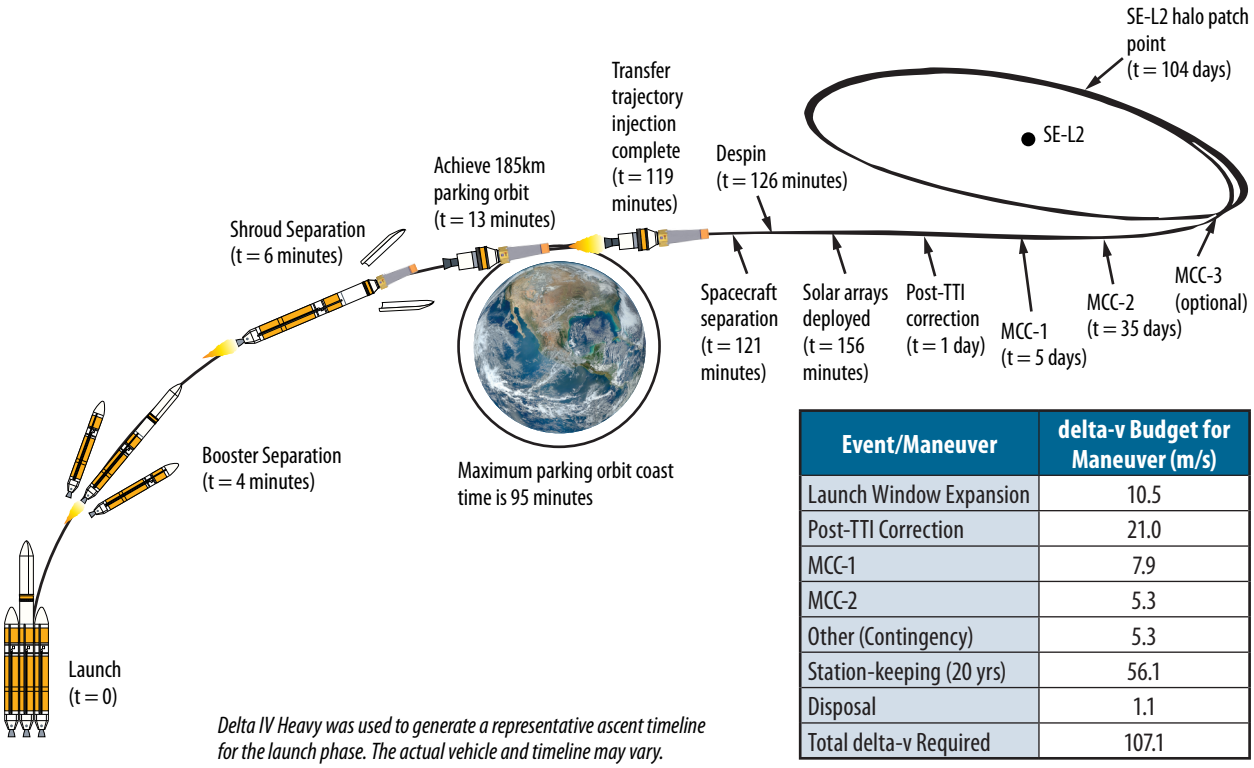

Event/Maneuver	delta-v Budget for Maneuver (m/s)
Launch Window Expansion	10.5
Post-TTI Correction	21.0
MCC-1	7.9
MCC-2	5.3
Other (Contingency)	5.3
Station-keeping (20 yrs)	56.1
Disposal	1.1
Total delta-v Required	107.1

Figure 6.28. Launch to orbit timeline and delta-v budget.

6.4.2 Guidance, Navigation, and Control

The GN&C system maintains knowledge of the spacecraft orientation, controls the maneuvers required to orient desired celestial targets within the telescope FOV, and holds each target attitude for the commanded duration. Table 6.15 highlights key parameters of this system. The *Lynx* system achieves the required 10-arcsecond absolute pointing accuracy and stability of ±0.17 arcsecond per second per axis after target acquisition and allows the Observatory to carry out a 90° slew maneuver in ~50 minutes. The minimum continuous observation time-on-target is 105 seconds, with longer observation times possible with appropriate momentum management. In addition, the GN&C system provides sufficient data for post-facto calculation of an absolute location on the sky to within a 1-arcsecond RMS radius and to reconstruct X-ray images within a 0.2-arcsecond RMS diameter.

Table 6.15. The GN&C subsystem meets derived science and mission requirements with low risk design solutions.

GN&C Subsystem Key Parameters	Value
Observations	1–20 targets per day, 1,000–100,000 s per observation
Orbit determination accuracy	30 km
Pointing accuracy	10 arcsec (3σ)
Onboard knowledge	4 arcsec
Ground aspect knowledge	1 arcsec absolute to sky
Stability	±0.17 arcsec per sec per axis
Slew performance	90° degree slew in 50 min

The *Lynx* GN&C system architecture is based on *Chandra's* PCAD design heritage. The *Lynx* design includes an SOA Ball Aerospace High-Accuracy Star Tracker (HAST) camera capable of simultaneously tracking 8 to 10 object images with 1- to 4-second readouts, three 3-axis strapdown Honeywell Miniature Inertial Measurement Units (MIMUs), two Adcole Coarse Sun Sensors, two Adcole Ultra-Fine Sun Sensors, and six Rockwell Collins TELDIX® RDR 68-3 reaction wheels sized to counteract environmental disturbance torques. To hold the target attitude, the star camera acquires and tracks known guide stars in the target vicinity, the MIMUs monitor rotational rates, and reaction wheels are commanded to spin as needed to compensate for disturbance torques (due primarily to solar wind and radiation pressure). The MIMUs and reaction wheels are used to maneuver to science targets.

Unloading of reaction wheel momentum due to environmental disturbance torques (primarily due to solar pressure) is assumed to occur once the reaction wheels reach a total momentum capacity of ~50%. The determination of disturbance torques is based on worst-case geometric offset of Observatory center of mass and center of pressure for a conservative estimate of propellant needed (Figure 6.29). This offset will be optimized (i.e., minimized) during detail design to grant an opportunity for higher propellant margin.

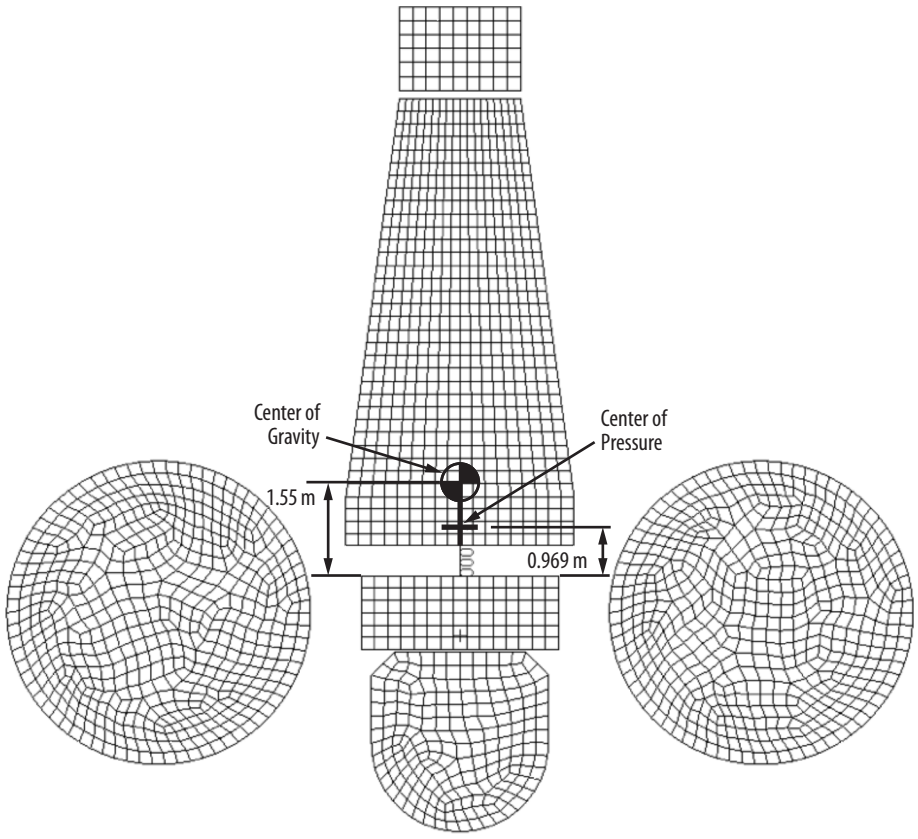

Figure 6.29. The *Lynx* center of gravity and center of solar pressure were included in the GN&C analysis and are sufficient. The design will be further optimized to improve propellant efficiency during preliminary design.

The *Lynx* SE-L2 orbit is free from Earth and Moon shadowing, allowing for uninterrupted observation of any target. However, no *Lynx* science instrument can tolerate direct solar radiation, so viewing is restricted to angles larger than 45° from the direction toward the Sun (Figure 6.30). This restriction makes about 15% of the sky inaccessible at any given moment, but no part of the sky remains inaccessible for more than three months of each year. In addition, the spacecraft and instrument designs take advantage of the hot and cold sides of the Observatory to locate radiators, fuel lines, etc., which imposes a constraint on the Observatory roll angle (rotation about boresight) of approximately ±15° to prevent impingement of direct sunlight on these surfaces.

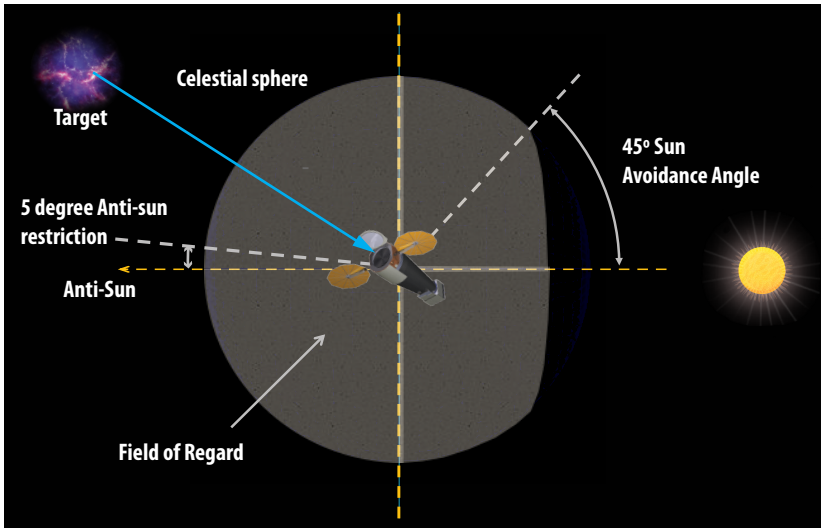

Figure 6.30. *Lynx* Field of Regard. *Lynx* can view the entirety of the celestial sphere less the 45° Sun avoidance cone imposed by the sunshield that is in place to protect the sensors from solar impingement.

The post-facto aspect solution makes use of the guide star positions, the fiducial light positions, and the integrated MIMU rate data to compute the solution for the pointing direction, roll, and gyroscope biases. It then interpolates the solution to the precise arrival time of each registered X-ray photon event, allowing each photon to be registered to its point of origin on the sky.

Ranging and Doppler velocity data are sufficient for station-keeping a satellite at a linear Lagrange point, such as the SE-L2 in the case of *Lynx* [583]. Deep Space Network (DSN) ranging and Doppler measurement data will be obtained during the three one-hour daily communication passes. Detailed simulations performed for the *JWST* mission showed that two 30-minute (alternately, two 3-hour) passes per day will measure the velocity to 6.5 (5.9) mm/s versus a requirement of 2 cm/s accuracy to maintain a halo-type orbit [584]. The simulation assumes that both northern and southern hemisphere DSN stations are used, and that the solar radiation pressure force can be modeled to 5%. Station-keeping maneuvers will be done approximately every three weeks. Approximately 2.5 m/s per year is the expected correction. Unloading angular momentum is not done with a perfect torque couples by thrusters. An unloading efficiency of 87% is expected, and thus 13% of the force produces orbital perturbation. In principle, ideal momentum unloading could contribute to the station-keeping. However, random orientations relative to the orbit will be assumed. Thus, for the 49 momentum dumps expected per year, a random walk delta-V of 1.6 cm/s per year is imparted, a small impact to the total 2.5 m/s adjustment.

The *Lynx* propellant budget is sized for the 2.5 m/s per year for a 20-year mission. A future study will determine if significant propellant can be saved via improved orbit determination. Candidates for the improved determination are use of the DSN delta-Doppler one-way ranging, or incorporating onboard cameras dedicated to tracking solar system objects including the Earth, Moon, and asteroids.

6.4.3 Power

As summarized in Table 6.16, the electrical power system is designed using all high-heritage components to generate, store, manage, and distribute required power to the Observatory throughout all phases of operation via a combination of deployable solar panels and onboard energy storage. Energy storage is supplied via five 28-V batteries, with one additional battery to ensure single-fault tolerance. The batteries are sized to provide launch power (743 W) for 156 minutes from launch to the completion of initial checkout and solar array deployment. Initial thermal analyses suggest that the LMA, OBA, HDXI, and XGS can be powered down during the launch phase. Survival heaters following the launch phase but prior to solar array deployment will be powered by onboard batteries until the solar arrays are deployed. A more detailed analysis will be conducted during Phase A that will contain the possible inclusion of additional batteries or a small body-mounted solar array panel, to provide additional survival power in the event of an anomaly before full solar array deployment.

Two UltraFlex™ deployable solar arrays with a total area of 51 m^2 are utilized to provide sufficient total power and are articulated to allow for full Sun illumination at any boresight pitch angle with respect to the Sun. The arrays are sized to meet the 7.4-kW peak operational power requirement (XGA inserted and LXM at the primary focus) with ~40% margin. The power system design accounts for expected degradation over a 20-year mission lifetime.

Table 6.16. The *Lynx* power system is designed to provide power throughout all phases of operation. All power values are in Watts.

Source	Launch (0 – 156 min)	Survival Mode (5 min) Battery Power Only	Normal Mode (LXM, XGS on, Downlink)
Avionics	551	546	1,812
GN&C	0	283	283
Propulsion	0	510	510
Mechanisms	0	0	210
Thermal	178	154	178
Total SCE Subsystems	**729**	**1,493**	**2,993**
LXM	14	14	2,205
HDXI	0	7	248
XGS	0	7	190
LMA Heater	0	593	1,346
OBA Heaters	0	438	438
Total Telescope	**14**	**1,059**	**4,427**
Total Observatory	**743**	**2,552**	**7,420**

6.4.4 Thermal

Thermal control and regulation of the LMA and OBA are critical to meeting Observatory performance requirements. The spacecraft thermal subsystem is designed to maintain the spacecraft and OBA at an average temperature of 283 K and the LMA at a warmer temperature than the spacecraft (293 K ± 0.25 K) (Table 6.17). The temperature of the mirrors will be controlled throughout assembly and alignment as well as in flight to minimize contamination. The Observatory-level thermal system design includes the use of a high-TRL thermal control approach with the use of conventional MLI, a siliconized Kapton sunshade, OSRs where appropriate, and redundant heaters and radiators.

Table 6.17. The Thermal subsystem uses active and passive design to maintain the required temperature envelope for all allowable sun angles, to meet science requirements, and to control possible contamination of the mirrors over the mission lifetime .

Thermal Subsystem Key Parameters	Value
LMA temperature	293 K ± 0.25K
SCE maximum average temperature OBA maximum average temperature ISIM maximum average temperature Translation table maximum average temperature	283 K
OBA average zone Temperature for full range of allowable sun angles	283 ± 2 K

The current DRM conceptual design uses advanced high-performance radiators to reduce mass. This technology has a clear path to TRL advancement; however, current flight-heritage radiator technology can meet the *Lynx* thermal performance requirements with a nominal mass increase.

A trade study of the OBA thermal control comparing passive and active control options concluded that a purely passive system of heat pipes and MLI could not maintain the required limit on temperature gradients at all pitch angles due to variation in heat pipe inputs on the bench. See Appendix B.6.6 for more details.

Another study was conducted to determine an alternative to the use of *Chandra*-heritage silverized Teflon MLI on the optical bench. This study was prompted by the more-rapid-than-predicted degradation of the *Chandra* MLI due to Ultraviolet (UV) exposure. Analysis of the *JWST*-heritage siliconized Kapton revealed poor thermal control in using this material as simply the outer MLI layer for the *Lynx* geometry. OSRs were also studied, and although the OSR solution provided the desired thermal performance, the support structure required to mount them to the optical bench was determined to have an unacceptably large mass impact. Following this study, an additional option was analyzed that included the use of a lightweight, flat, simple deployable sunshade of siliconized Kapton. Through a modest study of pitch and roll combinations, the preliminary analysis showed that this design produced similar performance to the OSR solution without significant additional mass (see Figure 6.31 and the *Lynx DRM Supplemental Design Package* for more details).

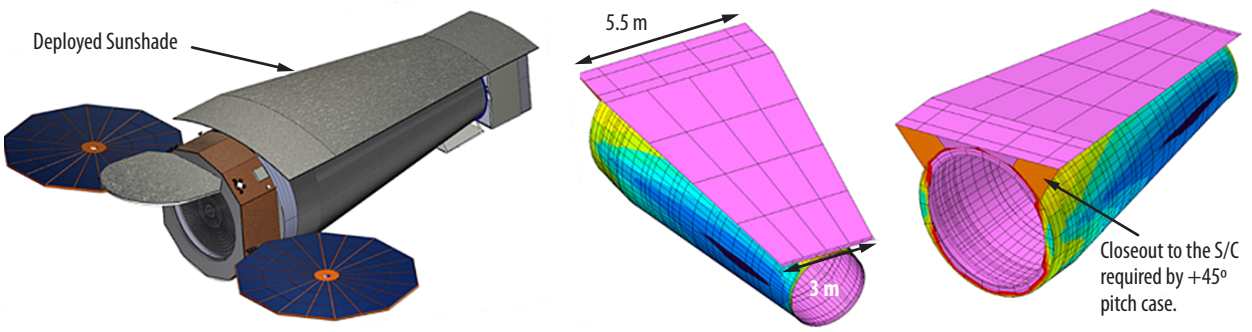

Figure 6.31. Schematic depiction of single-deployment Si-Kapton sunshade mounted on sun-facing side of OBA.

6.4.5 Avionics and Flight Software

The avionics equipment in the *Lynx* spacecraft is designed to perform the functions of GN&C, power switching, data storage, command management, uplink and downlink communications, and thermal control. These systems will draw heavily from heritage (e.g., *Mars Orbiter*, *Chandra*, *Spitzer*, and *JWST* designs). *Lynx* requirements allow the use of technologies that are readily available. Table 6.18 summarizes key parameters for this system.

Table 6.18. The Avionics and Flight Software (S/W) subsystem meets requirements with heritage design solutions.

Avionics and Flight Software Subsystem Key Parameters	Value
Total science data collection rate	240 Gbit/day (2.78 Mbps)
Total science memory storage	48 hours (~500 Gbit)
Total SCE memory storage	1 Tbit (1.4 Gbps capacity)
Flight software lines of code	100, 000
Flight software reuse (%)	68%

A temperature-controlled, ultra-stable oscillator (1 part in 10^9 per day) synchronizes all spacecraft control and data and command functions. A heritage flight computer system will be baselined, similar to that used for the Jet Propulsion Laboratory's (JPL's) *Mars Orbiter*, which is designed for long life in the SE-L2 environment. Based on analysis of the science instrument designs, the maximum science data rate is 240 Gbits per day. The spacecraft design assumes up to 48 hours of science data storage, with a total data storage capacity of 1 TB and spacecraft capacity of 1.4 Gbps. The *Lynx* flight software includes software for the spacecraft and science instruments. The spacecraft software will reside on the redundant spacecraft flight computers. Remote command and telemetry units interface between the spacecraft computer and the functional subsystems, including the focal plane instruments.

Flight software will control communications and data handling, attitude control, recorder management for housekeeping and science data, spacecraft health and safety monitoring, PCAD, electrical power, thermal control, and will be responsible for recognizing fault conditions and managing safe modes. Safe mode control will include a separate set of control processing electronics that operate with different software. The science instruments will include software that will reside on the electronics units developed by each science instrument provider. The flight software will incorporate new development only for mission-specific components and as needed for obsolescence. Examples of reuse of software algorithms include power management, C&DH, health and safety, executive services, and memory loads and dumps. Examples of *Lynx*-specific software components include instrument support, mission-specific operations concept support, power switching services, and mechanism control. Based on system design and Class A requirements, ~10^5 software lines of code are estimated for the *Lynx* flight software system, at ~68% reuse. All *Lynx* flight software development will comply with NASA Software Engineering Requirements per NASA Procedural Requirement (NPR) 7150.2, and NASA software safety standard 8719.13 as Class A Safety Critical software.

An internally redundant Safe Mode Electronics Unit (SMEU) (shown in Figure 6.32) is included to enable the Observatory hold position or to slew autonomously to a safe Sun angle in the event of out-of-range onboard parameters. See §6.7.2 for discussion on Safe Mode. Ka-band is not currently part of the SMEU; this will be part of a future trade during preliminary design.

The system design includes three heater controllers to maintain the design temperatures and thermal gradient requirements for key science and spacecraft systems. These controllers are designed with multiple zones, each with 100% redundant heaters and sensors. Figure 6.33 contains a schematic of the temperature control concept.

The *Lynx* avionics are susceptible to galactic cosmic rays and solar particle events at SE-L2. To mitigate resulting negative effects, the avionics design includes components that were specifically selected for a long life in a deep space environment. A more rigorous design, appropriate shielding, and careful parts selection during Phase A is needed (§6.6.2.1).

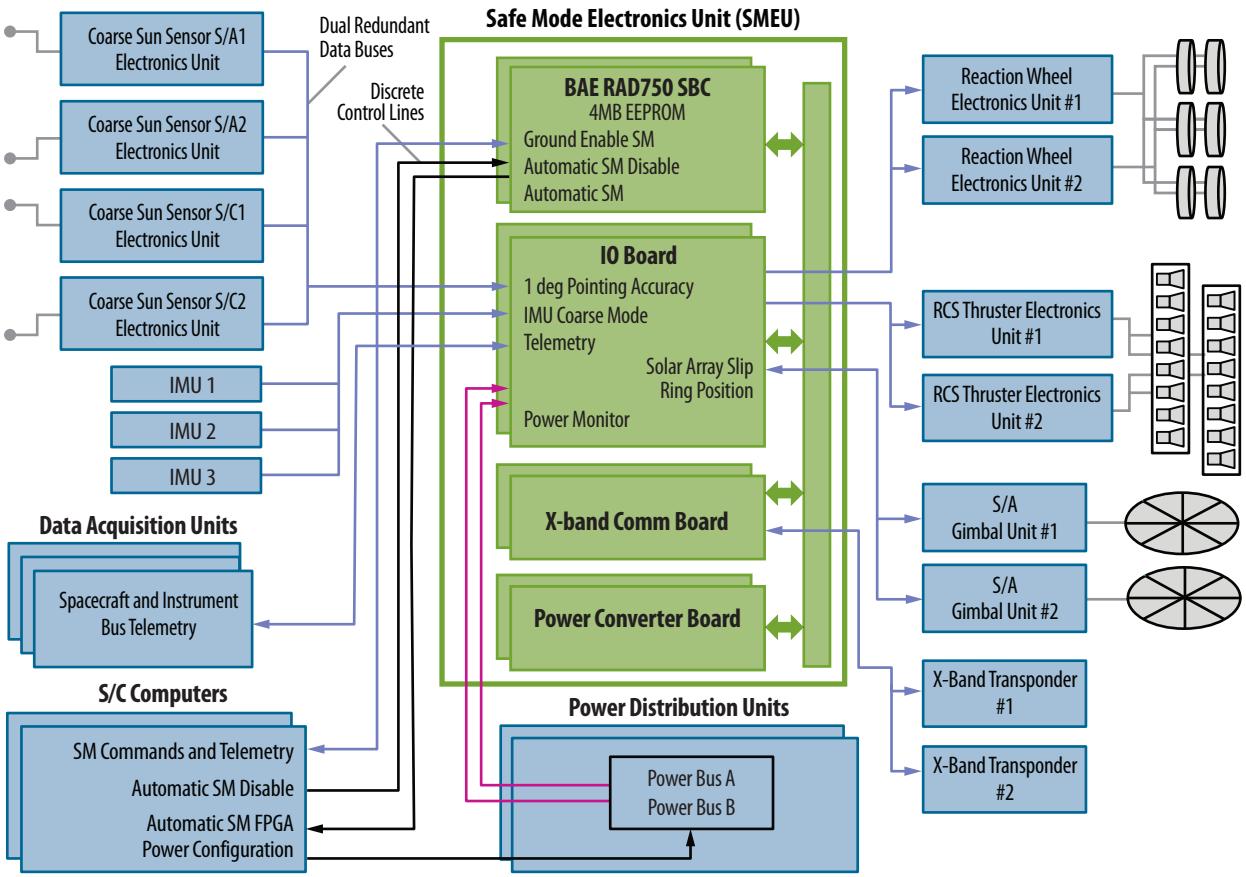

Figure 6.32. The internally redundant SMEU will provides autonomous safing capability.

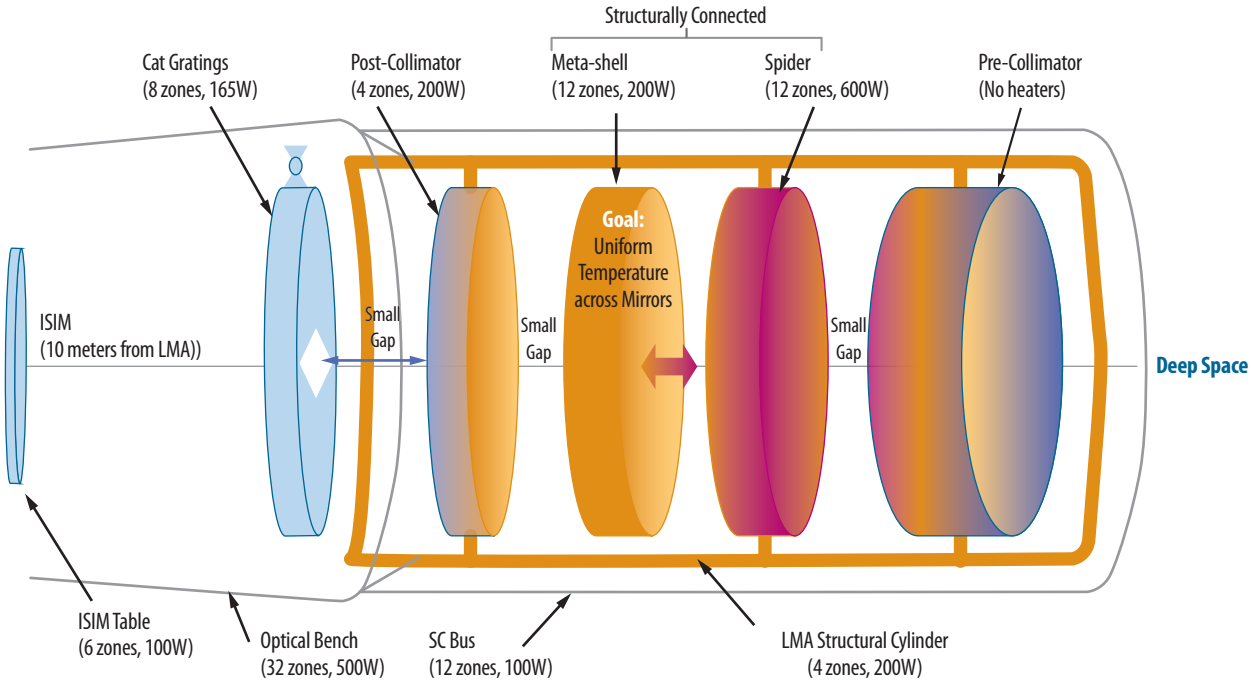

Figure 6.33. Thermal control concept. Multiple thermal zones designed to maintain temperatures and gradients for the mirror, instruments, optical bench and spacecraft. Conservative analysis used to determine number of and size of heater controllers. Power numbers reflect controller capability, not actual heater power required, which is smaller. The colors indicate the relative temperature gradient between elements.

6.4.6 Command and Data Handling

For communications with the ground, *Lynx* will utilize NASA's existing DSN system to provide Telemetry, Tracking, and Command (TT&C), ensuring high-reliability and high-data rate communications for downloading its science and spacecraft health data and uplinking commands. Table 6.19 summarizes the telemetry data rates and volume for the science instruments and spacecraft.

For the DRM, a flight-heritage communication system has been baselined that is similar to that used on the Mars Reconnaissance Orbiter, which supports data volumes up to 270 Gbits/day. It is also assumed that the *Lynx* communication system will utilize the high-heritage Ka-band for data downlink (per Space Communications and Navigation (SCAN) guidance) and X-band for low-rate uplink and backup telemetry. The current *Lynx* concept assumes high-flight heritage, phased-array antennas, avoiding the use of gimbaled antennas and their potential vibrations, providing more stability for the telescope during science operations.

With the guidance from NASA SCAN experts, the *Lynx* engineering team conducted a trade study on future DSN communications and capabilities. Technology for long-distance, space-based laser communications was demonstrated in NASA's 2013 Lunar Laser Communication Demonstration (LLCD), the space terminal that flew on the Lunar Atmosphere and Dust Environment Explorer (LADEE) spacecraft. The LLCD configuration demonstrated an error-free data transmission at a rate of 622 Mbps from lunar orbit. From the science perspective, there are benefits to considering higher data rates. First, the same volume of data could be downlinked in a much shorter time. Feasible data rates could be 5× or more higher than the current baseline. Alternately, larger volumes of data could be downlinked in the same amount of time. A trade study will be carried out during the *Lynx* detailed design phase to assess the state of the technology and applicability to *Lynx*.

Table 6.19. *Lynx* data volumes are modest and easily handled in the 2030s timeframe.

Source	Expected Volume	Data Rate	Comments
Science Data	240 Gbits/day	2.78 Mbps (maximum average)	Based on science objectives and known X-ray fluxes
LXM	< 200 Gbits/day*	200 kbps to 8 Mbps	Minimum rate is background. Maximum rate observations are scheduled for no more than 6 hours and interleaved with low-rate observations
HDXI	< 200 Gbits/day*	600 kbps to 6 Mbps	Minimum rate is background. Maximum rate observations are scheduled for no more than 6 hours and interleaved with low rate observations
Aspect	0.9 Gbits/day	10 kbps	8 stars per second, 4 gyro rates every 31 ms
Grating readout	<160 Gbits/day	600 kbps to 6 Mbps	Minimum rate is background. Maximum rate observations are scheduled for no more than 6 hours and interleaved with low rate observations. Used simultaneously with LXM or HDXI
Housekeeping	17 Gbits/day	200 kbps	Estimate. Flexible depending on mode.
Downlink Frequency	1–3 times/day; 1 hour each	22.2 Mbps	*Chandra*-like operations
Uplink Frequency	1–3 times/day; 1 hour each	< 1 Mbps	*Chandra*-like operations

*Only one of the LXM or HDXI takes celestial data at any time.

6.4.7 Mechanisms

Lynx mechanisms for the DRM were chosen to meet all science and mission requirements and to have low development risk. Requirements that the mechanisms must meet include operation in the intended environments, cycles sufficient to complete the 5-year baseline mission (and extendable to a 20-year mission) and to carry out ground processing and verification, reliability, repeatability, accuracy, torque, and motion range. Additionally, all *Lynx* mechanisms have been designed to be either internally redundant or grouped with redundant mechanisms. Most *Lynx* mechanisms have flight heritage, and others are high-TRL with very low development risk. In most cases, a representative off-the-shelf mechanism part number has been identified. As *Lynx* moves into preliminary design, mechanisms will be optimized to increase performance for reduce cost. A summary of mechanisms is provided in Table 6.20.

Table 6.20. *Lynx* mechanisms meet requirements within the current SOA.

System Element	Expected Performance	Mechanism Type/Example Part #	Mechanism TRL
Solar Panel Deployment	Single deployment	Deploys on boom using spring mechanism. Contains deployment and launch locks. Provided by supplier	9
Launch locks for XGA, ISIM, siliconized Kapton thermal sunshade	Single deployment	NEA Model 9106B	9
Forward contamination door/ sunshade deployment	Designed for 20 cycles open/close. Single deployment on-orbit	Moog Type 7 Harmonic Drive Rotary Actuators	9
Aft contamination door deployment	Designed for 20 cycles open/close. Single deployment on-orbit	Moog Type 7 Harmonic Drive Rotary Actuators	9
ISIM horizontal translation	750-mm horizontal translation 5-µm accuracy, 3-µm stability	PI LS-180 High-Load Stage (or similar)	6+
ISIM Focus	40-mm vertical translation	Moog Linear Actuator (or similar)	6+
HDXI and LXM filter adjustment	Open/Closed positions, lateral repeatability of inserted filter is estimated to be ±6 µm	Segment Brushless DC Motors	9
XGA deployment	Designed for 10,000 cycles, open/closed positions 200-µm stability along optical axis and 100-µm repeatability	Moog Type 7 Harmonic Rotary Actuators	9
XGD Focus	30-mm range with 1.25-µm step fine focus adjustment	Standa 8MT173V-30 (or similar)	6+

6.5 Launch Vehicle

Lynx is compatible with existing heavy-class launch vehicles, reducing the risk of meeting the constraints (vehicles capabilities in terms of mass, environments, center of gravity location, and dynamic envelope) of future (2030s) similar vehicles.

The *Lynx* Observatory will launch on a heavy-class launch vehicle of identical capability to those currently available (e.g., Delta IV Heavy). The ability to launch on this class vehicle allows launch flexibility, resulting in reduced risk and optimized cost and schedule. The outer diameter of the *Lynx* spacecraft is ~4.5 m in diameter, sufficient to fit into a standard 5-m-class fairing. The overall volume of the *Lynx* Observatory easily fits inside the payload dynamic envelope when the solar panels and sunshade door are retracted. No additional deployments are needed. Similarly, the maximum payload mass requirement is met with adequate margin (Figure 6.34).

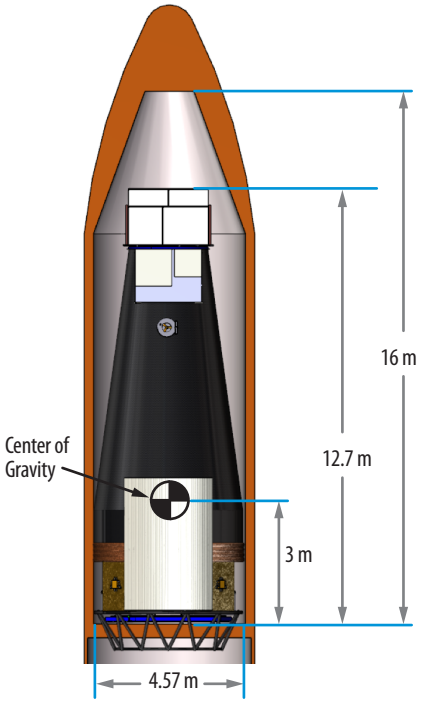

Lynx Launch Configuration Future Heavy-lift LV Shroud

Lynx Observatory Mass Summary	
Parameter	**Value**
Total Observatory Dry Mass (Basic)	5,763 kg
Total Propellant Mass (includes margin, Propellant, Residuals and Pressurant)	537 kg
Payload Adapter Mass‡	0 kg
Total Launch Mass (no MGA)*	6,300 kg
Future Heavy Launch Vehicle (LV) Capability	10,000 kg
Pre-Phase A Margin [24.5% MGA on Basic Dry Mass + Margin to LV Capability]	37%

‡Payload adaptor mass is not considered part of the payload as per NASA LSP guidance
*MGA is 24.5% of the Basic Mass. Total Observatory mass with MGA is 7712 kg. MGA is per AIAA depletion table for pre-Phase A design, and takes into account high-heritage spacecraft components.

Figure 6.34. *Lynx* Observatory Mass Summary. *Lynx* fits within the payload envelope and can launch on a future Heavy-class vehicle to SE-L2 with sufficient mass growth allowance and launch vehicle margin.

Due to the uncertainty regarding the specific launch vehicle with the payload envelope and lift capability to launch *Lynx* to SE-L2 in the 2030s, NASA's LSP has provided payload envelope, lift capability, and environments for generic vehicle class types (intermediate and heavy class), as well as for the SLS vehicles. Per current LSP guidance, the maximum payload mass to SE-L2 for the intermediate class launch vehicles in the 2030s is 6,500 kg, and for the heavy class launch vehicles is 10,000 kg. The *Lynx* DRM Observatory mass is 7,712 kg, which includes a 24.5% MGA per AIAA recommendations. Based on this information, a heavy-class vehicle meets the requirement to launch *Lynx* to SE-L2 with

an additional launch vehicle margin of 23%, which is sufficient for this stage of mission design and level of high-heritage hardware and systems.

Though the *Lynx* DRM assumes a baseline launch on a heavy class vehicle, a broad trade space regarding the availability and applicability of larger class vehicles such as SLS was explored. The goal of this study was to reduce the risk of launch vehicle availability in the 2030s even further and to provide options that could potentially minimize project cost and optimize schedule (see Appendix B.1.3).

One option worth mentioning is the possibility of launching *Lynx* on the SLS as a single payload with a co-manifested human crew. In this scenario, *Lynx* would be the only payload (other than crew) carried by the SLS, and would maintain its national importance of a Class A flagship mission. This scenario is akin to the space shuttle launching *Hubble*, the *Compton Gamma-Ray Observatory*, and *Chandra* flagship missions.

The current *Lynx* configuration easily meets the 10,000-kg and 7.2-m-diameter co-manifested payload envelope, but not the 8.4-m length limitation. A study was conducted via an industry Cooperative Agreement Notice (CAN) partnership to provide an initial design of an Extendable Optical Bench (EOB) that would allow the *Lynx* launch configuration to fit inside the SLS co-manifested payload envelope. The preliminary design includes three telescoping segments deployed on-orbit via lead screws. The overall concept is shown in Figure 6.35. See also supplemental *DRM Supplemental Design Package* for more details on the design and preliminary analysis.

An SLS co-manifested launch limits launch availability and does not allow for direct insertion to SE-L2 orbit, resulting in an increased total delta-V, propellant load, and other subsequent mass impacts. Cable management, thermal protection designs, and structural stability also need careful consideration. However, because this option could potentially result in significant cost savings to the project, it is worth exploring further at a future date.

The EOB option, in a general sense, provides a solution that would allow *Lynx* to fit into a variety of launch vehicles with shorter payload envelopes. However, this option comes at the added risk of increased number of mechanisms for deployment and additional ground testing and analyses to ensure on-orbit telescope performance is not compromised. As such, the solid OBA and standard heavy-lift vehicle for the 2030s as defined by LSP have been baselined for the *Lynx* DRM.

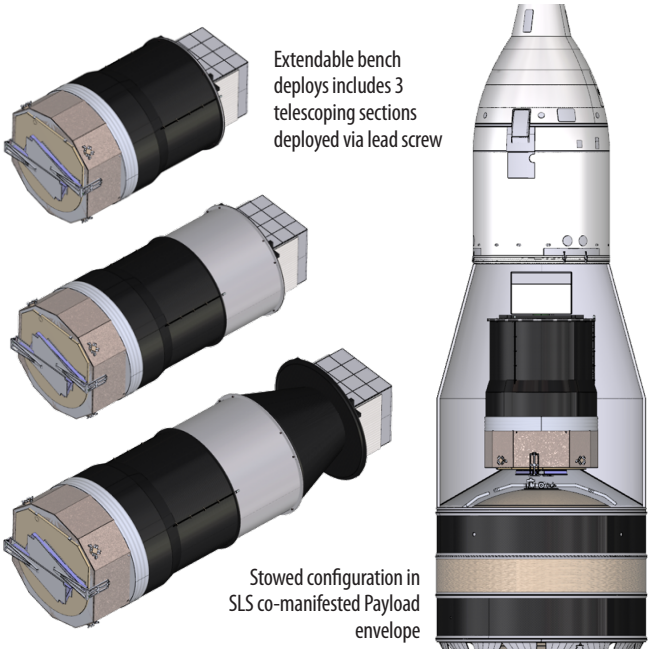

Figure 6.35. EOB design for SLS single-payload co-manifested with a human crew, trade-study option. Preliminary design and analysis shows feasibility, but with increased complexity and risk.

6.6 Systems Engineering and Integration

Lynx will use proven systems engineering principles and processes and apply them using state-of-the-art MBSE tools.

The *Lynx* Observatory will meet its science requirements by developing a robust requirements traceability that emphasizes the full system performance. Using MBSE tools, the *Lynx* team will develop all systems engineering products. MBSE allows for a simulation-driven, end-to-end lifecycle process that supports the development and maintenance of requirements and functional analysis/allocation, system analysis and control, and management. A preliminary model has already been generated by the *Lynx* team working with the University of Alabama in Huntsville (UAH) (Appendix C). Using this model, technical requirements will be developed per the processes outlined in NPR 7123.1, NASA Systems Engineering Processes and Requirements, with implementation details documented in the *Lynx* Systems Engineering Management Plan (SEMP), which will be developed as *Lynx* moves into pre-Phase A.

In pre-Phase A, stakeholder needs, goals, and objectives will be collected; the concepts of operations will be utilized to derive operational requirements; and technical requirements for the *Lynx* system will be derived. These top-level requirements will then be functionally decomposed and allocated through the requirements hierarchy.

The proposed *Lynx* requirements hierarchy, shown in Figure 6.36, takes into account the Work Breakdown Structure (WBS) and Product Breakdown Structure (PBS) to provide clear interfaces and divisions of responsibility between *Lynx* partners and future contractors.

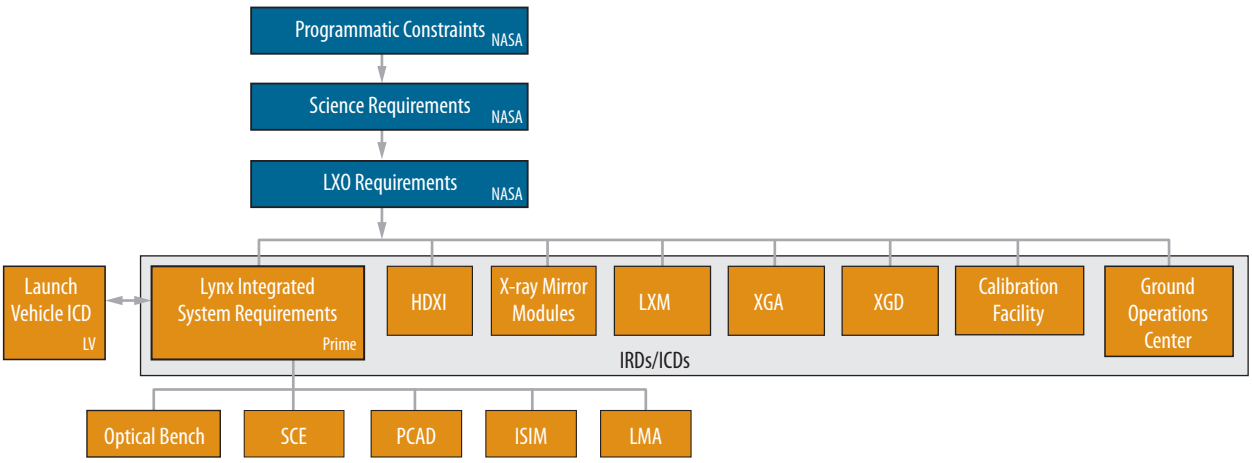

Figure 6.36. Requirements hierarchy tree. Interface Requirement Documents (IRDs) and Interface Control Documents (ICDs) are defined between interfacing elements.

During the study phase, the *Lynx* systems engineering team traced science- and mission-based requirements from the Mission Traceability Matrix to requirement implementation in the conceptual design (FO3) to show that all requirements can be met with margin in at least one feasible concept.

The spacecraft, optical bench, and ISIM element conceptual design shows that requirements can be met with low-risk, high-TRL design solutions. The *Lynx* flight system uses a robust, future-proof system architecture that does not require (but can take advantage of) new technologies to increase reliability and performance margin. This can be implemented on a subsystem level without costly system architecture changes as new capabilities become available. Details of the flight system conceptual design can be found in the *Lynx DRM Supplemental Design Package*.

The systems in the *Lynx* flight design requiring technology development in order to meet requirements are the optics and the instruments, and are detailed in the technology development plans in §7. The *Lynx* ground system concept leverages the existing *Chandra* ground system, using successful flight-proven approaches to meet all ground system requirements, as described in §6.7.4.

The *Lynx* systems-level engineering model and spares philosophy will apply the guidelines in NPR 8705.4 for Risk Class A projects, tailored to meet budgetary constraints. All new technologies such as the science instruments and the LMA will have engineering models or Engineering Development Units (EDUs). During Phase A, a cost-effective and risk-reducing approach will be used to identify the sparing level and specific spare items for each element and subsystem. This could be at the subsystem, box and/or component level, depending on a number of factors such as long-lead procurement times, criticality of the item, risk to the item, and cost and schedule impacts of not having a spare available. After launch, engineering models and unused spares will be configured to simulate on-orbit systems to validate software loads, for example, prior to uploading to *Lynx*. In this way, the investment in spares and engineering models will be leveraged even after launch of the flight system. During this study phase, a percentage was used to cost spares in the parametric cost models (§8.5.2).

The *Lynx* team will perform product Verification and Validation (V&V), ensuring that requirements are met, including those for the flight hardware and software. V&V will be performed at multiple levels of assembly and integration. The approach will be to verify subassemblies to the extent possible prior to integration to a higher-level system and then verify at the system level to ensure that requirements are still met when integrated. This approach will ensure that issues are identified as early as possible and will make locating their root causes easier, thereby saving schedule and cost. This approach will also ensure that possible interface issues are addressed at the integrated system level.

At the *Lynx* Observatory level, the protoflight V&V approach will be used. This is mainly driven by the prohibitive cost impact of a full, observatory-level qualification unit. This is technically acceptable due to the high TRL level of the proposed design solution for the spacecraft, optical bench, and ISIM elements. *Lynx* does not require any new technology in these elements to meet science and mission requirements. The *Lynx* Observatory's lower TRL elements (such as the optics and instruments) will have EDUs that are representative of the flight hardware and will be tested at qualification levels and durations. In addition, these flight units will still be tested at protoflight levels. This rigorous approach will confirm that the final products meet environmental and functional requirements and are able to support science operations.

The V&V methods used for *Lynx* will benefit from the lessons learned from *Chandra*. *Lynx* uses a *Chandra*-like system architecture, which will allow leveraging of the lessons learned from *Chandra's* verification and Assembly, Integration, and Test (AI&T) to develop a technically rigorous schedule and cost, as well as an efficient verification test flow.

MBSE tools will be used to deliver a technically correct and resource-efficient flow from requirements to verification activities, which will make configuration management, traceability, and verification more integrated as they are performed in the same model. At lower levels of verification, partners and suppliers may use other tools such as relational databases to perform V&V. These can be linked to the *Lynx* Observatory model to ensure an overall integrated V&V picture.

Validation, as separate from verification, will be addressed in two ways by the *Lynx* team. First, by ensuring that requirements fully address end user's needs, goals, objectives, and the intended operational modes and environment; validation can be addressed in verification activities. This is preferable because validation concerns can be addressed prior to flight. Second, during the on-orbit commissioning and calibration phase, the *Lynx* Observatory can be extensively fine-tuned to optimize science return and ensure efficient operations.

6.6.1 System-Level Error Allocations

The *Lynx* design architecture leverages the considerable investment *Chandra* made in detailed error budget development and adapts it. Using lessons learned from *Chandra*, *Lynx* will track error budgets at a higher system level and allocate error to the contributing elements/components across the system. This will provide increased flexibility as the design matures to avoid unnecessary conservatism of any one contributor to the error budget. This, in turn, avoids unnecessary development impacts to cost and schedule while still meeting science requirements at the system level with margin. Reserve has been included to account for any unknown elements that may contribute to the performance.

The *Lynx* team focused on three areas regarding error budget allocations: (1) on-axis image quality, (2) spectroscopic resolving power, and (3) effective area. These TPMs are critical to meeting the *Lynx* science goals. Each error budget provides a first-cut at the error allocations for each element affecting that particular TPM. Reserve usage for each TPM error budget will be tracked and monitored throughout the project.

6.6.1.1 On-Axis Image Quality

The *Lynx* on-axis imaging budget borrows from the *Chandra* budget to identify the main sources of error to imaging performance. This includes the finite optical quality of the LMA, misalignments (static and dynamic) between the X-ray mirrors and the focal plane instruments, and the quality of the aspect solution. The current program links the three main branches of the error budget and includes reserve to realize the 0.5-arcsecond on-axis image quality. This is different from the arrangement used in the legacy program, where the corresponding main sources of image degradation were separately specified (as per MSFC-SPEC-1836).

The current error budget architecture (Figure 6.37) links the main branches of the error budget, allowing for reallocation among these branches to harvest overperformance in one area to ease the allocation on another. This is a key lesson learned from other missions and demonstrates *Lynx*'s conservative approach to design to cost.

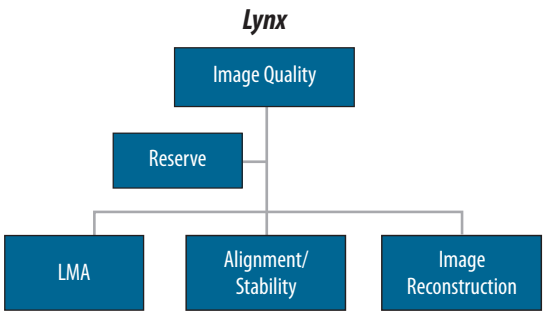

Figure 6.37. High-level error budget architecture for the LMA on-axis imaging. The main elements include the performance of the LMA, the alignment stability between the LMA and the focal plane instruments, and the ability to reconstruct an image. The latter is based on the ground aspect reconstruction of the arrival direction of each photon based on star camera and gyro rate data.

The 0.5-arcsecond HPD imaging required for *Lynx* is equivalent to an RMS diameter of 0.416 arcseconds. Figure 6.38 clearly indicates the dominant role LMA imaging quality plays in realizing the *Lynx* objective of 0.5-arcsecond image quality.

Image reconstruction errors (Figure 6.39) and alignment stability errors (Figure 6.40) are derived from detailed budgets from *Chandra* and populated with flight-proven values and analysis of the *Lynx* design. The use of flight-validated performance values in the aspect budget and the reapplication of the alignment tolerance analysis from *Chandra* gives high levels of confidence. Moreover, due to the root-sum-square addition involved in error budgets, small deviations both positive and negative have small influence at the top level. This means that there is little risk to performance from these values and small opportunity, such that the main focus of effort and resources should and will be on the LMA (Figure 6.41).

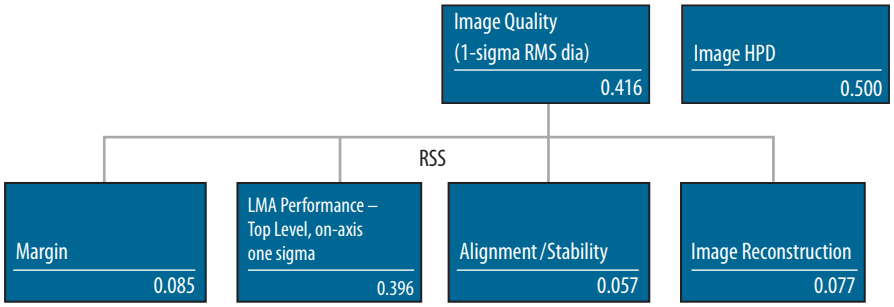

Figure 6.38. High-level error budget architecture for *Lynx* on-axis imaging at 1 keV. The main elements include the performance of the LMA, the alignment stability between the LMA and the focal plane instruments, and the ability to reconstruct an image. The latter is based on the ground aspect reconstruction of the arrival direction of each individual photon, based on star camera and gyro rate data. By linking these three error budgets, we can reallocate error and apply reserve across the three contributors to meet performance requirements with efficient use of cost and schedule resources.

The LMA budget follows lessons learned in the derivation of the *Chandra* imaging budget but also includes specific terms for the Silicon Meta-shell Optics implementation. The left-most branch of the budget contains the scattering terms, which are non-Gaussian and energy-dependent. The geometric branch shown on the right-hand-side is the result of finite tolerances in manufacture, alignment, and environment, which are Gaussian in nature and are energy-independent. The values for the various terms are the result of analysis and simulation using validated predictive tools. Energy-dependent terms are enclosed in the blue-outline boxes.

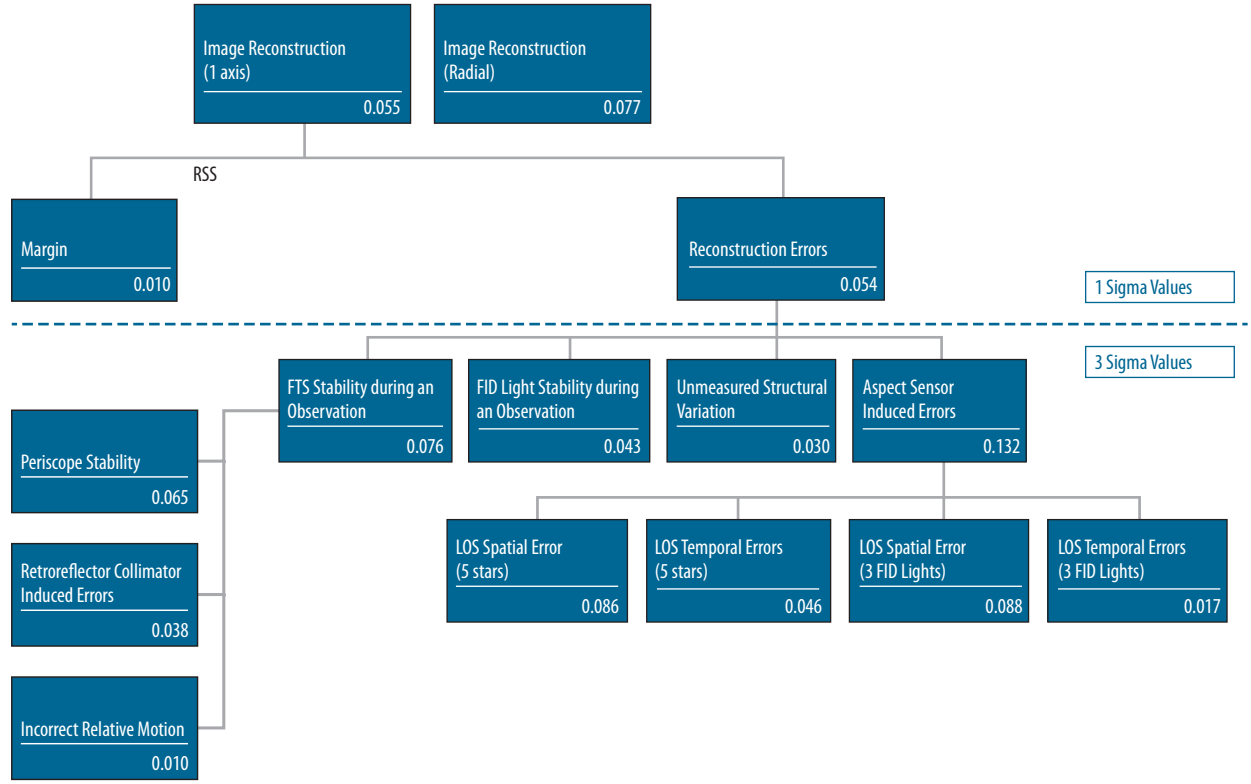

Figure 6.39. Aspect image reconstruction error budget.

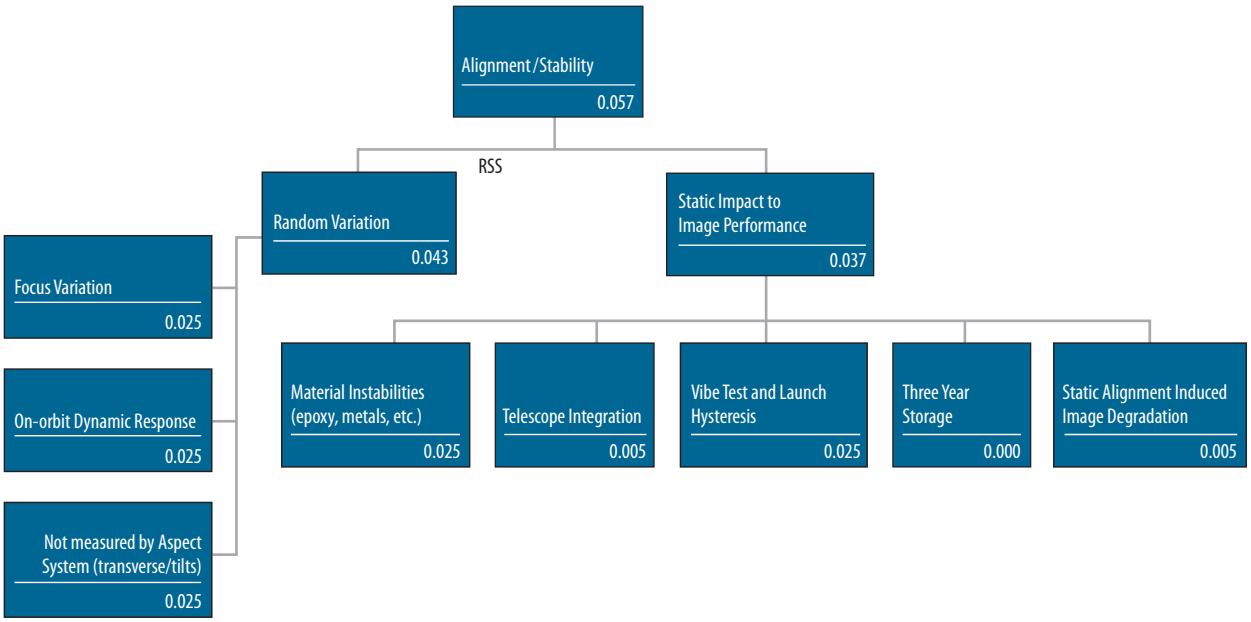

Figure 6.40. Alignment/stability budget for on-axis image quality. Telescope integration includes the degradation of imaging performance due to LMA integration in bench.

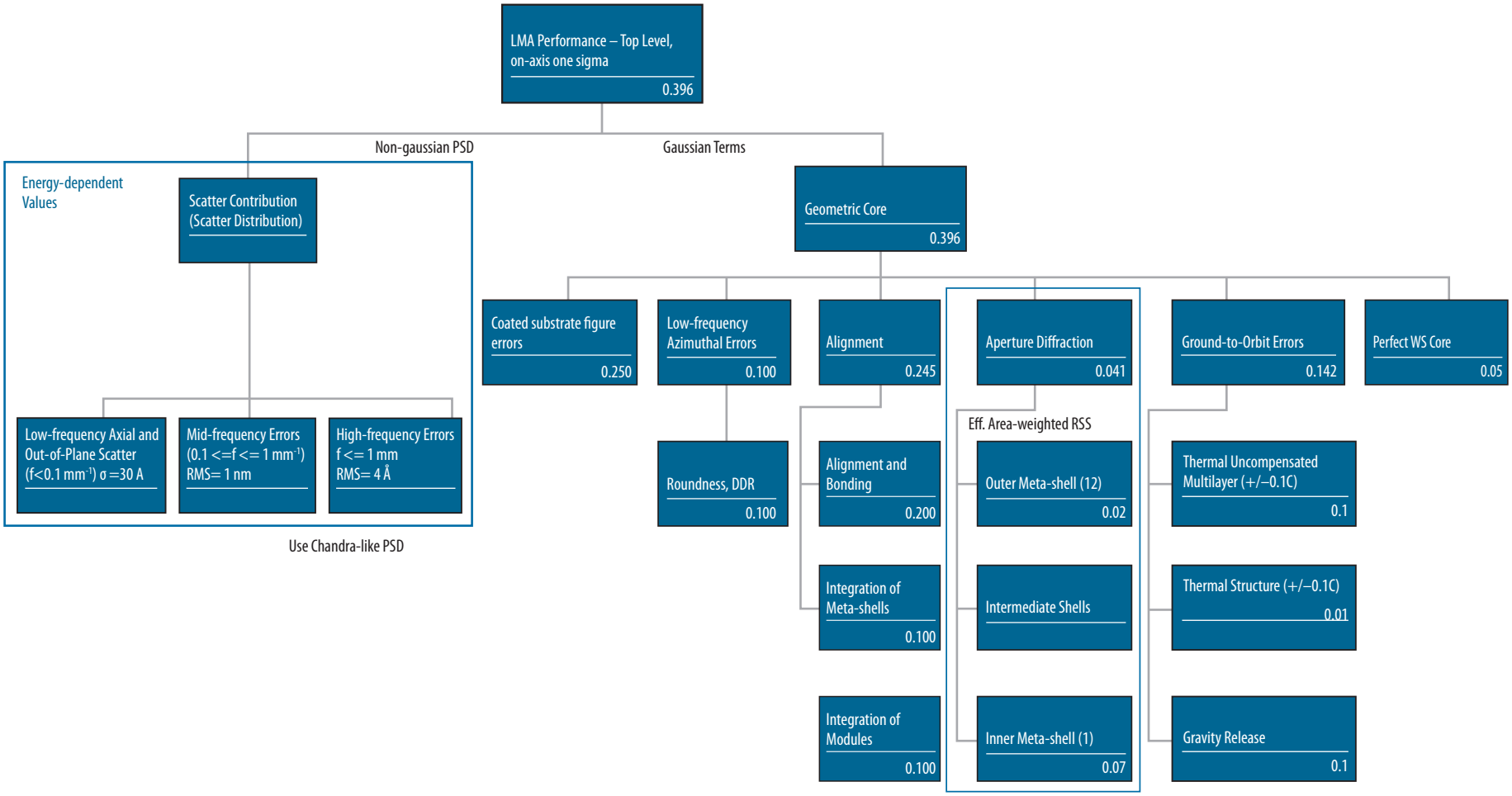

Figure 6.41. LMA top level imaging error budget.

6.6.1.2 Spectral Resolving Power

The *Lynx* XGS performance is characterized by the effective area (A_{eff}) and the spectral resolving power R. Both of these key TPMs are affected by the alignment of the XGA and XGD to the LMA. Integration of the XGA and XGD onto *Lynx* is straightforward, and SOA mechanisms provide more than sufficient tolerances to maintain critical alignments. Since the alignment tolerances required to meet the resolution requirement are tighter than those required to meet the effective area budget, only the resolving power error budget values are shown in Figure 6.42.

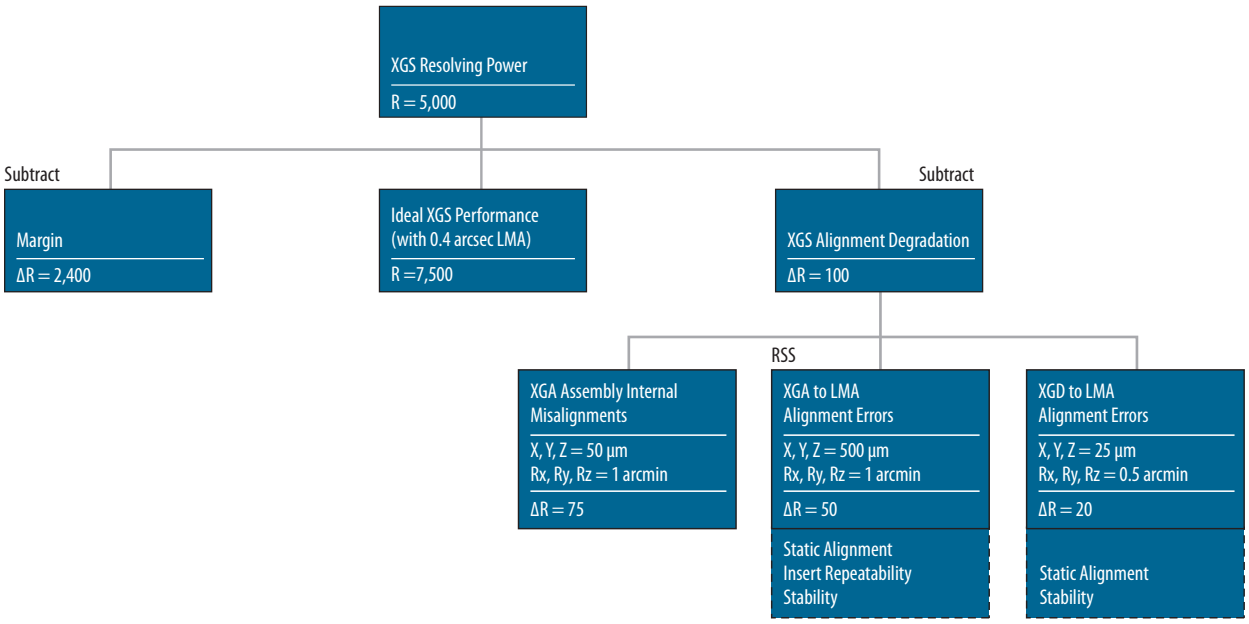

Figure 6.42. XGS resolving power R allocation error budget.

The branches of the spectroscopic error budget correspond to the finite tolerances in the assembly and integration of the XGA in the branch labeled "XGA Assembly Internal Misalignments." Alignment tolerances between the XGA and LMA are detailed in the branch labeled "XGA to LMA Alignment Errors." These tolerances include static alignment (installation), mechanism repeatability, and stability of the alignment during a measurement. The third branch of the tree focuses on detector alignment effects, including static alignment (installation) or resolution limits for the adjustable Degrees of Freedom (DOFs) and stability.

The error allocations are based on a combination of detailed ray-trace simulations and analytic approximations. The foundation for this analysis is ray-trace work done by the CAT-XGS team at MIT to establish the sensitivity of the CAT gratings to misalignments in the six rigid-body DOFs. The simulations initially assume a perfectly aligned CAT-XGS and include non-ideal effects such as the finite extent of the mirror PSF, astigmatism inherent in the design, and finite sizes of CAT gratings and CCD detectors (which cause deviation from the ideal Rowland torus geometry).

A ray-trace with 200,000 photons for three wavelengths in the XGA band were evaluated and A_{eff} and R were calculated. A_{eff} is the total effective area summed over all dispersed orders that fall on the XGD, and R is the average resolving power, where the resolving power from individual orders is

weighted by the number of photons in that particular order. Using this ray-trace simulation, sensitivities of the six rigid-body deviations from perfect alignment were computed. Figure 6.43 shows an example of the results from a set of simulations, with the top row showing the effects of translations and the bottom row showing the effects of rotations of the grating elements. The coordinate system used is aligned with the global system but centered on the individual grating element. Each figure shows the shift or rotation angle on the x-axis and then plots the spectral resolving power (R) with a solid line; the value for R can be seen on the left y-axis of the figure. Over-plotted is the effective area with dotted lines; the value can be seen on the right y-axis of the plot. Using this method, the sensitivities to facet misalignment within the XGA, the XGA alignment to the LMA, and the XGD to the LMA were determined.

For the XGA assembly internal alignments, small finite alignment tolerances of 50 μm for translations and 1 arcminute for rotations are posited as reasonable tolerances and show negligible impacts to the error budget. XGA to LMA alignment studies indicate that a shift along the x-axis (the optical axis) will not impact performance. Shifts along the other axes will have a negligible impact on A_{eff} but can result in reduced R for shifts larger than 1 or 2 mm.

Alignment requirements are set by R for all rotations. Rotation around the y-axis or z-axis will move some gratings "above" and others "below" the surface of the Rowland torus, dramatically widening the spot of the dispersed rays. Due to the long lever arm, gratings farthest away from the rotation axis have the largest effect. Tolerances for the alignment of the XGA door to LMA of 0.5 mm in translation and 1 arcminute in rotation are easily met and have minimal effect on A_{eff} or R.

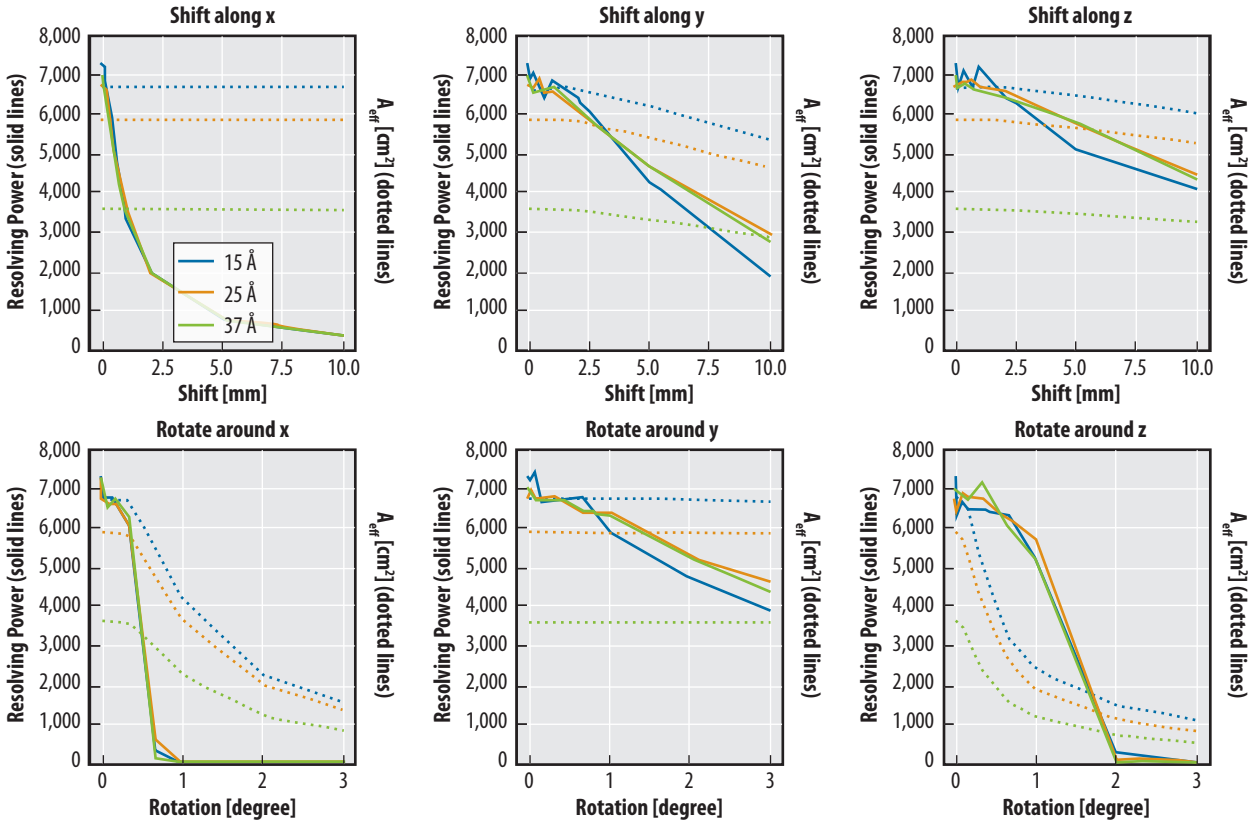

Figure 6.43. Sensitivity of R and A_{eff} to internal XGA tolerances.

The XGD-to-LMA alignment was also studied. A shift along x or a rotation around z will bring the XGD out of focus. Thus, these are the misalignments with the largest impacts. Fortunately, these are also the two DOFs that can be adjusted on-orbit with the planned XGD focusing mechanism. Since focus can be adjusted with a mechanism, the static allocation is just the mechanism resolution, which will be capable of positioning the detector within the depth of field of 25 μm.

6.6.1.3 Effective Area

The science requirement for at least 2-m² effective mirror area at 1 keV has been decomposed into a high-level error budget shown in Figure 6.44. The dominant terms are obscuration from the support structure and the thermal pre- and post-collimators, and the reflection efficiency of the mirror. To minimize the shadowing, the LMA is designed so that the structural elements of the spider align with elements of the pre- and post-collimators. The total obstructed geometric area is 13.5%, including 2% margin. The error budget will be maintained to manage margin and will become a TPM as the design matures. Contamination also contributes to effective area loss. To maintain the integrity of calibration, particulate contamination is separately controlled to cover no more than 0.005% of the mirror area, which was achieved for the *Chandra* mirrors. During ground handling, the mirror is covered and purged with a positive pressure of clean, dry nitrogen. On-orbit, the thermal control system keeps the mirror at a higher temperature than any surfaces in view to reduce the chance of volatile contaminants condensing on the reflecting surfaces. The grating assembly has been designed to minimize obscuration by aligning its structural elements to the mirror assembly. The mirror has been designed with excess geometric area to allow for the loss of tens of segments or even an entire module, while still preserving margin.

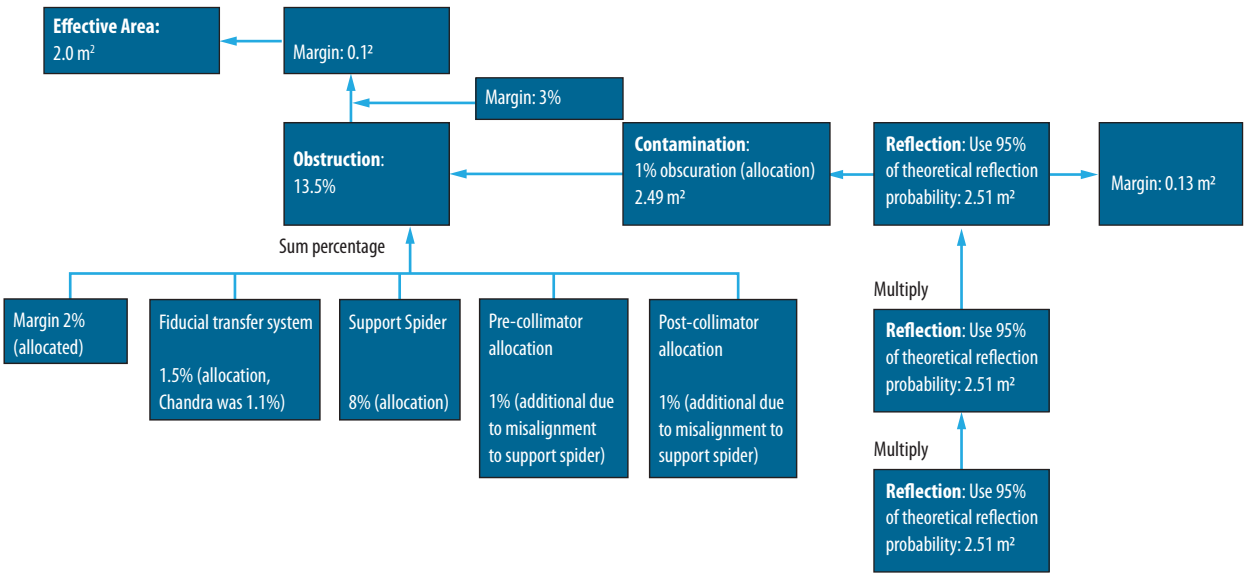

Figure 6.44. High-level block diagram of the error budget elements for the *Lynx* effective area.

6.6.2 Integrated Observatory Performance

The following analyses were completed during the concept study phase to address key performance parameters that directly enable the *Lynx* science mission. Results of these analyses have been incorporated into the *Lynx* conceptual design and are used to show that performance requirements are met with margin.

6.6.2.1 SE-L2 Natural Environment Analyses

The SE-L2 natural environment and the environment of the orbits around that point are relatively benign compared to those of geosynchronous and low-Earth orbits. For this and other reasons, this location will also be home to *JWST*, *WFIRST*, *Spectrum Roentgen Gamma (SRG)*, and *Athena*. *Lynx* will leverage knowledge from these missions regarding predicted (and eventually measured) environmental factors, and will incorporate this knowledge into the detailed design work during Phase A.

The ionizing radiation and meteoroid SE-L2 environments are the primary elements with the potential to influence *Lynx* performance and longevity. Preliminary consideration for each has been given, and mitigation for each is discussed in the relevant subsections that discuss the telescope and spacecraft detail (§6.3). Additional environmental factors have also been considered, such as the thermal properties, orbital attitude disturbance, and control. Additional considerations will be made during Phase A, such as the plasma environment and spacecraft charging.

Ionizing radiation in the form of solar particle events can cause single-event effects and degrade hardware. Galactic cosmic rays can upset avionics and contribute to the total hardware dose, and moderate energy protons (100–300 keV) can scatter down the optical path, creating background events and degrading detector performance. The total ionizing dose over a 20-year mission lifetime was estimated using the Space Environment Information System (SPENVIS). Preliminary analysis by the MSFC Natural Environments Branch of total ionizing dose concludes that there is minimal risk of single-event effects or hardware degradation over a 20-year mission lifetime (including transit and phasing orbits on the way to SE-L2) assuming a modest (2.5-mm-thick) aluminum shielding. For those particles that are scattered down the optical path, the *Lynx* design follows the *Athena* guideline [553] to place strong magnets around the optical path to divert, to the extent practical, focused low-energy protons and electrons away from the X-ray detectors.

In addition, the mass-limited fluxes and impact speed distributions of meteoroids — as defined by NASA's Meteoroid Environment Office, Meteoroid Engineering Model 3 — on various *Lynx* surfaces indicate minimal risk over the mission lifetime. These surfaces (e.g., radiators, solar panels, thermal blanketing, and similar structures) are sized to allow for predicted degradation. In particular, the modular design of the *Lynx* X-ray mirror elements allows for a small number of damaged mirror segments without measurable degradation to overall *Lynx* performance. Furthermore, it was determined by GSFC's Mission Design Lab that only a small number of meteoroid particles would potentially penetrate the laminated OBA structure and allow in scattered light over the extended 20-year mission.

6.6.2.2 Telescope Thermoelastic Analysis

A thermoelastic analysis of the *Lynx* telescope system was performed to estimate the order of magnitude of global deformations between the LMA and the focal plane due to predicted thermal gradients. Three of the available predicted gradients were used as input loads to the *Lynx* structural Finite Element Model (FEM), an image of which is shown in Figure 6.45. These gradients represented the steady state thermal gradient when oriented 45°, 90°, and 175° to the Sun. Displacements at the aft end of the OBA and at the center of the LMA spider were predicted for each gradient.

Assumptions for this analysis included:

1. Assuming that the structure is deformed at predicted thermal steady state conditions (as opposed to performing transient thermal analyses) is conservative.
2. The derived CTE based on *JWST*-heritage CTE data is achievable for the specific OBA composite layup design.
3. At the start of the *Lynx* service life, the system will be focused and aligned.

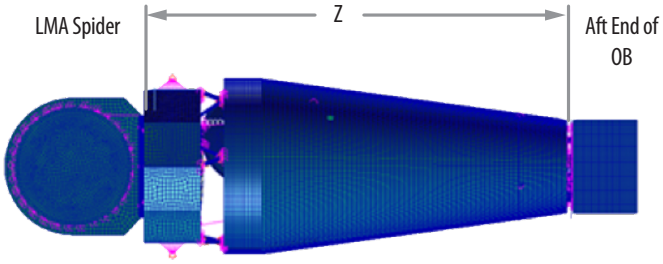

Figure 6.45. FEM used for telescope thermoelastic analysis. Results show an order of magnitude of margin of optical axis motion over error budget allocation.

Focus was expressed as the primary concern; therefore, thermal deformations were predicted in the z-axis (optical axis) direction. The difference between the predicted deformation at pairs of steady state thermal gradients (45° and 90°, 90° and 175°, and 45° and 175°) was considered a conservative estimate of changes in the structure's geometry.

Results indicated an estimated 2.5-μm optical axis relative motion between the center of the LMA spider and the center of the aft end of the OBA. The current error budget allocation for this motion is 25 μm, resulting in an estimated order of magnitude of error budget margin

6.6.2.3 Observatory On-Orbit Dynamic Analysis

A lesson learned from *Chandra* was that while jitter or relative motion between the mirrors and the focal plane was not an issue, resonances of the mirror shells due to Reaction Wheel Assembly (RWA) vibrations was. This issue was discovered during system testing and manifested as an impact to image quality. The solution at that time was to incorporate RWA passive isolators into the design. The *Lynx* design incorporates this lesson by including passive isolation for the RWA as well as for the LXM cryocooler to circumvent the risk of pertinent dynamics negatively affecting Observatory image quality. Detailed design and analysis of the passive isolation system will be conducted as the overall *Lynx* design matures.

A detailed dynamic analysis was performed to determine the relative motion perpendicular to the optical axis between the LMA and a point near the center of the focal plane. The *Lynx* structural FEM was used for this analysis. Existing reaction wheel specification data were used as inputs, and 1% damping was assumed. The predicted maximum relative motion was <0.004 μm, which is compared to the jitter error budget of 13 μm. Without the planned RWA passive isolation, three orders of magnitude of margin exist.

Vibrations associated with the LXM cryocooler will result in relative motion between detectors on the ISIM. The predicted motion between the HDXI and the XGD is planned future work. However, with isolation between the cooler and adjacent structure, there is no known reason to think pertinent motions will pose a significant engineering challenge. Detailed design and analysis of the cryocooler isolation systems will be conducted as the overall *Lynx* design matures.

6.6.2.4 Observing Efficiency Assessment

The *Lynx* conceptual design maximizes science observation time and minimizes time spent on non-science operations.

An analysis was performed using the conceptual Observatory design and conservative estimates to show a *Lynx* observing efficiency of 91.5%, including 3.3% of the time observing celestial calibration targets. Details of this analysis are provided in the *Lynx DRM Supplemental Design Package*. This observing efficiency provides a margin of an hour per day compared to the required minimum observing efficiency of 85%. The analysis used an example observing schedule from the *Chandra* project using 720 targets and a non-optimized observing schedule to be conservative. The time for each slew to target was based on the *Lynx* reaction wheel sizing and moments of inertia, and an additional 10 minutes of time was added to each slew maneuver to account for star acquisition and settling of any vibrations. Two 10-minute momentum dump intervals per week and one 10-minute station-keeping maneuver every three weeks were included. Instrument and spacecraft configuration will take place during slews, and communication to DSN will occur at any time including during science observations. Only nominal conditions were used in the study, with no safing actions or solar event shutdowns, as these were not intended for inclusion in the 85% requirement. The observing efficiency analysis and error budget allocation will be updated as the *Lynx* design matures.

6.6.3 Observatory Assembly, Integration, and Test

Many basic optics module and science instrument characteristics will be measured during subassembly, while only system-level ground X-ray calibration of the flight optics and instruments will be carried out at a dedicated calibration facility. Additional X-ray calibration at a continuum of energies using celestial sources and full-aperture illumination will be performed in-flight.

6.6.3.1 Ground Calibration

A key difference with *Chandra* calibration is the hierarchical design of the meta-shell optics planned for *Lynx*. This approach enables the PSF and effective area of individual optics modules to be mapped over a full range of energies and pitch and yaw angles with relatively modest Ground Support Equipment (GSE) and X-ray test facilities (preferably co-located with module production facilities). Visible light metrology is sufficient to verify module-to-module co-alignment within meta-shells and of meta-shells within the LMA. The LMA (protected from contamination) is then transported to a dedicated calibration facility for the final verification of the system at a small subset of X-ray energies and angles, thereby reducing schedule and cost.

After performing an assessment of available X-ray calibration facilities, the *Lynx* team decided to baseline the use of MSFC's X-ray and Cryogenic Facility (XRCF) for on-ground calibration activities of the LMA and scientific instruments. This facility was built in the 1990s for the *Chandra* project, is being considered for use by ESA's *Athena* project, and can accommodate the *Lynx* on-ground calibration campaign. Figure 6.46 shows a diagram of the instrument chamber.

Modifications to the facility are required and are under consideration for the *Athena* calibration campaign scheduled to take place in the FY28–FY29 timeframe. Anticipated XRCF modernization and upgrades include changes to the X-ray source system, X-ray detector system, X-ray data acquisition and control system, contamination control and monitoring system, thermal control system, and cleanroom facilities. The *Lynx* project will leverage these upgrades to reduce overall cost. Specific upgrades for *Lynx* will include but are not necessarily limited to mirror and instrument handling fixtures, a mirror reorientation fixture, focal plane instrument positioning fixtures, a high-speed detector, a metrology system, and other handling equipment. XRCF upgrades and usage are included in the project schedule and cost (§8).

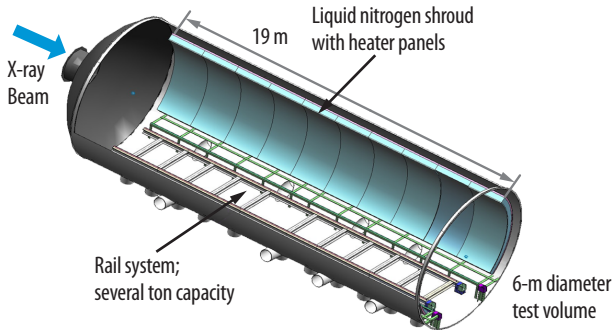

Figure 6.46. XRCF Instrument chamber accommodates *Lynx* on-ground calibration requirements.

Ground calibration of the LMA includes verification of effective area and PSF at highly oversampled spatial resolution. The diameter of the X-ray beam entering the XRCF test chamber is 1.46 m, allowing ~20% of the LMA aperture to be illuminated at one time. The plan is for the LMA to be aligned in the test chamber offset from the boresight of the beam and translated and/or rotated about its optical axis (under vacuum) to successively illuminate the entire LMA aperture as shown in Figure 6.47.

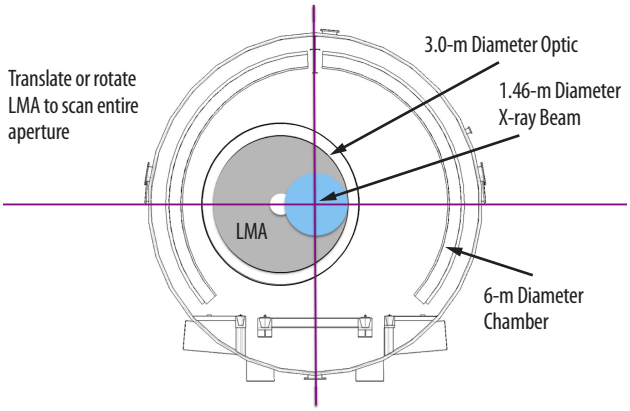

Figure 6.47. Schematic of the XRCF test chamber (outer circle), X-ray beam (blue) and X-ray mirror modules aperture (gray) viewed along the beam boresight. The X-ray mirrors can be translated and/or rotated about its optical axis to illuminate different ~20% portions of the full aperture.

Ground calibration of the XGA includes verification of the dispersion relation, effective area in all diffraction orders, and line response function. XGA calibration will require the LMA to ensure that it is properly aligned and that the grating deployment mechanism and the grating focal plane detector meet requirements.

Ground calibration of the HDXI (and XGD) and the LXM in tandem with the LMA is planned (see §8.4). The proposed LXM development schedule follows the approach used by the SXS instrument on *Hitomi* [585], is planned for the Resolve instrument on *XRISM*, and is similar to the approach planned for the *Athena* X-IFU. It is based on the development of an engineering model and a protoflight unit, with selected subsystem flight spares but no complete instrument spare. The engineering model will

undergo extensive qualification testing beyond the typical level of an EDU in order to space-qualify the design. The engineering model, not the flight unit, will be X-ray tested along with the LMA TRL demonstrator (§7.2.1) at the XRCF.

The X-ray calibration of *Lynx* will require a suite of GSE, including focal plane detectors and flight-like communications within a flight-like thermal environment. The calibration will be in two stages. The first is a six-month setup and rehearsal designed to test all GSE, communications, harnessing, and alignment procedures; validate performance simulations; verify data flow; and develop test schedules, handling procedures, and contamination control procedures. The calibration rehearsal will use engineering models of the optics and all science instruments. The six-month ground calibration of flight units (and LXM engineering model) will immediately follow the rehearsal as shown on the project schedule (§8.4). The rehearsal will be conducted within a 40-hour workweek, while the calibration of the flight equipment will utilize 24/7 operations.

6.6.3.2 *Lynx* Mirror Assembly Integration & Test

The LMA structure consists of the X-ray mirror module assembly, forward and aft contamination doors, barrel assembly, and structural mounts. The fiducial transfer system components are also integrated at this assembly step. The high-level LMA Integration and Test (I&T) flow is shown in Figure 6.48. LMA I&T begins with the availability of the validated mirror module assembly. The LMA test campaign includes pre-environmental functional testing, Electromagnetic Interference/Electromagnetic Compatibility (EMI/EMC) testing, Thermal Vacuum (TVAC) testing, first-motion testing of mechanisms, and post-environmental testing. All tests can be conducted using existing NASA and/or contractor facilities. Following testing, the LMA is shipped for integration into the XRT. LMA I&T is expected to take six months. An additional two months of risk mitigation has been assumed.

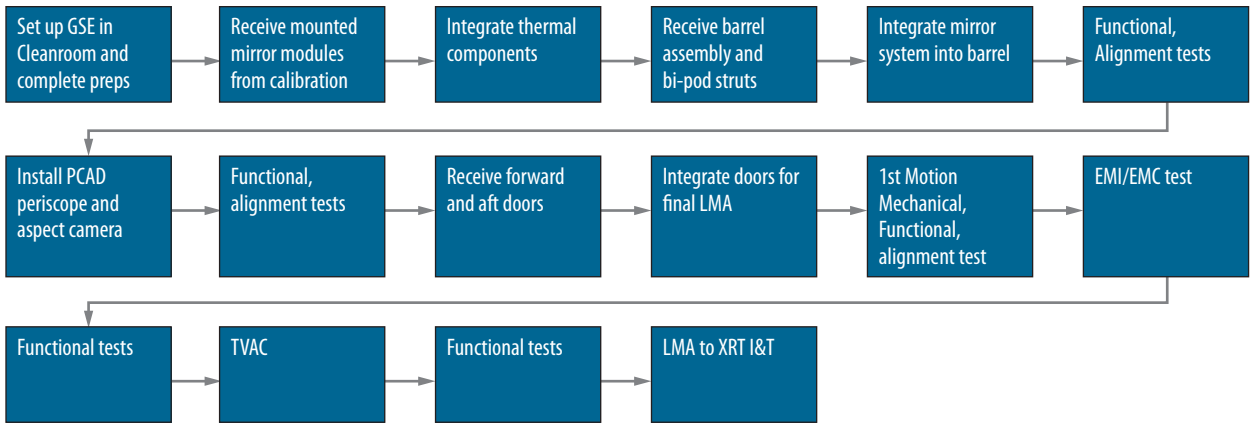

Figure 6.48. LMA I&T flow.

6.6.3.3 Integrated Science Instrument Module I&T

The ISIM assembly includes the LXM and HDXI mounted on the translation table, the XGD mounted on a stationary or "fixed" plate, electronics boxes, harnesses, and radiator panels. The high-level ISIM I&T flow is shown in Figure 6.49. ISIM I&T begins with the mounting of the translation mechanisms to the closeout plate and translation stage. The LXM is then integrated and aligned to the translation stage, followed by the HDXI. Then, the XGD is installed and aligned on the stationary closeout plate, followed by installation of the electronics boxes, harnesses, and thermal components. The test campaign includes pre-environmental functional testing, EMI/EMC testing, TVAC testing, first-motion testing of mechanisms, alignment, and post-environmental functional tests. All tests can be carried out at existing NASA and/or contractor facilities. Following testing, the ISIM is shipped for integration into the XRT. The ISIM I&T is on the *Lynx* critical path and is expected to take 14 months to complete. A critical path margin of two months has been added to this activity per critical path schedule margin guidelines.

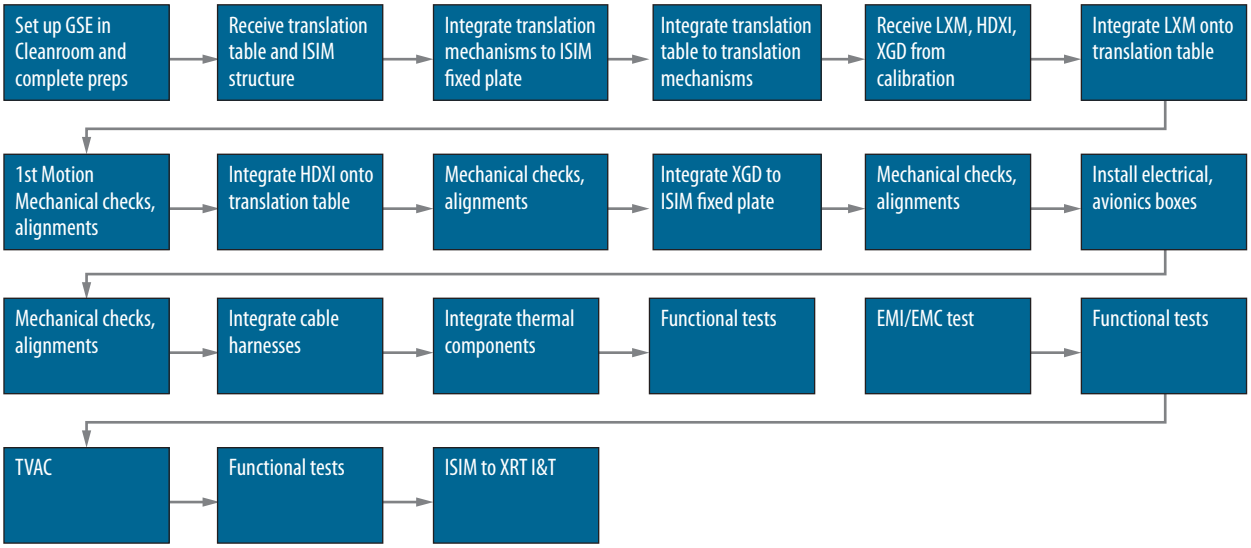

Figure 6.49. ISIM I&T flow.

6.6.3.4 X-ray Telescope I&T

The X-ray Telescope (XRT) assembly includes the XRT, XGA, OBA and electronics, harnesses, and thermal system components. The high-level XRT I&T flow is shown in Figure 6.50. XRT I&T begins with the integration and alignment of the XGA to the LMA. This assembly is then mounted to the OBA, and finally, the ISIM is integrated. The test campaign includes pre-environmental functional testing, single-motion mechanical testing, alignment tests, and PCAD system tests. All tests can be conducted at existing NASA and/or contractor facilities. Following testing, the XRT is shipped for integration into the SCE. The XRT I&T is on the *Lynx* project critical path and is expected to take 18 months to complete. A critical path margin of nine months has been added to this activity per critical path schedule margin guidelines.

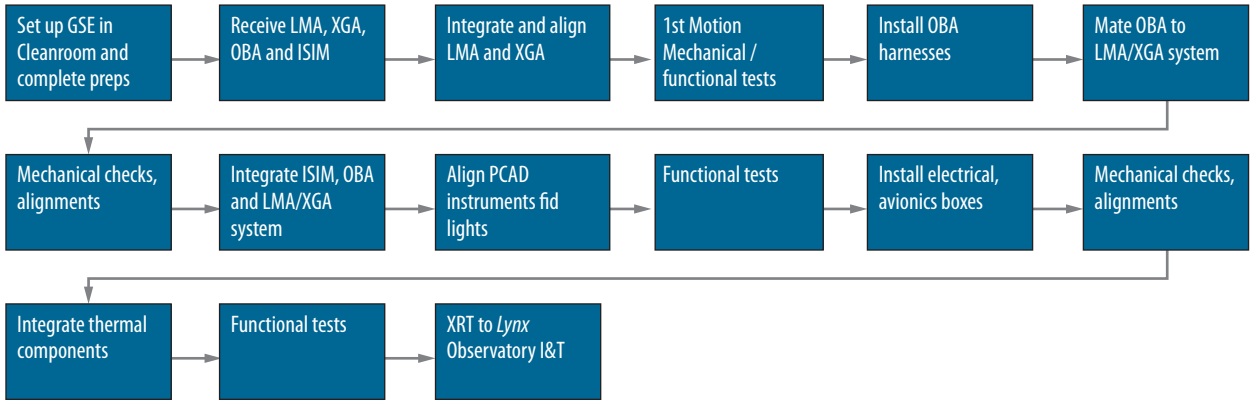

Figure 6.50. XRT I&T flow.

6.6.3.5 Spacecraft Element I&T

The SCE consists of the spacecraft and all of the subsystems, such as power, thermal, C&DH, GN&C, and propulsion. The high-level SCE I&T flow is shown in Figure 6.51. SCE I&T begins with integration of the propulsion system, followed by the GN&C, power system components, thermal components, C&DH system components, harnesses, and MLI. Spacecraft testing includes functional and performance testing, verification of all electrical interfaces, comprehensive performance test (pre- and post-), alignment checks, acoustics, shock and vibe, EMI/EMC, three-point thermal balance, end-to-end data flow, deployment testing of the solar arrays, sunshade and contamination doors, and mechanisms. All of these tests can be conducted at existing NASA and/or contractor facilities. Following testing, the SCE is shipped for integration with the XRT into *Lynx*. SCE I&T is expected to take eight months to complete. No additional margin is included for this activity. The *Lynx* spacecraft is a similar design to *Chandra*, which took seven months for I&T.

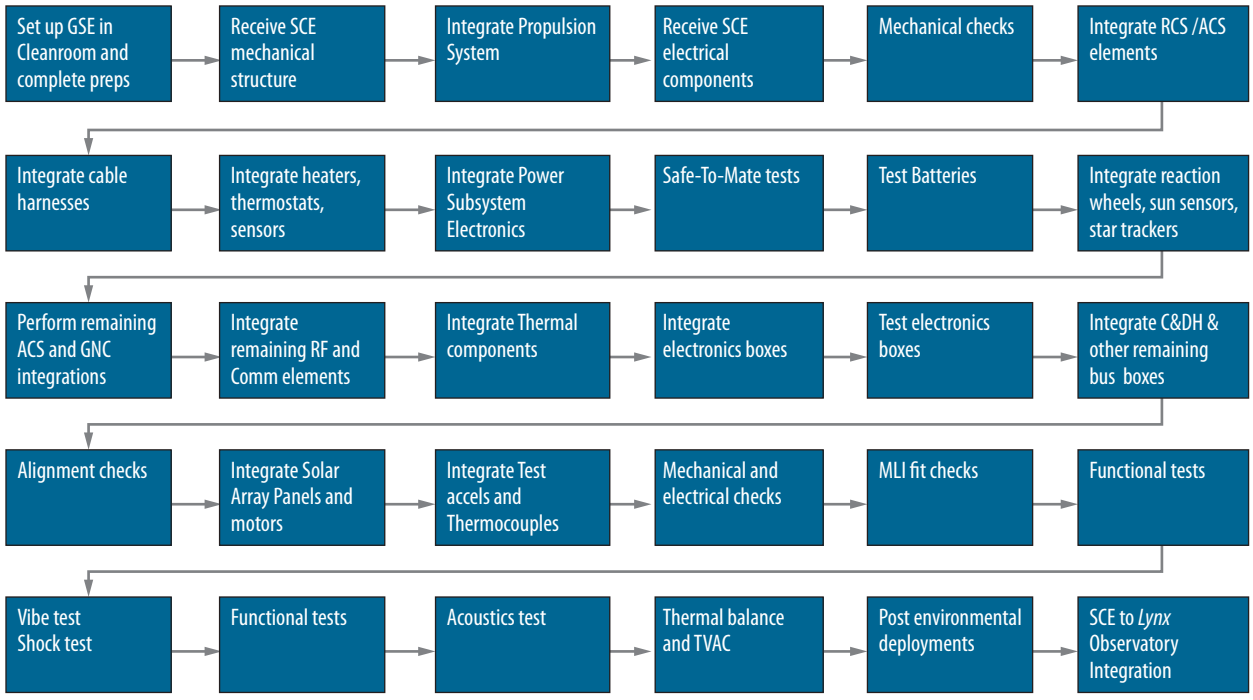

Figure 6.51. SCE I&T flow.

6.6.3.6 Observatory I&T

The *Lynx* Observatory I&T integrates the fully qualified XRT and SCE. The high-level *Lynx* I&T flow is shown in Figure 6.52. *Lynx* Observatory I&T includes ambient functional testing, alignments, leak checks, deployments, full Observatory functionality, and electrical/mechanical compatibility. The test campaign includes pre-and post-functional testing, cryogenic vacuum and thermal balance tests, EMI/EMC tests, and acceptance-level acoustic and vibration testing. Furthermore, data flow to the *Lynx* Science and Operations Center will take place during this phase of I&T. All of these tests can be conducted at existing NASA and/or contractor facilities. Following testing, *Lynx* is shipped to the launch site for the launch vehicle integration and is readied for flight. The *Lynx* Observatory I&T is on the project critical path and is expected to take six months to complete. Critical path margin of one month has been added to this activity per critical path schedule margin guidelines.

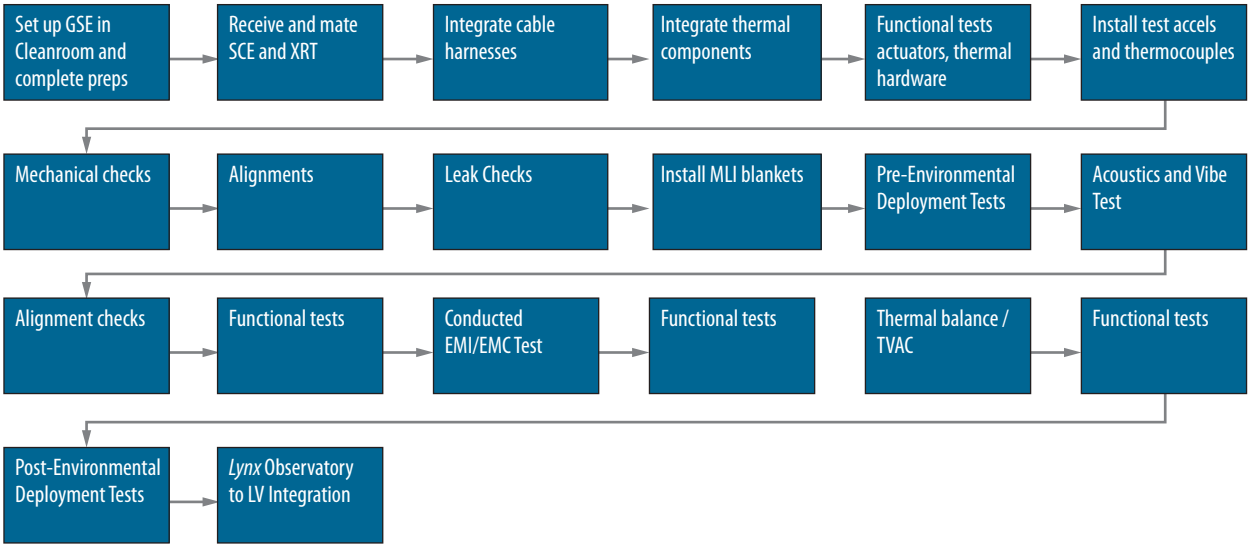

Figure 6.52. *Lynx* Observatory I&T flow.

Key operations during *Lynx* AI&T are performed to verify and validate system performance requirements. Given the commonalities between the *Lynx* and *Chandra* architectures, the AI&T flow for *Lynx* closely resembles the heritage assembly and test philosophy of *Chandra*. The overall AI&T flow is shown in Figure 6.53.

The AI&T activities and flow were developed by the *Lynx* systems engineering team consisting of MSFC and SAO systems engineers along with industry CAN partners with direct experience on the *Chandra* Observatory. This flow outlines the system-level integration sequence for *Lynx*, high-level tests at the end of each assembly sequence, and the assumed durations for each. This information was used as direct input into the late-Phase C/Phase D portions of the *Lynx* project schedule described in §8.4.

The *Lynx* Observatory architecture includes two primary elements: (1) the XRT and (2) the SCE. These elements are further broken down into subelements and assemblies as defined in Table 6.21.

A feasible assumption (based on *Chandra*) for subsystem Design, Development, Test, and Evaluation (DDT&E) is that the mirror modules, XGA, LXM, HDXI, and XGD are all government-furnished and that the prime contractor has DDT&E responsibility for the OBA and ISIM, as well as the entirety of the SCE. Further, it can be assumed that the prime contractor is responsible for integration of the mirror modules into the LMA, integration of the LXM, HDXI, and XGD into the ISIM; and for integrating the LMA, XGA, OBA, and ISIM into the XRT. It is assumed that all subassemblies are delivered to the next level of integration fully qualified to the extent practical. The XRT and SCE will be delivered to *Lynx* Observatory I&T as fully qualified units.

Table 6.21. *Lynx* Observatory primary elements, subelements, and subassemblies.

Primary Elements	Primary Subelements	Primary Subassemblies
XRT	LMA	X-ray Mirror Modules
		LMA Structures
		PCAD system
	XGA	GAS
	OBA	Magnetic Broom
	ISIM	LXM
		HDXI
		XGD
		ISIM Structures
SCE	Structural System	Secondary structures and mechanisms
	Thermal Control System	MLI, heaters
	Electrical Power System	Solar arrays, batteries
	C&DH System	Flight computer, controllers
	Communication System	Antenna, transponders
	GN&C System	Rxn Wheels, PCAD, Star Trackers, IRUs
	Propulsion System	MPS, RCS/ACS engines, tanks

Protoflight-level environmental testing will be performed at the subelement level, and acceptance-level vibration and acoustics testing will be performed at the Observatory level. Interface simulation hardware will be used during tests at lower levels of assembly to provide data for final analysis and verification. Testbeds, mock-ups, and engineering models and test units at the subelement level will be used as pathfinders to provide data and analysis to be used for final verification at the Observatory level. Specifically, engineering models of the X-ray Mirror Modules and scientific instruments will be used for calibration checkout, early testing, schedule risk mitigation for manufacturing, and assembly of these complex components.

Electrical Ground Support Equipment (EGSE) and Mechanical Ground Support Equipment (MGSE) will be developed and qualified to safely handle and align the flight hardware during AI&T, and special transportation equipment will be developed as needed to move flight hardware during assembly and test activities. A standard C-5 cargo plane can be utilized for transporting the large assemblies. Existing test facilities are anticipated to be used during the AI&T campaign for *Lynx*. Specifically, cryogenic vacuum testing can be performed at NASA Johnson Space Center Chamber A or GSFC Chamber 290. *Lynx* will require an ISO-7-class cleanroom facility such as the GSFC's Space Systems Development and Integration Facility (SSDIF) to mitigate contamination, specifically on the X-ray optics. Furthermore, the test and cleanroom facilities used for *Chandra* are still available and operational; however, this in no way presumes contractor preference or selection. Original *Chandra* partners as well as other aerospace contractors have developed new or improved facilities since that time that would be acceptable for this mission.

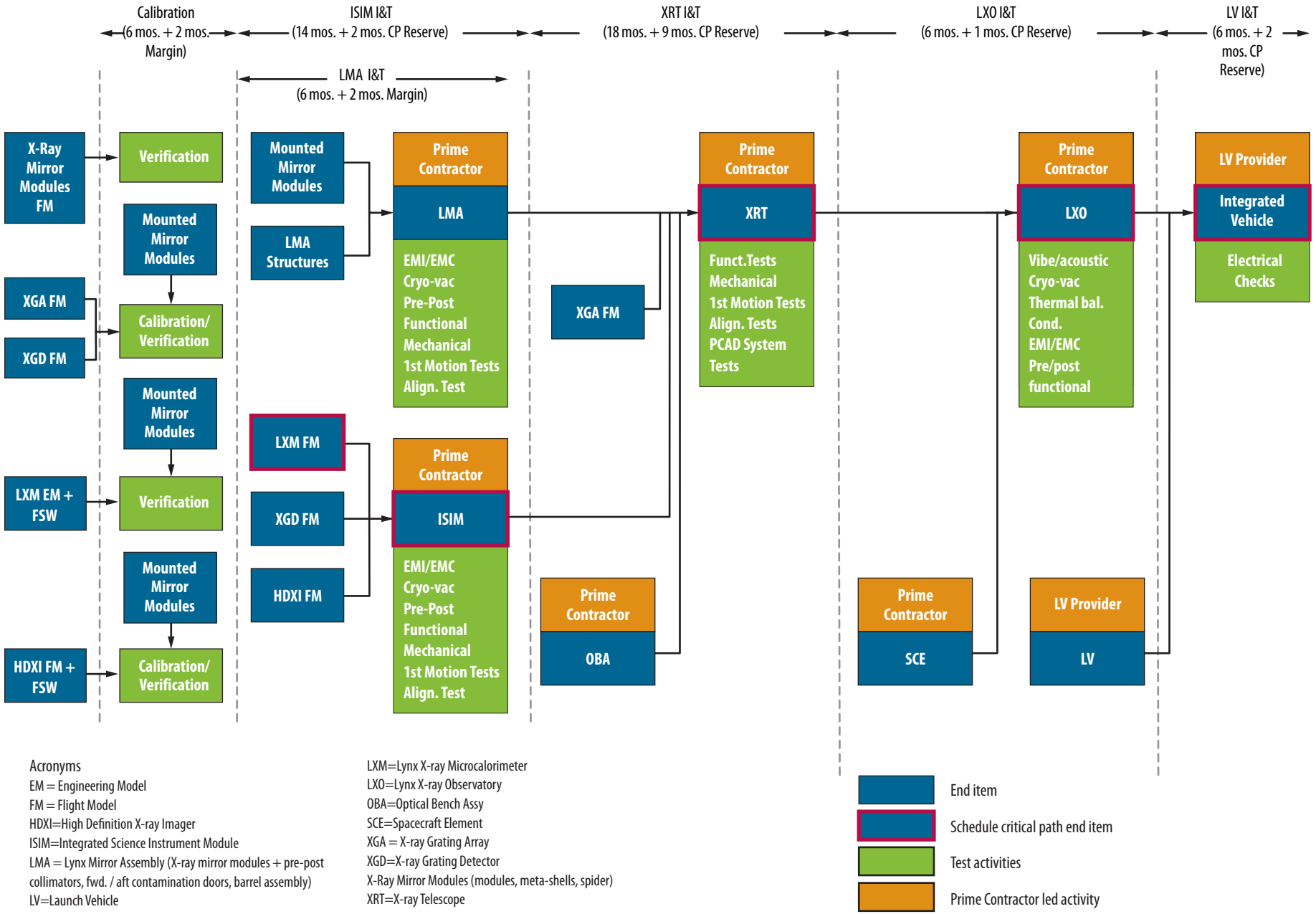

Figure 6.53. *Lynx* AI&T flow

6.7 Concept of Operations

The *Lynx* Observatory will serve the worldwide astronomical community as an efficient, long-lived scientific observing platform.

The concept of operations describes the fundamental on-orbit and ground support operations necessary to conduct the *Lynx* science program. In the *Lynx* paradigm (Figure 6.54), end users (referred to as general observers) conceive scientific experiments that define celestial targets, instrument configurations and observing modes, and durations of observations. The *Lynx* mission operations infrastructure then turns these definitions into scheduled programs of actions through mission planning and scheduling, commands the Observatory to execute the programs through operations activities, and ensures the resulting data are recovered, processed and validated, and then distributed to the general observers and the broader community in a timely manner. The *Lynx* Science and Operations Center sends commands to the Observatory and receives data from the Observatory through the DSN. The commands include all of the general observers' target and configuration requests, as vetted by mission support, and the spacecraft responds by positioning the proper instruments in the correct arrangements and photon-counting modes, and by slewing to and holding on targets. The process is made efficient by placing *Lynx* in an optimized observing environment capable of a long mission lifetime using flight-proven mission operations befitting a community-driven flagship mission, and maintaining data integrity and fidelity throughout.

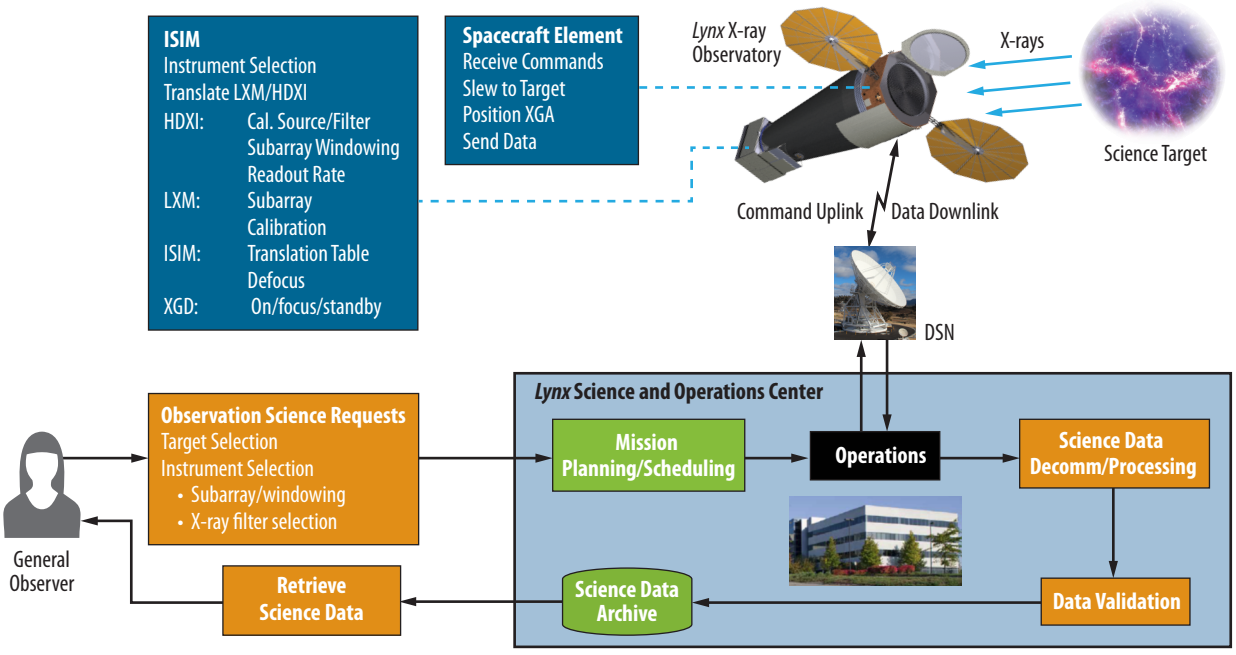

Figure 6.54. Concept of operations showing the cycle from user requests for observations to user receipt of science data. Following review, observation requests are processed by the *Lynx* Science and Operations Center into commands uplinked to the Observatory. Physical data from the Observatory flow through the DSN to the *Lynx* Science and Operations Center (which includes both mission and science operations), and ultimately to the observers, the general scientific community, and the public.

The *Lynx* Observatory is accommodated, with margin, in a standard heavy-lift vehicle for the 2030s. The SE-L2 orbit planned for *Lynx* easily meets the high observing efficiency requirement with a launch-to-orbit timeline sufficient to carry out all necessary performance verification and commissioning tasks. The subsequent science operations phase (§6.7.2) can fulfill the entire range of *Lynx* science objectives with enough flexibility to accommodate rapid response for unanticipated Targets of Opportunity (ToOs). There is sufficient propulsion for orbital maintenance, power, data, and communications capability during the science operations phase. See §6.4 for mission implementation details.

To best support the user community, *Lynx* ground operations (§6.7.4) are modeled after *Chandra*-proven practices and infrastructure. All *Lynx* science instruments are photon-counting detectors that accumulate event-based time, position, and energy data. These data (along with engineering data) are accumulated and temporarily stored on board before being periodically telemetered to the ground, where the data are then archived, processed, and distributed to the scientific community.

Finally, the *Lynx* concept of operations includes plans for the decommissioning and disposal of the Observatory and the preservation of science and engineering data and data products (§6.6.3).

6.7.1 Launch to Orbit — Cruise, Commissioning, and Check-Out

Lynx will launch in the mid-2030s under the current assumption that it will be integrated onto a heavy-class (expendable or recoverable) vehicle that will launch from NASA Kennedy Space Center (KSC). Following a Transfer Trajectory Insertion (TTI) maneuver, *Lynx* will be inserted into the 800,000-km, semi-major axis halo orbit around the SE-L2 libration point. As summarized in Appendix B.1.2, several orbits were analyzed for *Lynx*, including SE-L2, drift-away, Lunar Distant Retrograde Orbit, *Chandra*-type orbit, and Transiting Exoplanet Survey Satellite- (TESS-) like orbit. After careful consideration, the SE-L2 orbit was selected because it provides: (1) no eclipsing, (2) a stable thermal environment, (3) avoidance of trapped radiation belts, (4) high observing efficiency, and (5) moderate fuel and propulsion requirements relative to some of the other orbits considered. The observing efficiency is the percentage of real time *Lynx* will spend on science observations and takes into account the estimated times for slewing, thermal, and vibrational stabilization.

The estimated time to reach SE-L2 is 104 days. During this time, the spacecraft and telescope systems are powered on, allowed to outgas, and undergo system checks and initial calibration. Early orbit operations schedules are being developed for each of the telescope systems, with an integrated element that provides contamination mitigation during the outgassing and checkout phases.

6.7.2 On-Orbit Operations

The on-orbit operational modes are preplanned using a scheduling process that seeks to maximize the time on-target while accommodating all necessary spacecraft operations. The sequence of slews and dwell times are planned to achieve an observing efficiency of at least 85% [579], while staying within budgets for consumables, momentum unloading, and data storage. The mission schedule plan will be used to generate spacecraft and instrument commands, which are then uplinked to the spacecraft and stored. A sufficient number of commands will be loaded to ensure autonomous operations for 72 hours.

On-orbit operational modes can be classified as "Normal Pointing Mode" or "Maneuver Mode" with an additional "Safe Mode." ToOs are carried out using the Normal Pointing and Maneuver modes.

Normal Pointing Mode — Following on-orbit activation and checkout, *Lynx* will be primarily in Normal Pointing (also called "Science") Mode conducting an autonomous pre-planned program of celestial observations. In this mode, the telescope's optical axis is pointed within 10 arcseconds of a commanded celestial position, which is assured by locking on pre-planned stars at specific positions in the aspect star camera. The positions of the stars are constantly monitored and recorded for later downlink, along with the positions of fiducial lights in the focal plane projected onto the star camera image and inertial reference sensor data. All these data are needed to reconstruct the X-ray image on the ground with precise celestial coordinates. The X-ray camera uses its internal computer software to detect and recognize single photons as they arrive and tags them with arrival time, position, and energy (or, equivalently, wavelength).

When the XGA is inserted, the XGS-dispersed spectrum is directed onto the XGD, while the non-dispersed portion can be focused onto either focal plane instrument. Therefore, there are four observing configurations available for science observations:

1. XGS gratings inserted and LXM at the primary focus (XGS+LXM)
2. XGS gratings inserted and HDXI at the primary focus (XGS+HDXI)
3. HDXI as the primary with gratings retracted (HDXI only)
4. LXM as the primary focal plane instrument with gratings retracted (LXM only)

A typical scientific observing scenario may involve the spacecraft dithering the optical axis in a pattern on the focal plane in order to average the response over many pixels. Typical data collection times for *Lynx* are expected to range from ~1 ks up to a few hundred ks per pointing, limited only by angular momentum buildup. There is no practical limit for the total time on a single target via multiple pointings. Slews to new targets require only 1–3 ks.

The Nominal Pointing Mode is transparent to the selection or internal settings of the focal plane instruments. The *Lynx* data subsystem interfaces with each camera to collect CCSDS-standard encoded packets of data as they are assembled by the camera software. Data collection and time registration are synchronized by signals from the precision spacecraft clock. The data packets contain X-ray events, background events that mimic X-rays, and auxiliary configuration, timing, temperature, voltage, and current "housekeeping" data from the instrument. During the observation, the reaction wheel speeds are adjusted based on data from the star camera and gyros to absorb angular momentum generated by disturbance torques and thus keep the pointing direction within limits. At the commanded end time of the observation, the spacecraft computer sends signals to allow the X-ray camera(s) to transition to standby and prepares to enter the Maneuver Mode.

On-orbit calibration observations are performed as part of the Normal Pointing Mode science operations. See §6.7.3 for more details.

Maneuver Mode — In Maneuver Mode, a new target quaternion is loaded from the stored command sequence, and an eigen-axis rotation is computed for slewing the optical axis to the new position. The reaction wheel speeds are changed to generate appropriate torques on the Observatory, keeping the total angular momentum unchanged. The expected slew path is continuously compared to the gyro

rate data to ensure the maneuver is progressing properly. At the end of the maneuver, the star camera is commanded to acquire pre-determined acquisition stars. Deviations of these stars from their expected positions allows a fine update to the pointing direction, whereupon the star camera locks on guide stars used to hold during the observation, and the Observatory transitions to Normal Pointing Mode. The guide stars may include some or all of the acquisition stars. During Maneuver Mode, the ISIM and XGA mechanisms are used to place either the HDXI or the LXM at the mirror aim point, to insert or retract the XGA, and to adjust detector positions along the optical axis to nominal focus locations. Commands are sent to the focal plane instruments to configure for the upcoming observation. Reaction wheel momentum may be unloaded by firing the reaction control propulsion engines during Maneuver Mode.

Safe Mode — Safing actions are initiated autonomously by onboard detection of one or more preset sensor limit violations. Depending on the alarm, the Observatory may continue control by the spacecraft computer and either hold on stars at the current attitude ("Bright Star Hold Mode") or use coarse and fine Sun sensors to reorient normal to the Sun line ("Normal Sun Mode") while awaiting ground instructions to affect a recovery. Such alarms do not indicate any spacecraft system failures, and the onboard computer maintains control. In the presence of more significant alarms that might indicate possible hardware failures, the computer may switch to redundant subsystems and electronics, or may switch off the computers and transfer to the SMEU firmware to hold the vehicle in a safe, power-positive orientation (Safe Mode). The spacecraft is designed to be able to survive in Safe Mode indefinitely. Upon receiving telemetry, any anomalies will be recognized automatically by ground software and alarms relayed to mission operations personnel. The anomaly response will ensure that the spacecraft and instruments are safe, and will then develop and implement an appropriate recovery plan to return to Normal Mode observations. A hierarchy of safing actions will be defined.

The phased array antenna allows ground contacts and solid-state recorder data playback to take place in any mode, including Safe Modes.

Rapid Response Capabilities — Stored command loads can be interrupted and updated as needed to accommodate ToOs. In assessing the strategies for *Lynx* response to the ToOs, it is important to note that *Lynx* will fly in an astrophysical landscape shaped by transformative capabilities in the time domain. Detection rate of transient events will increase by orders of magnitude compared to the present. As a long-lived Great Observatory platform, ToO follow-up with *Lynx* will enable extraordinary advances in the astrophysical transient discovery space.

Optimistically, *Lynx* could respond to a ToO trigger within three hours of approval. This is possible for ~10% of triggers, and requires a 24-hour availability of the relevant mission planning and operations teams. Longer response times are possible with an increased probability and require less strain on mission operations. An 8-hour response can be achieved for ~100% of targets, still assuming that the relevant teams are available 24/7. A ToO turnaround response time of faster than 24 hours can be routinely guaranteed without additional strain on the mission operations.

The interruption and re-planning of command loads for a Risk Class A observatory like *Chandra* (and indeed *Lynx*) dominates the ToO response time. A review of procedures developed during two decades of *Chandra* operations suggests the following most optimistic scenario, in which it is possible for *Lynx* to respond within three hours for high-priority transient events (also shown graphically in Figure 6.55). This scenario still maintains the conservative risk posture appropriate for the Risk Class A Observatory:

1. **Community alerts triggered, and relevant *Lynx* team members are notified** — Following submission of the request, an alert mechanism is triggered to notify all relevant persons on the *Lynx* team of the urgent science event. Upon review, the request is approved. Procedures for quick approval of the ToO requests are developed with input from, for example, the *Lynx* User's Committee or its equivalent. The ToO response timeline starts from this point.

2. **Reschedule and review of the new observing schedule** — New schedule and satellite commands are generated on a timescale of minutes. Once the commands are generated, they are distributed to subsystem groups for review. Conducted in parallel, each review typically takes 1.5 hours to complete.

3. **Archiving of the approved schedule, transmitting to the DSN ground station, and DSN uplink** — This step takes 30 minutes. If it is completed during the normally scheduled DSN uplink, the new command load can be immediately sent to the spacecraft. This condition is satisfied for ToO observations approved within a time window from $t_{DSN,start}$–2 hours to $t_{DSN,end}$–2 hours. Assuming three DSN contacts per day and a 1-hour duration of the contact, the delay related to DSN contacts can be avoided for approximately one-eighth of the triggers.

4. **Satellite slewing and science observation** — Upon receiving a new command load, it takes 45 minutes for *Lynx* to perform a 90° slew, acquire guide stars, and start a new observation. For a smaller fraction of targets, the slew is shorter and the new observation can start sooner.

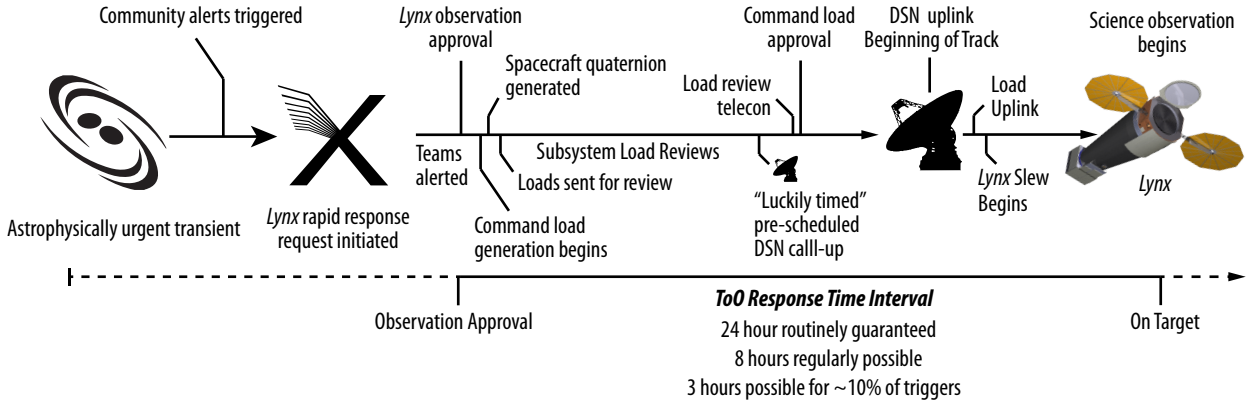

Figure 6.55. A summary of the technical and programmatic steps needed to plan, review, and uplink *Lynx* command loads following a ToO request. In some cases, the response time could be as short as three hours, though 24 is more typical.

6.7.3 On-Orbit Calibration

A set of standard celestial targets will be determined for on-orbit calibration use. These targets will be periodically observed to monitor the LMA, all science instruments, and aspect system performance. Calibration observations are planned, scheduled, and executed as part of Normal Pointing Mode operations (accompanied by Maneuver Mode slews) (see §6.7.2). Calibration measurements during the course of the mission science phase primarily monitor changes in performance characteristics such as detector background, energy resolution, energy gain, and filter throughput; grating line response function; system on- and off-axis PSF and optical alignment; and cross-calibration amongst the three *Lynx* science instruments. Some performance characteristics can be monitored parasitically using science observations without the need for separate calibration measurements. The same amount of calibration time as for *Chandra*, about 1 Ms per year, decreasing later in the mission to about 700 ks per year, has been budgeted for *Lynx*.

In addition, the HDXI and LXM contain in situ calibration sources that are mounted on their filter assemblies. Specifically, the LXM design includes a modulated X-ray source of pulsed X-rays at multiple energies similar to that used on *Athena*'s X-IFU [569] and *Hitomi's* SXS [576]. The HDXI includes a radioactive 55Fe source in its selectable filter mechanism. These onboard calibration sources allow calibration data acquisition during Normal Pointing Mode (see §6.7.2) when the given instrument is not being used as the primary instrument for an observation.

6.7.4 Ground Operations

All science and observatory data will be received, and all commands to *Lynx* will be generated by a co-located team of flight, science, and ground operations personnel. This team will be responsible for the spacecraft health and safety, carrying out all observational programs, monitoring and performing necessary maintenance, and retrieving and transmitting all data for processing, archiving, and distribution.

Several ground operations teams are necessary to plan *Lynx* operations and to process science data collection and distribution:

- The **Flight Operations Team** schedules, plans, generates spacecraft command sequences, uplinks, verifies spacecraft commands, and monitors real time data during communications with *Lynx*. The team performs engineering analysis of subsystems and diagnoses anomalies.
- The **Science Operations Team** is responsible for planning the mission schedule sequence by optimally scheduling targets provided by the *Lynx* user community. That team specifies the science instrument configuration for each observation and conducts on-orbit scientific instrument monitoring and calibration.
- The **Science Planning Team** coordinates with observers and with the staffs of other observatories to carry out coordinated multi-wavelength campaigns and to perform simultaneous observations.
- The **Science Data Team** performs standard data processing (with scientific validation and verification), archiving of data products, and distribution to the *Lynx* community, maintenance and distribution of calibration products and analysis tools, and archival search and retrieval services.

- The **Ground Operations Team** is responsible for supporting and maintaining all ground support hardware and software facilities used for scheduling, commanding, data flow, archiving, and communications. This includes facility infrastructure upkeep, network integrity, and facility security. Redundant critical systems will be provided for at a physically separate site.

A schematic of the *Lynx* data flow is shown in Figure 6.56. Communication to the *Lynx* Observatory from the *Lynx* Science and Operations Center will be through the DSN. One hour of telemetering during one to three daily contacts are envisioned during normal operations. Following data receipt and quality check, housekeeping data will be forwarded to the flight operations team for monitoring and safety checks while all data will be transmitted to the science data team for processing.

By analogy to *Chandra*, and accounting for differences, it is estimated that the ground software system will include 1.2 million logical lines of code. Standard data processing proceeds via automated pipelines, controlled by a parameter file derived from the archive defining observer requirements.

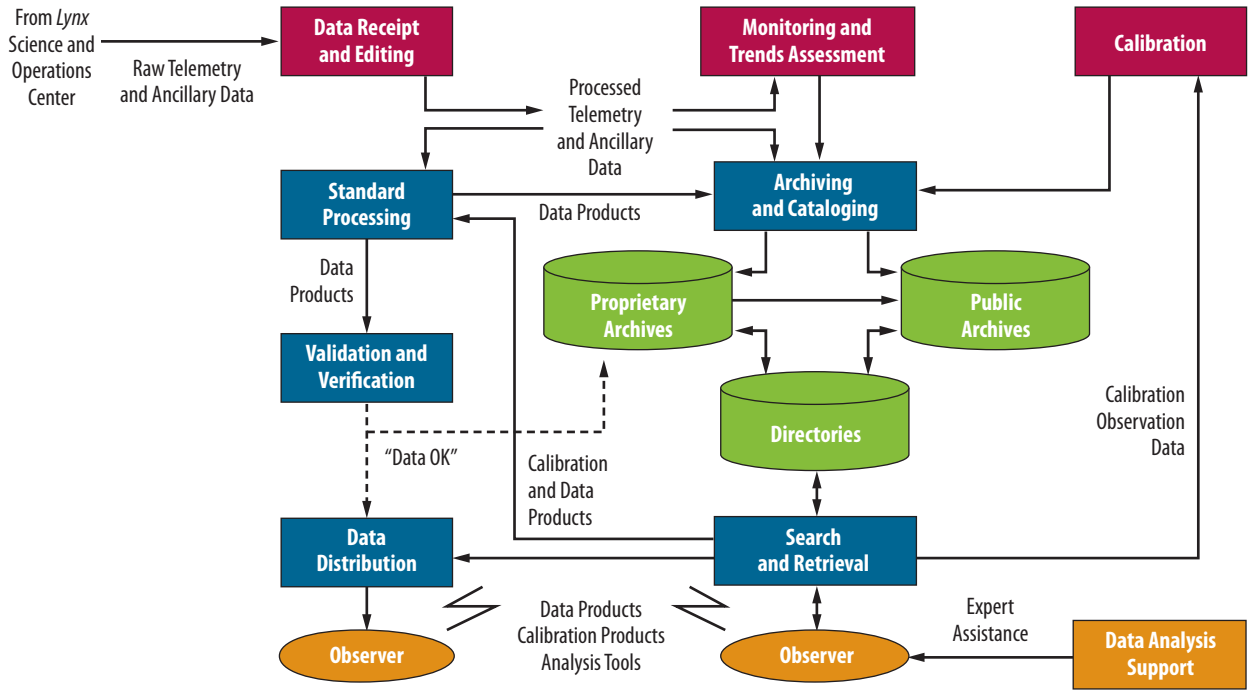

Figure 6.56. Data flow through the *Lynx* Science and Operations Center. Functional operations are performed by the science and the data operations teams, under the cognizance of the director's office.

Level 0 processing decommutates telemetry data. In Level 1 processing, the decommutated telemetry files have all camera events extracted (necessarily including both background and genuine X-ray photons), the aspect solution performed, and the time, celestial position, energy, and a quality flag tagged to each event. All products are archived and made available to the observer. In standard Level 2 processing, analysis tools are applied to generate a higher quality selection of celestial X-ray photon events. The Level 1 and 2 results go through an automated V&V process prior to ingesting into the archive and notifying the observer of their availability. Science-oriented software for data reduction and analysis will

comprise about one-third of the total data system. Processing tools will include the ability to model the mirror PSF as a function of energy and position at both low and high fidelities and the ability to model cosmic, instrumental, and in situ particle-induced backgrounds. ATOMDB [586] or a successor will be integrated with the analysis system to provide spectral line identifications and to model thermal plasmas. Tools will allow model fitting of spectra and of spatial structure. The data archive, data management, ingest, and distribution functions will comprise about one-third of the data system. This includes protection of proprietary data, the pipeline control software, search and retrieval tools, and interfaces to mirror archives. Remaining software will provide for proposal solicitation, management, planning, and peer review infrastructure, as well as science mission planning and scheduling tools.

Operations software will take advantage of Commercial Off-The-Shelf (COTS) systems for data transmission, raw data storage, communications, and assistance with mission planning and scheduling. Operations personnel will modify and configure these systems for *Lynx*-specific characteristics. A command and telemetry database will be developed and maintained. Software will monitor real time data, check for limit violations, and send out appropriate automated notices as needed. Monitoring and trends tools will provide data to subsystems engineers for detailed spacecraft performance assessment.

Table 6.16 from §6.4.6 shows the telemetry rates and data volume from the expected focal plane detectors. With the CCSDS packetization, the instantaneous data rates are allowed to exceed the telemetry downlink capacity so long as the onboard memory storage capacity of 480 Gbits is not exceeded. Only a very few sources will approach the maximum data rates shown in the table. Observations will be scheduled so that the daily average telemetry does not exceed 240 Gbits so that it can be downlinked at the 22.2-Mbps rate in three 1-hour contacts per day.

6.7.5 Serviceability

The science opportunities enabled by *Lynx* are greatly enhanced by its long mission lifetime. *Lynx* has been designed and provisioned to operate for 20 years at SE-L2 without significant reduction in capability, and with sufficient redundancy of key systems. Robotic serviceability will further help to ensure this long lifetime and could extend it further. To the extent practical under this study, the *Lynx* team has considered and incorporated robotic servicing design elements into the Observatory, consistent with guidance provided by the Satellite Servicing Projects Division (SSPD) at GSFC and the congressional mandate for all future observatory-class scientific spacecraft to include servicing.[†]

Lynx Observatory servicing is enabled primarily using "cooperative servicing aids" in the areas of remote survey, Rendezvous and Proximity Operations (RPOs), and capture to enable refueling and refurbishment (Figure 6.57). These servicing aids include standard interfaces and designs that are universally applicable to all new satellite missions, and are described in detail in [587].

Remote Survey — Allows the Observatory to be inspected from a distance in order to diagnose issues. *Lynx* will include retroreflectors installed on the tips of the antennas and solar panels, the OBA, and ISIM to facilitate this.

[†] *Public Law 111-267-Oct. 11, 2010, 124 Stat. 2833, Sec. 804. In-Space Servicing [https://www.congress.gov/]*

RPO — Rendezvous with a servicing satellite is enabled by the inclusion of specifically designed fiducial labels that are placed strategically across the Observatory. Once the servicing satellite is within 100 m of *Lynx*, proximity operations can commence (following capture). Prior to launch, closeout detailed photos using optical and IR will be taken of the Observatory at the launch site, with servicing in mind. Additionally, the forward *Lynx* sunshade door is designed to close in order to mitigate contamination of the optics from robotic servicing vehicle thruster plumes.

Capture — Standardized grapple fixtures will be installed on the forward and aft regions of the Observatory for easy capture by the servicing spacecraft. An external grounding point will be added to mitigate potential electrical differences between *Lynx* and the servicing spacecraft. During the detailed design phase, *Lynx* will consider implementing yet-to-be determined techniques to accommodate on-orbit loads during capture. While captured, refueling is possible with standardized valves designed specifically for robotic refueling [588], and MLI panels can be refurbished.

A more complete trade study will be carried out during pre-Phase A and Phase A and refined further as the *Lynx* design matures. This trade space will likely include (and is not limited to) spacecraft repair/replacements (e.g., thrusters and solar panels), replacing external sensors such as star trackers, repairing external mechanisms, and including test ports for on-orbit diagnostics. Designing for the replacement of the focal plane instruments is not practical based on their requirement to maintain translation and focus tolerances relative to the LMA and/or XGA, their integration into the ISIM translation stage, and in the case of LXM, its large mass. However, this could be revisited during the detailed design phase.

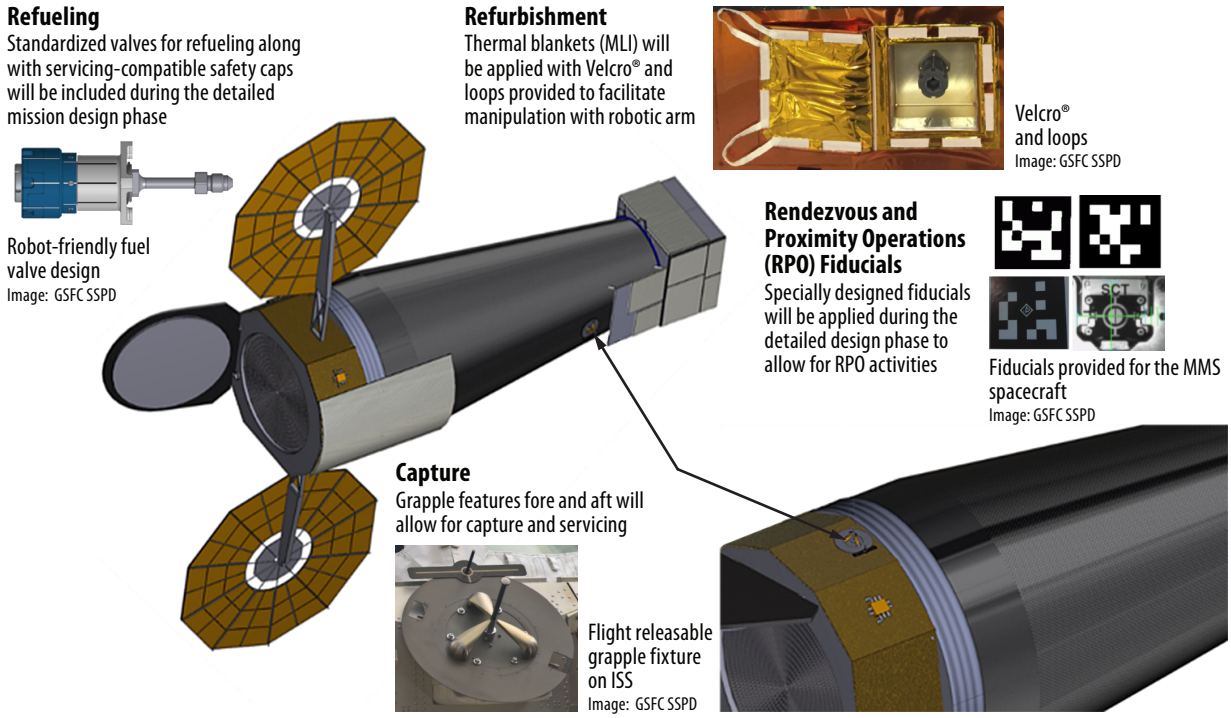

Figure 6.57. Future robotic servicing is enabled by incorporating servicing features into the *Lynx* design. Areas of servicing include remote survey, RPOs, and capture for refueling and MLI refurbishment.

6.7.6 End of Mission

After the 5-year baseline mission (with a potential extension up to 20+ years) of scientific discovery, *Lynx* will enter the end-of-mission operational phase. *Lynx* will comply with all applicable requirements in NASA-STD-8719.14, Process for Limiting Orbital Debris, and planning and compliance will be documented in an End of Mission Plan (EOMP). In the *Lynx* conceptual design, the delta-V budget and propellant load includes a disposal maneuver for end-of-mission. This will nudge *Lynx* out of its SE-L2 operational orbit and into a heliocentric disposal orbit. Although not required by NASA-STD-8719.14, *Lynx* can passivate (depletion of stored energy such as propellant and batteries) the Observatory to reduce future risk. After the operational mission is complete, the legacy of *Lynx* will live on in the archived scientific data, enabling astrophysical discoveries for years to come.

F02. *Lynx* System Block Diagram

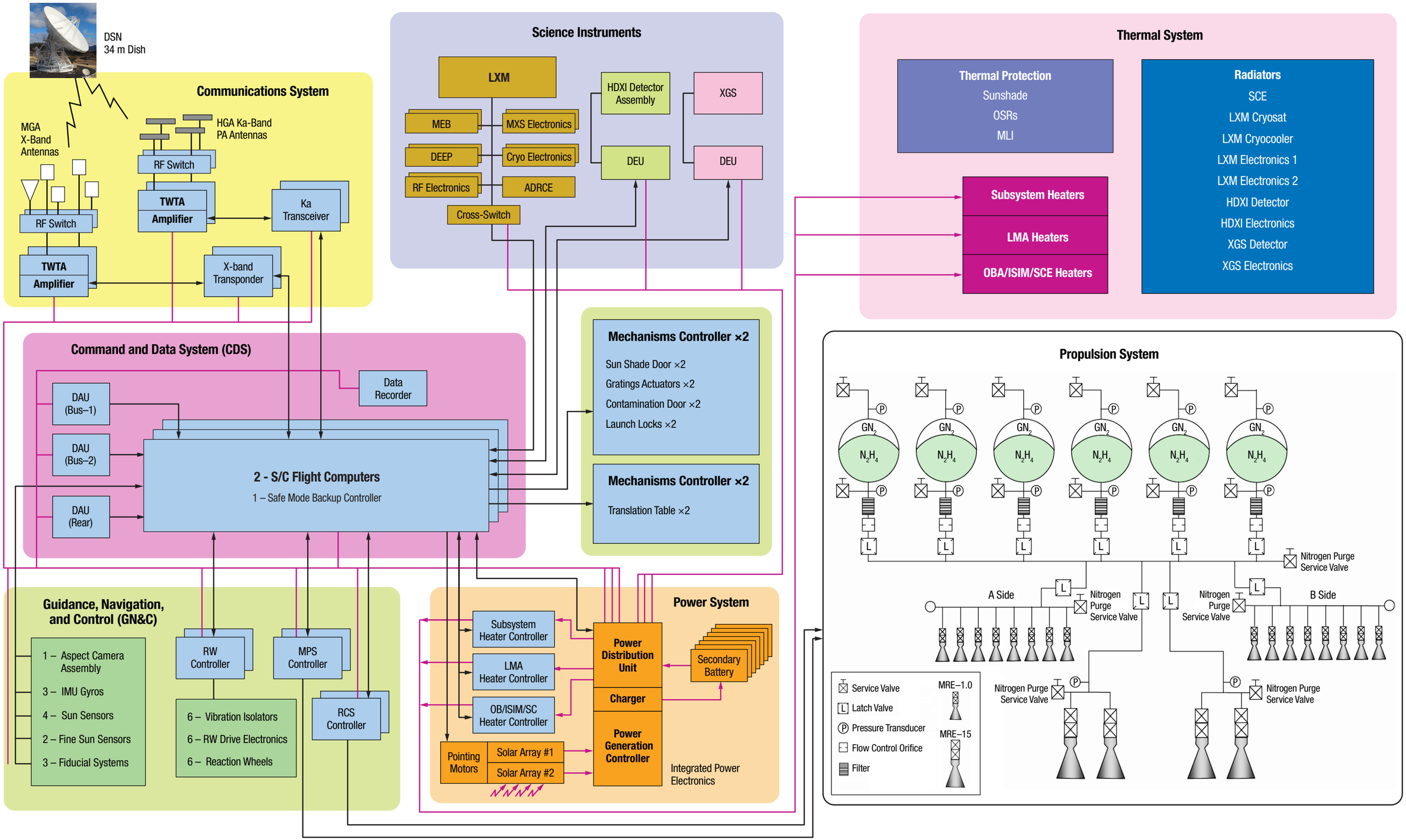

F03. *Lynx* Mission Trace Matrix

	A. Mission Functional Requirements		B. Mission Design Requirements		C. Spacecraft Requirements		D. Ground System Requirements		E. Operations Requirements	
	Requirement	DRM Design Confirmation	Requirement	DRM Design Confirmation	Requirement	DRM Design Confirmation	Requirement	DRM Design Confirmation	Requirement	DRM Design Confirmation
1	**Design for minimum observing efficiency of 85%**	Verified by simulation of a realistic target sequence. Study of *Lynx* Observing Efficiency*	• DRM requires 2.5 years to complete • Minimize on-orbit transients that reduce observing time • Provide propulsion to reach SE-L2, maintain orbit, and provide momentum management"	• To meet the *Lynx* effective collecting area requirement requires nesting large numbers of thin, lightweight, co-aligned, co-axial mirrors in order to optimize the available aperture. 85% efficiency verified by simulation of a realistic target sequence. 6.1.2, 6.4.5, and Study of a *Lynx* Observing Efficiency* • Design of attitude control system, CDMS, propulsion system, and thermal system minimizes non-science time. Thermal system can control temperatures within science requirements at any allowable pointing attitude and throughout maneuvers. • Propulsion system has adequate propellant load and control authority. Sufficient momentum unloading prop allocation.*	• Provide for attitude control • Provide ability to maneuver between celestial targets	• *Chandra*-proven mission operations and infrastructure will be implemented to ensure efficient, queued observing scheduling; *Chandra*-like pointing attitude control, stability, and knowledge consistent with subarcsecond imaging. (6.1.1) • The reaction wheel configuration, consisting of 6 wheels, along with the attitude control system thrusters, and MIMUs, provide for 3-axis control. The MIMUs and reaction wheels are used to maneuver to science targets. (6.4.2)	• Provide efficient mission planning and target sequencing • Derive aspect solution	• *Chandra* legacies include adopting an updated, state-of-the-art pointing and aspect determination system conceptually identical to *Chandra*'s PCAD, and implementing the *Chandra* operations and mission planning paradigm. (6.1.2) • A PCAD system is integrated with the telescope and spacecraft to provide a highly accurate aspect solution and to control pointing and dithering. (6.2)	• Acquire 1–20 targets/day • Provide for continuous data collection for 1–100 ks/target	• The GN&C system maintains knowledge of the spacecraft orientation, controls the maneuvers required to orient desired celestial targets within the telescope FOV, and holds each target attitude for the command duration. (6.4.2) • Assuming a maximum disturbance torque of 0.00037 Nm, the accumulated momentum in 100,000 s of continuous observation is 37 Nm. The momentum capacity for the baseline 6-wheel pyramid is 59.5 Nm, providing >60% margin. This allows continuous target pointing to meet/exceed the requirement.*
2	**Design for operation and survival in science orbit**	Observatory designed to survive in radiation and thermal environment at SE-L2. Spacecraft systems are designed to provide a stable platform and maintenance of the halo orbit, as well as keep the observatory attitude within mission guidelines for Sun avoidance. Environments* and Thermal Control*	• Provide solar power with battery storage • Provide propulsion for momentum-unloading maneuvers, station-keeping and EOL disposal • Design S/C surrounding X-ray mirrors to ease thermal management of the mirrors • Leverage hot/cold sides of observatory for thermal management • Design for Risk Class A • Provide for minimal on-orbit servicing • Provide for SE-L2 radiation and particle environment	• The power system batteries are sized to provide adequate power during launch and ascent, including survival power to the payload, prior to solar array deployment, with 40% margin. Solar arrays are sized to provide the maximum needed observatory power for 20 years.* • Propellant load and propulsion systems were designed to meet the requirements that flowed from the science objectives to the mission and spacecraft, including EOL disposal maneuver. • The spacecraft thermal subsystem is designed to maintain the spacecraft and OBA at an average temperature of 283 K, which allows the LMA to maintain positive thermal control at 293 K. (6.4.4)" • The use of MLI with a hot-side sunshade provides positive thermal control of the telescope, and pointing constraints provide a cold-side location for radiators for the instruments and electronics. (6.4.4) • Spacecraft components are fully redundant, for any credible failure, where required to meet the risk standard.* • Grapple fixture, reflectors are located on the observatory. Sunshade door can close during servicing.* • Charged particles exist as an omnidirectional flux, a portion of which can be concentrated through the LMA directly onto the focal plane. Relatively low (~90 C) sensor operating temperature and shielding on the HDXI enclosure will be used to mitigate the ambient particle flux, and a magnetic diverter will be used to divert the charged particle flux away from the focal plane. Micrometeoroid environment was modeled and has a near-zero percent chance of degrading performance. (6.3.2.2)	• Distribute needed power; peak <8 kW • Provide for communication with existing ground stations (DSN) • Maintain operating temperatures within required limits • Place instruments at optimum focus	• Power system is designed to deliver 4430 W to the payload at the end-of-life (20 years), which includes a 40% power margin for the instruments and an overall payload power margin of 30.5%.* • For communications with the ground, *Lynx* will utilize NASA's existing DSN system to provide telemetry, tracking, and command, ensuring high reliability and high data rate for communications for downloading its science and spacecraft health data and uplinking commands. (6.4.6) • Cooling for the sensor array is through a cold strap connection between the sensor array that conductively coupled to a SiC mosaic plate and the enclosure. The enclosure, along with its thermal load from the rest of the instrument through heat pipes that move along with the translation table. (6.3.2.1) • Strong space flight heritage (high TRL) and flight heritage mechanisms will be employed for focal plane instrument translation and focusing and for grating array insertion and retraction. (6.1.2)	• Monitor health and safety of observatory • Provide for on-orbit calibration	• All science and observatory data will be received and all commands to *Lynx* will be generated by a co-located team of Flight, Science, and Ground operations personnel. The team is responsible for the spacecraft health and safety, carrying out all observational programs, monitoring and performing necessary maintenance, and retrieving and transmitting all data for processing, archiving, and distribution. (6.7.4) • A set of standard celestial targets will be determined for on-orbit calibration use. These targets will be periodically observed to monitor LMA, all science instruments, and aspect system performance. (6.7.3)	• Maintain 45 degree Sun avoidance • Command instruments for data collection and standby • Restrict roll angle to manage thermal environment • Store commands for up to 72 hours autonomous operation	• Observations will be checked by the mission planning software to ensure observations remain outside the Sun-avoidance angle, and maneuvers between targets will be designed to avoid even momentary entry into this region. • The avionics equipment located in the *Lynx* spacecraft is designed to perform the functions of GN&C, thermal control, power switching, data storage, command management, and uplink of commands and downlink of data. (6.2, 6.4.5) • Thermal analysis informed the design such that this requirement is met.* • On board flight computer RAD750 can perform autonomous operations with flight control and operations software uplinks to non-volatile memory.*
3	**Design for accommodation of payload in launch vehicle**	Payload meets mass, and static and dynamic envelope requirements for generic heavy-class launch vehicle for the 2030s, as defined by LSP. Spacecraft, optical bench, and integrated science instrument module structure are sized to survive the launch environment as specified for Delta IV Heavy. See Section 6.4 and Configuration*	• Design for NASA-provided LV per LSP recommendations • Design to survive launch: fit w/ in static and dynamic envelope defined by LV; exceed minimum modal frequency requirements for LV	• Baseline configuration sized to fit within the LSP Future Heavy payload dynamic envelope provided.* • Observatory mass, volume, and dynamic analysis make *Lynx* compatible with multiple anticipated future heavy-class launch vehicles expected to be available in the 2030 timeframe including, the Space Launch System. (6.1.1)	Battery power until solar array deployment	Energy storage is provided via five 28-V batteries with one additional battery to ensure single fault tolerance. The batteries are sized to provide launch power (743 W) for 156 minutes from launch to the completion of initial checkout and solar array deployment, and for 5 minutes of survival mode. (6.4.3)	Plan initial on-orbit activation and checkout	For 156 minutes following launch, *Lynx* will rely on batteries to power minimal spacecraft systems, survival heaters for critical telescope elements, and to deploy the solar panels. During travel to SE-L2, the spacecraft and telescope systems are powered up, allowed to outgas, and undergo system checks and initial calibration. (6.7.1)	• Maintain optics and instruments in low-power mode prior to solar array deployment • Instrument initial V&V	• Energy storage is provided via five 28-V batteries with one additional battery to ensure single fault tolerance. The batteries are sized to provide launch power (743 W) for 156 minutes from launch to the completion of initial checkout and solar array deployment, and for 5 minutes of survival mode. Power will be provided to all attached architecture elements during initial checkout (2.6 hours) and solar array deployment per power schedule. Full power will remain available during final orbit insertion. (6.4.3.3*) • For 156 minutes following launch, *Lynx* will rely on batteries to power minimal spacecraft systems, survival heaters for critical telescope elements, and to deploy the solar panels. During travel to SE-L2, the spacecraft and telescope systems are powered up, allowed to outgas, and undergo system checks and initial calibration. (6.7.1) Note that the L2 halo orbit has no eclipse time to interrupt solar panel provided power.

*DRM Supplemental Design Package

F03. *Lynx* Mission Trace Matrix *continued*

	A. Mission Functional Requirements		B. Mission Design Requirements		C. Spacecraft Requirements		D. Ground System Requirements		E. Operations Requirements	
	Requirement	DRM Design Confirmation	Requirement	DRM Design Confirmation	Requirement	DRM Design Confirmation	Requirement	DRM Design Confirmation	Requirement	DRM Design Confirmation
4	**Provide data collection that is sufficient for uninterrupted observations by all science instruments**	On board computer provides for 1 Tbit of onboard data storage. Comm plan allows for sufficient downlink of data to satisfy maximum expected data rates from instruments, with margin. See Section 6.4.6 and C&DH*	• Use existing DSN ground station for communications • Use Ka-band for science data downlink (per SCaN guidance) • Use X-band for command uplink and engineering up/ downlink	• For communications with the ground, *Lynx* will utilize NASA's existing DSN system to provide telemetry, tracking, and command, ensuring high reliability and high data rate for communications for downloading its science and spacecraft health data and uplinking commands. (6.4.6) • A flight-heritage communication system will be baselined, similar to that used on the Mars Reconnaissance Orbiter, which supports data volumes up to 270 Gbits/day. The *Lynx* communication system will utilize the high heritage Ka-band for science data downlink. (6.4.6) • The *Lynx* C&DH system baselines X-band for low-rate uplink and backup telemetry. (6.4.6)	• 6 Mbps maximum instantaneous data collection rate • 1 Tbit onboard data storage • Provide for 240 Gb downlink/day • Translate science instruments to/ from primary aim point • Insert/retract XGS	• Using a standard 10Base-T Ethernet bus supports 10 Mbps rates. • Included in the Avionics equipment is a 1 Tbit mass data storage device, which provides 100% redundancy. • Following a *Chandra*-like DSN schedule of 3 one hour links per day at 22 Mbps achieves the 240 Gbits per day downlink requirement. • HDXI and LXM, along with their electronics and radiators, are mounted on a moveable platform that is part of the ISIM. The translation table assembly permits either instrument to be placed on-axis. (6.3) • On-board mechanisms will all have strong space flight heritage (high TRL) and flight heritage mechanisms will be employed for focal plane instrument translation and focusing and for grating array insertion and retraction. (6.3)	• Plan Normal (Science) Mode program • Provide L0 data to the • Operations Center with < 72 hours latency. • Provide for data archival, retrieval, and distribution to public • Plan instrument configuration to avoid excessive data collection	• *Lynx* will be primarily in normal pointing mode conducting an autonomous pre-planned program of celestial observation. The telescope optical axis is pointed within 10 arcsec of a commanded celestial position, which is assured by locking on pre-planned stars at specific positions in the aspect of the star camera. (6.7.2) • The 1 Tbit of on board memory stage provides a latency capability which exceeds the 48 hour requirement.* • All *Lynx* science instruments are photon counting detectors that accumulate event based time, position and energy data that are accumulated and temporarily stored on board before being periodically telemetered to the ground where it is processed, archived, and distributed to the scientific community. (6.7) • The Science Operations Team is responsible for planning the mission schedule sequence by optimally scheduling targets provided by the *Lynx* user community. That team specifies the science instrument configuration for each observation and carries out on-orbit scientific instrument monitoring and calibration. The Science Data Team performs standard data processing, archiving data products, and distribution to the *Lynx* community, maintenance, and distribution of calibration products and analysis tools, and archival search and retrieval services. (6.7.4)	Follow Normal (Science) Mode pre-planned observing program	*Lynx* will be primarily in normal pointing mode conducting an autonomous pre-planned program of celestial observation. The telescope optical axis is pointed within 10 arcsec of a commanded celestial position, which is assured by locking on pre-planned stars at specific positions in the aspect of the star camera. (6.7.2)
5	**Design for 5-year mission**	All Observatory systems designed for on-orbit life of at least 5 years with margin and not to preclude 20 years. See Section 6.4.1; Propulsion*	• Provide consumables for up to 20 years contingency • Provide for robust safe modes system	• Prop load is sized for 20 year mission, including momentum unloading and station-keeping.* • An internally redundant Safe Mode Electronics Unit (SMEU) is included to allow the observatory to autonomously slew to a safe Sun angle in the event of out of range on-board parameters. Safe mode control will include a separate set of control processing electronics that operate with different software. (6.4.5, 6.4.6)						
6	**Provide pointing control of the optical axis at desired targets.**	Pointing and propulsion systems were designed to meet the requirements that flowed from the science objectives to the mission and spacecraft. The design of the OBA and its attachments to the LMA and ISIM minimize telescope boresight variation. See Section 6.3.6, 6.4.2, and GN&C*	• Photon counting science instruments to record time, position, and energy for each event • Limited optical bench length variation keeps image in focus, and lateral boresight variation is tracked with a fiducial light system • Stability 0.17 arcsec/sec	• All *Lynx* science instruments are photon counting detectors that accumulate event-based time, position and energy data that are accumulated and temporarily stored on board before being periodically telemetered to the ground where it is processed, archived, and distributed to the scientific community. (6.7) • OBA is made of a low CTE material to minimize length variation and potential "hot-dogging" due to maneuvers changing the temperature profile, and the sunshield maintains cold-bias for positive heater control. Bipod struts to LMA are an a thermalized design and temperature-controlled, as is the flexure connection to the ISIM • The pointing control system incorporates hardware that has equivalent or better performance than the *Chandra* PCAD system, which allows the observatory to meet this requirement.*	• Pointing attitude to 10 arcseconds absolute • On-board knowledge 4 arcseconds	• The reaction wheel configuration, consisting of 6 wheels, along with the attitude control system thrusters, and MIMUs, provide for 3 axis control. 3-axis reaction wheel typically provides pointing accuracy of +/- 0.0001 deg (0.36 arcsec).* • Sensor suite includes Inertial Measurement Unit 3x plus High Accuracy Star Tracker for state updates (+/- 0.2 arcsec/axis, 1 sigma).*	• Post facto image reconstruction consistent with 0.2-arcsecond RMS system accuracy • Absolute celestial location to 1 arcsecond	• A *Chandra*-like PCAD system is integrated with the telescope and spacecraft to provide a highly accurate aspect solution and to control pointing and dithering. (6.2) • The GN&C system maintains knowledge of the spacecraft orientation, controls the maneuvers required to orient desired celestial targets within the telescope FOV, and holds each target attitude for the command duration. (6.4.2)	Monitor exact pointing attitude history and spacecraft alignment	The *Lynx* GN&C system has adopted *Chandra* heritage PCAD system. To hold the target attitude, the star camera acquires and tracks known guide stars in the target vicinity, the MIMUs monitor rotational and translational drift rates, and reaction wheels are commanded to spin, as needed, to compensate for disturbance torques. (6.3.6, 6.4.2)

*DRM Supplemental Design Package

7 *Lynx* Technology Development

The *Lynx* X-ray mirror assembly and three science instruments are the critical technologies that will enable the *Lynx* Observatory's revolutionary science. To date, significant development efforts have advanced these technologies to a Technology Readiness Level (TRL) of 3 or higher based on non-advocate estimates. Credible and executable technology development plans are in place to advance all components of these technologies to TRL 5 by the start of Phase A and to TRL 6 by the Preliminary Design Review. These plans have been independently and objectively assessed with respect to risk, cost, and schedule. These *Lynx* technology development plans will ensure that the telescope optics and instrument systems meet the scientific performance and programmatic requirements for the *Lynx* Observatory.

7.1 Four *Lynx*-Enabling Technologies

The *Lynx* Observatory will require the development of four enabling technologies: an X-ray mirror assembly and three science instruments. For purposes of in-depth cost, schedule, and system integration evaluation, the Silicon Meta-shell Optics, the hybrid Complementary Metal-Oxide Semiconductor (CMOS) High-Definition X-ray Imager (HDXI), the Critical-Angle Transmission (CAT) X-ray Grating Spectrometer (XGS), and the *Lynx* X-ray Microcalorimeter (LXM) have been designated as the Design Reference Mission-enabling technologies. (§6) These technologies have matured significantly and are all currently at TRL 3 or higher, with some elements or components at a higher TRL, as assessed by the most recent Physics of the Cosmos (PCOS) Technology Management Board assessment in 2019. In addition, multiple credible technology options are being independently developed for each of these four technologies (or for components of these technologies). Cultivating multiple technology options at this time will significantly diminish risk to the project.

Each technology contains several key elements that require maturation to TRL 6. Complete development plans for each technology (a.k.a., technology roadmaps) have been developed and are included as supplements to this report. The *Lynx* technology maturation plans were developed by expert teams—often with participation across multiple academic, industrial, and government institutions. The technology plans follow the development paths from the current State of the Art (SOA) to TRL 5 by the start of Phase A (Key Decision Point- (KDP-) A: October 1, 2024) and to TRL 6 by Preliminary Design Review (PDR): February 1, 2028). This schedule assumes a launch date of November 2036, technology development funding starting three years prior to KDP-A (FY22), and final architecture selection beginning eight months prior to KDP-A (§8.4). At currently anticipated funding levels, most enabling Design Reference Mission (DRM) technologies are expected to achieve TRL 4 by the start of directed funding, and there are no known fundamental physical challenges to reaching TRL 6 for any *Lynx*-enabling technology.

While this report is focused on the specific technologies selected for the DRM, the *Lynx* team recognizes the risks inherent in developing specialized technologies with characteristics that are beyond the SOA. For this reason, the program is supporting parallel "alternate technology" efforts for the mirror assembly and all three science instruments (or components of instruments) for the purpose of risk reduction. These include two alternate X-ray mirror assembly architectures—called the Full Shell Optics and the Adjustable Segmented Optics—and an alternative feasible XGS technology: the Off-Plane X-ray Grating Spectrometer (OP-XGS). Complete technology development plans for these three alternates are provided as supplements to this document. The HDXI development plan includes two architectures in addition to the hybrid CMOS technology: the monolithic CMOS and the advanced "digital" Charge-Coupled Device (CCD). All three HDXI technologies are included within a single development plan because, while they differ in architecture, they are nearly identical in functionality and require similar Observatory resources and interfaces. The LXM development plan includes alternative technologies for thermal sensor, readout multiplexing, and cryocooler subsystem components.

All the *Lynx* technology development plans present reviews of the SOA; descriptions of the technical elements being developed, tested, and verified; statements of TRL 4, 5, and 6 specific to each technology; assessments of the key milestone elements (with Advancement Degree of Difficulty (AD^2) evaluations[†] [626]) needed to advance each technology to successive TRL levels; and estimates of the associated schedules, costs, risks, and risk mitigations. In addition, a special section of the *Journal of Astronomical Telescopes, Instruments, and Systems* (*JATIS* Vol. 5(2), 2019) dedicated to *Lynx*-enabling technologies provides 20 open-access refereed articles with additional information on *Lynx* technology development plans.

Table 7.1 summarizes the enabling *Lynx* DRM technologies, their SOAs, the specific *Lynx* requirements driving their development, top-level challenges to advance their *Lynx*-specific TRLs, and a synopsis of the milestone(s) for TRL advancement to the next level. The following subsections highlight the most challenging technology development elements for each enabling technology.

The combination of significant relevant heritage and high current SOA ensures that further technology development for all four *Lynx*-enabling technologies is well within the experience base with a high degree of confidence that TRL 6 can be achieved with low schedule and cost risk. All technologies have analytically and experimentally demonstrated critical function and characteristic proof-of-concept while validating model predictions of key parameters.

The *Lynx* team recognizes the complex interrelationship among these four enabling technologies and the need to demonstrate required performance at a system level early in the development schedule. The natural juncture in the *Lynx* project development schedule for such a demonstration matches the X-ray mirror assembly and the X-ray Grating Array (XGA) TRL 6 maturation point in early 2027. A joint TRL 6 demonstration combining a mirror engineering unit—with representative components spanning the full range of the *Lynx* aperture diameters, with a complementary grating array portion of the XGS—is planned at this time in the program schedule. X-ray performance and environmental tests of this engineering model are planned at NASA Marshall Space Flight Center's (MSFC's) X-ray and Cryogenic Facility to accommodate the test article's large size. Ground Support Equipment (GSE) will be used for mirror and grating array X-ray performance.

[†]*AD2 is a bottoms-up assessment of the anticipated difficulty over the course of a technology maturation project. AD2 is determined through consideration of cost, schedule, and risk with a resulting value on a scale of increasing difficulty from 1 to 9.*

Table 7.1. *Lynx*-enabling technologies requiring technology maturation.

	Technology	Function	Development Challenges	Development Path	AD2 - Rationale
***Lynx* Mirror Assembly (LMA)**	Silicon Meta-shell Optics – Modular design with many thousands of thin, lightweight mirror segments integrated (via modules/meta-shells) into the *Lynx* Mirror Assembly **Current TRL = 3** 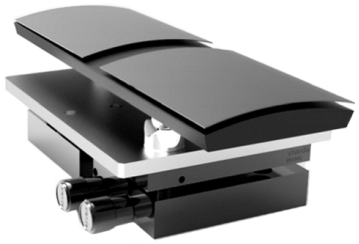	Provide high-resolution imaging over the large field of view and broad energy range needed to meet *Lynx* science goals	• Demonstrate a reliable fabrication process to mass produce quality mirror segments • Verify processes for assembling the required 611 mirror modules • Demonstrate assembly processes for 12 meta-shells • Demonstrate final assembly, alignment, and testing processes	• Develop alternate mirror technologies in parallel with baseline • Fabrication, alignment, coating, bonding, and qualification of single-mirror segment pairs (TRL 4) • Fully populating and qualifying multiple mirror modules and a single meta-shell (TRL 5) • Assembly and qualification testing of subscale (3 meta-shell) engineering model *Lynx* Mirror Assembly (TRL 6)	• TRL 4: $AD^2 = 3$ – All required fabrication processes (substrate, coating, bonding, alignment) demonstrated, process refinement for mass production to be developed • TRL 5: $AD^2 = 3$ – Alignment and bonding processes will carry over from TRL 4 development; iterative fabrication assembly process required to ensure throughput and environmental survivability is straightforward • TRL 6: $AD^2 = 3$ – As with TRLs 4 and 5, this is a relatively straightforward (albeit intricate) assembly, fit, and test phase that will likely require iterations; No fundamental barriers are apparent.
High-Definition X-ray Imager (HDXI)	Imaging spectrometer leveraging pixelated silicon sensor technology heritage from many ground- and space-based applications **Current TRL = 3** 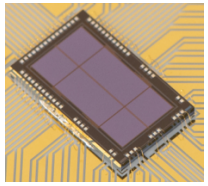 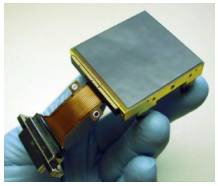 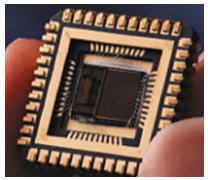	Provide large-format, high-throughput, sub-arcsec angular resolution at moderate spectral resolution over broad X-ray energy band to meet *Lynx* science goals	• Provide excellent low-energy X-ray response (high quantum efficiency) and fine spatial resolution at high frame rates • Demonstrate low detector noise, high pixel-to-pixel response uniformity, and reliable readout processing	• Demonstrate required sensor (with Application-Specific Integrated Circuit (ASIC)) noise, resolution, and quantum efficiency at high and low energies in representative multichannel sensor • Demonstrate required performance of integrated sensor/ASIC system of representative size before and after environmental testing • Demonstrate required performance of ¼-size focal plane in relevant environment before and after environmental testing	• TRL 4: $AD^2 = 5$ – Optimization of pixelated silicon sensors and ASICs is standard industry practice, but all science requirements must be demonstrated on a single custom sensor; may require long lead-times • TRL 5: $AD^2 = 2$ – Integrating a sensor/ASIC and associated readout electronics for evaluation to TRL 5 is largely an engineering activity • TRL 6: $AD^2 = 2$ – Combining multiple sensors and ASICs into an engineering model focal plane of pixelated silicon sensors has high heritage from many missions

Table 7.1. *Continued*

	Technology	Function	Development Challenges	Development Path	AD2 - Rationale
X-ray Grating Spectrometer (XGS	Very high resolving power, dispersive, soft X-ray spectrometer optimized for efficiency at astrophysically critical atomic line energies **Current TRL = 4** 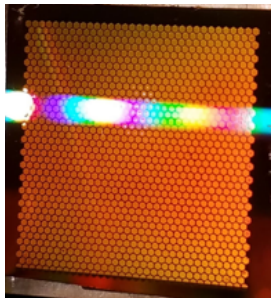	Provide high-throughput, very high resolving power, dispersive spectroscopy to meet *Lynx* science goals for bright, point-like sources	• Fabricate high- efficiency diffraction gratings (thin grating bars but deep device layers with low support structure obscuration) • Advance metrology for alignment and mounting to preserve energy resolution (Line Spread Function (LSF)). Develop "chirped" gratings to maintain LSF of large grating facets	• Develop alternate grating array technology in parallel with baseline • Increase depth and decrease width of grating bars using Deep Reactive-Ion Etching and KOH polishing solution • Leverage experience from past mission development as foundation for alignment metrology and assembly • Build toward TRL 6 large-scale prototype matched to LMA TRL 6 demonstrator	• TRL 5: $AD^2 = 3$ – Fabricating grating membranes with reduced structural obscuration is an incremental development but must pass environmental tests; conception and implementation of metrology infrastructure for mounting and alignment in brassboard is new development. • TRL 6: $AD^2 = 3$ – Fabricating larger grating membranes with designed grating bar widths and period chirp will leverage semiconductor and Micro-Electrical Mechanical Systems (MEMS) industry practices – most development is incremental
Lynx X-ray Microcalorimeter (LXM)	Large-format fine pixel microcalorimeter with three pixel array types providing a large range of scientific capabilities **Current TRL = 3** High-bandwidth microcalorimeter readout **Current TRL = 3** Focal Plane Assembly (FPA) and Optical Photon Blocking Filters **Current TRL = 4** Cryogenic cooling system **Current TRL = 4** 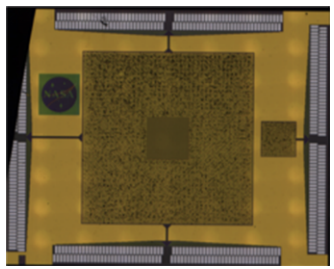	Provide high-spatial resolution energy dispersive imaging capabilities to meet multiple *Lynx* science goals	• Reduce slew rates for the thermal multiplexed pixels to adequately match the readout capabilities of the μMUX readout • Reduce thermal crosstalk • Avoid substantial energy degradation from crosstalk in readout circuitry at relevant mux factors • Advance cryocooler and ADR technologies to required TRL within schedule and budget	• Develop alternate sensor technology in parallel with baseline • Fabricate heat-sinking of arrays with buried wires through multiple approaches to achieve best thermal crosstalk reduction • Design readout components and operational parameters (e.g., tone power to amplifiers) to mitigate crosstalk • Leverage *Athena*'s X-ray Integral Field Unit (X-IFU) development for *Lynx* Focal Plane Array • Utilize two independent industry-based cryocooler design and development paths and choose best option	• TRL 4: $AD^2 = 3$ – Existing TES-based arrays lack only standard testing; μMUX readout needs optimization for bandwidth required – testing/modeling efforts indicate no fundamental design limits for LXM • TRL 5: $AD^2 = 3$ – Arrays require advancement in heatsinking – buried wire technology scale-up straightforward; significant carryover from ongoing development efforts for multiple terrestrial applications expected for readout advancement ($AD^2 = 4$); cryocooler advancement requires funding investment • TRL 6: $AD^2 = 2$ – Straightforward engineering advancement of arrays to full size; readout integration into new FPA geometry is AD2 = 4; new FPA is an engineering effort leveraged from *Athena* ($AD^2 = 3$) – blocking filter sizing and environmental testing not a technical challenge; cryocooler straightforward optimization between structural and thermal performance

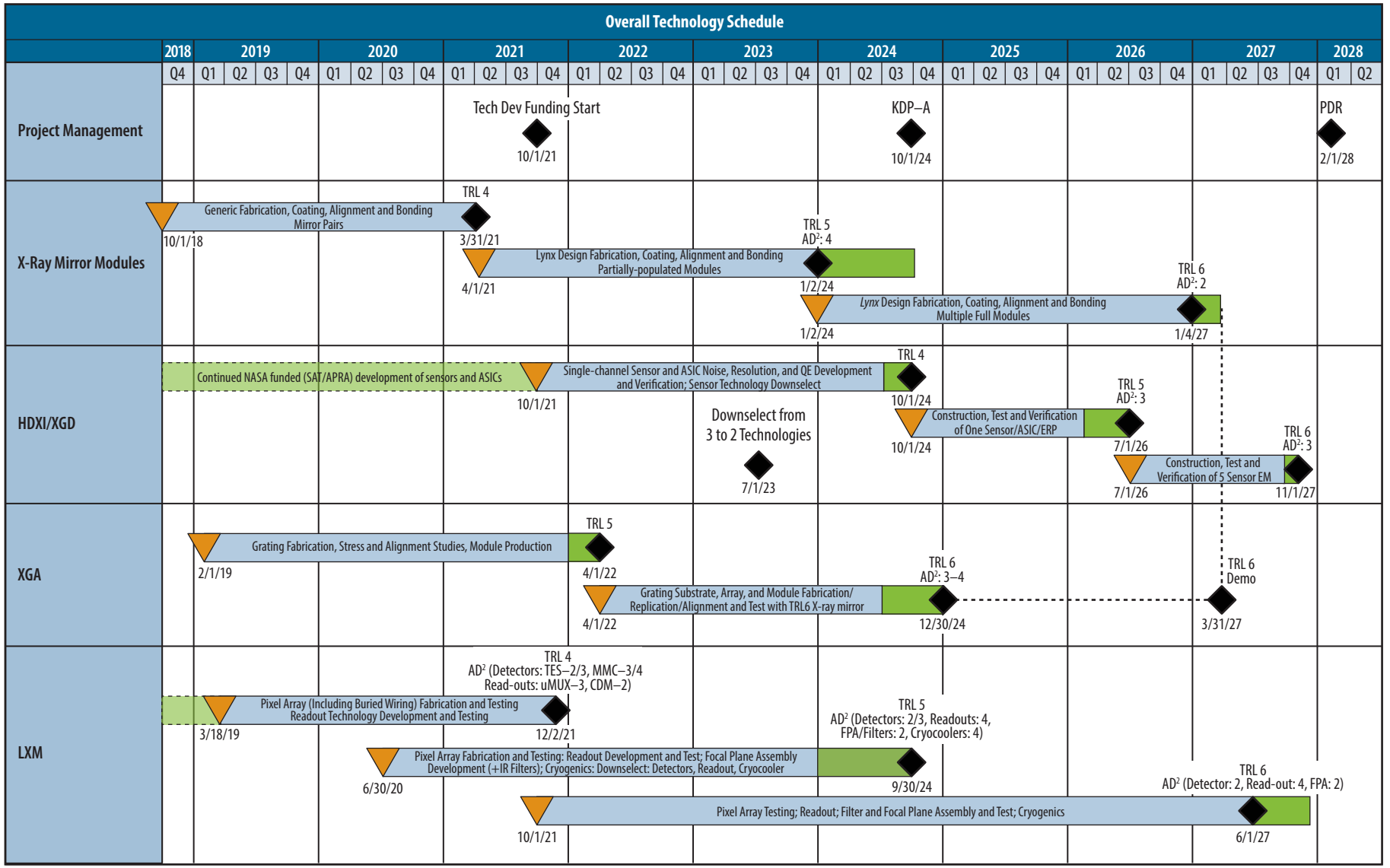

Figure 7.1. Development schedule to mature four *Lynx* enabling technologies to TRL 6 by mission PDR.

Figure 7.1 displays the overall project schedule (including margins) for developing the four DRM technologies to TRL 6 prior to PDR. The schedule is the result of grassroots analyses by the individuals and organizations active in the respective technology development efforts and reflect realistic estimates of workload, procurement lead time, and funding profiles as detailed in the supplemental development plans for each technology. A full project schedule is given in §8.4, and each technology development plan supplement provides schedules detailing individual development milestone tasks.

Most enabling DRM technologies will achieve TRL 4 by the start of directed funding, which is expected to begin in FY22. The exception is the HDXI, whose early technology progress is through iterative cycles of design improvement and fabrication. Anticipated funding allows only a few development cycles to be completed up to and during the pre-Phase A period, leading to a longer development path to TRL 4. In contrast, developing the HDXI to TRL 5 and 6 will be rapidly advanced.

All technologies described in this report are currently funded by NASA and other sources. Grassroots technology development (directed) and Phase A cost estimates are given for each *Lynx* technology in their individual technology development plans. The required funding estimated for the three-year pre-Phase A period for the four enabling technologies is in-family with *Wide Field Infrared Survey Telescope* (*WFIRST*) estimations, with Phase A funding estimated at a comparable level.

7.2 Optics Development

Lynx X-ray mirrors must enable leaps in sensitivity, spectroscopic throughput, survey speed, and most importantly, imaging performance over past or planned missions. Because of this critical significance, the *Lynx* team performed a comprehensive technology assessment trade study (Appendix B.2.1) of three X-ray optics technologies. The study evaluated each approach's ability to meet *Lynx* science requirements, their capacity for overcoming technical challenges, and the validity of their schedule, cost, and risk estimates. The study recommended the Silicon Meta-shell Optics assembly architecture (§7.2.1) to focus the Observatory DRM while maintaining the Full Shell Optics (§7.2.2) and the Adjustable Segmented Optics (§7.2.3) architectures as feasible alternatives. The study cited Silicon Meta-shell Optics as being the most mature of the three technologies with the shortest path to achieving TRL 5 and 6. Comprehensive technology development plans for all three architectures are provided in the supplemental documentation.

7.2.1 Silicon Meta-shell Optics

The DRM optics design for *Lynx* employs a highly modular approach to building, testing, and qualifying a mirror assembly [589]. In this approach, tens of thousands of similarly dimensioned, ~100-×-100-×-0.5-mm, lightweight mirror segments (and nonreflecting stray light baffles) are integrated into mirror modules by attachment (directly or indirectly) via other mirror segments onto module mid-plates. The mirror modules, in turn, are integrated into full-circumference meta-shells of different diameters before finally being integrated to create the *Lynx* X-ray mirror assembly (§6.3.1.1). The technology development

plan follows this hierarchy by first refining four technology elements through repetition: (1) fabrication, (2) coating, (3) alignment, and (4) bonding of single pairs of mirror segments (TRL 4). This is followed by partially to fully populating mirror modules (including environmental qualifying and X-ray testing; TRL 5). A TRL 6 engineering model demonstration of a *Lynx* Mirror Assembly (LMA) will contain numerous modules aligned and mounted within representative meta-shells whose parameters span the full range of the LMA. The full technology development plan to reach TRL 6 by Q4 2026 (well in advance of the start of Phase B) is contained in the *Silicon Meta-shell Optics Technology Roadmap.* The following is a summary of the key technology development elements from that document.

The Next Generation X-ray Optics group at NASA Goddard Space Flight Center (GSFC) has been continually developing the Silicon Meta-shell Optics technology since 2011. This technology combines the direct fabrication grind-and-polish method (proven for *Chandra's* sub-arcsecond optical performance) with mature production technologies widely used in the semiconductor industry, such as ion beam figuring and CNC machining. Critically, the technology uses a nearly ideal substrate (monocrystalline silicon) to fabricate extremely thin optical components.

The DRM optics design for *Lynx* uses monocrystalline silicon—an inexpensive staple of the semiconductor industry—for its mirror substrate material. Monocrystalline silicon, also known as single-crystal silicon, is a continuous crystal lattice free of grain boundaries. It can be ground, honed, lapped, cut, sliced, diced, and etched and remain free of internal stress. It is lightweight, stiff, and thermally conductive with a low coefficient of thermal expansion. Monocrystalline silicon is the ideal material for *Lynx* mirrors.

At present, numerous monocrystalline silicon mirror substrates have been repeatedly fabricated and (optically) demonstrated to meet figure requirements. A pair of uncoated mirrors aligned and bonded at four locations with silicon supports onto a breadboard silicon plate (as specified in the optical design) has achieved 1.3-arcsecond Half-Power Diameter (HPD) at 4.5 keV (Figure 7.2). Performance was demonstrated by full-illumination X-ray tests at the X-ray beamline at GSFC; simulations show that equivalent performance in the absence of gravity would be close to 0.5-arcsecond HPD. A similar module was independently measured at the PANTER 130-m X-ray beamline for its effective area at several different energies, agreeing within 2% with calculations

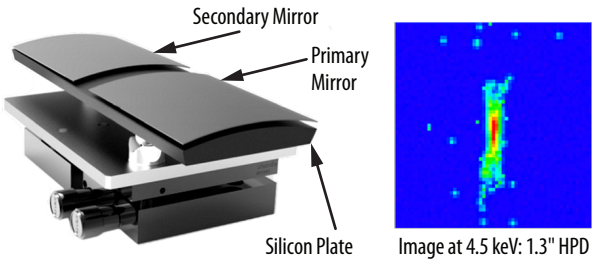

Figure 7.2. A primary and secondary mirror pair aligned and bonded on a breadboard silicon plate. The concave reflecting surface faces down in this photograph, and the four (per mirror) silicon supports are hidden between the reflecting surface and the silicon plate. Right: An X-ray image obtained with a fully-illuminating beam of 4.5-keV (Ti K) X-rays showing a half-power diameter of 1.3 arcseconds. The effective area at several energies were measured at MPEs PANTER X-ray beam line from a similar mirror pair and shown to agree with theoretical expectations within 2%.

based on atomic form factors. These demonstrations place the fabrication, alignment, and bonding development of the *Lynx* baseline optics at TRL 3. The PCOS Program assessed the Silicon Meta-shell Optics technology at TRL 3.

Table 7.2 summarizes the approach or strategy used to meet each of the mirror performance requirements derived from the *Lynx* science objectives, with items in square brackets correlating these strategies with specific milestones (M1, M2, etc.) identified in the complete *Silicon Meta-shell Optics Technology Roadmap*, the associated TRL, and the planned completion date.

Table 7.2. *Lynx* requirements on its mirror assembly derived from its science drivers and the strategy of the Silicon Meta-shell Optics technology to meet them.

LMA Requirements Derived from Science Requirements		Silicon Meta-Shell Optics Strategy to Meet LMA Requirements
Point Spread Function (PSF) (on-axis)	Better than 0.5 arcsec	1. Use of a Wolter-Schwarzschild optical prescription optimized for best off-axis response and use of mirror segments short in the axial direction (100 mm) to minimize effects of field curvature. [COMPLETE] 2. Use of modern proven and deterministic polishing technology and metrology techniques to make and fully qualify each mirror segment. [COMPLETE] 3. Use of traditional kinematic support for alignment and minimal constraint for permanent bonding of each mirror element to realize the performance potential of each mirror segment. [M3, TRL 4, Q4/2019]
PSF (10 arcmin off-axis)	Better than 1 arcsec	
Effective area	2 m^2 at 1 keV	1. Choose monocrystalline silicon to make thin (0.5-mm) mirror segments to efficiently pack the large mirror area into a small volume. [COMPLETE] 2. Coating of the mirror surface with iridium film and possibly other interference coating to enhance or maximize reflectivity. [M2, TRL 4, Q3/2019] 3. Incrementally fabricate and assemble up to 360 m^2 of mirror surface area [TRL 5, 6]
Mass	<2,500 kg	1. Use of monocrystalline silicon to make mirror segments that are geometrically thin and lightweight. [COMPLETE] 2. Use of the modular and hierarchical buildup process to minimize the mass of required mechanical structural and support material.

For an advanced optical assembly like the *Lynx* mirrors, performance must ultimately be viewed in the larger context of the Observatory's overall ability to meet scientific goals. Thus, errors affecting performance must be identified in a flowdown of requirements, and realistically allocated bounds must be assigned at the component or finer level. For the hierarchical meta-shell approach, the error allocations apply to the technology development elements (i.e., fabrication of mirror segments, coating, alignment, and bonding) at the mirror module level, and additional allocations are assigned for aligning and bonding into meta-shells and for aligning and attaching the meta-shells into the mirror assembly. A complete error budget (to be summed in quadrature) for the *Lynx* design, in units of angular distance, is given in Table 7.3. To meet *Lynx* requirements, the technology development plan must be executed within these error allocations at each stage of the process.

Table 7.3. Top-level angular resolution error budget guiding Silicon Meta-shell Optics technology development to meet *Lynx* requirements.

Major Steps	Cumulative HPD Req (arcsec, 2 reflections)	Error Sources	Allocation (or Req) (arcsec HPD, 2 reflections)	Technology Status as of Q1 2019 (arcsec HPD, 2 reflections)	Notes
Optical prescription	0.11	Diffraction	0.10	0.10	At 1 keV, weighted average of diffraction limits of all shells.
		Geometric PSF (on-axis)	0.05	0.05	On-axis design PSF is slightly degraded to achieve best possible off-axis PSF.
Fabrication of mirror segments	0.25	Mirror Substrate	0.20	0.40	Each pair of mirror segments must have a PSF better than 0.2-arsec HPD, based on optical metrology.
		Coating	0.10	0.20	Coating that maximizes X-ray reflectance must not degrade the mirror pair's PSF by more than 0.1 arcsec.
Integration of mirror segments into modules	0.34	Alignment	0.10	0.30	Each pair's image must be located within 0.1 arcsec of the module's overall image.
		Bonding	0.20	0.30	Bonding of a mirror pair must not degrade its PSF by more than 0.2 arcsec.
Integration of modules into meta-shells	0.36	Alignment	0.10	0.10*	Each module's image must be located within 0.1 arcsec of the meta-shell's image.
		Bonding	0.10	0.10*	Bonding must not shift the module's image by more than 0.1 arcsec.
Integration of meta-shells into mirror assembly	0.39	Alignment	0.10	0.10*	Each meta-shell's image must be located within 0.1 arcsec of the overall assembly's image.
		Attachment	0.10	0.10*	Permanent attachment of the meta-shell must not shift its image by more than 0.1 arcsec.
Ground-to-orbit effects	0.43	Launch shift	0.10	0.10*	Launch shift must not degrade PSF by more than 0.1 arcsec.
		Gravity release	0.10	0.14*	Disappearance of gravity must not degrade PSF by more than 0.1 arcsec.
		On-orbit thermal	0.10	0.16*	On-orbit thermal disturbance must not degrade PSF by more than 0.1 arcsec.
Mirror assembly on-orbit performance			0.43	0.70	On-axis PSF of the optics. Add effects of jitter and other effects to get the final Observatory-level PSF.

** Model performance estimates*

7.2.1.1 Key Elements and Milestones

Fabrication of Mirror Substrates — Numerous mirror substrates meeting performance requirements have been fabricated in recent months. Thus, the development work beyond the current TRL will refine the fabrication process to achieve higher efficiency at lower cost, as well as to fabricate a sufficient number of mirror segments (>100) for making multiple mirror modules (TRL 4 and 5) and mirrors of varying optical prescription (TRL 6). Ultimately, tens of thousands of flight-quality mirror segments will be needed for *Lynx*.

The fabrication process steps (Figure 7.3) to be refined and made more efficient in the technology development path start with a commercially procured block of monocrystalline silicon measuring 150 × 150 × 75 mm, into which a conical approximation contour is cut with a band saw and then lapped to generate a precision conical surface that is a zeroth- and first-order approximation to an X-ray mirror segment. A thin top layer is then cut from the block. To remove the damage caused by the cutting and lapping process, the silicon shell is etched in a standard industrial process with an HNA solution, a

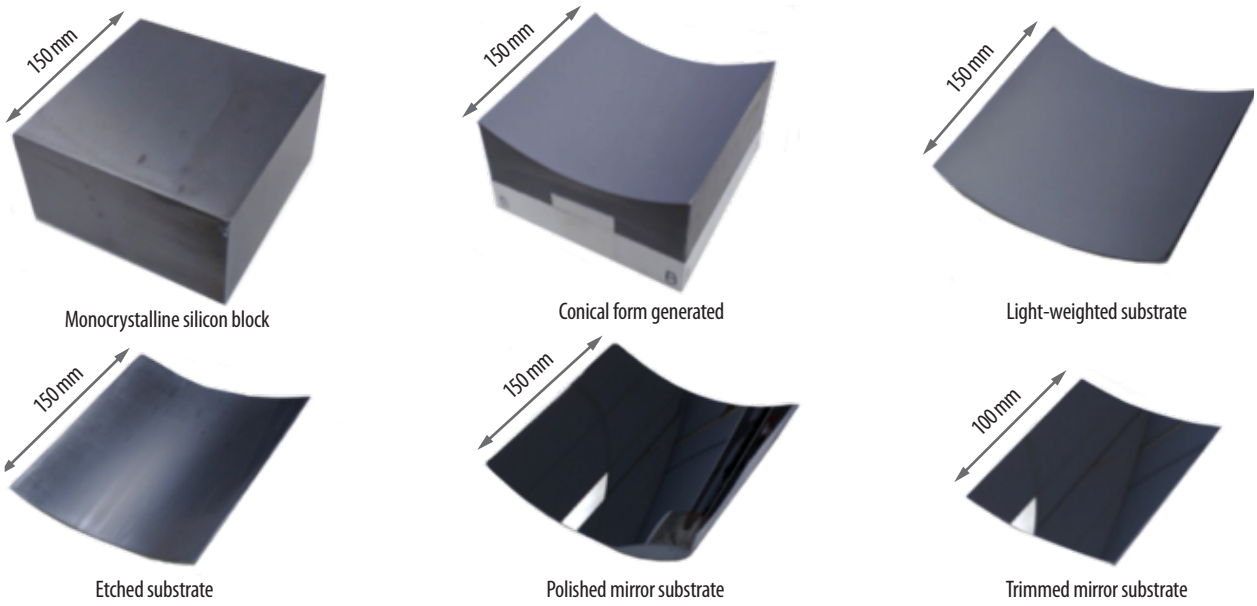

Figure 7.3. Six major steps of fabricating a mirror substrate. The process is highly amenable to automation and mass production methods, leading to high throughput and low cost.

mixture of hydrofluoric, nitric, and acetic acids. Following this etching step, the thin shell is a single crystal, free of any internal stress. The conical substrate is then polished with synthetic silk on a cylindrical tool to achieve required specularity and micro-roughness. This step results in a mirror substrate with a clear aperture of approximately 100 × 100 mm, and 0.5 mm thickness with roll-off errors near the four edges. The areas near the edges are removed with a dicing saw, resulting in a mirror substrate of the required size. The damage along the cut edges is removed via etching to again restore the pristine monocrystalline nature of the substrate.

The final step in fabricating the mirror substrate is a figuring process using an ion beam. The mirror substrate is first measured on an interferometer to produce a topographical map used to guide the ion beam to preferentially remove material where the surface is high.

The development plan for this technology element is to refine this fabrication process. Using no special equipment other than what is commonly available; the entire fabrication process used to complete one mirror segment currently takes about 15 hours labor time and less than two weeks of calendar time.

By TRL 6, a team of scientists, engineers, quality control personnel, and managers who are fully knowledgeable of the entire *Lynx* mirror production process will be in place. This team will include industry partners and other potential technology transfer recipients. At a minimum, as a first step of a technology transfer process, a list of potential suppliers, contractors, and industrial facilities that are technically ready to implement one or more production lines for making mirror segments, modules, and for integrating and testing those modules will be in hand. This plan includes the development of the mirror testing and qualification processes, including both science performance and environmental testing. Given the mass production nature involved in making the LMA, it is critical that there be three separate, efficient qualification processes: one for the modules, one for the meta-shell, and finally, one for the full mirror assembly. This is reflected in the calibration and assembly, integration, and test plans described in §6.6.3.2.

Mirror Coating — The mirror substrate needs a thin film coating to achieve high reflectance and meet effective area requirements. However, this coating introduces stress that can severely distort the figure of a mirror substrate. Preserving the substrate figure therefore requires a way to cancel or otherwise compensate for this effect to prevent the coating from degrading the mirror pair's Point Spread Function (PSF) by more than a budgeted 0.1 arcsecond.

The coating stress compensation plan is shown in Figure 7.4. Using the semiconductor industry's dry oxide growth process, the backside (i.e., the convex non-reflecting side) of the mirror substrate is coated with a layer of Silica (SiO_2). The SiO_2 exerts compressive stress on the substrate, causing it to distort. Then, a thin film of high-reflectivity iridium with an undercoat of chromium serving as a binding layer is sputtered onto the front side.

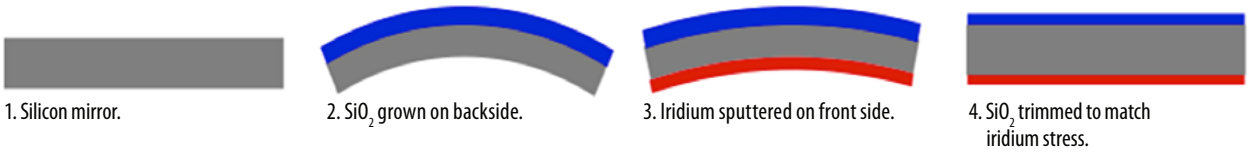

Figure 7.4. Illustration of mirror coating process to enhance X-ray reflectance while preserving the figure quality of silicon substrate: The distortion caused by the stress of the iridium thin film is precisely balanced or compensated for by the stress of the silica on the other side of the mirror substrate.

The compressive stress of the iridium film counteracts the SiO_2 stress and cancels some of the distortion, but significant distortion remains. The final step is to trim the thickness of the SiO_2 layer to achieve precise cancellation of stresses and restore the figure of the substrate. This trimming step is guided by precise figure measurement and finite element analysis.

Two trimming methods for restoring the mirror figure to within the error allotment are being studied. One recently demonstrated method involves the use of hydrofluoric acid chemical etching [590]. Another is through the use of an ion beam, the same as that used for final figuring the silicon substrate. Since ion beam figuring is a dry process, it has the advantage of being cleaner; however, unlike chemical etching, it must be done under vacuum. Both methods are expected to meet stress compensation requirements. In the end, the method with the higher efficiency and lower cost will be used. Refinement through experimentation is expected to be completed by Q3 2019, and mirror segments with the correct physical dimensions (including thickness) and coated with iridium will be built as single-pair modules and tested in Q2–Q4 2020. The condition of the coated surface will be verified with a Zygo surface profiler (or equivalent) to ensure micro-roughness requirements are met, and by X-ray measurement to ensure the effective reflectance requirements are met.

Mirror Alignment — In the Silicon Meta-shell Optics design, each mirror segment will have four supports at optimized locations that necessarily and sufficiently determine the location and orientation of its curved surface (just as three supports are needed for a planar surface). The alignment of the mirror segment is determined by the heights of the four supports. The alignment task is an iteration

of Hartmann measurements using a beam of visible light monitored by a CCD camera (shown in Figure 7.5) and precise grinding of the heights of the supports. The precision required to meet the 0.1-arcsecond budgeted alignment error translates into a support height error of as little as 25 nm in the worst case corresponding to the largest (outermost) radius of curvature. This level of precision is easily achievable with a deterministic grinding material removal process.

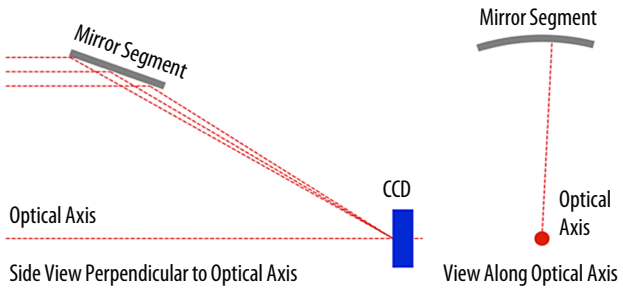

Figure 7.5. Illustration of the Hartmann setup using a beam of visible light to measure the location and orientation of the mirror segment being aligned.

As of early 2019, an X-ray mirror capable of being supported at four points and aligned to about 1 arcsecond Root Mean Square (RMS) error has been repeatedly demonstrated. This error is currently dominated by two metrology factors: (1) the size of the light source and (2) the diffraction of the visible light that degrades the ability to locate the centroids of Hartmann maps, thereby degrading the precision of mirror alignment. Solutions to both of these problems have been identified: a smaller pinhole will be used to reduce the light source size from its current 100 μm to 5 μm, and beam-reducing optics will be used to focus the diffraction spot size from about 30 mm down to 5 mm, significantly increasing the centroiding precision. This work is necessary to achieve TRL 4 and is expected to be completed by the end of 2019.

Co-aligning (and bonding) another mirror segment pair on top of the first (for TRL 5 demonstration) is simply a repetition of the same procedure. The only significant difference lies in the optical prescriptions of the mirror segments. This difference only entails the use of different tooling, which is procured commercially and does not present any technical issue. There is the possibility that the diameter of the supports may need to be made larger than that used in demonstrating TRL 4 to ensure that the module can sustain the vibration test environment. If larger diameter supports have to be used, the support grinding process would need to be refined to ensure an accurate top surface. There is no intrinsic technical difficulty, but additional time and effort would be needed to ensure the completion of TRL 5 demonstration.

Mirror Bonding — Mirror segments are bonded onto the four supports using epoxy adhesive. Figure distortion and alignment disturbance caused by epoxy shrinkage must be minimized such that bonding of a mirror pair does not degrade its PSF by more than the budgeted 0.2 arcseconds.

Bonding the mirror segment is a direct extension of the alignment process. Once the four supports have the correct heights as determined by the Hartmann measurements, the mirror segment is fixed with epoxy and vibrations are applied to help the mirror segment settle in its optimal configuration. The epoxy on each support is spread uniformly and compressed, and the mirror segment is permanently bonded once the epoxy is cured. Any local distortion caused by epoxy cure is minimal, as the diameter of the support is only a few times larger than the thickness of the mirror segment. The 0.5-mm-thick mirror segment is very stiff over the length scale of the support diameter.

As of early 2019, mirror segments have been repeatedly bonded using different epoxies, and multiple variables have been found that can affect the bonding quality: (1) epoxy type, (2) cure strain of the epoxy, (3) epoxy viscosity, (4) diameter of the supports, and (5) surface geometry of the support in contact with the mirror segment. Finite element analyses have reproduced these effects. Numerous additional experiments will be conducted in combination with finite element analyses to quantify the relationships among these variables and arrive at an optimal specification. This work is expected to be completed by Q2 2020. By Q3 2020, it is expected that single-pair modules capable of consistently meeting *Lynx* PSF and effective area requirements (as well as Field of View (FOV) requirements) will be successfully built and tested.

There remains a risk that epoxy shrinkage during cure may cause larger-than-expected figure distortion within the segment "stack" comprising a mirror module. If this risk materializes, the number of mirror segments bonded to a module may need to be reduced, therefore increasing the number of modules needed. This will effectively reduce strength requirements and enable the use of much smaller amounts of epoxy, leading to less distortion. The net consequence of this is a slight reduction in the effective area of the LMA, as more modules will lead to a slightly lower nesting efficiency.

7.2.1.2 Programmatic Considerations

The four basic elements of the Silicon Meta-shell Optics approach have been empirically demonstrated. Further technical and engineering development in the coming years will ready this technology for implementing the *Lynx* mission.

The main challenge for this optics design is the large numbers of mirror segments that need to be fabricated, coated, aligned, and mounted. This is mitigated by the hierarchical approach that reduces the mirror assembly production into a small number of highly repetitive, mature, and efficient routines. Nearly all future technology development steps for the LMA are incremental improvements upon the current TRL. These new developments are similar enough to existing experience that a single development approach may be taken with a high degree of confidence for success. Current NASA investments in Silicon Meta-shell Optics technology development, followed by directed *Lynx* technology development funding, will bring the mirror assembly to TRL 6, well within the schedule for *Lynx*.

The hierarchical approach for building the *Lynx* mirrors is also highly conducive to developing, refining, and perfecting a set of iterative work procedures that involve building and testing many hardware pieces at many different integration levels, guided by optical, thermal, and structural analyses. Thus, reaching TRL 6 will demonstrate that not only can the LMA be made to meet science performance and spaceflight environment requirements, but also that its production procedures meet the stringent schedule and cost requirements outlined in §8.5.2.1 and can be transferred to industrial partners for large-scale mirror production.

7.2.2 Full Shell Optics

The Full Shell Optics option for *Lynx* [591, 592] is a direct fabrication technology with direct lineage to *Chandra* that combines traditional grinding and polishing with precise metrology to produce finely figured, full-circumference mirrors. The advantages of full shells over segments lie in the simplified alignment requirements, the inherently greater structural integrity, and the lower susceptibility to coating-induced stresses and mounting-induced distortions. The direct fabrication process flow

encompasses substrate procurement and initial preparation, successively finer grinding/machining, polishing and super-polishing steps, and final post-fabrication figure correction using ion beam figuring [593] and/or differential deposition [594] techniques.

The full shell optics solution for *Lynx* is based upon low-density and low-coefficient of thermal expansion materials with high elastic modulus and high yield strength, such as lightweight metal alloys, glass, and fused silica. Detailed *Lynx*-specific optical designs and structural, thermal, and mechanical analyses of mirrors and mirror support structures during manufacture, integration, and flight have been provided in the *Full Shell Optics Technology Roadmap.* These analyses and simulations show that the full shell design can meet all scientific, technical, and programmatic evaluation criteria for *Lynx*.

The Full Shell Optics technology has been assessed at TRL 2 by the 2017 PCOS Technology Management Board. This assessment is based on X-ray testing in 2011 [595] of a directly fabricated fused silica shell. This shell was designed to meet the 10-arcsecond requirement of the Wide Field X-ray Telescope (WFXT) concept [596] and performed within a factor of two of that requirement. Direct fabrication Full Shell Optics is being funded by NASA's Internal Scientist Funding Model (ISFM) program at MSFC to develop processes based on lightweight metal and metal matrix composites substrates [592, 597] and by the Italian Space Agency (ASI) at the Brera Astronomical Observatory (OAB) based on glass and glass-like substrate materials [591, 598].

Performance, Issues and Challenges — To date, only moderate-size, ~0.5-m-diameter, thin full shell X-ray optics have been directly fabricated. Larger diameter thin mirrors are unwieldy and susceptible to large-scale distortions or damage during the manufacturing and handling processes. While there is little or no difficulty meeting reduced outer diameter requirements such as the 1.3-m^2 configuration (§10) with full shell technology, potential solutions for large-diameter shell fabrication risks include using alternative substrate materials, thicker substrates, or shell segments of limited azimuth rather than full shells. Another challenge is obtaining measurements of the mirror shell figure throughout the manufacturing process to monitor progress and plan further processing. If metrology cannot be performed in situ, then the production schedule will need to be extended to account for delays due to installation and re-alignment between metrology and fabrication processes.

There are no fundamental physical barriers to achieving TRL 3 and 4 (X-ray test of a modest diameter, breadboard-mounted, coated mirror shell demonstrating ~3 arcseconds or better HPD). Achieving TRL 5 requires multiple two-reflection shells (representing diameters up to 1 m) mounted on a single flight-like support structure and X-ray calibrated. While both mounting and alignment are new developments (e.g., documenting epoxy shrinkage and integrating shrinkage into models), similarity to existing experience is substantial and sufficient to warrant a single development path. Reaching TRL 6 is an extension of the TRL 5 milestone to larger diameter mirror shells. Attaining TRL 6 requires additional (larger) machines that can fabricate mirrors aligned in a vertical orientation. Conceptually, TRL 6 is merely a scaling from TRL 5, but costs are substantial, as are estimated lead times to procure shells and manufacturing hardware.

7.2.3 Adjustable Segmented Optics In development

The Adjustable Segmented X-ray Optics concept is designed to enable the fabrication, alignment, and mounting of lightweight X-ray optics with a figure that can be corrected to the desired precision after assembly. Adjustable X-ray Optics borrow from techniques to remove the blurring effects of atmospheric turbulence in active ground-based optical/Infrared (IR) applications. The technology can potentially ease segment fabrication requirements, thereby reducing segment cost and schedule. In addition to fabrication errors, the addition of addressable actuation is also motivated by the need to correct mounting-induced distortions, reflective coating stresses, and epoxy creep, and by the potential to correct for post-launch environmental (temperature) changes on-orbit.

Actuation is accomplished by the patterning of sputter-deposited Lead Zirconate Titanate (PZT) electrodes and necessary electrical contacts on the backs of individual mirror segment substrates. Applying a low DC voltage across the thickness of the PZT produces a stress in the piezoelectric material that introduces a localized bending of the mirror segment analogous to the bimetallic effect. The resulting "influence function" of the electrode can be well characterized, and algorithms for the overall figure correction of the mirror can be constructed and applied. Applications have been made to 0.4-mm-thick slumped glass (Corning Eagle XGTM), and plans are to use 0.5-mm-thick, single-crystal silicon mirror segments (equivalent to the *Lynx* DRM optics technology) instead.

The technology is currently at TRL 3, as assessed by the 2017 PCOS Technology Management Board. It has been under development jointly by the Smithsonian Astrophysical Observatory (SAO) and Penn State University (PSU), with funding since 2013 through NASA's Strategic Astrophysics Technology (SAT) and Astrophysics Research and Analysis (APRA) programs. A complete *Adjustable Segmented Optics Technology Roadmap* has been prepared for *Lynx*.

Performance, Issues and Challenges — An Adjustable Segmented Optics-based optical point design that satisfies *Lynx* science requirements has been developed, and a detailed imaging error budget is in development. In parallel, developments have led to both a mirror mounting scheme that satisfies the demands of minimizing induced distortions and an optical alignment metrology and processes that align mirror segment pairs to ~0.35 arcseconds RMS diameter. The mirror point design makes use of a modular approach as previously envisioned for Con-X and the International X-ray Observatory (IXO). The present design, which makes use of preliminary structural plans, includes three radial rows of modules — inner, middle, and outer — with 10 inner modules, 20 middle modules, and 40 outer modules. Each mirror segment is 200 mm long (axially), and segment azimuthal spans range from ~100 mm to ~220 mm.

Current development efforts are restricted to smaller mirror segments (i.e., 100 × 100 mm) to avoid large investments in larger PZT deposition and other processing equipment during the early development phase. The key areas to mature to TRL 4 are the addition of Zinc Oxide (ZnO) transistors to facilitate row-column addressing, the alignment of a mirror pair in a proof-of-concept mounting frame, the testing of this mirror pair in an X-ray beamline, and performance validation through simulations. Demonstrating the required TRL 5 performance will include the fabrication and testing of full-sized mirror segments. This will require either an investment in larger processing equipment or partnering with an industry supplier. Other key maturity elements that need to be demonstrated include the addition of strain gauges to monitor mirror figure and partially populating and environmentally testing at least two modules (including mass simulators as needed). The main hurdle in achieving TRL 6 is building and testing a higher fidelity, full-size, multi-module prototype that meets all *Lynx* requirements.

7.3 Science Instruments Development

There are three enabling technologies that provide the full range of imaging and spectroscopic capabilities needed for *Lynx* and define the science instrument suite: (1) the HDXI (§7.3.1); (2) the XGS (§7.3.2), which consists of an XGA mounted along the optical path just aft of the mirror assembly and a matched focal surface X-ray Grating Detector (XGD); and (3) the LXM (§7.3.4).

For the HXDI (and the similarly capable XGD), the *Lynx* team has identified three sensor technologies (discussed in §7.3.1) with the potential to meet all scientific requirements for *Lynx*.

For the XGS, two grating technologies have been identified as feasible for *Lynx*: (1) the CAT (§7.3.2) gratings and (2) the OP-XGS (§7.3.3). Both technologies are expected to meet *Lynx* diffraction efficiency and spectral resolution requirements, and reach TRL 6 well before PDR. The *Lynx* team conducted a trade study (Append B.5.1) in Q3 2018 to recommend one architecture to focus the design for the *Lynx* DRM. This study found that CAT gratings offer more relaxed alignment tolerances, making it easier to integrate within the Observatory and somewhat lower system mass, whereas off-plane gratings have higher diffraction efficiency, thereby requiring less aperture coverage to meet the effective area requirement and a smaller XGD footprint (and power consumption). Ultimately, the CAT-XGS was recommended for the DRM because of relative insensitivity to contamination, ease of implementing thermal controls, and greater simplicity of alignment.

7.3.1 High-Definition X-ray Imager

The HDXI instrument is an imaging X-ray spectrometer capable of achieving a minimum 22-×-22-arcminute² FOV while simultaneously achieving a fine angular resolution of 0.33 arcseconds (≤16-μm pixel size) to directly oversample the PSF of the mirrors. The *Lynx* HDXI configuration adopted for the DRM (§6.3.2) has twenty-one 1,024-×-1,024-pixel sensors arranged in a 5-×-5 tiling with the four corners excluded. The HDXI spectrometer must function at high quantum efficiency over the full *Lynx* bandpass from 0.2 to 10 keV. The HDXI instrument design is derived from the highly successful CCD-based X-ray imaging spectrometers built for *Chandra* and XMM-Newton. The challenge to HDXI sensor technology for *Lynx* is providing both excellent low-energy X-ray response and fine spatial resolution in a rapid readout, low-power operational environment. To meet this challenge, HDXI sensors must satisfy demanding requirements on detector noise, pixel-to-pixel response uniformity, and readout processing.

Three promising sensor technologies are being extensively studied and developed for *Lynx*. The first, hybrid CMOS sensors, under development by Teledyne Imaging Systems, use a thick, fully depleted silicon wafer bump-bonded to a Readout Integrated Circuit (ROIC) with multiple high-speed readouts, low power, and on-chip digitization [599]. Another is a monolithic CMOS sensor in development at Sarnoff Research Institute (SRI) [600] that features in-pixel, high-responsivity sense nodes and on-chip digitization for fast, low-noise operation. And third, an advanced, "digital" CCD being developed at the Massachusetts Institute of Technology's (MIT's) Lincoln Laboratories combines CMOS-compatible

operating voltages and high-speed, on-chip amplifiers with parallel CMOS signal chains for greatly increased framerate and lower power [601]. Each of these sensor technologies is illustrated in Figure 7.6.

The current performance of these three sensor technologies is compared to the *Lynx* requirements in Table 7.4. As can be seen, reducing read noise in the hybrid CMOS architecture, increasing depletion depth of the monolithic CMOS sensors, and increasing framerate in the digital CCD design are the key advancement requirements for the three sensor technologies, respectively.

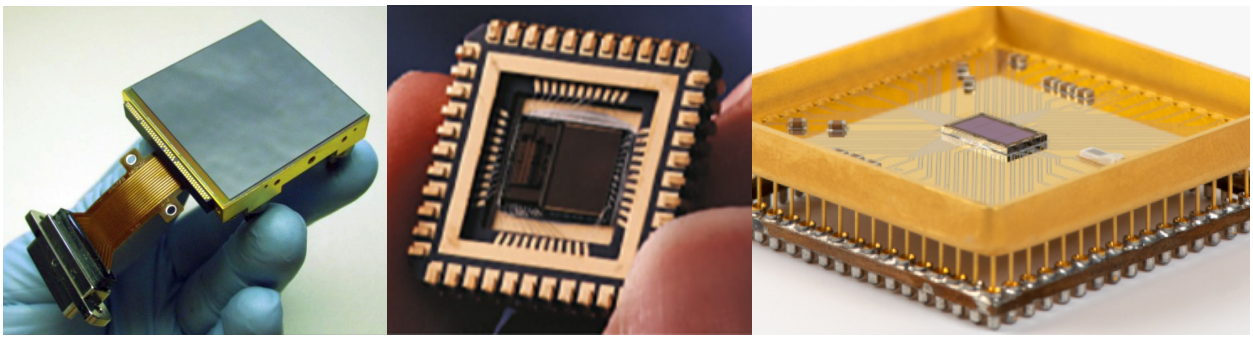

Figure 7.6. Prototypes of three sensor technologies under development for the *Lynx* HDXI. Left to right, these are the Teledyne/PSU hybrid CMOS sensor, the SRI/SAO monolithic CMOS sensor, and the MIT/Lincoln Laboratory's digital CCD.

Table 7.4. HDXI sensor requirements and current performance of a single detector device.

Parameter	Requirement	Current Performance		
		Hybrid CMOS	Monolithic CMOS	DCCD
Pixel size (μm)	≤16 × 16	12.5 × 12.5	16 × 16	8 × 8
Spectral resolution (eV, FWHM) at 0.5 keV at 6 keV	 <70 <150	 78 156	 60 (at 0.183 eV) 150	 Measurement not available 145
Read noise (electrons, RMS)	≤4	5.6	2.9	4.2
Single-sensor framerate (frame/s) × (frame size in Mpix)	≥100 × 1	>100 × 1 breadboard in design	20 × 1	4.7 × 0.5
Depletion depth (μm)	100	100	15	75
ASIC status		Developed; simplifying improvements are planned	In development	Breadboard in design

In addition to advancing the X-ray photon-counting imaging sensor technology, the HDXI technology development plan includes maturing readout electronics specific to each sensor architecture. The sensors convert incoming X-ray photons to electrical signals containing information about photon energy and interaction position, while readout electronics extract this information from sensor output signals and digitize it while also providing the timing and bias voltages required by the sensor. Readout electronics are expected to be implemented with Application-Specific Integrated Circuits (ASICs). Optimizing sensor-specific readout and control functions, operating temperatures, and developing flight packaging are the key advancements for the ASIC signal processors.

Specific milestones have been established along the TRL 6 development path for these elements, as documented and described in detail in the complete *HDXI Technology Roadmap*. The *Lynx* HDXI technology development plan is derived from experience with developing sensor technologies and

ASICs for previous missions by the teams at MIT, PSU, and SAO in consultation with experts at Lincoln Laboratory, Teledyne, and SRI and with support from the *Lynx* engineering and technical teams at MSFC and SAO.

These technologies differ primarily in their architecture, but not in their functionality; each has demonstrated proof of concept. At present, each of these technologies individually meets some, but does not simultaneously meet all, of the *Lynx* HDXI requirements, and each is assessed at TRL 3 for *Lynx* by the most recent PCOS Program Annual Technology Report. Each technology requires similar resources from the spacecraft, and all three have similar development paths. The development plan assumes initially funding all three options to minimize risk. During the course of pre-Phase A activities, a downselection to two technologies will precede a final downselection prior to Phase A.

The pixelated readout sensors for the *Lynx* XGS (§7.3.2) will require many of the same capabilities as the HDXI detectors. Therefore, no separate XGS sensor technology development plan is needed.

7.3.1.1 Key Elements and Milestones

The link between the science drivers and the performance requirements for the HDXI was detailed in §6.3.2. Here, those performance requirements are linked to the strategy to reach TRL 4 by the start of Phase A and to reach TRL 5 and 6 by mission PDR, as outlined in Table 7.5. A few additional performance parameters, such as radiation tolerance and temporal resolution, are omitted here for brevity but included in the full *HDXI Technology Roadmap*.

Table 7.5. HDXI technical requirements and the strategies to meet them.

HDXI Parameter	Requirement	HDXI Development Team's Strategy to Meet *Lynx* Requirements
Quantum Efficiency (excluding optical blocking filter)	≥0.85, 0.5–10 keV >0.1, 0.2–0.5 keV	1. Use of proven silicon wafer processes to develop sensors on high-resistivity material 2. Use of heritage from highly successful *Chandra*/ACIS and *Suzaku/XIS* among others 3. Use of demonstrated entrance window (backside) passivation to enhance low-energy spectral resolution and quantum efficiency
Field of view	22 x 22 arcminute (5k × 5k pixels)	1. Employ four-side abuttable sensors as demonstrated for *WFIRST* 2. Leverage ability to closely pack sensors and associated electronics successfully as shown on many other missions
Framerate—full frame	>100 frames s^{-1}	1. Use highly parallel sensor and readout architectures and high-responsivity output transistors 2. Use current generation Field Programmable Gate Array (FPGA) capabilities to perform event/island detection at these data rates

The sensor technology and associated analog signal processing ASICs are the primary elements of the HDXI that need further development to reach TRL 6 by PDR. Other HDXI electrical elements such as high-speed event recognition processors and large free-standing optical blocking filters require some development, but more importantly, integrated system level testing is required for the complete HDXI system to achieve TRL 6. Thus, the HDXI technology development plan has three major stages: (1) advancing the sensors and ASICs from their present TRL 3 to TRL 4, (2) demonstrating that two sensor/ASIC pairs operating in close proximity meet TRL 5 requirements, and (3) demonstrating that a fully functional, flight-like system of five 1,024-×-1,024-pixel sensor/ASICs with representative event recognition processors (and optical blocking filters) meets all science requirements, operates at required rates, and meets all TRL 6 performance requirements, including appropriate environmental tests. The general technology development strategy for the sensor and readout electronics elements is discussed below.

Two major development efforts are needed to advance the sensor and ASIC technologies to TRL 4. First, several dedicated device fabrication runs (three are planned) must be made to optimize a given sensor. Each such run entails a cycle of design improvement, lithographic mask production, wafer fabrication and test, device packaging, and laboratory characterization. The sensors must demonstrate low-noise performance at representative pixel rate, energy resolution, and quantum efficiency at high and low energies in a representative single-channel sensor before and after exposure to flight ionizing and non-ionizing radiation environments.

Second, and in parallel, several custom ASIC development runs must be made for each sensor technology. As with the sensors, dedicated fabrication runs are required for ASICs. Sensors and ASICs for each of the three technologies will initially be developed in parallel. An external review by subject matter experts and downselection to two sensor/ASIC technologies is planned in Q3 2023. The two ASIC/sensor combinations will then be tested to ensure adequate single- and multi-channel noise performance and radiation tolerance as needed to attain TRL 4 performance.

The risks and challenges to advancing the HDXI technology to TRL 4 are primarily attributable to budget and schedule if all the HDXI requirements cannot be demonstrated on a single architecture over the course of the TRL 4 development process. Funding three sensor technologies in the early stages of the *Lynx* mission is a risk mitigation approach that warrants a high degree of confidence for success based on past experience. A final downselect to a single architecture is planned at the start of Phase A following demonstration of TRL 4 performance.

To demonstrate TRL 5, an integrated system comprising two sensor/ASIC units of representative size operating in close proximity will be constructed and subjected to environmental tests. The two-sensor configuration will simulate multi-sensor focal plane operation, and the environmental testing will include vibration, thermal cycling, and (10-year equivalent) radiation exposure.

Finally, TRL 6 will be demonstrated using an engineering model including a quarter-scale focal plane with five flight-sized sensors and ASICs in a realistic geometry using flight-like sensor-to-ASIC electrical interconnects. This unit will be subjected to full environmental testing.

7.3.1.2 Programmatic Considerations

The HDXI technology development plan outlines significant upfront effort to develop sensors and ASICs optimized for *Lynx*. This process of developing mission-specific pixelated silicon sensors has been successfully executed for numerous astrophysics missions including *Chandra*, *Suzaku*, and *Hubble Space Telescope*, as well as a much larger number of missions outside astrophysics. Lessons learned from these past programs suggest advancement to TRL 4 requires new development that is similar to existing experience but that multiple development approaches should be pursued to provide a high degree of confidence for success. Thus, to reduce risk and ensure performance requirements are met, three separate sensor/ASIC development paths are funded for study early in the HDXI plan. Furthermore, development of large focal planes (as needed for TRL 5 and 6 demonstrations) has considerable heritage in industry, academia, and government laboratories. Achieving TRL 5 and 6 requires only straightforward engineering processes that will be tailored for the development of a configuration representative of the HDXI focal plane for testing across the range of anticipated environmental conditions. Finally, sufficient funded schedule reserve will be in place to mitigate the (low) risks of sensor/ASIC fabrication delays, the need for additional fabrication cycles to meet performance requirements, and additional packaging development effort.

7.3.2 Critical-Angle Transmission X-ray Grating Spectrometer

The *Lynx* XGS will provide high-throughput, high resolving power (R >5,000) spectra over the soft X-ray energy band. The XGS is comprised of the XGA mounted along the optical path just aft of the mirror assembly and the XGD located on the Integrated Science Instrument Module (ISIM) (§6.3.3; readout array performance requirements are similar enough to those of the HDXI that its development path is addressed in §7.3.1.)

The CAT grating design combines the high diffraction efficiency of specular reflection at grazing angles of incidence below the critical angle with the orders-of-magnitude relaxed alignment tolerances of transmission gratings to preserve the exquisite *Lynx* angular resolution in the resulting diffracted spectra leading to high spectral resolving power.

The CAT grating design combines the high diffraction efficiency of specular reflection at grazing angles of incidence below the critical angle with the orders-of-magnitude relaxed alignment tolerances of transmission gratings to preserve the exquisite *Lynx* angular resolution in the resulting diffracted spectra leading to high spectral resolving power.

The CAT grating is a blazed dispersive transmission grating optimized to achieve maximum efficiency in high diffraction orders near the astrophysically important, He-like O VII line energies. CAT grating bars are inclined by an angle less than the critical angle of total external reflection, relative to the incident X-rays, efficiently blazing into diffraction orders near the angle of specular reflection from the grating bar sidewalls (Figure 7.7).

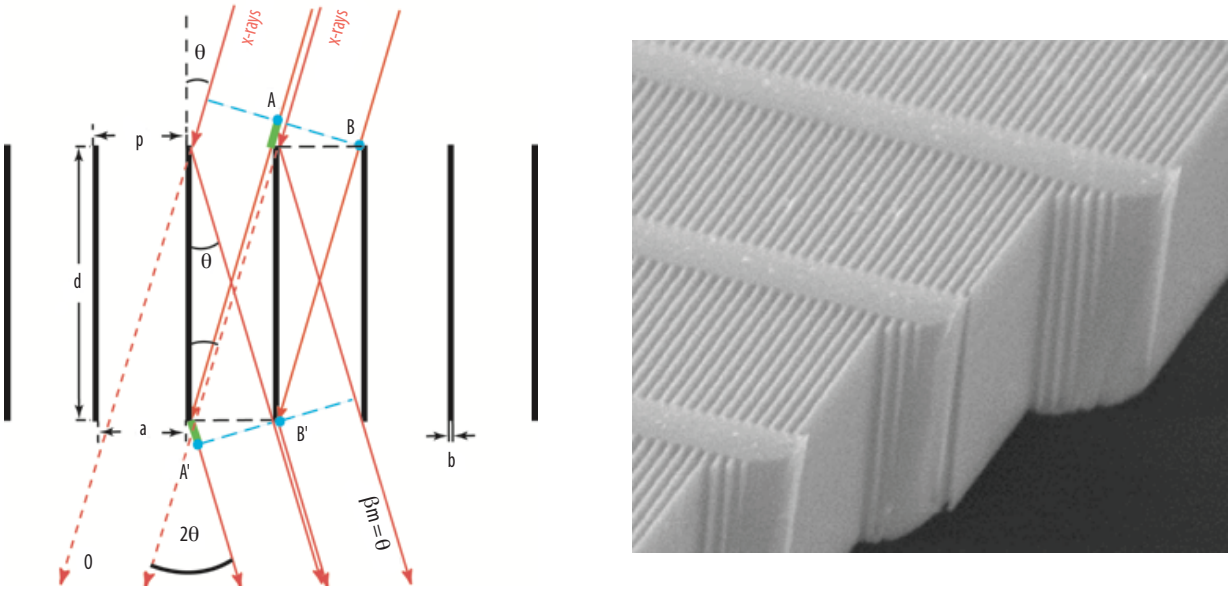

Figure 7.7 (Left) Schematic CAT grating of period p. The m^{th} diffraction order occurs at an angle β_m where the path length difference between AA' and BB' is $m\lambda$. Shown is the case of blazing in the m^{th} order where β_m coincides with the direction of specular reflection from the grating bar sidewalls ($|\beta_m| = |\theta|$). (Right) Scanning electron micrograph of a cleaved free-standing silicon grating membrane with 200-nm period grating bars and 5-μm period cross supports.

CAT gratings are being fabricated at MIT's Space Nanotechnology Laboratory; the same laboratory that produced gratings for *Chandra*, the *Solar and Heliospheric Observatory* (SOHO), the *Imager for Magnetopause-to-Aurora Global Exploration* (*IMAGE*), the *Geostationary Operational Environmental Satellite* (*GOES*), *Two Wide-Angle Imaging Neutral-Atom Spectrometers* (*TWINS*), and the *Solar Dynamics Observatory* (*SDO*). The full *CAT-XGS Technology Roadmap* has been developed by the CAT grating team at MIT with support from the *Lynx* engineering and technical teams at MSFC. The *Lynx* design is based on the Rowland torus concept used by the *Chandra* High-Energy Transmission Grating Spectrometer (HETGS; [607]), which was also built by MIT. The initial CAT grating design was conceived in 2005, and the technology has been under development since 2007 principally through NASA's APRA and SAT funding programs. The 2017 PCOS Program Annual Technology Report assessed the CAT-XGS technology at TRL 4.

CAT gratings are fabricated from Silicon-On-Insulator (SOI) wafers. The grating bars (Figure 7.8) and integrated Level 1 (L1) support structures are etched from the 4- to 6-µm-deep device layer side of the wafer, and a stiffer, hexagon-shaped Level 2 (L2) support mesh is etched from the thicker opposing handle layer, with the buried SiO_2 insulator layer between them removed from the open areas (Figure 7.8; center).

The resulting grating membrane (Figure 7.8; right) is bonded to a narrow frame comprising a grating facet. Hundreds or possibly up to 2,000 co-aligned and mounted facets (depending on facet size) are needed to populate a Grating Array Structure (GAS) for *Lynx* that densely tiles a large enough fraction of the mirror aperture to collectively meet the system effective area requirement.

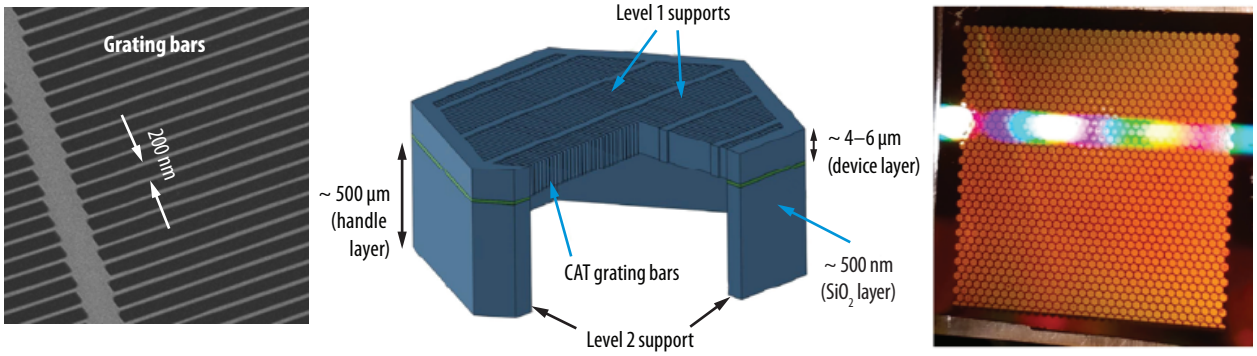

Figure 7.8. (Left) Micrograph of CAT grating bars. (Center) Schematic of CAT grating "unit cell" showing the structural hierarchy (not to scale). (Right) A 32-×-32 mm² CAT grating membrane. Note the honeycomb structure of the unit cell's hexagonal L2 mesh and the visible light diffraction due to the aligned L1 mesh in the device layer.

Grating membranes of 32 × 32 mm^2, yet slightly thinner than required for *Lynx*, have been fabricated, and individual platinum-coated facets of 10 × 30 mm^2 have demonstrated R >10,000 in 18th-order using Al-Kα radiation and illumination with an ~1-arcsecond mirror pair (Figure 7.9; [602, 605]). Facets with the same parameters have undergone thermal and vibration testing without any loss in X-ray performance [603]. These particular facets provide ~30% diffraction efficiency [604], which would fall short of the baseline design for *Lynx* by ~20%. Nevertheless, all the basic concepts of a CAT grating spectrometer have been demonstrated.

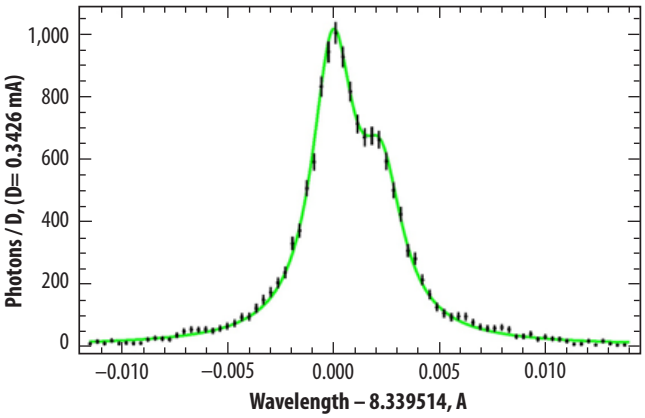

Figure 7.9. Spectrum of Al-K_α doublet (1.49 keV) in 18th-order from a single platinum-coated CAT grating measured at the NASA MSFC Stray Light Test Facility demonstrating R >10,000.

The MIT Space Nanotechnology Laboratory is currently producing 200-nm-period CAT gratings with 4-μm depths and 60-nm grating bar widths and facet areas up to 32 × 32 mm^2. The baseline design for *Lynx* calls for 5.7-μm-deep, 40-nm-wide grating bars with 200-nm period.

The CAT grating array optical design for *Lynx* has been developed using geometric ray-trace simulations [606] based on the DRM design mirror properties, grating sizes, and other grating properties, and optimized for resolving power. The main error terms for resolving power are misalignment and placement of individual grating facets, misalignment and placement of the grating array as a whole, grating facet period distortion, thermal gradients, aberrations in the optical design, deviation of detector surface from ideal placement (static and dynamic), and readout sensor pixelation.

7.3.2.1 Key Elements and Milestones

The key elements of the CAT-XGS design requiring maturation are improving the system effective area and preserving the spectral resolution. While preliminary ray-trace simulations supporting these design elements have been performed, additional work is anticipated in parallel with any future mirror assembly design modifications because the grating array layout is specific to the mirror assembly characteristics.

System Effective Area — Increasing grating depth increases diffraction efficiency, and reducing bar width increases throughput. While etching ultra-high-aspect ratio structures on the nanometer scale is challenging, the required etch depth has already been achieved using tools developed for the semiconductor and Micro-Electrical Mechanical Systems (MEMS) industries. Specifically, grating bars with 200-nm pitch, 6-μm depth, and L1 structures of the needed dimensions have been etched from bulk silicon using Deep Reactive-Ion Etching (DRIE), followed by a short potassium hydroxide polish to create nanometer-smooth grating bar sidewalls. Fabrication of a full grating membrane from an SOI wafer with the required device layer thickness will be part of TRL 5 development (Q4 2019). To further increase geometric throughput, all the support structures (L1, L2, and facet frames) need to be thinned by small amounts without compromising structural, thermal, or mechanical integrity. Larger

grating membranes will increase throughput and system effective area. Grating facets of 60 × 60 mm² are planned for TRL 6 demonstration (Q4 2022). The main challenge for the CAT-XGS fabrication of large-area grating facets with the required performance is process development on SOA fabrication tools from the semiconductor and MEMS industries, as well as development of some custom fabrication steps and optimization of support structures with the goal to maintain launch survival and to minimize membrane distortions due to bonding into facets. The larger the membrane area, the smaller the number of required grating facets, and the lower the ultimate cost of the grating array.

Spectral Resolution — Large grating facets are desired for reducing production schedule and cost and for improving throughput. However, large flat facets cannot continuously match the curved Rowland torus surface (§6.3.3.1). Deviations lead to aberrations that broaden the diffracted Line Spread Function (LSF), thus reducing resolving power below requirements for the largest facet sizes considered. The use of chirped gratings (i.e., imposing a variable grating period over the membrane) promises to recover resolving power. Current developments include patterning methods for 200-nm-period CAT gratings using 4× projection lithography with e-beam written masks, as is standard in the semiconductor industry. Fabricating large membranes with period chirp is scheduled for TRL 6 (Q3 2023).

Mounting and alignment distortions of grating membranes and facets need to be kept low to prevent grating period variations from impacting resolving power. The *Lynx* CAT grating array will consist of a large number of grating facets that must be arrayed on the Rowland torus to within well-defined tolerances. Facet alignment and bonding equipment and facet-to-GAS alignment and mounting equipment (including metrology infrastructure) will need to be designed, procured, and applied to reach TRL 5 brassboard (Q2 2021) and TRL 6 prototype (Q4 2023) demonstrations. The *Lynx* XGS strategy to meet science requirements is shown in Table 7.6.

Table 7.6. XGS requirements derived from *Lynx* science drivers and the strategy of the CAT grating technology to meet them. Values in [ ] refer to milestones, TRL, and expected completion date as given in the full *CAT-XGS Technology Roadmap*.

***Lynx* X-ray Grating Spectrometer Requirements Derived from Science Requirements**		**CAT XGS Strategy to Meet *Lynx* Requirements**
System effective area at OVII lines	4,000 cm²	1. Increase diffraction efficiency by fabricating deeper device layer (grating bar depth) [M1, TRL 5, Q4 2019] 2. Increase geometric throughput by decreasing obstruction due to support structures [M2,3, TRL 5, Q2 2020] 3. Fabricate larger grating membranes [M11, TRL 6, Q4 2022] 4. Fabricate thinner grating bars to increase throughput and diffraction efficiency [M9, TRL 6, Q4 2022]
Resolving Power	$R > 5{,}000$	1. Develop concept and metrology infrastructure for mounting and alignment to preserve LSF [M4, TRL 5, Q3 2020] 2. Develop "chirped" gratings to maintain LSF of large membranes [M12,13, TRL 6, Q3,Q4 2023]

7.3.2.2 Programmatic Considerations

Advancing from the demonstrated SOA to the *Lynx* performance requirements will require several stepwise advancements in grating fabrication, facet assembly, and precision alignment on the integrated grating assembly. However, there are no known physical barriers to achieving the required capabilities (i.e., formulating and applying the processes needed to produce the required number of finished

grating membranes, facets, and array structures are extensions and refinements of current practices). Identified risks are primarily matters of production and manufacturing scale and can be mitigated by design conservatism. For example, the system effective area requirement can ideally be met by reducing support structure obscuration as planned or by increasing the mirror aperture coverage from the current ~65%. The latter incurs greater mass and cost but remains a viable option lowering the overall risk posture. Steady and reasonable investment in technology development through NASA SAT funding, followed by *Lynx* technology development funding, is expected to bring the CAT-XGS to TRL 6 by Q3 2024, well in advance of mission PDR.

7.3.3 Off-Plane Reflective Grating Spectrometer

The reflection grating (also referred to as off-plane gratings or OP-XGS) concept for *Lynx* [608] is an alternative to the DRM grating architecture with a fully-developed *OP-XGS Technology Roadmap*. The reflection grating design utilizes a blazed grating to intercept light exiting the telescope optic to create a high-resolution dispersed spectrum. The light is incident nearly parallel to the grating grooves at grazing incidence. The small graze angles at X-rays allow close stacking of the gratings commensurate with the nesting of the X-ray optics. Large-format (~100-×-100-×-0.5-mm^3) gratings are fabricated using standard nanofabrication techniques [609]. The process begins by writing the groove pattern into a resist using an electron beam lithography tool. This pattern is transferred into a substrate to produce a master grating that can then be replicated hundreds to thousands of times using standard techniques such as substrate conformal imprint lithography. Once the gratings are replicated, they are aligned and mounted into modules appropriate to the telescope optic.

The OP-XGS reflection grating technology has been assessed at TRL 4 by the 2017 NASA PCOS Technology Management Board. The concept has been recently demonstrated on the suborbital *Water Recovery X-ray Rocket* (*WRXR*; [610]) and is slated to fly on the *Off-plane Grating Rocket Experiment* (*OGRE*; [611]). The latter includes a 12-shell polished silicon optic similar to the *Lynx* baseline design. Experiments using similar gratings [608] have demonstrated diffraction efficiency over 60% (exceeding the *Lynx* estimated requirement of 40%) and resolving power of R = ~8,000 (*Lynx* requirement is R = 5,000). The specific technology described here has been under development at PSU (and formerly at the University of Iowa) since 2011 through funding by NASA's SAT, APRA, and Roman Technology Fellowship (RTF) programs.

Performance, Issues and Challenges — The OP-XGS design requires a smaller fractional occultation of the mirror aperture, allows for a wider working energy range (0.2 to 2 keV), and a smaller focal plane footprint (fewer focal plane sensors) relative to the baseline CAT-XGS. However, the OP-XGS has more restrictive alignment tolerances and a greater mass XGA than the CAT-XGS design. The alignment allocation, including sensitivity to repeated insertions and retractions of the XGA, is captured in the overall error budget. As with the CAT-XGS, the XGS system resolving power is affected by these alignments and by other tolerances within this error budget.

There are two main challenges for the OP-XGS technology development. First, while blazed gratings have been fabricated for high efficiency and radial profiles (needed to diffract the converging telescope beam) have been fabricated for high resolving power, a large-format, radial blazed grating has not been tested to demonstrate both concurrently. At least four methods are under study that can

potentially be used to fabricate gratings of the required geometry. The highest risk for the most viable of these options is a decrease in diffraction efficiency because of increased scattering due to roughness caused by the radial profile not following the crystal structure of the silicon substrate.

The second challenge is achieving alignment per stringent *Lynx* requirements. A full error budget has not yet been validated specific to *Lynx*, but contributions have been identified that include grating-to-grating alignments within a module, module-to-module alignments within the array, array-to-mirror alignments, and mirror + XGA alignment to the focal plane. These alignments, along with factors such as the details of the telescope PSF, pointing knowledge, and detector pixelation will form the error budget for the spectral LSF, which will ultimately determine the performance of the OP-XGS. Concept designs and initial calculations argue that the tightest translational tolerance is on the order of 100 μm (1 σ), while the tightest alignment tolerance is around 5 arcseconds (1 σ). The WRXR grating module demonstrated ~10s of arcseconds (1 σ) angular alignment and translation alignments better than 100 μm (1 σ).

7.3.4 *Lynx* X-ray Microcalorimeter

LXM requires an over 30-fold increase in the number of X-ray absorbers (pixels) compared to *Athena*'s X-ray Integral Field Unit. This is being realized through significant technology investment that has already demonstrated (1) thermal multiplexers (a.k.a., "hydras") linking 25 pixels to a single temperature sensor; (2) fine-pitch, multilayer, superconducting wiring buried beneath planarized substrates—leveraged from superconducting digital electronics and quantum computing developments—enabling wiring of large-format arrays; and (3) readouts using Superconducting Quantum Interference Devices (SQUIDs) coupled to microwave resonators—using technology pioneered for infrared detectors—for a 10-fold advancement in the number of sensors read out on each signal chain without loss of energy resolution. A full-size, 102,800-pixel, *Lynx* X-ray Microcalorimeter array is under development today with fabrication scheduled for completion in 2019.

The LXM is a broadband, energy-dispersive, high spectral and spatial resolution imaging spectrometer focal plane instrument (§6.3.4). The LXM X-ray absorbers and sensors, operating at 50 mK, precisely determine incident photon energies by measuring the temperature rise from the heat they deposit. The LXM instrument concept builds upon substantial experience in developing microcalorimeter instruments for space, including *Astro-E*, *Astro-E2*, *Hitomi*, the *X-ray Imaging and Spectroscopy Mission* (*XRISM*) (launching in 2022), and *Athena* (slated for launch in 2031). The major technological differences of LXM from these predecessors are the 30-fold increase in the number of absorbers (10^5 pixels), their much finer pitch (25 to 50 μm), and the improved spectral resolution for a lower energy range subarray (<0.3 eV Full-Width Half-Maximum (FWHM)).

The LXM concept has been advanced by scientists and engineers from several low-temperature X-ray detector groups in the U.S. Key members of this group located at GSFC have substantial experience in developing all the microcalorimeter instruments listed above; most apropos being *Athena's* X-ray Integral Field Unit (X-IFU). Members of this group working on LXM are funded through NASA's APRA, SAT, and ISFM programs.

There are four elements to be matured from the current SOA to TRL 6 for the LXM: (1) the arrays of detectors, (2) the readout electronics, (3) the Focal Plane Assembly (FPA) and optical/IR photon blocking filters, and (4) the cryogenic cooling system. These technology elements were collectively assessed by the 2017 NASA PCOS Technology Management Board for *Lynx* at TRL 3; however, the first element is expected to reach TRL 4 before this year is out, the second element within another year, and the third and fourth elements are already at TRL 4. Parallel development paths are actively being funded for most of these elements, greatly enhancing the potential for rapid advancement while helping reduce technical and schedule risk. Detailed development plans for all baseline and alternative technologies are provided in the complete *LXM Technology Roadmap*.

To meet all the science objectives for *Lynx*, the LXM design consists of three types of pixel arrays with different performance capabilities. These are referred to as the Main Array (MA), Enhanced Main Array (EMA), and Ultra-High-Resolution Array (UHRA). Required performance characteristics for each array are listed in Table 6.11 of §6.3.4.1. The SOA performance of these arrays and of the associated multiplexing readout electronics are compared to the *Lynx* requirements in Table 7.7.

Table 7.7. LXM array and readout electronics derived requirements and current performance.

Parameter	Requirement	Current Performance		
Pixel Array	**MA / EMA / UHR**	**Main Array**	**Enhanced Main Array**	**Ultra-Hi-Res Array**
Pixel pitch (μm)	50 / 25 / 50	50	25	50
Array size	86,400/ 12,800 / 3,600	37,500	10,000	1,600
Hydra Factor	25 / 25 / 1	25	25	1
Spectral resolution in large-format prototype array (FWHM eV): Comment:	MA: 3 eV up to 7 keV EMA: 2 eV up to 7 keV UHRA: 0.3 eV up to 0.75 keV	Int. NEP $_{(no\ X\text{-}T)}$ = 2.7 eV Measured FWHM: 3.3 eV @ 1.5 and 6.4 keV No heat-sinking => high cross talk	Int. NEP$_{(no\ X\text{-}T)}$ = 1.2 eV Measured FWHM: 1.7 eV @ 1.5 keV (No heatsinking => high crosstalk)	Int. NEP $_{(no\ X\text{-}T)}$ = 0.26 eV Measured FWHM: 0.26 eV @ 3, 6 and 9 eV (Not yet measured at higher energies)
Performance in similar pixel type in other arrays		Measured FWHM in 20-absorber hydras (50 μm, 4.2 μm thick): 3.4 eV @ 5.4 keV	–	Measured FWHM in absorber of 4.2 μm: 0.7 eV at 1.5 keV
Multiplexing Readout				
Electrical multiplexing: Resonators/HEMT	400 / 100 / 667	128 TESs on single HEMT through 128 μMUX SQUID resonators (with 2-MHz bandwidth)		
Resonator bandwidth	1.4 MHz / 5.6 MHz / 0.86 MHz	Resonators of this BW successfully tested	Resonators produced – not yet tested	Resonators of this BW successfully tested
Resonator spacing	10 MHz / 40 MHz / 6 MHz	Most demanding spacing (6 MHz) demonstrated in 128-TES demonstration		

Int. NEP is the integrated Noise Equivalent Power, which is a measure of the achievable energy resolution calculated from the measured signal from X-ray events (responsivity) and the quiescent noise excluding thermal background crosstalk events (no X-T)

A fully wired **microcalorimeter array** prototype using the baseline Transition-Edge Sensor (TES) detector technology has been fabricated with over 55,000 pixels representing all three array types [612]. A full-size LXM microcalorimeter array is under development, with fabrication scheduled to be completed in late 2019. A central component of the MA and the EMA technology is the use of hydras linking multiple X-ray absorbers (pixels), each with a different thermal coupling, to a single TES microcalorimeter. The thermal conductance of each link is tuned so that the TES measures a different characteristic temperature profile for X-ray events absorbed in the different pixels (Figure 7.10). The shape of the pulse is measured to determine the event position.

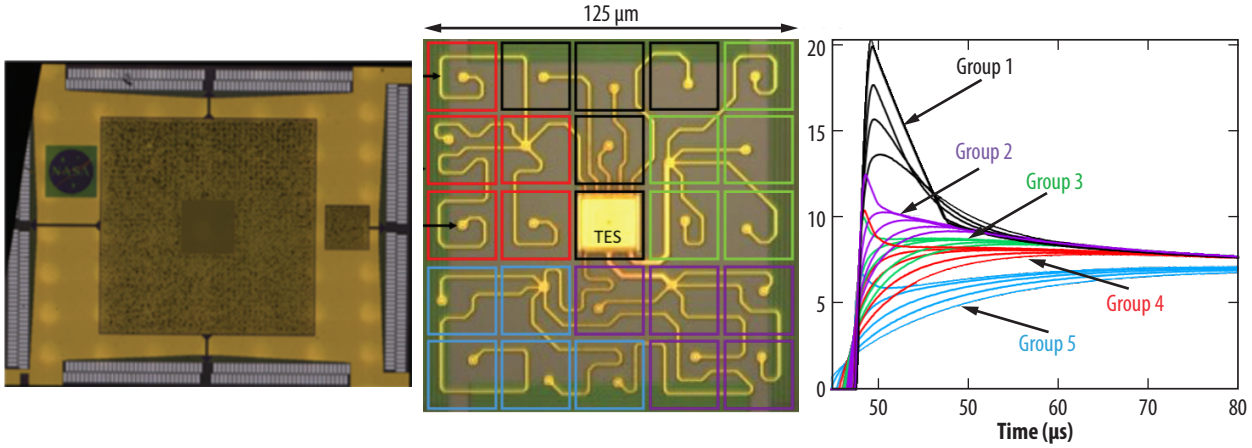

Figure 7.10. (Left) 50,000-pixel two-thirds linear scale LXM prototype detector array. The large square in the middle is the MA surrounding the EMA at its center. The UHRA is to the right. (Center) Single 25-pixel EMA hydra (25-µm pitch) prior to depositing absorbers. Colored squares delineate absorber locations. The TES is the large central square, the small dots are pixel contact stems, and narrow lines are thermal links connecting absorbers to the TES. Note the four "trunks," each "branching" into four more stems for a total of five pixels for each of five hydra groups (one trunk is the TES itself). (Right) Measured pulse shapes for all 25 pixels color-coded by group corresponding to center panel.

For use as an effective spectrometer, the combination of signals from all pixels in a hydra needs to produce a narrow spectrum, as shown [613] for the MA and EMA in Figure 7.11, ensuring high system energy resolution. The UHRA uses single-pixel detectors to maximize the energy resolution at low photon energies. The energy resolution of the UHRA has also been characterized (Figure 7.11, right panel), but not yet at representative energies because of the difficulty in producing a photon source with a sufficient intensity of 3 eV photons per pulsed laser-diode event.

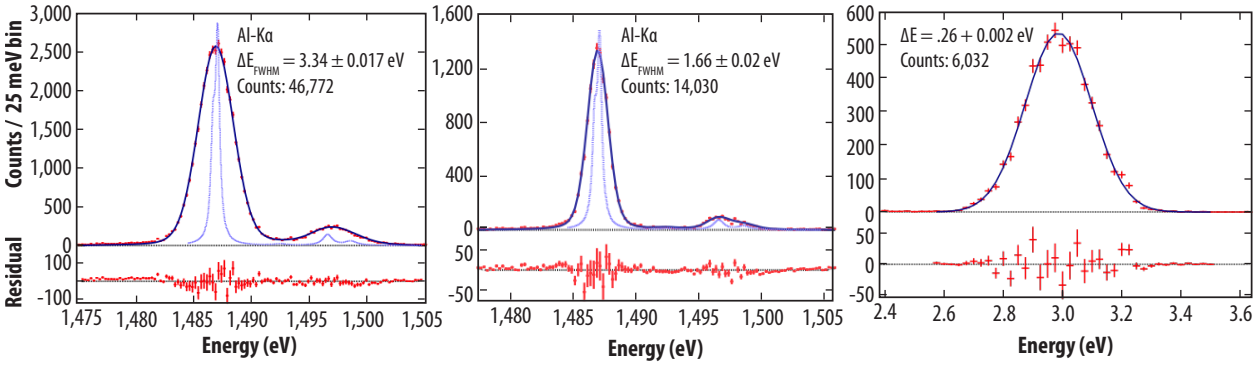

Figure 7.11. X-ray spectra measured by prototype LXM sensor arrays. (Left) Co-added Al-Kα for all 25-pixel MA hydras. (Center) Co-added Al-Kα for all 25-pixel EMA hydras. (Right) Single-absorber UHRA spectrum of a narrow-line ultraviolet laser diode source at 3 eV.

These first prototype arrays fabricated specifically for LXM incorporate microstrip-buried wiring layers, developed through a collaboration between GSFC and MIT Lincoln Laboratory. They are of suitable pitch and density to read out a full-scale array; however, the prototype does not yet incorporate a heatsink layer required to prevent noise from thermal crosstalk degrading the energy resolution. Improvements estimated for a device with suitable crosstalk heat-sinking are within LXM energy resolution requirements.

Readout electronics based on microwave SQUID multiplexing of up to 128 TESs have demonstrated good performance without energy resolution degradation from the readout [614, 615]. These demonstrations have shown microwave SQUID multiplexing is capable of providing the necessary bandwidth for single-absorber TESs, and components spanning the necessary parameter space to read out the high slew rates of the multi-absorber hydra microcalorimeters have been experimentally proven. The current technology assessment is TRL 3 because the readouts designed for each of the specific LXM pixel types have not yet been tested with LXM microcalorimeters and are likely to require some further iteration [616].

The microcalorimeter array, anti-coincidence detector, and cold readout components are packaged inside a **focal plane assembly** (**FPA**). At the instrument base temperature, the FPA provides thermal-mechanical isolation and electromagnetic shielding. The LXM will leverage much of the same technology in the mechanical design, thermal design, magnetic shielding, and design of the anti-coincidence detector as *Athena*'s X-IFU FPA [617] and is assessed at TRL 4. The design of the LXM FPA is summarized in [612]. The LXM will use a set of blocking filters mounted within the dewar that transmit the X-rays of interest while attenuating longer wavelengths to prevent performance degradation of the microcalorimeters and cooling chain [618]. Current technologies meeting LXM requirements are at TRL 4. Additional development will leverage highly from *Athena*'s X-IFU. Optical/IR blocking filters are at TRL 5.

The cryogenic **cooling system** envisioned for LXM is also assessed at TRL 4. Many cryostats have already been developed for space-based applications, and many cryocoolers that integrate into them are under development in the commercial sector. As the *Lynx* FPA develops, the cryocooler definition will improve, the vibration requirements will be better refined, and designs specific to *Lynx* will reach higher fidelity. Part of the cryogenic system, the Adiabatic Demagnetization Refrigerator (ADR), provides the 50-mK cooling, as has been demonstrated on *Hitomi* by an ADR lifting 0.4 μW from the detector array. To achieve the estimated 6 μW of cooling needed for the LXM, a Continuous ADR (CADR) will be needed. CADRs have been demonstrated at TRL 4 with four cooling stages operating between 4.5 K and 50 mK. For the LXM, a fifth stage operating continuously at 0.6 K must be demonstrated.

7.3.4.1 Key Elements and Milestones

Development paths for each of the four elements to be matured for LXM are outlined below. Table 7.8 lists the strategic approach used to mature these elements to meet the *Lynx* scientific goals.

Table 7.8. *Lynx* requirements on the LXM derived from its science drivers and the strategy of the LXM technology to meet them

Main Array	Requirement	LXM Development Team's Strategy to Meet *Lynx* Requirements
Energy Range	0.2 to 7 keV	Energy range is set by (1) design of TES transition width, (2) pixel heat capacities, and (3) readout capability. Already shown that (1) and (2) are possible up to 7 keV. Will trade detector energy resolution with readout capability to allow standard energy range >7 keV in normal operating mode and will adjust bath temperature (energy resolution) for mode extending to 15 keV.
Field of view	5 arcmins x 5 arcmins	The use of hydras with 25 pixels attached to each sensor and high-yield buried multilayered superconducting wiring makes this feasible with only a factor of 2 more sensors than *Athena*'s X-IFU. Prototypes with half this FOV area (two-thirds the linear dimension) have already been fabricated with wiring pitch consistent with fabrication of full-size array.
Pixel size	1 arcsec x 1 arcsec	Ion-milling of all-gold absorbers with the required quantum efficiency on 50-μm pitch has already been demonstrated. Area fill factor will be further optimized but current fill factor already acceptable.
Energy Resolution	3 eV (FWHM)	Have demonstrated 3.3 eV for 1.5 and 6.4 keV X-rays in a 25-pixel hydra, and have shown sensitivity will be <3 eV when suitable heat-sinking incorporated. Will optimize absorber thickness and TES design to optimize resolution and ease of readout.
Enhanced Main Array	**Requirement**	**LXM Development Team's Strategy to Meet *Lynx* Requirements**
Energy Range	0.2 to 7 keV	Strategy same as for main array.
Field of View	1 arcmin × 1 arcmin	Strategy similar to that of main array. Use 25-pixel hydras attached to each sensor and high-yield buried multilayered superconducting wiring.
Pixel Size	0.5 arcsec × 0.5 arcsec	Strategy same as for main array.
Energy Resolution	2 eV (FWHM)	Have demonstrated sensitivity in suitable 25-pixel hydras of 1.6 eV at 1.5 keV. Will optimize absorber thickness and TES design to optimize resolution and ease of readout.
Ultra-High-Resolution Array	**Requirement**	**LXM Development Team's Strategy to Meet *Lynx* Requirements**
Energy Range	0.2 to 0.75 keV	Basic strategy similar to main array, but main development and focus is on the engineering of the TES transition properties.
Field of View	1 arcmin × 1 arcmin	Fully wired full-size arrays utilizing buried superconducting multi-layered wires have already been designed, fabricated and tested. The FOV of this subarray is not a driver of technology development.
Pixel size	1 arcsec × 1 arcsec	Strategy same as for main array.
Energy Resolution	0.3 eV (FWHM)	This energy resolution has already been demonstrated for low-energy photons and needs to be demonstrated at energies in the bandpass of interest. Transition width will be engineered to optimize energy resolution and energy range to meet simultaneous requirements.
Readout	**Requirement**	**LXM Development Team's Strategy to Meet *Lynx* Requirements**
Flight qualify suitable HEMT amplifiers	HEMTs must adhere to requirements for > 10-years at L2.	Will flight-qualify suitable HEMT amplifiers working together with a suitable HEMT manufacturing company.
Microwave SQUID resonator components.	Readout (μMUX SQUID resonators) must meet noise, bandwidth, and resonator spacing requirements of each LXM subarray.	Design, fabricate, and test microwave SQUID circuitry with the appropriate noise level resonator bandwidths and resonance frequency spacing for the LXM to demonstrate that subarrays can be read out without significant energy resolution degradation from the readout. Special care will be taken to minimize crosstalk between signals at different resonator frequencies. Parallel technology effort to develop code division multiplexing option until TRL 5 is established by a readout technology.

Table 7.8. *Continued*

FPA	Requirement	LXM Development Team's Strategy to Meet *Lynx* Requirements
Magnetic shielding	Shielding factor $> 6 \times 10^5$ Ambient field < 1 μT	Use identical approach to magnetic shielding as has been developed and proven for the *Athena* X-IFU
Electrical wiring/ contacts	44 coaxial cables from 283 K to 50 mK	Regular semi-rigid coax cables from room temperature to HEMTs at 4.5 K. Will verify thermal conductance of low thermal conductivity of superconductivity coax cables for use from 4.5 K to 50 mK. Will integrate superconducting bump bonds for connections between TESs and μMUX readout. Will use superconducting microstrip flex under development at GSFC between detectors and readout.
Mechanical mounting	Kinematically mount detector and readout chips. Support low temperature stages with rigid low thermal conductance supports.	Implement application-specific kinematic mounting techniques developed for mounting filters on *Hitomi* SXS and evolved for the *Athena* X-IFU. Develop and test low thermal conductivity thrust cones between lowest temperature stages using low thermal conductivity thin fiberglass structures.
Cryogenics	**Requirement**	**LXM Development Team's Strategy to Meet *Lynx* Requirements**
Cooling from 283 K to 4.5 K	50 mW @ 4.5 K High reliability	Use of 4-stage pulse-tube cryocooler specially designed to meet cooling requirements as well as cooling of 3 thermal shields at intermediate temperatures. Parallel option of using 3-stage Turbo Brayton Coolers. Need to develop 4.5-K turbo-alternator.
Cooling from 4.5 K to 50 mK	Cooling: 250 μW @ 0.6 K 6 μW @ 50mK Heat generated: < 4 mW (avg.) @4.5 K	Further develop multistage continuous ADR similar to previous 4-stage ADRs but with additional 5th stage to provide required cooling at 0.6 K. Heat generated, while cyclical, will be time-averaged through thermal design to provide constant quiescent level of less than 4 mW.

Element 1: Microcalorimeter Arrays — To achieve TRL 4 for the LXM MA, EMA (25 absorber hydras), and UHRA (single-pixel readout), prototype arrays with suitable form factors are needed. A subset of pixels from each subarray type has already demonstrated energy resolution that is close to meeting all LXM requirements (Figure 7.11). It remains to verify that the energy resolution and pixel discrimination properties (for the MA and EMA hydras) are maintained when measurements are performed using suitable Nyquist inductors in the bias circuits. Previous measurements have shown no detrimental effects [619], but these measurements must be reproduced on LXM-compatible hydras to reach TRL 4.

At TRL 5, all three required pixel arrays will be fabricated on a single substrate (as already demonstrated) and tested for quantum efficiency, pixel uniformity, and radiation hardness. Also, at TRL 5, the integration of heatsinking (via a gold thermal ground plane underneath the array, where the substrate has been thinned in the region of the absorbers) suitable to minimize thermal crosstalk across a full-size array will be performance tested. The technical approach to heatsink advancement will be similar to one that has previously been successfully demonstrated at the necessary level. Scale-up of existing buried wiring technology is not expected to be an issue.

At TRL 6, a full-size, flight-like array with a pixel yield of >95% will be tested to verify that all performance and radiation hardness requirements are met. This test will be conducted with a full-scale demonstration FPA and readout electronics that support the operation of at least 25% of the pixels simultaneously. The AD^2 to TRL 6 is low because the development needed is only incremental due to the previously successful demonstration of large-scale detector fabrication. Once TRL 5 is established, the detector essentially already exists, and only fabrication yield and sensitivities to the environment need to be verified, which are not expected to be problematic.

There are no known fundamental barriers to straightforward technology advancement using standard engineering practices for the microcalorimeter arrays given the recent breakthroughs made in the development of smaller pixels, fine-pitch wiring, and hydras.

Element 2: Microcalorimeter Readout — To achieve TRL 4, the multiplexing focus will be on developing microwave SQUID circuits for each of the required pixel array types at reduced multiplexing factors to minimize design and fabrication time while still providing important information about the interactions between the sensors and the readout system. Some new development is needed to optimize the designs for the bandwidth required. At TRL 5, the requirement will be ramped up to full bandwidth and energy resolution that meets full requirements. Additionally, radiation hardness will be tested on the TRL 5 test article. At TRL 6, a scalable readout geometry will be developed to read out >25% of the full-scale pixel arrays simultaneously.

At TRL 4, a High-Electron Mobility Transistor (HEMT) amplifier suitable for flight qualification will be designed and fabricated. At TRL 5, a set of flight-like HEMT amplifiers, complete with requisite cabling, will be fabricated and included in the TRL 5 test setup. Upon reaching TRL 5, these flight-like amplifiers will have demonstrated that any energy resolution degradation after a 5-year equivalent radiation dose remains within the allowed range. The HEMT design will require no further development and can be used for TRL 6 system testing.

Room temperature readout electronics for LXM are currently at TRL 3. The progression to TRL 4 will proceed by assembling an appropriate set of room temperature readout electronics using commercial parts as a breadboard model spanning a bandwidth of 4–8 GHz and testing with low-temperature SQUID resonators. This will be carried out using a lesser performing Field Programmable Gate Array (FPGA) than the one envisioned for LXM, but will prove the concept for being able to read out a 1–2 GHz sub-band of the 4–8 GHz bandwidth. To progress to TRL 5, the breadboard components will be upgraded with flight-qualified components (a few components may need to be qualified through a NASA flight qualification process). This will again be a room temperature operation, and will demonstrate isolated readout of relevant pixel types at relevant multiplexing factors at frequencies ranging over the full bandwidth range of the HEMT. TRL 6 will be achieved by fabricating and testing a full-scale readout system, with at least one quarter of the array using flight-qualified parts.

Overall, the advancing the readout to TRL 5 is moderately challenging but has a high degree of confidence of success because of widespread industry needs identical to those of LXM. The scale-up of the low-temperature electronics to TRL 6, with integration into a new FPA geometry, is similarly challenging. The room temperature electronics have a clear and feasible development plan, requiring a straightforward but large engineering support effort.

Element 3: Focal Plane Assembly and Optical/Infrared Blocking Filter Assembly — The *Lynx* FPA design is leveraged from *Athena*'s, and as such, it is currently at TRL 4. Advancing to TRL 5 will require:

1. Design and testing of kinematic mounting approaches for the FPA chip and the anti-coincidence detector, and also the microwave SQUID resonator chips together with Nyquist inductors and bias resistors;

2. Simulations and experiments to determine whether there will be issues related to RF signals interfering with each other among the different microwave SQUID resonator chips; and

3. Verifying the thermal and mechanical properties of the T-300 cone-shaped thrust tubes used for mechanical support of the FPA between different temperature stages, as well as verification of the mechanical properties and the DC- and AC-shielding performance of the magnetic shields.

To progress to TRL 6, a full-scale model FPA attached to a CADR to provide representative temperatures/conditions for FPA operation will be designed, built, and tested. This will include appropriate interconnects and bump bonds. Advancing to TRL 6 represents a large engineering effort but will leverage *Athena's* similar FPA design.

It is likely that connectorized coaxial cables that are suitable in size and thermal conductance for the LXM FPA will be used between each HEMT and the readout at 50 mK. Currently, there are only limited data available on the properties of such interconnects. To progress to TRL 5, measurements must be made to verify that the thermal and mechanical properties are suitable. Superconducting flex (around-the-corner wiring) is needed to carry signals between the detector arrays and the multiplexer chips, and measurements must be made to verify that the thermal, mechanical, and electrical properties are suitable for the LXM. TRL 6 will be verified as a part of the full-scale demonstration model FPA's verification testing.

Optical blocking filters are already at TRL 5. Progressing to TRL 6 requires building a set of filters that are compatible with the FPA and cryostat designs, with appropriate kinematic mounts. Demonstration in the relevant environments will then be performed using a vibration table for mechanical verification.

Element 4: Cryogenic Cooling System — The commercial pulse tube cooler under consideration for LXM is currently at TRL 4, while the Reverse-Brayton (RB) cooler is at TRL 3. In order to advance the RB cooler to TRL 4, only the 4.5-K turboalternator stage remains to be demonstrated. Then, at TRL 5, the RB cooler must demonstrate launch load survivability, and TRL 6 requires integration into the TRL 6 LXM test article and performance verification.

Advancing the pulse tube cooler to TRL 5 involves the design, fabrication, and demonstration of the full cryocooler system performance as proposed for the LXM, meeting all the cryogenic performance requirements. Breadboard electronics will be used with flight-compatible electronics components and verify that the system meets performance requirements and is compatible with expected launch loads. Ultimately, TRL 6 will be achieved when an entire flight-like system is demonstrated with performance testing in pre- and post-launch load environments and with flight-like support electronics.

The LXM cryostat, which houses all components lower than room temperature, is based on design principles used for many previously flown cryostats. The design challenge is primarily a tradeoff between structural and thermal performance and is considered normal engineering work for experienced cryogenic engineers. Previous missions employing long-life dewars operating at this low temperature include the *Infrared Astronomical Satellite* (*IRAS*), *Cosmic Background Explorer* (*COBE*), the *Infrared Space Observatory* (*ISO*), *Suzaku*, *Hitomi*, *Spitzer*, and *Herschel*, among others. In the case of LXM, there will be no liquid helium, which simplifies the design. Nevertheless, the cryostat is considered TRL 5, and to advance to TRL 6, a cryostat design that meets the LXM's thermal and structural requirements is needed, and structural and/or thermal sample tests are needed where suitable data for specific materials used in the design do not currently exist.

The ADR for LXM is already at TRL 4. To raise the 50-mK CADR to TRL 5 requires adding to the system and demonstrating a high-performance magnetic shield, as well as demonstrating that meeting launch load vibrational requirements can be met. To advance to TRL 6, a secondary continuous stage operating at 0.6 K must be added. This is a straightforward addition of another stage and its support and heat switch. This TRL 6 unit will need to demonstrate 6-μW cooling at 50 mK.

7.3.4.2 Programmatic Considerations

As presented in detail in the *LXM Technology Roadmap*, alternative technologies are being independently funded and investigated for the thermal sensor, readout electronics, and cryocooler elements of the *Lynx* design. This approach helps to mitigate about one-third of the identifiable technical and schedule risks while simultaneously enhancing the potential for bringing new and innovative technological solutions to the program. Formal selection of baseline LXM technologies for these elements will be made soon after TRL 5 performance has been verified (i.e., near the start of Phase A).

The FPA is a special-purpose entity that needs to be integrated and tested with the rest of the instrument. This means the design, fabrication, and testing of the detectors and readout should start early, and these components should be at TRL 6 early. Thus, all the critical technologies needed for LXM will achieve TRL 4 by the start of pre-Phase A, funded through ongoing existing research and development programs, achieve TRL 5 nine months prior to the end of pre-Phase A, and the critical detector and readout technologies will achieve TRL 6 by the end of Phase A through a TRL 6 demonstration unit, with seven months of margin.

Beyond that, the overall LXM development approach is based upon that followed by the Soft X-ray Spectrometer (SXS) instrument on *Hitomi* and is similar to the approach planned for the *Athena* X-IFU. It is based on the development of an engineering model and a protoflight unit, with selected subsystem flight spares but no complete instrument spare. There is no qualification model at the instrument or subsystem level, but the engineering model is planned to undergo extensive qualification testing beyond the typical level of an engineering development unit in order to space-qualify the design. The philosophy behind this approach is to optimize schedule considerations, with time for proper feedback between the engineering and flight model construction, without adding risk.

The LXM's development will benefit greatly from the availability of additional experienced engineers and scientists becoming available during Phase A to complement the LXM development team following the launch and commissioning of *XRISM* and from the ramp-down of *Athena's* X-IFU activities during its Phase B. Furthermore, there are no major infrastructure upgrades needed, as the LXM program will leverage the substantial investment made for developing detectors for the X-IFU.

8 *Lynx* Design Reference Mission Programmatics

Lynx is a flagship NASA mission designed to execute an ambitious and revolutionary science program while maintaining a low risk posture, and delivering on technical, cost, and schedule commitments to ensure mission success. This approach enables a launch in the mid-2030s at a reasonable cost for a flagship mission, consistent with pre-Phase A concept maturity.

The Design Reference Mission (DRM) programmatic details describe a well-validated and achievable project management approach, as well as schedule and cost formulation representative of a mature mission design, enabling technologies that are rapidly progressing and relatively small-quantity, manageable technology development risks, and a strong use of heritage. In addition to the technology development roadmaps described in §7, the DRM is further enabled by project management practices and approaches that leverage substantial *Chandra* heritage and team experience. The result is a well-developed project organization, detailed WBS, feasible and achievable schedule, mitigatable risks, and credible and validated costing consistent with pre-Phase A formulation practices. The *Lynx* team understands the challenges related to developing and costing flagship class missions [620], and has taken a conservative approach throughout by including substantial margins and reserves to mitigate cost and schedule risks.

8.1 Project Classification and Authority

The *Lynx* DRM delivers on the transformative science program (§1 through §5), consistent with a NASA Flagship mission. *Lynx* is a Category 1 project as defined in NASA Procedural Requirements (NPR) 7120.5, *NASA Space Flight Program and Project Management Requirements*, and is classified as Risk Class A per NPR 8705.4, *Risk Classification for NASA Payloads*. This risk class is assigned due to the criticality of *Lynx* to NASA's strategic plan, very high national significance, and long mission lifetime. The *Lynx* project will be under the decision authority of the NASA Associate Administrator (AA) and the Science Mission Directorate (SMD) AA. The project will be part of the recently established Astrophysics Strategic Missions Program within the NASA SMD Astrophysics Division, and overall project management responsibilities will be assigned to the selected lead NASA Center.

The *Lynx* project will perform Lifecycle Reviews (LCRs) in accordance with the project management processes defined in NPR 7120.5 and with the systems engineering requirements in NPR 7123.1, *NASA Systems Engineering Processes and Requirements*. An independent Standing Review Board (SRB) will conduct the LCRs and make recommendations on the project's ability to proceed through the prescribed Key Decision Points (KDPs) and life-cycle phases.

8.2 Project Organization and Partnerships

The *Lynx* project organization mimics that of successfully implemented heritage flagship missions. The notional project structure for *Lynx* (Figure 8.1) encompasses the roles necessary to deliver and launch the Observatory, provide required levels of technical authority oversight and insight, and ensure overall mission success. While Centers and contractors have not been assigned responsibility for the *Lynx* mission, estimated costs were burdened with rates and fees typical of the Centers and contractors that might ultimately perform the mission. The resulting estimates are therefore useful for budgeting purposes. This organization is consistent with the project Work Breakdown Structure (WBS) and dictionary summarized in §8.5.1. Specific mission roles will be established prior to Phase A following the final architecture decision and Mission Concept Review (MCR). Strategic partnerships will take advantage of the existing resources (hardware and facilities) and workforce developed, over many years, for *Chandra*. These partnerships reduce risk through the implementation of lessons learned and significant stored knowledge of *Chandra* development through flight. Additionally, as a Flagship mission, *Lynx* welcomes continued international participation. An Acquisition Strategy Meeting will be conducted prior to Phase A to finalize decisions on international agreements, procurements, and partnerships.

The *Lynx* project will be staffed by the lead NASA Center (possibly supported by an external science team) to provide overall management and integration of mission elements, as well as lead project scientist functions. Specifically:

- WBS 01, Project Management (PM) functions include the management, integration, and direction of *Lynx* project activities, in compliance with Agency policies and procedures. The PM is responsible for programmatic business activities, control of the programmatic baseline, and resource management through rigorous project planning and control processes. The science payload manager for development of the X-ray mirrors and science instruments (the *Lynx* X-ray Microcalorimeter (LXM), High-Definition X-ray Imager (HDXI), and X-ray Grating Spectrometer (XGS)) will directly report to the PM.
- WBS 02, Systems Engineering (SE) functions include the technical design and performance of the mission. The Mission Systems Engineer (MSE) provides independent technical authority for *Lynx*.
- WBS 03, Safety and Mission Assurance (S&MA) functions include independent overview of S&MA activities and ensuring compliance with S&MA requirements.
- WBS 04, Project Scientist functions include leading the Science Working Group (SWG), ensuring the science content of the project, managing the technology development activities, and serving as the project interface to the *Lynx* science community.
- WBS 05, X-ray Telescope (XRT) management functions include overall Design, Development, Test, and Evaluation (DDT&E) of the telescope and its subsystems, as well as Integration and Test (I&T) and calibration of the telescope. It is assumed that these activities will be contractor-managed.
- WBS 06, Spacecraft Element (SCE) management functions include overall DDT&E of the SCE and its subsystems, as well as I&T of the SCE. It is assumed that these activities will be contractor-managed.
- WBS 07/09, Ground systems and mission operations functions include responsibility for the design, development, integration, test, implementation, and associated physical support equipment of the systems needed for commanding and operating the Observatory. This includes downlinking, processing, archiving, and distributing telemetry with the engineering and scientific data.

- WBS 08, Launch vehicle services functions include interfacing between the project and launch vehicle provider.
- WBS 10, Observatory I&T functions include management of the overall Observatory I&T program. It is assumed that these activities will be contractor managed.
- WBS 11, Outreach functions include responsibility for informing the public on *Lynx's* benefits to the community.

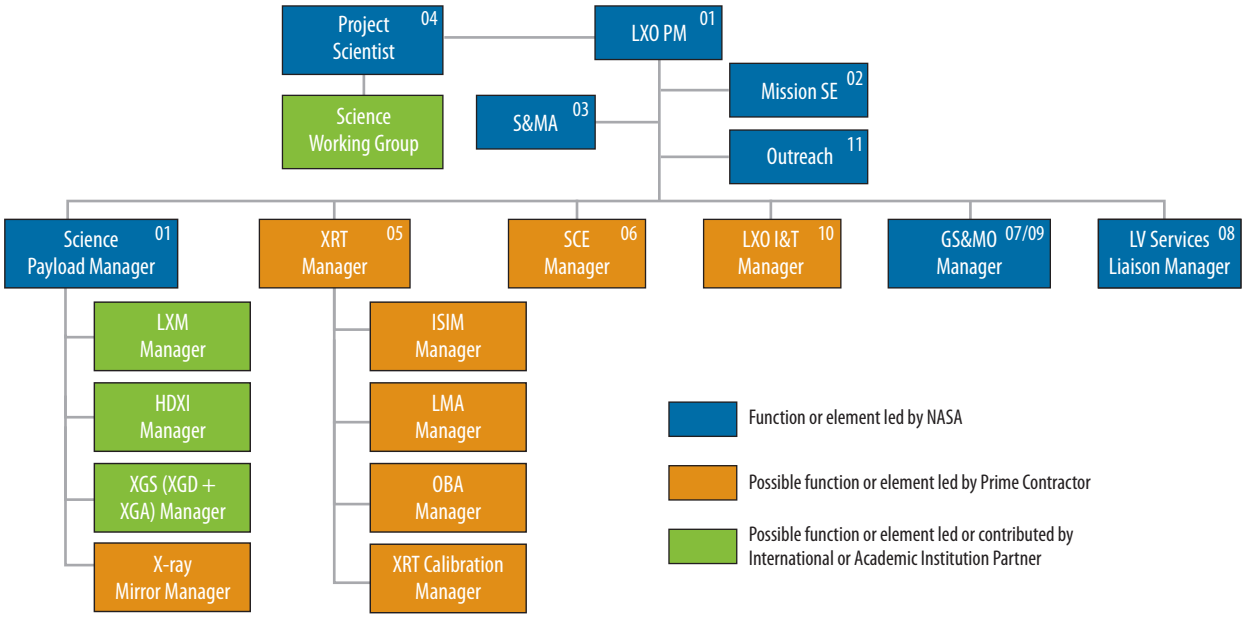

Figure 8.1. Notional *Lynx* project organization is consistent with NASA management practices and considers possible partnerships and prime contractor activities. Final organization will be defined following pre-Phase A procurement decisions and Mission Concept Review.

A prime contract is anticipated to be competitively selected for the DDT&E of the SCE, the XRT (including DDT&E of the Integrated Science Instrument Module (ISIM)), and the *Lynx* Mirror Assembly (LMA). The prime contractor will be responsible for overall integration for the Observatory, including systems I&T. The anticipated prime contract roles defined above are similar to the management approach used for *Chandra*.

The *Lynx* project will benefit from potential international and/or academic partnerships. Along with the intention of having a fully open scientific program similar to *Chandra* and XMM-Newton, and presumably *Athena*, potential areas of contribution could include instruments, building on existing collaborations, or even a distinct contribution to the spacecraft. The possibility of such contributions is being explored and discussions will continue through Phase A.

It is assumed that the science instruments will be provided by an academic institution, NASA or other government agency, or by an international partner, and that the X-ray mirrors will be provided by a contractor. Instrument providers will be selected through a NASA-issued Announcement of Opportunity (AO), and the X-ray mirror provider will be selected through a NASA-issued Request for Proposal (RFP). It is also assumed that a *Lynx* Science and Operations Center (§6.7) will be responsible for developing the ground system and leading Phase E under the direction of the lead NASA Center. The sequencing of the AOs and RFP are discussed in more detail in §8.4.

8.3 Risks and Risk Mitigation

Lynx project risks are well understood and mitigation plans are well defined. For the mirrors, HDXI and XGD sensors, and XGS gratings, multiple feasible (and funded) alternate technologies are available to mitigate technology development risks. Additionally, the LXM leverages strong heritage from similar, in-development flight instruments.

The *Lynx* design meets Risk Class A requirements that are consistent with NPR 8705.4. There are no credible single-point failures in the spacecraft or telescope designs, and the subsystems incorporate multiple redundancies throughout. A Failure Mode and Effects Analysis (FMEA) and Critical Items List (CIL) will be developed as required during project implementation to identify hardware items critical to the performance and safety of the mission, potential failure modes, and any resulting items requiring design improvements or corrective actions necessary to meet redundancy requirements. A summary of specific key redundancies for fault tolerance is provided in Table 6.14.

Level 1 Electrical, Electronic, and Electromechanical (EEE) parts, per the NASA Parts Selection List (NSPL), are included in the cost analysis, as are Engineering Models (EMs), prototypes, and component spares for the optics and instruments as described in §7. A protoflight Verification and Validation (V&V) approach will be used at the *Lynx* Observatory level due to the prohibitive cost impact of a full Observatory-level qualification unit. Lower Technology Readiness Level (TRL) subsystems, such as the optics and instruments, will have engineering development units tested at qualification levels. See §6.6 for more details on the *Lynx* V&V approach.

The *Lynx* team has identified and ranked the top project risks and defined the Likelihood (L) and Consequence (C) of risk occurrence on a scale of 1 to 5, with 1 being the lowest likelihood of occurrence and consequence to the Project and 5 being the highest. The project risk list is shown in Table 8.1, and Figure 8.2 provides 5-×-5 risk chart for these risks. The risks ratings are per the standard scale for consequence and likelihood, consistent with Goddard Procedural Requirements (GPR) 7120.4D, *Risk Management Reporting*. Project-level risks are defined as those with the potential to change the technical and/or programmatic baseline. In addition to project risks, each major technology under development will also carry risks as defined in the individual technology development roadmaps and summarized in §7. The risks fall under the general categories of technology maturation, manufacturability, and science impact. All of the *Lynx* risks, which are specific to the DRM, have credible mitigation

Table 8.1. Summary of top *Lynx* project risks.

Risk	Title	L	C	T	S	$
1	X-ray Mirror Module Assembly and Alignment	3	4		X	X
2	LXM Technical Maturation to TRL 6	3	3	X	X	X
3	X-ray Mirror Segment Industrialization	2	3		X	X
4	LXM Fabrication and Assembly	2	3		X	X
5	X-ray Mirror Technical Maturation to TRL 6	3	2	X	X	X
6	HDXI/XGD Detector Technology Maturation to TRL 6	2	2	X	X	X
7	Calibration Facility Availability	1	3		X	X

L = likelihood of risk occurrence; C = consequence of risk occurrence; T = technical risk; S = schedule risk; $ = cost risk

plans. It is important to note that multiple feasible technologies exist for the mirrors and instruments that might have a different set of opportunities and risks than those listed.

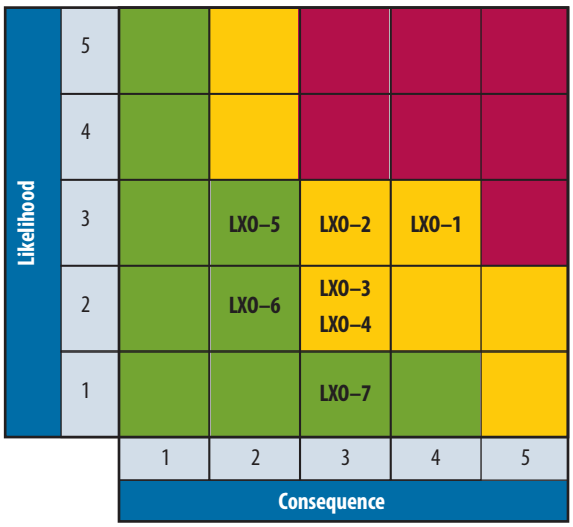

Figure 8.2. *Lynx* risk ranking. No red risks identified; all identified risks can be mitigated.

Risk 1 — X-ray Mirror Module Assembly and Alignment: If the ability to demonstrate and scale up the processes from a laboratory environment to the production levels needed to assemble and align the numerous X-ray mirror modules cannot be achieved while maintaining technical requirements, then the project cost and schedule will be impacted.

Mitigation: For each mirror system design under consideration, a technology development roadmap has been developed that includes early studies of mirror alignment and mounting processes. For the Silicon Meta-Shell Optics specifically, recent developments have shown the feasibility of producing a single aligned high-quality mirror segment pair that meets the necessary mirror figure. Further work is needed to prove full-scale feasibility of the necessary processes with requisite quality control to mount and align the many mirror segments into modules needed for flight. This work will take place during technology development. Starting at TRL 4, multiple partially-populated modules will be demonstrated. By TRL 6/PDR, a high-fidelity, qualification-tested, partially populated EM will be developed and will serve as pathfinder for the technology, as well as the manufacturing and assembly processes. For the Silicon Meta-Shell Optics technology, the EM will consist of three meta-shells (outer, middle, inner) with three fully populated modules in each that serve as a testbed for demonstrating technical and assembly processes. Nine months of DDT&E schedule margin have been added to the Silicon Meta-shell Optics delivery to flight unit calibration/verification. This margin includes three months to delivery of the TRL 6/PDR demonstration unit to cover issues that arise during technology maturation and an additional six months of margin for issues that arise during the manufacturing and assembly process of the flight unit.

Impact: Increased cost and schedule to meet technical requirements.

L × C: 3 × 4

Risk 2 — LXM Technical Maturation to TRL 6: If the LXM is unable to achieve requisite technology maturation and performance to TRL 6, then the mission science and/or technology development cost and schedule will be compromised.

Mitigation: A detailed *LXM Technology Roadmap* that includes cost, schedule, and risk has been developed for the LXM, which is based on extensive experience from previous and planned space-based X-ray microcalorimeters. Technology developments from the *Hitomi* SXS, *Athena* X-ray Integral Field Unit (X-IFU), and *X-Ray Imaging and Spectroscopy Mission* (*XRISM*) Resolve X-ray microcalorimeter instruments will be leveraged as applicable for the LXM (§6.3.4). Individuals supporting *Athena* X-IFU development also support LXM development from pre-Phase A onward, and those supporting the *XRISM* Resolve instrument will support the LXM from Phase A onward. The large-scale fabrication

of detectors is low risk since detectors have already been produced with scale and performance close to requirements, utilizing proven processes with high yield and reliability. For the read-out, the main risk is the number of read-out channels needed and, therefore, how much cooling power is required (and thus spacecraft resources such as power), rather than whether or not it will reach TRL 6. The LXM read-out uses microwave Superconducting Quantum Interference Device (SQUID) resonators that are not difficult to fabricate in comparison to components under development for missions operating at longer wavelength. (For LXM, relatively few resonators per feedline are needed and thus resonance frequency accuracy is not critical). The LXM DRM design requires the read-out of 7,600 sensors—not a major scale-up from the number of sensors in the *Athena* X-IFU—and naturally leads to a focal plane assembly that is 4 inches in diameter at 50 mK (similar to the X-IFU) and with relatively standard optical blocking filter sizes. Several industry studies have been initiated to investigate the LXM cryogenic design to identify the solution space (mass, volume, and complexity versus cost) for this already mature subsystem. Two Cooperative Agreement Notice (CAN) studies were carried out during this study, specifically to investigate the maturity of these systems and to consider their maturity as part of the LXM system. Periodic reviews will be conducted as needed to ensure requisite development milestones are met and that conservative cost and schedule reserves have been applied. As part of the detailed *LXM Technology Roadmap*, a high-fidelity, full-assembly EM will be developed to serve as a pathfinder for Observatory assembly, integration, and test. Six months of DDT&E schedule margin to TRL 6 have been included in the LXM development schedule to cover issues that may arise during technology maturation.

Impact: Reduced science capability or increased cost and schedule for technology development.

L × C: 3 × 3

Risk 3 — X-ray Mirror Segment Industrialization: If the manufacturing process used to fabricate mirror segments cannot be scaled to the required industrial-scale production levels while still meeting the technical requirements, then the project cost and schedule will be impacted.

Mitigation: For each mirror system design under consideration, an early study of manufacturability and production of the mirror elements has been initiated through industry partnerships and as part of overall technology development considerations. For the Silicon Meta-shell Optics specifically, recent developments have shown that producing multiple high-quality segments that meet the necessary mirror figure is feasible within the *Lynx* program cost and schedule. Further work is needed to prove full-scale manufacturing feasibility with requisite quality control to produce the quantity of segments required for flight (§8.5.2.1). An advantage of the Silicon Meta-shell Optics design is the nearly identical sizes and shapes of mirror segments regardless of location within the X-ray mirror assembly, and realization of cost and schedule savings via the utilization of several parallel processes in the manufacturing of these elements. Optimization of the manufacturing process (number of parallel machine lines, polishing lines, coating lines, etc.) will lead to a reduction in cost and schedule once the process steps have been defined and proven to yield segments and modules meeting project requirements. A high fidelity, partially populated EM will be developed as part of the TRL 6/PDR demonstration to serve as pathfinder for the technology and manufacturing processes. For Silicon Meta-shell Optics, an assumed 10% for spares has been included in the cost model to account for quality and other issues during the manufacturing process. Furthermore, via industry partnership, a queuing theory-based

model has been developed for the production time and cost of the LMA to determine the most efficient cost and schedule path through the manufacturing process, including but not limited to identification of gating process(es) and the number of parallel manufacturing lines necessary to prevent pileup [621]. Finally, if schedule and cost challenges arise, mirror pairs can be eliminated from the design for up to a 50% reduction in effective area as discussed in §9. In this case, mass dummies would replace the eliminated mirror pairs, thus saving the time and cost for mirror polishing, coating and ion beam figuring. This option would not decimate the *Lynx* science program, but would necessitate longer exposure times. Nine months of DDT&E schedule margin have been added to the Silicon Meta-shell Optics delivery to flight unit calibration/verification. This margin includes three months to delivery of the TRL 6/PDR demonstration unit to cover issues that arise during technology maturation, and an additional six months of margin for issues that arise during the manufacturing and assembly process of the flight unit.

Impact: Increased cost and schedule to meet technical requirements.

L × C: 2 × 3

Risk 4 — LXM Instrument Fabrication and Assembly: If the LXM and its subsystems and components cannot be fabricated, assembled, tested, and integrated within the projected timescale, then the critical path project schedule margin will be eroded at increased project life-cycle cost.

Mitigation: The DDT&E schedule for the LXM is based on the *LXM Technology Roadmap* and leverages the DDT&E plan from the *Athena* X-IFU, as applicable. A full, high-fidelity LXM EM is planned prior to Critical Design Review (CDR) to serve as a pathfinder for the manufacturing and assembly processes. A team of scientists and engineers at GSFC possess substantial experience in the development of instrumentation of this type. This team developed the detectors, focal plane assembly, filters, Adiabatic Demagnetization Refrigerator (ADRs), etc. for *Astro-E*, *Astro-E2* and *Hitomi*; have applicable experience for I&T, calibration, etc.; and a proven record of having developed space-flight hardware on schedule. This GSFC team is currently focused on delivering similar hardware for the Resolve instrument on *XRISM*, which is scheduled to launch in 2022. The team will likely be available for the full LXM development life cycle. In an almost ideal time-scale, they will be available to complement the separate technology development team currently focused on developing TES detectors and readout for the *Athena* X-IFU at the start of Phase-A. The gradual ramp-down of *Athena* X-IFU activities will likely fit well with the ramp up of LXM detector development work. DDT&E schedule margin of four months plus an additional five months of critical path reserve has been added to the project schedule for LXM delivery to ISIM I&T to account for issues that may arise during the fabrication and assembly process.

Impact: Critical path schedule duration and increased project cost.

L × C: 2 × 3

Risk 5 — X-ray Mirror Technical Maturation to TRL 6: If the X-ray mirrors are unable to achieve requisite technology maturation and performance, then the mission science and/or technology development cost and schedule will be compromised.

Mitigation: Technology development roadmaps (§7) have been developed for the three different *Lynx*-feasible, actively funded X-ray mirror technologies. Each technology will receive continued funding during pre-Phase A development and a final selection (based on technology maturation and proximity to reaching TRL 5 by the start of Phase A) will be made by the time of the *Lynx* Mission Concept Review (MCR) to ensure that the most mature and capable technology is selected for the mission. Carrying the three technology developments in parallel and making periodic schedule and technology advancement-driven downselect decisions provides risk mitigation among the candidates and optimization of science return. Each of these roadmaps identifies a set of unique risks and mitigation plans. The Silicon Meta-shell Optics technology chosen for the DRM has already validated the basic process of mirror segment fabrication and alignment through X-ray testing. Conservative cost and schedule reserves on the Silicon Meta-shell Optics technology have been applied, and periodic reviews will be carried out as needed to ensure that developmental goals are met. Furthermore, a high-fidelity, partially-populated EM will be developed as part of the TRL 6/PDR demonstration to serve as a pathfinder for the technology and manufacturing processes. Three months of DDT&E schedule margin to TRL 6 has been added to the mirror development schedule to account for issues that may arise during technology maturation.

Impact: Reduced science capability or increased cost and schedule for technology development.

L × C: 3 × 2

Risk 6 — HDXI/X-ray Grating Detector Technology Maturation to TRL 6: If the HDXI and X-ray Grating Detector (XGD) are unable to achieve requisite detector technology maturation and performance, then the mission science and/or technology development cost and schedule will be compromised.

Mitigation: An *HDXI Technology Roadmap* has been developed, and because XGD requirements are met with the same sensors as those for HDXI, the *HDXI Technology Roadmap* is sufficient for both. Though the hybrid CMOS-sensor technology has been selected for the DRM, there are at least two other sensor technologies of similar maturity that can meet *Lynx* requirements. Each of these sensor technologies (hybrid CMOS, advanced Charge-Coupled Device (CCD), and monolithic CMOS) have demonstrated proof-of-concept and are assessed at TRL 3. Each technology will be developed until a predefined downselect milestone in 2023, at which point the two most advanced technologies will proceed with development to TRL 4. These two selected sensor technologies will be funded to achieve TRL 4 by the start of *Lynx* project Phase A. The challenges to developing the HDXI and XGD are primarily confined to achieving TRL 4 performance. Once these fundamental capabilities have been demonstrated, subsequent development efforts focus on the assembly and testing of larger sensor/ASIC arrays and higher fidelity testing with respect to flight conditions. These are considered essentially engineering activities and advancement to TRLs 5 and 6 is expected to be straightforward. A single sensor technology will be selected for TRL 5. Downselect decisions will be based on the cost and schedule to meet remaining TRL milestones and ability to meet *Lynx* performance requirements. Carrying the three technology developments in parallel and making periodic, schedule-driven downselect decisions mitigates risk among the candidates. If none of the advanced technologies makes the requisite progress, the use of existing CCD technology may be utilized, though with reduced capability. Three months of pre-Phase A schedule margin and five months of DDT&E schedule margin to TRL 6 is included in the HDXI and XGD schedules to cover issues associated with technology maturation.

Impact: Reduced science capability or increased cost and schedule for technology development.

L × C: 2 × 2

Risk 7 — Calibration Facility Availability: If NASA Marshall Space Flight Center's (MSFC's) X-ray and Cryogenic Facility (XRCF) is chosen as the calibration facility for the *Athena* mission, and if the *Athena* calibration activity is significantly delayed, the *Lynx* schedule will be impacted.

Mitigation: Currently, the *Athena* mission's notional schedule indicates that the flight unit calibration activities will take place from approximately mid-FY28 to around mid-FY29. The current *Lynx* project schedule has rehearsal and flight unit calibration activities taking place around mid-FY31 to late FY32. To impact the *Lynx* critical path, the *Athena* calibration activity would need to slip by approximately 2.5 years. This issue is currently considered a "watch" item.

Impact: Schedule duration and increased project cost.

L × C: 1 × 3

8.4 Life-cycle Schedule and the Critical Path

The *Lynx* project schedule reflects inputs and development planning from technology, engineering, and industry partner teams. It leverages heritage and analogous AI&T, mission and ground operation, and on-ground calibration planning, and is aligned with NASA project requirements, the WBS, and cost analysis, resulting in a credible path to a launch in the mid-2030s.

The schedule development process included multiple iterations to ensure appropriate completeness and alignment of activities and durations, ultimately resulting in the integrated product shown in Figure 8.3. The project schedule covers all aspects of the Phase A – E portions of the lifecycle. Pre-phase A technology development schedules, outlining milestones, detailed development activities, and associated costs and risks are included in the individual *Lynx* technology development roadmaps and summarized in §7. The technology development schedules include funded margin for achieving each TRL. Pre-Phase A is expected to start October 2021, be 3 years in duration, and end with final technology downselect and architecture decisions. The project lifecycle schedule is detailed in its composition, consistent with the technology development plans and analogous *Chandra* integration activities, and credible for the pre-Phase A stage of development; however, it is still notional. Further development and optimization will take place following final technology and contractor selection during the late pre-Phase A/early Phase A timeframe. Specific analysis to optimize the manufacturing and assembly of the X-ray mirrors to determine the most cost- and schedule-efficient number of parallel manufacturing lines will also take place in the late pre-Phase A/early Phase A timeframe. The approach used for this analysis is described in §8.5.2.1. Additional schedule optimization opportunities include, but are not limited to, AI&T sequencing and on-ground calibration planning with respect to availability of the HDXI and XGD for the duration of the calibration campaign for end-to-end testing.

The schedule for specific elements was determined through various means including, but not limited to:

- Key milestone phasing for the X-ray mirrors and science instruments consistent with costing, technology development (§7), and current DDT&E plans.

- Input from the *Chandra* prime contractor for similar and assumed contracted activities for *Lynx*.
- Input from the *Chandra* science operations team for activities associated with ground systems and mission operations.
- Input from the *Lynx* calibration team, which includes *Chandra* and *Athena* calibration team members, for activities related to X-ray and Cryogenic Facility (XRCF) modernization and on-ground calibration.

The schedule was developed utilizing Government Accountability Office (GAO) *Best Practices for Project Schedules*, consistent with pre-Phase A project maturity. Schedule planning included identification of all milestones and KDPs consistent with NPR 7120.5, as summarized in Table 8.2. Key *Lynx* phase durations, summarized in Table 8.3, were compared to, and validated against, the *Chandra* Actual and *WFIRST* In-Guide Schedules for a 2025 Launch Readiness Date (LRD) where applicable for comparable activities. The *Lynx* schedule is aligned with the WBS and mission cost estimate. Key project-level milestones are indicated along the top row of the schedule. The planned start and delivery dates for all major elements of the project are identified.

All of the *Lynx* technologies for the X-ray mirrors and instruments will receive continued technology development funding during the Pre-Phase A period. A technology review will take place approximately 12 months prior to the start of Phase A to downselect to the individual mirror and instrument technologies most ready to reach TRL 5 by the start of Phase A, TRL 6 by PDR, and meet *Lynx* requirements.

As discussed in §7, there are multiple, actively funded technologies with similar maturity levels currently in development for the optics and science instrument suite, capable of meeting

Table 8.2. Key event dates.

Project Milestone	Approximate Milestone Date
Technology Development / Start of Pre-Phase A	10/2021
Architecture Decision	2/2024
MCR	8/2024
KDP-A / Start of Phase A	10/2024
SRR/MDR	2/2026
KDP-B / Start of Phase B	10/2026
PDR	2/2028
KDP-C / Start of Phase C	4/2028
CDR	11/2029
Start of X-ray Mirror Module, XGD & HDXI Flight Unit Calibration	12/2031
Delivery of LXM Flight Unit to ISIM I&T	6/2032
Delivery of X-ray Mirror Modules to LMA I&T	8/2032
Delivery of LMA to XRT I&T	4/2033
Delivery of ISIM to XRT I&T	10/2033
SIR	6/2035
KDP-D / Start of Phase D	7/2035
ORR	3/2036
LRD	10/2036
KDP-E / Start of Phase E	11/2036
End of Primary Mission	11/2041

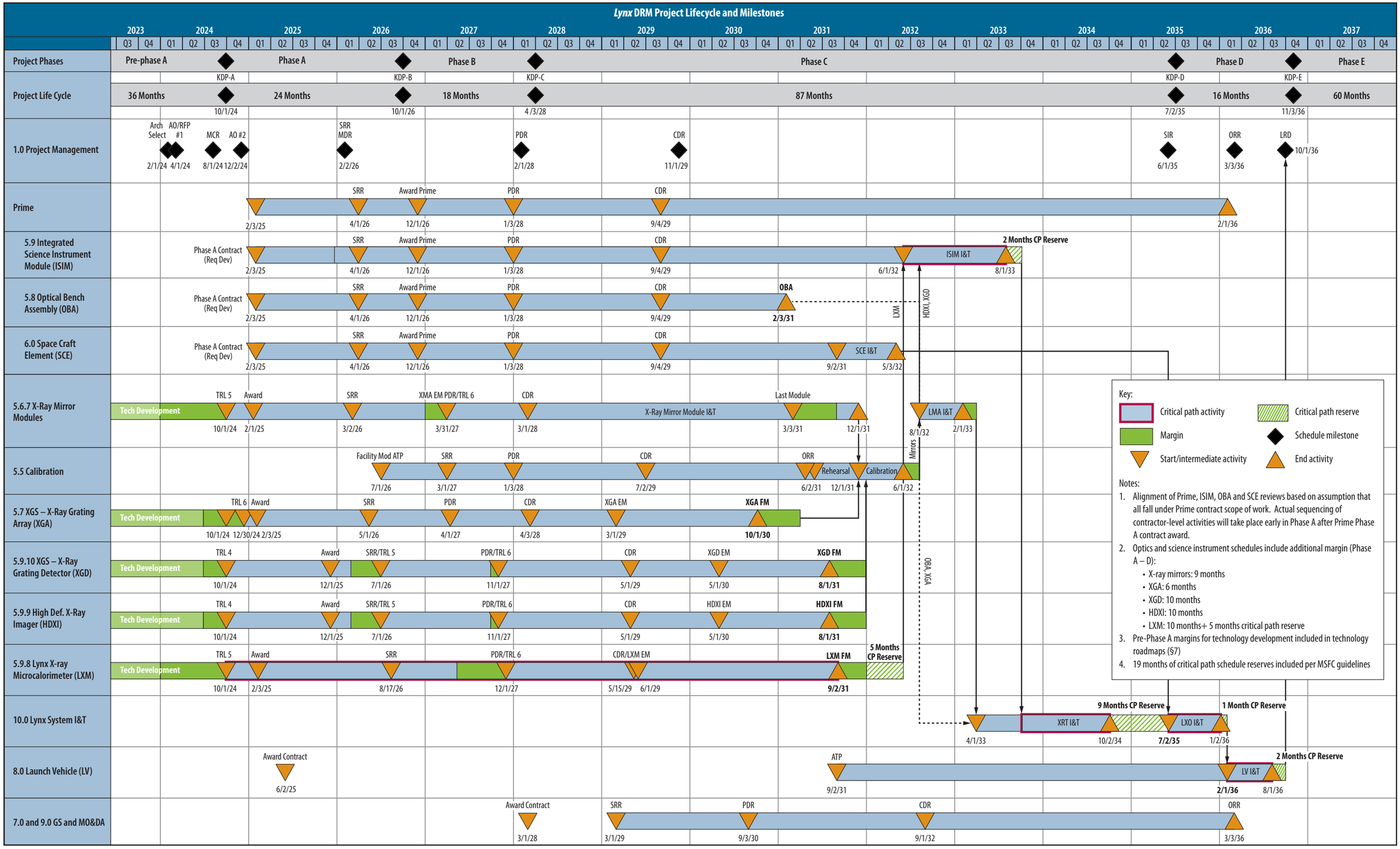

Figure 8.3. *Lynx* project life-cycle schedule.

mission requirements. These technologies will continue receiving funding through the pre-Phase A period. Carrying these multiple technologies lowers the project risk posture in that downselect decisions will be made in the pre-Phase A timeframe based on the ability of each technology to meet the remaining TRL 5 and TRL 6 maturity and project milestones, and *Lynx* requirements. Final selection of the mirror, XGA and LXM technologies will be made by the architecture selection milestone of February 2024.

As described in the *HDXI Technology Roadmap,* three separate sensor technologies are currently under development for the HDXI and XGD. An intermediate downselect will take place by July 2023, and the final downselect will take place by the start of Phase A, again based on maturation advancement and ability to meet *Lynx* requirements. As noted in the schedule, the selected sensor technologies are expected to be at TRL 4 by the start of Phase A. The challenges to developing the HDXI and XGD are primarily confined to achieving TRL 4 performance. Once these fundamental capabilities have been demonstrated, subsequent development efforts focus on the assembly and testing of larger sensor/ASIC arrays with higher fidelity testing with respect to flight conditions. These are considered essentially engineering activities and advancement to TRL 5 and TRL 6 is expected to be straightforward. Three months of pre-Phase A schedule margin is included in the technology development schedule to cover issues associated with technology maturation. Furthermore, aggressive development efforts are already underway for all three sensor/ASIC architectures and significant advances may reasonably be expected before the pre-Phase A period begins.

It is assumed that a single prime contractor will be responsible for DDT&E of the ISIM, Optical Bench Assembly (OBA), and SCE, as well as I&T of the LMA, the telescope, and the Observatory. Alignment of the ISIM, OBA, and SCE DDT&E milestones reflects this assumption. An RFP will be released after the architecture selection milestone for a prime contractor Phase A contract award by February 2025, enabling the development of system requirements. Detailed schedules and sequencing of any contractor-led elements will be developed after selection. The remaining prime development contract will be awarded in Phase B.

The critical path was calculated based on the longest duration of activities through the project schedule. The *Lynx* critical path runs through the LXM DDT&E, and through ISIM, XRT, Observatory and launch vehicle I&T activities. The X-ray mirror development path through DDT&E only lags the LXM DDT&E path by ~1 month in this schedule. It is recognized that the actual development schedule and critical path analysis will take place in Phase A following decisions on the final architecture and Observatory element providers. Nineteen months of schedule reserves were added to the critical path activities, consistent with guidance from MSFC 7102.1, Table 17-3, *Standard Schedule Margin for Programs/Projects*. In addition to the critical path reserves, margin has been added to the X-ray mirrors and science instrument schedules to account for uncertainties associated with technology development, DDT&E, and key integration activities. Schedule margin has also been added to the on-ground calibration and LMA I&T to account for uncertainties associated with these activities. Critical path and schedule reserves are summarized in Table 8.3.

Table 8.3. Key phase duration table.

Project Phase	Duration (months)	Comments
Pre-Phase A (Technology Development)	36	Pre-Phase A duration based on technology development schedules and assumed funding levels (comparable to *WFIRST*)
Phase A (Conceptual Design): KDP-A to KDP-B	24	Phase A duration based on technology development schedules and funding (comparable to *WFIRST* levels).
Phase B (Preliminary Design): KDP-B to KDP-C	18	Phase B duration based on assumed technology development funding and all technologies reaching TRL 6 by PDR
Phase C (Detailed Design): (KDP-C to KDP-D)	87	Phase C includes development of X-ray mirrors (and integration into LMA) and 3 science instruments, mirror and instrument on-ground calibration, ISIM I&T, and XRT I&T. X-ray mirror development assumes multiple parallel manufacturing lines to be optimized during Phase A. LXM schedule comparable to *Athena* X-IFU. *Chandra* Phase C duration similar except for no analogous LXM, and *Chandra* SIM integration took place during Observatory I&T in Phase D. *WFIRST* Phase C shorter due to less complex design (2 science instruments and no ISIM)
Phase D (I&T): KDP-D to KDP-E	16	Phase D includes integration of XRT and SCE to become the LXO. *Chandra* Phase D also included integration of SIM during Observatory I&T. *Lynx* assumes ISIM integration during XRT I&T in Phase C
Phase E (Primary Mission Ops): KDP-E to KDP-F	60	*Lynx* planned operational lifetime is 5 years, extendable to 20 years with on-board consumables
Start of Phase A to SRR	16	
Start of Phase B to PDR	16	
Start of Phase C to CDR	19	
Start of Phase C to SIR	86	
Start of Phase D to LRD	15	
Phase B to X-ray Mirror Delivery to Calibration	62 (53+9)	*Lynx* mirror DDT&E includes additional 9 months of schedule margin
Phase B to LXM Delivery to ISIM I&T	68 (53+*10*+**5**)	LXM DDT&E includes additional 10 months of schedule margin and **5** months of critical path reserve
Calibration (Flight Unit)	8 (6+2)	On-ground calibration similar to *Chandra* with exception of additional science instrument (LXM EM); Schedule includes additional 2 months of margin
LMA I&T	8 (6 + 2)	LMA I&T involves integration of the X-ray mirror module assembly, pre- and post-collimators, contamination doors, and other structures into the barrel structure; Schedule includes 2 months of margin
ISIM I&T	16 (14+**2**)	ISIM I&T is more complex than *Chandra* SIM actual due to mechanisms and additional instrument; Schedule includes **2** months of critical path reserve
Telescope I&T	27 (18+**9**)	XRT I&T involves integration of LMA, XGA, OBA, and ISIM; Schedule includes **9** months of critical path reserve
SCE I&T	8	*Lynx* SCE comparable to *Chandra* actual; No additional margin included
Observatory I&T	7 (6+**1**)	*Lynx* Observatory I&T comparable to *Chandra* actual; Schedule includes **1** month critical path reserve
Launch Site Activities	8 (6+**2**)	*Lynx* LV Integration comparable to *Chandra* actual; Schedule includes **2** months critical path reserve

Linkages between key elements are shown in Phase C of the schedule, consistent with the AI&T activities described in §6.6.3.

It is assumed that on-ground calibration will take place at the MSFC XRCF as described in §6.6.3.1. Development of a new calibration facility is not required for *Lynx*, but modernization of this *Chandra*-era asset may be required. The XRCF is under consideration as the calibration facility for *Athena*. If selected for *Athena*, facility modernization costs including but not limited to additional X-ray sources, detectors, data acquisition systems, and system-specific GSE, will be encumbered by the *Athena* project.

The *Lynx* schedule and costing are conservative in assuming that XRCF will not be selected by *Athena*, and this work will be encumbered by the *Lynx* project. XRCF modernization activities occur in parallel with Observatory development; major reviews are shown in the schedule. Completion of these activities will coincide with the *Lynx* on-ground calibration during Phase C.

On-ground calibration and environmental testing facilities capable of meeting *Lynx* requirements currently exist and are expected to be available in the 2030s. No new Observatory-level calibration facility construction is needed or included in the schedule or costing.

The development of ground systems, mission operations, and the science data analysis system will occur in parallel with the Observatory development, with major reviews shown in the schedule. The procurement strategy for these systems will be determined at the pre-Phase A Acquisition Strategy Meeting.

It is assumed the selection of the launch vehicle provider will take place in Phase A prior to the project System Requirements Review (SRR) and Mission Definition Review (MDR) to enable close coordination of critical design interfaces between the Observatory elements and the launch vehicle.

The schedule supports an October 2036 launch readiness, with plans for a nominal five years of mission operations. Additional onboard consumables extend the mission life to 20 years.

8.5 Cost

The relatively straightforward *Lynx* Observatory design, technology maturation and evolution, and use of rich *Chandra* heritage and lessons learned enabled the development of a detailed parametric estimate and BOE, as well as multiple independently-developed validation cost estimates that yielded favorable comparisons. The sum total of this effort is a thoroughly and credibly costed pre-formulation stage mission.

The *Lynx* team developed a parametric mission cost estimate for Phase A through the first five years of operation, consistent with *GAO Best Practices for Estimating and Managing Costs* and guidelines and requirements described in the *NASA Cost Estimating Handbook*. The following sections describe the methodologies and summary results of the *Lynx* mission costing effort. Details and results for the entirety of this effort are included in the *Lynx* Costing Book, which is unavailable to the public.

The process for the development of the parametric estimate includes additional levels of rigor, lending to its credibility. This includes the use of:

- Multiple parametric models for all elements
- In-family comparisons at the subsystem level
- Subject Matter Expert (SME) inputs at the component level for all elements
- A transparent and clearly defined BOE and estimating process
- Multiple independently conducted cost estimates and/or assessments using different approaches

The parametric estimate includes 30% reserves on the Phase B–D cost (excluding launch vehicle and fee) and 10% fee on the assumed contractor portions. The estimate is aligned with the WBS, project schedule, Master Equipment List (MEL), and Power Equipment List (PEL), and includes funded schedule reserves to cover development risks discussed in §8.3 and §8.4. The launch vehicle cost was a pass-through per NASA Headquarters (HQ) guidance. The estimate incorporates high *Chandra* architecture heritage, robust and high-TRL spacecraft components and design, and a detailed and credible path forward for all DRM technologies (§6 and §7).

The validation estimates range from –11% to +28% of the parametric estimate, and the 40% confidence level (CL) results from the uncertainty analyses were within 1% of the parametric estimate. These independently conducted validation estimates provide credibility of the *Lynx* parametric estimate. (Figure 8.4).

The mission parametric estimate was validated through several separately conducted means to strengthen its credibility. The validation approaches include a *Chandra* analogous estimate, grassroots estimate, a non-advocate Independent Cost Estimate (ICE) with uncertainty analysis and an independent, contracted Cost and Technical Evaluation (CATE) with uncertainty analysis. The parametric estimates for the LMA, HDXI/XGD, and SCE were separately validated with in-family comparisons to historic missions.

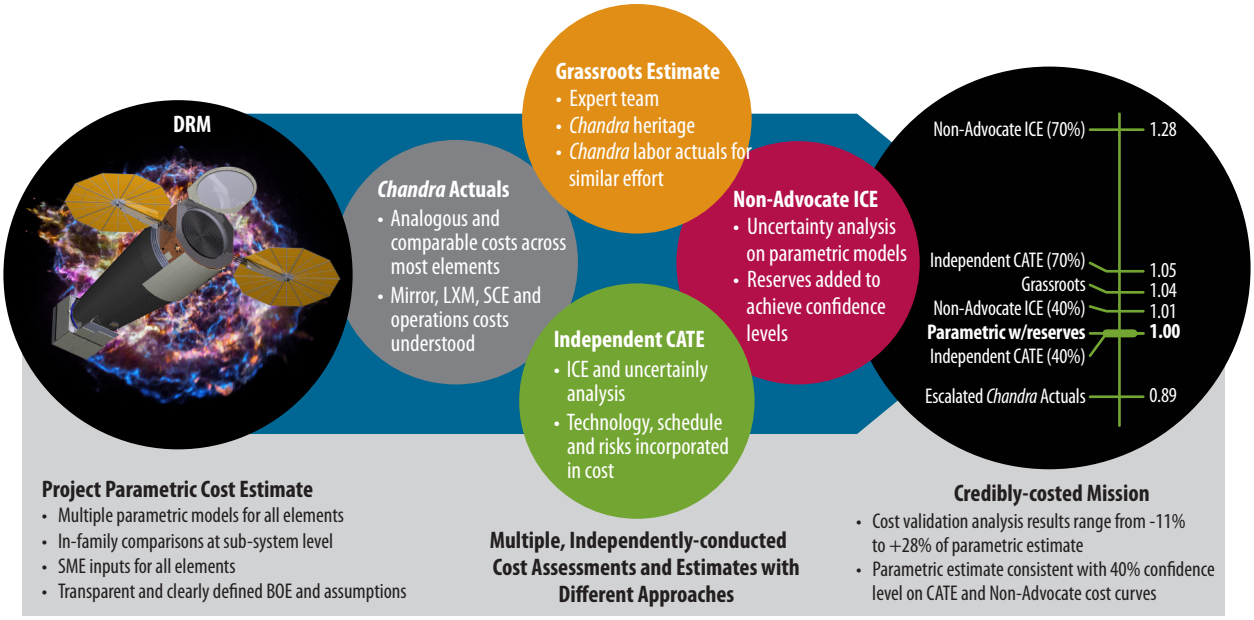

Figure 8.4. The *Lynx* parametric estimate is normalized to 1 and compared with multiple independently conducted cost analyses including a comparison to escalated *Chandra* actuals, grassroots estimate, non-advocate ICE with uncertainty analysis, and an independent CATE with uncertainty analysis. These validation estimate results are within a band of –11 to +28% of the *Lynx* parametric estimate. The 40% CL on the uncertainty analysis cost curves are within 1% of the parametric estimate. These results validate the credibility of the *Lynx* mission cost estimate.

The total *Lynx* DRM parametric mission cost is in the range of $4.8B at a 40% CL to $6.0B at a 70% CL in Fiscal Year 2020 Dollars (FY$20) and $6.5B at a 40% CL to $8.2B at a 70% CL in Real Year Dollars ($RY).

Analysis of the trade space on the science return per dollar indicates that the *Lynx* DRM produces the most scientifically and technically capable architecture that meets the science goals. Details of this analysis are discussed in §9.

8.5.1 Work Breakdown Structure

The *Lynx* Observatory WBS is structured similarly to the *Chandra* WBS and is consistent with guidance provided in the *NASA WBS Handbook* (NASA/SP-2016-3404). The structure allowed for development of an analogous cost comparison to *Chandra*, discussed in §8.5.3.1. The WBS is defined to Level 3 for all elements and to Level 6 for the XRT and SCE due to the in-depth knowledge and details of these systems. A summary of the key WBS elements associated with the DRM and their definitions is provided in Table 8.4. The fully expanded version of the WBS is provided in Appendix E.

The WBS provides the organizational scheme for the overall project, the structure for the cost model, and serves as the genesis of the Product Breakdown Structure (PBS) for all delivered hardware elements.

8.5.2 Cost Estimation Methodology

The primary cost estimate for *Lynx* was developed using parametric modeling, consistent with pre-formulation design maturity. Parametric cost estimation and analysis for the *Lynx* spacecraft, mirror, instruments, and mission utilized the industry-standard Project Cost Estimating Capability (PCEC), SEER®-H (Space Guidance), PRICE® TruePlanning® Space Missions, and PRICE®-H models. The NASA Instrument Cost Model (NICM) was used as a validation model for the instrument estimates. The launch vehicle cost was a pass-through as directed by NASA HQ and based on guidance from the Launch Services Program Office. The estimate for the LXM, discussed in more detail below, was developed by GSFC using PRICE®-H and was a pass-through for the *Lynx* mission estimate. The parametric cost models use Cost-Estimating Relationships (CERs) derived from the analysis of historical data with similar space programs and projects. These models have tailorable inputs allowing specific modifications to closely match the development approach for the *Lynx* optics and scientific instruments. The ability to tailor inputs is critical for these technologies given the uniqueness of Flagship missions in general [620] and the paucity of specific X-ray mission analogies in the historical databases from which the CERs are drawn.

PCEC is a publicly available parametric model developed and maintained by MSFC's Engineering Cost Office that is used to estimate the cost of spacecraft, launch vehicles, and human space flight systems. PCEC contains over 43 planetary and Earth-orbiting spacecraft missions and provides estimates at the subsystem level, which are all documented within the Cost Analysis and Data Requirements (CADRe) database.

Table 8.4. Summary WBS and definitions.

WBS	Elements
	***Lynx* X-ray Observatory Project**
01	**Project Management** – This element includes the management, business and administrative planning, organizing, directing, coordinating, controlling, approval processes used to accomplish overall project objectives not associated with specific hardware or software elements as well as review planning, project reserves, project planning and control and configuration management, and science payload management.
02	**Systems Engineering** – This element includes the technical and management efforts of directing and controlling the mission-level engineering efforts for this project, system requirements development, verification, integrated test planning, and system and mission analysis including system architecture development, and technical oversight
03	**Safety and Mission Assurance** – This element includes the overall efforts of directing and controlling the safety and mission assurance elements of the project, including verification of practices and procedures, safety and mission assurance management, reliability analysis, quality assurance, and mission safety.
04	**Science and Technology** – This element includes managing and directing the science investigation aspects, science support for Phases A–D as well as leading, managing, and performing the technology demonstration elements of the project. Included is the technology development effort to TRL 6 for the X-ray mirror modules (04.03), LXM (04.04), HDXI (04.05) and the XGS (04.06) which includes the XGA and XGD subassemblies.
05	**X-ray Telescope (XRT)** -This element includes management (05.01), systems engineering (05.02), product assurance (05.03), integration and testing of the XRT and its subsystems (05.04), on-ground calibration (05.05) and calibration facility modernization (05.12). This element also includes the DDT&E of the X-ray mirror modules and its integration into the LMA with its associated structural and thermal elements, DDT&E of the LXM, HDXI and the XGS (XGA+XGD), DDT&E of the ISIM and its sub-assemblies, integration of the LXM, HDXI and XGD into the ISIM, and DDT&E of the OBA. The completed XRT is delivered to the Observatory I&T in WBS 10.
05.06	*Lynx* Mirror Assembly (LMA)
05.06.07	X-ray Mirror Modules
05.07	X-ray Grating Spectrometer (XGS) – X-ray Grating Array (XGA)
05.08	Optical Bench Assembly (OBA)
05.09	Integrated Science Instrument Module (ISIM)
05.09.08	*Lynx* X-ray Microcalorimeter (LXM)
05.09.09	High Definition X-ray Imager (HDXI)
05.09.10	X-ray Grating Spectrometer (XGS) - X-ray Grating Detector (XGD)
06	**Spacecraft Element (SCE)** – This element includes management (06.01), system engineering (06.02), product assurance (06.03), and I&T (06.04) and DDT&E of the spacecraft element and its subsystems: FSW (06.05), GSE (06.06), Structures (06.07), TCS (06.08), EPS (06.09), C&DH (06.10), Communications (06.11), GN&C (06.12) and Propulsion (06.13). The completed SCE is delivered to the Observatory I&T in WBS 10.
07	**Mission Operations** – This element covers the totality of Mission Operations and Science Activity (and all associated support) during Phase E, commencing at the end of on-orbit checkout and running through the end of the primary science mission. This element includes tracking, commanding, receiving/processing telemetry, analyses of system status, trajectory analysis, orbit determination, maneuver analysis, and disposal of remaining end-of-mission resources. It also includes all aspects of science operations, mission planning and target scheduling, data analysis, archiving, scientific investigations and reporting.
08	**Launch Vehicle Services** – This element includes the launch vehicle as well as management and implementation of activities required to place the observatory directly into its operational environment. This element includes activities to support integration and testing of the observatory into the launch vehicle.
09	**Ground Systems** – This element covers the total development of the Mission Operations Systems (MOS) and Ground Data Systems (GDS), representing the Phase A–D effort to design, develop, integrate, test, and verify the software and hardware to support MOS/GDS activities on the ground. It includes development of all MOS and GDS-required testbeds, support equipment, and facilities, and development and implementation of procedures, documentation, and training required to conduct mission and science operations.
10	**Systems Integration and Test** – This element includes management and implementation of activities to perform observatory-level integration and testing. The element includes hardware, software, procedures, and unique GSE and facilities required to perform the integration and testing of the XRT to the SCE as well as I&T at the observatory level. This element also includes sustaining engineering support for telescope and observatory subsystems through on-orbit checkout.
11	**Public Outreach** – This element includes all aspects of public outreach for the project including but not limited to press releases, media support, videos, models, website development to inform the public of the benefits of the project.

PCEC was selected for the overall mission level and spacecraft estimate because of its following benefits:

- Aligns with standard NASA WBS structure and fully captures NASA efforts under WBS 1, 2, 3, 5, and 10 elements
- Provides full access to the data and analysis used to develop the CERs and related statistics
- Contains data that are normalized to minimize subjective inputs
- Incorporates the Space Operations Cost Model (SOCM) to estimate Mission Operations and Data Analysis functions for Phases B

Chandra and other flagship mission costs provide calibration factors. *Chandra* actuals, SEER-H®, and PRICE® TruePlanning® provides validation for the PCEC mission and spacecraft estimates.

SEER® and PRICE® are commercial cost models that employ large databases as tools for spacecraft and instrument cost estimation. SEER-H® was selected for the HDXI, XGS (XGA+XGD), and LMA estimates because it uses historical data that allows for a more accurate assessment of costs related to detectors and mirror segments. PRICE® TruePlanning® and NICM estimates, and *Chandra* actuals, provide validation for the LMA, instruments, and spacecraft. Furthermore, the SEER® risk analysis capability provides a coefficient of variation ranging from 0.3 to 0.5, consistent with Air Force guidance for space systems as input distribution for the PCEC mission model.

The GSFC Instrument Design Lab (IDL) developed a cost estimate for LXM using the PRICE-H® tool. While this instrument incorporates heritage and design elements from past and planned X-ray missions, it does not have any direct analogies or historical analogies that provide an easy comparison. The GSFC estimate was developed with input from SMEs for the detector technology and manufacturing, X-ray calibration sources, and Flight Software (FSW) testbed and associated hardware development. This estimate was incorporated as a pass-through in the *Lynx* PCEC mission cost model.

The approach to parametric costing of the LMA was given special consideration, as the LMA assembly does not have applicable analogous historical comparisons (§8.5.3.1). The manufacturing of the LMA's many mirror segments (§6.3.1) is of particular importance, and unlike *Chandra*, can take advantage of a highly parallelized manufacturing scheme.

8.5.2.1 LMA Manufacturing Approach and Cost Considerations

The LMA consists of the X-ray mirror modules, integrated with the pre-and post-collimators, contamination doors, and barrel structure. The unique feature of the LMA and key to the *Lynx* science program is the X-ray mirror module assembly. Understanding and preparing for the manufacturing of the mirror modules and the many mirror segments that populate them is a surmountable challenge with a solution that builds upon substantial laboratory work already accomplished. The *Lynx* team recognizes that a fully vetted LMA manufacturing and assembly process must be demonstrated early in the project to demonstrate mission viability.

Industrialization of the manufacturing process and mirror assembly are the subject of two of the top project risks, as discussed in §8.3. Current studies are ongoing and will continue through Phase A to prove out the manufacturability and assembly of the mirrors as part of TRL advancement. The X-ray mirror module TRL 6 demonstration, which includes nine fully populated modules assembled within three meta-shells, will also serve as a test bed for the manufacturing and assembly processes.

The mirror module assembly consists of 611 modules, populated with a total of 37,492 mirror segments that are mounted to a common structural element called the "spider." A single ring (of a given diameter) consists of multiple identical modules to create a meta-shell. There are 12 meta-shells that form the LMA, enabling *Lynx* to meet its effective area requirement. Each mirror segment has the same thickness (0.5 mm) and roughly the same dimensions (100 mm × 100 mm). Within the modules for a given meta-shell, the radius of curvature of the mirror segments does not change significantly. This modular design allows for parallel manufacturing (by meta-shell), and this is reflected in the *Lynx* parametric cost analysis.

Inputs and Assumptions for Parametric Costing — The parametric costing utilizes an understanding of the LMA fabrication and assembly process, obtained with the detailed input and review by the Silicon Meta-shell Optics team through multiple technical interchange and face-to-face discussions, throughout the course of this study.

The parametric cost model includes all elements required for fabrication and assembly of the LMA. At a high level, there are essentially six cost areas; three are independent of the manufacturing process: (1) the materials for the mirror elements, or consumables, (2) the labor hours to assemble the meta-shells into the LMA, and (3) the *Lynx* specific tooling such as lapping and polishing tools. The elements of cost that depend on the detailed design of the manufacturing process are (4) machine (server) costs, (5) facility costs such as rent, utilities, maintenance, and (6) level-of-effort costs such as management, systems engineering, procurement, quality assurance, and record keeping.

Details for the process and elements are applied during the selection of cost model parameters. Some of the key SEER-H® model inputs include:

- The use of a learning curve to take advantage of the large quantity of similar (but individually produced) mirror segments and mirror modules
- A decrease in the "Percent New Design" at the meta-shell level to account for the benefits of a largely repeatable production process:
  - "Make" was used for the first meta-shell (80% new design)
  - "Major Modification" was used for the second meta-shell (65% new design)
  - "Average Modification" was used for the remaining meta-shells (15% new design)
- The staggering of the development start for the second and third meta-shells to benefit from the development of first meta-shell
- The use of "Minor Design Changes" after the development of second meta-shell
- Concurrent development and production timeline to take advantage of the use of 12 production lines for the meta-shells
- A model hierarchy that reflects each meta-shell as a separate subsystem

The Silicon Meta-shell Optics team also provided guidance on input parameters for prototype definition and spares at the mirror module level consistent with the *Lynx* sparing philosophy. Mass inputs were per the Silicon Meta-shell Optics team-provided MEL.

In parallel, the GSFC team developed a detailed grassroots estimate (Table 8.11, *(*WBS 05.06.07*)* and *Lynx Cost Book*). This estimate includes costs for unique tooling such as for lapping and polishing, capital equipment for mirror fabrication and coating, and labor to produce the mirror assembly.

The estimate includes assumptions for process steps and time to complete based on laboratory experience to date, and based on the project schedule (Figure 8.3), estimates the number of machines and parts processed per machine per week to manufacture the 611 mirror modules and assemble the 12 meta-shells. This estimate takes into account the industrialization of the repeatable manufacturing and assembly process, which is key to the cost effectiveness of the Silicon meta-shell design.

The X-ray mirror module parametric estimate was within 4% of the GSFC grassroots estimate and found to be "in-family" with historical x-ray telescope assemblies (Figure 8.7).

Manufacturing Process and Optimization — Based on laboratory work already accomplished to produce and align segment pairs, the Silicon Meta-shell Optics team has developed a detailed flow for the steps required to manufacture the X-ray mirror modules, which are the dominant component in the LMA (Table 8.5). This analysis establishes, by measurement, the time required for each step in the process; identifies capital equipment for mirror fabrication and coating, along with unique tooling for lapping, polishing and the like; sizes and scopes the needed facilities; and estimates the labor necessary to produce the mirror assembly. At this relatively early point in the program, the *Lynx* team has conservatively assumed 12 parallel manufacturing lines, or one per meta-shell, to shorten the overall manufacturing time enabling the work to fit within the overall *Lynx* project schedule (Figure 8.3) by taking advantage of the modular nature of the mirror assembly.

Table 8.5. List of LMA process steps and associated time to complete each step.

	Step	Name	Calendar Time (h)
Element Fabrication	1	CNC Grinding	4
	2	Lapping (buffing and measurement on FizCam)	8
	3	Slicing	3
	4	Coarse edge treatment	1
	5	Etch	1
	6	Polishing (FizCam)	20
	7	Smoothing (FizCam)	4
	8	CNC Grinding	4
	9	Trimming	2
	10	Final Etching	3
	11	FizCam measurement, IBF	3
Coating	12	Cleaning and oxidizing the backside	10
	13	Sputter Ir coating	10
	14	Anneal	10
	15	FizCam measurement, IBF	3
Align and Bond	16	Measure height and locations of 8 spacers	0.5
	17	Fabricate 8 spacers	4
	18	Attach spacers and cure	2
	19	Measure radial heights of 8 spacers and trim to tolerance	3
	20	Align mirror by fine-grinding guided by Hartmann	4
	21	Bond mirror and cure, return to Step 16 to complete module	10

A CAN study was initiated to develop an analytic method for optimizing the LMA manufacturing process. This approach is based on industrial engineering methodology, and the first assessment of the LMA manufacturing process has been reported in the literature [621], indicating that the baseline approach is feasible.

The CAN study derives a method that identifies the optimal number of machines (servers) required for each process step in order to minimize idle, or down time, over the entire manufacturing process. Servers for a single production line include all manufacturing and metrology machines needed to carry out the mirror fabrication, coating, alignment, and bonding. There are 21 identified steps in the manufacturing process (Table 8.5) [622]. Assuming one production line per meta-shell means that there are 12*21=252 server sets to be procured. To be conservative, the full quantity of 252 servers was assumed for the parametric and grassroots cost estimates. Equipment for the servers is a mix of commercially available interferometers, grinders, slicers, etchers, ion-beam figuring machines, cleaners, coaters, ovens and the like, along with hardware unique for *Lynx* such as lapping, trimming, and polishing tools, and machines. Required equipment has been identified and costed based on prices for the commercially available items and costs for developing *Lynx* unique tools during the laboratory demonstration work. For example, individual lapping and polishing tools range in cost from $10K to $125K. The grassroots estimate for equipment is ~40% of the total estimated cost. By far the dominant labor effort is that required to fabricate, align, and bond a mirror segment. Based on laboratory experience to date as summarized in Table 8.4, and including ~10% margin, the number of labor hours to produce a mirror segment, which includes direct labor, overhead, and quality assurance, is conservatively estimated at 61 hours. Summed over the full number of segments, the total labor equates to ~1,150 person years, which equates to roughly 288 equivalent persons per year, for a 4-year effort. This effort (plus 6 months of funded schedule margin) is supported by the project schedule (Figure 8.3). While this labor force to produce the mirror segments is considerable, the estimate is conservative and based on non-optimized processes. Labor costs have been estimated using a mix of levels and capabilities and a range or associated rates leading to a labor cost estimated at ~55% of the total grassroots cost.

The simple approach of procuring a complete set of servers for each meta-shell does not account for the fact that each step in the process will be completed at a different rate or that the number of modules and mirror segments in each of the 12 meta-shells differ, indicating that further optimization is possible. Table 8.5 shows that the rate-limiting step is polishing, which is twice as long as the next longest step. Since all of the steps after polishing take less time, there is idle time for those servers. Removing this idle time by optimizing the use of the servers would result in significant cost savings to the project. Adding more servers for the polishing step (or other steps among the most time-consuming) would reduce the time required to flow through those "bottle-neck" stages. This optimization process indicates that the parametric and grassroots estimates are somewhat conservative and that further trades involving the numbers of lines, servers, and related labor costs has the potential to reduce costs. A very preliminary, first pass suggests that a reduction in number of servers of order 30% is possible [621], but a much more thorough analysis will be performed during pre-Phase A to assess pros and cons of 12 completely separate lines (as baselined at this point) versus a more integrated flow and more cost-effective use of servers and resources.

8.5.2.2 Parametric Cost Ground Rules and Assumptions

The ground rules and assumptions (GR&A) for the *Lynx* mission level parametric cost estimate process are summarized in Table 8.6.

Table 8.6. General GR&A for *Lynx* cost estimate.

Parameter	Value
Baseline cost	$FY20 per NASA inflation tables
Phased mission cost	$RY per NASA inflation tables
Fee	10% applied to Spacecraft, ISIM, OBA, and LMA (X-ray mirror modules + associated structures); no fee for science instruments (assumed NASA or university-developed)
Reserves	30% on Phases B–D, excluding launch services and fee
Design approach	Protoflight
Mission risk class	A
Parts class	Unmanned space class S1; redundancies provided in MEL (Appendix D)
Flight unit quantity	1
Spares	10% for all subsystems
Phase A estimate	5% of DDT&E + Flight Unit total
Public outreach estimate	1% of XRT (WBS 05) + SCE (WBS 06) totals

Specific cost model inputs for LMA, HDXI, XGS (XGA+XGD) and the spacecraft are provided in Table 8.7. The integrated mission cost estimate was modeled using PCEC, with the mirror, instrument, and spacecraft models, and the SOCM operations model as inputs. The LV was not modeled, as the estimate was provided as a pass-through. As described in §8.5.2, the LXM cost was modeled by GSFC using PRICE-H®, and treated as a pass-through as well.

Table 8.7. Parametric cost model input parameters.

Parameter	SEER-H® (Space Guidance)	PRICE® (Space Missions)	PCEC
Operating Environment	**LMA, HDXI, XGS (XGA+XGD), SCE**: Space unmanned, science, command and control, Earth-orbiting (SE-L2)	**LMA, HDXI, XGS (XGA+XGD), SCE:** Space unmanned, Earth-orbiting (SE-L2)	**SCE, Mission**: Earth-orbiting (SE-L2)1
Platform	**LMA, HDXI, XGS (XGA+XGD), SCE**: Space unmanned	**LMA, HDXI, XGS (XGA+XGD), SCE**: Space unmanned	N/A
Standard	**LMA, HDXI, XGS (XGA+XGD), SCE**: Science, command & control	**LMA, HDXI, XGS (XGA+XGD)**: Payload, Class A mission **SCE**: Class A mission	**SCE, Mission**: Robotic spacecraft
Acquisition Category	**LMA, HDXI, XGS (XGA+XGD), SCE**: Based on component and production plan; varies for individual components from "make" to "space procure to print"	**LMA, HDXI, XGS (XGA+XGD), SCE**: Based on component and production plan; varies for individual components from "new" to "minimum modification"	**SCE, Mission**: Based on subsystem heritage factor, parts rating (flagship mission), operating environment
Level	**LMA, HDXI, XGS (XGA+XGD), SCE**: Component	**LMA, HDXI, XGS (XGA+XGD), SCE**: Component	**SCE**: Subsystem **Mission**: NASA and contractor
Structures Complexity	**LMA, XGS (XGA+XGD), HDXI, SCE**: Primary/secondary structures knowledge base defaults, nominal complexity **LMA-specific**: Optics knowledge base, high to very high complexities, learning curve applied for subsequent modules	**LMA, XGS (XGA+XGD), HDXI, SCE**: Defaults based on environment, subsystem and function **LMA-specific**: Optics subsystem, high to very high complexities, learning curve applied for subsequent modules	**SCE**: Defaults based on environment and subsystem **Mission**: N/A

Table 8.7. *Continued*

Parameter	SEER-H® (Space Guidance)	PRICE® (Space Missions)	PCEC
Mechanisms Complexity	**LMA, XGS (XGA+XGD), HDXI, SCE**: Component-specific knowledge bases, defaults and unmanned space operations	**LMA, XGS (XGA+XGD), HDXI, SCE**: Defaults based on environment, subsystem and function	**SCE**: Defaults based on environment, subsystem, and function **Mission**: N/A
Multiples of Same Component	**LMA, XGS (XGA+XGD), HDXI, SCE**: Multiple at next higher level of assembly	**LMA, XGS (XGA+XGD), HDXI, SCE**: Multiple at next higher level of assembly	**SCE**: Multiple at next higher level of assembly **Mission**: N/A
Electronics Complexity	**LMA, XGS (XGA+XGD), HDXI, SCE**: Component-specific knowledge bases, defaults, and unmanned space operations **XGD-specific**: Detector electronics unit (DEU) electronics box—conductive cooling knowledge base defaults—modification minor (15% new)	**LMA, XGS (XGA+XGD), HDXI, SCE**: Price complexity calibration **XGD-specific**: Electronics box—20% new	**SCE**: Defaults based on environment, subsystem, and function **Mission**: N/A
Thermal Components	**LMA**: Thermal control knowledge base—passive; spider heaters active; make **XGA**: N/A **HDXI**, **XGD**: Component-specific knowledge base defaults **SCE**: Component specific knowledge base defaults	**LMA, XGS (XGA+XGD), HDXI, SCE**: Price default complexity	**SCE**: Defaults based on environment, subsystem, and function **Mission**: N/A
Power	Per power schedule (Table 6.16)	Per power schedule (Table 6.16)	Per power schedule (Table 6.16)
Communication	**LMA, XGS (XGA+XGD), HDXI:** N/A **SCE**: Component knowledge base, Std. RF X Band and Ka Band TWTA for SE-L2 (1200W Ka Band Transponder)	**LMA, XGS (XGA+XGD), HDXI**: N/A **SCE**: Component knowledge base, Std. RF X Band & Ka Band TWTA for SE-L2 (1200W Ka Band Transponder)	**LMA, XGS (XGA+XGD), HDXI**: N/A **SCE**: earth-orbiting, Std. RF X Band and Ka Band TWTA for SE-L2 (1,200 W Ka Band Transponder)
Propulsion	**LMA, XGS (XGA+XGD), HDXI**: N/A **SCE**: Weight-based, component-based	**LMA, XGS (XGA+XGD), HDXI**: N/A **SCE**: Weight-based, component-based	**LMA, XGS (XGA+XGD), HDXI**: N/A **SCE**: MPS—86N, 4 thrusters; RCS—5N, 16 thrusters
Quantities[2]	**LMA**: 10% prototype for structural items except for spider and meta-shell structures #1, #6, and #12 (50% to capture quantity for the EM), 4% prototype for mirror segments and modules,10% spares **XGA**: 10% prototype for structural items and spares **HDXI, XGD, SCE**: 65% prototype (10% wrap ETUs, 1 EDU (55% flight-quality unit), 10% spares	**LMA**: 10% prototype for structural items except for spider and meta-shell structures #1, #6, and #12 (50% to capture quantity for the EM), 4% prototype for mirror segments and modules,10% spares **XGA**: 10% prototype for structural items and spares **HDXI, XGD, SCE**: 65% prototype (10% wrap ETUs, 1 EDU (55% flight-quality unit), 10% spares	**SCE**: 65% prototype (10% wrap ETUs, 1 EDU (55% flight-quality unit), 10% spares

Notes: 1. Earth-orbiting environment selected for PCEC mission cost model based on Wilkinson Microwave Anisotropy Probe (WMAP) mission, a U.S. system at SE-L2, and classified as near-Earth orbiting. This choice of Earth operating environment is supported by similarities in the mission design and operation requirements for Lynx at SE-L2 and Chandra at High Earth Orbit (HEO). 2. Spares, prototype, Engineering Test Unit (ETU), and Engineering Development Unit (EDU) factors based on development philosophy described in §6.6.

8.5.2.3 Parametric Cost Basis of Estimate

The parametric basis of estimate (BOE) summarized in Table 8.8 provides a basis for the cost estimate by WBS element, and summarizes key parametric model assumptions.

Table 8.8. BOE for parametric estimate by project WBS.

WBS	WBS Title
01	**Project Management**
Basis of the Estimate: PCEC used for this WBS element. This estimate used a CER in the PCEC tool that utilizes data on Lead Organizations, flight systems organizations, heritage and parts ratings, and from similar projects. Reserves at 30% to Phase B–D costs.	
02	**Systems Engineering**
Basis of the Estimate: PCEC used for this WBS element. The CER provided estimates for the Government and Contractor SE cost per month at the Project-, Payload-, and Spacecraft-level based on data from mission destination and flight system power for similar projects.	
03	**Safety and Mission Assurance**
Basis of the Estimate: PCEC used for this WBS element. The CER provided estimates for the Government and Contractor S&MA cost per month at the Project-, Payload-, and Spacecraft-level based on data from mission destinations, lead organizations, and flight system power for similar projects.	
04	**Science and Technology**
Basis of the Estimate: PCEC used for this WBS element. The CER provided estimates for the Government and Contractor Science and Technology cost based on the Astrophysics science category factor, applied to the sum of WBS 1–3, 5–7, and 9–11.	
05	**X-ray Telescope (XRT)**
Basis of the Estimate: PCEC used to estimate the structural and mechanical portions of the XRT subsystem. However, the level of detail provided in the MELs made PRICE® and SEER® more suitable tools to estimate the LMA (05.06), the X-ray mirrors (05.06.07), the XGA (05.07) and the ISIM instruments (LXM: 05.09.08, HDXI: 05.09.09 and XGD: 05.09.10). PRICE® does not estimate X-ray optics and sensors well, so SEER® was used for instruments with these components. Also, SEER® provides an embedded Monte Carlo generation capability that provides input distribution into the PCEC model. Although the instrument's mass and power are well outside the dataset in NICM, NICM was used to provide an additional point of comparison as PCEC does not estimate instruments. Note: The GSFC-provided PRICE® estimate for the LXM was a pass-through.	
06	**Spacecraft Element (SCE)**
Basis of the Estimate: PCEC used to estimate the spacecraft costs because of the level of the data provided. PCEC also allowed the other estimates to be throughput with Monte Carlo input data and Monte Carlo analysis to be performed on the overall estimate. Used a 10% fee and 30% reserves. Flight Software costs are included in the GN&C, Communications, and C&DH Estimates in the mission level estimate. A proto-flight design approach is used, 65% prototype, flight unit of 1, and 10% spares to all subsystems. These percentages are similar/typical of Pre-Phase A efforts.	
07	**Mission Operations**
Basis of the Estimate: PCEC used for this WBS element. Utilized the near earth CER based on the daily data volume, mission type, tracking network, management mode, science team role, science team size, and quantity and type of instruments.	
08	**Launch Vehicle Services**
Basis of the Estimate: Throughput from NASA HQ following direction from the Launch Service Program (LSP).	
09	**Ground Systems**
Basis of the Estimate: PCEC used for this WBS element. Used Mission Operations (MO) and Data Analysis (DA) Phase B–D and near-Earth CER based on the flight system dry mass, mission type, tracking network, management mode, science team role, science team size, and quantity and type of instruments.	
10	**Systems Integration and Test**
Basis of the Estimate: PCEC used for this WBS element. This CER calculates a monthly cost during I&T based on the mission duration, payload organization, flight system power, total payload mass, and number of payload elements. The monthly charge per phase is determined based on the database average for this type of mission.	
11	**Public Outreach**
Basis of Estimate: Used 1% of Phase B–D costs. Historically, public outreach has been 1–2% of the project payload and flight system cost.	

8.5.3 Cost Validation

Multiple cost validation exercises conducted separately from the parametric analysis provided additional peer reviews, sensitivity analyses, and independent crosschecks—further strengthening the credibility of the *Lynx* parametric estimate.

The primary cost estimate for the *Lynx* mission is the parametric estimate, which is consistent with pre-Phase A for concept formulation. The credibility of this estimate is strengthened by the SME inputs on the component level for every Observatory element. Further validation of the parametric estimate includes a detailed comparison to *Chandra*, a grassroots assessment developed by a team of highly qualified experts on both *Lynx* and *Chandra*, development of a non-advocate ICE with uncertainty analysis, and development of an independent, contracted cost and technical evaluation (CATE) with uncertainty analysis. In-family comparisons to the LMA, HDXI and XGD assembly, and spacecraft provides additional validation of the parametric estimate for these elements. The approaches to each of these validation methodologies are outlined below.

8.5.3.1 *Chandra* Analogy

The huge gains in capability that *Lynx* provides do not directly translate to a huge cost increase over inflated ($FY20) *Chandra* actuals due to extensive, existing knowledge-base and lessons learned from past X-ray missions, existing spacecraft hardware, and recent advancements in X-ray mirror and science instrument maturity. As a result, the *Lynx* parametric mission cost estimate is within 11% of the escalated ($FY20) *Chandra* actual cost.

Given the strong heritage from the *Chandra* mission and availability of actual costs, *Lynx* parametric cost estimates were compared with *Chandra* actuals normalized to $FY20. Detailed comparisons were performed at the subsystem level for the spacecraft, at the instrument and mirror levels for the telescope, operations, and at the mission level.

Lynx mission formulation and technology development have directly benefitted from having a science community and a contractor base with extensive and applicable experience from working on *Chandra* and other recent X-ray missions. Even though personnel and contractors will change, an exceptionally solid mission concept and cost basis for *Lynx* are developed with inputs and lessons learned from the current personnel base. The *Lynx* DRM uses an over-arching observatory and ground system architecture similar to that of *Chandra*, enabling *Lynx* to take advantage of lessons learned while also taking different approaches as necessary.

The analogous and comparable *Chandra* elements leveraged on *Lynx*, which include the spacecraft, the HDXI and XGS assembly, and operations are summarized in Table 8.9. Items less amenable to direct leveraging from *Chandra* are the X-ray mirrors (and LMA) and the LXM. However, as discussed below, these costs are well understood. For the spacecraft, almost all *Lynx* performance requirements are the same as those on *Chandra*, primarily due to having the same angular resolution requirement. Observatory-wide error budgets for mass, power, thermal, and end-to-end performance, discussed in

§6.6.1, demonstrate that the requirements are well understood and achievable. The *Lynx* design utilizes current high-heritage spacecraft components, analogous to those on *Chandra*. While *Lynx* will ultimately use SOA elements, no new specific technology developments are required.

The mission cost estimate reflects the overall utilization of *Chandra* heritage. The *Lynx* PCEC parametric modeling includes heritage factors with settings of "major modification" (3 on a 1–10 scale) for all spacecraft subsystems and flight systems except structures, and a setting of "new but standard process" for structures. Parameters for mission type, mission destination, and operating environment, which influence the communication and mission operations cost estimates, are set to the same normalization as WMAP, which operated at Sun-Earth L2 (Table 8.7, note 1). Inclusion of these heritage factors lowers the parametric cost estimate.

Table 8.9. Summary comparison of key *Chandra* and *Lynx* spacecraft, telescope elements, and operations.

Observatory Element	*Lynx* vs. *Chandra* Requirements	Comments
Spacecraft		
Propulsion	Comparable except *Lynx* requires more fuel to maintain L2 orbit	Momentum management is similar. *Lynx* does not require internal spacecraft engines to reach final orbit.
GN&C	Comparable	*Lynx* requirements are similar for pointing accuracy and control, aspect determination, slew speed, and frequency.
Power	Analogous *Lynx* ~3x *Chandra*	*Lynx* uses different solar panels and battery technology. However, the power design philosophy is similar and high TRL hardware already exists.
Thermal	Comparable	Thermal requirements are similar for the OBA and LMA, but due to aging of *Chandra* Multi-Layer Insulation (MLI), an additional offset layer and small sunshade is included for *Lynx*.
Avionics and Flight Software	Comparable	Thermal control, power switching and management, data storage, command management, and uplink and downlink communications require *Lynx*-specific flight software, but the design philosophy is similar.
C&DH	Comparable except *Lynx* data storage and downlink rates are nearly 100x *Chandra*	Frequency of DSN contacts for uplink and downlink is similar to *Chandra*. Increased requirements for data storage and downlink rate can be met with already existing high TRL hardware.
Telescope		
Mirror Assembly	Comparable requirements, but implementation involves a very different approach	*Lynx* mirror fabrication and assembly is very different from *Chandra*. *Lynx* Mirrors are segmented and made of a different material. *Lynx* requires the integration of ~37,500 segments to form the LMA. Demonstrated laboratory production of multiple mirror segments, along with plans for mass production, plus modularity of the assembly provide a sound basis for the cost estimate.
HDXI	Analogous	Similar to primary imager on *Chandra* in terms of functionality and spacecraft resource requirements, even though *Lynx* HDXI will use SOA technologies.
XGS	Comparable	Grating array structure and mechanisms for *Lynx* designed similar to *Chandra* grating array. Detector system is also similar in terms of required spacecraft resources. *Lynx* grating array is much larger than *Chandra* gratings and uses a different design.
LXM	Not Analogous	LXM is a unique instrument that leverages heritage and design from JAXA and ESA missions. There is no *Chandra* analogy. LXM costs are well understood given high heritage with other similar instruments (*Hitomi* SXS, *XRISM* Resolve and *Athena* X-IFU).
Operations	Comparable	Nearly all of the hardware and software requirements and algorithms are available for designing ground operations and science systems. Software heritage is substantial.

Spacecraft Comparisons — Table 8.10 provides a look at two *Chandra* spacecraft subsystems also specified on *Lynx* for which current costing information is readily available.

Table 8.10. Cost comparison between inflated *Lynx* actuals and current vendor estimates for two spacecraft subassemblies.

Subsystem	*Chandra* Actual Cost	*Chandra* Cost ($FY20)	Current Vendor Estimate
Reaction Wheels (6 flt.+1 spare) plus drive electronics and isolation system	$1.95M	$3.82M	$1.0–$2.0M Range due to uncertain cost for quality control
Aspect camera assembly	$28.5M (1 optic with flip mirror and 2 readouts)	$55.9M	$30M–$35M (2 complete camera assemblies)

Although not necessarily representative for all spacecraft subsystems, these two examples show that costs have not escalated as quickly as predicted by NASA inflation factors. This assessment is directly relevant to the overall spacecraft cost comparisons since most *Lynx* spacecraft subsystems requirements are met by those used on *Chandra*, so hardware with demonstrated performance is already available.

Labor costs comprise the largest cost element at the full systems level for the spacecraft, with the subsystem hardware costs being a significant, albeit lower, contributor. The data above suggest that the hardware costs for various *Lynx* spacecraft subsystems are likely to be somewhat lower than the inflated *Chandra* actuals, while the labor required should not differ substantially from *Chandra*. These considerations provide additional support for the parametric estimates for the spacecraft being at a level comparable to the inflated *Chandra* actuals.

Telescope Comparisons — The *Lynx* telescope elements are based on technologies currently at TRL 3 or higher. The LMA and science instrument requirements, their current state of development, and their technology development plans to achieve TRL 6 are presented in §6 and §7. Although further technology development is required, the development plans for the payload elements are well understood, leading to credible parametric estimates for each as described in this section and in the *Lynx Cost Book*. The required pre-Phase A and Phase A technology development funding has been identified and is at a level consistent with existing NASA funded development opportunities and that of other similar programs.

***Lynx* Mirror Assembly** — The X-ray mirrors are the dominant component of the LMA, and are akin to the mirror elements within the *Chandra* High Resolution Mirror Assembly (HRMA). The *Lynx* X-ray mirrors have a collecting area ~30x the HRMA, comparable on-axis angular resolution, and a sub-arcsecond point spread function over a FOV 20x the corresponding FOV for *Chandra*. The sub-arcsecond angular resolution over the much larger FOV for *Lynx* results from making small changes to the mirror prescription from the *Chandra* Wolter-1 to the *Lynx* Wolter-Schwarzschild, along with the use of substantially shorter mirror segments on *Lynx*, with no accompanying cost drivers. The tighter nesting of the thinner *Lynx* mirror segments results in a 3-m diameter, which is 2.5x larger than the HRMA. The focal length and focal plane plate scales are identical for *Lynx* and *Chandra*. The LMA is described in detail in §6.3.1.

Design and capability differences between the *Lynx* LMA and *Chandra* HRMA do not translate directly into large differences in cost primarily due to readily available mirror segment Silicon material and cost efficiencies borne out of the repetitive manufacturing processes for the LMA segments and modules (§8.5.2). The estimated cost of the LMA is within 6% of the escalated ($FY20) HRMA actual cost.

A key factor for the basis of the *Lynx* mirror costs, in addition to the ready availability of high-quality monocrystalline silicon, is the demonstrated laboratory performance of the machinery needed to polish, shape, and smooth the *Lynx* segments, along with the metrology to measure and confirm their performance. This situation can be contrasted with *Chandra* for which all of the equipment had to be developed almost from scratch.

In contrast to HRMA, the LMA is modular, lending itself to a "mass production, assembly line" approach. This systematized manufacturing approach is the essential factor constraining the *Lynx* mirror costs (§8.5.2). While the approximately 37,500 mirror segments represent a large increase relative to *Chandra's* eight mirror elements, the process is quickly transformed from the specialized, "one-at-a-time" *Chandra* approach to a relatively straightforward manufacturing process for *Lynx*. For *Lynx*, handling and shaping small segments (even very thin ones) is substantially easier than dealing with large, heavy *Chandra* elements. *Chandra* polishing required many months for each element, while *Lynx* segments can be done in a few days, with many segments being fabricated, aligned, and assembled simultaneously. The time, labor, and equipment costs for fabricating these mirrors are well understood and have been applied to project the *Lynx* mirror costs (§8.5.2).

The planned assembly line process for *Lynx* keeps the production time for the total ensemble of segments comparable to the polishing time for the *Chandra* elements; the projected costs are comparable in $FY20. In addition, a few pairs of segments have already been aligned at close to the precision required for *Lynx*; demonstration of flight-like alignment is included as part of the technology development plan to achieve TRL 6. While *Chandra* had only eight elements, mounting and aligning them was very challenging. For *Lynx*, dealing with and assembling many more small, light-weight segments is also challenging, but is expected to evolve into a "routine" process for which the required time and associated costs are already approximately known.

Ultimately, the modularity of the *Lynx* mirrors provides a "safety valve" against schedule slip, cost growth, and/or depletion of mass margins, as mirror pairs can be eliminated from the design for up to a 50% reduction in effective area (§9). In this case, mass dummies would replace the eliminated mirror pairs, thus saving the time and cost for mirror polishing, coating, and ion beam figuring. While this option would necessitate longer exposure times, a reduced area would not decimate the science program. This ability to react to challenges to cost and schedule during DDT&E provides overall project flexibility and reduces cost and schedule risk. This modular approach also supports having reasonable numbers of spare segments at the 10% level, allowing replacement of broken or non-performing pieces during the manufacturing or assembly process or in a worst-case scenario, simple deletion of a module or a shell. Note that while *Chandra* had spare blanks for each element, none of these were polished, thereby making any potential replacement a more time-consuming and expensive proposition. In terms of modularity and spares, the approach to the *Lynx* mirrors is far more robust and cost-effective than what was available for the *Chandra* HRMA.

***Lynx* Science Instruments** — Though the *Lynx* and *Chandra* science instruments use different technologies, meaningful comparisons can be made. The *Lynx* HDXI and XGD are designed to use similar technologies and both have substantial similarities to the *Chandra* Advanced CCD Imaging Spectrometer (ACIS). However, the *Lynx* detectors provide significant increases in capability through higher quantum efficiency at lower energies, active pixel sensing, faster readout, and radiation hardness (§6.3.2). These *Lynx* detectors do not require technology breakthroughs, just advancements over the current state of the art to couple with the LMA to provide leaps forward in sensitivity (100×) and FOV (20×), with high-angular resolution imaging and survey capabilities relative to *Chandra*. Similar considerations apply to the XGA, which will have on the order of 100× the throughput and 10x the resolving power of the *Chandra* gratings, enabling tremendous advances for spectroscopy of point-like sources such as stars and active galactic nuclei (§6.3.3). *Lynx* costs for each of these instruments are projected to be ~30% higher on average than the inflated *Chandra* costs for ACIS and the High Energy Transmission Gratings (HETG). These estimates are conservative when taking into account ongoing advances in the semi-conductor industry, which have resulted in cost growth rates for sensors, electronics, and similar hardware that are lower than the standard inflation rate applied to escalate the *Chandra* actuals.

The one instrument on-board *Lynx* that does not have a direct analogue from *Chandra* is the LXM. The LXM cost estimate, however, does take into account other heritage and leveraged design elements from planned missions while allocating substantial funding for this new capability. Coupled with the capabilities of the LMA, the LXM provides breakthroughs for high-resolution spectroscopy of extended sources such as clusters of galaxies, galactic halos, and supernova remnants, to name a few (§2.2, §3.3). There have been great advances in the technology development for this type of instrument, both in the laboratory and through flight development for a series of Japanese missions. Those missions include *Hitomi*, where the performance capabilities of the SXS instrument were demonstrated before the premature loss of the mission, and *XRISM*, currently under construction. The LXM also benefits substantially from investments by NASA and ESA in the *Athena* X-IFU, which is a similar detector albeit with fewer pixels, less demanding spatial resolution, and no extra-high spectral resolution subarray as is planned for the LXM. Through the use of thermal and electronic multiplexing, the LXM has a comparable number of readout channels to *Athena* and thereby comparable cooling requirements (§6.3.4).

The LXM design leverages successes and developments related to *Hitomi's* SXS and *Athena*'s X-IFU instruments. Vibration isolation necessary to avoid performance degradation related to the cryocooler relies on heritage from *Hitomi*. The LXM also includes an assembly with a modulated X-ray source capable of providing pulsed X-ray lines at multiple energies and is similar to that used on *Hitomi* for in-flight calibration. Infrared/optical blocking filters that are necessary to block long-wavelength photons from reaching the microcalorimeter array are also included and based on the *Hitomi* and *Athena* designs. The ADR baselined for the LXM and its control electronics are adapted from those used on *Hitomi*, with additional stages of similar design being added to provide further cooling power. The burst disc, filter wheel, pump-out port, by-pass valve, dewar door mechanism, and event signal processor electronics and software are based upon those developed for and used on *Hitomi*. Since the baseline sensor technology uses Transiting Exoplanet Survey Satellites (TESs), there are many advances being made for *Athena* that will be leveraged for the LXM, such as the focal plane assembly that houses the sensor array, the cold read-out, and the anticoincidence detector for reducing background events.

Operations Comparisons — The direct transfer of *Chandra* experience to *Lynx* also applies to the development and operation of the ground system, starting with a baseline to co-locate the science and operations centers and form an integrated team for all relevant activities. Even with the change from High-Earth Orbit (HEO) to an L2 orbit, *Lynx* requirements are similar to those of *Chandra*. The HEO has to deal with regular passages through trapped radiation zones, while the L2 has an added requirement for station keeping. Nearly all of the hardware and software requirements and algorithms are already available for scoping the ground operations and science systems and for guiding their development, testing, and utilization. Software heritage is substantial, although *Lynx* anticipates new coding for a mission in the 2030s and beyond, utilizing more powerful hardware and software platforms available in that timeframe. Understanding the operations scope, and taking advantage of less expensive computer hardware and cost reductions from evolved *Chandra* operations, reduces cost and risk for *Lynx* relative to *Chandra*. This is especially the case for the first several years where the *Chandra* learning curve was still quite steep. One area where *Lynx* requires capabilities that are more sophisticated is the analysis of the detailed, high-resolution spectra obtained with the XGS and LXM. Overall, the combined ground system development and actual *Lynx* operations are comparable to the *Chandra* inflated costs, even after folding in an increased level of funding for *Lynx* science grants compared with *Chandra* levels. The parametric estimate for *Lynx* ground system development and operations is based on the Space Operations Cost Model (SOCM) that uses *Lynx* baselines for mission destination, operating environment, length of development, number of instruments, center or PI-led effort, single or multi-operations center, length of mission, size of science team, and several other parameters.

In comparing *Lynx* to *Chandra*, the spacecraft plus two out of the three *Lynx* instruments are not substantially different from evolutions of the *Chandra* equivalents and do not require significant breakthroughs or new inventions. Mission operations are particularly well understood, with plans and cost estimates derived from *Chandra* experience. The ability to produce a *Lynx* mirror at a cost similar to *Chandra's* can be tracked to tangible technological advances, along with a mirror design amenable to mass production. The LXM is quickly gaining technology maturity from laboratory efforts and from other X-ray missions (*Hitomi*, *XRISM*, *Athena*)., and can be viewed as a well-understood evolution of the *Athena* X-IFU (in which *Lynx* instrument leads are already involved). Given the achievements in key technology areas and the development plans to achieve TRL 6 for the LMA and the science instruments over the next several years, *Lynx* costs in $FY20 only modestly exceed the *Chandra* costs inflated to $FY20.

8.5.3.2 Grassroots Estimate

The detailed grassroots estimate for project Phases A–E is within 4% of the parametric estimate.

The *Lynx* team developed a DRM grassroots estimate to validate the parametric estimate. The grassroots estimate was developed for each Level 2 WBS code, and in some cases, down to the WBS 3 level. A skilled and diverse team of experts including *Chandra* project and prime contractor team members and *Lynx* science, engineering, and technology team members provided estimate inputs for the individual WBS elements. The estimates consist of a mix of *Chandra*-analogous estimates, scaled *Chandra* actuals for prime contract activities, and true grassroots based on development planning.

For the prime contractor portions of the grassroots estimate, an analysis of actual *Chandra* prime and subcontractor labor hours was performed via an industry CAN partnership. The prime contractor efforts for *Lynx* approximate the same scope for *Chandra* and include contract management; mission assurance; telescope and science instrument module subcontract management; observatory systems engineering and Assembly, Integration, and Test (AI&T); spacecraft DDT&E; and observatory commissioning. Actual *Chandra* labor hours were collected by WBS; scaling factors ranging from 1.0 to 1.5 were applied based on knowledge of the design, scope of work, and schedule durations of both the *Chandra* and *Lynx* projects. An hourly labor rate was derived by averaging the actual *Chandra* average contractor rate (inflated to $FY20) and an average Department of Labor rate for aerospace industry workers. The derived average fully wrapped contractor labor rate was used for the prime portions of the grassroots estimate. Material costs were estimated at 50% of labor costs for those WBS codes involving development of flight hardware and GSE.

The grassroots estimate was developed for Phase A–E (first 5 years of operation) and aligned with the *Lynx* DRM project schedule. The Phase A estimate was based on ~150 civil servants and support contractors for WBS 1, 2, 3, and 4, which is similar to the number of personnel that supported the *Chandra* project in Phase A. An average fully loaded labor rate in $FY20 for MSFC personnel was applied to that level of support. Additionally, it was assumed that support from the Prime contractor for a Phase A requirements development contract would be 30 personnel at the derived average fully wrapped contractor rate. The Phase A estimate includes the technology development cost estimates (§7), and Phase A estimate for WBS 9. Phase A (and pre-Phase A) funding estimates include project office support for management, oversight, risk mitigation, and requirements development associated with technology development efforts. The technology development estimates for Phase A are consistent with the rapidly advancing technology maturation and funding projected during the pre-Phase A period.

The launch vehicle is included in the total grassroots estimate, and uses the same LSP-provided pass-through as for the project parametric estimate. Fee and 30% reserves were applied only to those contracted portions not based off *Chandra* actuals. It was assumed that the estimates based on *Chandra* actuals represent the final cost with 100% of the reserves consumed.

Table 8.11 summarizes the grassroots BOE by WBS. This high-level summary is supported by an extended BOE that is part of the *Lynx Cost Book*. This extended BOE includes details such as a breakdown of assumed labor rates, materials, and equipment. In some cases, Rough Order Magnitude (ROM) cost estimates were provided by the vendor. A summary of personnel who prepared each grassroots WBS estimate and their qualifications is include in Appendix E.

Table 8.11. *Lynx* BOE for grassroots estimate.

WBS	WBS Title
01	**Project Management**
Basis of Estimate: Task-based estimate developed from project milestones and deliverables and captures the annual average number of personnel based on *Chandra* project actuals per the project manager. FTE fully loaded cost from the MSFC average rate table for Science Office personnel escalated to FY$20 was used with additional funding for supplies and travel to calculate total cost for this WBS. Includes project management, project planning and control analysts, project coordinators, scheduler support, configuration and data management support, contract support, supplies, and travel costs.	
02	**Systems Engineering**
Basis of Estimate: Task-based estimate developed from project milestones and deliverables, and captures the annual average number of personnel based on *Chandra* project actuals per the project manager. FTE fully loaded cost from the MSFC average rate table for Science Office personnel escalated to FY$20 was used with additional funding for supplies and travel to calculate total cost for this WBS. Includes Chief Engineer (oversight; NASA-provided Independent Technical Authority (ITA), systems engineering, requirements development & verification, materials support and independent review of analytical integration and requirements, ICDs, and verification products provided by the Prime Contractor.	
03	**Safety & Mission Assurance**
Basis of Estimate: Task-based estimate developed from project milestones and deliverables, and captures the annual average number of personnel based on *Chandra* project actuals per the project manager. FTE fully loaded cost from the MSFC average rate table for Science Office personnel escalated to FY$20 was used with additional funding for supplies and travel to calculate total cost for this WBS. Includes Safety and Mission Assurance support for payload development and testing, reliability analysis, quality assurance and mission safety. Chief Safety Officer oversight is NASA-provided Independent Technical Authority.	
04	**Science & Technology**
Basis of Estimate: Includes science and technology management, science support (project Phases A–D) and *Lynx* optics and instrument technology development (Phase A). Estimate is based on 3% of WBS 1, 2, 3, 5, 6, 7, 9, 10 and 11. Same % was used in parametric. Includes the Phase A estimates for technology development for the DRM technologies as per the technology development plans (§7).	
05	**X-ray Telescope (XRT)**
05.01 – 05.04	Telescope management, systems engineering, product assurance, I&T (Prime Contract)
Basis of Estimate: This WBS includes the DDT&E efforts associated with the XRT including the management, systems engineering, product assurance integration and test, GSE, the structure, thermal control system, and integration of the LMA, OBA, ISIM, and fiducial transfer components of the Pointing Control and Aspect Determination system. This element also includes Prime Contractor management, product assurance, and systems engineering activities. The telescope contractor portion of this estimate is based on a review of actual *Chandra* WBS level 4 labor hours, rolled up to level 2 and an applied weighted complexity factor of 1.2 based on review of lower level details. The weighted factor was derived by comparison of the *Chandra* and *Lynx* designs, complexities and mass differences, and scaled time spans based on project schedules. Overall, the *Lynx* XRT is more complex than *Chandra* due to the number of interfaces, overall size, and tight alignment tolerance. The estimate includes the LMA and XRT AI&T including the flight OBA and doors, mechanisms, telescope control electronics and cabling, and thermal hardware. The size of the GSE will drive more manufacturing, materials, and assembly.	
05.05	Telescope Calibration
Basis of Estimate: The *Lynx* ground calibration activities are assumed to be carried out at the MSFC XRCF as was done for *Chandra* in the 1990s. The calibration schedule and planned procedures are based on *Chandra* experience adjusted to better incorporate on-orbit calibration plans that are expected to considerably reduce ground calibration activities. This effort includes the calibration rehearsal activities to practice handling and calibration procedures using EM models for the LMA, XGA, LXM, HDXI and XGD, as well as the calibration of the flight mirrors and grating array to the flight grating and HDXI and XGD detectors. The high-fidelity LXM EM will be used for ground calibration. This estimate includes both MSFC Full-Time Equivalent/Work Year Equivalent (FTE/WYE) and Prime Contractor WYE efforts to perform the *Lynx* ground calibration campaign. The MSFC portion of this estimate is a bottom-up pricing out of FTE/WYE specific tasks. The cost is based on average fully loaded rates for MSFC Science Office and XRCF personnel. The Prime portions of this estimate are based on actual *Chandra* hours with a scaling factor of 1.3 to account for the additional size and complexity of the *Lynx* system and the addition of the LXM instrument. The effort for the rehearsal and flight calibration activities will take ~2 additional months vs. that for *Chandra*. The Prime contractor portion also includes efforts to provide mirror module assembly-to-XRCF interface hardware necessary for X-ray calibration.	

Table 8.11. *Continued*

WBS	WBS Title
05.06	*Lynx* Mirror Assembly
Basis of Estimate: This WBS includes the DDT&E efforts associated with the LMA including the management, systems engineering, integration and test, GSE, the structure, thermal control system, and integration of the X-ray mirror module assembly, barrel, and pre-and post-collimators. The telescope contractor portion of this estimate is based on a review of actual *Chandra* WBS level 4 labor hours, rolled up to level 2 and an applied weighted complexity factor of 1.2 based on review of lower level details. The weighted factor was derived by comparison of the *Chandra* and *Lynx* designs, complexities and mass differences, and scaled time spans based on project schedules. This WBS compares to the HRMA Flight and GSE hardware and integration with similar complexity but with a diameter of 3× time larger than *Chandra*. All handling operations and gravity offloading need to reflect the constraints due to critical alignments (0.1 arcsec). A high-fidelity verification test article similar to the VETA-II on *Chandra* is also included for qualification testing. Actuator and electronics verification test sets and GSE fixtures are included. LMA shipping and purge GSE is included.	
05.06.07	X-ray Mirror Modules
Basis of Estimate: The X-ray mirror module estimate is based on work completed by the GSFC Silicon Meta-shell Optics team and technology status as of September 2018. The estimate includes equipment and labor costs of mirror segment fabrication, mirror segment coating, integration of segments into modules, module testing, integration of modules into meta-shells, and integration of meta-shells into the final X-ray mirror module assembly. The estimate includes facility costs for integration of the mirror module assembly into the LMA. The cost model reflects the number of labor hours based on a fully loaded rates for junior workers (technicians, project support etc.), and senior workers (engineers, scientists, etc.), as well as major equipment costs and small consumable items needed. For GSE, past purchasing prices inflated to FY$20 and/or recent quotations solicited from vendors were used. 30% has been added to cover the price to account for upkeep and servicing contracts that are an essential part of operations. The estimate also includes an additional 10% to cover the procurement work associated with the equipment. For consumables, the estimate is based on usage experience, in combination with experience with many recent purchases. Labor hours are based on fabrication, coating, alignment, and bonding of mirror segments. This estimate does not include the development of the TRL 6 engineering model (included in WBS 4 estimate for Phase A activities).	
05.07	X-ray Grating Array (XGA)
Basis of Estimate: The XGA estimate is for the CAT XGA, and is based on the *Chandra* HETG experience with grating fabrication and testing, and recent costing for the proposed X-ray Arcus Midex mission. Costs consist of labor (estimated FTE effort and duration for each milestone), new tools and equipment, consumables (boules, wafers, chemicals, etc.), costs for MIT Lincoln Labs to develop their processes and run batches through their fab, and services and fees (use of outside tools, machining costs, deposition services, etc.). Estimates for development includes: Build up fabrication and characterization infrastructure, establish documentation protocols, perform fabrication test runs, refine and optimize fabrication process steps, acquire custom SOI wafers, build assembly and alignment infrastructure, refine and optimize frame design, and long-lead time orders, personnel ramp-up (hiring and training) for the fabrication and characterization ("production"). Two scenarios are considered: Large gratings (2/wafer, ~ 800) and small gratings (7/wafer, ~ 2,050). We estimate that an XGA populated with large gratings is cheaper by ~ $4.5M, mostly due to labor savings from the smaller number of gratings to be characterized and handled. For the purpose of this estimate, the smaller gratings are assumed. This estimate does not include the engineering model delivered post-CDR that will consist of a flight like grating array structure, several qualification-tested grating facets and mass dummies (part of WBS 4 estimate). This EM will be used to space qualify the design.	
05.08	Optical Bench Assembly (OBA)
Basis of Estimate: This WBS includes the DDT&E efforts associated with the OBA including the management, systems engineering, integration and test, GSE, the structure, thermal control system, and magnetic broom. The telescope contractor portion of this estimate is based on a review of actual *Chandra* WBS level 4 labor hours, rolled up to level 2 and an applied weighted complexity factor of 1.5 based on review of lower level details. The weighted factor was derived by comparison of the *Chandra* and *Lynx* designs, complexities and mass differences, and scaled time spans based on project schedules. Specifically, for this WBS, the differences are based on the increased optical bench diameter, increased size impacts on the GSE, and the thermal heater system and blanketing areas. Key alignment datums for ISIM and LMA will be engineered into the OBA for reference during XRT assembly. GSE fixtures will be manufactured to support assembly of the large composite structures and fittings, and rotation fixture to support final integration steps prior to XRT integration. GSE handling equipment will also serve as shipping supports.	
05.09	Integrated Science Instrument. Module (ISIM)
Basis of Estimate: This WBS includes the DDT&E efforts associated with the ISIM including the management, systems engineering, integration and test, GSE, the structure, electronics system, thermal control system, and translation table mechanisms, as well as integration of the Government-furnished science instruments (LXM, HDXI. and XGD), as well as overall I&T for the ISIM. This estimate is based on analogy using *Chandra* Prime Contractor actual labor hours to design and build the ISIM, integrate the instruments, perform mechanism life tests and SIM environmental testing. The ISIM for *Lynx* is estimated to be more complex by a factor 1.5 over the *Chandra* ISIM due to 3 instruments to be installed, co-aligned and maintained (versus 2 for *Chandra*), accommodation of the LXM (a state-of-the-art cryogenic instrument) and its cryocoolers and a much more complex dynamics environment than *Chandra* (which had no coolers).	

Table 8.11. *Continued*

WBS	WBS Title
05.09.08	*Lynx* Microcalorimeter (LXM)
Basis of Estimate: The LXM BOE is based upon two rounds of costing carried out by the GSFC Cost Estimating, Modeling & Analysis Office following an Instrument Design Laboratory that was also carried out at GSFC, and is based upon a MEL that was produced during this laboratory in June 2017, and updated in June 2018. The estimate is based upon a combination of sources for the various subsystems in an attempt to provide the best possible estimate, which is different for the various different components. Where possible, the costs were based on the costs of nearly identical heritage components of the Soft X-ray Spectrometer instrument on Astro-H, inflated to $FY20. Detailed new grassroots estimates were made for the detector focal plane assembly, the majority of the adiabatic demagnetization refrigerator, and also the main detector read-out electronics. These were done by GSFC SMEs, and checked by the GSFC Costing Office to ensure all costs such as design, review, integration, and testing costs had been included. For the cryocooler, quotations were acquired from the two companies considered most able to provide cryocoolers meeting the LXM 4.5 K cooling and micro-vibration requirements, and with the most advanced TRL. For these quotations, the development costs for Pre-Phase A and Phase A costs were kept separate from the main instrument costs and are included in the roadmap separately. These quotations include the cost of all models of cryocoolers needed for the project and are included in the *Lynx Cost Book*. The highest quotation was used to be conservative. Parametric estimates obtained using PRICE-H® were used for some of the items for which grass-roots estimates were not available, such as for the cryostat other than the cryocooler, the cost of GSE, environmental testing, spares and the cost of selected environmental test units. For the LXM, an EM and a proto-flight unit will be developed, with selected subsystem flight spares but no complete instrument spare. The EM will undergo extensive qualification testing beyond the typical level of an EDU in order to space-qualify the design.	
05.09.09	High Definition. X-ray Imager (HDXI)
Basis of Estimate: This estimate is based on actual costs for the *Chandra* ACIS instrument, which to a zeroth-order approximation is a reasonable comparison to the *Lynx* HDXI. Although the *Lynx* HDXI is more capable than ACIS, 30 years of technical progress provides the extra capability at the same real cost. The estimate is derived from 533M financial reports during the Phase B–D development period (January 1993 through August 1999), escalated to FY$20. The estimate includes project management, systems engineering and integration, reliability and QA, DDT&E activities, detector assembly, detector electronics assembly, digital processor assembly, instrument integration and verification, GSE, CCD fabrication, fabrication facility and support, instrument flight software, flight operations and data analysis, science support and mission management, Lincoln Laboratory engineering and ACIS (2-chip) calibration support. The GSFC IDL developed a separate grassroots/parametric-based estimate for the HDXI in February 2018. This estimate included DDT&E costs for the instrument based on the IDL design and CBE mass of 80.4kg, flight software, GSE, testing, flight spares and ETU. The total point design estimate was within 3% of the grassroots estimate.	
05.09.10	X-ray Grating Detector (XGD)
Basis of Estimate: The estimate for the *Lynx* XGD is based on similarity with the ACIS/HDXI, but scaled down to reflect the simpler layout and fewer sensors. Both instruments on *Lynx* are assumed to utilize the same sensor technology and follow a similar development path. Because *Lynx* is considering HDXI and XGD as separate instruments, developed by separate teams, most of the development and test costs will be incurred separately for each. ACIS included both an imaging array (4 CCDs) and a grating readout array (6 CCDS). The total raw detector cost was about 15% of the total ACIS instrument cost. Therefore, assuming only a grating readout on ACIS, the cost would have been about 10% (60% of 15%) less. A separate estimate for the XGD was obtained that assumed the use of an existing and commercially available CCD technology. This cost was within 9% of the grassroots ACIS/HDXI estimate.	
05.12	*Lynx* Calibration Facility
Basis of Estimate: This effort includes calibration facility-related work necessary to perform the rehearsal and flight calibration activities described in WBS 05.05. This includes facilities upgrades and modernization, GSE, DDT&E, labor, (e.g., technical, facility management, scientific, and IT support) and material costs. This effort is considered comparable to the estimates recently developed by MSFC XRCF staff in anticipation of calibration of *Athena*, currently in development by ESA, and anticipated to go through calibration in the FY28–FY29 timeframe. Anticipated calibration facility modernization and upgrades to the 1990s-era XRCF include changes to the X-ray source system, X-ray detector system, X-ray data and acquisition control system, contamination control and monitoring system, thermal control system and cleanroom facilities. GSE for *Lynx* calibration includes mirror and instrument handling fixtures, mirror reorientation fixture, focal plane instrument positioning fixtures, high-speed detector, metrology system, and other handling equipment. This estimate includes both MSFC FTE/WYE and Prime Contractor WYE efforts to upgrade the existing XRCF facilities, develop test GSE requirements, define interfaces, and perform test planning and procedure development. The MSFC portion of this estimate is a bottom-up pricing out of FTE/WYE specific tasks. The cost is based on average fully loaded rates for MSFC Science Office and XRCF personnel. The Prime portion of this estimate is based on actual *Chandra* hours with a scaling factor of 1.0. The facility efforts are expected to be of lower scope as the facility and interface definitions already exist, some *Chandra* GSE can be re-used, so there is less new hardware. This new hardware is more complex, due to the size and tighter alignment tolerances for *Lynx*. Net assessment is that the overall effort will be the same.	

Table 8.11. *Continued*

WBS	WBS Title
06	**Spacecraft Element**
Basis of Estimate: Estimate is based on analogy using *Chandra* Prime Contractor labor actuals for this WBS element with modifications applied for assessed differences between the *Chandra* and *Lynx* spacecraft bus designs. Like *Chandra*, the Prime Contractor will have the responsibility for DDT&E activities associated with the spacecraft bus. Sub-elements include Management, Systems Engineering, Product Assurance, Integration and Test, and Ground Support Equipment, as well as all of the Spacecraft Bus subsystems (FSW, Structures, Thermal Control, EPS, C&DH, Communications, GN&C and Propulsion. For this element, the Prime contractor effort was scaled at 1.5 over the *Chandra* effort based on increased mass and power requirements for *Lynx*.	
06.05	Flight Software
Basis of Estimate: In addition to the analogous *Chandra* estimate, a separate grassroots estimate for FSW was developed by the MSFC software engineering branch using the Constructive Cost Model (CoCoMo). Two estimates were generated: one using customized parameters based MSFC software team experience and the other using Class A software defaults. Only C&DH software was included in this exercise (no instrument software). 104,739 software lines of code (SLOC) was estimated by the GSFC Mission Design Lab (MDL) for the *Lynx* spacecraft. It is assumed that this element is include the in Prime contractor's scope already. This grassroots estimate is provided for information and does not contribute to the total.	
07	**Mission Operations**
Basis of Estimate: The *Lynx* cost model for Mission Operations in Phases E–F was developed by analogy using the actual costs for the corresponding *Chandra* WBS elements with modifications applied for assessed differences between the *Chandra* and *Lynx* requirements, while also taking into account efficiencies developed over the course of the *Chandra* operations to date, which are directly applicable to *Lynx*. The detailed assessment included review of *Chandra* MO actuals for phase E–F, identification of any differences with the *Lynx* hardware and operations, development of a *Lynx* cost model populated with *Chandra* labor and Other Direct Costs (ODC), and revisions made to the above for noted differences. This element also includes grants for the *Lynx* general observer program.	
08	**Launch Vehicle Services**
Basis of Estimate: This cost is based on direction from NASA HQ and from LSP and includes the Full Mission costs for launch services for a composite heavy-class LV based on today's prices escalated out to the *Lynx* 2035 LRD. Included in this cost is the standard launch provider services defined in the NASA Launch Services (NLS) II contract terms and conditions, as well as additional mission unique services necessary to meet the mission requirements as defined by the spacecraft project (e.g., additional doors, special cleaning, additional analyses cycles, etc.). Integrated Services covers payload processing at the launch site and LSP's support-service contractor costs that will eventually be directly charged to the individual mission work performed. Finally, this element includes the station needed for downrange station telemetry coverage. The stations used during the mission are dependent on the mission-unique trajectory to meet the spacecraft requirements. Per LSP, actual heavy-class vehicles that will exist in 2030s are unknown, so this cost includes a large degree of uncertainty.	
09	**Ground Systems**
Basis of Estimate: The *Lynx* cost model for Ground Systems in Phases A–D was developed by analogy using the actual costs for the corresponding *Chandra* WBS elements with modifications applied for assessed differences between the *Chandra* and *Lynx* requirements. The detailed assessment included review of *Chandra* Ground Systems actuals for Phase A–D, identification of any differences with the *Lynx* hardware and operations, development of a *Lynx* cost model populated with *Chandra* labor and ODC, and revisions made to the above for noted differences.	
10	**Systems Integration and Test**
Basis of Estimate: Estimate is based on analogy using *Chandra* Prime Contractor labor actuals for this WBS element with modifications applied for assessed differences between the *Chandra* and *Lynx* Observatory I&T efforts. This WBS includes I&T management and systems engineering, GSE, facilities and all work necessary to integrate the XRT with the SCE and perform system-level testing. The scaling factor for I&T management is assumed to be 0.8 for *Lynx* due to the shortened schedule for this activity. The factor for GSE is assumed to be 1.5 for *Lynx* due to increased complexity associated with a heavier spacecraft and telescope. The factor for I&T execution is assumed to be 1.0 due to similar effort and testing. The average overall scaling factor is 1.05 for *Lynx*.	
11	**Public Outreach**
Basis of Estimate: This element provides the resources to carry out a mission-related public outreach and communication for the project. The same resources as for *Chandra* are assumed for *Lynx* in the model. This provides for website and social media support, graphics and video generation, outreach to the public, and press and image releases at ~2/month.	

8.5.3.3 Independent Cost Estimate (ICE) and Uncertainty Analysis

The MSFC Engineering Cost Office performed a non-advocate, independent cost estimate and uncertainty analysis of the *Lynx* parametric estimate and concluded that "…the independent risk assessment results are consistent with historical NASA mission cost growth behavior." The 40% CL on the non-advocate cost curve is within 1% of the *Lynx* parametric estimate.

At the request of NASA HQ, the MSFC Engineering Cost Office developed a non-advocate ICE and performed an uncertainty analysis to validate and determine the CL in the parametric estimate. The ICE addressed the uncertainty in the estimating methods, input parameters, design complexity, and fee. The analysis was performed in FY$20 and $RY, using NASA escalation factors for Phases B–E, exclusive of launch vehicle costs and reserves, to derive the cost basis for the assessment.

Input and model uncertainties were calculated for estimates performed using the PCEC tool. Input uncertainty was modeled using a triangular distribution, and model uncertainty was calculated using prediction intervals. Estimates performed for the LMA and science instruments using the SEER® and PRICE® models were assumed to be at a 25% CL. Coefficients of variation (CV), a rough measure of uncertainty, were in the 40% to 50% range. This resulted in conservatism in the range of results. The calculated overall CV of 35% on the derived cost basis is consistent with Air Force guidance for new space systems. Higher CVs for the mirror assembly and instruments reflect the amount of new design and technology development for these elements.

A Monte Carlo simulation on the input models provided a cost curve with CLs ranging from 10%–90% as shown in Figure 8.5. Reserve amounts to achieve corresponding confidence levels were calculated based on the delta between the derived cost basis (parametric estimate for Phases B–E exclusive of launch vehicle and reserves) and the cost at the 50% and 70% CLs on the resulting cost curve. Based on this analysis, the *Lynx* parametric estimate with 30% reserves on B–D costs (exclusive of launch vehicle) has a 38% CL on the independent cost curve. An analysis of 132 historic NASA projects [623] concludes that typically, project estimates with reserves, have ~15% CL. Thus, the *Lynx* parametric estimate with 30% reserves on Phases B–D (less launch vehicle) represents a substantially better reserve posture than historical NASA projects.

The resulting analysis yielded a cost range from $4.9B at a 40% CL to $6.2B at 70% CL in $FY20, and $6.7B at 40% CL to $8.5B at 70% CL in $RY, using NASA escalation factors.

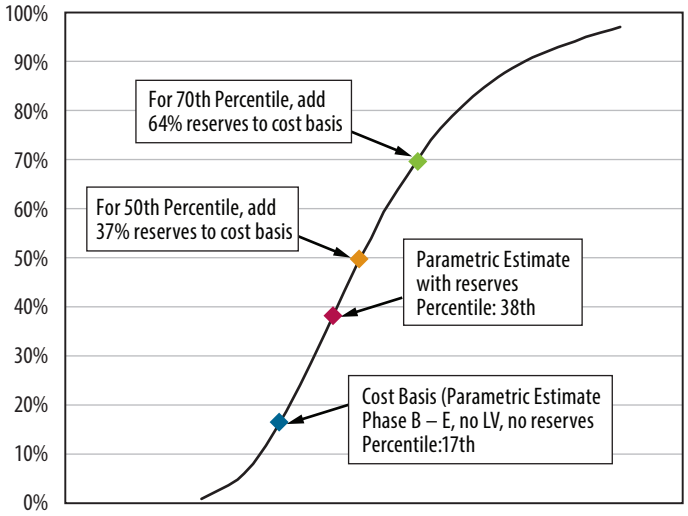

Figure 8.5. The *Lynx* parametric cost estimate with 30% reserves on Phase B–D (exclusive of LV) represents a 38% CL. To achieve a 50% CL, 37% reserves need to be applied to the cost basis. For 70% CL, 64% reserves need to be added to the cost basis.

8.5.3.4 Independent Cost Analysis and Technical Evaluation

The independently developed cost analysis and technical evaluation (CATE) validated the *Lynx* parametric cost estimate and found it, "…reasonable, credible, reproducible, and consistent with the DRM parameters." The 40% CL on the CATE cost curve is within 1% of the *Lynx* parametric estimate.

To further validate the cost estimate and ensure incorporation of cost and schedule risks, the *Lynx* team procured the services of MCR Solutions, LLC to develop an independent risk-based life-cycle project cost estimate and schedule forecast. For this assessment, MCR developed a detailed, independent parametric cost estimate (MCR ICE), analyzed the project schedule (§8.4) with respect to development durations for similar missions, analyzed the *Lynx* Technology Development section (§7), and assessed the DRM architecture (§6) to determine critical missing or underestimated development costs and schedule risks. These analyses were used as inputs into Monte Carlo-based analyses to produce the cumulative distribution functions for the total project and key lower level elements of the WBS that resulted in a total cost probability distribution for the predicted life-cycle cost and schedule realism. The resulting "S-curves" for total project cost and schedule provide an assessment of the project parametric cost estimate and execution plan.

MCR Cost and Schedule Estimating Methodology — The *Lynx* team provided source information to MCR for the CATE analysis including the detailed project parametric costing BOE, project schedule, WBS, technology development roadmaps, DRM MEL and PEL, engineering analyses, and technical papers [624], as well as the non-advocate ICE (§8.5.3.3), and grassroots estimate (§8.5.3.2) for comparison. The CATE methodology for development of the MCR ICE followed the GAO and NASA best practices approaches for cost estimation. The CATE utilized some of the same NASA parametric cost estimating models used in the project parametric estimate, as shown in Table 8.12. Crosscheck models indicated in the table were used for validation of the ICE. PCEC emulated an Earth-orbiting robotic environment and SEER-H® used the unmanned space platform.

Table 8.12. Assignment of primary and secondary models and methods for CATE estimate.

Cost Element (WBS)	Primary and Cross-Check Models and Methods
1.0 Project Management 2.0 Systems Engineering 3.0 Safety & Mission Assurance 4.0 Science & Technology	PCEC and SEER-H®
5.0 X-ray Telescope (XRT)	PCEC at higher WBS-level; except where noted below; SEER-H® for lower-level detail of WBS 5.06, 5.07, 5.09; 10% fee on most instruments. See Section 5 for details on fee.
5.06 LMA	PCEC for primary; SEER-H® for crosscheck.
5.07 X-Ray Grating Assembly (XGA)	Detailed model for primary using SEER-H® and TRL maturity based on MCR paper; PCEC for crosscheck.
5.09 Integrated Science Instrument Module (ISIM)	SEER-H® and PCEC as a crosscheck.
5.09.08 *Lynx* X-Ray Microcalorimeter (LXM)	Detailed model for primary using SEER-H® and TRL maturity with NICM as a crosscheck.
5.09.09 High-Definition X-Ray Imager (HDXI)	Detailed model using SEER-H® and TRL maturity with NICM as a crosscheck.
5.09.10 X-Ray Grating Detector (XGD)	Detailed model using SEER-H® and TRL maturity with NICM as a crosscheck.

Table 8.12. *Continued*

Cost Element (WBS)	Primary and Cross-Check Models and Methods
5.05 XRT Calibration	Throughput from Northrop Grumman, analogy estimate based on *Chandra* 1990 design.
5.12 *Lynx* Calibration Facility	Throughput from Northrop Grumman, analogy estimate based on *Chandra* 1990 design.
6.0 Spacecraft Element (SCE)	PCEC and SEER-H®, including flight software.
7.0 Mission Operations	PCEC, SOCM, and *Chandra* analogy.
8.0 Launch Vehicle Services	PCEC and SEER-H® plus throughput for LSP (launch vehicle).
9.0 Ground Systems	PCEC using MO and DA Phase B–D CER; Project grassroots estimate used as roots crosscheck.
10.0 Systems Integration & Test	PCEC and SEER-H®
11.0 Public Outreach	Calculated as a percentage of project costs and PCEC
Schedule	Project-provided schedule; MS Project; @Risk; basis of cost reserve

The MCR CATE used the same inputs and ground rules and assumptions established for the project parametric estimate, specifically:

- Project-provided WBS
- Model input mass, as provided by the MEL, including design redundancy and contingencies
- Achievement of TRL 6 for all instruments by PDR
- Contractor fee was included in selected elements consistent with project parametric estimate; fee was not applied to:
  - WBS 1–4, project management, systems engineering, S&MA, science and technology
  - WBS 5.07, 5.09.08, 5.09.09, and 5.9.10, Instruments
  - WBS 5.05 and 5.12, Telescope Calibration
  - WBS 7 and 9, Operations
  - WBS 8, Launch Vehicle Services
  - WBS 11, Public Outreach
- The total cost estimate was apportioned among project phases, as follows:
  - Pre-Phase A costs were not included in the estimate
  - Phase A: estimated as 5% of the total phase B–D cost
  - Phase B–D: parametric models and select throughput values
  - Phase E: parametric model based on 5-year operating life
- Flight software was estimated by PCEC from engineering data proposing 140 Kilo Source Lines of Code (KSLOC) with 60% reused, adjusted to 96.845 Equivalent Source Lines of Code (ESLOC)
- Throughput estimate values were the derived from the project-provided Grassroots estimate for:
  - WBS 5.5, XRT Calibration
  - WBS 5.12, *Lynx* Calibration Facility Modernization
  - WBS 8.0, Launch Vehicle

As a first step in evaluating the estimate credibility, both the project parametric cost estimate and the non-advocate ICE were evaluated against the MCR CATE estimate range, e.g., at the low to high boundaries before assignment of cost reserve and confidence assessment. At level 2 of the WBS, values were noted to be "within family."

Crosschecks were made for validation at lower WBS levels using more than one cost method (model, throughput or an analogue source) and at higher WBS levels, comparing cost and schedule with *Chandra* and other relevant projects.

Schedule Analysis — MCR analyzed the *Lynx* project schedule (§8.4) using a Monte Carlo schedule risk assessment. The project schedule was based on an analogy to *Chandra*, other-project actual cost experience, and MSFC policy. It was supplemented with historical schedule estimates (in months) derived from credible other scientific projects. These detailed schedule estimates at lower-level WBS elements are consistent with an optimized project execution schedule and fit into the generally-accepted time-cost trade curve [625] shown in Figure 8.6, where dollars and months are optimized during project planning. Project execution uncertainty incorporates variations in time and cost from the fundamental plan resulting in explainable variances. All *Lynx* cost/time solutions fall within expected limits.

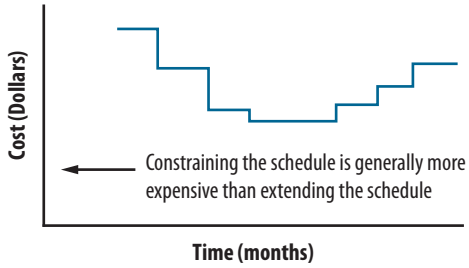

Figure 8.6. Bathtub concept illustrating juxtaposition of optimum cost/time solutions and changes when there is schedule acceleration or delay. This is a nominal-shaped bathtub curve generated by a commercial cost model illustrating cost sensitivity to schedule.

MCR determined that the project schedule demonstrates an estimate confidence greater than 50% for launch readiness based on a task duration range of –5% to +20% for all tasks both with and without planned schedule margin.

The analysis indicates that the current plan with the programmed schedule margin and schedule visibility tasks has a high confidence of meeting launch vehicle integration. While the plan as configured consumes some of the planned schedule margin, it provides adequate reserves accounting for the "unknown-unknown" risks, resulting in a high confidence credible plan.

Uncertainty Analysis — An important purpose of cost and schedule risk is to determine the total likely project cost and reserves that will assure an adequate budget and funding confidence level for successful project execution of *Lynx*. As with the non-advocate ICE, several models with different correlation factors were applied for sub-elements to establish reserve amounts:

- **PCEC**: elements modeled using an assumed triangular risk distribution; mode uncertainty calculated using prediction intervals. The estimate intervals were established by the MEL parameters and TRL analysis as:
  - Lower (L) bound: design weights without contingency
  - Most Likely (L) value: design weights with contingency
  - Higher (H) bound: design weights with contingency plus TRL adjustment to development cost

- **SEER-H®**: elements modeled using an assumed triangular risk distribution; mode uncertainty calculated using prediction intervals. The model provided output values for the lower, most likely, and high bounds of the estimate.
- **NICM**: used to crosscheck the instruments and validate "in family" only. Due to the limited number of X-ray instrument data points, spectrometers and particle instruments were used as analogies.
- **@Risk®**: lower-level uncertainties combined to determine the top-level correction.

A primary consideration in calculating cost and schedule risk was the project requirement of starting development at low TRLs and assuming a cost and schedule to achieve TRL 5 at the start of Phase A and TRL 6 by PDR. Adjustments to PCEC and SEER-H® non-recurring cost estimates were based on MCR's NASA database of TRL development cost factors, as discussed above.

Other risk considerations included flight software development and instrument development. Operational risks (failure on-orbit) were not considered in this estimate.

The resulting analysis yielded a cost range of $4.8B at 40% CL to $5.1B at 70% CL in $FY20, and $5.7B at a 40% CL to $6.1B at a 70% CL in $RY.

8.5.3.5 In-Family Comparisons

The overall *Lynx* mission parametric cost model is modular and built with multiple, detailed subsystem cost models used for individual elements, as described above. Use of multiple cost models provides validation of the individual subsystem estimates, and thus veracity of the overall mission estimates. The modularity of the mission cost estimate lends itself to further validation with element-level, in-family comparisons to similar elements on historical missions. There is general scarcity of available, comparable, X-ray mission-level cost data that allows for in-family comparisons; however, data exists for comparisons of the LMA (Figure 8.7), HDXI and XGD assembly (Figure 8.8), and spacecraft (Figure 8.9). The *Lynx Cost Book* includes these comparisons with actual costs.

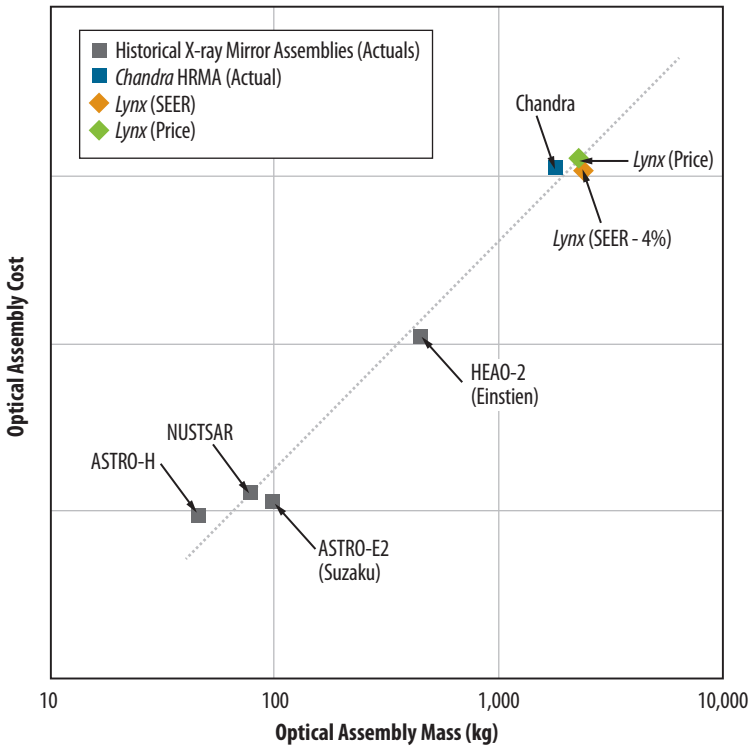

Figure 8.7. LMA in-family comparison to historical, U.S.-developed X-ray telescope optical assemblies.

Validation missions used to compare the LMA to historical X-ray telescope optical assemblies was selected from X-ray telescope missions with available cost and technical data. Foreign missions were excluded due to data unavailability.

Historical cost data for the in-family comparison of the HDXI and XGD assembly was selected from spectrometer instruments with total B–D cost data in NICM, excluding spectrometers, spectrographs, photometers, and radiometers designed for wavelengths longer than infrared.

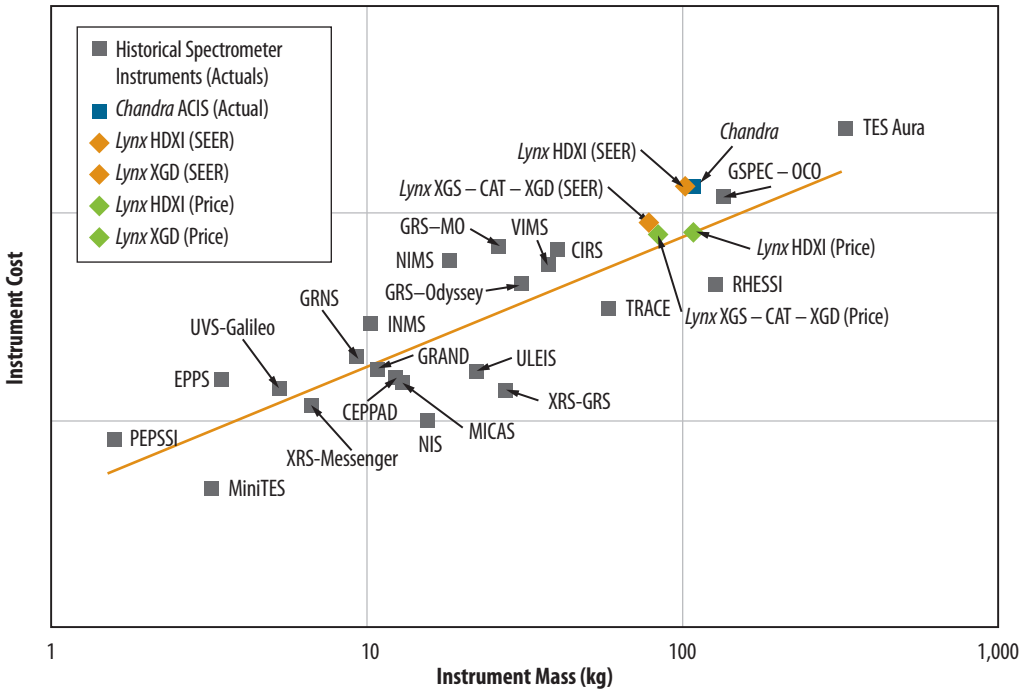

Figure 8.8. HDXI and XGD assembly in-family comparison to comparable spectrometer instruments.

Historical cost data for in-family comparison of the *Lynx* spacecraft element was selected from similar unmanned NASA missions with available cost data.

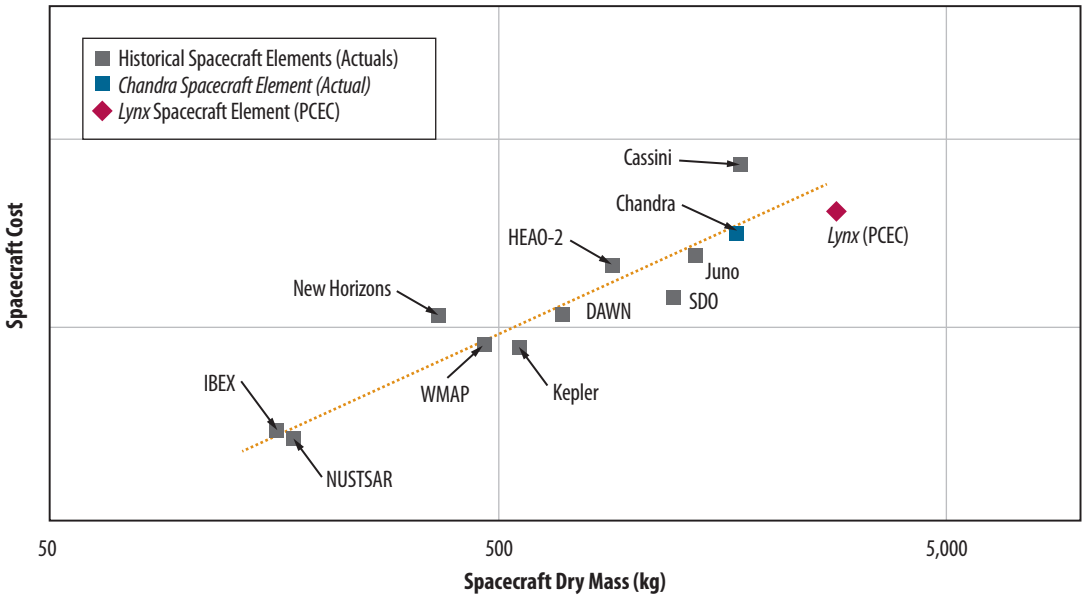

Figure 8.9. *Lynx* spacecraft element in-family comparison to comparable NASA project spacecraft.

The *Lynx* parametric estimate was developed with a thorough understanding of the Observatory architecture, design considerations and programmatic construct. Multiple, detailed cost models were developed for the primary elements of the telescope and spacecraft, with special attention on the development of the cost models for the X-ray mirrors and instruments given the absence of comparable X-ray technologies and missions in available cost data sets. These models were used to estimate the overall *Lynx* mission cost. Several validation analyses were undertaken by the *Lynx* team to provide credibility of the parametric mission estimate. These included a comparison to escalated ($FY20) *Chandra* actual costs, development of an independently conducted grassroots estimate, an independent non-advocate ICE with uncertainty analysis, and an independently conducted, contracted CATE with ICE and uncertainty analysis. As summarized in Table 8.13, the *Lynx* mission parametric estimate was within a –11% to +28% range of the validation results, and the 40% CL on the cost curves developed as part of the non-advocate ICE and CATE were consistent to within 1% of the *Lynx* mission cost, all resulting in a thoroughly and credibly-costed mission for pre-Phase A formulation.

Table 8.13. Comparison summary of cost validation results to parametric estimate.

Validation Cost Estimate	Delta from Mission Parametric Estimate (%)
Chandra comparison	–11%
Independent CATE (40% CL)	0%
Non-adv. cost analysis (40% CL)	+1%
Grassroots	+4%
Independent CATE (70% CL)	+5%
Non-adv. cost analysis (70% CL)	+28%

8.5.4 Cost Contributions

The *Lynx* team welcomes international participation in the *Lynx* project. Potential areas of contribution could include instruments, building on existing collaborations related to *Athena* and others that offer a distinct contribution to the spacecraft, and calibration support. Specific cost contributions will be sought out and defined more formally during pre-Phase A.

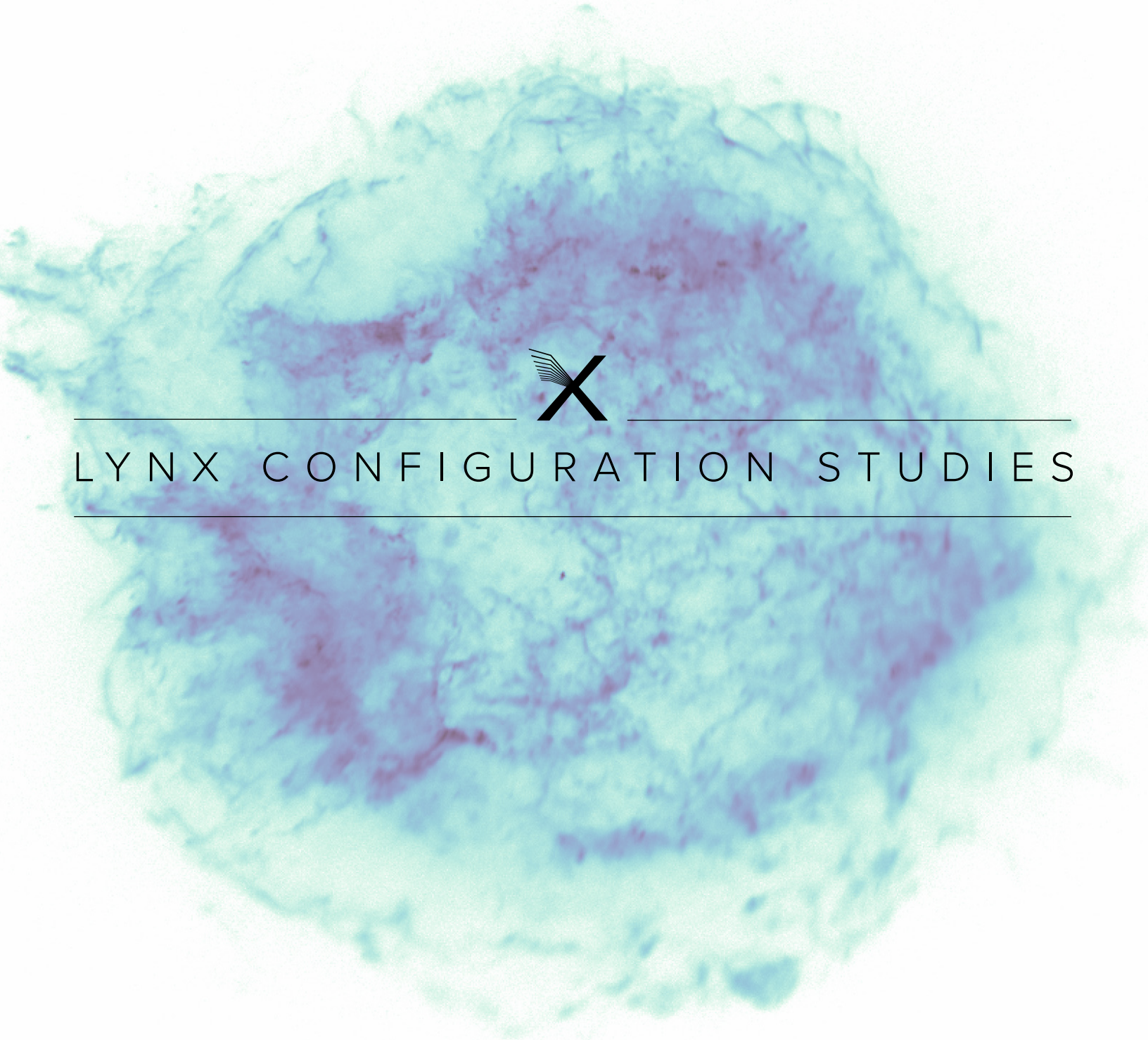

LYNX CONFIGURATION STUDIES

9 *Lynx* Observatory Configuration Trade Space

The *Lynx* Design Reference Mission Observatory configuration is designed to provide the maximum science-per-dollar. To confirm this, the *Lynx* team conducted a high-level trade study of multiple Observatory configurations. Smaller configurations do not lead to significant cost reductions and result in substantial science losses. Larger configurations have increased capability but are sub-optimal in the science-per-dollar sense.

The nature of the *Lynx* Observatory trade space is multifaceted because it is designed to carry out a broad, Great Observatory-class science program. The *Lynx* team considered multiple configurations to assess the Observatory science capability as a function of cost. This analysis shows that the *Lynx* Design Reference Mission (DRM) is the optimal configuration in terms of science-per-dollar, while fully achieving the identified mission objectives (§6.1.1).

9.1. Trade Configurations

Sampling the broad *Lynx* trade space required a detailed design and costing for two designs that acted as anchor points for this trade. Significant effort was spent detailing all aspects of the DRM (§6) and a second, less capable configuration, dubbed the "1.3-m² Configuration" (which is its mirror effective area at 1 keV). This reduced configuration also has a less capable *Lynx* X-ray Microcalorimeter (LXM) and reduced X-ray Grating Spectrometer (XGS) effective area. The design and cost analyses for this 1.3-m² Configuration are presented in §10. The costs for all other configurations listed in Table 9.1 were obtained by taking appropriate deltas and scaling from the two anchor points.

The Observatory configurations that were considered included combinations of reduced *Lynx* Mirror Assembly (LMA) effective area at 1 keV, while preserving the shape of the effective area curve across the bandpass, and science instrument capability. In all cases, the High Definition X-ray Imager (HDXI), matching the angular resolution and field of view (FOV) provided by the *Lynx* mirrors, was considered essential. However the *Lynx* team considered reductions in capability for XGS and LXM, as well as complete removal. The *Lynx* team also considered a poorer angular resolution of 2 arcseconds (compared to 0.5 arcsecond for the DRM).

Table 9.1. The *Lynx* team studied a variety of configurations. The two anchor points are called out in the table. The 1.3m² Configuration should not be considered a preferred option to the DRM, as it is merely an anchoring point to provide reference for the multiple configurations that were considered. Checkmarks indicate the configurations studied. Bold checkmarks indicate the two "anchor point" configurations with full mission design and cost analyses.

Instrument Configuration					
Effective Area (Diameter and Focal Length)	**Nominal LXM and HDXI, scaled XGS**	**Nominal HDXI, reduced LXM, scaled XGS**	**Nominal HDXI and LXM, no XGS**	**Nominal HDXI, scaled XGS, no LXM**	**Nominal HDXI, no LXM and no XGS (imaging only)**
2.1 m^2 [d=3 m, f=10 m]	**✓** – DRM		✓	✓	✓
1.3 m^2 [d=2.3 m, f=10 m]		**✓** – 1.3-m^2 Configuration	✓	✓	✓
0.8 m^2 [d=1.8 m, f=10 m]	✓		✓	✓	✓
3.0 m^2 [d=3.6 m, f=12 m]	✓				
4.1 m^2 [d=4.2 m, f=14 m]	✓				
2.1 m^2, 2 arcsecs PSF	✓				

The configurations with a reduced mirror effective were assessed by removing both outer and inner meta-shells from the DRM LMA design while maintaining a focal length of 10 m. A shorter focal length results in unacceptable reductions of the effective area above ~ 4 keV, and so these options are not viable. For configurations with larger effective area, a simplified approach was applied to the optical design. The DRM optical design already populates the input telescope aperture with nearly maximally packed mirror segments. Therefore, any substantial increase of the effective area must come from increasing the diameter of the mirror system. In addition, for the DRM design, the grazing angle for the outer mirror shells is close to the maximum for reflecting 1 keV photons. Therefore, any increase of the telescope diameter must be accompanied by a corresponding increase of the focal length. A transformation of the LMA along these lines, maintaining a uniform increase of the effective area across the band, results in the number of mirror segments and assembly mass scaling as $\sim D^2$. Scalings informed by the *Lynx* parametric cost model and historical trends were applied to estimate the cost for these larger configurations (§9.3.2).

9.2. Impact on Science

The science capability loss and gain is assessed via the estimated effect of the Observatory configuration changes on the notional observing plan (§5, Table 5.1) for the science pillars. The notional *Lynx* observing plan is a diverse collection of generally multi-object and multi-purpose programs, and it serves as a fair representation of the community-driven science program for *Lynx* in the 2030s. This approach allows science "scores" to be assigned for each element of the program, followed by estimates of how the science value of that element scales with available exposure time.

The process of assigning scores requires an assessment of the relative importance of the science that *Lynx* will be able to do in addition to its pillars — the "Observatory/Discovery" portion of the program. Examples of such science are given in §4. More importantly, *Lynx* must provide opportunities for observations that address today's "unknown unknowns" — questions as of yet unasked. The ensemble of *Lynx* observations, as well as the discoveries across astrophysics, will drive these questions. As such, equal total weights, $w = 0.5$, were assigned by the *Lynx* team for both the Pillars and the Observatory/Discovery portions of the program.

History shows that for major astrophysical missions such as *Hubble*, *Chandra*, *Spitzer*, and *Compton*, unanticipated discoveries are at least as important as the execution of their original science goals. This study accounts for this by assigning equal weight to both the *Lynx* science pillars and the Observatory/Discovery portions of the program.

Next, the science of the three pillars was separated into sub-themes, followed by programs, and then, within some of the science programs, into specific classes of observations. A uniform division of the science scores was used at each level of this hierarchy. More specifically, each pillar was assigned a weight of $w = 0.5/3=0.167$, the three sub-themes of the second pillar were assigned $w = 0.167/3 = 0.0556$ and so on down to the lowest level of single-type observations, typically performed with a single science instrument. This hierarchy and the scores are documented in Table 9.2.

The scores assigned to individual programs enable an estimate of the science impact of removing science instruments from the Observatory, because some of the programs become completely unfeasible in this case. For these configuration changes, those programs' science scores were removed from the overall total. For completeness, the impact of removing the instruments was also estimated for the Observatory/Discovery portion of the program. This was done under the assumption that the pillars portion of the program is a fair representation of the mix of target types, instrument choices, and observation modes for the Observatory/Discovery portion. Several methods (such as using each instrument's total exposure time, the number of targets, computing the fractional exposure time, aggregated science score) lead to a similar conclusion: the HDXI, LXM, and XGS instruments will contribute approximately 30%, 50%, and 20% to the Observatory/Discovery program, respectively. These percentages are consistent with the *Lynx* team assessment of historical trends of imaging versus spectroscopic observations on major NASA missions and provide a reasonable initial assumption.

Table 9.2. *Lynx* notional observing plan with weights.

Science Theme	Weight	Sub-theme	Program	Weight	Typical Observations	Weight	Instrument	Science with 30% less area	Science with 50% less area
The Dawn of Black Holes	0.167	Black hole dawn	1.1 Origin of supermassive black holes seeds*	0.083	Surveys over 1 deg^2 to depth fx = 1.6^{-19} [0.5–2 keV] plus a deeper survey over 400 arcmin^2 to fx = 7–20 erg/s/cm^2	0.083	HDXI	0.700	0.500
		From dawn to noon	1.2 Growth of supermassive black holes from cosmic dawn through cosmic noon to the present, relations between AGN and environments, triggering and quenching AGNs, relationship to star formation activity	0.083	Survey down to fx = 2^{-18} over up to 2 deg^2		HDXI	0.850	0.700
The Invisible Drivers of Galaxy and Structure Formation	0.167	State of diffuse baryons z = 0	2.1 State of diffuse baryons in galactic halos—direct imaging*	0.028	Survey of ~15 low-redshift isolated (spiral galaxies), pushing 10% thermodynamic (gas density) measurements to 0.5 r500 for M ~3^{12} and to r200 for M ~1^{13}	0.028	HDXI	0.850	0.700
			2.2 State of diffuse baryons in galactic halos—absorption line spectroscopy*	0.028	Observe ~80 AGN sightlines (fagn ~1^{-11}) to detect ~60 absorption line systems in the foreground galaxy halos, detection limits for absorption lines are EW ~3 mÅ and down to 1 mÅ for r > r200, same Milky Way Halo	0.028	XGS	0.700	0.500
		High-z probes	2.3 State of gas and feedback measurements in high-redshift galaxy clusters and groups	0.028	Gas temperature, density, and metallicity profiles in ~30 clusters and groups at z >2, 6 Msec LXM observations	0.028	LXM/main array	0.850	0.700
			2.4 Characterization of the first galaxy groups at z = 3–4	0.028	HDXI observations of ~10 high-z galaxy groups	0.028	HDXI	0.850	0.700
		Feedback	2.5 Spectroscopic survey of AGN to determine energetics of the AGN feedback	0.011	Soft-band spectroscopy with *R* >1,000 down to 0.2 keV to measure density-sensitive spectral features, 3 Msec XGS, LSM / ultra-high resolution array	0.011	XGS, LXM/ultra-high resolution subarray	0.850	0.700
			2.6 Characterize the supply side of AGN energy feedback	0.011	Measure thermodynamic state of diffuse gas near the Bondi radius of SMBHs in nearby elliptical galaxies	0.011	LXM/enhanced spatial resolution subarray	0.850	0.700
			2.7 Measure the energetics and effects of AGN feedback on galactic scales*	0.011	Observe AGN-inflated bubbles in the ISM of low-redshift elliptical galaxies	0.006	LXM/enhanced spatial resolution subarray	0.850	0.700
					Spectro-imaging of extended narrow emission line in nearby spiral galaxies	0.006	LXM/enhanced spatial resolution subarray	0.850	0.700
			2.8 Understand the energetics and mechanics of the supernovae-driven galactic winds*	0.011	Observe galaxy winds in ~20 objects, with the ability to characterize velocities <100 km/s on arcsec scales, 2.5 Msec LSM / ultra-high spectral resolution array	0.011	LXM/enhanced spatial resolution subarray	0.700	0.500
			2.9 Galaxy cluster-scale feedback	0.011	LXM observations of nearby galaxy clusters to constrain plasma physics effects in the cluster cores	0.011	LXM/main array	0.850	0.700
The Energetic Side of Stellar Evolution and Stellar Ecosystems	0.167	3.1 Stellar coronal physics, impact of stellar activity on planet habitability, accretion on young stars		0.042 c	Spectroscopic survey of 80 stars within 10 p	0.021	XGS	0.875	0.650
					Transit spectroscopy of planets around dwarf stars down to super-earth regime	0.021	XGS, LXM/ultra-high resolution subarray	0.875	0.700
		3.2 Young forming regions		0.042	Surveys to detect entire mass distribution of stars in active star forming regions to d = 5 kpc			0.870	0.700
		3.3 Endpoints of stellar evolution: SNRs*		0.042	Targeted observations of the youngest SNRs in the Milky Way, up to ~50 objects	0.021	LXM/main array	0.800	0.750
					Statistics and typing of SNRs in different environments in nearby galaxies	0.021	LXM/main array	0.700	0.500
		3.4 Endpoints of stellar evolution: X-ray binary populations		0.042	Survey of X-ray binary populations and ISM in nearby galaxies 2 Msec LXM		HDXI, LXM	0.850	0.700
Observatory/Discovery Program	0.500					0.500	50% LXM, 30% HDXI, 20% XGS	0.840	0.700

For simplicity, the assumption was that the science capability loss associated with removing science instruments could not be recouped by added exposure time for the remaining instruments. Moreover, the team verified that even with reasonable prescriptions for a redistribution, the DRM configuration still clearly yields the greatest ratio of science to cost (Table 9.3).

Table 9.3. Relative science capability and cost of different mission configurations.

Configuration description	Capability	Relative cost	Science/$
DRM	1.00	1.00	1.00
DRM, no LXM	0.60	0.87	0.69
DRM, no XGS	0.84	0.94	0.90
DRM, imaging only	0.43	0.80	0.54
1.3 m^2 effective area	0.77	0.95	0.81
1.3 m^2, imaging Only	0.34	0.75	0.45
1.3 m^2 - no XGS	0.63	0.88	0.71
1.3 m^2 - no LXM	0.46	0.81	0.57
4.2 m mirror diameter	1.36	1.48	0.92
3.6 m mirror diameter	1.18	1.24	0.95
2 arcsec angular resolution	0.20	0.97	0.21
0.8 m^2 effective area	0.50	0.92	0.55
0.8 m^2, no XGS	0.41	0.85	0.48
0.8 m^2, no LXM	0.29	0.78	0.37
0.8 m , imaging only	0.21	0.66	0.32

Changes in the mirror effective area for most of the *Lynx* programs are equivalent to changes in the exposure time, with decreased area equating to decreased exposure time. For relatively small changes, the science value of individual programs changes approximately as the inverse of statistical uncertainties, effectively scaling as $\sim A^{0.5}$ as the mirror area decreases. This trend continues to ~50% of the nominal area, at which point a big loss of value occurs in the sense that the program can no longer address the corresponding pillar goals. The $A^{0.5}$ trend is not universal, however. For deep surveys of high-z Supermassive Black Hole (SMBH) seeds, absorption line spectroscopy of the Circumgalactic Medium (CGM), measurements of galaxy wind feedback, Supernova Remnant (SNR) observations, and spectroscopic survey of stars, the goals are centered around covering a maximally wide parameter space or observing diversity of properties in a large sample of objects, resulting in a $\sim A$ trend. The science value of the Observatory/Discovery portion is assumed to scale as $A^{0.5}$, reflecting the predominant scaling in the pillars portion of the program. The t_{exp} scalings in the Table 9.2 for these programs reflect the assessment of the science value changes in these situations.

9.2.1. Science Threshold

Throughout this trade study, it was critical to identify the crucial observational capabilities necessary to accomplish the science pillars, maintain ample time for Observatory/Discovery program, and avoid compromising the ability to transform astrophysics in the 2030s and beyond. Because of the complex nature of this task, the *Lynx* team undertook several approaches. The *Lynx* team wanted to be as objective as possible while recognizing that assigning simple numerical scores or rankings might not be adequate for this task.

The science capability threshold is defined as the point at which *Lynx* would lose its ability to execute one or more of its science pillars or to carry out Observatory/Discovery science. These scenarios were deemed unacceptable for a Flagship-class mission for the 2030s. However, configurations both above and below this threshold were considered to allow for a better understanding of how the costs scaled with mission capability.

Maintaining a posture that is appropriate for a Flagship mission and above an acceptable science threshold requires three essential *Lynx* capabilities: (1) large effective area, (2) high-spectral resolution over the entire bandpass, and (3) high-spatial resolution over a large field of view.

Reductions in the mirror effective area larger than 50% of the DRM configuration would result in a configuration below the science threshold. Similarly, the loss of either the LXM or XGS would place the mission below the science threshold. In reviewing the configurations that remove one or both of these instruments, the result is that the amount of science lost per dollar saved does not support removing either instrument.

In addition to maintaining the DRM science instruments, preserving the high-angular resolution is central for the execution of the *Lynx* science and is essential for a 2030s observatory-class X-ray mission. One of the configurations in the trade space (2-arcsecond angular resolution) formally demonstrated the devastating impact of such angular resolution degradation on the *Lynx* science. For this configuration, the notional observing plan was reviewed and programs that could still be carried out with a 2-arcsecond Point Spread Function (PSF) were identified. Primarily, these programs are a subset of the grating spectroscopy programs that do not require high spatial resolution. The total weight of these programs is only 0.2. None of the science pillars can be executed at this level of spatial resolution, although there are still interesting options in the Observatory/Discovery portion of the program. The overall assessment was that a 2-arcsecond configuration is well below the science threshold for a flagship mission.

9.3. Cost Changes

9.3.1. Summary of the 1.3-m² Configuration Costs

Compared to the DRM, the 1.3-m² configuration features a smaller diameter mirror assembly that is accommodated by a smaller-diameter spacecraft and Optical Bench Assembly (OBA) (§10.1.5). With this configuration, the *Lynx* team explored the cost impact of small changes in the instrument design, such as reducing the LXM FOV from the DRM 5 arcminutes down to 4 arcminutes. This smaller diameter mirror assembly also resulted in a reduced X-ray Grating Array (XGA) effective area (and physical diameter).

The cost changes associated with minimal changes in the science instrument configurations are small (§10.4.3). There is a small reduction of cost in the spacecraft, mostly due to a mass reduction in the primary structures. The cost of the OBA is reduced due to the smaller diameter; however, the mass reduction is small since the thickness of the OBA had to be increased to accommodate the new observatory center of gravity (§10.2.2). However, these savings are almost entirely offset by the introduction of an additional launch adaptor required to mate this reduced diameter to the standard ~5-m fairing. The total cost of the spacecraft and the OBA for the 1.3-m² configuration is within 1% of that for the DRM. The smaller mirror effective area results in a 19% reduction of the mirror assembly cost, and it is this component that drives a 5% reduction of the estimated mission cost compared to the DRM.

The fact that a 38% reduction in the mirror effective area only results in a 19% reduction of the mirror assembly cost reflects the modular design of the LMA, its highly parallelize-able assembly process, and the mass-production nature of manufacturing and assembling the required number of mirror segments (§8.5.2.1).

9.3.2. Mirror Cost Scaling

The key point for comparing the cost estimates for the different mirror assembly configurations is that they have nearly-identical upfront costs associated with technology development, manufacturing readiness, and in the design and engineering of the mirror structure and related subsystems (e.g., thermal). Each configuration requires nearly identical numbers of mirror prototypes, and therefore has the same cost for prototype production and testing. The main difference between configurations is the number of mirror segments and mirror modules produced and assembled into meta-shells. These differences play a role only during the mass-production phase, and therefore the cost reduction is modest.

In the *Lynx* parametric cost models, a "learning curve" setting is used to represent the acquired experience and hence reduced costs of the module production as multiple modules and meta-shells are built (§8.5.2). Moreover, historical data on the X-ray mirror costs are used to estimate the impact of the learning curve and mass production. The X-ray mirrors for the *NuSTAR* and *SRG*-ARTX-C telescopes are good examples. In both cases, the mirror systems consisted of multiple modules, and a large number of reflecting elements within each module. In these cases, the average cost of the subsequent modules was 11% of that of the first module produced. For *Chandra*, where the mirror manufacturing process was not set up for mass production, the cost of the first set of mirrors was ~2× that of each of the three subsequent sets (§8.5.3.1).

The parametric model cost difference for the *Lynx* DRM and 1.3-m² configurations is captured by a model that assumes that the cost of the first produced meta-shell is more than the cost of the subsequent meta-shells due to the applied learning curve (§8.5.2.1). The percentage difference in cost for producing subsequent meta-shells is ~10% of the cost of the first meta-shell. This scaling is consistent with historical X-ray mirror manufacturing experience and is used to estimate the mirror costs for the larger and smaller effective area configurations. The results are summarized in Table 9.4.

Table 9.4. Summary of mirror configurations assessed for *Lynx* and their scaled cost compared to the DRM.

	Configuration				
Mirror Assembly Diameter (Configuration)	**1.8-m (0.8-m²)**	**2.3-m (1.3-m²)**	**3.0-m (DRM – 2.1-m²)**	**3.6-m (3.0-m²)**	**4.2-m (4.1-m²)**
Number of meta-shells	5	7	12	17	24
Relative parametric model cost	—	0.81	1.0	—	—
Relative cost from simple scaling	0.67	0.76	1.0	1.26	1.55

Impact of the coarser angular resolution on cost — The potential cost reductions associated with a coarser angular resolution (2 arcsecond) are assessed and the manufacturing process envisioned for the Silicon Meta-shell Optics technology has been reviewed (§7). No steps in the fabrication, alignment, and mounting process were identified that could be eliminated or significantly shortened because of more relaxed angular resolution requirements. Potential savings might appear during the technology development phase, if the required TRL levels are reached faster because of more relaxed requirements. Coarser spatial resolution allows one to use a larger pixel size in the HDXI detector, which can also accelerate the pace of its technology development, but will only modestly reduce the cost of the flight unit. XGS and LXM technology development costs would not be impacted, though there would be an impact to the science (i.e., resolving power and spatial resolution, respectively). To be conservative in the mission configuration tradeoff analysis, the cost reduction for a 2-arcsecond configuration was assumed to be $100M.

9.3.3. Instrument Suite Costs

The costs reductions associated with changes in the science instrument suite were estimated for the DRM configuration by using the parametric estimates for the costs of the instrument plus the cost of any components uniquely associated with that instrument, such as mechanisms. Relevant spacecraft systems, such as power and thermal, were also appropriately scaled. As a result, the cost reductions associated with removing the LXM instrument include the ISIM translation mechanism and substantially reduced power and a simplified thermal system. The costs of the XGS instrument include the XGA insertion mechanisms and a reduced footprint of the ISIM. Table 9.5 shows the costs reductions associated with three possible instrument suite changes, as a percentage of the total DRM cost estimate.

Table 9.5. Potential cost savings from *Lynx* instrument changes.

	No LXM	No XGS	No LXM and XGS (HDXI only)
Cost Reduction	–13.3%	–6.5%	–19.9%

Identical absolute cost reductions for instrument removals were applied to smaller and larger mission configurations, which is a sufficient assumption for the purposes of this analysis.

9.3.4. Larger Mission Cost Scaling

Configurations larger than the DRM were assessed by assuming that all cost growth is associated with the increased diameter and focal length of the X-ray mirror modules and of the spacecraft and OBA. The cost of the science instruments is assumed to not change, even though, in reality, these costs would increase because physically larger detector planes would be needed to cover the same area on the sky and larger grating arrays would be required to cover the same fraction of the input aperture. Higher costs of science instruments for configurations larger than the DRM only strengthen the conclusions regarding these options.

The mirror cost scaling is shown in Table 9.4. The mass of the mirror and the OBA increase as the diameter times the focal length or by D^2. The larger configurations also require a larger diameter spacecraft. The spacecraft and OBA masses increase approximately in proportion to the mass of the mirror assembly. The associated cost growth is ~ $\text{mass}^{1.1}$ as established by historical data on the costs of NASA science mission spacecraft (§8.5.3.5, Figure 8.8). This simple scaling captures the increased demands on the spacecraft structures, power and thermal systems, larger solar pressure torque and moments of inertia, larger Δv for station keeping, etc. It is recognized that this scaling is approximate, but the largest configuration considered is only 40% larger than the DRM. Therefore, the accuracy should be sufficient for this high-level study.

Observatory configurations larger than the *Lynx* DRM cannot fit into heavy-class launch vehicles fairings and exceed their maximum payload mass capacity. Therefore, these configurations would require super-heavy class launch vehicles such as the SLS. The NASA Launch Services Program (LSP) guidance available at the time of this study recommends a cost delta of +$100M associated with the super-heavy class launchers. A higher cost difference would only strengthen the conclusions provided here. Note that the 0.8-m^2 configuration may be launched with a medium-class launch vehicle, so the corresponding cost reductions were assumed. Again, if such configurations required a heavy-class launcher, this would only further increase the cost.

9.4. Results

The Observatory configuration "science-per-dollar" is the primary metric for assessing the optimized configuration for *Lynx*. Figure 9.1 plots the relative science capability per unit cost (or "science-per-dollar") versus the relative science capability, normalized to 1.0 for the DRM on both axes and provided in Table 9.3. Larger circles show the two anchor points in the trade space with full mission design and cost analyses. Open circles show those configurations where scaling was used for the cost of the mirror and spacecraft to extrapolate beyond the range covered by the anchor points.

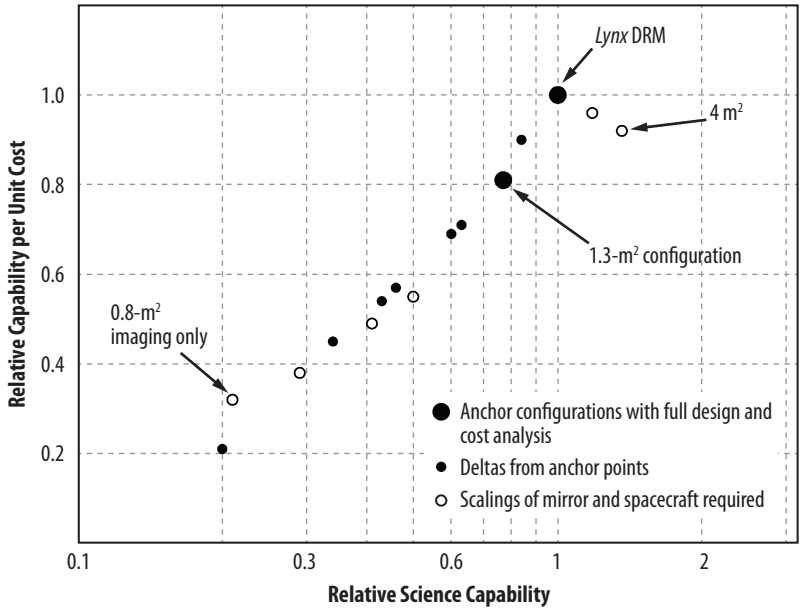

Figure 9.1. *Lynx* Observatory configurations trade, illustrating the optimal *Lynx* DRM configuration providing the maximum "science per dollar".

The DRM configuration is optimal and maximizes the "science-per-dollar." Approaching the DRM from the less capable missions on its left, the mission cost grows slowly for increasingly more capable configurations. The primary reason for the relatively slow cost growth in this regime is efficient amortization of upfront costs associated with the development of the 0.5-arcsecond-capable Observatory (telescope and spacecraft) and upfront costs related to production of the first sets of X-ray optics. The mass-production nature of the X-ray mirror manufacturing results in a slow increase of the mirror cost with assembly diameter. These two factors led to a significant increase in science capability-per-dollar shown by the rather steep slope approaching the DRM.

The larger configurations must endure increased spacecraft costs related to the increased mirror assembly diameter and focal length. There is an added cost associated with the need for a more capable launch vehicle; and there is a slower growth in science capabilities. To fully capitalize on the extra effective area for the larger configurations, *Lynx* would need angular resolution better than 0.5 arcsecond, with the next natural science break point estimated by the *Lynx* team to be at a PSF level of ~0.1 arcsecond HPD. An X-ray observatory with such angular resolution would be capable, e.g., of detecting individual X-ray binaries in the z=10 galaxies and resolving well inside the Bondi radius of supermassive black holes in nearby galaxies. However, achieving the 0.1-arcsecond PSF would require a new set of breakthroughs in both the X-ray mirror and detector technologies that go well beyond the expected state of the art for the next decade. The *Lynx* DRM, with its 0.5-arcsecond angular resolution, is already orders of magnitude more capable than any other X-ray telescope existing or planned, and is capable of executing the *Lynx* science pillars while providing significant time for an Observatory/Discovery science program.

A final comment is in order regarding mission configurations with effective area somewhat smaller than the 2.1-m^2 provided by the DRM. *Lynx* science can tolerate moderate reductions of this type. However, as argued above, substantial cost savings are not projected from reducing the mirror effective area. Instead, a possibility of meeting basic science requirements with a smaller mirror assembly should be viewed as an option to improve cost and schedule margin for manufacturing the LMA.

The Observatory configuration trade study shows that the *Lynx* DRM configuration maximizes the science-per-dollar metric. Smaller configurations lead to only modest cost reductions and result in increasingly larger and eventually unacceptable science losses. Larger configurations have increased capability but lack the higher angular resolution to maximize their science return. Their substantially higher cost and likely longer schedule are inconsistent with the NASA Astrophysics budget and the Decadal timeframe.

10 *Lynx* 1.3-M² Configuration

The 1.3-m² configuration detailed design, schedule, cost, and assessed science return provides a trade-space anchoring point used to confirm that the *Lynx* Design Reference Mission (DRM) provides an optimal architecture that maximizes the science return for the cost.

The Observatory configuration trade study described in §9 is strengthened by the detailed knowledge provided by the in-depth study of a reduced-capability configuration. The configuration studied has a mirror effective area of 1.3-m² at 1 keV, and reduced X-ray Grating Spectrometer (XGS) and *Lynx* X-ray Microcalorimeter (LXM) capabilities. This configuration was chosen as one of two anchor points (in addition to the DRM) in the configuration trade space.

The 1.3-m² configuration offers a significantly reduced mirror effective area at the expense of increasing the on-orbit time needed to achieve the science pillars to nearly the full 5-year mission lifetime. This configuration is just above the *Lynx* science threshold, which is defined as the point at which the program is no longer able to address the goals defined by the science pillars. Reductions in the mirror effective area larger than 50% of the DRM configuration result in a configuration that is below the science threshold. As mentioned in §9, the loss of any of the science instruments would place the mission below the science threshold.

The reduced effective area for this configuration is accomplished by reducing the number of meta-shells from 12 to 7, thereby reducing the grating array effective area and increasing the time needed for the highest resolution spectroscopy (the system angular resolution is not affected because the focal length is not diminished in this configuration). The High-Definition X-Ray Imager (HDXI) remains unchanged, as there were no credible cost savings in reducing the HDXI Field of View (FOV) or other HDXI science performance capabilities. Importantly, the requirements to maintain high-angular resolution across the 22 × 22 arcminute FOV were not relaxed, as this capability was deemed essential across nearly all *Lynx* science objectives. However, this configuration does have modest reductions in LXM Main Array (MA) FOV from 5 × 5 arcminutes to 4 × 4 arcminutes. This impacts the spatially resolved spectroscopy of the largest apparent-size objects such as nearby supernova remnants, clusters of galaxies, and diffuse or extended galactic sources.

The *Lynx* Mirror Assembly (LMA) effective area for this configuration is ~2/3 that of the DRM configuration. This decrease allows for a smaller diameter spacecraft bus and Optical Bench Assembly (OBA), but essentially leaves unchanged the Integrated Science Instrument Module (ISIM) (Figure 10.1). The focal length was not changed, resulting in a slightly larger depth-of-field and correspondingly relaxed

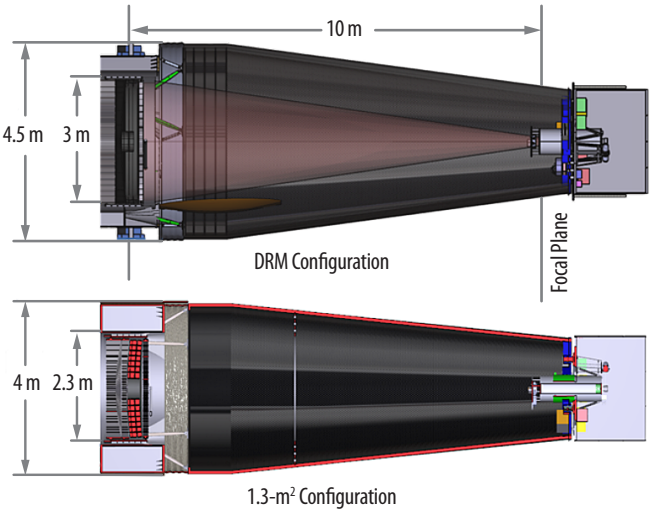

Figure 10.1. (Top) *Lynx* DRM observatory configuration and (Bottom) 1.3-m² configuration with critical dimensions shown.

focus and alignment tolerances. All DRM technologies (i.e., Silicon Meta-shell Optics, Hybrid Complementary Metal-Oxide Semiconductor (CMOS) HDXI, Critical-Angle Gratings (CAT-XGS), LXM relevant technologies) are also assumed for this configuration.

The prime goal for this choice was to provide a detailed analysis for a representative configuration significantly smaller than the DRM and to enable approximate analyses for even smaller configurations for the Observatory configuration trade study described in §9. A detailed design analysis was completed, and a project schedule and cost were generated for this configuration such that the science impact as a function of cost and risk could be assessed and compared directly to the DRM.

The primary characteristics of this configuration in comparison to the DRM are summarized in Table 10.1. Detailed analysis of every major subsystem for the 1.3-m² Configuration, summarized in the sections below, indicates minimal savings of mass and power, and ultimately of cost (§10.4.3). The amount of science lost due to reduced capability for this configuration is not offset by acceptable savings in cost, schedule, and risk as detailed in (§9.3.1, Figure 9.1).

10.1 Telescope Design Details Overview

The telescope elements (i.e., the LMA and science instruments) for the 1.3-m² Configuration in comparison to the DRM are discussed in the following sections. The impact to the science is discussed in §9.

10.1.1 *Lynx* Mirror Assembly — Reduced Effective Area

The reduced *Lynx* configuration has an effective area of 1.3-m² at 1 keV, decreased from 2.1-m² for the DRM Configuration by removing the outer three and inner two meta-shells. This roughly 1/3 reduction in the effective area of the DRM LMA is taken approximately uniformly across the full *Lynx* bandpass (Figure 10.2, Left). The resulting outer diameter of the 1.3-m² Configuration LMA is 2.3-m, compared to 3-m for the DRM (Figure 10.2, Right).

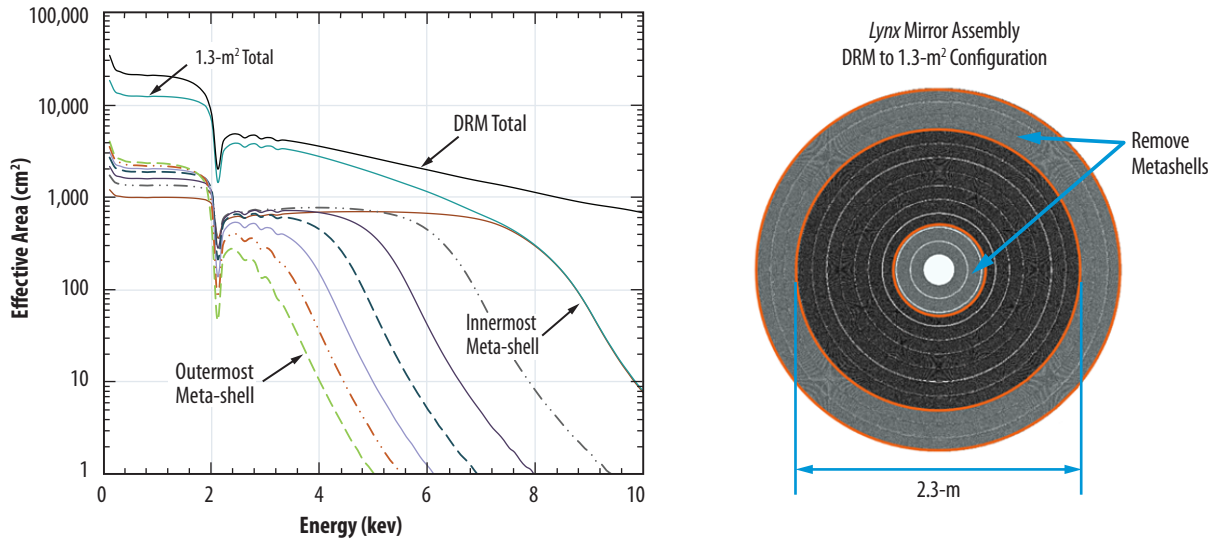

Figure 10.2. (Left) Plot of the LMA effective area for the 1.3-m² Configuration as a function of meta-shell, compared to the total LMA effective area for the DRM. (Right) The 1.3-m² Configuration (shown in dark gray) has five fewer meta-shells than the DRM does, resulting from removing the three outer and two inner DRM meta-shells.

From an Observatory architecture standpoint, this reduction in LMA size necessitates a smaller diameter spacecraft, contamination doors, sunshade, and OBA. The resulting mass savings is minimal, resulting in a mass savings of less than 10% (609 kg) over the DRM (Table 10.1).

Table 10.1. Requirements and *Lynx* Observatory total mass and power estimates based on detailed design and analysis of major observatory elements that include the payload and spacecraft systems.

Requirement	1.3-m² Configuration	DRM
LMA Effective Area at 1 keV	1.3-m²	2.1-m²
XGA Effective Area	~3,000 cm²	~4,400 cm² (4,000 cm² Required)
LXM Main Array FOV	4 × 4 arcminutes	5 × 5 arcminutes
Characteristic	**1.3-m² Configuration**	**DRM**
Total Mass (with Margin)	7,103 kg	7,712 kg
Power (with Margin) Launch Survival Science Mode	 720 W 2,552 W 7,356 W	 743 W 2,552 W 7,420 W

10.1.2 High Definition X-ray Imager — No Reductions

A study was carried out by the *Lynx* team to determine a possible reduced configuration HDXI that fit within the context of this reduced-capability configuration. HDXI is described in detail in §6.3.2. Capabilities that were considered for reduction included lower readout rate, the use of fewer but larger sensors, reduced high-energy Quantum Efficiency (QE), reduced FOV, removal of the filter wheel assembly, elimination of windowing capability, and the use of larger pixels for reduced spatial resolution. The team concluded that there were no HDXI capability reductions that would result in an appreciable cost, schedule, or risk savings, and still be consistent with the *Lynx* science goals.

10.1.3 X-Ray Grating Spectrometer — Reduced Effective Area

The XGS consists of a retractable X-ray Grating Array (XGA) located immediately behind the LMA and an X-ray Grating Detector (XGD) assembly located on the ISIM (§6.3.3). The 1.3-m² Configuration has a smaller diameter XGA that is consistent with the reduced LMA effective area as shown in Figure 10.3, but requires that the Resolving Power, R = 5,000, remain unchanged. By keeping the focal length the same as that of the DRM, this is easily achieved.

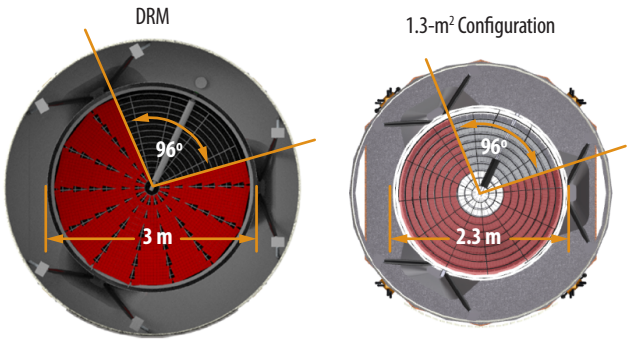

Figure 10.3. The XGA effective area was reduced by approximately the same amount as the LMA across the *Lynx* bandpass.

The XGA effective area was reduced by approximately the same amount as the LMA across the *Lynx* bandpass. This effective area is shown in Figure 10.4 and is compared to that of the DRM. Conservative estimates have been made for both cases.

As for the DRM, the 1.3-m² Configuration assumes that the HDXI technology will be used for the XGD. The length of the XGD assembly on the ISIM is driven by the longest wavelength photons (Figure 10.5) and on the required resolving power. Because the bandpass remains unchanged between configurations, the XGD 1.3-m² Configuration requires the same number of sensors as the DRM.

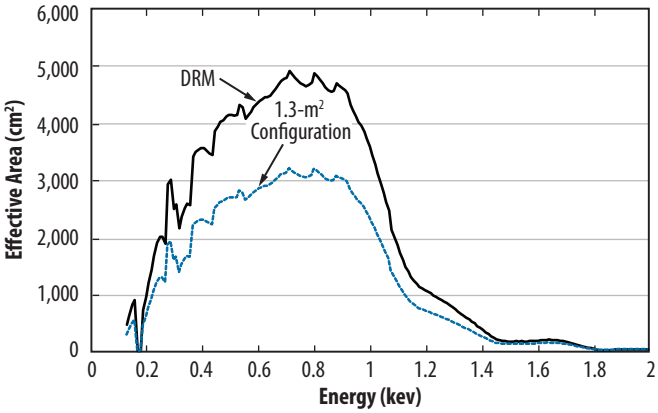

Figure 10.4. The DRM effective area is the black curve and the blue dashed curve is the 1.3-m² Configuration effective area. The analysis neglects drops at certain wavelengths due to XGD chip gaps.

10.1.4 LXM—Reduced Field of View

The LXM DRM focal plane array consists of three different styles of pixels in three different arrays and are described in §6.3.4. For the 1.3-m² Configuration, the *Lynx* LXM team considered multiple reduction options that included eliminating either the Enhanced Main Array (EMA) or the Ultra-High Resolution Array (UHRA), switching from the baseline readout to a slightly more complex, but higher TRL readout multiplexing scheme, and reducing the FOV of the Main Array.

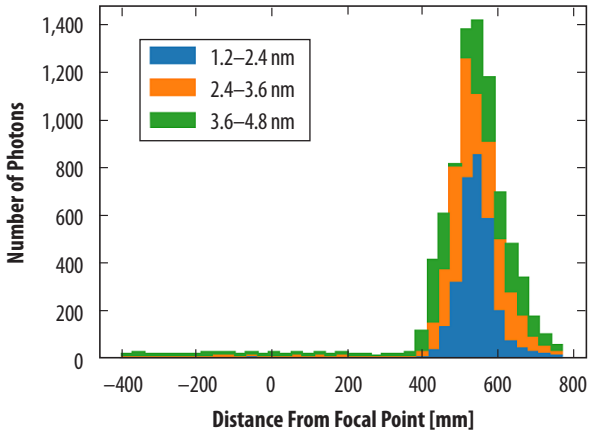

Figure 10.5. Number of photons as a function of the distance from the *Lynx* focal plane.

Extensive discussions within the *Lynx* team on the loss to the *Lynx* science goals related to the elimination of the EMA or UHRA concluded that these were not viable options, especially given the relatively minimal cost savings (§10.4.3) and development risk mitigation. To assess the cost of using the higher TRL readout electronics, a cost exercise was carried out at Goddard Space Flight Center (GSFC). The results indicated a higher cost for these electronics than what was baselined for the DRM, suggesting that the baselined electronics be selected for the 1.3-m² Configuration as well. Reducing the FOV of the MA is a viable and acceptable option, so the *Lynx* team assessed the trades associated with this reduction.

The MA for the DRM Configuration consists of 1-arcsecond pixels over a 5-arcminute FOV, with a 0.2 to 7–keV energy range. The 1.3-m² Configuration MA is designed to maintain the same pixel size and energy resolution as the DRM LXM, but with a reduced MA FOV of 4 arcminutes. The result is a small cost reduction in detector fabrication and readout electronics. The impact to the DRM cryocooler, one of the driving cost elements for the LXM, is small, as the reduction in heat load is minimal.

10.1.5 Optical Bench + Pointing Control and Aspect Determination

The primary impact to the OBA (§6.3.6) is that the 1.3-m² Configuration design has a smaller diameter that is consistent with the reduced LMA. Interfaces (use of bipods) between the LMA and the OBA, and between the OBA and the spacecraft, remain unchanged from the DRM.

Reducing the OBA diameter near the LMA requires the thickness of the optical bench to be increased over that of the DRM. Since the Observatory is launched inverted, with the ISIM at the top of the stack, the optical bench thickness had to be increased to meet the stiffness requirements for launch. This mass increase is reflected in the overall Observatory mass given in Table 10.1.

The Pointing Control and Aspect Determination (PCAD) system (also described in §6.3.6) for the 1.3-m² Configuration is the same as the DRM. Since the focal length did not change, the aspect system did not change between configurations.

10.2 Spacecraft Design Details

The 1.3-m² Configuration spacecraft elements were designed to accommodate the reduced LMA diameter. Changes from the DRM were primarily in the areas of mechanical, structural, thermal, and power. Most elements required no changes from that of the DRM design. Table 10.2 summarizes the impact to each spacecraft element. Detailed analyses are found in the *1.3-m² Configuration Supplemental Design Package*.

Only those elements that changed due to the reduced LMA are discussed below.

Table 10.2. Subsystem elements that were changed from that of the DRM are listed.

Subsystem	1.3-m² Configuration
Observatory Architecture	Smaller spacecraft diameter, OBA, LMA, XGA, and inclusion of payload adaptor
Structures	Increased OBA thickness
Avionics	Updated heater controllers for reduced LMA
Power and Thermal	Updated to include reduced heaters on the smaller LMA and XGA
Mechanisms	No Change
Environments	No Change
GN&C	No Change
Propulsion	No change
Dynamics	No analysis – Forward Work

10.2.1 Configuration

The large reductions in mirror assembly size and science capabilities resulted in a modest reduction in the spacecraft mass. The mass savings are primarily from reducing the spacecraft inner and outer diameters to accommodate the new LMA size. The smaller spacecraft diameter requires an additional adaptor to mate the Observatory to a standard fairing size (Figure 10.6). This additional mass must be included with the mass of the Observatory, and is bookkept in the MEL for this configuration.

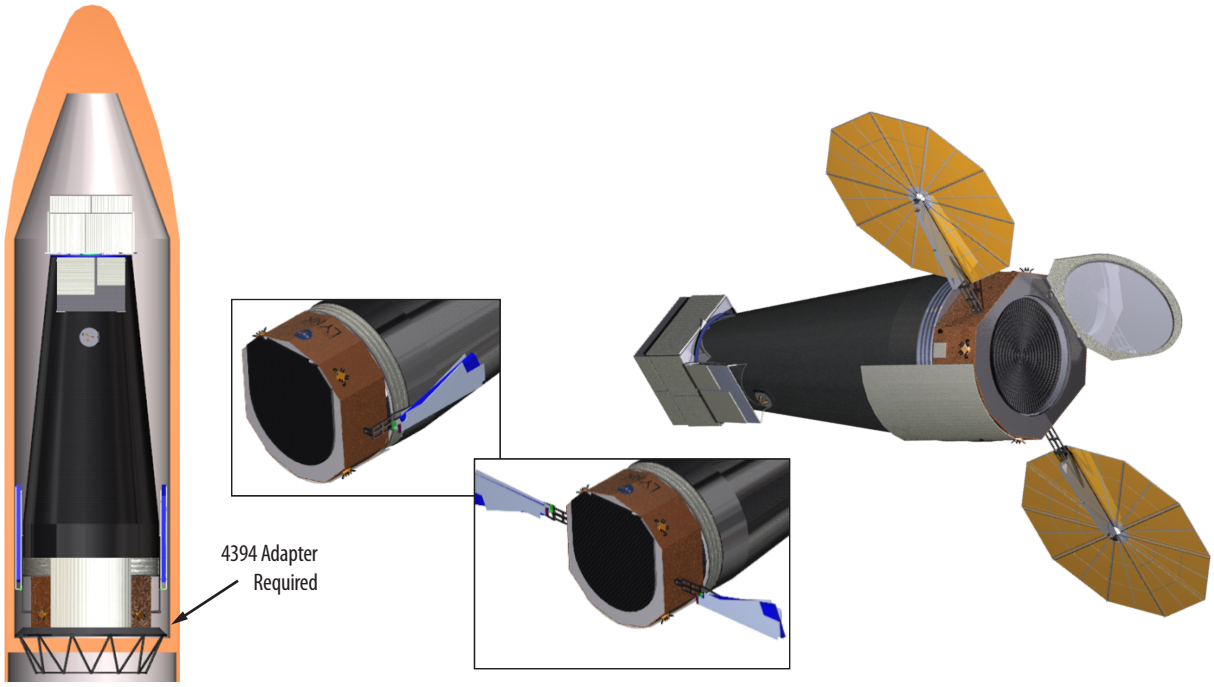

Figure 10.6. (Left) 1.3-m² configuration of *Lynx* inside of a future heavy-class launch vehicle. An adaptor plate is required to mate the Observatory to a standard 5-m fairing. (Top-Right) Solar panels are retracted for launch and (Mid-Right) partially and (Bottom-Right) fully deployed.

10.2.2 Structures

A detailed structural analysis was performed on the 1.3-m² Configuration, taking into account the new mass and Center of Gravity. All primary structures met or exceeded requirements as defined in NASA-STD-5001B for strength and stability, once the thickness of the OBA was increased. The first lateral-constrained normal mode of 9.45 Hz satisfies the Delta IV heavy requirement of 8Hz with an additional 15% margin. Analysis indicates that launch locks are required on the LMA barrel to spacecraft (three locations), on the forward contamination door to LMA barrel (six locations), aft-contamination door to subsystem support ring (six locations), XGA frame to OBA (six locations), and on the ISIM to OBA (four locations).

10.2.3 Avionics and Thermal Control

The 1.3-m² Configuration resulted in minimal changes to the avionics. The primary modification from the DRM was an update to the heater controllers. The heater controllers were updated to account for the reduced LMA, XGA, OBA, and spacecraft size. The number of heaters and temperature sensors were reduced and the heater cabling and the sensor wiring were recalculated. The result was a minimal reduction in heater controller and cabling mass and reduced heater control enclosures for the LMA, XGA, OBA, and spacecraft. Heater controller power was reduced by 32 W.

10.2.4 Power

The primary reduction in power for the 1.3-m² Configuration of the *Lynx* Observatory was due to the reduction in heaters for the smaller LMA, XGA, OBA, and spacecraft. Table 10.3 summarizes the power requirements for the non-science phases.

The total reduction for the launch phase is 23 W for the 1.3-m² Configuration, with minimal savings across the board. Power savings up to a few hundred watts (predicted to be ~2/3 the power required to heat the DRM LMA) are expected for when the Observatory is on orbit and operating in science mode. Currently, the analysis for the 1.3-m² Configuration assumes a conservative estimate for power for the LMA, which is similar to that of the DRM. These power savings are not expected to result in a significant cost savings for this configuration.

Table 10.3. Breakdown of the power requirements for the 1.3-m² configuration of *Lynx*, for all phases except for on-orbit science mode operation.

Source	Launch (0 – 156 min)	Checkout (156 min – 21 days)	Cruise (21 – 104 days)	Safe Hold	Survival (5 min) Battery Power Only
Subsystems					
Avionics	533	1,411	1,411	673	546
GN&C	0	283	283	283	283
Propulsion	0	510	510	510	510
Mechanisms	0	0	0	0	0
Thermal	174	174	174	178	154
Totals (Subsystems)	**707**	**2,377**	**2,377**	**1,643**	**1,492**
Payload					
Microcalorimeter	13	14	434	434	14
HDXI	0	249	249	7	7
XGS	0	190	190	7	7
Mirror Heater	0	700	700	1339	593
Optical Bench Heaters	0	403	403	438	438
Totals (Payload)	**13**	**1,556**	**1,976**	**2,225**	**1,059**
Total Spacecraft - 1.3 m² configuration	**720**	**3,933**	**4,353**	**3,868**	**2,552**
Total Spacecraft - DRM	**743**	**3,991**	**4,411**	**3,875**	**2,552**

10.3 Mission Design Details

Given that the 1.3-m² configuration must be able to carry out *Lynx* science pillar goals, no significant changes in the Mission Design were required. The target orbit of SE-L2, transfer trajectory, ascent profile, delta-V budget and timeline, and launch vehicle class (heavy-class) are identical to those for the *Lynx* DRM.

10.4 Programmatics

Like the DRM, the 1.3-m² configuration is required to be a Category 1 project, Risk Class A, suitable for a Flagship mission. The project organization and leadership, and Agency Governance Model do not change as described in §8.1.

A risk assessment, project schedule, and cost have been established for this configuration and findings are summarized in the following sections.

10.4.1 Risk Assessment

The top project risks for the 1.3-m² Configuration, shown in Table 10.4, are the same as those discussed in §8.3 and listed in Table 8.1. None of these risks requires modification.

Table 10.4. Summary of top *Lynx* 1.3-m² configuration Program risks. Risks (2), (3), and (4) Likelihood and Consequence have been changed from that of the DRM to reflect the reduced capability of this configuration.

Risk	Title	L	C	T	S	$
1	X-ray Mirror Module Assembly and Alignment	3	4		X	X
2	LXM Technical Maturation to TRL 6	3	3	X	X	X
3	X-ray Mirror Segment Industrialization	2	3		X	X
4	LXM Fabrication and Assembly	2	3		X	X
5	X-ray Mirror Technical Maturation to TRL 6	3	2	X	X	X
6	HDXI/XGD Detector Technology Maturation to TRL 6	2	2	X	X	X
7	Calibration Facility Availability	1	3		X	X

L = likelihood of risk occurrence; C = consequence of risk occurrence; T = technical risk; S = schedule risk; $ = cost risk

Risk 1 — X-ray mirror module assembly and alignment: Because the manufacturing schedule has been reconsidered to account for the reduced number of mirror segments, modules, and meta-shells, the same risk as for the DRM exists. If the schedule is extended due to inability to industrialize the process, there will be cost and schedule impacts. The reduced manufacturing schedule decreases the likelihood that mirror assembly will be on the project critical path.

Risk 2 — LXM technical maturation to TRL 6: The only change to the LXM is that the 1.3-m² Configuration has a slightly smaller MA, which has no impact on the technology maturation to TRL 6.

Risk 3 — X-ray mirror segment industrialization: The potential to increase schedule margin before mirror delivery with fewer mirror segments to fabricate would decrease the likelihood of this risk, but not significantly. The *Lynx* team deemed that this was not a significant enough impact to demote the likelihood from a 2 to a 1.

Risk 4 — LXM instrument fabrication and assembly: The only change to the LXM is that the 1.3-m² Configuration has a slightly smaller MA, which has little impact on the fabrication and assembly. There would be fewer pixels to calibrate, but not a significant enough impact to lower the current risk rating.

Risk 5 — X-ray mirror technical maturation to TRL 6: Because the angular resolution requirement for the 1.3-m² Configuration is the same as that of the DRM, the technical maturation is unaffected.

Risk 6 — HDXI/X-ray Grating Detector technology maturation to TRL 6: The XGS resolving power requirement and relative effective area drives the maturation for the gratings. The resolving power for the 1.3-m² Configuration is the same as that of the DRM. The effective area coverage is a reduction that is equivalent to the percentage reduction of the LMA, and so is effectively unchanged.

Risk 7 — Calibration facility availability: Because the mirror production schedule has been reduced by nine months, there is a slight increased risk that the calibration for *Lynx* would overlap that of *Athena*, if *Athena* were to be calibrated in the MSFC X-ray and Cryogenic Facility (XRCF). The *Lynx* team did not feel that this risk increase was significant enough to warrant changing the risk score.

10.4.2 Lifecycle Schedule and the Critical Path

The life-cycle schedule for the 1.3-m² Configuration is shown in Figure 10.7. The primary difference between this schedule and that of the DRM is a reduction in fabrication time for the mirror modules and the XGS gratings. The reduction in the number of required X-ray mirror modules in this configuration results in a ~9-month reduction in the mirror module schedule, allowing for an earlier start to calibration efforts. Final calibration still requires the availability of the flight model HDXI and XGD, whose development schedules are unchanged in this configuration. Therefore, the total duration for flight calibration efforts increases by ~6 months. As with the DRM, the calibrated HDXI and XGD are needed for ISIM I&T following calibration. With the DRM, the ISIM I&T begins with the availability of the LXM, followed ~2 months later with the availability of the HDXI and XGD following calibration. In the 1.3m² Configuration, the HDXI and XGD are available ~1 month before the LXM. The ISIM I&T effort is unchanged in the 1.3m² Configuration, therefore, the 1 month earlier start in this critical path activity results in **only a ~1 month earlier LRD of September 1, 2036**. The XGA fabrication reduction is ~4 months, with has no impact to the critical path.

10.4.3 Cost

The total *Lynx* 1.3-m² Configuration Phase A–E (first 5 years of operation) cost with fee is around ~$0.3B less than the cost of the DRM.

As with the DRM estimate, the parametric estimate for the 1.3-m² Configuration includes project level reserves of 30% on the Phase B–D costs less fee and Launch Services Program (LSP)-provided launch vehicle pass-through cost for a heavy-class vehicle. The estimate range is considered credible for the pre-formulation stage of the study given high *Chandra* architecture heritage, robust and high TRL spacecraft components and design, a detailed and credible path forward for all of the DRM technologies, and detailed and thorough parametric estimates for the mirror assembly, LXM, and XGA, which were developed in the same manner as for the DRM and updated to reflect the design changes for this configuration. The parametric estimate for this configuration serves as the primary estimate. The lower estimate (at a 40% Confidence Level (CL)) compares favorably to the *Chandra* mission actual cost of $4.3B, escalated to $FY20, and is in line with an independent cost estimate and high CLs. Detailed cost information is included in the *1.3-m² Supplemental Design Package*.

The parametric cost estimate for the 1.3-m² Configuration utilized the same cost models and methodologies as for the DRM that are described in §8.5.2.

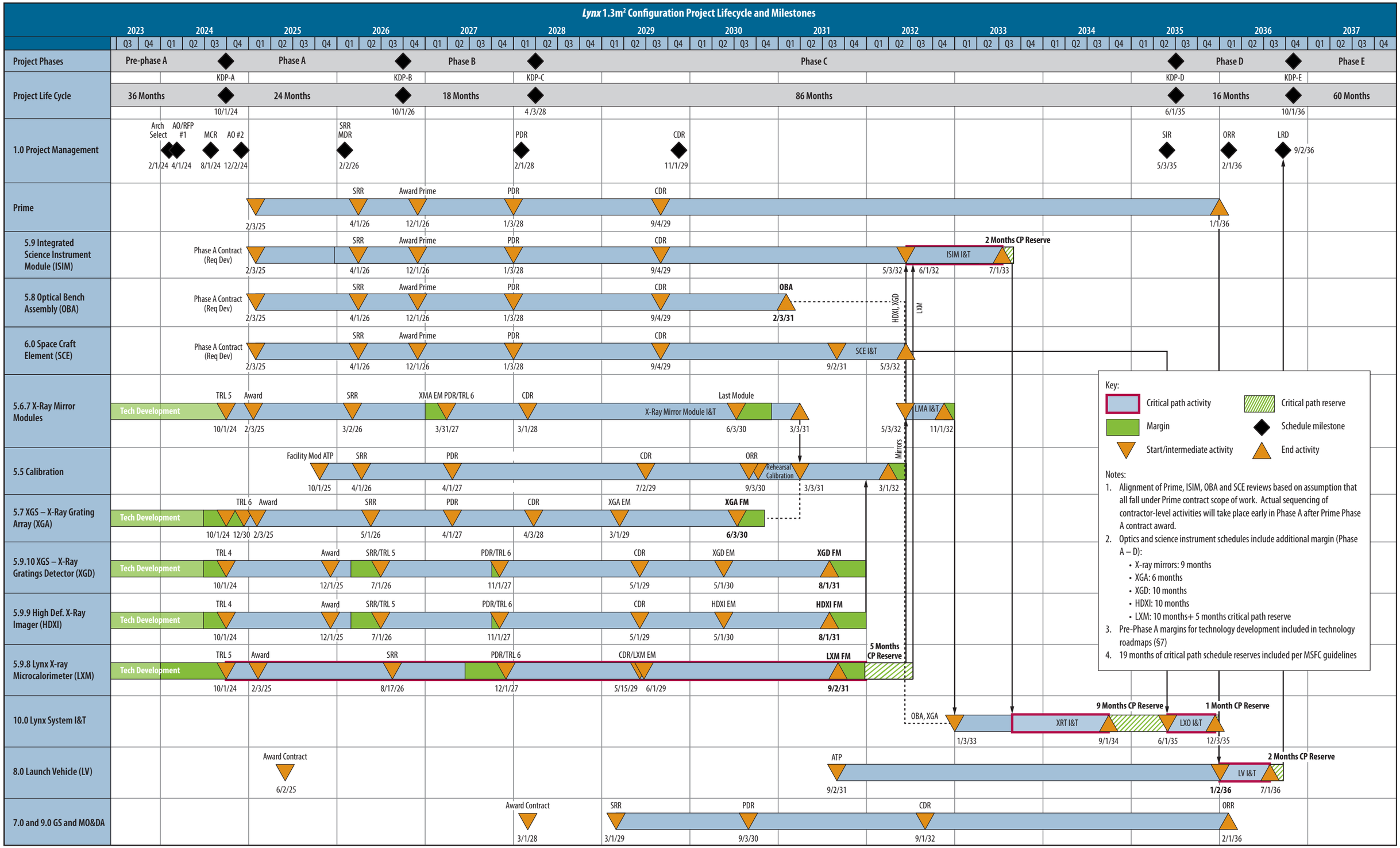

Figure 10.7. *Lynx* 1.3-m² configuration project life-cycle schedule

10.4.4 Work Breakdown Structure

As with the DRM Configuration, the 1.3 m² Configuration estimate was based on the project Work Breakdown Structure (WBS) structure as described in §8.5.1. There were no changes in the WBS for the 1.3-m² Configuration.

10.4.5 Cost Estimation Methodology

The cost estimation methodology for the 1.3-m² Configuration followed that of the DRM Configuration estimate methodology, as described in §8.5.2. Specific parametric model inputs for the LMA and XGA were different for the 1.3-m² Configuration in order to account for the reduced number of meta-shells for the LMA. An updated cost model for the LXM was developed by GSFC and used as throughput into the overall *Lynx* mission cost model for this configuration. The LXM cost model accounted for the reduced LXM focal plane array. These changes are summarized below. All other costing Ground Rules and Assumptions (GR&A) and methodologies are unchanged from the DRM estimate.

LMA parametric model input changes:

- Removed five meta-shells (three outer and two inner) from the LMA cost model.
- Changed mass of thermal pre-collimator, spider, post-collimator, forward and aft contamination doors, and mirror barrel structure per the MEL for the 1.3-m² Configuration. The MEL is provided in the *1.3-m² Supplemental Design Package*.
- The LMA EM unit assumes the use of different meta-shells from those for the DRM.
- LMA new first meta-shell (innermost) acquisition category changed from "Average Modification" (15% new design) to "Make" (80% new design).
- LMA new second meta-shell acquisition category changed from "Average Modification" to "Major Modification" (65% new design). "Average Modification" was used for the remaining meta-shells (15% new design).
- XGA parametric model input changes:
- XGA reduced in size consistent with the reduced LMA.
- LXM parametric model input changes:
- The number of thermal readouts (§6.3.4.1) reduced in proportion to MA (~factor of 2).
- Reduction in electronics assemblies scaled roughly by number of electronic readouts (§6.3.4.1) and reduction of MA.

10.4.6 Cost Validation

The *Lynx* 1.3-m² Configuration cost estimate was validated with a side-by-side comparison by WBS of the analogous *Chandra* costs as described in §8.5.3.1 for the DRM Configuration. A grassroots estimate was not developed for the 1.3-m² Configuration. The *Chandra* analogous estimate agreed to within a few percent of the parametric estimate and provides a high confidence in the reasonableness of the estimate. In addition, as with the DRM, the *Lynx* parametric estimates for the 1.3-m² Configuration LMA, science instruments, and spacecraft element were compared to historical observatory missions. The parametric estimates for these assemblies are within family. This historical comparison further reinforced the reasonableness of the *Lynx* estimate.

10.4.7 Independent Cost Assessment

Per request of NASA Headquarters, the MSFC Engineering Cost Office developed a non-advocate Independent Cost Estimate (ICE) and performed an uncertainty analysis to validate and determine the CL in the 1.3-m² Configuration parametric cost estimate. As with the DRM independent assessment, the ICE addressed the uncertainty in the estimating methods, input parameters, design complexity, and fee. The analysis was performed in $FY20 and $RY, using NASA escalation factors, for Phases B–E, exclusive of launch vehicle costs and reserves, to derive the cost basis for the assessment. All assumptions used in the DRM assessment described in §8.5.2 remained the same for the 1.3-m² Configuration, and all other details for the analysis methodology remain unchanged as described in §8.5.2.

A Monte Carlo simulation on the input models provided a cost curve with CLs ranging from 10% to 90% as shown in Figure 10.8. Reserve amounts to achieve corresponding CLs were calculated based on the delta between the derived cost basis (parametric estimate for Phases B–E exclusive of launch vehicle and reserves) and the cost at the 50% and 70% CLs on the resulting cost curve. Based on this analysis, the *Lynx* parametric estimate with 30% reserves on B–D costs (exclusive of launch vehicle and fee) has a 39% CL on the independent cost curve. As with the DRM, and as described in §8.5.3.3, the parametric estimate for the 1.3-m² Configuration with reserves represents a substantially better reserve posture than historical NASA projects.

The resulting analysis yielded a cost range of $4.6B at a CL of 40% to $5.8B at a CL of 70% in $FY20, and $6.3B at a CL of 40% to $7.9B at a CL of 70% in $RY. The 40% CL in $FY20 on the non-advocate cost curve is within 1% of the *Lynx* parametric estimate for the 1.3-m² Configuration.

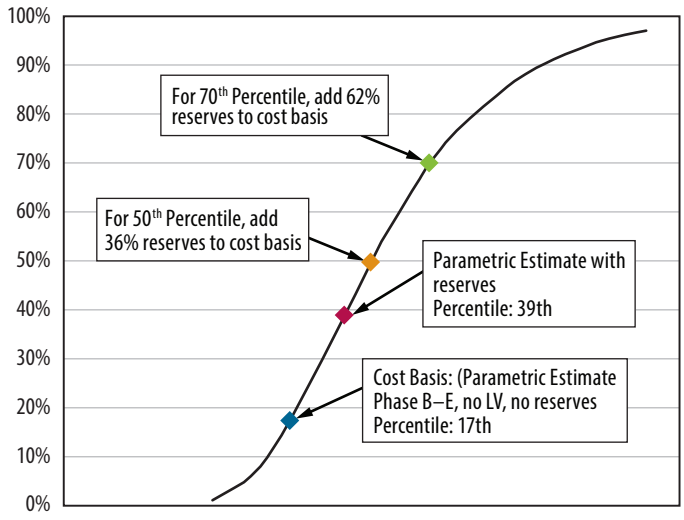

Figure 10.8. The *Lynx* parametric cost estimate with 30% reserves represents a 39% CL. To achieve a 50% CL, 36% reserves need to be applied to the cost basis. For 70% CL, 62% reserves need to be added to the cost basis.

APPENDICES & REFERENCES

Appendix A. *The* Fundamentals *of Lynx* Science Performance

A.1 Source Confusion Limit and Angular Resolution Requirements

In very crowded fields, telescopes suffer from source confusion caused by significant fluctuations in the background induced by a large number of unresolved and/or undetected sources. Confusion manifests itself as significant centroid shifts and as large fluctuations in the flux of detected sources on top of purely statistical noise. The effects become severe and uncontrollable at flux levels at which images contain 1/50 to 1/15 sources per beam[627]. For PSF $\gtrsim 1''$, source confusion is the main limiting factor preventing X-ray telescopes from reaching the flux levels needed to detect $z = 10$ black hole seeds (§1.1.3) or resolve cores of young star forming regions in the Milky Way (§3.1).

The main parameter controlling the source confusion is the number of sources per one PSF beam near the detection threshold. The effective solid angle of the beam is defined as $\Omega_b = \int \mathrm{PSF}\, d\Omega$, where the PSF is normalized to 1 at its peak (Condon [628]). The *Lynx* PSF here is assumed to be Gaussian. This is appropriate, e.g., in cases when angular resolution is limited by small misalignments of a large number of mirrors. This is indeed expected to be one of the main contributors to the *Lynx* PSF. For a Gaussian PSF, the beam solid angle is $\Omega_b \approx 1.13 \times \mathrm{FWHM}^2 \approx 1.18 \times \mathrm{HPD}^2$, where HPD is the 50% power diameter of the PSF. Effects of confusion become strong at levels below

$$b = q^2/(3-\gamma) \text{ beams per source,} \qquad \text{(A.1)}$$

where γ is the differential slope of the $\log N - \log S$ distribution and $q \approx 5$ is the "quality factor" [628].

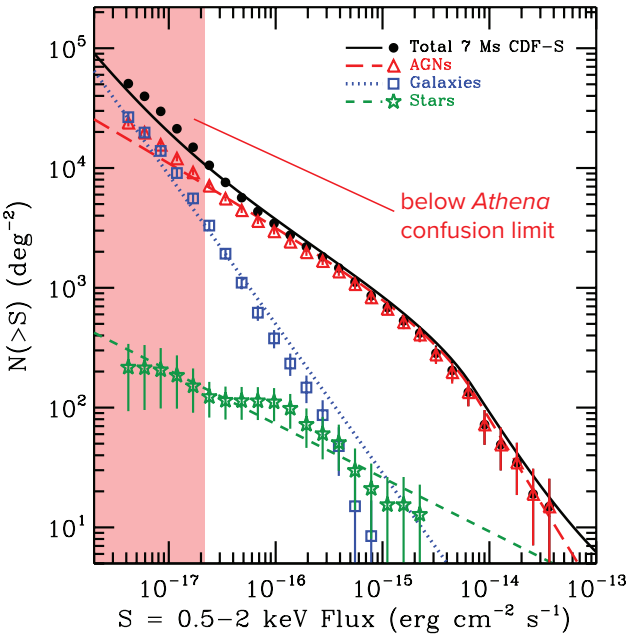

Fig. A.1— *Chandra* $\log N - \log S$ distribution observed in the 7 Msec deep survey (reproduced from [95]). Extrapolation of this function to low fluxes is used to compute *Lynx* confusion limits. Shaded region shows fluxes below the anticipated *Athena* confusion limit (5″ PSF, HPD).

We now need to estimate γ near the flux limits appropriate for *Lynx*. The $\log N - \log S$ distribution observed in the deepest *Chandra* surveys shows an upturn very near the flux limit achieved in its 4 Msec surveys (Lehmer et al. [629]). This upturn is now very clearly observed in the 7 Msec pointings ([95], reproduced in Fig. A.1), and is associated with the integrated flux of X-ray binaries in $z \lesssim 3$ galaxies. This dominant source component is modeled in Lehmer et al. Their model is reliable and well-constrained because it describes sources originating in relatively low-redshift galaxies via a well-known process (XRB activity

associated with star formation) and can be calibrated using a well-established distribution of star formation rates in the not-so-distant Universe. Therefore, extrapolations of the Lehmer et al. model to low fluxes can be used to compute the effect of source confusion.

The results are shown in Fig. A.2. A steep slope of the $\log N - \log S$ function below $f_x = 10^{-17}$ erg s^{-1} cm^{-2} corresponds to a quickly increasing confusion flux limit as the PSF degrades. For sub-arcsecond PSFs, confusion limits are below the sensitivity target in the *Lynx* deep surveys. However, already for a 2″ PSF, the confusion limit is an order of magnitude higher than the target. Such levels of angular resolutions are unacceptable. The confusion limit for *Athena* (5″ PSF) is above the sensitivity levels achieved in the 4 Msec *Chandra* survey, and is a factor of ~ 200 above the *Lynx* sensitivity targets.

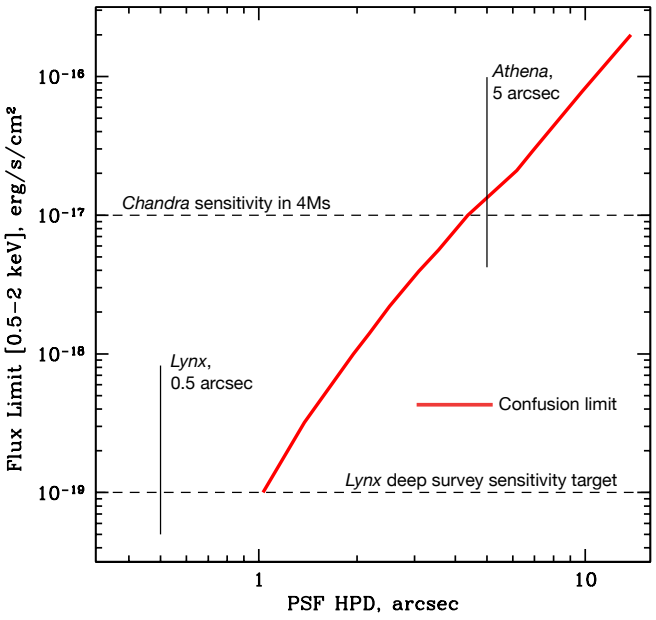

Fig. A.2— Confusion limit in the 0.5–2 keV band as a function of angular resolution for a Gaussian PSF.

A.2 XRBs in High-*z* Galaxies

The main science goal for deep surveys with *Lynx* is detection of black hole seeds in $z \approx 10$ galaxies (§1.1), which have relatively low mass and L_X. Therefore, a possible contamination of X-rays flux from massive black holes by the integrated emission of X-ray binaries in the host galaxy should be considered.

Highest-z galaxies detected by *Hubble* are compact, < 1 kpc half-light radius [630], which corresponds to < 0.5″ angular diameter at $z = 10$. Such galaxies will be barely resolved with *Lynx* if at all. The X-ray spectrum of XRBs is expected to be softer than that of the BH seeds (see below), which will serve as an additional discriminator. However, the safest approach is to limit the analysis to X-ray fluxes sufficiently above the floor set by the XRB emission.

A key point to note here is that we expect a strong correlation between near-IR (NIR) magnitude of high-z galaxies and the integrated flux of their XRBs. The total flux of high-mass X-ray binaries (which will dominate the total XRB emission [391]) reflects the on-going star formation in the host galaxy. The observed NIR magnitude also reflects star formation, because at $z = 10$, the observer-frame NIR corresponds to the UV emission in the source rest frame (e.g., $\lambda = 1.65$ μm corresponds to 1,500 Å at $z = 10$).

At low redshifts, a strong correlation between the star formation rate and the XRB flux is indeed observed [631, 632], $L_X \propto$ SFR. This correlation is well understood, and can be successfully derived from the population synthesis models (e.g., [391]). The specific X-ray output, L_X/SFR, depends on the high-mass end of the stellar IMF and on the metallicity of the stellar population. At low

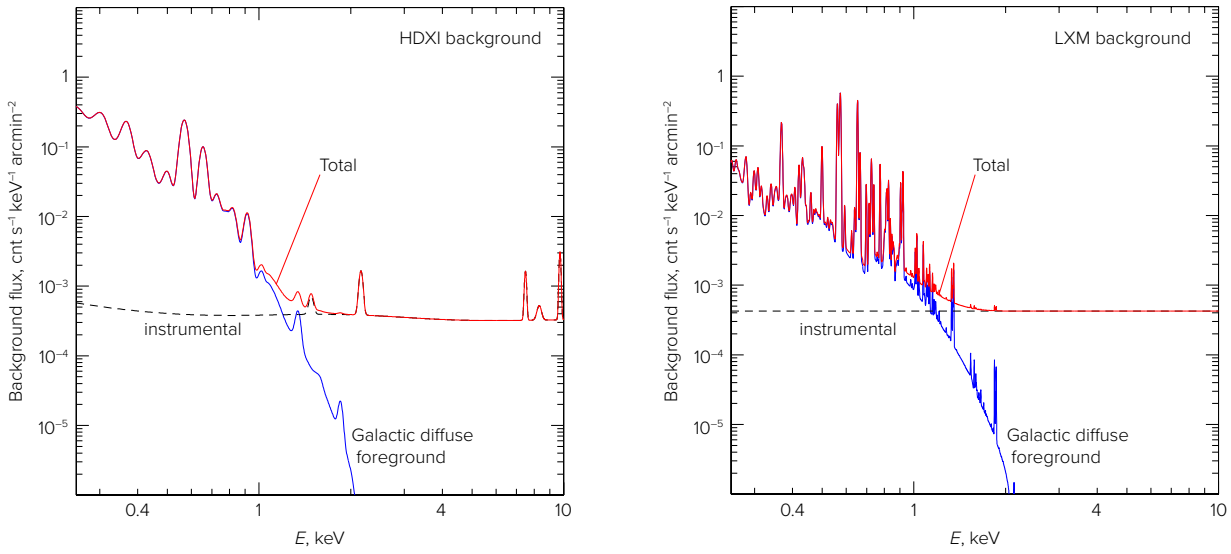

Fig. A.3— Predicted spectra of diffuse backgrounds for the *Lynx* HDXI and LXM instruments. Backgrounds are normalized to a solid angle of 1 arcminute^2 on the sky (for the 10-m focal length, 1 arcmin^2 = 0.0846 cm^2). Below ~ 1.5 keV, the background is dominated by the diffuse Galactic foreground (a model from Hickox & Markevitch [640] is used here). This signal is astrophysical in origin, and varies proportionally to the telescope effective area. The instrumental background is dominated by secondary X-rays produced by charged particles. For HDXI, it is assumed to be identical to the *Chandra* ACIS-I background. For LXM, predictions for the *Athena* XIFU instrument are adopted.

redshifts, this has indeed been seen [631–637], L_X [2–10 keV]/SFR = 4×10^{39} erg s^{-1} $M_\odot^{-1}$ yr, which is in a good agreement with predictions of the population synthesis models of Fragos et al. [391]. This model generically predicts that the L_X/SFR ratio increases almost ten-fold for low-metallicity stellar populations expected in high-z galaxies. Therefore, the adopted value of the X-ray luminosity of XRBs in high-z galaxies is 4×10^{40} erg s^{-1} for each $M_\odot$ yr^{-1} of star formation. Using Kennicutt's relation between UV luminosity and star formation rate [638], corrected for lower metallicities following Madau & Dickinson [136], we have:

$$f_{\rm XRB,\,0.5–2\,keV} = 1.0 \times 10^{-19}\,{\rm erg\ s^{-1}\ cm^{-2}}\ 10^{0.4\,(30-{\rm m})},$$

where m is the apparent galaxy magnitude in the band that corresponds to the rest-frame wavelength 1,500 Å. The coefficient here is computed for an X-ray spectrum with cutoff at $E \approx 6$ keV, as observed at low redshifts [394, 639]. Note that, in this case, one expects virtually no source photons detected above ~ 1 keV. This is in strong contrast with the power-law spectra expected for the black hole seeds. Therefore, the presence of the spectral cutoff can be established even for relatively faint sources and used as a discriminator between the XRBs and black hole seed emission.

To conclude, there is a natural X-ray flux "floor" set by the XRB emission, and the level of this floor depends on the depth of the counterpart OIR survey. For the m ≈ 30 surveys expected from *JWST* and *WFIRST*, the XRB floor is around $f_x = 10^{-19}$ erg s^{-1} cm^{-2}, which represents a natural target for the deep surveys with *Lynx* aimed at detection of black hole seeds in the early Universe. This X-ray flux level corresponds to the XRB emission from galaxies with a 5 $M_\odot$ yr^{-1} star formation rate at $z = 10$. For objects with *a priori* known locations, *Lynx* can reach down to $f_x \approx 5 \times 10^{-20}$ erg s^{-1} cm^{-2} in a ~ 4 Msec survey (Fig. A.5 below), which corresponds to SFR ~ 2 $M_\odot$ yr^{-1}.

A.3 Faint Point Source Detection and Sensitivity Projections

Reaching $f_x \sim 10^{-19}$ erg s^{-1} cm^{-2} flux limits (two orders of magnitude below the sensitivity of deepest *Chandra* observations) is obviously a challenge. As discussed above, source confusion will not be a limiting factor for *Lynx* at these flux levels. Instead, the main limiting factor for *Lynx* is the diffuse background, which is both astrophysical and instrumental in origin. The expected background is discussed below, followed by a summary of the faint source detection approach projected for *Lynx*, as well as results of Monte-Carlo simulations of detection thresholds as a function of exposure time.

A.3.1 Expected *Lynx* background

In its deepest exposures, *Lynx* will resolve close to 100% of the cosmic X-ray background originating from discrete X-ray sources. Therefore, only truly diffuse background components need to be considered. The first component is the instrumental background, dominated by the secondary X-rays generated by charged particles interacting with the detector itself and detector housing. For the LXM instrument, this component can be substantially reduced by employing an anti-coincidence shield, as designed for the *Athena* XIFU instrument. The instrumental background predictions developed for the *Athena* XIFU [641] were adapted for the LXM instrument. For the HDXI, the particle-induced background per unit area was assumed to be identical to that of the *Chandra* ACIS-I detector.

Below ~ 1.5 keV, the background will be dominated by emission of the Milky Way halo. Its spectrum and intensity has been measured with *ROSAT* [642], *XMM-Newton* [643], and with *Chandra* by Hickox & Markevitch [640]. All of these results are consistent, but for *ROSAT* and *XMM-Newton* it is a challenge to separate the truly diffuse Galactic foreground from the residual cosmic X-ray background generated by discrete sources that will be detected and masked out in *Lynx* images. Therefore, the Hickox & Markevitch measurements derived from the deepest *Chandra* pointings are used. The results are shown in Fig. A.3. The soft Galactic component follows the same model for the HDXI and LXM instruments, the only differences being the energy resolution of these detectors and a different throughput at the very soft energies.

The shape of the expected *Lynx* background spectrum is very different from that of the typical sources dominated by the power-law continuum. Therefore, source detection can be significantly optimized by choosing the appropriate energy band. For traditional source detection methods operating on single-band images, the most optimal band for *Lynx* is $\approx 0.7 - 2$ keV. This spectral difference can be exploited to further lower the source detection threshold. A next-generation detection procedure is described below. It maximizes information utilized for detection of faint sources and optimally combines data from different energies so that there is no need to restrict detection to, e.g., the 0.7–2 keV band.

A.3.2 Next-generation source detection methods

Images obtained with focusing X-ray telescopes have low background levels, enabling extremely faint detection limits. Sources with only ten, five, or even fewer photos collected over weeks of observing time can be confidently detected. Currently, the standard approaches for X-ray source detection are based on a convolution of single-band images with a filter approximating the telescope PSF [644, 645]. This method is close to, but is not, theoretically optimal for detecting faint sources in images

dominated by Poisson noise. *Lynx* will push limits in sensitivity, and therefore more sophisticated and optimized analysis techniques are required. The derivation of an improved detection filter based on the likelihood function is described below. It can be easily generalized for combining the data from multiple energy bands. This method is close to being theoretically optimal. Compared with traditional approaches, it leads to approximately a factor of two savings in exposure time needed to reach the given sample purity at a given flux threshold in the *Lynx* deep images.

Single-band optimal filter — Source detection can be thought of as a statistical test of whether a source with a positive flux exists at a given location. The goal is to minimize the probability of missing real sources, e.g., because of unnecessary high detection thresholds, while also minimizing a number of "false positives" — statistical fluctuations mistaken as sources with positive flux. The Neyman-Pearson lemma [646] suggests that the likelihood ratio provides the most statistically powerful test in this case.

For faint sources on top of high background and uniform, white noise, a convolution of the image with the PSF is equivalent to performing the likelihood ratio test (c.f. [647]). This is the regime found in optical and NIR images, and the convolution with the PSF has been widely used as a detection filter throughout astronomy. However, X-ray images are in a different regime of statistical noise, and therefore the optimal filter is different, as shown below.

For a Poisson-dominated image noise, the likelihood function can be written as

$$-\ln L = \sum_i \ln\, m_i - \iint m, \tag{A.2}$$

where the sum is over the location of detected photons, and m_i is the image model evaluated at each point i. In the case of a single, isolated point source on top of a uniform background, the model can be written as $m = f \times P + b$, where P is the PSF image ($\iint P = 1$), f is the total source flux, and b is the background brightness. Substituting this into eq. (A.2), we have

$$-\ln L = \sum_i \ln\left(f\, P_i + b\right) \;-\; B \;-\; f,$$

where $B = \iint b$. The likelihood ratio test is equivalent to analyzing the difference in the log-likelihoods computed for models with and without the source,

$$\Delta \ln L = \sum_i \ln\left(f\, P_i + b\right) - \sum_i \ln b - f = \sum_i \ln\left(f\, P_i/b + 1\right) \;-\; f. \tag{A.3}$$

The first term in this equation is a convolution kernel that can be thought of as the optimal detection filter,

$$\Phi = \ln\left(\frac{f}{b}\, P + 1\right). \tag{A.4}$$

Filter Φ is the optimal filter for searching for sources with flux f on top of a uniform background b. In the limit of very faint sources, where $f \to 0$, it reduces to the expected shape of the PSF itself, $\Phi \approx P$.

That the filter shape depends on the flux of the target sources is a complication of little significance. One should simply develop the filter for sources near the target detection threshold and then use it

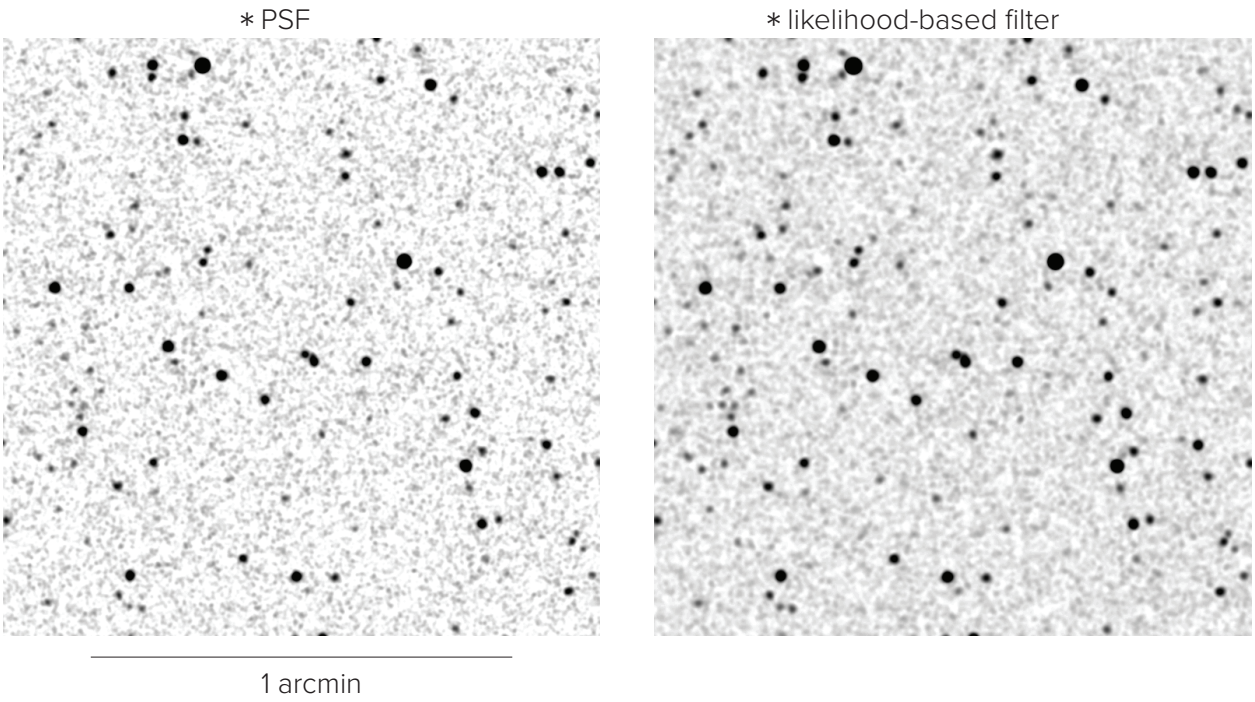

Fig. A.4— Examples of source detection in a 4 Msec *Lynx* HDXI exposure using a traditional detection filter based on convolution with the PSF *(left)*, and the optimal likelihood-based filter given by eq. (A.5). Traditional detection is performed in the optimal single energy band (0.7–2 keV), while the likelihood-based detection uses a broader band, 0.3 – 3 keV. Images are normalized to the same source brightness. The likelihood filter results in a much suppressed level of noise, leading to lower false detection probabilities and the possibility of reaching fainter flux levels for the same exposure time.

for all sources. The filter will be suboptimal for sources far above the threshold, but such sources will be confidently detected in any case.

One possible procedure for setting the target detection thresholds is based on the required sample purity or false detection probability. The thresholds themselves can be established via Monte-Carlo simulations. For real sources with flux f, the convolution with filter Φ produces a peak with an average amplitude

$$C_{\rm peak} = f \iint P \ln\left(f\,P/b + 1\right).$$

$C_{\rm peak}$ can be precomputed for given b and f. The analysis of simulated Poisson images with uniform background b and convolved with filter Φ provides the probability that the level $C_{\rm peak}$ in the convolved image is exceeded by purely statistical fluctuations. The factor f is then increased until that probability is below a pre-defined level. The resulting f serves as the threshold and defines the optimal detection filter.

Extension to multiple energy bands — Since the detection filter in eq. (A.4) is proportional to the log of the likelihood function, it enables an extremely straightforward combination of the data in multiple energy bands in a statistically optimal way: simply adding the convolutions in individual (narrow) energy bands is equivalent to the logarithm of the combined likelihood function,

$$\Delta \ln L = \sum_{i,j} \ln\left(f\,\frac{P_{i,j}\,s_j}{b_j} + 1\right) \tag{A.5}$$

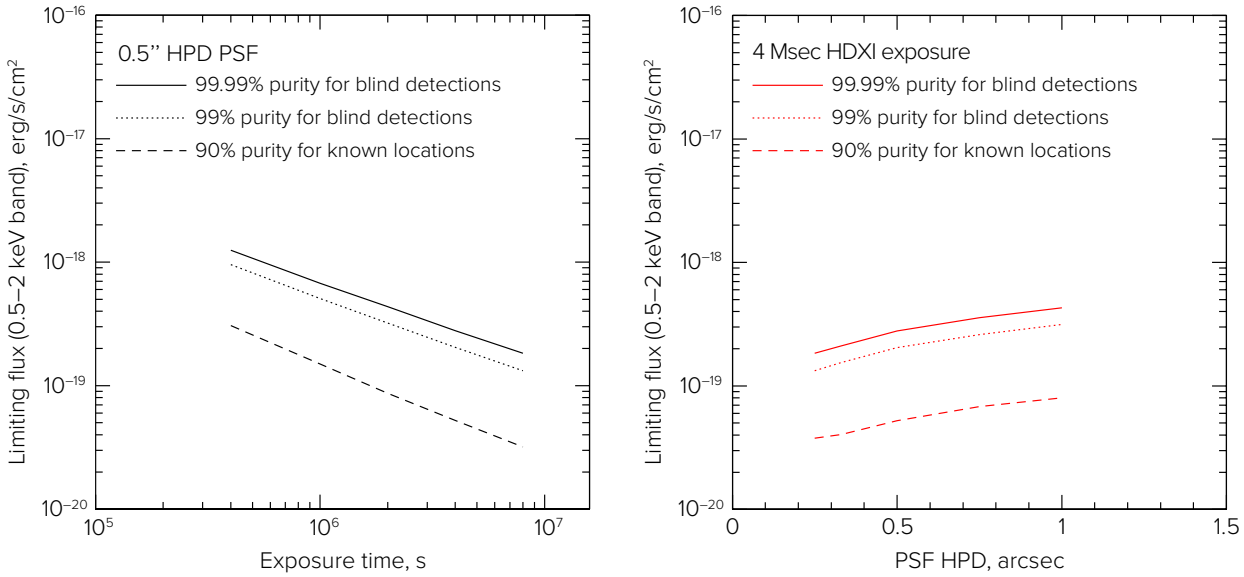

Fig. A.5— *Lynx* limiting sensitivity as a function of exposure time *(left)* and PSF size *(right)*. Detection thresholds are computed for different levels of required sample purity, and different detection modes (blind detections and search around known locations such as high-z JWST galaxies). The limiting fluxes are quoted in the observed 0.5–2 keV energy band, even though the optimal detection is performed over a somewhat wider 0.3–3 keV energy band (see text). A flux limit of 6×10^{-20} erg s^{-1} cm^{-2} achievable for known locations in a 4 Msec exposure for the on-axis 0.5″ PSF corresponds to 5 photons detected in the 0.3–3 keV band.

where the sum is over the detected photon positions i as before and the detected photon energies j, $s(E)$ is the source spectrum, b_j is the background brightness at energy j, $P_{i,j}$ is the PSF evaluated at location i and energy j, and f is the total source flux. Further simplifications to computing the convolution given by eq. (A.5) are possible if, e.g., the PSF is energy independent, but such cases are beyond the scope of this analysis.

The threshold for optimal detection in a wide energy band will depend on the source spectrum. This is a strength of this new technique, since it opens the possibility of searching for specific classes of sources (power-law, strongly absorbed, etc.) in a statistically optimal way.

An example of the likelihood-based optimal detection performance is shown in Fig. A.4. The method leads to a factor of ≈ 10 improvement of sample purity for a given source flux, or nearly a factor of 2 reduction in exposure time needed to achieve the required sample purity for a given source flux. Approximately half of these gains comes from using a more optimal shape for detection filter (eq. (A.4)), the rest coming from a statistically optimal combination of the data from a wider energy band.

A.3.3 Sensitivity projections

Limiting sensitivities computed for the detection of power-law sources with $\Gamma = 2$ in *Lynx* HDXI images with exposures ranging from 400 ksec to 8 Msec are shown in Fig. A.5. The variation of detection thresholds with the PSF size is shown in the right panel of the same Figure. These results show that flux limits ≈ 10^{-19} erg s^{-1} are achievable in the deep *Lynx* exposure for sample purities corresponding to detection around *a priori* known source locations (e.g., high-z *JWST* galaxies). Exceptionally high sample purities (> 99.99% for blind detections) will be achieved for somewhat

higher flux levels, $f_x = (2-3) \times 10^{-19}$ erg s^{-1} cm^{-2}. For reference, a flux level of 10^{-19} erg s^{-1} cm^{-2} in the 0.5–2 keV band corresponds to 8 photons detected in the 0.3–3 keV detection band in a 4 Msec exposure.

As shown in Fig. A.5, flux limits scale with exposure more slowly than $t_{\rm exp}^{-1}$, and they also improve somewhat for smaller PSF sizes. This indicates that the diffuse background is affecting source detection. The background is dominated by the astrophysical component (Fig. A.3) whose intensity scales as the telescope effective area. As a consequence, the exposure times needed to achieve a given flux threshold are approximately inversely proportional to the effective area.

A.4 Considerations for X-ray Gratings

Grating spectrometers are essential instruments for future X-ray missions, and existing technologies provide 50 – 1,500-fold higher throughput compared to current orbiting instruments. The characteristic temperature of galaxies, galaxy clusters, stars, neutron stars, black hole accretion disks, and exploding objects occurs at T > 0.5×10^6 K. At temperatures of 0.5–100×10^6 K, diagnostic emission and absorption lines are from metals (i.e., O, C, Fe, Mg, Si, Ne), and most have energies in the X-ray band. Of these lines, the strong oxygen lines at 10^6 K (O VII Heα and O VIII Lyα, at 21.6Å and 18.9Å) are particularly important because of the oxygen abundance relative to other metals and the variety of environments where they are detected. To measure line profiles and detect faint lines, the resolution must be close to the thermal width, which for the oxygen lines is $54 \times (T_6)^{1/2}$ km s^{-1}, where T_6 is the temperature in units of 10^6 K. This suggests a spectral resolution target of R = 5,000 – 10,000, matching the thermal widths of the oxygen lines for $T = 10^{5.5} - 10^6$ K. A resolving power of 5,000 is therefore used as a requirement for the XGS instrument. At this level, spectral resolution plays an insignificant role on the detectability of faint absorption lines from the CGM and Cosmic Web, because an internal kinematic structure with Δv of at least a few tens of km s^{-1} is expected in these settings (Fig. A.7). Overall, for the nominal XGS design with A = 4,000 cm^2 and R = 5,000, absorption lines with equivalent widths of 0.5–1 mÅ will be detectable, and that the kinematic structure can be measured starting from EW ≈ 2 mÅ.

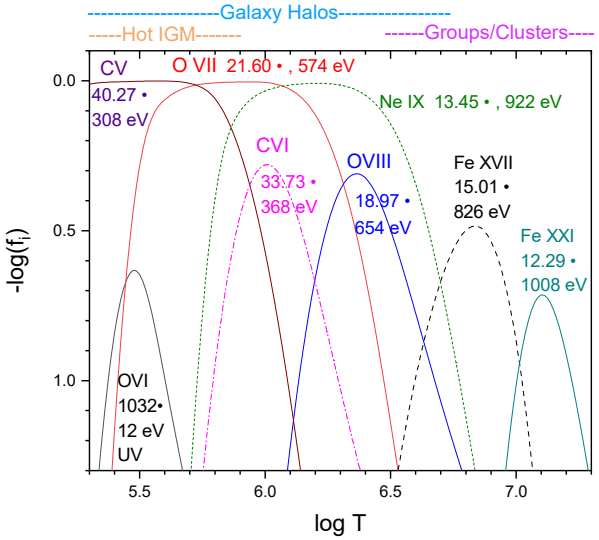

Fig. A.6— Ionization states for strong absorption lines in the CGM around galaxies and groups. Many of the important ions and strong resonance lines are in the soft X-ray band (12.29–40.27 Å⟺ 0.31–1.01 keV), and most are already detected in the MW hot halo. Other ions not shown here, but detectable, are N VI, N VII, S XI, S XII, Si X, Si XI, Fe XIX, and Fe XXII. Approximate temperature ranges of the primary hosts for intergalactic absorption are indicated on top.

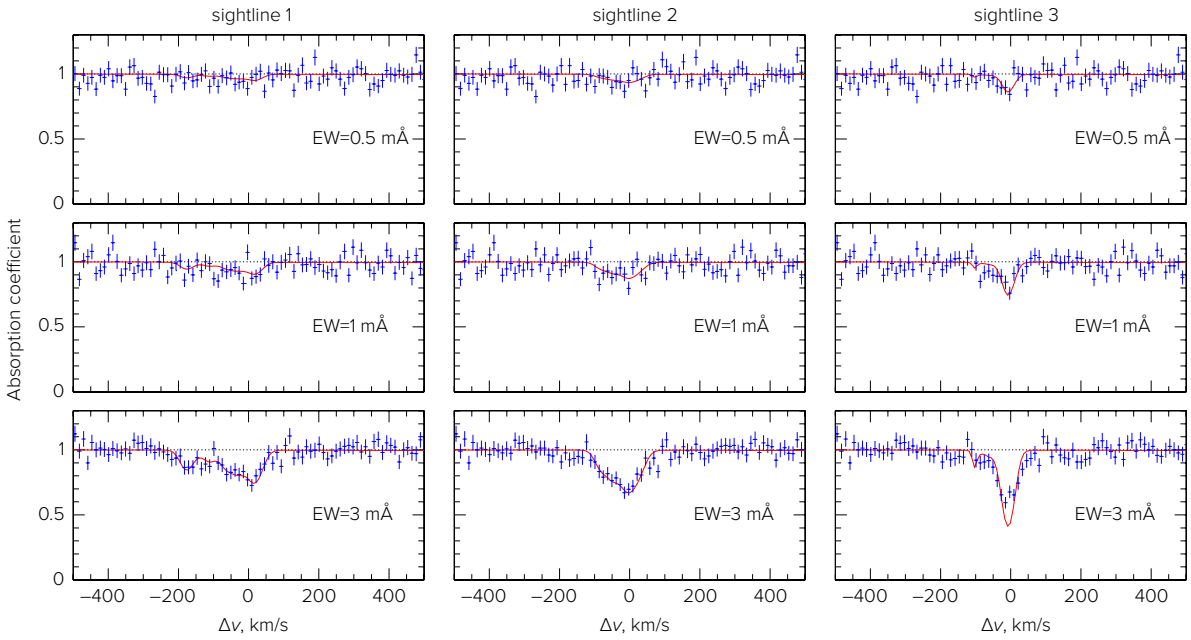

Fig. A.7— Simulated XGS absorption spectra of O VII in the CGM, observed in a 300 ksec *Lynx* pointing at a background AGN with $f_x = 10^{-11}$ erg s^{-1} cm^{-2}. The line profiles were obtained from different sightlines through the EAGLE simulations (see discussion in §A.5 below). The absorption lines were rescaled to integrated equivalent widths of 0.5, 1, and 3 mÅ. Red lines show the intrinsic line profiles. Simulated spectra (blue data points) contain effects of spectral resolution (R = 5,000) and Poisson noise. Only sightline 3 contains a sufficiently narrow line for which the instrumental spectral resolution becomes apparent.

A.5 Sensitivity projections for CGM and Cosmic Web

The assessment of the feasibility of observing the CGM is based on analyzing mock observations generated from several modern numerical simulations of galaxy formation, including EAGLE, FIRE, MUFASA, Illustris-TNG, and Agertz & Kravtsov zoom-in simulations. These simulations generally reproduce the observed stellar populations but use different numerical models, subgrid physics, and prescriptions for feedback. These outputs provide a representative range of predictions of what *Lynx* can see in the galactic halos (Fig. A.8).

All of these simulations lead to a consistent picture. Galaxy halos are the brightest in the soft X-ray band, $E < 0.7$ keV, because of their low temperatures. However, the emission is dominated by a small number of bright spectral lines (notably, O VII and O VIII transitions). The contrast of the CGM continuum emission relative to the unavoidable foreground from the Milky Way halo is low, making CGM density measurements in the soft band impossible, except for the very inner radii. At higher energies, $E > 0.7$ keV, the CGM spectrum has a stronger continuum component, and the foreground Milky Way halo emission is much weaker. Therefore, the gas density can be derived using the CGM emission in this energy band. Simultaneous solid detections of the CGM flux in three spectral bands, 0.4–0.7, 0.7–1.05, and 1.05–1.5 keV, are sufficient for ≈ 10% determination of gas density, and ~20% determination of temperature and metallicity. Detections in only two bands constrain a degenerate combination of density, metallicity, and temperature. Detection only in the soft band provides a measure of the O line flux, which is very difficult or even impossible to convert to thermodynamic quantities. Therefore, X-ray observations aiming at a detailed characterization

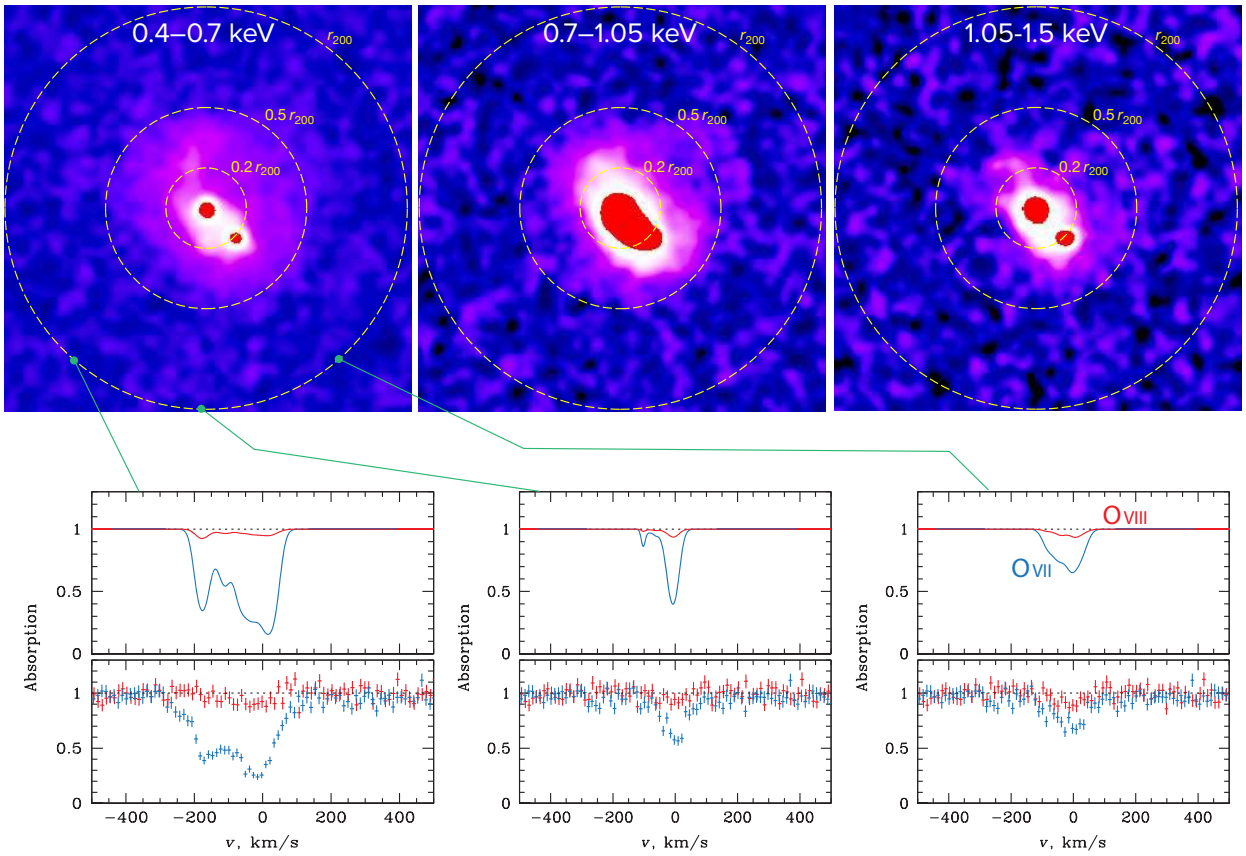

Fig. A.8— Mock *Lynx* observations of a $M_{\rm tot} = 3\times10^{12}\,M_\odot$ galaxy at $z = 0.03$ generated using an output from the EAGLE simulation. The top panels show 500 ksec HDXI images in three energy bands (the virial radius, r_{200}, corresponds to 9′), including the realistic noise from astrophysical and instrumental backgrounds, detection and removal of background point sources, etc. The CGM can be mapped out to $\sim 0.5\,r_{200}$ in all three bands. The bottom panels show simulated O VII and O VIII absorption spectra (300 ksec XGS observations, $f_{\rm AGN} = 10^{-11}$ erg s^{-1} cm^{-2}) at three arbitrary lines of sight located near the virial radius. Solid lines show the ideal absorption spectra derived from simulation output, including thermal broadening and random velocities, whose data points indicate what *Lynx* will observe with XGS at spectral resolution $R = 5{,}000$. Note the strong variations of absorption spectra for different lines of sight, emphasizing the complex kinematic and multiphase structure of the CGM. *Lynx* will provide very high signal-to-noise measurements of the O VII line, and solid detections of O VIII. A joint analysis of the O VII and O VIII lines will constrain the distribution of random velocities and temperatures in each of the lines of sight.

of the CGM must have the sensitivity for solid detections in all three of the 0.4–0.7, 0.7–1.05, and 1.05–1.5 keV bands. This requirement can be satisfied with *Lynx* to at least half the virial radius in galaxies with mass as low as $\approx 3\times10^{12}\,M_\odot$ (see below).

An alternative approach for measuring CGM temperatures is possible using the LXM, whose spectral resolution is sufficient to separate the O VIII and O VII emission lines in the CGM from those in the MW halo for $z > 0$ galaxies. This increases the CGM contrast in the soft band by a factor of ~10, and the O VIII and O VII lines will be detectable to $\approx 0.5\,r_{200}$ for galaxies with $M_{\rm tot} \approx 3\times10^{12}\,M_\odot$ or higher. Flux ratio in the O VII and O VIII lines is a sensitive temperature indicator, such that a simple detection of both lines constrains the gas temperature to better than 10%. However, solid measurements of the CGM continuum emission in the soft band are still impossible, even with the microcalorimeter spectral resolution. To constrain gas density and metallicity, one needs to detect the CGM emission at $E > 0.7$ keV.

All simulations in our suite show the expected X-ray emission from the CGM of the Milky Way-type galaxies at large radii to be very faint, certainly well below the *Chandra* and *XMM-Newton* limits. Its detection is challenging even for next-generation X-ray missions. The limiting factor is the low expected contrast of the CGM emission relative to the astrophysical and instrumental diffuse backgrounds, which leads to an unavoidable level of systematics. Based on the *Chandra* experience, the systematic uncertainties will be approximately 1% of the foreground/background in the corresponding energy band. In addition, imaging of the CGM at $E \gtrsim 0.7$ keV is severely affected, unless most of the cosmic X-ray background is resolved into discrete sources, for which arcsecond resolution is required (e.g., Figs. A.1 and A.2). Mock simulations of long exposures show that the residual background fluctuations from sources below the *Athena* confusion limit are at least a factor of 10 above the Poisson noise-dominated residual fluctuations for *Lynx*. Moreover, *Athena* mirrors will not be protected from stray light, which will introduce additional large-scale non-uniformities in the background. These two factors will introduce severe fundamental limitations on *Athena*'s ability to map diffuse gas in galactic halos and Cosmic Web filaments. In contrast, *Lynx* will be limited almost exclusively by statistical noise. Mapping the CGM can be accomplished with *Lynx* to at least half the virial radius in galaxies with mass as low as $\approx 3 \times 10^{12}\ M_\odot$. A sample of what *Lynx* can observe in galactic halos is shown in Fig. A.8.

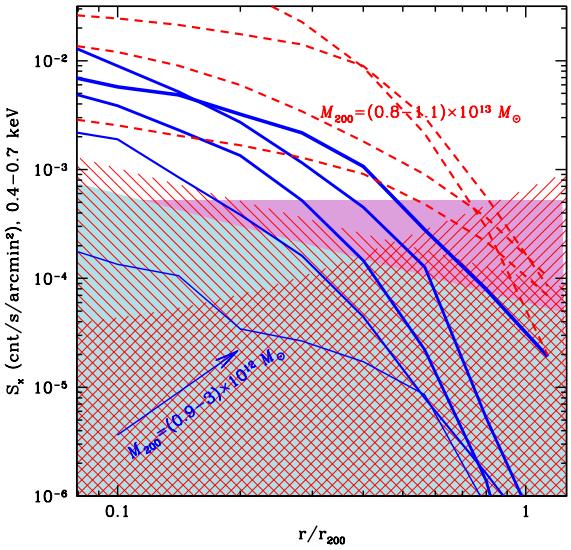

Fig. A.9— Surface brightness profiles of representative simulated galaxies in the 0.4–0.7 keV band, together with the estimated levels of statistical and systematic uncertainties. Solid blue corresponds to a 5 σ level of statistical fluctuations of the *Lynx* background. Solid purple corresponds to 3% of the background, indicative of the level of unavoidable systematics. Red hashed regions indicate uncertainties for *Athena*: residual surface brightness fluctuations (decreasing with radius) and stray light (increasing with radius).

Summary of mock observation analysis for CGM in emission — Figures A.9–A.11 show results from the mock data analysis of the CGM observations with *Lynx* and *Athena*, illustrating the following key findings:

- In the soft band, 0.4–0.7 keV, the sensitivity of *Lynx* and *Athena* is similar. For both observatories, the main limiting factor is low contrast of the observed signal relative to the unavoidable background dominated by the diffuse Milky Way emission.
- At $E > 0.7$, *Athena* is significantly less sensitive than *Lynx* because of the higher level of background fluctuations due to undetected or confused background sources. This sensitivity difference reaches an order of magnitude in the 1–1.5 keV band. *Athena* stray light is another important limiting factor for these studies.
- At 500 ksec, *Lynx* statistical uncertainties are similar to the level of unavoidable systematics. Therefore, the nominal soft-band effective area of 2 m^2 of the *Lynx* Design Reference Mission (§6) is a good configuration choice from the point of view of CGM studies.

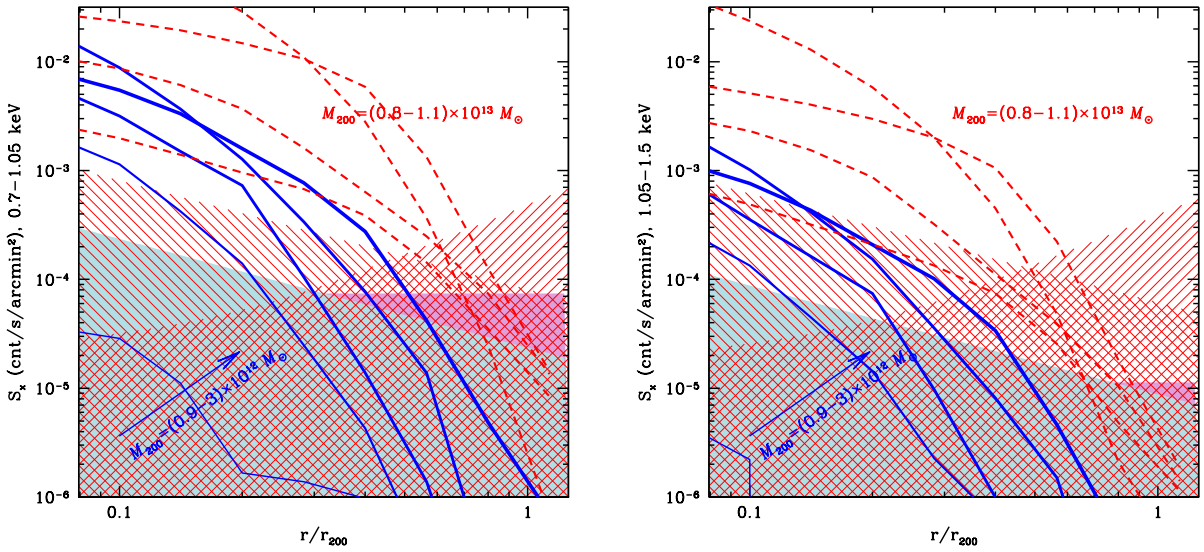

Fig. A.10— Same as Fig. A.9, but for the 0.7-1.05 keV and 1.05-1.5 keV bands (*left and right, respectively*).

- Overall, *Lynx* is capable of providing detailed information on the state of hot gas at half the virial radius for galaxies down to $\approx 3 \times 10^{12}\,M_\odot$. *Athena* is fully sensitive only for $M_{\rm tot} \gtrsim 8 \times 10^{12}\,M_\odot$ galaxies.

Absorption line studies of the CGM — Numerical simulations also enable assessment of how far down in the mass scale the hot CGM can be probed via absorption line studies. EAGLE simulations in particular provide spectral line profiles, including full thermal broadening and kinematic information. Examples of predicted absorption spectra for sight lines at the virial radius of $M_{\rm tot} = 10^{12}\,M_\odot$ galaxies are shown in Fig. A.8. Overall, the mock analysis shows that O VII absorption should be routinely detectable with the XGS in this regime; O VIII is also detectable in many cases. The O VIII/O VII flux ratio is a sensitive temperature diagnostic, so detection of both lines should constrain the CGM temperature rather well. This is an important characteristic of the CGM thermodynamic state, even though the gas density cannot be derived from the oxygen absorption lines.

The kinematic structure of O VII and O VIII is complex, but it can be characterized rather well in the stronger detection cases, opening a door to a new diagnostic of the hot CGM in L^* galaxies. Because of the complex, non-Gaussian structure of the line-of-sight velocity distribution, proper characterization of the lines requires a spectral resolving power at least matching the expected thermal width of the oxygen lines, $R \approx 5{,}000$.

To assess how many absorption line measurements of the CGM halos are possible with *Lynx*, the RASS-6dFGS catalog of bright AGN [648] was used as a representative sample of appropriate background sources. The probability of intercepting each sight line with a CGM absorption system at a given fraction of the virial radius depends on the AGN redshift and galaxy mass. The mass is relevant because it strongly affects the number density of galaxies (via the dark matter halo mass function, $dn/dM \sim M^{-2}$, for low M), and because the impact parameter scales with mass as $r \propto M^{1/3}$. Integrating the mass function [649] and folding in AGN redshifts and fluxes, a 5 Msec survey of 80 X-ray bright AGN should yield ~ 30 measurements of absorption line systems near the virial radius of galaxies with $M_{\rm tot} = 10^{12}\,M_\odot$, with data quality similar to that shown in Fig. A.8. Many more

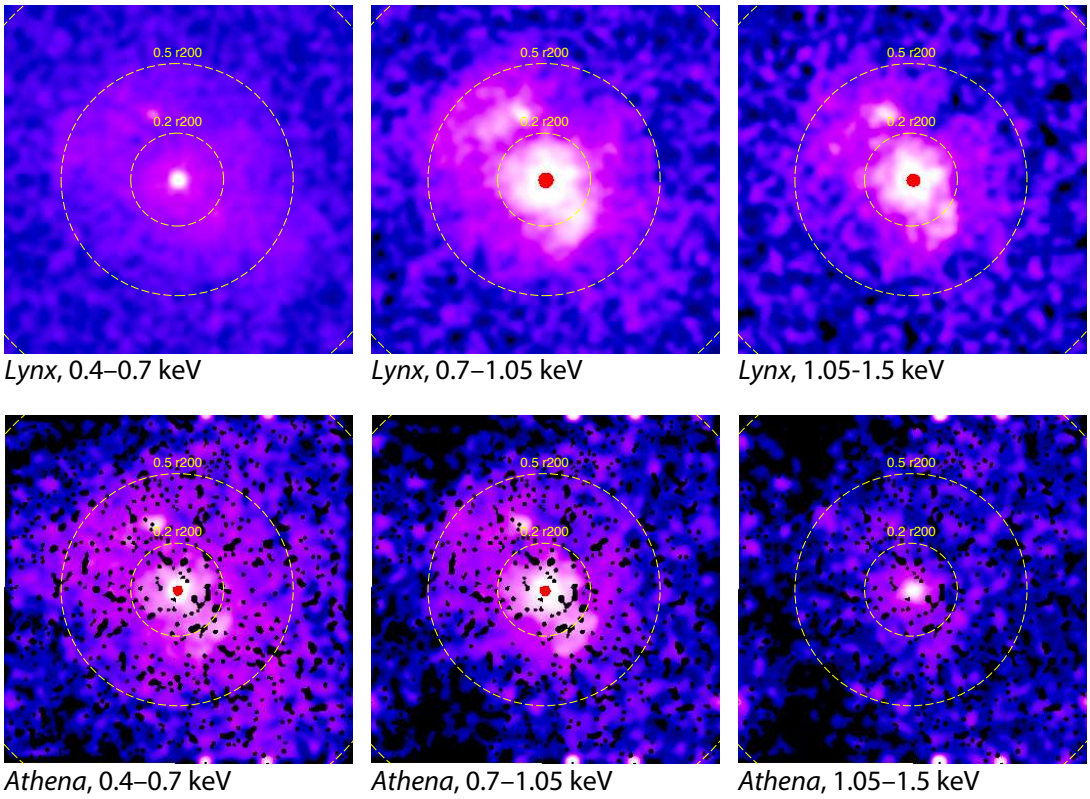

Fig. A.11— Simulated 500 ksec observation of an EAGLE galaxy with $M_{\rm tot} = 8 \times 10^{12}\, M_\odot$ with the *Lynx* HDXI *(top)* and *Athena* WFI *(bottom)* detectors. Each panel is 20 arcminute on a side. The color scale in all panels is normalized to the individual level of noise.

detections in the same sample of AGN are expected from higher-mass systems and from the Cosmic Web filaments [195]. Such a survey can be substantially optimized by measuring galaxy redshifts near the AGN sightlines in advance of the X-ray observations.

Detectability of Cosmic Web in emission — *Lynx*' ability to detect and remove discrete X-ray sources contributing to the cosmic X-ray background, and its low instrumental background (relative to astronomical signals), enable detection of extremely low surface brightness structures. This capability can be exploited for detection of hot gas in the Cosmic Web filaments converging on galaxy clusters. On the largest angular scales (appropriate for the mapping of the Cosmic Web), the limiting factor for *Lynx* will be systematic 1%-level background uncertainties, as shown in Figs. A.9–A.10. A possible observing scenario is to select a rich supercluster at $z \sim 0.1$ and survey a 10 deg^2 region around it with 100 ksec HDXI pointings. The point source sensitivity in each pointing will exceed that of the 7 Msec *Chandra* deep field, so the cosmic X-ray background will be nearly completely resolved into sources. Detectable surface brightness in the 0.7–1.5 keV band is only a few counts per 100 ksec per arcmin^2. Mock X-ray brightness maps derived from numerical simulations clipped to this limit show that *Lynx* will be capable of mapping the Cosmic Web in emission (see Fig. 4.7). Assuming a $\approx$ 1 Mpc line-of-sight depth appropriate for the expected size distribution of Cosmic Web filaments [401], the brightness limit can be converted to the corresponding gas density threshold. This estimate suggests that *Lynx* will be sensitive to structures with density contrasts of only $\rho/\langle\rho\rangle \approx 50$.

Only a minor fraction of the area in the survey concept described here will be covered by high surface-brightness regions of low-z galaxy clusters. The majority of the area will be suitable for, e.g., traditional AGN and distant galaxy cluster surveys, in addition to studies of the low-z Cosmic Web filaments. Such a survey is therefore multi-purpose and can constitute one of the *Lynx* "Legacy" fields (§4.4.1).

B. *Lynx* Trade Studies

The *Lynx* mission concept development depends upon quantitative and qualitative assessments and comparisons with respect to performance, cost, schedule, and risk of identified realistic alternatives to achieving the *Lynx* scientific goals. These trade studies are an integral part of the decision-making activities performed by the *Lynx* team throughout the course of this study.

This section outlines the mission-level, optics, science instrument, and spacecraft trade studies undertaken by the *Lynx* team in order to achieve the most acceptable technical solutions among viable alternatives. The purpose of this section is to document the trades undertaken as well as their outcomes to enable traceability. The following entries list the candidate choices, the selection criteria used, and the evaluation leading to the trade choice. References given point to the locations in the body of this report that are relevant to the given trade.

B.1 Mission-Level Trades

B.1.1 Configuration Architecture

Candidates:

- *Chandra*-like with spacecraft bus forward encircling *Lynx* Mirror Assembly (LMA), with mirror focused on a choice of focal plane cameras and insertable grating spectrometer (**SELECTED**)
- Distributed spacecraft bus components
- Simultaneous use of gratings and focal plane detectors via multiple mirror modules

Selection Criteria:

- Thermal control and stability
- Heritage
- Structural integrity and robustness for launch
- Assembly, Integration, and Test (AI&T) flow
- Efficiency of instrument use

Evaluation:

Grazing-incidence X-ray telescope payloads with two reflections will be somewhat longer than their focal lengths with mass distributed primarily at both ends of the optical bench. Thermal management favors the location of the spacecraft bus at the optics end of the optical bench. Therefore, like *Chandra*, the *Lynx* design places the spacecraft bus surrounding the LMA to ensure tight control of the mirror temperature and gradients. All previous high-resolution X-ray telescopes — namely *Einstein*, *ROSAT*, *XMM/Newton*, and *Chandra* — have used this configuration. Use of heritage gives confidence that the Observatory can be designed to meet structural and thermal requirements. The configuration allows the spacecraft to be developed, assembled, and tested independently of and in parallel to the optics and science instruments. Many scientific objectives do not require the use of simultaneous gratings or

multiple focal plane cameras. Therefore, a grating array fixed in the optical path or a secondary X-ray optics to simultaneously illuminate multiple instruments were rejected because they would significantly increase the time (decrease the efficiency) necessary to meet all the scientific objectives. This trade study was performed by the *Lynx* engineering team.

Reference: §6.4 Design of Spacecraft and Subsystems, Figure 6-4

B.1.2 Orbit

Candidates:

- Sun-Earth L2 (SE-L2) (SELECTED)
- High-Earth orbit, *Chandra*-like ellipse
- Drift-away orbit, Spitzer-like
- Lunar resonant, Transiting Exoplanet Survey Satellite- (TESS-) like
- Lunar Distant Retrograde Orbit (LDRO)
- Low-Earth Orbit (LEO)

Selection Criteria:

- Observing efficiency (must be capable of 85%)
- Lifetime (must not be limited to less than 20 years)
- Delta-V to achieve and maintain orbit (desired to be minimal)
- Radiation dose (desired to be minimal)
- Thermal environment (desired to be most stable)

Evaluation:

The LEO option did not meet efficiency requirements and was eliminated. Table B.1 shows the evaluation of the other candidates. "A" scored as 1.0, "B" as 0.75, and "C" as 0.5. The SE-L2 and TESS/lunar resonant were the top two candidates.

SE-L2 was chosen based on its smaller delta-V — which results in less mass for propellant and propellant tanks — and for the lack of eclipses, which results in simpler operations and a reduced number of batteries and lower battery mass. The *Lynx* engineering team performed the trade study, and the decision was made by the Science and Technology Definition Team (STDT).

Reference: §6.7.1 Launch to Orbit – Cruise, Commissioning, and Checkout

Table B.1. *Lynx* orbit trade.

	Total Score	Science Observing	Launch Vehicle	Delta-V	Duration	Thermal	Comm	Environment	Serviceability
Max Points	100	15	10	15	10	15	15	15	5
SE-L2	91	A	A	A	A	A	B	B	B
Drift-away	81	A	A	A	C	A	C	B	C
LDRO	84	A	A	C	A	B	A	B	B
CTO	73	B	B	B	A	C	A	C	C
TESS	86	A	A	B	A	B	A	B	C

B.1.3 Launch Vehicle

Candidates:
- Launch Services Program- (LSP-) defined heavy-class (SELECTED)
- Space Launch System (SLS)
- SLS co-manifested payload
- Intermediate-class (as defined by LSP)

Selection Criteria:
- Mass capability meets or exceeds *Lynx* Observatory estimate
- Fairing geometry meets or exceeds *Lynx* Observatory estimate

Evaluation:
While details of the Launch Vehicle (LV) fleet available at the time of *Lynx*'s anticipated launch is highly uncertain, total Observatory mass and geometry comparison to anticipated LV mass and fairing size capabilities are central to mission cost and payload architecture. A trade study assessing heavy-class, SLS (alone or as co-manifested payload), and intermediate-class LV options was performed by the *Lynx* engineering team in accordance with NASA's LSP and SLS program recommendations.

Given the mass and volume of the as-presented *Lynx* Observatory and the LSP-provided guidelines for payload mass to SE-L2 and payload volume for LVs in the 2030s, the *Lynx* study selected the "heavy-class" LV as the baseline for all structural, propulsion, and orbital mechanics design analyses.

The feasibility of launching the *Lynx* Observatory as a co-manifested payload on the SLS is also appealing, and design scenarios for meeting SLS co-manifested requirements have been considered as well. Launching as a co-manifested payload significantly reduces the cost of LV services (WBS 08), as the LV cost is assumed to be a "contributed" cost. However, as a co-manifested payload, launch availability is reduced, and propulsion requirements to SE-L2 are increased.

The LSP-provided mass to SE-L2 and payload volume of the "intermediate-class" launch vehicle for the 2030s is not sufficient to carry the as-presented *Lynx* Observatory. Although a larger *Lynx*-specific payload shroud could be designed for the intermediate-class vehicle and/or an Extended Optical Bench (EOB) could be designed to be compatible with the LSP-provided intermediate-class payload volume, significant payload mass reductions would be required to utilize this as-provided vehicle class.

Reference: §6.5 Launch Vehicle

B.2 Optics

B.2.1 *Lynx* Mirror Assembly Trade

Candidates:
- Silicon monocrystalline meta-shell (SELECTED)
- Slumped glass adjustable via piezoelectric elements
- Full-circumference shells

Selection Criteria:

- Optical performance must meet science requirements for area, energy range, and angular resolution over a defined Field of View (FOV)
- Highest technology readiness
- Best demonstrated performance
- Credibility of roadmap to reach required on-orbit performance
- Minimal mass and cost
- Credibility of cost estimate

Evaluation:

The *Lynx* STDT, recognizing that a credible and feasible path to maturing the LMA was crucial to a compelling and executable *Lynx* mission concept and—following deliberations within the *Lynx* Optics Working Group (OWG) and Study Office and corroborated by a *Lynx* Interim Report Red Team recommendation—commissioned a trade study in January 2018 to recommend a reference mirror design that demonstrates a technological path to realizing the science envisioned by the STDT. The trade study was specifically chartered to provide a recommendation for one Design Reference Mission (DRM) concept for the mirror assembly architecture to focus the design for the Final Report and identify any feasible alternates.

The *Lynx* Mirror Architecture Trade (LMAT) Working Group represented scientific and technical leadership across academia, NASA, and industry, including international participation. Using public evaluation criteria, this community working group conducted an open science, technical, and programmatic evaluation in a series of meetings from February through July of 2018. The team reached a broad consensus on the recommendation and the basis for the recommendation after amassing over 650 pages of documents and committing over 5,000 manhours of study and deliberations.

The study used the Kepner-Tregoe decision analysis method facilitated by Gary Blackwood of the Jet Propulsion Laboratory (JPL). The process began with agreeing on evaluation criteria and their weights (Figure B.1), followed by documenting descriptions of the technology options, evaluating these options against the criteria, reaching consensus on the evaluation, documenting potential risks and opportunities, and finally making a recommendation that accounted for these risks and opportunities. Leading evaluation criteria that drove the recommendation were the current and near-future demonstrated performance and technology development plans. Relative simplicity of mirror assembly production process and test as well as relative impact of technical accommodation to the spacecraft were also discriminating factors.

The LMAT recommended the Silicon Meta-shell Optics as the DRM concept mirror assembly architecture to focus the design for the Final Report. The Full Shell Optics and Adjustable Segmented Optics technologies were determined to be feasible alternates. The Silicon Meta-shell Optics technology was deemed the most mature with the shortest path to achieving Technology Readiness Level 5 (TRL 5) by Key Decision Point A (KDP-A) and TRL 6 by Preliminary Design Review (PDR). It uses the shortest mirrors, which leads to improved off-axis Point Spread Function (PSF) performance relative to the other designs, but also requires the largest quantity of mirror elements to be produced, aligned, and bonded, resulting in the longest estimated production schedule. Full Shell Optics, conversely, has potentially the shortest schedule (fewest mirror shells) but was deemed most challenging to produce very thin high-quality mirrors of large diameter. The Adjustable Segmented Optics design was determined

to have a short production and installation schedule due to the relaxed figure error tolerances afforded by adjustability, but the many steps in the process had yet to be demonstrated and the application of actuated control at the system level was deemed likely to adversely affect the A&IT schedule.

MUSTS										
	Science	Per definitions / analysis of SET								
M1	Optical performance will meet requirements flowing down from Science Trace Matrix					Y		Y		Y
	Technical	Per definitions / analysis of TET								
M2	Credible roadmap from today's status to predict flight on-orbit performance					Y		Y		Y
M3	Performance modeling tools related to current results are demonstrated to be credible					Y		Y		Y
M4	Repeatable fabrication process based on current status					Y		Y		Y
M5	Credible error budget					Y		Y		Y
M6	Expected to survive launch					Y		Y		Y
	Programmatic	Per definitions / analysis of PET								
M7	Show a credible plan to meet TRL 4-6					Y		Y		Y
M8	Produce the mirror assembly within the Program schedule allocation					Y		Y		Y
WANTS		***Key***	***Driving***	***Weights***						
	Technical	Per definitions / analysis of TET								
W1	Highest predicted technology readiness at Astro2020 by March 2020	K	D	12	7	small-significant	7	small-significant	10	BEST
W2	Relative demonstrated performance	K	D	12	4	**SIGN./VL**	4	**SIGN./VL**	10	BEST
W3	Relative credibility of roadmaps from today's status to predict flight on-orbit performance (reflected M2)	K	D	12	5	SIGN. DIFFERENCE	5	SIGN. DIFFERENCE	10	BEST
W4	Relative simplicity of mirror assembly production process and test	K	D	10	8	small difference	10	BEST	10	BEST
W11	Relative complexity and accuracy of ground calibration of mirror assembly	K	D	6	8	small difference	10	BEST	10	BEST
W13	Relative impact of technical accommodation (cost, mass,	K	D	10	8	small difference	5	SIGN. DIFFERENCE	10	BEST
	Technical Sub total					400		402		620
	Programmatic									
W12	Relative cost and credibility of grass-roots cost estimate of the mirror assembly through delivery	K		10	10	WASH	10	WASH	10	WASH
W18	Best assessment of the schedule to mirror assembly delivery (reflects M8)	K	D	6	8	small difference	10	BEST	8	small difference
	Programmatic Sub Total			100		148		160		148
	Final Total				548		562		768	SELECTED

Figure B.1. Kepner-Tregoe *Lynx* Mirror Assembly Trade study outcome. Evaluation criteria as determined by science, technology, and programmatics teams (SET, TET, and PET, respectively) were classified as Musts and Wants. The three technologies evaluated were (last three columns; left to right) Adjustable Segmented, Full Shell, and Silicon Meta-shell Optics. All three technologies met the Must criteria and were deemed feasible.

Reference: §6.3.1.1 LMA Design Overview, §7.2 Optics Development Overview

B.2.2 Other Optics Trades

B.2.2.1 High Energy Effective Area

Candidates:

- Primary configuration (SELECTED)
- Modification with extended capability for mirror effective area above 10 keV and to LXM for Quantum Efficiency (QE) at these energies, including potential use of multilayer optics coating

Selection Criteria:
- Science return for cost

Evaluation:
The possibility of enhancing *Lynx* science capabilities by extending the performance range to higher X-ray energies has been discussed by the STDT. This may be a Phase A trade to enable additional science beyond the current *Lynx* science requirements. The STDT carried out the science trade, while the LXM instrument lead estimated the cost impact to this instrument. No assessment was made of the cost or schedule impacts to the mirror development before this modification was tabled.

Reference: §6.3.4.1 LXM Design Overview

B.2.2.2 LMA Fabrication

Candidates: (CHOICE PENDING STUDIES TO BE COMPLETED)
- Number of parallel lines for each process step
- Degree of automation for each process line

Selection Criteria:
- Length of schedule
- Cost of production equipment
- Cost of labor
- Risk of schedule slip

Evaluation:
The manufacturability and production of the mirror components has been recognized as a risk, and a study to identify areas to reduce the overall development schedule and cost for this portion of the project will be performed by the *Lynx* study office. The trade has been undertaken by *Lynx* study office personnel, industry partners, and the Silicon Meta-Shell Optics technical lead.

Reference: §8.3 Risks and Risk Mitigation

B.3 Science Instruments—LXM

B.3.1 Pixel Array Types

Candidates:
- 1-arcsecond pixels, 5-×-5-arcmin FOV, 3 eV-resolution (SELECTED – MAIN ARRAY)
- 0.5-arcsecond pixels, 1-×-1-arcmin FOV, 2 eV resolution (SELECTED – ENHANCED MAIN ARRAY)
- 1-arcsecond pixels, 1-×-1-arcmin FOV, 0.3 eV resolution (SELECTED – ULTRA-HIGH-RESOLUTION ARRAY)
- 5-arcsecond pixels, 20-×-20-arcmin FOV, 1 eV resolution Extended Array
- 0.5-arcsecond pixels, 20-×-20-arcsecond FOV, 1.5 eV resolution High-Resolution Inner Array

Selection Criteria:
- Satisfy science objectives
- Minimal cost, risk, complexity

Evaluation:
Three-pixel array types (the Main Array, Enhanced Main Array, and Ultra-High-Resolution array) span the scientific needs of *Lynx*. The trades of various focal plane arrays and subarrays necessary to carry out *Lynx* science objectives was discussed by STDT, including a face-to-face meeting in January 2018 where it was decided that three of the original five array types are necessary to cover all the important *Lynx* science objectives while simplifying the demands on the instrument. The trade study was conducted by the Instrument Working Group in conjunction with the STDT.

Reference: §6.3.4 *Lynx* X-ray Microcalorimeter

B.4 Science Instruments—HDXI

B.4.1 Focal Plane Field of View

Candidates:
- 22-arcminute diameter (SELECTED)
- 46-arcminute diameter

Selection Criteria:
- Satisfy science requirements
- Minimize cost, complexity
- Minimize mass, power

Evaluation:
The LMA PSF degrades slowly with off-axis distance, but certain scientific enhancements may be possible if the High Definition X-ray Imager (HDXI) detector FOV extends beyond that needed to meet the *Lynx* grasp requirement for sub-arcsecond resolution. This trade was made by the STDT in consultation with the *Lynx* Instrument Working Group and their recommendations.

Reference: §6.3.2.1 HDXI Design Overview

B.4.2 Sensor Architecture (Phase A selection)

Candidates:
- Hybrid Complementary Metal-Oxide Semiconductor (CMOS)
- Monolithic CMOS
- Digital Charge-Coupled Device (CCD) with CMOS readout

Selection Criteria:
- Low-energy response
- High-energy response
- Readout noise and energy resolution

Evaluation:
Three technologies were identified by the *Lynx* Instrument Working Group as candidates for meeting the scientific requirements for the HDXI. These technologies differ primarily in their architecture, but not in their functionality; each has demonstrated proof of concept. At present, each of these technologies

individually meets some, but does not simultaneously meet all, of the *Lynx* HDXI requirements, and each is assessed at TRL 3 for *Lynx* by the most recent Physics of the Cosmos (PCOS) Technology Review Board. Each technology requires similar resources from the spacecraft, and all three have similar development paths. The development plan assumes, during the course of pre-Phase A activities, a downselection to two technologies will precede a final downselection prior to Phase A.

Reference: §6.3.2.1 HDXI Design Overview, §7.3.1 High-Definition X-ray Imager

B.5 Science Instruments—XGS

B.5.1 Gratings Architectures

Candidates:
- Critical-Angle Transmission (CAT) gratings (SELECTED)
- Off-Plane Gratings (OPG)

Selection Criteria:
- Meets science requirements per the *Lynx* STDT
- Evidence of a repeatable fabrication process
- Ease of accommodation in the Observatory
- Shows a clear instrument-level requirements flowdown to grating elements
- Launch survivability

Evaluation:
The two technologies identified by the *Lynx* Instrument Working Group both meet the required effective area, energy resolution and bandwidth requirements, and are acceptable grating architecture choices. A trade study following the Kepner-Tregoe process was conducted with evaluation criteria, weights, and scores developed through consensus. The X-ray Grating Spectrometer (XGS) technologies were evaluated on science and technology criteria (not cost or schedule). Both technologies were deemed feasible and capable of meeting science and technical requirements (both are currently at TRL 4). The CAT grating was deemed to require less alignment precision, less contamination control, and less stringent thermal control.

Reference: §6.3.3.1 XGS Design Overview, §7.3 Instrument Development Overview

B.6 Spacecraft

B.6.1 Star Camera

Candidates:
- Single camera, internally redundant (SELECTED)
- Dual co-aligned cameras
- Dual offset cameras

Selection Criteria:
- Serve for real-time pointing control

- Serve for ground aspect reconstruction
- Redundancy
- Minimum mass, power

Evaluation:
Dual-offset cameras give the best measurement of roll angle; however, the measurement accuracy required to reconstruct 0.5-arcsecond images means that a very small, 2-deg2 FOV allows enough lever arm to measure roll to the accuracy needed. Star cameras should be aligned with the X-ray telescope to obtain the best measurement of celestial location. Failure of the glass optical elements or of the structural support is non-credible. Therefore, only one co-aligned star tracker is necessary and sufficient.

Reference: §6.4.2 Guidance, Navigation, and Control

B.6.2 Pointing Stability

Candidates:
- Precision gyros and reaction wheels (SELECTED)
- Control moment gyros

Selection Criteria:
- Mass and cost
- Hold to 0.17 arcseconds per second stability
- Stay within 10 arcseconds of target
- Mission heritage

Evaluation:
Control moment gyros are very massive and expensive. They can give much greater stability than is required, since the Observatory counts each single X-ray photon and can reconstruct an image via post facto knowledge of where the telescope was pointing.

Reference: §6.4.2 Guidance, Navigation, and Control

B.6.3 Data Storage

Candidates:
- Consultative Committee for Space Data Systems- (CCSDS-) compliant packets (SELECTED)
- Fixed format (e.g., time division multiplexed)

Selection Criteria:
- Flexibility for variable data rates
- Contemporary standard

Evaluation:
Time-Division Multiplexing (TDM) forces a fixed maximum data rate and results in large blocks of "zeroes" telemetered for weak sources. CCSDS packets allow mission planning to interleave observations, resulting in counting rates requiring much higher-than-average telemetry balanced by low-rate observations.

Reference: §6.4.6 Command and Data Handling

B.6.4 Antenna

Candidates:
- Phased array (SELECTED)
- Gimbaled antenna

Selection Criteria:
- Power to support communication at SE-L2
- Impact on pointing

Evaluation:
Both antennas can provide needed db margin for communications. Phased array avoids vibrations from the use of gimbaled antenna.

Reference: §6.4.6 Command and Data Handling

B.6.5 Safe Mode Control

Candidates:
- Independent control processing electronics and firmware (SELECTED)
- Redundant computer

Selection Criteria:
- Robust against single failures
- Robust spacecraft safing while unknown anomalies are diagnosed
- Minimize hardware, complexity, mass, and power

Evaluation:
Redundant computers, which are included already to protect against computer hardware failure, are subject to single-point failure due to running the same software. Independent control processing electronics run different software, which is concentrated on fewer tasks just to stabilize the vehicle in power-positive configuration.

Reference: §6.4.5 Avionics and Flight Software

B.6.6 Observatory and OBA Thermal Control

Candidates:
- Active control, cold-biased with heaters (SELECTED)
- Passive control, heat pipes, and Multilayer Insulation (MLI)

Selection Criteria:
- Robust control at all pitch angles, 45° to 175°
- Maintain required thermal environment for possible 20-year mission

Evaluation:
Development of a detailed integrated thermal model of the Observatory, including the thermal control of the LMA and Optical Bench Assembly (OBA), was performed by a *Lynx* study office-industry

partnership. A separate OBA trade comparing passive and active thermal control options concluded that the use of heat pipes and MLI alone (a purely passive control system) could not maintain the required limit on gradients at all pitch angles due to the variation of the heat input to one side of the bench.

Reference: §6.4.4 Thermal

B.6.7 Thermal Coverings

Candidates:
- Ag-Teflon MLI, with offset Si-coated Kapton shield (SELECTED)
- Second-surface quartz mirrors (Optical Solar Reflectors)
- Si-Kapton MLI
- Ag-Teflon MLI

Selection Criteria:
- Stability over 20 years in L2 environment
- Low value of absorptance: 0.1 to 0.3, low α/ε ratio.
- Low mass

Evaluation:
Quartz mirrors were eliminated as a significant mass penalty. Ag-Teflon was eliminated due to the significant increase in α to values >0.5. Si-coated Kapton is relatively stable, but starts with α>0.3 andα/ε >0.5. Ag-Teflon shielded by Si-coated Kapton provides the desired thermal environment and stability.

Reference: §6.4.4 Thermal

B.6.8 Communications Trade

Candidates:
- Ka-band (SELECTED for telemetry downlink
- X-band (SELECTED for command uplink and status downlink
- S-band
- Optical

Selection Criteria:
- Conservatively meet *Lynx* data volume and data rate estimates
- High flight heritage; low obsolescence risk

Evaluation:
A trade study performed by the *Lynx* engineering team, with guidance from NASA/Space Communications and Navigation (SCaN) experts on future Deep Space Network (DSN) communications capabilities, was concluded and reported in April 2017. *Lynx* bandwidth requirements do not require capabilities beyond the data rates provided by Ka-band. Ka-band for data return (downlink) and X-band for low-rate command uplink and status downlink were selected for *Lynx*. Optical (laser) communications TRL was deemed too low to use in the design but is a promising technology that may be considered for future analysis.

Technology for long-distance space-based laser communications was demonstrated in NASA's 2013 Lunar Laser Communication Demonstration (LLCD), the space terminal which flew on the Lunar Atmosphere and Dust Environment Explorer (LADEE) spacecraft. Using a (gimballed) 10-cm satellite-based telescope (which is the analog of an antenna in the optical regime), a 0.5-W laser transmitter, and a ground station comprised of four 40-cm telescopes, LLCD demonstrated error-free data transmission at a rate of 622 Mbps from lunar orbit.

In the near future, NASA plans two more laser communications demonstrations, and, on the timescale of *Lynx*, laser communications would be a feasible option. Moreover, with its orbit about SE-L2, unlike missions to the Moon or Mars, *Lynx* would always be viewed in the nighttime sky, significantly reducing demands on the ground station in terms of thermal loading from the Sun and noise introduced by the sky brightness.

From the science perspective, there are two complementary benefits to considering higher data rates. First, the same volume of data could be downlinked in a much shorter time. Feasible data rates could be 5× or higher than the current baseline, enabling additional time for science observations. Alternately, larger volumes of data could be downlinked in the same amount of time. Doing so could enable new observational possibilities, particularly in the time domain. Table B.2 summarizes the *Lynx* radio frequency-based baseline telecommunications, LLCD, the two near-term NASA laser communications demonstrations, and an illustrative extrapolation to the SE-L2 distance of *Lynx*. The illustrative *Lynx* with laser communications is not meant to suggest a specific implementation (as there is ample trade space to consider), but only illustrate that much higher data rates could be achieved for *Lynx*.

Table B.2. Comparison of the *Lynx* baseline telecommunications, near-term NASA laser communications, and an illustrative *Lynx* case.

System	Data Rate (Mbps)	Range (x106 km)	Flight Terminal Aperture (cm)	Transmitter Power (W)	Ground Station
Lynx baseline Ka-band radio	22	1.5	N/A	N/A	DSN 34 m antenna
LLCD	620	0.5	10	1	0.8 m telescope
Optical to Orion (O2O)[1]	80	0.5	10	1	0.4 m telescope
Deep Space Optical Communications (DSOC)[2]	20	150	22	4	5 m telescope
Illustrative *Lynx* w/Laser Communications	32,000	1.5	22	4	2 m telescope

[1] O2O system is scheduled to be included on the Orion crew capsule of Exploration Mission-2 (EM-2), with a planned launch in 2022. It will have an architecture similar to LLCD, but will use more commercially built subsystems, notably the space modem and the ground detectors. Because the Orion data transmission requirements (80 Mbps) are lower than those for the LLCD, only a single 40-cm ground telescope is planned.
[2] DSOC system is manifested on the Psyche Discovery mission, with a planned launch in 2022. The requirements include demonstrating laser communications over ranges comparable to the distance to Mars, but, as an illustration of capability, DSOC will provide approximately 10 Mbps at ranges of 1 au.

Reference: §6.4.6 Command and Data Handling

B.6.9 Orbital Insertion

Candidates:
- Parking orbit (SELECTED)
- Direct insertion

Selection Criteria:
- Launch window flexibility
- Maximal payload mass

Evaluation:
A direct insertion allows for greater payload mass at the expense of fewer launch opportunities and shorter launch windows. A circular parking orbit allows more flexibility in targeting the outgoing transfer trajectory. Analysis showed a modest mass increase of 2%–3% in payload mass was possible (but not guaranteed) by direct insertion and that the performance may not increase due to range safety considerations. Direct ascent maneuvering designed to expand the launch window could further decrease performance, and the direct injection burns could exceed the burn-time limit of the engines. The parking orbit was chosen because the modest possible increase in mass from the direct ascent was outweighed by the flexibility of the parking orbit. The trade study was performed by the *Lynx* engineering team with consultation with the NASA LSP.

Reference: §6.4.1 Propulsion

B.6.10 Optical Bench Assembly

Candidates:
- Fixed optical bench (SELECTED)
- Extendable optical bench

Selection Criteria:
- Launch vehicle fairing accommodation
- Structural stability
- Stable length. Sensitivity to thermal changes.
- Minimal mechanisms and risk

Evaluation:
The OBA is a precision metering system with tight tolerances. Epoxy fiber composites can be laid out to have very small coefficients of thermal expansion, allowing excursion of several degrees Celsius to still be within the mirror assembly depth of focus. However, depending upon LV fairing constraints, the 10-m focal length *Lynx* payload may need to be accommodated using a one-time extendable (rather than fixed-length) OBA. Consideration of an extendable bench may facilitate LV flexibility with modest impacts on mass and cost. Due to a lowered center of gravity when stowed, the payload will experience reduced launch loads with the EOB. To a first order, the EOB option was considered feasible; however, further detailed analysis with the engineering team and industry partners is required to fully assess this option. Conversely, a fixed OBA eliminates the extra mechanism and deployment operation that would be required by an EOB. Additional mechanisms and deployments add risk.

Reference: §6.3.6 Optical Bench Assembly, §6.5 Launch Vehicle

B.6.11 Placement of Optical Axis on Selected Instrument

Candidates:
- Moveable focal plane assembly (SELECTED)
- Moveable mirror

Selection Criteria:
- Precision of locating the optical axis on the focal plane camera
- Mass and complexity of required mechanisms.
- Thermal control and stability of mirror on-orbit
- Structural integrity and mass distribution
- Ground calibration and verification

Evaluation:
An early appraisal of the distribution of mass within the *Lynx* Observatory indicated that, similar to *Chandra*, structural integrity would be maintained within reasonable mass budgets for a moveable instrument platform. Qualified mechanisms and motors could implement either choice. Ground verification of the moveable mirror positioning accuracy and the integrity of the optics in all required positions were considered a risk in view of gravity effects. Thermal control and stability were considered to be more tractable if the mirror maintains an identical configuration with respect to its surroundings. In view of the precision required to achieve sub-arcsecond angular resolution, a translating table affixed to the Integrated Science Instrument Module (ISIM) is baselined by the *Lynx* engineering team and associated instrument teams.

Reference: §6.3.5 Integrated Science Instrument Module

C. *Lynx* Model-Based Systems Engineering

The *Lynx* team plans to follow well-established systems engineering policies and processes and will implement them using state-of-the-art tools and methodology. The team has started implementing those new tools during the *Lynx* Study Phase.

The *Lynx* Study Office has partnered with the University of Alabama in Huntsville on the development of the Model-Based Systems Engineering (MBSE) tool for the *Lynx* X-ray Observatory. The objectives of the *Lynx* Observatory model during the Study Phase are to provide requirement traceability framework for the identification of relationships between science and mission goals to engineering design decisions, model the WBS, and identify the logical interfaces between the physical elements.

As the *Lynx* project advances into pre-Phase A, the *Lynx* model will expand to include all applicable systems engineering products and tasks such as formal system requirements, requirements logical decomposition and allocation to lower level elements, error budgets and analysis results showing current calculations and margins to those budgets, traceability, interface management, configuration management, define and track Measures of Effectiveness (MOEs), Measures of Performance (MOPs), and Technical Performance Measures (TPMs) as appropriate and will link these systems engineering products to design solutions. This allows rapid and efficient technical management, assessment, and decision analysis as the design matures. As the *Lynx* project moves into the verification and validation phase, the *Lynx* model will be used to track compliance to requirements to ensure that the Observatory will be able to fully enable science goals.

The systems engineering processes performed by the model are illustrated using Systems Modeling Language (SysML) diagrams. The Study Phase requirements traceability diagrams show the relationship between the three types of requirements identified: science traceability, mission traceability, and Ground Rules and Assumptions (GR&A). A freeform diagram captures the schema for the traceability from science goals to the GR&A. Bridge requirements were created to help narrow the gap in the relationship between GR&A with their respective mission traces. These requirements are written in the form of a "shall statement" and provide clarity as to how a specific GR&A can trace to a broader mission capability. Stereotypes were created and are used on all requirements to differentiate between the three types. Lastly, a generic table was generated to illustrate the trace between a requirement and all of its associated requirements. Other generic tables capture GR&A without a trace relationship to the mission traceability requirements for visibility of traceability for the systems engineering team.

All of the WBS elements were modeled as blocks, and their associated hierarchical decomposition is illustrated on multiple Block Definition Diagrams (BDDs). The *Lynx* WBS is composed of the organizational tasks as well as the end product hardware. The MBSE tool enables the visualization of the structural hierarchy of the elements and allows for the identification of interfaces among the elements illustrated in an Internal Block Diagram (IBD). Item flows such as data being passed or how the path power is distributed among the subsystems are just a few examples that are visually enabled by IBDs. MBSE usage in the *Lynx* project facilitates the communication between members of the team by the visual presentation of data that is dynamically presented from various views versus document based-exchange.

An online demonstration of the *Lynx* MBSE model can be accessed via the link below.

https://drive.google.com/drive/folders/1Xr_G1Kv8ZgW1MvEDQG84ZGtSJiyFq5OO?usp=sharing

1. Highlight all folders/files.
2. Right-click.
3. Select Download All (the download may take some time).
4. Once downloaded to your computer, unzip the file.
5. Enter the folder and open *Lynx*HTML

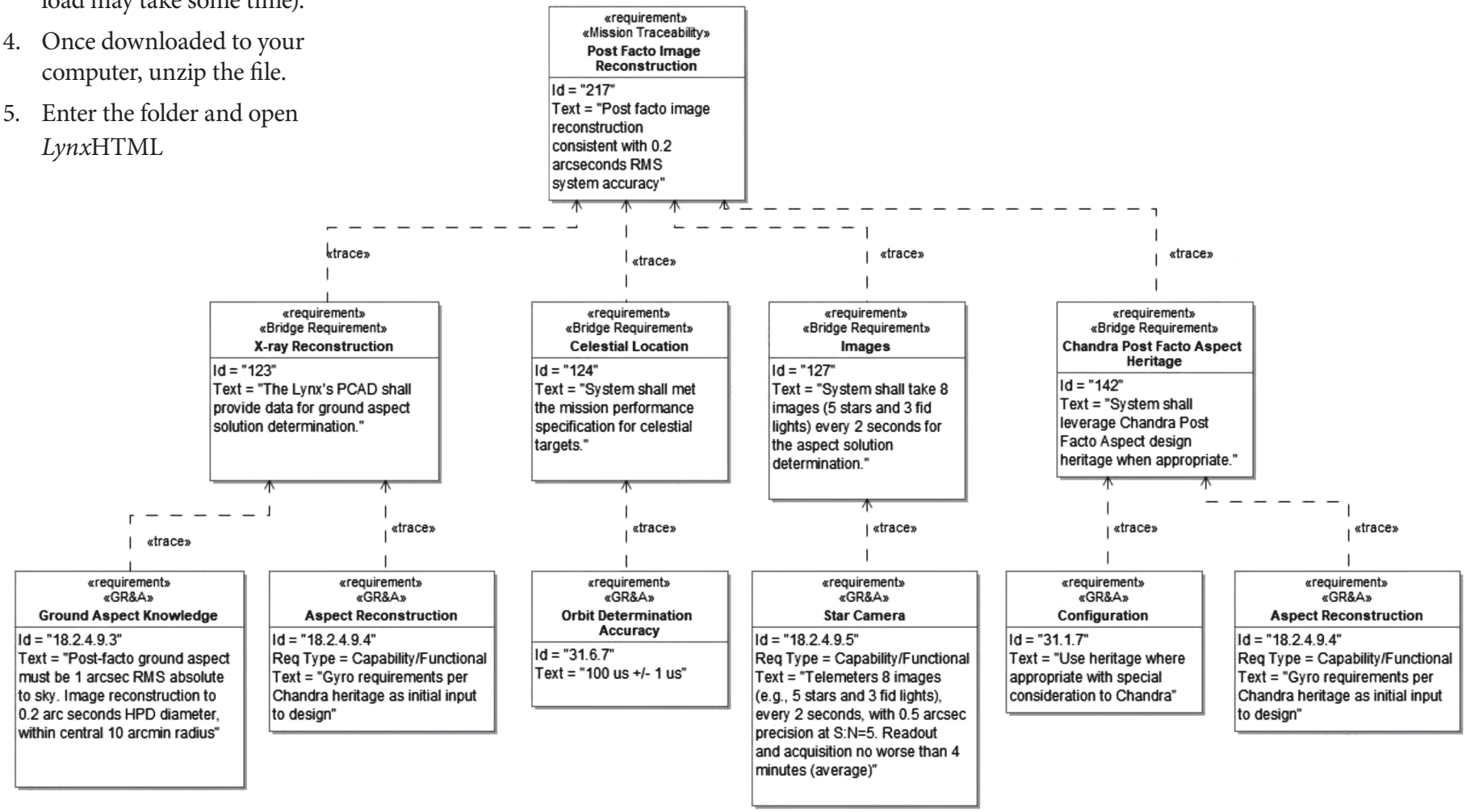

Figure C.1. Requirement trace example from *Lynx* MBSE tool.

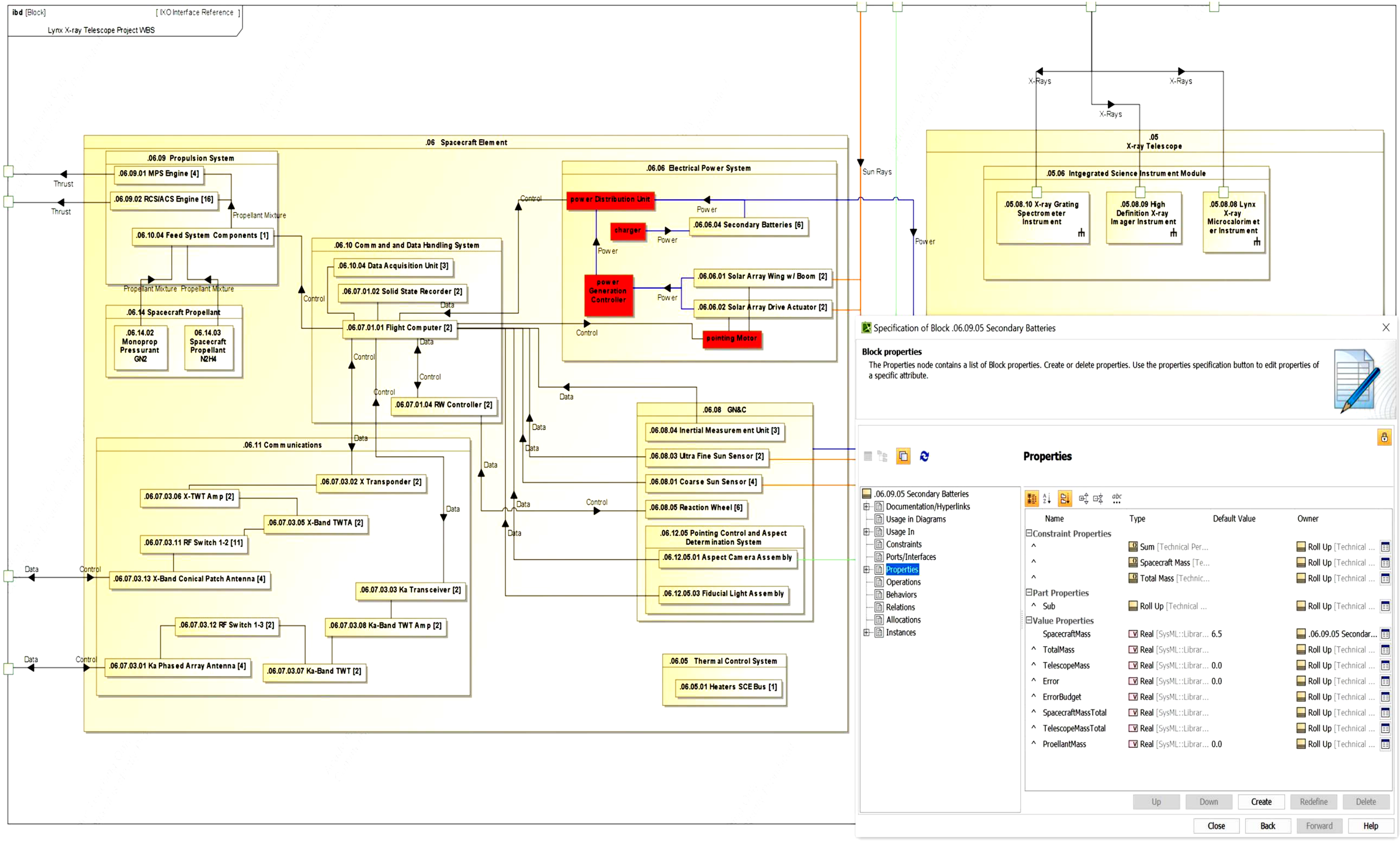

Figure C.2. Diagram from the *Lynx* MBSE tool showing IBD and the ability to display engineering data for each element in the diagram (example mass from the MEL).

D. Master Equipment List/Power Equipment List

Table D.1. *Lynx* Master Equipment List for the DRM.

WBS1	WBS1 Desc	WBS2	WBS2 Desc	WBS3 Desc	WBS5	WBS5 Desc	Basic Mass (kg)	MGA (kg)	Predicted Mass (kg)	TRL	Example Model, Manufacturer, and Part No. if available
09	X-ray Telescope (XRT)	05.06	*Lynx* Mirror Assembly (LMA)	X-ray Mirror Modules	05.06.07.04	X-ray Mirror Modules Optical Elements (segments, modules)	888.92	222.23	1,111.15		
					05.06.07.05	X-ray Mirror Modules Meta-Shell Forward / Aft Ring Structure	59.19	14.80	73.99		
					05.06.07.06	X-ray Mirror Modules Spider Structure	308.00	77.00	385.00		
				LMA Thermal Control	05.06.08.01	LMA MLI	3.42	0.68	4.11	9	
					05.06.08.02.01	LMA Pre-Collimator Assembly	118.82	29.71	148.53		
					05.06.08.02.02	LMA Post-Collimator Assembly	182.84	45.71	228.55		
					05.06.08.03	Spider Heaters	20.00	4.00	24.00	9	
				LMA Contamination Control Door Assemblies	05.06.09.01.01	FCD Structure	21.34	5.34	26.68		
					05.06.09.01.02	FCD Motor	15.40	3.85	19.25	9	Moog Type 7 Rotary Actuators
					05.06.09.01.03	FCD Motor Mount	12.00	3.00	15.00		
					05.06.09.01.04	Forward Door Hold Down Mechanisms (Launch Locks)	4.20	1.26	5.46	9	NEA Model 9106B
					05.06.09.02.01	Aft Contamination Door (ACD) Structure	21.60	5.40	27.00		
					05.06.09.02.02	ACD Motor	15.40	4.62	20.02	9	Moog Type 7 Rotary Actuators
					05.06.09.02.03	ACD Motor Mount	12.00	3.00	15.00		
					05.06.09.02.04	Aft Door Hold Down Mechanisms (Launch Locks)	4.20	1.26	5.46	9	NEA Model 9106B
				LMA Barrel Assembly	05.06.10.01	Barrel Structure	163.30	40.83	204.13		
					05.06.10.02	Subsystem Ring	28.67	7.17	35.84		
					05.06.10.03	LMA Flexures	2.20	0.55	2.75		
		05.06 Total					**1,881.51**	**470.40**	**2,351.90**		
		05.07	X-ray Gratings Array (XGA)	XGA Elements (gratings, facets)	05.07.06	XGA Elements (gratings, facets)	15.23	3.81	19.04		
				XGA Grating Array Structure (GAS)	05.07.07	XGA Grating Array Structure (GAS)	22.28	5.57	27.85		
				Grating Array Motor	05.07.08	Grating Array Motor	15.40	4.62	20.02	9	Moog Type 7 Rotary Actuators
				Grating Array Motor Mount	05.07.09	Grating Array Motor Mount	12.00	3.00	15.00		
				Gratings Array Structure Hold Down Mechanisms (Launch Locks)	05.07.10	Gratings Array Structure Hold Down Mechanisms (Launch Locks)	4.20	1.26	5.46	9	NEA Model 9106B
		05.07 Total					**69.11**	**18.26**	**87.36**		
		05.08	Optical Bench Assembly (OBA)	Magnetic Broom	05.08.05	Magnetic Broom	28.00	7.00	35.00		
				OBA TCS	05.08.06.01	OBA Heaters	50.00	10.00	60.00	9	
					05.08.06.02	OBA MLI	71.27	14.25	85.53	9	
					05.08.06.03	OBA OSR Support Structure	-	-	-	TBD	
					05.08.06.04	Observatory Sunshade	44.40	22.20	66.60	5	
				OBA Structure	05.08.07	OBA Structure	407.84	101.96	509.80		
		05.08 Total					**601.51**	**155.41**	**756.93**		
		05.09	Integrated Science Instrument Module (ISIM)	ISIM TCS	05.09.06.01	TTA Heaters	2.22	0.44	2.67	9	
					05.09.06.02	ISIM Heaters	8.76	1.75	10.51	9	
					05.09.06.03	TTA MLI	5.06	1.01	6.08	9	
					05.09.06.04	ISIM MLI	19.96	3.99	23.95	9	
					05.09.06.05	Radiator, LXM Cryostat	5.33	1.07	6.39	4 (TRL 9 are available)	
					05.09.06.06	Radiator, LXM Cryocooler	2.32	0.46	2.78	4 (TRL 9 are available)	
					05.09.06.07	Radiator, LXM Electronics 1	10.91	2.18	13.09	4 (TRL 9 are available)	
					05.09.06.08	Radiator, LXM Electronics 2	12.57	2.51	15.09	4 (TRL 9 are available)	
					05.09.06.09	Radiator, HDXI Detector Assembly	7.82	1.56	9.39	4 (TRL 9 are available)	
					05.09.06.10	Radiator, HDXI DEU	2.78	0.56	3.34	4 (TRL 9 are available)	
					05.09.06.11	Radiator, XGD Assembly	5.73	1.15	6.88	4 (TRL 9 are available)	
					05.09.06.12	Radiator, XGD DEU	2.31	0.46	2.77	4 (TRL 9 are available)	
					05.09.06.13	Radiator, Mounting Plate XGD	11.52	2.30	13.82	9	
					05.09.06.14	Subsystem Cold Plates and Survival Heaters	64.33	12.87	77.20	9	

Table D 1. *Continued*

WBS1	WBS1 Desc	WBS2	WBS2 Desc	WBS3 Desc	WBS5	WBS5 Desc	Basic Mass (kg)	MGA (kg)	Predicted Mass (kg)	TRL	Example Model, Manufacturer, and Part No. if available
				ISIM Structural System	05.09.07.01	ISIM Box	98.07	24.52	122.59		
					05.09.07.02	Translation Table Assembly (TTA)	75.26	18.82	94.08		
					05.09.07.02.02	LXM Struts	5.06	1.27	6.33		
					05.09.07.02.03	LXM Strut Fittings	4.95	1.24	6.19		
					05.09.07.02.04	Translation Table Hold Down Mechanisms (Launch Locks)	1.02	0.31	1.33	9	
					05.09.07.03.01	Horizontal TTA mechanisms	129.00	38.70	167.70		
					05.09.07.03.02	Vertical TTA Mechanisms	19.80	5.94	25.74		
					05.09.07.04	Mounting Plate XGD	58.65	14.66	73.31		
					05.09.07.05	XGD Fine Focus Motor w/ Tilt Offset	7.00	2.10	9.10		
					05.09.07.01	ISIM Box	98.07	24.52	122.59		
				Lynx X-ray Microcalorimeter (LXM) Instrument	05.09.08.05	LXM Electronics System (includes avionics)	145.94	36.48	182.42		
					05.09.08.07	LXM Thermal Control System (heat pipes)	72.00	18.00	90.00		
					05.09.08.08	LXM Miscellaneous Hardware (includes GSE stays)	24.13	6.03	30.16		
					05.09.08.09	LXM Harnesses	33.78	8.44	42.22		
					05.09.08.10	LXM Instrument Deck Assembly	28.34	7.09	35.43		
					05.09.08.11	LXM Dewar Assembly	163.75	40.94	204.69		
				High Definition X-ray Imager (HDXI) Instrument	05.09.09.07	HDXI Thermal Interface Material	0.25	0.06	0.31		
					05.09.09.08	HDXI Miscellaneous Hardware	3.81	1.14	4.95		
					05.09.09.09	HDXI Harnesses	9.70	3.01	12.70		
					05.09.09.10	HDXI Detector Assembly (DA)	51.60	16.00	67.60		
					05.09.09.11	HDXI Detector Electronics Unit (DEU)	15.02	3.30	18.32		
				X-ray Gratings Detector (XGD) Instrument	05.09.10.07	XGD Assembly	19.24	5.19	24.43		
					05.09.10.08	XGD Detector Electronics Unit (DEU)	38.77	8.14	46.91		
		05.09 Total					**1,166.76**	**293.70**	**1,460.47**		
05 Total							**3,718.89**	**937.77**	**4,656.66**		
06	Spacecraft Element (SCE)	06.07	SCE Structural System	Spacecraft Bus	06.07.01	Spacecraft Bus	361.84	90.46	452.30		
				Interface Struts (OBA/Bus/LMA)	06.07.02.01	Struts	94.34	23.59	117.93		
					06.07.02.02	Strut Fittings	27.48	6.87	34.35		
				Secondary Structures	06.07.03	Secondary Structures	238.78	59.70	298.48		
				Sunshade Door Assembly (SDA)	06.07.04.01	Sunshade Door	32.95	8.24	41.19		
		06.07 Total					**755.40**	**188.85**	**944.24**		
		06.08	SCE Thermal Control System	Heaters, SCE Bus	06.08.01	Heaters, SCE Bus	36.11	7.22	43.33	9	
				Multilayer Insulation (MLI), SCE Bus	06.08.02	Multilayer Insulation (MLI), SCE Bus	44.74	8.95	53.68	9	
				Radiator SCE Bus	06.08.03	Radiator SCE Bus	78.90	15.78	94.68	4 (TRL 9 are available)	
				SSD MLI	06.08.04	SSD MLI	13.73	2.75	16.47	9	
				Heaters, Propulsion Tanks	06.08.05	Heaters, Propulsion Tanks	0.50	0.10	0.60	9	
				MLI, Propulsion Tanks	06.08.06	MLI, Propulsion Tanks	2.50	0.50	3.00	9	
		06.08 Total					**176.47**	**35.29**	**211.76**		
		06.09	SCE Electrical Power System (EPS)	Solar Array Wing (with Boom)	06.09.01	Solar Array Wing (with Boom)	109.00	27.25	136.25	9	
				Solar Array Drive Actuator	06.09.02	Solar Array Drive Actuator	10.00	2.50	12.50	9	
				Integrated Power Electronics	06.09.03	Integrated Power Electronics	59.00	14.75	73.75		
				Secondary Distribution	06.09.04	Secondary Distribution	10.40	2.60	13.00		
				Secondary Batteries	06.09.05	Secondary Batteries	39.00	9.75	48.75		
				Cabling	06.09.06	Cabling	137.00	68.50	205.50		
				Solar Array Deployment Mechanism	06.09.07	Solar Array Deployment Mechanism	10.40	2.60	13.00	9	
		06.09 Total					**374.80**	**127.95**	**502.75**		

Table D 1. *Continued*

WBS1	WBS1 Desc	WBS2	WBS2 Desc	WBS3 Desc	WBS5	WBS5 Desc	Basic Mass (kg)	MGA (kg)	Predicted Mass (kg)	TRL	Example Model, Manufacturer, and Part No. if available
		06.10	SCE Command and Data Handling (C&DH) System	Flight Computer	06.10.01	Flight Computer	22.00	1.10	23.10	8	JPL, Uses BAE Systems RAD750 SBC
				Safe Mode Electronics Unit	06.10.02	Safe Mode Electronics Unit	17.80	2.67	20.47	6	TBD/Custom
				Solid State Recorder	06.10.03	Solid State Recorder	14.00	0.42	14.42	9	EADS Astrium CORECI
				Data Acquisition Unit	06.10.04	Data Acquisition Unit	9.54	0.48	10.02	9	L3 Cincinnati Electronics, DTP-503 Telepak
				MPS Controller	06.10.05	MPS Controller	14.00	2.10	16.10	6	TBD/Custom
				RCS Controller	06.10.06	RCS Controller	14.00	2.10	16.10	6	TBD/Custom
				RW Controller	06.10.07	RW Controller	14.00	2.10	16.10	6	TBD/Custom
				LMA Heater Controller	06.10.08	LMA Heater Controller	23.00	3.45	26.45	6	TBD/Custom
				SC/OBA/ISIM Heater Controller	06.10.09	SC/OBA/ISIM Heater Controller	19.00	2.85	21.85	6	TBD/Custom
				Avionics / Propulsion Heater Controller	06.10.10	Avionics / Propulsion Heater Controller	24.00	3.60	27.60	6	TBD/Custom
				Translation Table Controller	06.10.11	Translation Table Controller	4.00	1.00	5.00	6	PI USA, C-884.6DC
				Doors/Gratings Controller	06.10.12	Doors/Gratings Controller	10.00	1.50	11.50	8	MOOG/Broad Reach
				Instrumentation and Monitoring	06.10.13	Instrumentation and Monitoring	47.30	11.83	59.13	9	Assortment of sensors, temp, press, strain, etc.
				Avionics Cabling	06.10.14	Avionics Cabling	30.00	7.50	37.50	6	TBD/Custom
				Heater and Temp Sensor Cabling	06.10.15	Heater and Temp Sensor Cabling	105.60	26.40	132.00	6	TBD/Custom
		06.10 Total					**368.24**	**69.09**	**437.33**		
		06.11	SCE Communications	Ka Phased Array Antenna	06.11.01	Ka Phased Array Antenna	10.92	2.18	13.10	8	Messenger X-band MER
				X Transponder	06.11.02	X Transponder	6.40	0.19	6.59	9	General Dynamics SDST
				Ka Transceiver	06.11.03	Ka Transceiver	38.40	1.92	40.32	8	Harris Ka-band SDR
				Ka Diplexer	06.11.04	Ka Diplexer	2.00	0.40	2.40	8	Custom Microwave Inc.
				X-Band TWTA	06.11.05	X-Band TWTA	4.00	0.20	4.20	9	Thales, TH4604C
				X-TWT Amp	06.11.06	X-TWT Amp	5.00	0.25	5.25	8	Thales
				Ka-Band TWT	06.11.07	Ka-Band TWT	4.00	0.20	4.20	9	Thales, TH4626C
				Ka-Band TWT Amp	06.11.08	Ka-Band TWT Amp	5.00	0.25	5.25	8	Thales
				Waveguides	06.11.09	Waveguides	5.10	1.02	6.12	6	TBD/Custom
				RF Combiner	06.11.10	RF Combiner	1.20	0.12	1.32	6	TBD/Custom
				RF Switch 1-2	06.11.11	RF Switch 1-2	6.60	0.66	7.26	8	L3 SW-509 MER
				RF Switch 1-3	06.11.12	RF Switch 1-3	1.20	0.12	1.32	8	L3 SW-509 MER
				X-Band Conical Patch Antenna	06.11.13	X-Band Conical Patch Antenna	2.00	0.20	2.20	6	S-band Surrey MER
				X-Band MGA Array	06.11.14	X-Band MGA Array	0.25	0.05	0.30	8	L3 Narda 640,WR90
				Coax Cabling, Misc	06.11.15	Coax Cabling, Misc	11.00	1.65	12.65	6	TBD/Custom
		06.11 Total					**103.07**	**9.42**	**112.49**		
		06.12	SCE Guidance, Navigation and Control (GN&C) System	Coarse Sun Sensor	06.12.01	Coarse Sun Sensor	0.40	0.06	0.46	9	Adcole Course Sun Sensor
				Ultra Fine Sun Sensor	06.12.02	Ultra Fine Sun Sensor	4.00	0.60	4.60	9	Adcole Fine Sun Sensor
				Inertial Measurement Unit	06.12.03	Inertial Measurement Unit	13.50	2.03	15.53	9	Honeywell, Miniature Inertial Measurement Unit (MIMU)
				Reaction Wheel System	06.12.04.01	Reaction Wheels	45.60	6.84	52.44	9	Rockwell Collins, TELDIX RDR 68-3
					06.12.04.02	Reaction Wheel Drive Electronics	7.50	1.13	8.63	9	Rockwell Collins, TELDIX RDR 68-3
					06.12.04.03	Reaction Wheel Isolation System	24.00	3.60	27.60	9	Rockwell Collins, TELDIX RDR 68-3
				Pointing Control and Aspect Determination (PCAD) System	06.12.05.01	Aspect Camera Assembly	42.20	10.55	52.75	9	Ball, CT-601 High Accuracy Star Tracker
					06.12.05.02	Periscope	8.00	1.20	9.20	9	Ball
					06.12.05.03.01	Fiducial Light	0.60	0.09	0.69	9	Ball
					06.12.05.03.02	Fiducial Light Controller Assembly	2.90	0.44	3.34	9	Ball
				Star Tracker System	06.12.06.01	Star Tracker Camera Head (DTU micro ASC)	1.50	0.23	1.73	9	Danish Technical University (DTU)
					06.12.06.02	Star Tracker Double Data Processing Unit (DPU) (Internally Redundant)	1.12	0.17	1.29	9	Danish Technical University (DTU)
		06.12 Total					**151.32**	**26.92**	**178.24**		

Table D 1. *Continued*

WBS1	WBS1 Desc	WBS2	WBS2 Desc	WBS3 Desc	WBS5	WBS5 Desc	Basic Mass (kg)	MGA (kg)	Predicted Mass (kg)	TRL	Example Model, Manufacturer, and Part No. if available
		06.13	SCE Propulsion System	Main Propulsion System (MPS) Engine	06.13.01	Main Propulsion System (MPS) Engine	2.00	0.30	2.30	6	Northrop Grumman MRE-15
				Reaction Control System (RCS)/Attitude Control System (ACS) Engine	06.13.02	Reaction Control System (RCS)/Attitude Control System (ACS) Engine	17.60	2.64	20.24	9	Northrop Grumman MRE-1.0
				Propellant Tanks	06.13.03	Propellant Tanks	60.75	9.11	69.86	5	ATK 80274, modified
				Feed System Components	06.13.04.01	Service Valve	2.55	0.26	2.81	9	Moog C71465-001, Moog C71466-001
					06.13.04.02	Latch Valve	6.50	0.65	7.15	9	Wright Components Inc., 15512-1
					06.13.04.03	Flow Control Orifice	5.46	0.55	6.01		
					06.13.04.04	Filter	1.74	0.17	1.91	9	Vacco F1D10785-01
					06.13.04.05	Pressure Transducer	3.68	0.37	4.05	9	Paine 213-36-450-02
				Miscellaneous Hardware	06.13.05	Miscellaneous Hardware	14.69	3.67	18.37		
		06.13 Total					**114.97**	**17.72**	**132.69**		
		06.14	SCE Propellant	Propellant (N2H4)	06.14.01	Propellant (N2H4)	488.60	-	488.60		
		06.14 Total					**488.60**	**-**	**488.60**		
		06.15	SCE Non Propellant Fluids	Residual Propellant (N2H4)	06.15.01	Residual Propellant (N2H4)	24.40	-	24.40		
				Monoprop Pressurant (GN2)	06.15.02	Monoprop Pressurant (GN2)	23.31	-	23.31		
		06.15 Total					**47.71**	**-**	**47.71**		
		06.16	Payload Adapter	Payload Adapter	06.16.01	Payload Adapter	-	-	-		
		06.16 Total					**-**	**-**	**-**		
06 Total							**2,580.58**	**475.24**	**3,055.82**		
Grand Total							**6,299.47**	**1,413.01**	**7,712.48**		

Notes:
1. Engineering Models (EM) for optics and science instruments + 10% spares assumed for costing
2. TRLs and example models noted where information is available and/or specific items included in DRM
3. For items with identified TRL and no example model, it is assumed parts are commonly available and no technology development is required
4. High TRL radiators available, but with mass impact

E. Work Breakdown Structure

Table E.1. *Lynx* work breakdown structure.

Lynx X-ray Observatory Work Breakdown Structure		
WBS Code	Level	WBS Elements
01	2	**Project Management**
01 01	3	Project Management
01 02	3	Project Planning and Control
01 03	3	Configuration Management
02	2	**Systems Engineering**
02 01	3	Systems Engineering Management
02 02	3	Requirements Development & Verification
02 03	3	System and Mission Analysis
03	2	**Safety and Mission Assurance**
03 01	3	Safety and Mission Assurance Management
03 02	3	Reliability Analysis
03 03	3	Quality Assurance
03 04	3	Mission Safety
04	2	**Science and Technology**
04 01	3	Science and Technology Management
04 02	3	Science Support (Phase A - D)
04 03	3	X-ray Mirror Assembly (XMA) Technology Development
04 04	3	Lynx X-Ray Microcalorimeter (LXM) Technology Development
04 05	3	High Definition X-ray Imager (HDXI) Technology Development
04 06	3	X-Ray Grating Spectrometer (XGS (Array (XGA) + Detector (XGD)) Technology Development
05	2	**X-ray Telescope (XRT)**
05 01	3	XRT Management
05 02	3	XRT Systems Engineering
05 03	3	XRT Product Assurance
05 04	3	XRT Integration and Test
05 05	3	XRT Calibration
05 06	3	Lynx Mirror Assembly (LMA)
05 06 01	4	LMA Management
05 06 02	4	LMA Systems Engineering
05 06 03	4	LMA Integration & Test (includes calibration)
05 06 04	4	Reserved
05 06 05	4	Reserved
05 06 06	4	LMA Ground Support Equipment (GSE)
05 06 07	4	X-ray Mirror Modules
05 06 07 01	5	XMA Management
05 06 07 02	5	XMA Systems Engineering
05 06 07 03	5	XMA Integration and Test (includes calibration)
05 06 07 04	5	XMA Optical Elements (segments, modules)
05 06 07 05	5	XMA Meta-Shell Forward / Aft Ring Structure
05 06 07 06	5	XMA Spider Structure
05 06 08	4	LMA Thermal Control
05 06 08 01	5	LMA MLI
05 06 08 02	5	LMA Collimators
05 06 08 02 01	6	LMA Pre-Collimator Assembly
05 06 08 02 02	6	LMA Post-Collimator Assembly
05 06 08 03	5	Spider Heaters
05 06 09	4	LMA Contamination Control Door Assemblies
05 06 09 01	5	Forward Contamination Door (FCD)
05 06 09 01 01	6	FCD Structure
05 06 09 01 02	6	FCD Motor
05 06 09 01 03	6	FCD Motor Mount
05 06 09 01 04	6	Forward Door Hold Down Mechanisms (Launch Locks)
05 06 09 02	5	Aft Contamination Door (ACD)
05 06 09 02 01	6	Aft Contamination Door (ACD) Structure
05 06 09 02 02	6	ACD Motor
05 06 09 02 03	6	ACD Motor Mount
05 06 09 02 04	6	Aft Door Hold Down Mechanisms (Launch Locks)

Table E.1. *Lynx* work breakdown structure. *Continued*

05	06	10					4	LMA Barrel Assembly
05	06	10	01				5	Barrel Structure
05	06	10	02				5	Subsystem Ring
05	06	10	03				5	LMA Flexures
05	07						3	X-ray Gratings Array (XGA)
05	07	01					4	XGA Management
05	07	02					4	XGA Systems Engineering
05	07	03					4	XGA Integration & Test (includes calibration)
05	07	04					4	XGA Controller
05	07	05					4	XGA Ground Support Equipment (GSE)
05	07	06					4	XGA Elements (gratings, facets)
05	07	07					4	XGA Grating Array Structure (GAS)
05	07	08					4	Grating Array Motor
05	07	09					4	Grating Array Motor Mount
05	07	10					4	Gratings Array Structure Hold Down Mechanisms (Launch Locks)
05	08						3	Optical Bench Assembly (OBA)
05	08	01					4	OBA Management
05	08	02					4	OBA Systems Engineering
05	08	03					4	OBA Integration & Test
05	08	04					4	OBA GSE
05	08	05					4	Magnetic Broom
05	08	06					4	OBA TCS
05	08	06	01				5	OBA Heaters
05	08	06	02				5	OBA MLI
05	08	06	03				5	OBA OSR Support Structure
05	08	06	04				5	Observatory Sunshade
05	08	07					4	OBA Structure
05	09						3	Integrated Science Instrument Module (ISIM)
05	09	01					4	ISIM Management
05	09	02					4	ISIM Systems Engineering
05	09	03					4	ISIM Integration & Test
05	09	04					4	ISIM Electronics System
05	09	05					4	ISIM GSE
05	09	06					4	ISIM TCS
05	09	06	01				5	TTA Heaters
05	09	06	02				5	ISIM Heaters
05	09	06	03				5	TTA MLI
05	09	06	04				5	ISIM MLI
05	09	06	05				5	Radiator, LXM Cryostat
05	09	06	06				5	Radiator, LXM Cryocooler
05	09	06	07				5	Radiator, LXM Electronics 1
05	09	06	08				5	Radiator, LXM Electronics 2
05	09	06	09				5	Radiator, HDXI Detector Assembly
05	09	06	10				5	Radiator, HDXI DEU
05	09	06	11				5	Radiator, XGD Assembly
05	09	06	12				5	Radiator, XGD DEU
05	09	06	13				5	Radiator, Mounting Plate XGD
05	09	06	14				5	Subsystem Cold Plates and Survival Heaters
05	09	07					4	ISIM Structural System
05	09	07	01				5	ISIM Box
05	09	07	02				5	Translation Table Assembly (TTA)
05	09	07	02	01			6	TTA Mounting Plate
05	09	07	02	02			6	LXM Struts
05	09	07	02	03			6	LXM Strut Fittings
05	09	07	02	04			6	Translation Table Hold Down Mechanisms (Launch Locks)
05	09	07	03				5	TTA Mechanisms
05	09	07	03	01			6	Horizontal TTA mechanisms
05	09	07	03	02			6	Vertical TTA Mechanisms
05	09	07	04				5	Mounting Plate XGD
05	09	07	05				5	XGD Fine Focus Motor w/ Tilt Offset

Table E.1. *Lynx* work breakdown structure. *Continued*

05	09	08			4	Lynx X-ray Microcalorimeter (LXM) Instrument
05	09	08	01		5	LXM Management
05	09	08	02		5	LXM Systems Engineering
05	09	08	03		5	LXM Integration & Test (includes calibration)
05	09	08	04		5	LXM Software
05	09	08	05		5	LXM Electronics System (includes avionics)
05	09	08	06		5	LXM Ground Support Equipment (GSE)
05	09	08	07		5	LXM Thermal Control System (heat pipes)
05	09	08	08		5	LXM Miscellaneous Hardware (includes GSE stays)
05	09	08	09		5	LXM Harnesses
05	09	08	10		5	LXM Instrument Deck Assembly
05	09	08	11		5	LXM Dewar Assembly
05	09	09			4	High Definition X-ray Imager (HDXI) Instrument
05	09	09	01		5	HDXI Management
05	09	09	02		5	HDXI Systems Engineering
05	09	09	03		5	HDXI Integration & Test (includes calibration)
05	09	09	04		5	HDXI Software
05	09	09	05		5	HDXI Avionics
05	09	09	06		5	HDXI Ground Support Equipment (GSE)
05	09	09	07		5	HDXI Thermal Interface Material
05	09	09	08		5	HDXI Miscellaneous Hardware
05	09	09	09		5	HDXI Harnesses
05	09	09	10		5	HDXI Detector Assembly (DA)
05	09	09	11		5	HDXI Detector Electronics Unit (DEU)
05	09	10			4	X-ray Gratings Detector (XGD) Instrument
05	09	10	01		5	XGD Management
05	09	10	02		5	XGD Systems Engineering
05	09	10	03		5	XGD Integration & Test (includes calibration)
05	09	10	04		5	XGD Software
05	09	10	05		5	XGD Ground Support Equipment (GSE)
05	09	10	06		5	XGD Miscellaneous Hardware
05	09	10	07		5	XGD Assembly
05	09	10	07	01	6	XGD Electronics
05	09	10	07	02	6	XGD Thermal
05	09	10	07	03	6	XGD Structures
05	09	10	07	04	6	XGD Mechanisms
05	09	10	08		5	XGD Detector Electronics Unit (DEU)
05	09	10	08	01	6	XGD DEU Avionics
05	09	10	08	02	6	XGD DEU Power
05	09	10	08	03	6	XGD DEU Thermal
05	09	10	08	04	6	XGD DEU Structures
05	10	12			3	Reserved
05	11	13			3	Reserved
05	12	14			3	Lynx Calibration Facility
06					**2**	**Spacecraft Element (SCE)**
06	01				3	SCE Management
06	02				3	SCE Systems Engineering
06	03				3	SCE Product Assurance
06	04				3	SCE Integration & Test
06	05				3	SCE Flight Software (FSW)
06	06				3	SCE Ground Support Equipment (GSE)
06	07				3	SCE Structural System
06	07	01			4	Spacecraft Bus
06	07	02			4	Interface Struts (OBA/Bus/LMA)
06	07	02	01		5	Struts
06	07	02	02		5	Strut Fittings
06	07	03			4	Secondary Structures
06	07	04			4	Sunshade Door Assembly (SDA)
06	07	04	01		5	Sunshade Door
06	07	04	02		5	SSD Motor
06	07	04	03		5	SSD Motor Mount

Table E.1. *Lynx* work breakdown structure. *Continued*

06 08	3	SCE Thermal Control System
06 08 01	4	Heaters, SCE Bus
06 08 02	4	Multilayer Insulation (MLI), SCE Bus
06 08 03	4	Radiator SCE Bus
06 08 04	4	SSD MLI
06 08 05	4	Heaters, Propulsion Tanks
06 08 06	4	MLI, Propulsion Tanks
06 09	3	SCE Electrical Power System (EPS)
06 09 01	4	Solar Array Wing (with Boom)
06 09 02	4	Solar Array Drive Actuator
06 09 03	4	Integrated Power Electronics
06 09 04	4	Secondary Distribution
06 09 05	4	Secondary Batteries
06 09 06	4	Cabling
06 09 07	4	Solar Array Deployment Mechanism
06 10	3	SCE Command and Data Handling (C&DH) System
06 10 01	4	Flight Computer
06 10 02	4	Safe Mode Electronics Unit
06 10 03	4	Solid State Recorder
06 10 04	4	Data Acquisition Unit
06 10 05	4	MPS Controller
06 10 06	4	RCS Controller
06 10 07	4	RW Controller
06 10 08	4	LMA Heater Controller
06 10 09	4	SC/OBA/ISIM Heater Controller
06 10 10	4	Avionics / Propulsion Heater Controller
06 10 11	4	Translation Table Controller
06 10 12	4	Doors/Gratings Controller
06 10 13	4	Instrumentation and Monitoring
06 10 14	4	Avionics Cabling
06 10 15	4	Heater and Temp Sensor Cabling
06 11	3	SCE Communications
06 11 01	4	Ka Phased Array Antenna
06 11 02	4	X Transponder
06 11 03	4	Ka Transceiver
06 11 04	4	Ka Diplexer
06 11 05	4	X-Band TWTA
06 11 06	4	X-TWT Amp
06 11 07	4	Ka-Band TWT
06 11 08	4	Ka-Band TWT Amp
06 11 09	4	Waveguides
06 11 10	4	RF Combiner
06 11 11	4	RF Switch 1-2
06 11 12	4	RF Switch 1-3
06 11 13	4	X-Band Conical Patch Antenna
06 11 14	4	X-Band MGA Array
06 11 15	4	Coax Cabling, Misc
06 12	3	SCE Guidance, Navigation and Control (GN&C) System
06 12 01	4	Coarse Sun Sensor
06 12 02	4	Ultra Fine Sun Sensor
06 12 03	4	Inertial Measurement Unit
06 12 04	4	Reaction Wheel System
06 12 04 01	5\	Reaction Wheels
06 12 04 02	5	Reaction Wheel Drive Electronics
06 12 04 03	5	Reaction Wheel Isolation System
06 12 05	4	Pointing Control and Aspect Determination (PCAD) System
06 12 05 01	5	Aspect Camera Assembly
06 12 05 02	5	Periscope
06 12 05 03	5	Fiducial Light Assembly
06 12 05 03 01	6	Fiducial Light
06 12 05 03 02	6	Fiducial Light Controller Assembly

Table E.1. *Lynx* work breakdown structure. *Continued*

06 12 06	4	Star Tracker System
06 12 06 01	5	Star Tracker Camera Head (DTU micro ASC)
06 12 06 02		Star Tracker Double Data Processing Unit (DPU) (Internally Redundant)
06 13	3	SCE Propulsion System
06 13 01	4	Main Propulsion System (MPS) Engine
06 13 02	4	Reaction Control System (RCS)/Attitude Control System (ACS) Engine
06 13 03	4	Propellant Tanks
06 13 04	4	Feed System Components
06 13 04 01	5	Service Valve
06 13 04 02	5	Latch Valve
06 13 04 03	5	Flow Control Orifice
06 13 04 04	5	Filter
06 13 04 05	5	Pressure Transducer
06 13 05	4	Miscellaneous Hardware
06 14	3	SCE Propellant
06 14 01	4	Propellant (N2H4)
06 15	3	SCE Non Propellant Fluids
06 15 01	4	Residual Propellant (N2H4)
06 15 02	4	Monoprop Pressurant (GN2)
06 16	3	Payload Adapter
07	**2**	**Mission Operations**
07 01	**3**	Management
07 02	**3**	Systems Engineering
07 03	**3**	Science Operations (Phase E - F)
07 04	**3**	Science Data Systems
07 05	**3**	Science Instrument Teams (Phase E - F)
07 06	**3**	Operations
07 07	**3**	Grants Program
08	**2**	**Launch Vehicle Services**
08 01	3	Launch Vehicle Liaison
08 02	3	Launch Vehicle Integration and Test
09	**2**	**Ground Systems**
09 01	**3**	Management
09 02	**3**	Systems Engineering
09 03	**3**	Science Operations (Phase A - D)
09 04	**3**	Science Data System
09 05	**3**	Science Instrument Teams (Phase A - D)
09 06	**3**	Operations
09 07	**3**	Grants Program
10	**2**	**Systems Integration and Test**
10 01	3	I&T Management
10 02	3	I&T Systems Engineering
10 03	3	Lynx Observatory [XRT+SCE] Assembly, Integration & Test
10 04	3	Observatory I&T GSE
10 05	3	Observatory I&T Facilities
10 06	3	Observatory Test and Checkout
11	**2**	**Public Outreach**

Acronyms

$FY	Fiscal Year Dollars
$RY	Real Year Dollars
AA	Associate Administrator
ACH	Atomic Cooling Halos
ACIS	Application Specific Integrated Circuit
ACO	Advanced Concepts Office
ACS	Attitude Control System
ACT	Atacama Cosmology Telescope
ACTDP	Advanced Cryocooler Development Program
AD2	Advancement Degree of Difficulty
ADA	Aft Door Assembly
ADR	Adiabatic Demagnetization Refrigerator
AGN	Active Galactic Nuclei
AI&T	Assembly Integration and Test
AIAA	American Institute of Aeronautics and Astronautics
Al	Aluminum
ALD	Atomic Layer Deposition
ALMA	Atacama Large Millimeter/submillimeter Array
AO	Announcement of Opportunity
APD	Astrophysics Projects Division
APRA	Astrophysics Research and Analysis
APS	Active Pixel Sensor
ASCA	Advanced Satellite for Cosmology and Astrophysics
ASI	Italian Space Agency
ASIC	Application-Specific Integrated Circuit
ASM	Acquisition Strategy Meeting
BBXRT	Broadband X-ray Telescope
BDD	Block Definition Diagrams
BH	Black Hole
BHMF	Black Hole Mass Function
BOE	Basis of Estimate
C&DH	Command and Data Handling
CADR	Continuous Adiabatic Demagnetization Refrigerator
CADRe	Cost Analysis and Data Requirements
CAN	Cooperative Agreement Notice
CAP	Command Action Procedure
CAT	Critical Angle Transmission
CAT-XGS	Critical Angle Transmission Gratings
CATE	Cost and Technical Evaluation
CC	Core Collapse
CCD	Charge-Coupled Device
CCO	Central Compact Object
CCSDS	Consultative Committee for Space Data Systems
CDR	Critical Design Review
CE	Chief Engineer
CER	Cost-Estimating Relationship
CGM	Circumgalactic Medium
CIL	Critical Items List
CL	Confidence Level
CLA	Coupled Loads
CME	Coronal Mass Ejection
CMOS	Complementary Metal-Oxide Semiconductor
COBE	Cosmic Background Explorer
CoCoMo	Constructive Cost Model
COS	Cosmic Origins Spectrograph
COTS	Commercial Off-The-Shelf
CPR	Critical Path Reserve
CTE	Coefficient of Thermal Expansion
CTO	Chandra-type Orbit
CV	Coefficient of Variation
CXB	Cosmic X-Ray Background
DD	Double-Degenerate
DDT&E	Design, Development, Test, and Evaluation
DEEP	Digital Electronics and Event Processor
DEM	Differential Emission Measure
DEU	Detector Electronics Unit
DM	Dark Matter
DOF	Degrees of Freedom
DRIE	Deep Reactive-Ion Etching
DRM	Design Reference Mission
DSN	Deep Space Network
EAGLE	Evolution and Assembly of GaLaxies and their Environments
EDU	Engineering Development Unit
EEE	Electrical, Electronic, and Electromechanical
EGSE	Electrical Ground Support Equipment
ELT	Extremely Large Telescopes
EM	Electromagnetic (radiation, probe)
EM	Engineering Model
EMA	Enhanced Main Array

EMC	Electromagnetic Compatibility
EMI	Electromagnetic Interference
EOB	Extendable Optical Bench
EOL	End-of-Life
EOR	Epoch of Reionization
EPB	Event Processing Board
EPS	Electrical Power System
ERP	Event Recognition Processor
ESA	European Space Agency
ESLOC	Equivalent Source Lines of Code
ESO	European Southern Observatory
ETU	Engineering Test Unit
EUV	Extreme Ultraviolet
EW	Equivalent Width
FDA	Forward Door Assembly
FEM	Finite Element Model
FEMB	Front-End Motherboard
FIRE	Feedback In Realistic Environments
FMEA	Failure Mode and Effects Analysis
FOM	Figure of Merit
FOT	Flight Operations Team
FOV	Field of View
FPA	Focal Plane Assembly
FPGA	Field Programmable Gate Array
FSW	Flight Software
FTE	Full-Time Equivalent
FTS	Fiducial Transfer System
FU	Flight Unit
FWHM	Full Width at Half Maximum
FY	Fiscal Year
GA	Grating Array
GAO	Government Accountability Office
GAS	Grating Array Structure
GDS	Ground Data Systems
GMC	Giant Molecular Cloud
GN&C	Guidance, Navigation, and Control
GO	General Observer
GOES	Geostationary Operational Environmental Satellite
GOT	Ground Operations Team
GPI	Gemini Planet Imager
GPR	Goddard Procedural Requirements
GPU	Graphics Processing Unit
GR&A	Ground Rules and Assumptions
GSE	Ground Support Equipment
GSFC	Goddard Space Flight Center
GW	Gravitational Wave
HAST	High Accuracy Star Tracker
HDXI	High Definition X-ray Imager
HEMT	High-Electron Mobility Transistor
HEO	High-Earth Orbit
HERA	Hydrogen Epoch of Reionization Array
HETG	High-Energy Transmission Grating
HETGS	High-Energy Transmission Grating Spectrometer
HiCIAO	High-Contrast Coronographic Imager for Adaptive Optics
HNA	HF/Nitric/Acetic Acid
HOD	Halo Occupation Distribution
HPD	Half-Power Diameter
HQ	Headquarters
HRMA	High-Resolution Mirror Assembly
HST	Hubble Space Telescope
I&T	Integration and Test
IBD	Internal Block Diagram
ICD	Interface Control Document
ICE	Independent Cost Estimate
IDL	Instrument Design Lab
IFU	Integral Field Unit
IGM	Intergalactic Medium
IMAGE	Imager for Magnetopause-to-Aurora Global Exploration
IMF	Initial Mass Function
INAF	Instituto Nazionale Di Astrofisica
INTEGRAL	INTErnational Gamma-Ray Astrophysics Laboratory
IR	Infrared
IRAS	Infrared Astronomical Satellite
IRD	Interface Requirements Document
IRU	Inertial Reference Unit
ISFM	Internal Scientist Funding Mode
ISIM	Integrated Science Instrument Module
ISM	Interstellar Medium
ISO	Infrared Space Observatory
ITA	Independent Technical Authority
IXO	International X-ray Observatory

JATIS	Journal of Astronomical Telescopes, Instruments, and Systems
JPL	Jet Propulsion Laboratory
JWST	James Webb Space Telescope
KDP	Key Decision Point
KSC	Kennedy Space Center
KSLOC	Kilo Source Lines of Code
L1	Level 1 (requirements)
L2	Level 2 (requirements)
L2	Sun-Earth Lagrangian L_2 point
LADEE	Lunar Atmosphere and Dust Environment Explorer
LCR	Lifecycle Review
LDRO	Lunar Distant Retrograde Orbit
LEO	Low-Earth Orbit
LETG	Low-Energy Transmission Grating
LIGO	Laser Interferometer Gravitational-Wave Observatory
LISA	Laser Interferometer Space Antenna
LL	Lincoln Laboratory
LLCD	Lunar Laser Communication Demonstration
LMA	Lynx Mirror Assembly
LMAT	Lynx Mirror Architecture Trade
LMC	Large Magellanic Cloud
LRD	Launch Readiness Date
LSC	Lynx Science Center
LSE	Lead Systems Engineer
LSF	Line Spread Function
LSP	Launch Services Program
LSS	Large Scale Structure
LSST	Large Synoptic Survey Telescope
LV	Launch Vehicle
LXM	Lynx X-ray Microcalorimeter
LXO	Lynx X-ray Observatory
MA	Main Array
MAC	Mass Acceleration Curve; Molecular Absorber Coating
MBSE	Model-Based Systems Engineering
MCR	Mission Concept Review
MCR	MCR Technologies, LLC
MDL	Mission Design Lab
MDR	Mission Definition Review
MEB	Main Electronic Box
MEL	Master Equipment List
MEM	Meteoroid Engineering Model
MEMS	Micro-Electrical Mechanical Systems
MGA	Mass Growth Allowance
MGSE	Mechanical Ground Support Equipment
MIMU	Miniature Inertial Measurement Unit
MIRI	Mid-Infrared Instrument
MIT	Massachusetts Institute of Technology
MLI	Multilayer Insulation
MOE	Measure of Effectiveness
MOP	Measure of Performance
MOS	Mission Operations Systems
MPE	Max Planck Institute for Extraterrestrial Physics
MPS	Main Propulsion System
MSE	Mission Systems Engineer
MSFC	Marshall Space Flight Center
MUSE	Multi Unit Spectroscopic Explorer
MW	Milky Way
MXS	Modulated X-ray Source
ngVLA	Next Generation Very Large Array
NICER	Neutron star Interior Composition Explorer
NICM	NASA Instrument Cost Model
NIR	Near-Infrared
NPR	NASA Procedural Requirements
NS	Neutron Star
NSL	NASA Launch Services
OAB	Astronomical Observatory of Brera
OBA	Optical Bench Assembly
OBC	Onboard Computer
OBF	Optical Blocking Filter
OCC	Operations Control Center
ODC	Other Direct Costs
OGRE	Off-plane Grating Rocket Experiment
OIR	Optical Infrared
OP	Off-Plane
OP-XGS	Off-Plane X-ray Grating Spectrometer
OPG	Off-Plane Gratings
ORR	Operational Readiness Review
OSR	Optical Solar Reflector
OWG	Optics Working Group
PBS	Product Breakdown Structure
PCAD	Pointing Control and Aspect Determination

PCEC	Project Cost Estimating Capability
PCOS	Physics of the Cosmos
PDR	Preliminary Design Review
PEL	Power Equipment List
PLATO	PLAnetary Transits and Oscillations of stars
PM	Project Management
POP	III Population III
PRICE	Programmed Review of Information for Costing and Evaluation
PS	Project Scientist
PSF	Point Spread Function
PSU	Pennsylvania State University
PZT	Lead Zirconate Titanate
QE	Quantum Efficiency
RB	Reverse Brayton
RCS	Reaction Control System
REDSTAR	Resource Data Analysis and Retrieval
RFP	Request for Proposal
RGS	Reflection Grating Spectrometer
RM	Relative Motion
RMS	Root Mean Square
ROIC	Readout Integrated Circuit
ROSAT	Roentgen Satellite
ROSES	Research Opportunities in Space and Earth Sciences
RRM	Risk Reduction Margin
RTF	Roman Technology Fellowship
RWA	Reaction Wheel Assembly
RXTE	Rossi X-ray Timing Explorer
S&MA	Safety and Mission Assurance
SAO	Smithsonian Astrophysical Observatory
SAT	Strategic Astrophysics Technology
SCaN	Space Communications and Navigation
SCE	Spacecraft Element
SD	Single-Degenerate
SDO	Solar Dynamics Observatory
SDSS	Sloan Digital Sky Surveys
SE	Systems Engineering
SE-L2	Sun-Earth L2
SE&I	Systems Engineering and Integration
SEMP	Systems Engineering Management Plan
SFR	Star Formation Rate
SI	Science Instrument
SiGe HBT	Silicon-Germanium Heterojunction Bipolar Transistor
SiO2	Silica
SIR	System Integration Review
SKA	Square Kilometer Array
SLOC	Software Lines of Code
SLS	Space Launch System
SLTF	Stray Light Test Facility
SMBH	Supermassive Black Hole
SMC	Small Magellanic Cloud
SMD	Science Mission Directorate
SME	Subject Matter Expert
SMEU	Safe Mode Electronics Unit
SMO	Silicon Meta-shell Optics
SN	Supernova
SNe	Supernovae
SNR	Supernova Remnant
SOA	State of the Art
SOCM	Space Operations Cost Model
SOHO	Solar and Heliospheric Observatory
SOI	Silicon-On-Insulator
SOT	Science Operations Team
SPHERE	Spectro-Polarimetric High-contrast Exoplanet REsearch
SQUID	Superconducting Quantum Interference Device
SRB	Standing Review Board
SRI	Sarnoff Research Institute
SRR	Systems Requirement Review
SSDIF	Systems Development and Integration Facility
SSS	Shell Supporting Structure
Pan-STARRS	Panoramic Survey Telescope and Rapid Response System
STDT	Science and Technology Definition Team
STM	Science Traceability Matrix
SWG	Science Working Group
Swift/BAT	Swift/Burst Alert Telescope
SXS	Soft X-ray Spectrometer
SysML	Systems Modeling Language
SZ	Sunyaev-Zeldovich
TBD	To Be Determined
TBR	To Be Resolved
TCS	Thermal Control System

TDE	Tidal Disruption Events
TDM	Time-Division Multiplexing
TES	Transition-Edge Sensor
TESS	Transiting Exoplanet Survey Satellite
TGCAT	Transmission Grating Data Archive and Catalog
ToO	Target of Opportunity
TPM	Technical Performance Measure
TRL	Technology Readiness Level
TT&C	Telemetry, Tracking, and Command
TTA	Translation Table Assembly
TTI	Transfer Trajectory Insertion
TWINS	Two Wide-Angle Imaging Neutral-Atom Spectrometers
UAH	University of Alabama in Huntsville
UFO	Ultra-Fast Outflow
UHR	Ultra-High-Resolution
UHRA	Ultra-High-Resolution Array
ULX	Ultraluminous X-ray
USAF	United States Air Force
UV	Ultraviolet
VLT	Very Large Telescope
V&V	Verification and Validation
W-I	Wolter Type I
W-S	Wolter-Schwarzchild
WBS	Work Breakdown Structure
WFIRST	Wide-Field Infrared Survey Telescope
WFXT	Wide Field X-ray Telescope
WHIM	Warm Hot Intergalactic Medium
WRXR	Water Recovery X-ray Rocket
WSS	Wolter-Schwarzchild-Saha
WYE	Work Year Equivalent
X-IFU	X-ray Integral Field Unit
XARM	X-ray Astronomy Recovery Mission
XEUV	X-ray-Extreme Ultraviolet
XGA	X-ray Grating Array
XGD	X-ray Grating Detector
XGS	X-ray Grating Spectrometer
XIS	X-ray Imaging Spectrometer
XLF	X-ray Luminosity Function
XMA	X-ray Mirror Assembly
XMM	X-ray Multi-Mirror
XRB	X-ray Binaries
XRCF	X-ray and Cryogenic Facility
XRISM	X-Ray Imaging and Spectroscopy Mission
XRT	X-ray Telescope
XUV	X-ray and Extreme Ultraviolet
YSO	Young Stellar Objects
ZnO	Zinc Oxide
μMUX	Microwave SQUID Multiplexer

References

[1] in *Special Section on the* Lynx *X-Ray Observatory, J. Astron. Telesc. Instrum. Syst., 2019, 5(2)*, all of the papers are open source and online at: `https://tinyurl.com/yxrd6w38`

[2] Natarajan, P. et al., 2019, in *"Disentangling nature from nurture: tracing the origin of seed black holes"; Astro2020 science white paper*, `http://tinyurl.com/y3ytdq3e`

[3] Greene, J. E., 2012, Nature Communications, 3, 1304

[4] Gallo, E. et al., 2019, in *"Towards a high accuracy measurement of the local black hole occupation fraction in low mass galaxies"; Astro2020 science white paper*, `http://tinyurl.com/y44u9j4j`

[5] Greene, J. et al., 2019, in *"The Local Relics of of Supermassive Black Hole Seeds"; Astro2020 science white paper*, `http://tinyurl.com/y699fg7r`

[6] Wrobel, J. et al., 2019, in *"Intermediate-Mass Black Holes in Extragalactic Globular Clusters"; Astro2020 science white paper*, `http://tinyurl.com/y68q88dk`

[7] Kormendy, J. & Ho, L. C., 2013, ARA&A, 51, 511

[8] Soltan, A., 1982, MNRAS, 200, 115

[9] Yu, Q. & Tremaine, S., 2002, MNRAS, 335, 965

[10] Martini, P., 2004, Coevolution of Black Holes and Galaxies, 169

[11] Rees, M. J., 1984, ARA&A, 22, 471

[12] Woods, T. E. et al., 2018, arXiv e-prints, arXiv:1810.12310

[13] Fan, X. et al., 2001, AJ, 122, 2833

[14] Willott, C. J. et al., 2010, AJ, 139, 906

[15] Venemans, B. P. et al., 2013, ApJ, 779, 24

[16] Mortlock, D. J. et al., 2011, Nature, 474, 616

[17] Wu, X.-B. et al., 2015, Nature, 518, 512

[18] Bañados, E. et al., 2018, Nature, 553, 473

[19] Smith, A., Bromm, V. & Loeb, A., 2017, Astronomy and Geophysics, 58, no. 3, 3.22

[20] Madau, P., Haardt, F. & Dotti, M., 2014, ApJ, 784, L38

[21] Volonteri, M., 2012, Science, 337, 544

[22] Volonteri, M. & Bellovary, J., 2012, Reports on Progress in Physics, 75, no. 12, 124901

[23] Haiman, Z., 2013, in T. Wiklind, B. Mobasher & V. Bromm, eds., *The First Galaxies*, *Astrophysics and Space Science Library*, vol. 396, 293

[24] Natarajan, P., 2014, General Relativity and Gravitation, 46, 1702

[25] Schleicher, D. R. G., 2018, arXiv e-prints, arXiv:1807.06055

[26] Wise, J. H., 2018, arXiv e-prints, arXiv:1807.06080

[27] Barkana, R. & Loeb, A., 2001, Phys. Rep., 349, 125

[28] Haiman, Z. & Loeb, A., 2001, ApJ, 552, 459

[29] Whalen, D., Abel, T. & Norman, M. L., 2004, ApJ, 610, 14

[30] O'Shea, B. W. et al., 2005, ApJ, 628, L5

[31] Johnson, J. L. & Bromm, V., 2007, MNRAS, 374, 1557

[32] Milosavljević, M. et al., 2009, ApJ, 698, 766

[33] Haiman, Z., 2004, ApJ, 613, 36

[34] Oh, S. P. & Haiman, Z., 2002, ApJ, 569, 558

[35] Lodato, G. & Natarajan, P., 2006, MNRAS, 371, 1813

[36] Lodato, G. & Natarajan, P., 2007, MNRAS, 377, L64

[37] Omukai, K., 2001, ApJ, 546, 635

[38] Shang, C., Bryan, G. L. & Haiman, Z., 2010, MNRAS, 402, 1249

[39] Wolcott-Green, J. & Haiman, Z., 2011, MNRAS, 412, 2603

[40] Wolcott-Green, J., Haiman, Z. & Bryan, G. L., 2017, MNRAS, 469, 3329

[41] Dijkstra, M. et al., 2008, MNRAS, 391, 1961

[42] Visbal, E., Haiman, Z. & Bryan, G. L., 2014, MNRAS, 445, 1056

[43] Regan, J. A. et al., 2017, Nature Astronomy, 1, 0075

[44] Fernandez, R. et al., 2014, MNRAS, 439, 3798

[45] Tanaka, T. L., 2014, Classical and Quantum Gravity, 31, no. 24, 244005

[46] Wise, J. H. et al., 2019, Nature, in press; e-print arXiv:1901.07563

[47] Hirano, S. et al., 2017, Science, 357, 1375

[48] Schauer, A. T. P. et al., 2017, MNRAS, 471, 4878

[49] Inayoshi, K., Li, M. & Haiman, Z., 2018, MNRAS, 479, 4017

[50] Bromm, V. & Loeb, A., 2003, ApJ, 596, 34

[51] Hosokawa, T., Omukai, K. & Yorke, H. W., 2012, ApJ, 756, 93

[52] Hosokawa, T. et al., 2015, ArXiv e-prints, arXiv:1510.01407

[53] Sakurai, Y. et al., 2016, MNRAS, 459, 1137

[54] Haemmerlé, L. et al., 2018, MNRAS, 474, 2757

[55] Alexander, T. & Natarajan, P., 2014, Science, 345, 1330

[56] Inayoshi, K., Haiman, Z. & Ostriker, J. P., 2016, MNRAS, 459, 3738

[57] Sakurai, Y., Inayoshi, K. & Haiman, Z., 2016, MNRAS, 461, 4496

[58] Omukai, K., Schneider, R. & Haiman, Z., 2008, ApJ, 686, 801

[59] Devecchi, B. & Volonteri, M., 2009, ApJ, 694, 302

[60] Ricarte, A. & Natarajan, P., 2018, MNRAS, 481, 3278

[61] Vito, F. et al., 2016, MNRAS, 463, 348

[62] Vito, F. et al., 2018, MNRAS, 473, 2378

[63] Pacucci, F. et al., 2015, MNRAS, 454, 3771

[64] Natarajan, P. et al., 2017, ApJ, 838, 117

[65] Haehnelt, M. G., 1994, MNRAS, 269, 199

[66] Sesana, A., Volonteri, M. & Haardt, F., 2007, MNRAS, 377, 1711

[67] Berti, E. & Volonteri, M., 2008, ApJ, 684, 822

[68] Sesana, A. et al., 2011, Phys. Rev. D, 83, 044036

[69] Klein, A. et al., 2016, Phys. Rev. D, 93, no. 2, 024003

[70] Tanaka, T. & Haiman, Z., 2009, ApJ, 696, 1798

[71] Habouzit, M., Volonteri, M. & Dubois, Y., 2017, MNRAS, 468, 3935

[72] Alvarez, M. et al., 2019, in *"Unique Probes of Reionization with the CMB:From the First Stars to Fundamental Physics"; Astro2020 science white paper*, `http://tinyurl.com/y34ukydz`

[73] Pacucci, F. et al., 2019, in *"Detecting the Birth of Supermassive Black Holes Formed from Heavy Seeds"; Astro2020 science white paper*, `http://tinyurl.com/y4m4bl8j`

[74] Dijkstra, M., Sethi, S. & Loeb, A., 2016, ApJ, 820, 10

[75] Dijkstra, M., Gronke, M. & Sobral, D., 2016, ApJ, 823, 74

[76] Visbal, E. & Haiman, Z., 2018, ApJ, 865, L9

[77] Bellovary, J. et al., 2011, ApJ, 742, 13

[78] Volonteri, M. et al., 2017, ApJ, 849, 155

[79] Ricarte, A. & Natarajan, P., 2018, MNRAS, 474, 1995

[80] Snyder, G. F. et al., 2017, MNRAS, 468, 207, `https://archive.stsci.edu/prepds/illustris/`

[81] Lehmer, B. D. et al., 2016, ApJ, 825, 7

[82] Visbal, E., Haiman, Z. & Bryan, G. L., 2015, MNRAS, 453, 4456

[83] Agarwal, B. et al., 2012, MNRAS, 425, 2854

[84] Driver, S. P. & Robotham, A. S. G., 2010, MNRAS, 407, 2131

[85] Moster, B. P. et al., 2011, ApJ, 731, 113

[86] Mason, C. A., Trenti, M. & Treu, T., 2015, ApJ, 813, 21

[87] Hickox, R. C. et al., 2014, ApJ, 782, no. 1, 9

[88] Chen, C.-T. J. et al., 2013, ApJ, 773, no. 1, 3

[89] Yang, G. et al., 2017, ApJ, 842, no. 2, 72

[90] Powell, M. C. et al., 2018, ApJ, 858, no. 2, 110

[91] Brusa, M. et al., 2010, ApJ, 716, no. 1, 348

[92] Nandra, K. et al., 2015, ApJS, 220, no. 1, 10

[93] LaMassa, S. M. et al., 2016, ApJ, 817, no. 2, 172

[94] Civano, F. et al., 2016, ApJ, 819, no. 1, 62

[95] Luo, B. et al., 2017, ApJS, 228, no. 1, 2

[96] Chen, C. T. J. et al., 2018, MNRAS, 478, no. 2, 2132

[97] Merloni, A. et al., 2012, arXiv e-prints, arXiv:1209.3114

[98] Mereminskiy, I. A. et al., 2018, Astronomy Letters, 44, no. 2, 67

[99] Marchesi, S. et al., 2016, ApJ, 827, no. 2, 150

[100] Merloni, A., Heinz, S. & di Matteo, T., 2003, MNRAS, 345, no. 4, 1057

[101] Gültekin, K. et al., 2019, ApJ, 871, no. 1, 80

[102] Starikova, S. et al., 2011, ApJ, 741, no. 1, 15

[103] Mendez, A. J. et al., 2016, ApJ, 821, no. 1, 55

[104] Allevato, V. et al., 2016, ApJ, 832, no. 1, 70

[105] Plionis, M. et al., 2018, A&A, 620, A17

[106] Yang, G. et al., 2018, MNRAS, 480, no. 1, 1022

[107] Fornasini, F. M. et al., 2018, ApJ, 865, no. 1, 43

[108] Hopkins, P. F. et al., 2005, ApJ, 625, no. 2, L71

[109] Blecha, L. et al., 2018, MNRAS, 478, no. 3, 3056

[110] Risaliti, G., Maiolino, R. & Salvati, M., 1999, ApJ, 522, no. 1, 157

[111] Liu, T. et al., 2017, ApJS, 232, no. 1, 8

[112] Zappacosta, L. et al., 2018, A&A, 618, A28

[113] Stern, D. et al., 2005, ApJ, 631, no. 1, 163

[114] Alexander, D. M. et al., 2008, ApJ, 687, no. 2, 835

[115] Gandhi, P. et al., 2009, A&A, 502, no. 2, 457

[116] Goulding, A. D. et al., 2011, MNRAS, 411, no. 2, 1231

[117] Civano, F. et al., 2015, ApJ, 808, no. 2, 185

[118] Lansbury, G. B. et al., 2017, ApJ, 846, no. 1, 20

[119] Masini, A. et al., 2018, ApJ, 867, no. 2, 162

[120] Lemons, S. M. et al., 2015, ApJ, 805, 12

[121] Foord, A. et al., 2017, ApJ, 841, no. 1, 51

[122] Lee, N. et al., 2019, ApJ, 874, no. 1, 77

[123] Volonteri, M. & Natarajan, P., 2009, MNRAS, 400, 1911

[124] Volonteri, M., 2010, A&A Rev., 18, no. 3, 279

[125] Agarwal, B. et al., 2016, MNRAS, 459, no. 4, 4209

[126] Valiante, R. et al., 2018, MNRAS, 476, 407

[127] Sijacki, D. et al., 2015, MNRAS, 452, no. 1, 575

[128] Pacucci, F., Natarajan, P. & Ferrara, A., 2017, ApJ, 835, no. 2, L36

[129] Dashyan, G. et al., 2018, MNRAS, 473, no. 4, 5698

[130] Dickey, C. et al., 2019, arXiv e-prints, arXiv:1902.01401

[131] Stone, N. C. & Metzger, B. D., 2016, MNRAS, 455, no. 1, 859

[132] Werner, N. et al., 2013, Nature, 502, no. 7473, 656

[133] Urban, O. et al., 2017, MNRAS, 470, no. 4, 4583

[134] De Grandi, S. & Molendi, S., 2001, ApJ, 551, no. 1, 153

[135] Leccardi, A. & Molendi, S., 2008, A&A, 487, no. 2, 461

[136] Madau, P. & Dickinson, M., 2014, ARA&A, 52, 415

[137] Ettori, S. et al., 2015, A&A, 578, A46

[138] Mantz, A. B. et al., 2017, MNRAS, 472, no. 3, 2877

[139] McDonald, M. et al., 2016, ApJ, 826, no. 2, 124

[140] Greene, J. E. et al., 2014, ApJ, 788, no. 1, 54

[141] Powell, M. C. et al., 2018, A&A, 618, A27

[142] Ruszkowski, M. et al., 2019, in *"Supermassive Black Hole Feedback"; Astro2020 science white paper*, `http://tinyurl.com/y6affway`

[143] Churazov, E. et al., 2016, MNRAS, 463, no. 1, 1057

[144] McNamara, B. R. & Nulsen, P. E. J., 2007, ARA&A, 45, 117

[145] Fabian, A. C., 2012, ARA&A, 50, 455

[146] Zhuravleva, I. et al., 2014, Nature, 515, 85

[147] Hitomi Collaboration et al., 2016, Nature, 535, no. 7610, 117

[148] Tombesi, F. et al., 2010, A&A, 521, A57

[149] Allen, S. W. et al., 2006, MNRAS, 372, no. 1, 21

[150] Springel, V., 2005, MNRAS, 364, no. 4, 1105

[151] Henriques, B. M. B. et al., 2015, MNRAS, 451, 2663

[152] Behroozi, P. S., Wechsler, R. H. & Conroy, C., 2013, ApJ, 770, 57

[153] Werk, J. K. et al., 2014, ApJ, 792, 8

[154] Tumlinson, J. et al., 2011, Science, 334, 948

[155] Hummels, C. B. et al., 2013, MNRAS, 430, 1548

[156] Oppenheimer, B. D. et al., 2016, MNRAS, 460, 2157

[157] Nelson, D. et al., 2018, MNRAS, 477, 450

[158] Tumlinson, J., Peeples, M. S. & Werk, J. K., 2017, ARA&A, 55, 389

[159] Rees, M. J. & Ostriker, J. P., 1977, MNRAS, 179, 541

[160] White, S. D. M. & Rees, M. J., 1978, MNRAS, 183, 341

[161] White, S. D. M. & Frenk, C. S., 1991, ApJ, 379, 52

[162] Kereš, D. et al., 2005, MNRAS, 363, 2

[163] Dekel, A. & Birnboim, Y., 2006, MNRAS, 368, 2

[164] Balogh, M. L. et al., 2001, MNRAS, 326, 1228

[165] Martin, C. L., 2005, ApJ, 621, 227

[166] Rupke, D. S., Veilleux, S. & Sanders, D. B., 2005, ApJS, 160, 115

[167] Strickland, D. K. & Heckman, T. M., 2009, ApJ, 697, 2030

[168] Cicone, C. et al., 2014, A&A, 562, A21

[169] Heckman, T. M. & Best, P. N., 2014, ARA&A, 52, 589

[170] Springel, V. & Hernquist, L., 2003, MNRAS, 339, 312

[171] Oppenheimer, B. D. & Davé, R., 2006, MNRAS, 373, 1265

[172] Schaye, J. et al., 2010, MNRAS, 402, 1536

[173] Schaye, J. et al., 2015, MNRAS, 446, 521

[174] Nelson, D. et al., 2018, MNRAS, 475, 624

[175] Hopkins, P. F. et al., 2018, MNRAS, 480, 800

[176] Oppenheimer, B. D. et al., 2018, MNRAS, 481, 835

[177] Anglés-Alcázar, D. et al., 2017, MNRAS, 472, L109

[178] Bower, R. G. et al., 2017, MNRAS, 465, 32

[179] Weinberger, R. et al., 2017, MNRAS, 465, 3291

[180] Davies, J. J. et al., 2018, ArXiv e-prints, arXiv:1810.07696

[181] Schawinski, K. et al., 2014, MNRAS, 440, 889

[182] Bregman, J. N. et al., 2018, ApJ, 862, 3

[183] Keeney, B. A. et al., 2017, ApJS, 230, 6

[184] Peeples, M. S. et al., 2014, ApJ, 786, 54

[185] Shull, J. M., Danforth, C. W. & Tilton, E. M., 2014, ApJ, 796, 49

[186] Sutherland, R. S. & Dopita, M. A., 1993, ApJS, 88, 253

[187] Gupta, A. et al., 2012, ApJ, 756, L8

[188] Fielding, D. et al., 2017, MNRAS, 466, 3810

[189] Hodges-Kluck, E. J., Miller, M. J. & Bregman, J. N., 2016, ApJ, 822, 21

[190] Ji, S., Oh, S. P. & Masterson, P., 2018, arXiv e-prints, arXiv:1809.09101

[191] Butsky, I. S. & Quinn, T. R., 2018, ApJ, 868, 108

[192] Planck Collaboration et al., 2013, A&A, 557, A52

[193] Schaan, E. et al., 2016, Phys. Rev. D, 93, no. 8, 082002

[194] Battaglia, N. et al., 2017, JCAP, 11, 040

[195] Bregman, J. et al., 2019, in *"A Survey of Hot Gas in the Universe"; Astro2020 science white paper*, `http://tinyurl.com/y2d22nye`

[196] Tremblay, G. et al., 2019, in *"Galaxy Winds in the Age of Hyperdimensional Astrophysics"; Astro2020 science white paper*, `http://tinyurl.com/y6sygscu`

[197] Barcons, X. et al., 2017, Astronomische Nachrichten, 338, 153

[198] Nicastro, F. et al., 2018, Nature, 558, 406

[199] Kovács, O. E. et al., 2019, ApJ, 872, 83

[200] Bregman, J. N. et al., 2015, Journal of Astronomical Telescopes, Instruments, and Systems, 1, no. 4, 045003

[201] Qu, Z. & Bregman, J. N., 2018, ApJ, 862, 23

[202] Somerville, R. S. & Davé, R., 2015, ARA&A, 53, 51

[203] Veilleux, S., Cecil, G. & Bland-Hawthorn, J., 2005, ARA&A, 43, no. 1, 769

[204] Schneider, E. E. & Robertson, B. E., 2015, ApJS, 217, no. 2, 24

[205] Schneider, E. E. & Robertson, B. E., 2018, ApJ, 860, no. 2, 135

[206] Schneider, E. E., Robertson, B. E. & Thompson, T. A., 2018, ApJ, 862, no. 1, 56

[207] Tremblay, G. R. et al., 2016, Nature, 534, no. 7606, 218

[208] Tremblay, G. R. et al., 2018, ApJ, 865, no. 1, 13

[209] Behroozi, P. S., Conroy, C. & Wechsler, R. H., 2010, ApJ, 717, 379

[210] Zhang, D., 2018, Galaxies, 6, no. 4, 114

[211] Mac Low, M.-M. & Ferrara, A., 1999, ApJ, 513, no. 1, 142

[212] Martin, C. L., Kobulnicky, H. A. & Heckman, T. M., 2002, ApJ, 574, 663

[213] Thuan, T. X. et al., 2004, ApJ, 606, no. 1, 213

[214] Sormani, M. C. et al., 2018, MNRAS, 481, 3370

[215] Sormani, M. C. & Sobacchi, E., 2019, MNRAS, 486, 215

[216] Oppenheimer, B. D., 2018, MNRAS, 480, 2963

[217] Stevens, A. R. H. et al., 2017, MNRAS, 467, 2066

[218] Miller, M. J., Hodges-Kluck, E. J. & Bregman, J. N., 2016, ApJ, 818, 112

[219] Lehner, N. & Howk, J. C., 2011, Science, 334, 955

[220] Richter, P. et al., 2017, A&A, 607, A48

[221] Kataoka, J. et al., 2018, Galaxies, 6, no. 1, 27

[222] Ponti, G. et al., 2019, Nature, 567, no. 7748, 347

[223] Dobler, G. et al., 2010, ApJ, 717, no. 2, 825

[224] Su, M., Slatyer, T. R. & Finkbeiner, D. P., 2010, ApJ, 724, no. 2, 1044

[225] Crocker, R. M. & Aharonian, F., 2011, Phys. Rev. Lett., 106, no. 10, 101102

[226] Lacki, B. C., 2014, MNRAS, 444, L39

[227] Guo, F. & Mathews, W. G., 2012, ApJ, 756, no. 2, 181

[228] Inoue, Y. et al., 2015, PASJ, 67, no. 3, 56

[229] Revnivtsev, M. et al., 2009, Nature, 458, no. 7242, 1142

[230] Nazé, Y., Rauw, G. & Manfroid, J., 2008, A&A, 483, no. 1, 171

[231] Yadav, R. K. et al., 2016, ApJ, 833, L28

[232] Favata, F. & Micela, G., 2003, Space Sci. Rev., 108, 577

[233] Wright, N. J. et al., 2013, Astronomische Nachrichten, 334, 151

[234] Kuhn, M. A. et al., 2014, ApJ, 787, 107

[235] Kuhn, M. A., Getman, K. V. & Feigelson, E. D., 2015, ApJ, 802, 60

[236] Brickhouse, N. S. et al., 2010, ApJ, 710, 1835

[237] Cleeves, L. I. et al., 2015, ApJ, 799, 204

[238] Owen, J. E., Ercolano, B. & Clarke, C. J., 2011, MNRAS, 412, 13

[239] Mac Low, M.-M. & Klessen, R. S., 2004, Reviews of Modern Physics, 76, 125

[240] Alves, J. & Bouy, H., 2012, A&A, 547, A97

[241] Megeath, S. T. et al., 2012, AJ, 144, no. 6, 192

[242] Megeath, S. T. et al., 2016, AJ, 151, no. 1, 5

[243] Getman, K. V. et al., 2005, ApJS, 160, no. 2, 353

[244] Pravdo, S. H. et al., 2001, Nature, 413, no. 6857, 708

[245] Tsujimoto, M. et al., 2005, ApJS, 160, no. 2, 503

[246] Mamajek, E. E., 2009, in T. Usuda, M. Tamura & M. Ishii, eds., *American Institute of Physics Conference Series*, *American Institute of Physics Conference Series*, vol. 1158, 3–10

[247] Wolk, S. J. & Walter, F. M., 1996, AJ, 111, 2066

[248] Allen, L. E. et al., 2004, ApJS, 154, no. 1, 363

[249] Winston, E. et al., 2010, AJ, 140, no. 1, 266

[250] Townsley, L. K. et al., 2003, ApJ, 593, no. 2, 874

[251] Wolk, S. J. et al., 2002, ApJ, 580, no. 2, L161

[252] Feigelson, E. D. et al., 2005, ApJS, 160, no. 2, 379

[253] Johnstone, C. P. et al., 2015, ApJ, 815, L12

[254] Kochukhov, O. & Lavail, A., 2017, ApJ, 835, L4

[255] Kastner, J. H. et al., 2002, ApJ, 567, no. 1, 434

[256] Brickhouse, N. S. et al., 2010, ApJ, 710, no. 2, 1835

[257] Telleschi, A. et al., 2007, A&A, 468, no. 2, 541

[258] Güdel, M. et al., 2007, A&A, 468, no. 2, 529

[259] Güdel, M. & Telleschi, A., 2007, A&A, 474, no. 2, L25

[260] Curran, R. L. et al., 2011, A&A, 526, A104

[261] Brickhouse, N. S. et al., 2012, ApJ, 760, no. 2, L21

[262] Argiroffi, C. et al., 2009, A&A, 507, no. 2, 939

[263] Sacco, G. G. et al., 2008, A&A, 491, no. 2, L17

[264] Adams, F. C. & Gregory, S. G., 2012, ApJ, 744, no. 1, 55

[265] Donati, J. F. et al., 2007, MNRAS, 380, no. 4, 1297

[266] Günther, H. M. et al., 2007, A&A, 466, no. 3, 1111

[267] Günther, H. M., Huenemoerder, D. P. & Schulz, N. S. S., 2015, Resolving kinematics in young stars

[268] Preibisch, T. et al., 2005, ApJS, 160, 401

[269] Rutledge, R. E. et al., 2000, ApJ, 538, no. 2, L141

[270] Wright, N. J. et al., 2018, MNRAS, 479, no. 2, 2351

[271] Cook, B. A., Williams, P. K. G. & Berger, E., 2014, ApJ, 785, no. 1, 10

[272] Williams, P. K. G., Cook, B. A. & Berger, E., 2014, ApJ, 785, no. 1, 9

[273] Hussain, G. A. J. et al., 2012, MNRAS, 423, 493

[274] Wright, N. J. et al., 2011, ApJ, 743, 48

[275] Lingam, M. & Loeb, A., 2018, JCAP, 5, 020

[276] Johnstone, C. P. et al., 2015, A&A, 577, A28

[277] Garraffo, C., Drake, J. J. & Cohen, O., 2016, ApJ, 833, L4

[278] See, V. et al., 2016, MNRAS, 462, 4442

[279] Cohen, O. et al., 2017, ApJ, 834, 14

[280] Chung, S. M. et al., 2004, ApJ, 606, 1184

[281] Aschwanden, M. J. et al., 2016, Space Sci. Rev., 198, 47

[282] Antonucci, E., Dodero, M. A. & Martin, R., 1990, ApJS, 73, 147

[283] Antonucci, E. et al., 1982, Sol. Phys., 78, 107

[284] Poppenhaeger, K., Schmitt, J. H. M. M. & Wolk, S. J., 2013, ApJ, 773, no. 1, 62

[285] Wolk, S. et al., 2019, in *"X-ray Studies of Exoplanets"; Astro2020 science white paper*, `http://tinyurl.com/y6kqc2h6`

[286] Vidal-Madjar, A. et al., 2003, Nature, 422, no. 6928, 143

[287] Linsky, J. L. et al., 2010, ApJ, 717, no. 2, 1291

[288] Lecavelier des Etangs, A. et al., 2012, A&A, 543, L4

[289] Lavie, B. et al., 2017, A&A, 605, L7

[290] McCray, R. & Fransson, C., 2016, ARA&A, 54, 19

[291] Badenes, C., Maoz, D. & Draine, B. T., 2010, MNRAS, 407, no. 2, 1301

[292] Ferrand, G. & Safi-Harb, S., 2012, Advances in Space Research, 49, no. 9, 1313

[293] Sasaki, M. et al., 2012, A&A, 544, A144

[294] Maggi, P. et al., 2016, A&A, 585, A162

[295] Garofali, K. et al., 2017, MNRAS, 472, no. 1, 308

[296] Dewey, D. et al., 2008, ApJ, 676, no. 2, L131

[297] Bhalerao, J. et al., 2015, ApJ, 800, no. 1, 65

[298] Hitomi Collaboration et al., 2018, PASJ, 70, no. 2, 16

[299] Long, K. S. et al., 2010, ApJS, 187, no. 2, 495

[300] Xi, L. et al., 2019, ApJ, 874, no. 1, 14

[301] Yamaguchi, H. et al., 2016, ApJ, 820, no. 1, L3

[302] Orlando, S. et al., 2015, ApJ, 810, no. 2, 168

[303] Lopez, L. A. et al., 2011, ApJ, 732, no. 2, 114

[304] Vink, J., 2012, A&A Rev., 20, 49

[305] Yamaguchi, H. et al., 2014, ApJ, 785, no. 2, L27

[306] Maoz, D., Mannucci, F. & Nelemans, G., 2014, ARA&A, 52, 107

[307] Nomoto, K. & Leung, S.-C., 2017, *Thermonuclear Explosions of Chandrasekhar Mass White Dwarfs*, 1275

[308] Seitenzahl, I. R. & Townsley, D. M., 2017, *Nucleosynthesis in Thermonuclear Supernovae*, 1955

[309] Yamaguchi, H. et al., 2015, ApJ, 801, no. 2, L31

[310] Martínez-Rodríguez, H. et al., 2017, ApJ, 843, no. 1, 35

[311] Radice, D. et al., 2018, Journal of Physics G Nuclear Physics, 45, no. 5, 053003

[312] Hughes, J. P. et al., 2000, ApJ, 528, no. 2, L109

[313] DeLaney, T. et al., 2010, ApJ, 725, no. 2, 2038

[314] Safi-Harb, S. et al., 2019, in *"High-Resolution X-ray Imaging Studies of Neutron Stars, Pulsar Wind Nebulae and Supernova Remnants""; Astro2020 science white paper*, `http://tinyurl.com/y2sz4mgv`

[315] Faucher-Giguère, C.-A. & Kaspi, V. M., 2006, ApJ, 643, no. 1, 332

[316] Holland-Ashford, T. et al., 2017, ApJ, 844, no. 1, 84

[317] Katsuda, S. et al., 2018, ApJ, 856, no. 1, 18

[318] Marchant, P. et al., 2016, A&A, 588, A50

[319] Zezas, A. et al., 2019, in *"X-ray binaries: laboratories for understanding the evolution of compact objects from their birth to their mergers"; Astro2020 science white paper*, `http://tinyurl.com/y6sqg4oh`

[320] Fragos, T. & McClintock, J. E., 2015, ApJ, 800, no. 1, 17

[321] Qin, Y. et al., 2018, A&A, 616, A28

[322] Qin, Y. et al., 2019, ApJ, 870, no. 2, L18

[323] Bhattacharya, D. & van den Heuvel, E. P. J., 1991, Phys. Rep., 203, no. 1-2, 1

[324] Tauris, T. M. & van den Heuvel, E. P. J., 2006, *Formation and evolution of compact stellar X-ray sources*, vol. 39, 623–665

[325] Farris, B. D. et al., 2014, ApJ, 783, 134

[326] Haiman, Z., 2017, Phys. Rev. D, 96, no. 2, 023004

[327] The LIGO Scientific Collaboration et al., 2018, arXiv e-prints, arXiv:1811.12907

[328] Shoemaker, D. & LIGO Scientific Collaboration, 2019, in *Bulletin of the American Astronomical Society*, *BAAS*, vol. 51, 452

[329] Pooley, D. et al., 2018, ApJ, 859, no. 2, L23

[330] Barnes, J. E. & Hernquist, L., 1996, ApJ, 471, 115

[331] Artymowicz, P. & Lubow, S. H., 1994, ApJ, 421, 651

[332] Artymowicz, P. & Lubow, S. H., 1996, ApJ, 467, L77

[333] MacFadyen, A. I. & Milosavljević, M., 2008, ApJ, 672, 83

[334] Cuadra, J. et al., 2009, MNRAS, 393, 1423

[335] Roedig, C. et al., 2011, MNRAS, 415, 3033

[336] Nixon, C. J., King, A. R. & Pringle, J. E., 2011, MNRAS, 417, L66

[337] Shi, J.-M. et al., 2012, ApJ, 749, 118

[338] D'Orazio, D. J., Haiman, Z. & MacFadyen, A., 2013, MNRAS, 436, 2997

[339] Gold, R. et al., 2014, Phys. Rev. D, 90, no. 10, 104030

[340] Farris, B. D. et al., 2015, MNRAS, 447, L80

[341] Tang, Y., Haiman, Z. & MacFadyen, A., 2018, MNRAS, 476, 2249

[342] Paczynski, B., 1977, ApJ, 216, 822

[343] Roedig, C., Krolik, J. H. & Miller, M. C., 2014, ApJ, 785, no. 2, 115

[344] Reynolds, C. S. & Nowak, M. A., 2003, Phys. Rep., 377, no. 6, 389

[345] Miniutti, G. & Fabian, A. C., 2004, MNRAS, 349, 1435

[346] Dai, X. et al., 2010, ApJ, 709, no. 1, 278

[347] Jiménez-Vicente, J. et al., 2015, ApJ, 806, no. 2, 251

[348] Guerras, E. et al., 2017, ApJ, 836, no. 2, 206

[349] Kocsis, B., Haiman, Z. & Menou, K., 2008, ApJ, 684, 870

[350] Lang, R. N. & Hughes, S. A., 2008, ApJ, 677, 1184

[351] McWilliams, S. T. et al., 2011, Phys. Rev. D, 84, no. 6, 064003

[352] Phinney, E. S., 2009, in *Astro2010 White Paper*, arXiv:0903.0098

[353] Abbott, B. P. et al., 2017, Phys. Rev. Lett., 119, no. 16, 161101

[354] Metzger, B. D., 2017, arXiv e-prints, arXiv:1710.05931

[355] Haggard, D. et al., 2017, ApJ, 848, no. 2, L25

[356] Margutti, R. et al., 2017, ApJ, 848, no. 2, L20

[357] Mooley, K. P. et al., 2018, Nature, 554, no. 7691, 207

[358] Ruan, J. J. et al., 2018, ApJ, 853, no. 1, L4

[359] Margutti, R. et al., 2018, ApJ, 856, no. 1, L18

[360] Piro, L. et al., 2019, MNRAS, 483, no. 2, 1912

[361] Remillard, R. A. & McClintock, J. E., 2006, ARA&A, 44, no. 1, 49

[362] Bright, J. S. et al., 2018, MNRAS, 475, no. 3, 4011

[363] Pooley, D. et al., 2007, ApJ, 661, no. 1, 19

[364] Blaes, O., 2007, in L. C. Ho & J. W. Wang, eds., *The Central Engine of Active Galactic Nuclei*, *Astronomical Society of the Pacific Conference Series*, vol. 373, 75

[365] Event Horizon Telescope Collaboration et al., 2019, ApJ, 875, no. 1, L1

[366] Kara, E. et al., 2019, Nature, 565, no. 7738, 198

[367] Uttley, P. et al., 2014, A&A Rev., 22, 72

[368] Moustakas, L. et al., 2019, in *"Quasar microlensing: Revolutionizing our understanding of quasar structure and dynamics"; Astro2020 science white paper*, `http://tinyurl.com/y5eokw8z`

[369] Krawczynski, H., Chartas, G. & Kislat, F., 2019, ApJ, 870, no. 2, 125

[370] Chartas, G. et al., 2017, ApJ, 837, no. 1, 26

[371] Chartas, G. et al., 2019, in *"A New Era for X-ray Lensing Studies of Quasars and Galaxies"; Astro2020 science white paper*, `http://tinyurl.com/yxwba5la`

[372] Frank, J. & Rees, M. J., 1976, MNRAS, 176, 633

[373] Hills, J. G., 1975, Nature, 254, no. 5498, 295

[374] Rees, M. J., 1988, Nature, 333, no. 6173, 523

[375] Jonker, P. G. et al., 2019, arXiv e-prints, arXiv:1906.12236

[376] Fender, R. & Belloni, T., 2004, ARA&A, 42, no. 1, 317

[377] Auchettl, K., Guillochon, J. & Ramirez-Ruiz, E., 2017, ApJ, 838, no. 2, 149

[378] Komossa, S. & Bade, N., 1999, A&A, 343, 775

[379] Khabibullin, I., Sazonov, S. & Sunyaev, R., 2014, MNRAS, 437, no. 1, 327

[380] Shiokawa, H. et al., 2015, ApJ, 804, no. 2, 85

[381] Guillochon, J. & Ramirez-Ruiz, E., 2015, ApJ, 809, no. 2, 166

[382] Hayasaki, K., Stone, N. & Loeb, A., 2016, MNRAS, 461, no. 4, 3760

[383] Kaspi, S. et al., 2002, ApJ, 574, no. 2, 643

[384] Danehkar, A. et al., 2018, ApJ, 853, no. 2, 165

[385] Miller, J. M. et al., 2006, Nature, 441, no. 7096, 953

[386] Neilsen, J., Remillard, R. A. & Lee, J. C., 2011, ApJ, 737, no. 2, 69

[387] Basu-Zych, A. et al., 2019, in *Bulletin of the American Astronomical Society*, *BAAS*, vol. 51, 70

[388] Mesinger, A., Ferrara, A. & Spiegel, D. S., 2013, MNRAS, 431, 621

[389] NWNH, 2010, *New Worlds, New Horizons in Astronomy and Astrophysics*

[390] Fragos, T. et al., 2013, ApJ, 776, no. 2, L31

[391] Fragos, T. et al., 2013, ApJ, 764, no. 1, 41

[392] Madau, P. & Fragos, T., 2017, ApJ, 840, 39

[393] Mirabel, I. F. et al., 2011, A&A, 528, A149

[394] Kaaret, P., 2014, MNRAS, 440, L26

[395] Pacucci, F. et al., 2014, MNRAS, 443, 678

[396] Das, A. et al., 2017, MNRAS, 469, 1166

[397] McQuinn, M., 2012, MNRAS, 426, 1349

[398] Fialkov, A. et al., 2017, MNRAS, 464, 3498

[399] Ma, Q. et al., 2018, MNRAS, 480, 26

[400] Bahé, Y. M. et al., 2017, MNRAS, 470, 4186

[401] Dolag, K. et al., 2006, MNRAS, 370, no. 2, 656

[402] Cen, R. & Ostriker, J. P., 1999, ApJ, 514, 1

[403] Davé, R. et al., 2001, ApJ, 552, 473

[404] Davé, R. et al., 2010, MNRAS, 408, 2051

[405] Savage, B. D. et al., 2011, ApJ, 731, 14

[406] Danforth, C. W. et al., 2016, ApJ, 817, 111

[407] Fabian, A. C. et al., 2003, MNRAS, 344, L43

[408] Willis, J. P. et al., 2013, MNRAS, 430, no. 1, 134

[409] Mantz, A. et al., 2019, BAAS, 51, no. 3, 279

[410] LSST Dark Energy Science Collaboration, 2012, arXiv e-prints, arXiv:1211.0310

[411] Benson, B. A. et al., 2014, in *Proc. SPIE, Society of Photo-Optical Instrumentation Engineers (SPIE) Conference Series*, vol. 9153, 91531P

[412] De Bernardis, F. et al., 2016, in *Proc. SPIE, Society of Photo-Optical Instrumentation Engineers (SPIE) Conference Series*, vol. 9910, 991014

[413] Ade, P. et al., 2019, JCAP, 2019, no. 2, 056

[414] Stacey, G. J. et al., 2018, in *Proc. SPIE, Society of Photo-Optical Instrumentation Engineers (SPIE) Conference Series*, vol. 10700, 107001M

[415] Abazajian, K. N. et al., 2016, in *CMB-S4 Science Book, First Edition*, arXiv:1610.02743

[416] Mantz, A. et al., 2019, in *"The Future Landscape of High-Redshift Galaxy Cluster Science"; Astro2020 science white paper*, `http://tinyurl.com/yxlj5zwq`

[417] Ettori, S. et al., 2013, arXiv e-prints, arXiv:1306.2322

[418] Pointecouteau, E. et al., 2013, arXiv e-prints, arXiv:1306.2319

[419] Gaspari, M., Ruszkowski, M. & Sharma, P., 2012, ApJ, 746, 94

[420] McDonald, M. et al., 2018, ApJ, 858, 45

[421] Aird, J. et al., 2015, MNRAS, 451, no. 2, 1892

[422] Ehlert, S. et al., 2015, MNRAS, 446, no. 3, 2709

[423] Miller, T. B. et al., 2018, Nature, 556, no. 7702, 469

[424] Jiang, L. et al., 2018, Nature Astronomy, 2, 962

[425] Riess, A. G. et al., 2019, ApJ, 876, no. 1, 85

[426] Abbott, T. M. C. et al., 2018, Phys. Rev. D, 98, no. 4, 043526

[427] Allen, S. W., Evrard, A. E. & Mantz, A. B., 2011, ARA&A, 49, no. 1, 409

[428] Timmes, F. et al., 2019, in *"Catching Element Formation In The Act ; The Case for a New MeV Gamma-Ray Mission: Radionuclide Astronomy in the 2020s"; Astro2020 science white paper*, `http://tinyurl.com/y694lrj3`

[429] Fukugita, M. & Peebles, P. J. E., 2004, ApJ, 616, 643

[430] Gallazzi, A. et al., 2005, MNRAS, 362, 41

[431] Rafelski, M. et al., 2012, ApJ, 755, 89

[432] Lehner, N. et al., 2019, arXiv e-prints, arXiv:1902.10147

[433] Rahmati, A. & Oppenheimer, B. D., 2018, MNRAS, 476, 4865

[434] Cen, R. & Ostriker, J. P., 2006, ApJ, 650, 560

[435] Cen, R., 2012, ApJ, 753, 17

[436] Churazov, E. et al., 2019, BAAS, 51, no. 3, 325

[437] Corrales, L. et al., 2019, in *"Astromineralogy of interstellar dust with X-ray spectroscopy"; Astro2020 science white paper*, `http://tinyurl.com/y4ypjhda`

[438] Jenkins, E. B., 2009, ApJ, 700, no. 2, 1299

[439] Valencic, L. et al., 2019, in *"Probing the Structure of Interstellar Dust from Micron to Kpc Scales with X-ray Imaging"; Astro2020 science white paper*, `http://tinyurl.com/y5cxy45u`

[440] McKee, C. F. & Ostriker, E. C., 2007, ARA&A, 45, no. 1, 565

[441] Heyer, M. & Dame, T. M., 2015, ARA&A, 53, 583

[442] Onus, A., Krumholz, M. R. & Federrath, C., 2018, MNRAS, 479, 1702

[443] Khullar, S. et al., 2019, arXiv e-prints, arXiv:1902.00934

[444] Goodman, A. A. et al., 1998, ApJ, 504, no. 1, 223

[445] Rathborne, J. M. et al., 2015, ApJ, 802, no. 2, 125

[446] Uehara, K. et al., 2017, in R. M. Crocker, S. N. Longmore & G. V. Bicknell, eds., *The Multi-Messenger Astrophysics of the Galactic Centre*, *IAU Symposium*, vol. 322, 162–163

[447] Federrath, C. et al., 2016, ApJ, 832, no. 2, 143

[448] Churazov, E. et al., 2017, MNRAS, 465, 45

[449] Churazov, E. et al., 2019, in *"Probing 3D Density and Velocity Fields of ISM in Centers of Galaxies with Future X-Ray Observations"; Astro2020 science white paper*, `http://tinyurl.com/y6bg3lr5`

[450] Lee, J. C. & Ravel, B., 2005, ApJ, 622, 970

[451] Lee, J. C. et al., 2009, ApJ, 702, 970

[452] Corrales, L. R. et al., 2016, MNRAS, 458, 1345

[453] Hoffman, J. & Draine, B. T., 2016, ApJ, 817, 139

[454] Zeegers, S. T. et al., 2017, A&A, 599, A117

[455] Overbeck, J. W., 1965, ApJ, 141, 864

[456] Mathis, J. S. & Lee, C.-W., 1991, ApJ, 376, 490

[457] Draine, B. T., 2003, ApJ, 598, 1026

[458] Pooley, D. et al., 2019, in *"The Most Powerful Lenses in the Universe: Quasar Microlensing as a Probe of the Lensing Galaxy"; Astro2020 science white paper*, `http://tinyurl.com/yyvfejdk`

[459] Calzetti, D. et al., 2019, in *"How Do Stars Form? Open Questions on the Stellar Initial Mass Function"; Astro2020 science white paper*, `http://tinyurl.com/y58hcwql`

[460] Schechter, P. L. et al., 2014, ApJ, 793, no. 2, 96

[461] National Academies of Sciences, E. & Medicine, 2018, *Exoplanet Science Strategy* (Washington, DC: The National Academies Press)

[462] Drake, J. et al., 2019, in *"High-Energy Photon and Particle Effects on Exoplanet Atmospheres and Habitability"; Astro2020 science white paper*, `http://tinyurl.com/yygedrtl`

[463] Owen, J. E. & Jackson, A. P., 2012, MNRAS, 425, no. 4, 2931

[464] Drake, J. et al., 2019, BAAS, 51, no. 3, 113

[465] Brain, D. A. et al., 2016, Journal of Geophysical Research (Planets), 121, no. 12, 2364

[466] Wood, B. E. et al., 2014, ApJ, 781, no. 2, L33

[467] Wood, B. E. et al., 2005, ApJ, 628, L143

[468] Wargelin, B. J. & Drake, J. J., 2002, ApJ, 578, no. 1, 503

[469] Drake, J. J. et al., 2013, ApJ, 764, 170

[470] Segura, A. et al., 2010, Astrobiology, 10, no. 7, 751

[471] Airapetian, V. S. et al., 2016, Nature Geoscience, 9, no. 6, 452

[472] Crosley, M. K. & Osten, R. A., 2018, ApJ, 856, 39

[473] Crosley, M. K. & Osten, R. A., 2018, ApJ, 862, 113

[474] Alvarado-Gómez, J. D. et al., 2019, (Submitted to ApJ Letters)

[475] Argiroffi, C. et al., 2019, Nature Astronomy, 328

[476] Haisch, B. M. et al., 1983, ApJ, 267, 280

[477] Moschou, S.-P. et al., 2017, ApJ, 850, no. 2, 191

[478] Bhardwaj, A., Lisse, C. M. & Dennerl, K., 2014, in T. Spohn, D. Breuer & T. V. Johnson, eds., *Encyclopedia of the Solar System* (Boston: Elsevier), 1019, third ed.

[479] Wargelin, B. J. et al., 2004, ApJ, 607, no. 1, 596

[480] Dennerl, K., 2008, Planet. Space Sci, 56, no. 10, 1414

[481] Elsner, R. F. et al., 2005, JGR: Space Physics, 110, no. A1, A01207

[482] Bhardwaj, A. et al., 2007, JASTP, 69, no. 1, 179

[483] Branduardi-Raymont, G. et al., 2008, JGRA, 113, no. A2, A02202

[484] Dunn, W. R. et al., 2017, Nature Astronomy, 1, no. 11, 758

[485] Gladstone, G. R. et al., 2002, Nature, 415, 1000

[486] Bodewits, D. et al., 2007, A&A, 469, 1183

[487] Bhardwaj, A. et al., 2007, Planet. Space Sci., 55, 1135

[488] Snios, B. et al., 2016, ApJ, 818, no. 2, 199

[489] Jackman, C. M. et al., 2018, JGR: Space Physics, 123, no. 11, 9204

[490] Ness, J.-U., Schmitt, J. H. M. M. & Robrade, J., 2004, A&A, 414, no. 3, L49

[491] Bhardwaj, A. et al., 2005, ApJ, 624, no. 2, L121

[492] Branduardi-Raymont, G. et al., 2010, A&A, 510, A73

[493] Tremblay, G. R. et al., 2018, LPI Contributions, 2100, 3024

[494] Lisse, C. M. et al., 1996, Science, 274, no. 5285, 205

[495] Kharchenko, V. et al., 2003, ApJ, 585, L73

[496] Bodewits, D. et al., 2004, Physica Scripta, 70, no. 6, C17

[497] Snios, B., Lichtman, J. & Kharchenko, V., 2018, ApJ, 852, no. 2, 138

[498] Markevitch, M. et al., 2019, in *"Physics of cosmic plasmas from high angular resolution X-ray imaging of galaxy clusters"; Astro2020 science white paper*, `https://tinyurl.com/y4b44cac`

[499] Caprioli, D. et al., 2019, arXiv e-prints, arXiv:1903.08751

[500] Sanders, J. et al., 2018, Chandra News, 25, 1

[501] Loeb, A., 2002, New Astronomy, 7, no. 6, 279

[502] Sijacki, D. & Springel, V., 2006, MNRAS, 371, 1025

[503] Su, K.-Y. et al., 2017, MNRAS, 471, no. 1, 144

[504] Su, K.-Y. et al., 2019, MNRAS, 487, no. 3, 4393

[505] Hopkins, P. F. et al., 2019, arXiv e-prints, arXiv:1905.04321

[506] Schekochihin, A. A. et al., 2008, Phys. Rev. Lett., 100, no. 8, 081301

[507] Kunz, M. W., Schekochihin, A. A. & Stone, J. M., 2014, Phys. Rev. Lett., 112, no. 20, 205003

[508] Komarov, S. V. et al., 2016, MNRAS, 460, no. 1, 467

[509] Roberg-Clark, G. T. et al., 2018, ApJ, 867, no. 2, 154

[510] ZuHone, J. A., Markevitch, M. & Lee, D., 2011, ApJ, 743, no. 1, 16

[511] ZuHone, J. A. et al., 2013, Astrophys. J., 762, 69

[512] Ichinohe, Y. et al., 2017, MNRAS, 467, no. 3, 3662

[513] Wang, Q. H. S. & Markevitch, M., 2018, ApJ, 868, no. 1, 45

[514] Kraft, R. P. et al., 2017, ApJ, 848, no. 1, 27

[515] Su, Y. et al., 2017, ApJ, 834, no. 1, 74

[516] Schuecker, P. et al., 2004, A&A, 426, 387

[517] Zhuravleva, I. et al., 2015, MNRAS, 450, no. 4, 4184

[518] Wang, Q. H. S., Markevitch, M. & Giacintucci, S., 2016, ApJ, 833, no. 1, 99

[519] Werner, N. et al., 2016, MNRAS, 455, no. 1, 846

[520] Ichinohe, Y. et al., 2019, MNRAS, 483, no. 2, 1744

[521] Fox, D. C. & Loeb, A., 1997, ApJ, 491, no. 2, 459

[522] Markevitch, M. et al., 1996, ApJ, 456, 437

[523] Markevitch, M. & Vikhlinin, A., 2007, Phys. Rep., 443, no. 1, 1

[524] Russell, H. R. et al., 2012, MNRAS, 423, no. 1, 236

[525] Wang, Q. H. S., Giacintucci, S. & Markevitch, M., 2018, ApJ, 856, no. 2, 162

[526] Vink, J. & Laming, J. M., 2003, ApJ, 584, 758

[527] Eriksen, K. A. et al., 2011, ApJ, 728, L28

[528] Laming, J. M., 2015, ApJ, 805, 102

[529] van Weeren, R. J. et al., 2019, Space Sci. Rev., 215, 16

[530] Kaastra, J. S., Bykov, A. M. & Werner, N., 2009, A&A, 503, 373

[531] Brunetti, G. & Lazarian, A., 2007, MNRAS, 378, 245

[532] Brunetti, G. & Lazarian, A., 2011, MNRAS, 410, 127

[533] in *Special Section on the* Lynx *X-Ray Observatory, J. Astron. Telesc. Instrum. Syst., 2019, 5(2)*, all of the papers are open source and online at: `https://tinyurl.com/yxrd6w38`

[534] Weisskopf, M. C. et al., 2000, in J. E. Truemper & B. Aschenbach, eds., *Proc. SPIE*, *Society of Photo-Optical Instrumentation Engineers (SPIE) Conference Series*, vol. 4012, 2–16

[535] Chase, R. C. & van Speybroeck, L. P., 1973, Appl. Opt., 12, 1042

[536] Chandra X-ray Center, Chandra Project Science, MSFC & Chandra IPI Teams, 2018, The Chandra Proposers' Observatory Guide, Version 21.0

[537] Zhang, W. W. et al., 2019, Journal of Astronomical Telescopes, Instruments, and Systems, 5, 021012

[538] Civitani, M. M. et al., 2019, Journal of Astronomical Telescopes, Instruments, and Systems, 5, 021014

[539] Kilaru, K. et al., 2019, Journal of Astronomical Telescopes, Instruments, and Systems, 5, 021010

[540] Bishop, N. et al., 2019, Journal of Astronomical Telescopes, Instruments, and Systems, 5, 021005

[541] DeRoo, C. T. et al., 2018, Journal of Astronomical Telescopes, Instruments, and Systems, 4, 019004

[542] Arenberg, J. W., 2019, Journal of Astronomical Telescopes, Instruments, and Systems, 5, 021016

[543] 2016, Structural Design and Test Factors of Safety for Spaceflight Hardware, https://standards.nasa.gov/standard/nasa/nasa-std-5001

[544] Garmire, G. P. et al., 2003, in J. E. Truemper & H. D. Tananbaum, eds., *Proc. SPIE*, *Society of Photo-Optical Instrumentation Engineers (SPIE) Conference Series*, vol. 4851, 28–44

[545] Turner, M. J. L. et al., 2001, A&A, 365, L27

[546] Strüder, L. et al., 2001, A&A, 365, L18

[547] Koyama, K. et al., 2007, PASJ, 59, 23

[548] Falcone, A. D. et al., 2019, Journal of Astronomical Telescopes, Instruments, and Systems, 5, 021019

[549] Hull, S. V. et al., 2019, Journal of Astronomical Telescopes, Instruments, and Systems, 5, 021018

[550] Bautz, M. W. et al., 2019, Journal of Astronomical Telescopes, Instruments, and Systems, 5, 021015

[551] Kenter, A. et al., 2017, in *Proc. SPIE*, *Society of Photo-Optical Instrumentation Engineers (SPIE) Conference Series*, vol. 10397, 1039703

[552] https://wwwastro.msfc.nasa.gov/spectops/magbroom/

[553] Ferreira, I. et al., 2018, in *Proc. SPIE*, *Society of Photo-Optical Instrumentation Engineers (SPIE) Conference Series*, vol. 10699, 106994A

[554] 2019, Users Guide to the XMM-Newton Science Analysis System, https://tinyurl.com/y2rmag57

[555] Günther, H. M. & Heilmann, R. K., 2019, Journal of Astronomical Telescopes, Instruments, and Systems, 5, 021003

[556] McEntaffer, R. L., 2019, Journal of Astronomical Telescopes, Instruments, and Systems, 5, 021002

[557] Canizares, C. R. et al., 2005, PASP, 117, no. 836, 1144

[558] Paerels, F., 2010, Space Sci. Rev., 157, no. 1-4, 15

[559] Beuermann, K. P., Braeuninger, H. & Truemper, J., 1978, Appl. Opt., 17, no. 15, 2304

[560] Bandler, S. R. et al., 2019, Journal of Astronomical Telescopes, Instruments, and Systems, 5, 021017

[561] Risaliti, G. et al., 2013, Nature, 494, no. 7438, 449

[562] Fabian, A. C. et al., 2017, MNRAS, 467, no. 3, 2566

[563] Nardini, E. et al., 2015, Science, 347, no. 6224, 860

[564] Lansbury, G. B. et al., 2014, ApJ, 785, no. 1, 17

[565] Bauer, F. E. et al., 2015, ApJ, 812, no. 2, 116

[566] Kara, E. et al., 2015, MNRAS, 446, no. 1, 737

[567] Walton, D. J. et al., 2018, ApJ, 856, no. 2, 128

[568] Hitomi Collaboration et al., 2016, Nature, 535, no. 7610, 117

[569] Barret, D. et al., 2016, in *Proc. SPIE*, *Society of Photo-Optical Instrumentation Engineers (SPIE) Conference Series*, vol. 9905, 99052F

[570] Smith, S. J. et al., 2019, Journal of Astronomical Telescopes, Instruments, and Systems, 5, 021008

[571] Irwin, K. D. & Hilton, G. C., 2005, in C. Enss, ed., *Cryogenic Particle Detection*, *Topics in Applied Physics*, vol. 99, 63–150

[572] Mates, J. A. B. et al., 2017, Applied Physics Letters, 111, no. 6, 062601

[573] Bennett, D. A. et al., 2019, Journal of Astronomical Telescopes, Instruments, and Systems, 5, 021007

[574] DiPirro, M. et al., 2019, Journal of Astronomical Telescopes, Instruments, and Systems, 5, 021006

[575] Eckart, M. E. et al., 2019, Journal of Astronomical Telescopes, Instruments, and Systems, 5, 021020

[576] de Vries, C. P. et al., 2018, Journal of Astronomical Telescopes, Instruments, and Systems, 4, 011204

[577] Macculi, C. et al., 2016, in *Proc. SPIE*, *Society of Photo-Optical Instrumentation Engineers (SPIE) Conference Series*, vol. 9905, 99052K

[578] Muhlfelder, B. et al., 2001, Verification of payload on-orbit radiation environment, S0610, https://tinyurl.com/yxqsulmq

[579] Delorme, Y. et al., 2005, in *Sixteenth International Symposium on Space Terahertz Technology*, 444–448

[580] Frunzio, L., Cristiano, R. & Pagano, S., 1998, Japanese Journal of Applied Physics Supplement, 37, no. S2, 40

[581] Barth, J. L., Isaacs, J. C. & Poivey, C., 2000, The Radiation Environment for the Next Generation Space Telescope, https://tinyurl.com/y3wpvq5v

[582] Sakai, K. et al., 2019, Journal of Astronomical Telescopes, Instruments, and Systems, 5, 021013

[583] Farquhar, R. W., 1970, Libration point satellite stationkeeping control, https://tinyurl.com/yybpldjv

[584] Yoon, S., Rosales, J. & Richon, K., 2014, no. 20140008973 in 24th International Symposium on Space Flight Dynamics, https://tinyurl.com/yx947s54

[585] Eckart, M. E. et al., 2018, Journal of Astronomical Telescopes, Instruments, and Systems, 4, 021406

[586] Foster, A. R. et al., 2012, ApJ, 756, no. 2, 128

[587] On-Orbit Satellite Servicing Study Project Report, 2010, https://tinyurl.com/y23o8tym

[588] Cooperative Service Valve Fact Sheet, 2017, https://tinyurl.com/yyynvvbn

[589] Zhang, W. W. et al., 2019, Journal of Astronomical Telescopes, Instruments, and Systems, 5, 021012

[590] Yao, Y. et al., 2019, Journal of Astronomical Telescopes, Instruments, and Systems, 5, 021011

[591] Civitani, M. M. et al., 2019, Journal of Astronomical Telescopes, Instruments, and Systems, 5, 021014

[592] Kilaru, K. et al., 2019, Journal of Astronomical Telescopes, Instruments, and Systems, 5, 021010

[593] Civitani, M. et al., 2018, in *Proc. SPIE*, *Society of Photo-Optical Instrumentation Engineers (SPIE) Conference Series*, vol. 10699, 106990T

[594] Kilaru, K., Kolodziejczak, J. & Atkins, C., 2017, in *Proc. SPIE*, *Society of Photo-Optical Instrumentation Engineers (SPIE) Conference Series*, vol. 10399, 103991F

[595] Civitani, M. M. et al., 2012, in *Proc. SPIE*, *Society of Photo-Optical Instrumentation Engineers (SPIE) Conference Series*, vol. 8443, 84430Q

[596] Murray, S. S. et al., 2008, in *Proc. SPIE*, *Society of Photo-Optical Instrumentation Engineers (SPIE) Conference Series*, vol. 7011, 70111J

[597] Gubarev, M. et al., 2016, in *Proc. SPIE*, *Society of Photo-Optical Instrumentation Engineers (SPIE) Conference Series*, vol. 9905, 99051V

[598] Civitani, M. M. et al., 2017, in *Proc. SPIE*, *Society of Photo-Optical Instrumentation Engineers (SPIE) Conference Series*, vol. 10399, 103990W

[599] Hull, S. V. et al., 2019, Journal of Astronomical Telescopes, Instruments, and Systems, 5, 021018

[600] Kenter, A., Kraft, R. & Gauron, T., 2018, in *Proc. SPIE*, *Society of Photo-Optical Instrumentation Engineers (SPIE) Conference Series*, vol. 10762, 1076209

[601] Bautz, M. W. et al., 2019, Journal of Astronomical Telescopes, Instruments, and Systems, 5, 021015

[602] Heilmann, R. K. et al., 2016, in *Proc. SPIE*, *Society of Photo-Optical Instrumentation Engineers (SPIE) Conference Series*, vol. 9905, 99051X

[603] Heilmann, R. K. et al., 2017, in *Proc. SPIE*, *Society of Photo-Optical Instrumentation Engineers (SPIE) Conference Series*, vol. 10399, 1039914

[604] Heilmann, R. K. et al., 2018, in *Proc. SPIE*, *Society of Photo-Optical Instrumentation Engineers (SPIE) Conference Series*, vol. 10699, 106996D

[605] Heilmann, R. K. et al., 2019, Appl. Opt., 58, no. 5, 1223

[606] Günther, H. M. & Heilmann, R. K., 2019, Journal of Astronomical Telescopes, Instruments, and Systems, 5, 021003

[607] Canizares, C. R., Schattenburg, M. L. & Smith, H. I., 1986, in J. L. Culhane, ed., *Proc. SPIE*, *Society of Photo-Optical Instrumentation Engineers (SPIE) Conference Series*, vol. 597, 253–260

[608] McEntaffer, R. L., 2019, Journal of Astronomical Telescopes, Instruments, and Systems, 5, 021002

[609] Miles, D. M. et al., 2018, ApJ, 869, no. 2, 95

[610] Miles, D. M. et al., 2018, in *Proc. SPIE*, *Society of Photo-Optical Instrumentation Engineers (SPIE) Conference Series*, vol. 10699, 106996K

[611] Donovan, B. D. et al., 2018, in *Proc. SPIE*, *Society of Photo-Optical Instrumentation Engineers (SPIE) Conference Series*, vol. 10699, 106993U

[612] Bandler, S. R. et al., 2019, Journal of Astronomical Telescopes, Instruments, and Systems, 5, 021017

[613] Smith, S. J. et al., 2019, Journal of Low Temperature Physics, submitted, arXiv:1908.02687

[614] Mates, J. A. B. et al., 2017, Applied Physics Letters, 111, no. 6, 062601

[615] Yoon, W. et al., 2018, Journal of Low Temperature Physics, 193, no. 3-4, 258

[616] Bennett, D. A. et al., 2019, Journal of Astronomical Telescopes, Instruments, and Systems, 5, 021007

[617] Jackson, B. D. et al., 2016, in *Proc. SPIE*, *Society of Photo-Optical Instrumentation Engineers (SPIE) Conference Series*, vol. 9905, 99052I

[618] Eckart, M. E. et al., 2019, Journal of Astronomical Telescopes, Instruments, and Systems, 5, 021020

[619] Smith, S. J. et al., 2019, Journal of Astronomical Telescopes, Instruments, and Systems, 5, 021008

[620] Bitten, R. E., Shinn, S. A. & Emmons, D. L., 2019, in *2019 IEEE Aerospace Conference*, 1–13

[621] Arenberg, J. W., 2019, Journal of Astronomical Telescopes, Instruments, and Systems, 5, 021016

[622] Arenberg, J. & Zhang, W., 2019, in *AAS/High Energy Astrophysics Division*, AAS/High Energy Astrophysics Division, 109.45

[623] Prince, A., 2017, ICEAA Professional Development & Training Workshop

[624] 2019, Journal of Astronomical Telescopes, Instruments, and Systems, 5, `https://tinyurl.com/yxrd6w38`

[625] Kelly, E. V., 2009, PMI Global Congress 2009, `https://tinyurl.com/yxjwtlso`

[626] Cole, S. K. et al., 2013, Technology Estimating: A Process to Determine the Cost and Schedule of Space Technology Research and Development, `https://tinyurl.com/yxrcvyxz`

[627] Hogg, D. W., 2001, AJ, 121, no. 2, 1207

[628] Condon, J. J., 1974, ApJ, 188, 279

[629] Lehmer, B. D. et al., 2012, ApJ, 752, no. 1, 46

[630] Bouwens, R. J. et al., 2004, ApJ, 611, no. 1, L1

[631] Lehmer, B. D. et al., 2010, ApJ, 724, no. 1, 559

[632] Mineo, S. et al., 2014, MNRAS, 437, no. 2, 1698

[633] Prestwich, A. H. et al., 2013, ApJ, 769, 92

[634] Basu-Zych, A. R. et al., 2013, ApJ, 774, 152

[635] Douna, V. M. et al., 2015, A&A, 579, A44

[636] Basu-Zych, A. R. et al., 2016, ApJ, 818, 140

[637] Brorby, M. et al., 2016, MNRAS, 457, 4081

[638] Kennicutt, R. C., Jr., 1998, ARA&A, 36, 189

[639] Yukita, M. et al., 2016, ApJ, 824, no. 2, 107

[640] Hickox, R. C. & Markevitch, M., 2007, ApJ, 661, no. 2, L117

[641] von Kienlin, A. et al., 2018, in *Proc. SPIE*, *Society of Photo-Optical Instrumentation Engineers (SPIE) Conference Series*, vol. 10699, 106991I

[642] Snowden, S. L. et al., 1997, ApJ, 485, no. 1, 125

[643] Galeazzi, M. et al., 2007, ApJ, 658, no. 2, 1081

[644] Vikhlinin, A. et al., 1995, ApJ, 451, 542

[645] Freeman, P. E. et al., 2002, ApJS, 138, no. 1, 185

[646] Neyman, J., Pearson, E. S. & Pearson, K., 1931, Phil. Trans. of the Royal Society of London, Series A, 231, 289

[647] Pratt, W. K., 1978, *Digital Image Processing* (Wiley)

[648] Mahony, E. K. et al., 2010, MNRAS, 401, no. 2, 1151

[649] Klypin, A. A., Trujillo-Gomez, S. & Primack, J., 2011, ApJ, 740, no. 2, 102

SCIENCE WORKING GROUP MEMBERS

Working Group co-chairs are listed in ***Bold***

Cycles of Baryons In *&* Out *of* Galaxies

Joel Bregman
Juna Kollmeier
Andrey Kravtsov
Mehmet Alpaslan
Gabriella Alvarez
Camille Avestruz
Akos Bogdan
Massimiliano Bonamente
Lia Corrales
Massimiliano Galeazzi
Oleg Gnedin
Li Jiangtao
Dong-Woo Kim
Ralph Kraft
Fabrizio Nicastro
Susan Nulsen
Benjamin Oppenheimer
Frits Paerels
Scott Randall
Mateusz Ruszkowski
Kosuke Sato
Grant Tremblay
Eugenio Ursino
Lynne Valencic
Alexey Vikhlinin
Norbert Werner
Noriko Yamasaki

First Accretion Light

Niel Brandt
Piero Madau
Daniel Stern
James Aird
Nico Cappelluti
Francesca Civano
Andrea Comastri
Paolo Coppi
Anastasia Fialkov
Francesca Fornasini
Elena Gallo
Mélanie Habouzit
Zoltan Haiman
Philip Kaaret
Demosthenes Kazanas
Ildar Khabibullin
Joseph Lazio
Bin Luo
Mar Mezcua
Takamitsu Miyaji
Dan Schwartz
Ohad Shemmer
Benny Trakhtenbrot
Cristian Vignali
Fabio Vito
Marta Volonteri

Evolution of Structure *&* AGN Populations

Steven Allen
Ryan Hickox
Tesla Jeltema
Daniel Stern
James Aird
Felipe Andrade-Santos
Camille Avestruz
David Ballantyne
Elizabeth Blanton
Rebecca Canning
Chien-Ting Chen
Francesca Civano
Ashkbiz Danehkar
Abraham Falcone
Francesca Fornasini
Elena Gallo
Danielle Gurgew
Demosthenes Kazanas
Michael Koss
Erwin Lau
Adam Mantz
Kyoko Matsushita
Michael McDonald
Beatriz Mingo
Takamitsu Miyaji
Daisuke Nagai
Ming Sun
Benny Trakhtenbrot
Sara Turriziani
Panayiotis Tzanavaris
Stephen Walker
Reinout van Weeren
Cristian Vignali

X-rays *in the* Multiwavelength/Messenger Era

Robert Petre
Randall Smith
Vallia Antoniou
Esra Bulbul
Becky Canning
Chien-Ting Chen
Valerie Connaughton
Ashkbiz Danehkar
Yuichiro Ezoe
Abe Falcone
Federico Fraschetti
Suvi Gezari
Richard Griffiths
Hans Guenther
David Kieda
Albert Kong
Michael Koss
Peter Maksym
Adam Mantz
Herman Marshall
Michael McCollough
Patrick Motl
Frits Paerels
Alberto Sadun
Marcos Santander
Gregory Sivakoff
Francesco Tombesi
Grant Tremblay
Eleonora Troja
Sara Turriziani
Tonia Venters

SCIENCE WORKING GROUP MEMBERS

continued from previous page

Physics *of* Feedback

Megan Donahue
Christopher Reynolds
Nahum Arav
Elizabeth Blanton
Laura Brenneman
Teddy Cheung
Ashkbiz Danehkar
Massimo Gaspari
Oleg Gnedin
Martin Hardcastle
Sebastian Heinz
Julie Hlavacek-Larrondo
Edmund Hodges-Kluck
Chritine Jones
Alvaro Labiano
Sibasish Laha
Peter Maksym
Alex Markowitz
Herman Marshall
Francesco Massaro
Eileen Meyer
Jon Miller
Brian Morsony
Emanuele Nardini
Joey Neilsen
Paul Nulsen
Scott Randall
Mateusz Ruszkowski
Eric Schlegel
Norbert Schulz
Dan Schwartz
Paul Sell
Aneta Siemiginowska
Gregory Sivakoff
Lukasz Stawarz
Douglas Swartz
Makoto Tashiro
Francesco Tombesi
Grant Tremblay
Norbert Werner
Dan Wilkins
Mihoko Yukita
Shuo Zhang
Irina Zhuravleva

Physics *of* High Density Matter *&* Accretion

Feryal Özel
Frits Paerels
Christopher Reynolds
Frederick Baganoff
Slavko Bogdanov
Laura Brenneman
Deepto Chakrabarty
Filippo D'Ammando
Keigo Fukumura
Massimiliano Galeazzi
Javier Garcia
Hans Guenther
Sebastien Guillot
Craig Heinke
Paul Hemphill
Jeroen Homan
Erin Kara
Oleg Kargaltsev
Denis Leahy
Simin Mahmoodifar
Peter Maksym
Herman Marshall
Michael McCollough
Jon Miller
Cole Miller
Patrick Motl
Emanuele Nardini
Joey Neilsen
Eric Perlman
David Pooley
Bettina Posselt
Dimitrios Psaltis
Roger Romani
Norbert Schulz
Gregory Sivakoff
James Steiner
Francesco Tombesi
John Tomsick
Eleonora Troja
Giacomo Vianello
Dan Wilkins
Shuo Zhang
Michael Zingale

Stellar Lifecycles

Laura Lopez
Rachel Osten
Dave Pooley
Andy Ptak
Jeff Andrews
Vallia Antoniou
Frederick Baganoff
Aya Bamba
Arash Bodaghee
Slavko Bogdanov
Daniel Castro
Robin Corbet
Lia Corrales
Federico Fraschetti
Hans Guenther
Kenji Hamaguchi
Craig Heinke
David Huenemoerder
Margarita Karovska
Vinay Kashyap
Albert Kong
Denis Leahy
Maurice Leutenegger
Michael McCollough
Rodolfo Montez
Lidia Oskinova
Thomas Pannuti
Dan Patnaude
Sangwook Park
Paul Plucinsky
Katja Pottschmidt
Samar Safi-Harb
Manami Sasaki
Eric Schlegel
Norbert Schulz
Paul Sell
Gregory Sivakoff
Pat Slane
Douglas Swartz
John Tomsick
Eleonora Troja
Panayiotis Tzanavaris
Maureen van den Berg
Brad Wargelin
Ben Williams
Brian Williams
Scott Wolk
Andreas Zezas

LYNX SCIENCE SUPPORT OFFICE

GRANT **TREMBLAY**
Science Support Office Lead

JOHN **ZuHONE** FRANCESCA **CIVANO**
ERIC **MANDEL** BENJAMIN **OPPENHEIMER** DAN **PATNAUDE**
Center *for* Astrophysics | Harvard *&* Smithsonian

MICHAEL **McDONALD** DAVID **PRINCIPE** HANS MORITZ **GÜNTHER**
MIT Kavli Institute *for* Astrophysics *&* Space Research, Massachusetts Institute *of* Technology

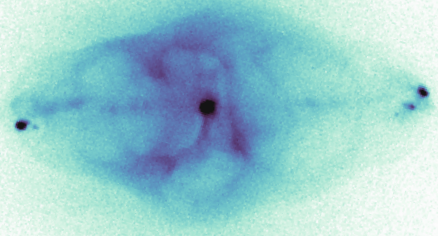

ADDITIONAL CONTRIBUTORS

Tom Alcroft
Julián David Alvarado-Gómez
Marcelo Alvarez
Jonathan Arenberg
Antara Basu–Zych
Roger Brissenden
Akos Bogdan
Slavko Bogdanov
Herve Bourdin
Laura Brenneman
Nancy Brickhouse
Esra Bulbul
Rebecca Canning
Eugene Churazov
Jason Conry
Lia Corrales
Romeel Davé
Larry David
Jeremy Drake
William Dunn
Ian Evans
Clarke Esmerian
Giuseppina Fabbiano
Anastasia Fialkov
Elena Gallo
Julie Hlavacek-Larrondo
Edmund Hodges-Kluck
Una Hwang
Ildar Khabibullin
Sibasish Laha
Martin Laming
Bret Lehmer
Andrew MacFadyen
W. Peter Maksym
Adam Mantz
Maxim Markevitch
Alex Markowitz
Jonathan McDowell
Andrei Mesinger
Joey Neilsen
Paul Nulsen
Salvatore Orlando
Fabio Paccuci
Paul Plucinsky
Katja Poppenhauger
Scott Randall
Arnold Rots
Mateusz Ruszkowski
Evan Schneider
Pat Slane
Bradford Snios
Emanuele Sobacchi
Mattia Sormani
Nicholas Stone
Ming Sun
Yike Tang
Francesco Tombesi
Lynne Valencic
Reinout Van Weeren
Eli Visbal
Fabio Vito
Stephen Walker
Rainer Weinberger
Nastasha Wijers
Belinda Wilkes
Scott Wolk
Andreas Zezas
Irina Zhuravleva

LYNX ENGINEERING SUPPORT TEAM

ALEX **DOMINGUEZ**
Team Lead

RANDY **HOPKINS**
Team Lead

ANDREW **SCHNELL**
Team Lead

MICHAEL **ALLISON** JEFF **APPLE** MIKE **BAYSINGER**
TYRONE **BOSWELL** JENNIFER **BRACKEN** TERESA **BROWN**
TERRY **BROWN** PETE **CAPIZZO** BILL **COOKE**
LEO **FABISINSKI** ALEX **FEW** JAY **GARCIA**
ERIC **GILLIGAN** LEVIN **GUILLERMO** JIM **HOWARD**
J. BRENT **KNIGHT** JOE **MINNOW** EMILY **MITCHELL** JACK **MULQUEEN**
BEN **NEIGHBORS** RACHEL **RIVERA** MITCHELL **RODRIGUEZ**
JUSTIN **ROWE** IAN **SMALL** JAMES **STURM**
ROB **SUGGS** STEVE **SUTHERLIN**

NASA Marshall Space Flight Center | Advanced Concepts Office

Lynx Mirror Assembly Trade Team (LMAT)

Gary Blackwood
Lynn Allen
Jon Arenberg
Charlie Atkinson
Jaya Bajpayee
Chip Barnes
Terri Brandt
David Broadway
Vadim Burwitz
Marta Civitani
Lester Cohen
Casey DeRoo
Daniel Evans
Mark Freeman
Jessica Gaskin
Karen Gelmis
Paul Glenn
Jennifer Gregory
Ryan Hickox
Steve Jordan
Gabe Karparti
Bernard Kelly
Kiran Kilaru
Gary Matthews
Ryan McClelland
Ted Mooney
John Nousek
Feryal Özel
Frits Paerels
Robert Petre
Denise Podolski
Bill Purcell
Paul Reid
Rita Sambruna
Mark Schattenburg
Eric Schwartz
Peter Solly
Daniel Stern
Doug Swartz
Alexey Vikhlinin
Dave Windt
William Zhang

Model-Based Systems Engineering Team

Marc Gethers
Ashleigh Lynch
Elizabeth Patterson
Isabeta Rountree
Dale Thomas

Technology Assessment & Roadmap Team

Robert Bitten
Angie Buckley
Frank Curran
Brett Drake
Linda Herrel
Mark Skinner

Cost & Technical Evaluation Team

Hank Apgar
Patrick Malone

INDUSTRY PARTNERS & REVIEW TEAMS

LOCKHEED MARTIN CORPORATION
Greg Feller, David Frank, Allison Nordt, & Jeff Olson

NORTHROP GRUMMAN CORPORATION
Jonathan Arenberg, Charlie Atkinson, Mike McEachen, & Perry Knollenberg

BALL AEROSPACE & TECHNOLOGIES CORP.
Steve Jordan, Mark Kilpatrick, & Bill Purcell

HARRIS CORPORATION
Keith Havey, Ted Mooney, & Lynn Allen

LUXEL, INC.
Ben Zeiger

HYPRES, INC.
Deepnarayan Gupta

CREARE, INC.
Mark Zagarola

ORBITAL ATK
Mike McEachen

NATIONAL INSTITUTE *for* STANDARDS & TECHNOLOGY
Charles Tarrio

LABORATORY *for* ATMOSPHERIC & SPACE SCIENCES
Andrew Jones

LYNX RED TEAM

CHRYSSA **KOUVELIOTOU**
Chair

JAYA **BAJPAYEE** VADIM **BURWITZ** JAN-WILLEM **DEN HERDER**
DIETER **HARTMANN** GABE **KARPATI** PATRICK **MALONE**
JOHN **NOUSEK** WILT **SANDERS** LEISA **TOWNSLEY** DAVID **WEINBERG**

LYNX STUDY OFFICE COSTING & SCHEDULE

ROBBIE **HOLCOMBE**
Lead

TERESA **BROWN** GREGG **GELMIS** SPENCER **HILL**
ANDY **PRINCE** AMBERLY **STAPLER** VIRGINIA **TICKLES**
NASA Marshall Space Flight Center

LYNX INSTRUMENT & OPTICS WORKING GROUP MEMBERS

Instrument Working Group

Mark Bautz
Ryan Allured
Simon Bandler
Douglas Bennett
Akos Bogdan
Casey DeRoo
Michael DiPirro
Benjamin Donovan
Megan Eckart
Abraham Falcone
Enectali Figueroa-Feliciano
Hans Moritz Günther
Ralf Heilmann
Kent Irwin
Ralph Kraft
Benjamin Mates
Dan McCammon
Randy McEntaffer
Drew Miles
Jeffrey Olson
Kevin Ryu
Kazuhiro Sakai
Dan Schwartz
Stephen Smith
Vyshnavi Suntharalingam
Doug Swartz
Daniel Swetz
James Tutt
Joel Ullom
Wonsik Yoon
Ben Zeiger
Thomas Stevenson
James Chervenak

Optics Working Group

Lester Cohen
Mark Schattenburg
Ryan Allured
Carolyn Atkins
Stefano Basso
Wayne Baumgartner
Michael Biskach
Stephen Bongiorno
Jay Bookbinder
David Broadway
Brandon Chalifoux
Kai-Wing Chan
Marta Civitani
Daneile Cocco
Vincenzo Cotroneo
Jaqueline Davis
Casey DeRoo
Manel Errando
Daniel Evans
Abe Falcone
Charly Feldman
Mark Freeman
Terry Gaetz
Mauro Ghigo
Hans Guenther
Danielle Gurgew
Ralf Heilmann
Mourad Idir
Anders Jakobsen
Diab Jerius
Kiranmayee Kilaru
Jeff Kolodziejczak
Vladimir Kradinov
Ralph Kraft
Herman Marshall
James Mazzarella
Ryan McCelland
Steve O'Dell
Takashi Okajima
Howard Padmore
Giovanni Pareschi
Giancarlo Parodi
Kurt Ponsor
Lisa Poyneer
Brian Ramsey
Paul Reid
Raul Riveros
Oliver Roberts
Timo Saha
Timo Saha
Bianca Salmaso
Dan Schwartz
Eric Schwartz
Peter Solly
Harvey Tananbaum
Susan Trolier-McKinstry
James Tutt
Mel Ulmer
Gabriele Vecchi
David Windt
Youwei Yao
William Zhang

Calibration Working Group

Wayne Baumgartner
Larry David
Jeremy Drake
Megan Eckart
Jessica Gaskin
Dale Graessle
Diab Jerius
Jeff Kegely
Ralph Kraft
Paul Plucinsky
Dan Schwartz
Doug Swartz

LAYOUT, ARTWORK, & BRANDING

Report Manager
Jared Austin

Report Layout
Jennie Mitchell, Jared Austin, Alexey Vikhlinin, Jessica Gaskin, Karen Gelmis, & Grant Tremblay

Technical Writing Support
Jared Austin, Troy Farsoun, Kay Glover, & Eric Mandel

***Lynx* Communications Working Group**
Samantha Johnson, **David Pooley**, Terri Brandt, Megan Donahue, Antonella Fruscione, Jessica Gaskin, Karen Gelmis, Bernard Kelly, Rodolfo Montez, & Grant Tremblay

***Lynx* Branding & Graphic Design Lead**
Grant Tremblay

***Lynx* Wordmark Design**
Tanya Borman-Voit | Design Five Seven

Artwork & Graphic Contributors
Seán Doran, Niko Maisuradze, David O. Miller, Jennie Mitchell, Michael Tremmel, & Evan Schneider

Credits for additional artwork used on our website and promotional materials can be found at
WWW.LYNXOBSERVATORY.ORG / CREDITS

X-RAY OBSERVATORY
LYNX
WWW.HIDDENCOSMOS.ORG

ACKNOWLEDGMENTS & THANKS

Lynx, our vision for a new epoch of discovery, is the joint achievement of a large international community whose expertise spans the disciplines of physics, astrophysics, optics, and aerospace engineering. This concept study has involved thousands of hours of community effort to provide scientific insight and engineering design solutions that exceed the most rigorous standards.

Lynx is possible only because NASA continues to encourage bold dreams, assiduously planning for discoveries that will be made by future generations. *Lynx* is one of four Large Mission Concept Studies funded by NASA for the 2020 Decadal Survey. The *Lynx* Team appreciates the opportunity afforded by NASA to design a reference mission concept for a New Great Observatory, alongside our friends and colleagues on the *LUVOIR*, *HabEx*, and *Origins Space Telescope* teams.

The history of NASA astrophysics has shown that Large Missions become something more than a pursuit of important but defined science goals: they become discovery platforms for the questions we have not yet thought to ask. To that end, we are honored to present our vision of a revolutionary X-ray observatory that will accelerate the expansion of discovery.


WWW.LYNXOBSERVATORY.ORG